SERC

CENTRAL LASER FACILITY ANNUAL REPORT 1992

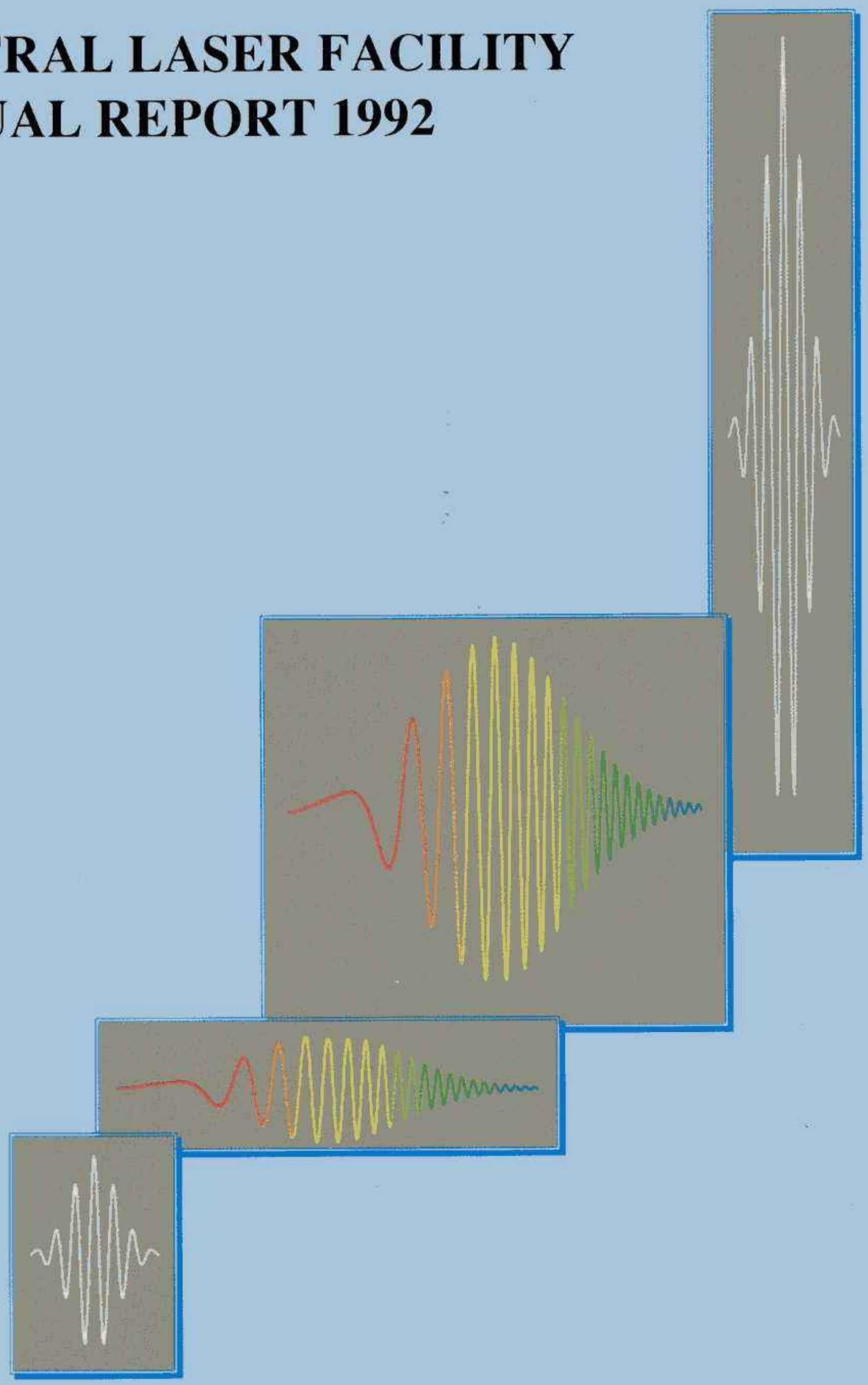

RUTHERFORD APPLETON LABORATORY

ANNUAL REPORT TO THE LASER FACILITY COMMITTEE 1992

5 April 1991 to 4 April 1992

SERC CENTRAL LASER FACILITY
RUTHERFORD APPLETON LABORATORY
CHILTON
DIDCOT
OXON
OX11 0QX

Telephone 0235 821900
Telefax 0235 445888

Rutherford Appleton Laboratory Report RAL-92-020

Cover design representing chirped pulse amplification and compression used for generating ultra-bright laser beams.

ACNOWLEDGEMENTS

It is a pleasure to acknowledge the skilled work of the team who have produced this report. Particular thanks are due to Chris Ayling and Katharine Higgs in connection with the production of text, and to Nic Allen and Chris Reason for the organisation of production.

Chapter and Section editing was undertaken by Colin Danson, Abdeslem Djaoui, Chris Edwards, Graeme Hirst, Chris Hooker, Andy Kidd, Andrew Langley, Peter Norreys, Tony Parker, Chris Reason, Ian Ross, Mick Shaw, Phil Taday, Sue Tavender, Bill Toner and Mike Towrie.

Once again, the camera-ready format has been very helpful to the production team and much of the material has been prepared by Facility users in their own Institutes and they too deserve many thanks particularly for, in some cases, meeting very tight deadlines for reports on experiments close to the end of the reporting year.

The document has been produced by RAL Reprographics service with the assistance of Swindon Press for the printing of the cover. Winner of the cover design competition was Professor Chang Zenghu and his representation of CPA laser operation was produced using Word for windows software with the assistance of Nic Allen and Chris Reason.

M H Key

PREFACE

M H Key
Head of the Central Laser Facility

At the end of the year to 31 March 1992, I am pleased to be able to observe that the problems and uncertainties highlighted in my comments at this time last year have been resolved. A productive year's work has been accomplished. The SERC wide ban on recruitment which was causing attrition of our staff has been lifted and our course for the mid term has been clarified.

An important aspect of the new plans arose from extensive consultation with the University user community of the high power lasers Vulcan and Sprite. An enthusiastic consensus was established to emphasise the development of the lasers for the generation of ultra-high brightness beams with both the glass and KrF facilities. Plans to this effect were proposed to the Science Board and late in the year were approved for funding through a novel mechanism linking participating University groups from Southampton, St Andrews and Imperial College in a joint project with CLF staff. The emphasis is on the short-term provision of new capabilities exploiting to the maximum degree the existing facilities.

In the next one to two years the ultra-bright KrF laser pumped Raman beams on the Sprite facility will be enhanced to provide two-beam operation at power approaching 2 TW in 10 ps. Pulses as short as 100 femtoseconds of energy more than 1 Joule will be generated in a single beam from the KrF amplifiers. The glass laser facility will be provided with generation, preamplification and target irradiation equipment for operation by Chirped Pulse Amplification and Compression to give powers up to 50 TW in 1 picosecond in a single beam. On a 4-year timescale a new larger aperture KrF amplifier will be constructed and incorporated into the Sprite system and the new configuration (Titania) will provide 4 Raman beams of exceptional brightness and power up to 20 TW in 10 ps.

Use of the high power laser facilities during the year has been vigorous with some 2,500 high power laser shots provided for experimenters. The Sprite facility has been brought to a fully operational status alongside Vulcan. In total 17 experimental campaigns were completed. One of these was the first by a European team, from Pisa in Italy, financed through Brussels as a pilot project in the CEC's Large Facilities Programme.

Among many notable scientific achievements it is a pleasure to draw attention to the first demonstration of saturated and near-diffraction limited operation of an XUV laser at 23 nm and the exploitation of the beam for high resolution microscopy and preliminary studies of coherence leading towards its deployment in holography. Studies of the transport of Planckian XUV radiation in low Z materials, which are of great interest in the context of laser fusion, have been pursued vigorously with some excellent experimental results and theoretical analyses. Important changes have been observed in the nonlinear interactions of intense laser beams with preformed plasmas using a variety of beam smoothing techniques relevant to laser fusion. Radiographic studies have included new high resolution XUV probing of inhomogeneities in laser-produced plasmas and α-particle radiography to study hydrodynamic instability. The recent availability of Sprite, as a scheduled user facility, has seen the first substantial X-ray laser experiments exploiting the Raman beam as well as significant investigations of the production of ultra-dense plasmas by exceptionally prepulse free irradiation of solids. Theoretical work has been intensive amongst groups with a close interest in the experimental programme and there has been particular progress in the modelling of X-ray lasers and in the development of atomic and radiation physics theory applicable to radiation transport studies. Substantial advances were made towards the provision of the CPA mode of operation of Vulcan as well as towards both ultra-short pulses and better quality Raman beams on Sprite and the X-ray laser programme will shortly benefit from work done to set up a two plasma generator/amplifier configuration exploiting all eight beams of Vulcan.

The work of the Laser Support Facility has been notable for its breadth as evidenced by the technical reports from 34 user groups working in different fields of chemistry, biology and physics. Users have access to both picosecond and nanosecond lasers at RAL of which there are more than seven configurations available as well as to eight different laser systems and ancillary equipment through the loan pool.

Particular progress has been made this year in bringing picosecond Raman spectroscopy of transient states to the point where spectra can be acquired with run times as short as two seconds for determinations of kinetic data for example from trans-stilbene and caratenoids. The nanosecond studies by Raman spectroscopy have produced extensive results including the first Raman spectrum of solvated Buckminsterfullerene and the first direct observation of the separation of geminate ion pairs. In biology the Raman technique has yielded detailed information on the behaviour of a single base in an oligonucleotide chain. Physics results have included the first experimental determination of the phase boundary of solidification of a 2D electron fluid in a Gallium Arsenide hetero junction.

The user community of the Laser Support Facility has begun this year a review of its future programme and it is hoped to complete this process in the course of 1992 leading to definition, in particular of the future specification of picosecond and femtosecond laser systems for the LSF and also of the more general future development of the Facility.

The most solid record of the achievements of the scientific users of the CLF is contained in the publications listed in the Appendix to this report, of which there are cited more than 140 in the refereed literature. My thanks are due to the Facility users for their continuing support of the Facility, for their dedication and enthusiasm in their different branches of research and for their considerable achievements recorded in this report.

The staff of the CLF have succeeded through this year in sustaining the operation and development of the facilities despite the attrition of their numbers through the recruitment ban and have contributed particularly to formulating the technical plans for the future and carrying out the development of the facilities.

In conclusion, it has been a good year which has set definite goals for the mid-term. This will provide both a stimulus and scientific opportunities for Facility users and staff.

ORGANISATION AND MANAGEMENT OF THE CENTRAL LASER FACILITY

W T Toner

The Central Laser Facility (CLF) is funded by the Science Board of the Science and Engineering Research Council and the programme is managed by the Laser Facility Committee (LFC) chaired by Professor R J Donovan FRSE. The LFC delegates responsibility to the Director of the Rutherford Appleton Laboratory for the operations of the facility.

The expenditure of the CLF for the period covered by this report, April 1991 to March 1992 was £3.6M. Fifty three man years of effort were used and the staff costs and overheads amounted to 55% of the allocation. The resources were divided between the three programmes of the Facility as shown in Figure 1, where users' travel and subsistence and provision for administration have been aggregated into the technical programme costs.

The major facilities provided by the CLF and their principal scientific applications are listed in Table 1. The Nd Glass Laser VULCAN is the main facility for experiments using high-power lasers by UK user groups and their overseas collaborators. Developments during the year include the first trials of CPA operation made in collaboration with a University laser group. The results of this work are contained in Section A of this report.

The KrF laser, SPRITE, is now regularly scheduled for plasma experiments and for development trials of new methods of short pulse amplification and the production of high brightness beams. The development and testing of pulsed power modules for the next generation of KrF lasers has continued. The work on KrF laser development and experiments is reported in Section B.

The Laser Support Facility provides small lasers and a laser-plasma X-ray source and covers all areas of research supported by the Science Board. The experiments are frequently multi-disciplinary in character. Some work is partially supported through the Eureka programme. Results from the programme of the LSF make up Section C of this report.

An engineering support group including a target preparation service, a small group giving theoretical support by maintaining computer codes and a laser R&D group service all CLF activities. Figure 2 shows the divisional and group structure of the CLF in the year up to 31st March.

Use of the CLF by UK research workers in Higher Education Institutes (HEI's) is free of charge to those successful in a peer review process. The cost of travel to the facility and some incidental costs of the research are borne by the CLF out of its allocation from the Board. The costs of research assistants and expenditure in HEI laboratories may be sought by application to the SERC for a research grant. The Laser Facility Committee funds users wholly or mainly using the CLF and the subject committees of the Science Board also award grants to users of the Facility.

Grant holders may bid for time on the facilities of the CLF by application to one of the two selection panels: the High Power Laser Panel chaired by Dr T A Hall and the Laser Support Facility Panel chaired by Professor D Phillips. The panels meet three times a year to determine the relative priority of the bids for time in a specific four month schedule period. A small proportion of the time may be allocated by the Panels to applicants without grant support. Following the recommendation of the Panels as to priority, and taking account of logistical factors, schedules are prepared by CLF staff which are then discussed, modified as necessary and approved by open committees of facility users.

The SERC encourages use of the CLF by industry or other organisations on the basis of payment for the full costs of laser time. Such use is limited to 10% of available laser time.

International collaboration in the research programme is extensive through collaborative participation in approved experiments of UK University groups and through agreements negotiated with the CLF and SERC. Funds from the European Commission were granted during the year for a pilot experiment giving access to the VULCAN facility for an experimental study of laser plasma interactions by research workers from Pisa, Italy in collaboration with the Imperial College group which is currently in progress.

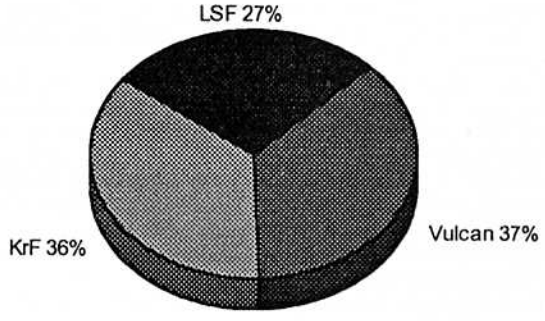

Figure 1 Breakdown of Science Board allocation by programmes.

TABLE 1: Major Programmes at the CLF

Nd Glass Laser Facility	Laser Support Facility	High Power KrF Lasers
Laser plasma interactions and energy transport	Photochemistry, Photobiology, Nonlinear Optics	Research and development in Raman beam combining and novel architectures for high power lasers.
Shocks in solids		Research and development in large scale KrF amplifiers
Laser compression of matter and dense plasmas	High field atomic physics Laser Loan Pool Raman facility	Short pulse laser-plasma interaction studies
XUV lasers and applications of laser produced plasma sources	Picosecond laser High repetition rate X-ray source	
Engineering Service Laser R&D Service Theoretical Support Service		

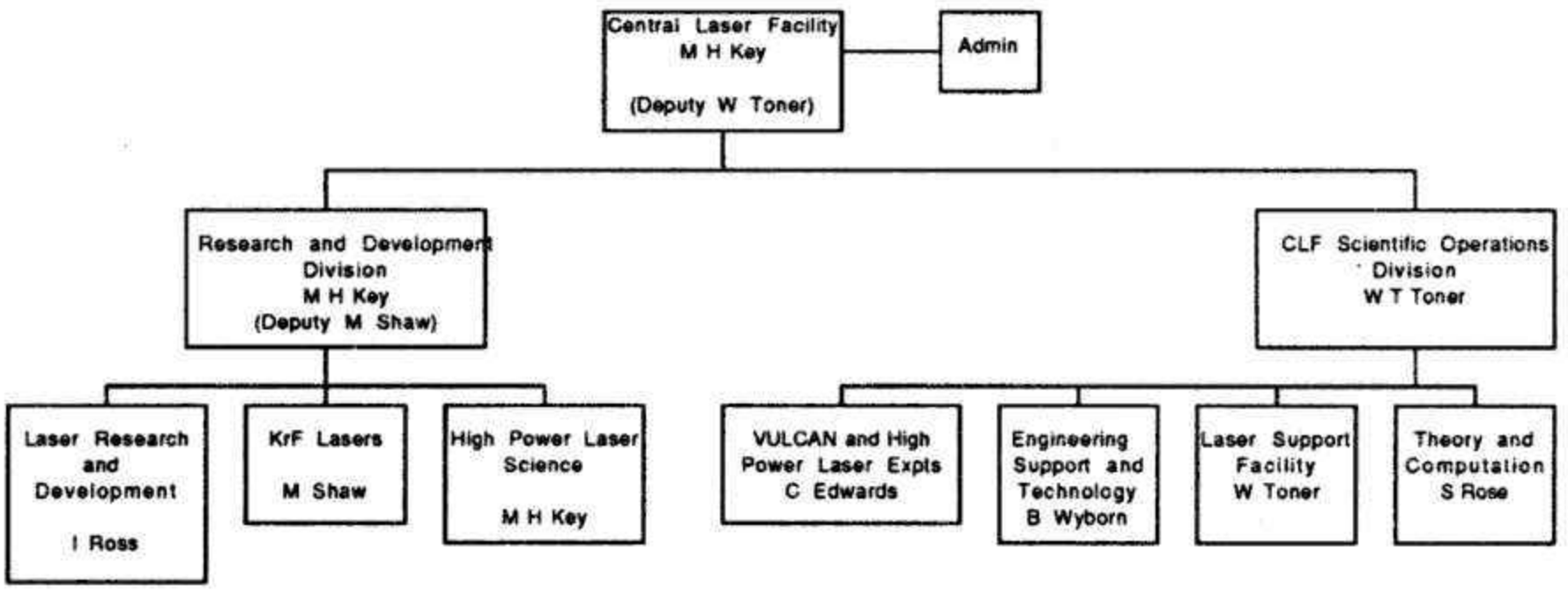

VULCAN PROGRAMME (W Toner) .....

KrF PROGRAMME (M Key, Dep M Shaw) .....

LASER SUPPORT FACILITY (W Toner) .....

ADMINISTRATION PROGRAMME (M Key, Dep N Allen) .....

Figure 2: Divisional and Group Structure of the Central Laser Facility and Programme Management

SATURATED AND NEAR-DIFFRACTION LIMITED OPERATION OF A Ge XXIII LASER AT 23.6 nm

A Carillon[7], H Z Chen[8], P Dhez[7], L Dwivedi[4], J Jacoby[8], P Jaegle[7], G Jamelot[7], Jie Zhang[2], M H Key[1,2], A Kidd[1], A Klisnick[7] R Kodama[8], J Krishnan[4], C L S Lewis[6], D Neely[6], P Norreys[1], D O'Neill[6], G J Pert[3], S A Ramsden[3,5], J P Raucourt[7], G J Tallents[4], J Uhomoibhi[6]

[1] Central Laser Facility, SERC Rutherford Appleton Laboratory, UK
[2] Clarendon Laboratory, University of Oxford, Oxford, OX1 3EU, UK
[3] Department of Physics, University of York, York YO1 5DD, UK
[4] Department of Physics, University of Essex, Colchester, CO4 3SQ, UK
[5] Department of Physics, University of Hull, Hull, HU6 7RX, UK
[6] Department of Pure and Applied Physics, Queens University of Belfast, Belfast, BT7 1NN, UK
[7] LSAI, Universite de Paris-Sud, Bat 350, 91405 Orsay, France
[8] Scientific Visitor at the Central Laser Facility and University of Oxford

The Ge XXIII laser has been successfully operated in several laboratories now using 1.05 μm neodymium glass laser drivers and solid slab targets. It has the highest reported efficiency of producing gain with gl/P up to 70 TW^{-1}. [1]

In our earlier work we measured the gain and both time and angularly resolved spectra from the Ge laser[2], then studied in detail the gain as a function of irradiance[3]. This initial work used three beams of the six beam Vulcan Nd:glass laser.

Deploying the additional three beams 180° opposed in another line focus enabled a double plasma experiment with compensation for refractive deviation of the beam. 200 fold enhancement of the emission from a 22 mm long source plasma was demonstrated with an additional 14 mm amplifying plasma[4].

We now report the use of this double plasma configuration with an XUV mirror to double-pass the double plasma. This increases the gain length to the level required for saturation of amplification and reduces the Fresnel number to a value less than unity giving conditions for near diffraction limited operation. The mirror increased the laser output by a factor of typically 30x which is much larger than has been observed in previously reported experiments with XUV mirrors and similar to recent observations in a collaborative experiment at Osaka University[5].

The mirror was a Mo/Si multilayer with a measured reflectivity at 23.6 nm of 28%[6]. It was concave with a radius of curvature of 13 cm and was positioned 2 cm from the 22 mm plasma, which in turn was separated 0.6 mm axially from the 14 mm plasma. The targets were evaporated stripes of germanium on glass substrates. They were in a pre-adjusted assembly with a lateral separation of 200 μm ± 10 mm (determined from previous work to give the best coupling between the two plasmas)(4). The mirror was also pre-aligned to the axis of the X-ray laser which was shown from previous measurements(4) to be shifted by refraction by 10 mrad from the plane of the target surface. The line foci were placed on the germanium stripes with ±15 mm and ± 1 mrad accuracy.

Three beams produced the 22 mm long line focus. Their 18 mm line foci were displaced axially to form a line focus up to 26 mm long in which a 22 mm long and 120 μm wide Ge stripe target was placed. The other three beams had 18 mm line foci superimposed to irradiate a 14 mm long 160 μm wide Ge stripe target. The intensity in the line foci was $2.3 \pm 0.5 \times 10^{13}$ W cm^{-2} and the 1.05 μm laser pulses were of duration 0.5 ns.

A flat field grazing incidence XUV spectrometer with a 1200 line/mm grating recorded the axial spectrum[2].

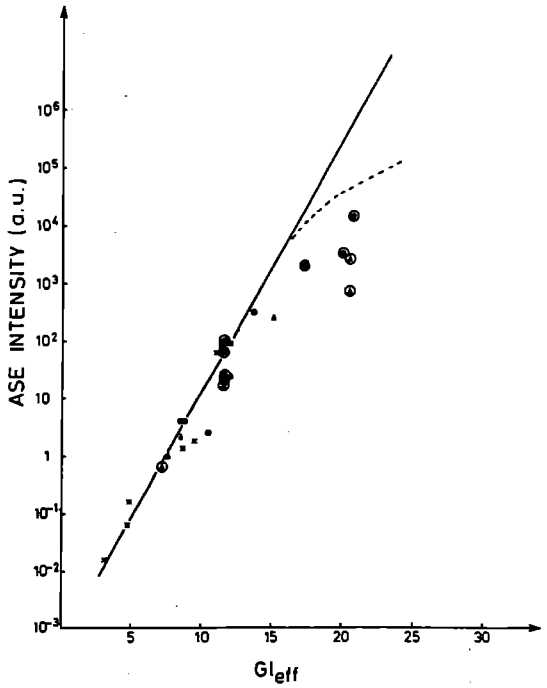

Fig 1 The peak ASE intensity in arbitrary units vs effective gain length Gl_{eff}. Solid circles are from time resolved spectra. Triangles are from time resolved angular distribution of emission. Those shots with mirrors are circled. Crosses are from our previous experiment[2]. The solid line shows intensity proportional to exp (Gl_{eff}) and the broken line shows our model calculations of the effect of saturation.

Overlap of higher orders was eliminated by use of two parallel Au mirrors at 8° grazing incidence which cut out radiation at wavelengths < 5 nm. The mirrors were located behind the 80 μm wide entrance slit of the spectrometer and the slit was 15 cm from the end of the plasma. Variable attenuation up to x 10^5 was obtained with aluminium filters. A KAP crystal spectrometer recorded the X-ray resonance spectra of Ge XXIII with spatial resolution along the plasma[3]. The uniformity of the irradiation along the line focus was optimised by observation of the ratio of the neon-like to fluorine-like spectral lines[3].

Axial spectra were recorded in three ways. Time averaged spectra with angular resolution were obtained using Kodak 101 XUV film in the focal plane. Time resolved spectra were obtained by placing an XUV streak camera slit across the spectrum at the angular peak of emission. In addition, a novel observation was made in which the 23.6 nm spectral line was aligned along the slit of the streak camera so that the streak displayed the temporal

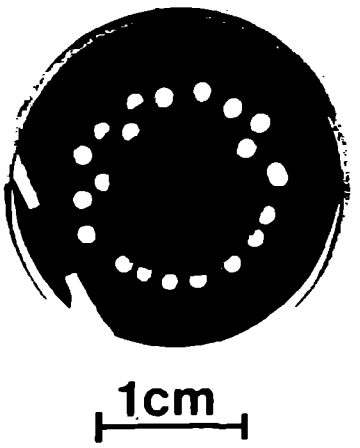

Fig 2 Photograph of the XUV mirror after use showing damaged regions similar in size to the protection aperture.

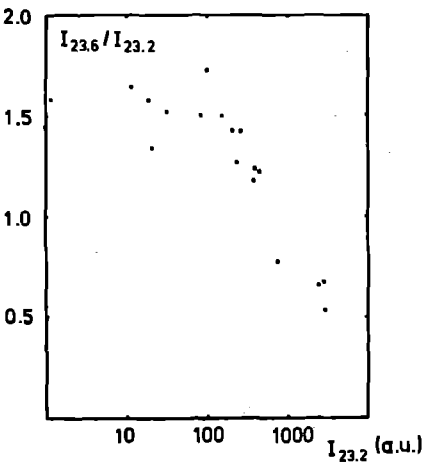

Fig 3 Ratio of intensity I_{236}:I_{232} against intensity of I_{232} (in arbitrary unit).

variation of the angular distribution of the emission, see Section A1.2 ibid.

Time resolved spectra were obtained for single plasmas of 22 mm length with and without the mirror and for double plasmas (22 + 5 mm, 22 + 9 mm and 22 + 14 mm) with and without the mirror. Relative intensities were obtained by densitometry of streak records as in our previous work [3]. The intensity data are plotted in Fig 1 against the effective gain length gl of the system. For the single target plasmas, the effective gl is simply the length multiplied by the gain coefficient 4 ± 0.5 cm^{-1}. The gain coefficient was determined from the exponential form and fitted slope of the unsaturated data with $gl \leq 12$ in Fig 1. Data from our previous study [2] of gain in a single plasma are also included in Fig 1 to show the similarity of their exponential growth of intensity. Intensities are shown with an arbitrary normalising factor to match the two sets of data.

The unsaturated single plasma results with the mirror were used to determine the effective feedback fraction from the mirror into the plasma by matching outputs with a mirror to those without mirrors. With the mirror and a single plasma of length l_1 the effective gl was $2gl_1 + \ln\eta$ where η is the feedback fraction from the mirror. From the typically 30-fold increase in output brightness for the 22 mm plasmas obtained by adding the mirror it was established that the effective feedback from the mirror was $\eta = 1.7\ (\pm^{1}_{0.7}) \times 10^{-2}$. This is significantly less than the measured 28% reflectivity[19] of the mirror. A photograph of the mirror used in the work is shown in Fig 2. It was moved from shot to shot and damage spots equal in size to the protective aperture in front of the mirror were produced on every shot. It seems probable that damage during the laser pulse significantly reduced the effective reflectivity in operation from its initial value. The mechanism has not been identified but thermal radiation seems the most probable cause.

A further refinement was to consider the temporal variation of the gain. This was deduced from the time variation of the ASE brightness for the 22 mm plasmas. The proportionality $I(t) \sim \exp(g(t)l)$ was used with the maximum g value being 4 cm^{-1}. The finite transit time of the radiation through the system for the double plasmas and with the mirror was then assessed to determine the slightly reduced effective gain coefficient for the different cases in order to plot effective gl values in Fig 1. This correction was limited to a maximum reduction of time averaged gain to 3.4 cm^{-1} for the longest double plasma and mirror combination.

The data in Fig 1 show an exponential increase for effective gl values less than about 14 above which they roll over into saturated behaviour for effective gl values up to 20.5. We believe this was the first reported unequivocal demonstration of saturation of an XUV laser and of the effective use of a mirror to significantly increase the gain length of the laser[7]. Subsequent work from SIOM in China has shown similar results[8] and saturation of the Se XXV laser has recently been reported from LLNL[9].

Confirmation of the saturated behaviour was obtained first by numerical modelling of the relative intensity of ASE in a homogeneous plasma column with the same length and transverse dimensions of the gain region (100 μm x 60 μm) as used in this experiment[10]. The results in Fig 1 show reasonable consistency between the observed gain saturation and that predicted. The model computes the laser output in units of the saturation intensity and its results have been scaled to fit the experimental data in the unsaturated range of ($gl < 12$) in Fig 1.

The magnitude of the saturation intensity I_s is given by $h\nu/\sigma\tau$, where τ is the gain recovery time and σ the stimulated emission cross-section. $I_s = 1.3 \times 10^{10}$ W cm^{-2} for the 23.6 nm J = 2-1 transition and 2x higher for the 23.2 nm J = 2-1 accompanying transition. This difference is responsible for the change in ratio of intensity 23.6:23.2 nm illustrated in Fig 3. At small gain lengths the 23.6 nm line is about 1.6 times more intense than the 23.2. There is a very slow change in the ratio with exponentiating intensity but a rapid change over the last decade of intensity increase into the saturation region of Fig 1. In the limit of strongly saturated behaviour the 23.2 nm transition is 2 times more intense than the 23.6 as expected for a saturated laser. The behaviour of this line ratio confirms the occurrence of saturation. If roll-over of exponential growth of intensity were due to a loss of gain due to refraction, the effect would be the same for both the J = 2-1 doublet lines. The strongly differential behaviour can only be explained by saturation.

The exit aperture of the gain region was, as discussed previously, approximately 100 μm x 60 μm and this, together with length and mirror curvature establishes a Fresnel number for the system of 0.8. At this Fresnel number the Van Cittert Zernicke theorem predicts that the radiation field at the exit from the system would be approximately single mode in a homogeneous plasma for saturated gain. The optical system is effectively semi-confocal with the focal point of the mirror (focal length L = 6.5 cm) close to the exit end of the second plasma. The beam waist of a confocal mode is of diameter $(\frac{2\lambda L}{\pi})^{1/2}$ which for the present example is 44 μm.

Measurement of the time resolved divergence in the plane of the target normal gave the results shown in Fig 4. For a single plasma of length 22 mm the divergence of 8.8 mrad is about twice that computed for an optically uniform gain medium of 60 μm width and 22 mm length with $gl = 8.4$.

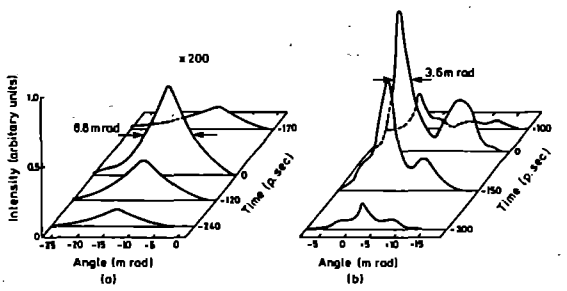

Fig 4 ASE intensity (in arbitrary units) plotted as a function of both angle and time from streak camera data

(a) 22 mm single target without mirror,
(b) double target (22 mm + 14 mm) with mirror.

The double plasma with the mirror shows in Fig 4 a burst of emission (superimposed on a broader background) which is significantly more localised in angle and time with angular width of 3.6×10^{-3} radians and duration 150 psec. This angular divergence is approximately 8x the angular width of an ideal semi-confocal mode implying a circa 5 μm spatial coherence length.

The VCZ theorem for a homogeneous plasma suggests about 2x larger coherence length. The increase of beam divergence above the level expected for an optically uniform medium can be qualitatively understood through refraction producing changes in angle of the order of the observed divergence (3.6 mrad) over a transverse scale of the order of the inferred spectral coherence length (5 μm). Subsequent measurements of the coherence reported in Section A1 have confirmed this conclusion.

The brightness of the source was deduced from time integrated spectra recorded on Kodak 101 film of calibrated sensitivity. The spectral intensities provide a value for the emitted energy per steradian which, with the estimated source aperture of 60 μm x 100 μm, gives a source brightness of 1.2×10^{14} W cm^{-2} sterad^{-1}. The accuracy of this value is limited by the uncertainty in the film calibration, grating reflectivity, and beam divergence in the dispersion plane to within a factor of 4. The output pulse duration was assumed to be 250 psec as observed in the streaked spectra. The peak angularly resolved brightness measured for different lengths of plasma with and without mirrors, is also plotted in Fig 1, with an arbitrary intensity scaling to match the unsaturated data from the time resolved spectra. The additional data give further support to the observation of saturation.

In conclusion we have shown that by use of a double plasma and an XUV mirror, gain saturation has been reached in an XUV laser at 23.6 nm. The system has been operated with a Fresnel number close to unity and the beam divergence is about 8x diffraction limited. The brightness of the source reached values of approximately 1.3×10^{14} W cm^{-2} sterad^{-1}.

REFERENCES

1. M H Key, J Mod Opt 35 575 (1988).

2. D M O'Neill, C L S Lewis, D Neely, J Uhomoibhi, M H Key, A McPhee, G J Tallents, S A Ramsden, A Rogoyski, E A McLean, Opt Comm 75 406 (1990).

3.. D Neely, C L S Lewis, D N O'Neill, J Uhomoibhi, M H Key, S J Rose, G J Tallents, S A Ramsden, Opt Comm 87, 231 (1992).

4. C L S Lewis, D Neely, D M O'Neill, J Uhomibhi, M H Key, Y Al-Hadithi, G J Tallents and S A Ramsden, Opt Comm (in press).

5. Some of us: (C L S Lewis, D Neely, D O'Neill) recently participated in a joint experiment at the University of Osaka, Japan where similarly high enhancement of output from a Ge XXIII laser was observed with a plane mirror half cavity.

6. The mirror was coated by C M Falco, J M Slaughter and D Schulze, Laboratory for X-ray Optics, Opt Sciences Center, Univ of Arizona, Tucson on an ultra smooth substrate machined by Carl Zeiss Ltd. Its reflectivity was measured by M Kühne of Phys Techn Bundesanstalt Inst Berlin, to be 30% at the 24.00 nm spectral peak and 28% at 23.60 nm.

7. C L S Lewis, D M O'Neill, D Neely, J Uhomoibhi, R Burge, G Slark, M Brown, A Michette, P Jaeglé, A Klisnick, L Dwivedi, H Z Shen, M H Key, R Kodama, P Norreys, S J Rose, J Zhang, G J Pert, S A Ramsden,, Ultrashort Wavelength Lasers, Ed S Suckewer, Proc SPIE 1551, 49 (1992).

8. S Wang, Y Gu, S Fen, G Zhou, S Yu, Y Ni, J Wu, G Han, Z Zhou, B Wan, Z Tao, H Peng, J Sheng, T Zhang, Y Shao, G Zhang, Z Lin, S Wang, W Chen, D Fan, Science in China 34 B88, (1991).

9. B J MacGowan, L B DaSilva, D J Fields, C J Keane, J A Koch, R A London, D L Matthews, S Maxon, S Mrowka, A L Ostenheld, J H Scofield, G Shimkaveg, J E Trebes and R S Walling, Phys Fluids (in press).

10. E C Harvey, C J Hooker, M H Key, A K Kidd, J M D Lister, M J Shaw and W Leland, J Appl Phys, 70 5238 (1991).

TIME-RESOLVED MEASUREMENTS OF THE ANGULAR DISTRIBUTION OF LASING AT 23.6 nm IN Ne-LIKE GERMANIUM

R Kodama[1], D Neely[2], L Dwivedi[3], M H Key[1,6], J Krishnan[3], C L S Lewis[2], D O'Neill[2], P Norreys[1], G J Pert[4], S A Ramsden[4,5], G J Tallents[3], J Uhomoibhi[2] and J Zhang[6]

[1]Rutherford Appleton Laboratory
[2]Queens University of Belfast
[3]University of Essex
[4]University of York
[5]University of Hull
[6]University of Oxford

INTRODUCTION

Collisional excitation of Ne and Ni like ions has been successfully exploited to produce XUV laser beams through high gain amplification of spontaneous emission [1]. The X-ray laser media have steep density gradients which can refract the X-ray beam from the region of the amplifying medium. Knowledge of the X-ray beam refraction is therefore crucial to optimising x-ray laser devices and consequently there have been several experimental [2-4] and theoretical [5] studies of the angular distribution of X-ray laser beams.

As a result of the time dependence of the electron density gradient in a laser-produced plasma, the refraction of the X-ray laser beam changes temporally affecting both the beam divergence and pointing direction. Therefore, temporally resolved measurements are necessary to investigate these phenomena [4].

In this paper we present time-resolved measurements of the angular distribution of a soft X-ray Ne-like Ge laser. The time-dependent distribution of the laser output at a wavelength of 23.6 nm produced from a slab target has been recorded.

EXPERIMENTAL SETUP

Experiments were carried out using the VULCAN Nd glass laser system. Laser pulses of 1.06 μm wavelength were focused to lines of 22 mm length x 100 μm width using 3 beams onto germanium (Ge) targets at intensities of 2.3 ± 0.5 x 10^{13} W/cm^2 with off-axis tilted mirrors [6]. Each beam generated 14 mm-long line focii and by displacing these along the axis it was possible to achieve reasonable illumination uniformity for targets of up to 22mm length. The targets consisted of 0.5 μm-thick stripes of Ge of 110±20 μm width. These were deposited on optically flat (λ/4) 1.5 mm-thick glass plates which had been overcoated with a 0.25 μm thick layer of pure hydrocarbon plastic. The pulse shape of the laser, monitored with an optical streak camera was flat topped for 500 psec with a 200 psec rise time. Lasing at 23.6 nm along the plasma line was obtained with a gain-length of 8 and a gain coefficient of 3.5±0.3 cm^{-1} from 22 mm-long targets [2,7].

The time-resolved angular distribution of the X-ray laser was measured by an X-ray streak camera coupled to a flat field grazing-incidence spectrometer as shown in Fig 1. The X-ray spectra were dispersed by a flat field grating of an average 1200 grooves/mm pitch [8]. The variation of intensity along each dispersed spectral line showed the angular distribution of the source [2]. Higher order shorter wavelength X-rays were suppressed using a gold reflection filter [9] and the signal level was controlled with an Al-foil filter. The spectral entrance slit of 75 μm width was oriented perpendicular to the target surface in order to measure the refraction of the X-ray laser in the direction of the plasma expansion. The slit of the streak camera was carefully positioned parallel to and centred on the 23.6 nm lasing line. The streak slit width was set at 800 μm corresponding to a temporal resolution of 20 psec. However, the spectral line width of the lasing transition was less than 50 μm at the streak slit plane and so the temporal resolution is limited by the streak camera operation to ~10 ps. Using a wider streak slit than the line width of the X-ray laser ensures all the lasing radiation is collected, but also means that the background from the continuum emission around the lasing line is recorded. The ratio of the signal to the background level was estimated to be >2 from time integrated data recorded on calibrated KODAK 101-07 film through the streak slit.

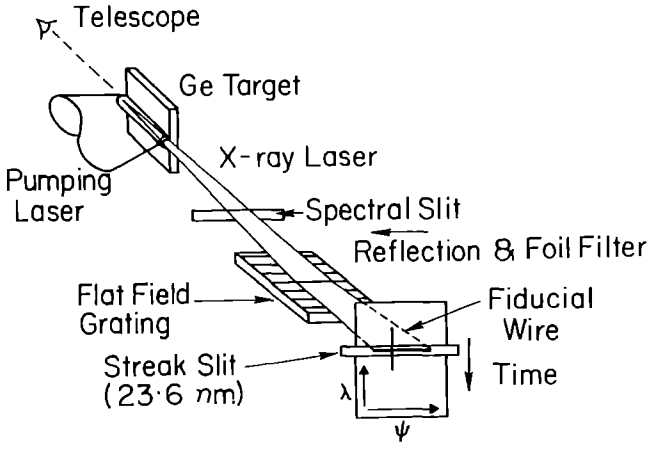

Figure 1
Experimental configuration for temporal-resolved measurements of beam angular distribution. The streak slit is centred on a parallel to the 23.6 nm lasing line.

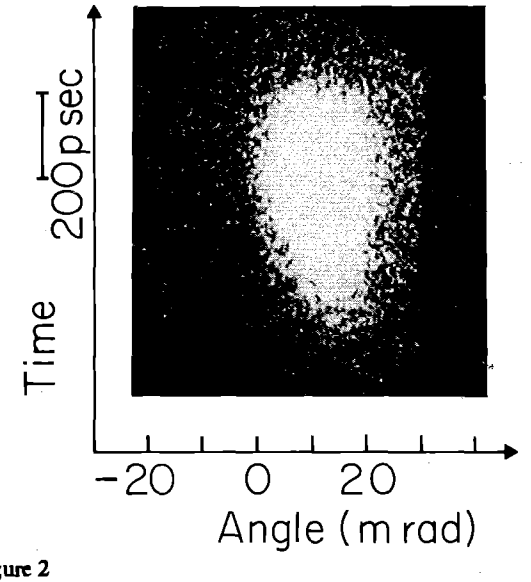

Figure 2
Typical X-ray streak image of the angular distribution with a 22 mm long target.

The angular acceptance range of the system was ±18 mrad. A wire positioned 12 mrad from the plane of the target on the streak camera entrance slit (see Fig 1) was used to provide an absolute pointing fiducial. The angular resolution of the measurements, defined by the size of the source and the distance to the detector, was 0.6±0.2 mrad. A gold photocathode of thickness 200 Å supported on 1 μm Al foil was used for the X-ray steak camera. The streak images were recorded through an image intensified system on individually calibrated ILFORD HP5 film.

RESULTS AND DISCUSSION

Figure 2 presents a typical streak image showing the temporal behaviour of the angular distribution of the 23.6 nm-lasing line with a 22 mm-length target. The sharp cut in the right-hand side of the image is caused by the limited collection angle of the spectrometer. The angle of peak intensity as a function of time is plotted in Fig 3(a) for the data shown in Fig 2. Figure 3(b) shows the temporal history of intensity along the peak intensity of the distribution. Early in time the X-ray laser output peaks at 14.5 mrad to the target surface, then gradually sweeps inwards to 9.5 mrad to the target surface in 500 ps.

The angle of the peak intensity to the target surface is influenced by refraction of the beam in the plasma. The refractive index η of a plasma depends on the free-electron density as $\eta = (1-n_e/n_c)^{1/2}$. Assuming a simple density gradient varying as $n(t) = n_o\,(1-x/L(t))$ where L(t) is the plasma scalelength, the refractive angle θ (t) of the beam is simply described as a function of the scalelength by $\theta(t) \sim A/L(t)$ where A is a constant for small angles and for small indices of refraction. The change of plasma scalelength in the travelling time ($\simeq$ 70 ps) of the ASE pulse can be estimated at ~7μm assuming an ion acoustic velocity of 10^7 cm/s, but is ignored in this approximate treatment. Using $\theta(t) \sim A/L(t)$ we can see that early in time, density gradients are steeper and the X-ray laser would be expected to be refracted more, as is indeed observed.

Figure 4 shows the angular profile changes with time of the figure 2 streak image. Beam profiles at three different times; (a) the X-ray laser peak (0), (b) 220 psec before the peak of the X-ray laser, and (c) 190 psec after the peak are plotted in Fig 4. The beam divergence (FWHM) is 7.8 mrad, 8.8 mrad, and 12 mrad at times -220 psec, 0 psec (the peak intensity) and +190 psec, respectively. An estimate of the time-integrated divergence from -300 psec to +200 psec has been made by adding the time-resolved streak data. A time integrated divergence of 9.8 mrad is obtained which is slightly larger than the divergence at the laser intensity peak. Broadening of the time integrated profile occurs due to the temporal change of the peak intensity in the angular distribution which moves from 14.5 mrad to 10 mrad over 500 psec of X-ray laser emission.

The broadening of the profile by 4 mrad over the 500 psec of X-ray lasing is consistent with the temporal change of the thickness (D) of the effective gain region in plasmas. In the simplest situation, the beam divergence is a function of D/B where B is the length of the laser medium (constant in time). Assuming that the gain linearly changes with electron density in isothermal blow-off plasmas, the thickness of the gain region will vary linearly with the density gradient. In this simple situation, the divergence φ will change temporally as φ (t) ~ D(t)/B~L(t). Therefore a small divergence early in time can be attributed to the steeper density gradient early in time. As we have seen the time-dependent beam pointing is also consistent with the temporal change of the peak intensity of angular distribution ie, there is more refraction early in time due to steeper density gradients early in time. A more detailed discussion of the dependence of the beam divergence and refraction on the gain length will be left to a future publication. In particular, the variations of the plasma scalelength and width changes during the travelling time of the X-ray pulse need to be examined in detail to understand the temporal variation of the x-ray laser output.

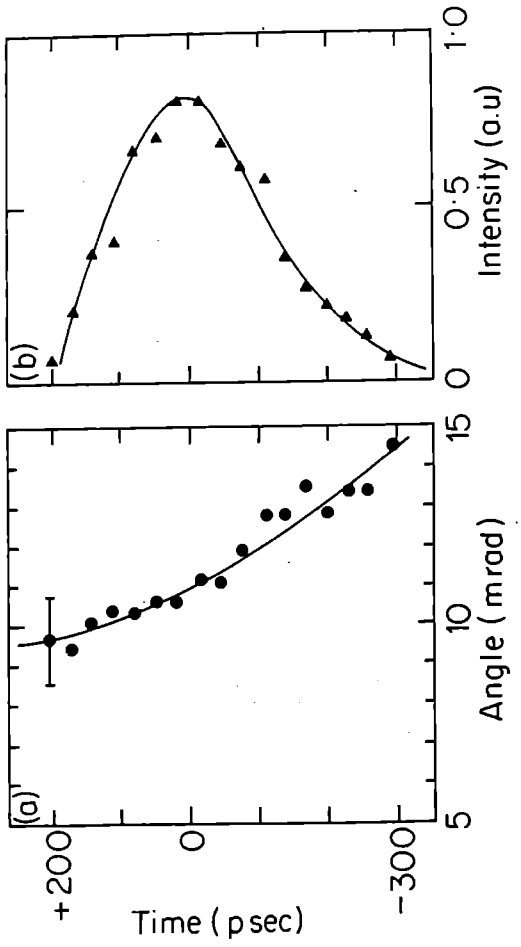

Figure 3
(a) Temporal trajectory of the peak intensity of the angular profile and, (b) angular width of the X-ray intensity. Time zero is at the peak of X-ray intensity.

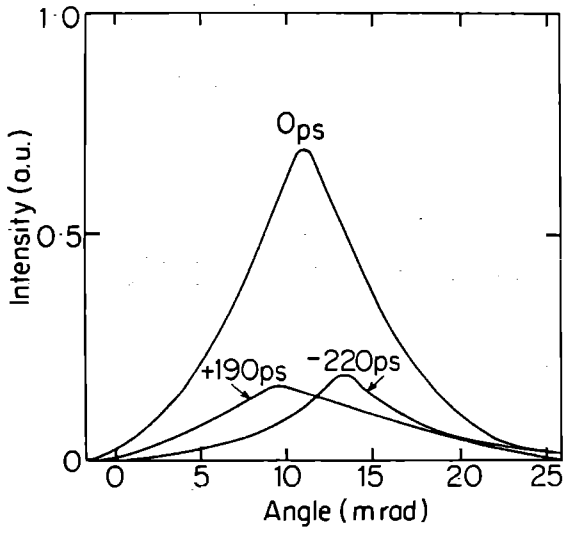

Figure 4
Angular profiles of the 23.6 nm lasing line at various times (a) X-ray laser peak (0 ps), (b) -220 psec before the peak, and (c) +190 psec after the peak.

CONCLUSION

We have presented time-resolved measurements of the angular distribution of a soft X-ray laser output. The angular profile of a 23.6 nm lasing line with a gain length of 8 created from a laser-produced Ne-like Ge plasma has been measured. The angular peak intensity is located at a large angle (14.5 mrad) to the target surface early in time and gradually sweeps to smaller angles (9.5 mrad) more closely parallel to the target surface. The divergence broadens with time from 7.8 mrad to 12 mrad. The change of the peak intensity pointing and the broadening of the angular profile with time have been shown to be consistent with a simple description of the time dependence of refraction and divergence due to density gradients in the plasma.

REFERENCES

[1] D Matthews, E Chandler, L da Silva, D Fields, W Goldstein, C Keane, J Koch, R London, B MacGowan, S Maxon, J Nilsen, A Osterheld, M Rosen, J Scofield, G Shimkaveg, R Stewart and J Trebes, in 'X-ray Lasers 1990', G Tallents, Ed (IOP, Bristol) p205 (1991).

[2] D M O'Neill, C L W C Lewis, D Neely, J Uhomoibhi, M H Key, A MacPhee, G J Tallents, S A Ramsden, A Rogoyski, E A McLean and G J Pert, Optics Comm 75, (1990) 406.

[3] S Suckewer, C H Skinner, D Kim, E Valeo, D Voorhees, and A Wouters, Phys Rev Lett 57, (1986) 1004; T Boehly, R S Craxton, R Epstein, M Russotto and Yaakobi, Optics Comm 79, (1990) 57.

[4] B J MacGowan, S Brown, E M Campbell, M Eckart, P Hagelstein, C Keane, R London, D Matthews, D Nilson, T Phillips, M Rosen, J Scofield, G Shimkaveg, A Simon, R Stewart, J Trebes, D Whelan, B Whitten and J Woodworth, SPIE Proceedings 688 (1986) 36; J L Bourgade, C Reverdin, J Bruneau, M Charet, D Desenne, A Dulieu, H Dumont, M Louis-Jacquet, R Sauneuf and P Troussel, 'X-ray Lasers:1990' Ed G J Tallents (IOP: Bristol) p69.

[5] R A London, Phys Fluids 31, (1988) 184; B Boswell, D Sharts, T Boehly, and B Yaakobi, Phys Fluids b2, (1990) 436.

[6] I N Ross, O Willi, G P Kiehn, R Corbett, C L S Lewis, L P Shorrock, M H Key and C J Hooker, Appl Optics 26, (1987) 1584.

[7] D Neely, C L S Lewis, J Uhomoibhi, D O'Neill, S A Ramsden, M H Key, B Shiwai, N Tragin and G J Tallents, Optics Comm in press.

[8] T Kita, T Harada, N Nakano and H Kuroda, Appl Opt 22, (1983) 512.

[9] C L S Lewis, D Neely and A R Damerell, RAL Annual Report RAL-90-026, (1990), 73 (unpublished).

PRELIMINARY REPORT OF A COHERENCE MEASUREMENT OF THE NE-LIKE GE SOFT X-RAY LASER.

T. Barbie=, P. Bilfort=,D. Carlo=, M. Carter=, S. Mrowka, J. Trebes=, K. Nugent', C. L. S. Lewis*, D. Neely*, D. M. O'Neill*, J. O. Uhomoibhi*, L. Dwivedi", J. Krishnan", G. J. Tallents", G. Jamelot", J. P. Raucourt", M. H. Key+, R. Kodama+, P. Norreys+and S. A. Ramsden#.

= L.L.N.L., University of California, Livermore, CA 94550, U.S.A.
' University of Melbourne, Australia.*
Department of Pure and Applied Physics, Queen's University of Belfast, N.Ireland.
"Department of Physics, University of Essex, Colchester, England.
"Universite de Orsay, Paris, France,
+ Central Laser Facility, SERC Rutherford Appleton Laboratory, Chilton, England.
# Department of Physics, University of Hull, Hull, England.

INTRODUCTION

Taking a hologram requires that the spatial coherence length of the illumination beam at the object plane is of similar size or larger than the object. To access the potential of the Vulcan pumped Ge laser for such applications we carried out a collaborative experiment with the group from L.L.N.L.[1] In this experiment we measured the spatial coherence of our standard Ge target and investigated ways of modifying and improving it. The data analysis is at a preliminary stage, and the following account only outlines the experimental work undertaken. A complete account will be given at a later stage.

EXPERIMENTAL

Six 1.06μm, 110mm diameter beams from the Vulcan glass laser were used in target area east at R.A.L. to illuminate standard Ge slab targets[2]. The pulse length used was ~650ps and the average intensity on target was $2x10^{13}$ Wcm^{-2}. The following target geometries were tested :-

(i) 22mm
(ii) 22+14mm
(iii) 22+14mm bow-tie
(iv) 22mm +mirror
(v) 22+14mm + mirror

Five different mirrors were available. These were:-

(i) Planar
(ii) Concave r= 130mm
(iii) Convex r= 23mm
(iv) Convex r= 11mm
(v) Convex r= 6mm
r = radius of curvature

The coherence of the soft X-ray laser beam was measured using interference from a random slit array. As the coherence of the sampled portion of the beam increases, the interference pattern fringe visibility increases. Figure 1 shows the calculated intensity distribution which would be obtained if the slit array is illuminated by a fully coherent source. The slit array consisted of twenty randomly spaced slits cut into a $1mm^2$ substrate, which was placed ~0.7m from the end of the soft X-ray laser. After propagating through the random slit array the beam traversed a further 4m before being deflected through 123°

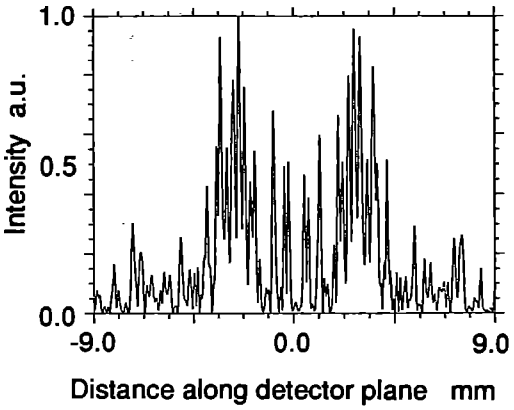

Figure 1 Calculation showing the expected interference pattern generated when the random slit array is illuminated with a fully coherent wave front.

using a 33.5° incidence, multi-layer mirror. The combination of the multi-layer mirror and an Al filter acts to restrict the bandpass of the instrument to ~2nm centered around 23nm. The interference pattern from the slit array was detected using either Kodak 10101 film, for time integrated results, or a Kentec streak camera for time resolved measurements. To measure the vertical and horizontal coherence from a target geometry, it was necessary to first record the horizontal information on one shot, then rotate both the random slit array and the detector through 90° and take another shot.

RESULTS

Figures 2a and b show the temporally resolved interference pattern with the slit array in a vertical orientation, generated from

:- 2a) a single 22mm target.

:- 2b) a 14+22mm target + mirror.

The temporal window displayed is approximately 1ns for both shots. From figures 2a and b we clearly observe an increase in fringe visibility as the gain length product of the plasma is increased from $\alpha L \sim 8$ to $\alpha L > 16$.

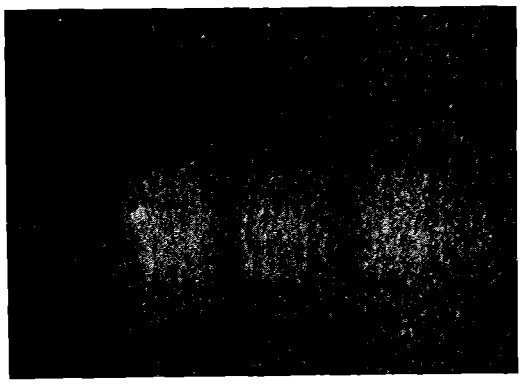

Figure 2a Temporally resolved interference pattern observed from a 22mm Ge slab target.

CONCLUSION

The coherence of the Ne-like Ge slab soft X-ray laser has been studied for a wide range of target geometries. Preliminary indications are that the Ge slab laser is more coherent than the Se exploding foil system of similar gain length product. This could be due to the stronger refractive gradients present in the Ge slab system. Work on theoretically predicting the expected coherence from the Ge slab system is presently underway[3]. The experimental data requires 2-D image processing and considerable analysis. Detailed results will be reported in next years annual report.

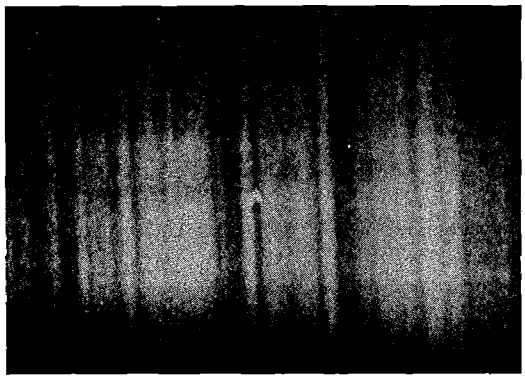

Figure 2b Temporally resolved interference pattern observed from a 22+14mm+ mirrorGe slab double target with d=2.5mm, s=300μm see reference[2] for target geometry.

---

[1] J. E. Trebes, K. A. Nugent, S. Mrowka, R. A. London, T. W. Barbee, M. R. Carter, J. A. Koch, B. J. MacGowan, D. L. Matthews, L. B. Da Silva, G. F. Stone and M. D. Feit, Phys. Rev. Lett 68, 5, (1992) p588-591

[2] C. Lewis, D. M. O'Neill, D. Neely, J.O. Uhomoibhi, R. Burge, G. Slark, M. Brown, A. Michette, P. Jeagle, A. Klisnick, A. Carillon, G. Jamelot, J. P. Raucourt, G. J. Tallents, J. Krishnan, L. Dwivedi, H. Z. Chen, M. H. Key, R. Kodama, P. Norrays, S. J. Rose, J. Zhang, G. J. Pert and S. A. Ramsden, Vol 1551, SPIE, July1991, p49-54

[3] G. J. Pert, M. Lightbody and P. Holden, University of York

DEMONSTRATION OF SUB-MICRON SPATIAL RESOLUTION FOR AN IMAGING MICROSCOPE USING THE COLLISIONALLY EXCITED Ne-LIKE GERMANIUM X-RAY LASER AT 23.6/23.2 nm.

R E Burge, M T Browne, P Charalambous, G E Slark and P J Smith

Physics Department, King's College, Strand, London, WC2R 2LS

INTRODUCTION

X-ray microscopy using synchrotron soft X-ray radiation has now achieved a spatial resolution of about 50 nm.[1] Applications to cell biology using whole wet cells are now being made at this resolution which is intermediate between optical and electron microscopy. Further, using synchrotrons, preliminary experiments in X-ray holography, aimed at the determination of three-dimensional macromolecular biological structure and cell organisation, have been carried out using both in-line[2] and Fourier transform[3] holography.

The X-ray laser brings two potential benefits over the use of synchrotrons. First, a bright field image in a single sub-nanosecond laser pulse, and, second, the use of - the expected - high laser spatial and temporal coherence, plus high X-ray brightness, to produce a hologram in a single pulse, with the possibility of three-dimensional reconstruction; certain limitations to the spatial coherence have not yet been overcome. Concerning the first advantage, the expectation is that specimen structure will be impressed on the in-flight transmitted wave before the processes of biological beam damage have time to react. The timescales are in msec for significant Brownian motion, molecular re-arrangement due to bond cross-linking, thermal damage processes etc.

Collisionally excited Ne-like Ge radiation has been made available to us by the Belfast Group headed by Dr C. Lewis, using the VULCAN X-ray laser at RAL. The radiation is in the form of a doublet with components of about equal intensity at 23.6 nm and 23.2 nm. This very soft radiation (less than 20% transmission through 100 nm protein) provides a means to investigate the physics of imaging and holography with X-ray lasers, in advance of further source development towards higher laser energy, and correspondingly thicker specimens, such as the 4.5 nm wavelength radiation available at the Nova X-ray laser installation.

Our first experiments have been directed towards (a) installing a full-field (imaging) zone plate microscope at the VULCAN laser, (b) evaluating the optical performance of the microscope in terms of the edge resolution of test images recorded on film in a single laser shot.

INSTRUMENTATION

A schematic diagram of the optical system of the microscope is shown in Figure 1. A Schwarzchild condenser produces a laser focus at, or near, the specimen plane, and the final image is focused by a zone plate objective on X-ray film. The entire optical system is under vacuum. There are significant experimental problems involved in the accurate location of the specimen with respect to the condenser focus and the zone plate with respect to the specimen. These have been reduced by, in effect, installing a Michelson interferometer, using white light fringes characterising the optical path difference between, respectively, the rear surfaces of the specimen and of the zone plate, following movement of a plane mirror mounted on an accurate micrometer.

The microscope was designed to have a resolution, as limited by the zone plate objective, of 60 nm. This figure for the resolution defines the necessary numerical apertures of the matching objective and condenser as 0.28. At this aperture, the fabrication procedures for the zone plate, made by the King's College E-beam method of enhanced carbon contamination, have to be corrected for spherical aberration. The corresponding zone plate objective focal length for Ge radiation is 156 μm and the depth of focus is 0.2 μm. The two mirrors of the Schwarzchild condenser were coated with multilayers of Si and Mo and gave normal incidence reflection coefficients of about 3% for Ge radiation. It is estimated that the ratio of the X-ray intensity of the laser irradiation at the

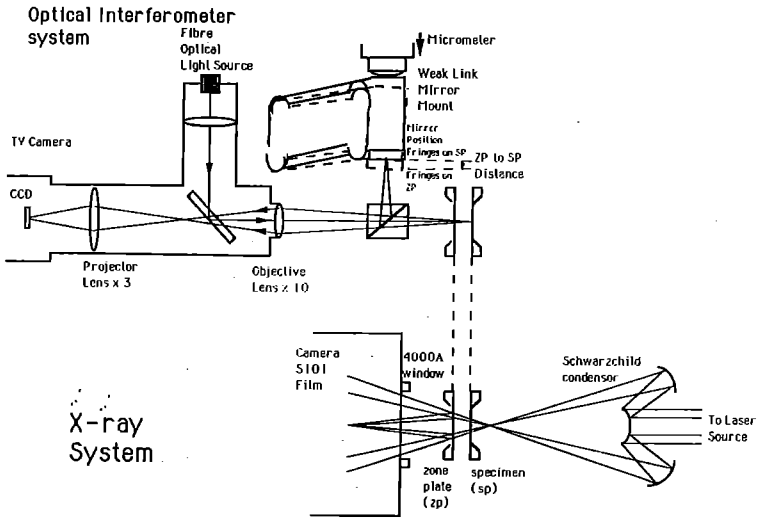

Figure 1 The optical system of the full field X-ray laser microscope

specimen, as compared with background radiation transmitted due to the passband of the multilayer coatings was about 50:1. Further barriers for other radiation to which the photographic film will respond were provided by Al filters.

The specification of a numerical aperture of 0.28 for the condenser produced a focused spot at the specimen only 2 to 3 μm across, which made identification of required specimen regions very difficult in relation to an interval of 20 to 40 minutes between laser shots. Consequently, most images were gained with the specimen displaced by a few μm from the condenser focus to give a larger Hollow cone of illumination due to the annular outer Schwarzchild mirror.

RESULTS

An image taken with a single laser shot on Kodak S101 film is shown in Figure 2, of a test object made in the form of a chequer-board of Au squares, 0.8 μm across with centre to centre separation of 2 μm. The test object was drawn by E-beam lithography on a stable membrane of silicon nitride 50 nm in thickness.

The axial alignment of the optical system is very critical and it was found possible to make creative use of misalignment to separate the two superimposed images, one for each X-ray wavelength. A consequence is that the zone plate aperture is not completely filled with radiation, giving related reduction in resolution, but the sharp edges on the displaced images produced by the misalignment allow a measurement of the lower limit for the point-to-point resolution, which would not otherwise be achievable due to the blurring of the superimposed equal-intensity images from the two wavelengths.

Taking the average width of the edge as measured from the 10% to 90% intensity points gives a resolution value of about 0.15 μm, which is considerably broadened by the large grain size of the photographic emulsion. The measured resolution is twice the expected zone plate resolution. However, the value is significantly sub-micron and consistent with the combined effects of axial displacement of the optical system, the fact that the E-beam edge profile is not infinitely sharp and with photographic broadening.

REFERENCES

1. A.G. Michette, G.R. Morrison & C.J. Buckley, Eds. 'X-ray Microscopy III, Springer-Verlag, Berlin, March 1992.

2. C. Jacobsen, M. Howells, J. Kirz & S. Rothman, Journ. Opt. Soc. Amer. A, 7, 1847-1861, (1990).

3. I. McNulty, J. Kirz, C. Jacobsen, E. Anderson & M.R. Howells. Nucl. Instrum. Math. in Phys. Res. A291, 74-79, (1990).

4. C.J. Keane, N.M. Ceglio, B.J. MacGowan, D.L. Matthews. D.G. Nilson, J.E. Trebes & D.A. Whelan, J. Phus. B; At. Mol. Opt. Phys. 22, 3343-3362, (1989).

Figure 2. X-ray image or Au test object of 0.8 μm wide gold squares. Optical axis displaced to separate independent images of chequer-board images at 23.6 nm and 23.2 nm (seen as chevron patterns). Hollow cone condenser illumination.

COLLABORATIVE WORK AT THE INSTITUTE OF LASER ENGINEERING ON THE NE-LIKE GE XUV LASER SCHEME

D M O'Neill[1], C L S Lewis[1], D Neely[1], Y Kato[2], M Yamanaka[2], H Daido[2], H Shiraga[2], H Azuma[2], K Murai[2], Y Gang[2], E Miura[2], M Ohmi[2], H Takaben[2], T Kanabe[2], M Takagi[2], S Nakai[2].

[1]Department of Pure and Applied Physics, The Queen's University of Belfast, N. Ireland.
[2]Institute of Laser Engineering, Osaka University, Suita, Osaka, 565 Japan.

INTRODUCTION

During February and March 1991, we carried out further studies of the Ne-like Ge collisional excitation scheme[1,2,3] in a very productive collaboration using the GEKKO XII glass laser at the Institute of Laser Engineering, Osaka University. The performance of exploding foil[4] and single/double slab target[5] geometries has been evaluated. In particular, we have examined efficiency of gain production and coherence properties in normal (single pass) and half-cavity (double pass) operation. The planar XUV multilayer mirror used for half-cavity operation had a measured reflectivity of ~ 35% at 23.6 nm and a bandpass halfwidth of ~ 2.5 nm[6].

EXPERIMENTAL DETAILS

The Gekko XII glass laser at ILE, operating at 1.053 μm, delivered ~ 1.10±0.03 kJ per beam to the target plane in a ~ 1 ns (fwhm) Gaussian shaped pulse. The laser beam was focussed to a line of 6 cm length, using a combination of cylindrical and aspherical lenses, resulting in an average irradiation intensity of ~ 1.7 x 10^{13} W/cm^2. The X-ray emission distribution observed with a crossed slit camera imaging at ~ 1 keV indicated that the focal width varied over the length from ~ 50 μm in the narrowest regions, which were separated by ~ 2.8 cm, up to ~ 160 μm at the centre and ~ 180 μm at either end. Target lengths varied from 2 to 5 cm and were always centred in the line focus distribution.

A flat-field grazing incidence spectrometer[7] viewed the plasma axially or at 10 mrad either side of the target axis. The off axis positioning was necessary to intercept the peak signals from slab targets, whose XUV lasing outputs generally emerge in an off axis direction due to refraction effects. In time-integrated mode, spectra were recorded, over ~ 10 mrad field of view, on Kodak 101-01 film. In time resolved mode, the timing slit of the Hamamatsu XUV streak camera was positioned at 10 mrad to the target axis -the time-integrated peak of the lasing output. Streaked spectra were recorded digitally using a cooled CCD array.

A high resolution grazing incidence spectrometer[8] (Hettrick Scientific, model 170.5-25) was used to record time-integrated spectra of lasing and non-lasing lines. The theoretical resolving power of the spectrometer as used was 12000 at 23 nm. A measure of the longitudinal coherence length was deduced from the halfwidth of the lasing lines[4].

Recent measurements of the spatial coherence of the Ne-like Se XUV laser used a uniformly redundant slit array to measure the coherence in one dimension[9]. Here, a pair of pinholes of 40 μm diameter and 100 μm separation were arranged in a two-dimensional periodic array[10] of 10 x 10. The pairs of pinholes were precisely machined by electric discharge on a 50 μm thick substrate at 300 μm intervals in both x and y dimensions. The pinhole array was positioned at 2.34 m from the exit plane of the XUV laser and in close contact with a concave (1.6 m radius of curvature) XUV mirror angled at ~ 20 mrad to the incident beam. The far field image of the pinhole array was recorded at 1.21 m from the mirror on Kodak 101-07 film. The limited mirror bandwidth of ~ 2.5 nm, centred on 23.4 nm, and an Al filter of 0.8 μm thickness ensured that only the 23.2 and 23.6 nm lines were recorded.

Removing the pinhole array and replacing the film with a photoresist, allowed a measurement of the energy of the XUV laser beam to be made.

In addition to these diagnostics, a crystal spectrometer provided information on the ionisation balance of the plasmas produced.

RESULTS

Exponential growth of intensity with length was observed on five spectral lines at 19.6, 23.2, 23.6, 24.7 and 28.6 nm as in previous work. Plasma lengths ≥ 4.5 cm, exhibited a reduction of the observed intensity indicative of near threshold irradiation conditions in the edge regions. Fitting of the time-resolved and time-integrated data to the Linford formula[11] produced gain coefficients on the two strongest J = 2-1 lines at 23.2 and 23.6 nm in the region of 3.0 cm^{-1} for both slab and exploding foil targets. These values were consistent with expectations[3]. No indication of amplification saturation was observed up to the maximum gL value of 13.5±0.9.

Signal intensities at 23.2 and 23.6 nm recorded from 4 cm long single beam irradiated slab targets were ~ 2x those from the double beam irradiated exploding foil targets of similar length indicating that, under these conditions, the slabs are ~ 2x more efficient.

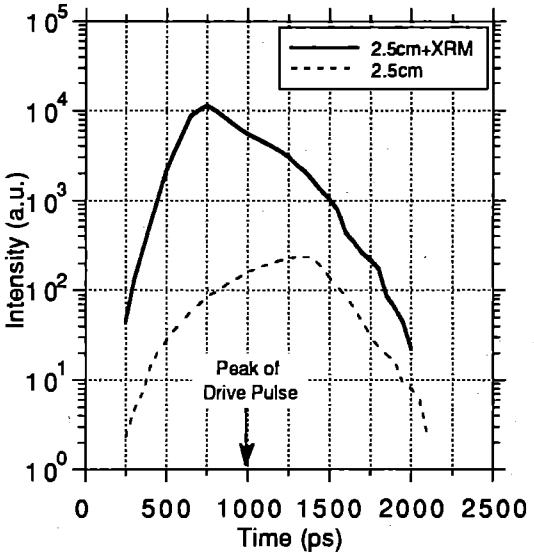

Figure 1 Output at 23.2 nm from 2.5 cm slab target with and without planar XUV mirror.

The time resolved output at 23.2 nm line from a 2.5 cm slab target with and without a planar XUV mirror aligned, shown in figure 1, shows a factor of ~ 100x increase in the rising edge of the pulse. The effect of the mirror is more clearly seen in figure 2 which shows the time dependence of the enhancement factor, calculated by ratioing the signal recorded with the XUV mirror to that without. Since the shot-to-shot timing jitter in the streak camera was $\leq \pm 200$ ps, the factor was calculated with a relative timing shift of dt $\leq \pm 200$ ps introduced between the signals shown in figure 1. For all cases, significant enhancement is observed in the early phases. The subsequent rapid decline of the effect we attribute to the mirror damaging[12]. Nevertheless, the peak intensity values reached are similar to those from a ~ 4 cm long single pass target.

Enhancement factors calculated at late times are subject to large errors due to the low signal levels recorded both with and without the mirror.

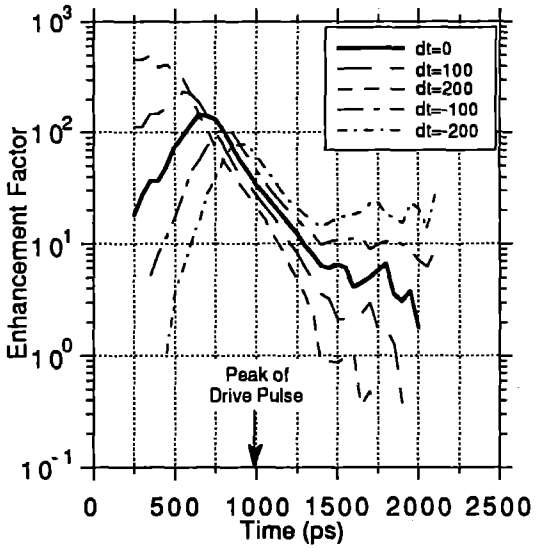

Figure 2 Enhancement of the output at 23.2 nm from a 2.5 cm slab target with an XUV mirror over that from a similar target with no mirror. In order to take account of possible streak camera shot-to-shot jitter, the ratios shown have been calculated with a relative timing shift between the outputs in figure 1 of dt$\leq \pm 200$ ps.

The beam divergence at 23.2 and 23.6 nm decreased from 8.5±2.0 to 5±1 mrad in going from 2 cm to 4 cm lengths. Since the beam direction may change during the laser pulse, the instantaneous beam divergence is probably smaller than these values[13].

Using a concave multilayer mirror, the beams at 23.2 and 23.6 nm were focussed to a ~ 600 μm spot size on PMMA photoresist. The combined energy of the two lines estimated from a single shot onto the photoresist was ~ 0.2 mJ for a 4 cm long target. From the measured temporal fwhm of 690 ps for both lines, we conclude that each line reached a peak power > 0.1 MW.

The spectral widths of the lasing lines, measured for plasma lengths of ~ 4 cm, of $\Delta\lambda_l/\lambda_l = 1.0\pm0.4 \times 10^{-4}$, correspond to a longitudinal coherence length of $\lambda_l^2/\Delta\lambda_l = 210$ μm. The ratio of spectral widths of lasing to non-lasing lines, $\Delta\lambda_l/\Delta\lambda$ was 0.4±0.15. This is slightly larger than the expected value[4] of $1/\sqrt{gL}$ where gL ~ 10. However, with the instrument operating close to its' theoretical limit, the measured spectral widths of the lasing lines could be subject to instrumental broadening.

Analysis of the far field diffraction patterns of the 2-D pinhole array for 4 cm exploding foil plasma lengths produced data consistent with simulations based on a Gaussian source of radius ~ 55 μm[4]. This corresponds to spatial coherence of ~ 160 μm at 2.34 m.

REFERENCES

[1] T N Lee et al Phys Rev Lett **54** 1584 (1987)
[2] D M O'Neill et al Opt Comm **75** 406 (1990)
[3] D Neely et al Opt Comm **87** 231 (1992)
[4] Y Kato et al in preparation
[5] C L S Lewis et al Opt Comm (1992) in press
[6] The Mo-Si multilayer mirrors used in this experiment were fabricated at Canon Research Centre of Canon Inc.
[7] T Harada and T Kita Appl Opt **19** 3987 (1988)
[8] M C Hettrick et al Appl. Opt. **27** 200 (1988)
[9] J E Trebes et al LLNL ICF Quarterly Report UCRL-LR-105821-91-2, Jan-Mar 1991 p72
[10] B J Thompson J Opt Soc Am **56** 1157 (1966)
[11] G J Linford et al Appl Opt **13** 395 (1974)
[12] C L S Lewis et al in preparation
[13] R Kodama et al Opt Comm (1992) in press

OBSERVATIONS OF LASING ACTION FROM Ne-LIKE Se SLAB TARGETS.

D. Neely*, C. L. S. Lewis*, D. M. O'Neill*, J. O. Uhomoibhi*, L. Dwivedi", J. Krishnan",
G. J. Tallents", M. H. Key+, R. Kodama+, P. Norreys+ and S. A. Ramsden#.

* Department of Pure and Applied Physics, Queen's University of Belfast, N.Ireland.
"Department of Physics, University of Essex, Colchester, England.
+ Central Laser Facility, SERC Rutherford Appleton Laboratory, Chilton, England.
# Department of Physics, University of Hull, Hull, England.

INTRODUCTION

Lasing action on Ne-like Ge (Z=32) 3p-3s transitions from 1.06μm driven slab targets has been extensively investigated at R.A.L.[1]. Gain length products of $\alpha L > 16$ have been achieved using a double target and half cavity geometry[2]. Extrapolation of this scheme to shorter wavelengths, using selenium (Z=34) as the target material was investigated during Oct-Nov91. Gain production efficiencies E_g (the gain length product achieved, divided by the driving laser power required) on the two dominant J=2-1 20.6 and 21.0nm transitions at a target irradiance of $1.9 \pm 0.3 \times 10^{13}$ Wcm^{-2} are $E_g \sim 15$ TW^{-1}. This is about 2/3 of that achieved using Ge targets at similar intensity, and is encouraging in terms of further isoelectronic scaling of this system at R.A.L.

EXPERIMENTAL

This experiment was carried out in target area east of the Vulcan glass laser facility. Three 1.06μm laser beams were used to illuminate 100 $\pm$ 10μm wide Se slab targets of effective lengths 6.5$\pm$0.5mm, 13.7 $\pm$0.5mm and 22.0 $\pm$ 0.5mm. An overhead KAP crystal spectrometer looking in the 0.9 - 1.05nm region was used to monitor the F to Ne 3s - 2p resonance line ratio and also to measure the target lengths.

The split field alignment system[3] was set up for 22mm long targets and was not readily usable for shorter lengths. Instead, we masked the unwanted portion of the 22mm Se stripes with a pure CH plastic and shot as normal. This resulted in coaxial Se and CH plasmas being formed along the line focus. The emission from the carbon in the plastic mask contaminates the axial spectrometer Se data. However, in the spectral region of interest only the carbon Balmer α 18.2nm line is sufficiently intense to be observable.

A flat-field 1200 l/mm grazing incidence axial spectrometer operated with a 75 $\pm$ 5 μm wide entrance slit was used to record the lasing emission's angular intensity distribution on Kodak 10101 film. The spectrometer had a $\pm$ 21mrad field of view in the horizontal plane around the chamber axis. To attenuate unwanted 9-17nm emission a 0.4 $\pm$ 0.1μm thick Al foil transmission filter was used for all shots. The laser drive pulse was 650 $\pm$ 50ps long, and the average target irradiance at which the targets were shot was $1.9 \pm 0.3 \times 10^{13}$ Wcm^{-2}.

THE ANAMALOUS SCALING BEHAVIOUR OF 18.2NM EMISSION

Densitometer traces of the flat-field spectra covering the 17-27nm spectral range taken at 15mrad from the axis obtained on the three Se slab targets shot are shown on *figure 1*. The non-linear growth of five transition at 18.2, 20.6, 21.0, 22.0 and 26.3nm are clearly observable. The transitions at 20.6, 21.0, 22.0 and 26.3nm all increase exponentially as the target length is increased. The 18.2nm emission increases as the target length is decreased. The emission at 18.2nm is composed of at least two elements. There is a J=0-1 Ne-like Se line at 18.244nm and a hydrogenic carbon Balmer α emission line at 18.217nm, as shown on *figure2*. When the J=0-1 A transition (see table 1 for line designation) is dominant it can clearly be observed as a narrow feature lying to the long wavelength side of this emission. As the J=0-1 line becomes weaker it blends in with the Carbon emission and can not be readily resolved. The lengths of all the substrates shot were constant but, as the Se stripe's length decreased, the mask's length increased. Thus, at

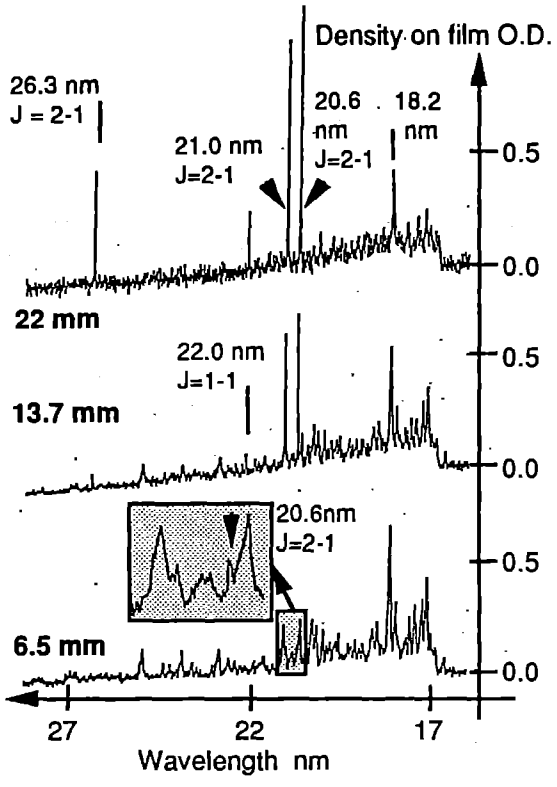

Figure1 Densitometer traces from Se slab targets showing the observed non linear growth with target length of five transitions.

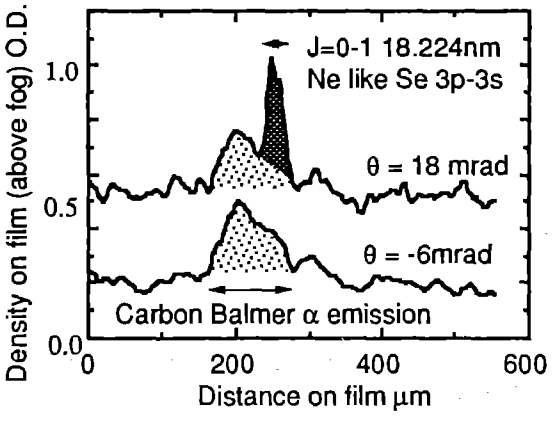

Figure 2 Densitometer traces showing blending of the J=0-1 Se 18.244nm 3p-3s emission, and carbon Balmer α 18.217nm emission.

shorter Se target lengths the C emission, which is almost linearly dependent on the mask's length, becomes brighter explaining the 'strange' behavior of the 18.2nm emission.

ANGULAR DISTRIBUTION AND POINTING DIRECTION OF THE LASING BEAMS

The angularly dependent spectrally integrated output intensities I(θ) from the J=2-1 20.6, 21.0 and 26.3 nm lines and the J=1-1 22.0nm line from target lengths of 22 and 13.7mm were measured. At the shorter target length of 6.5mm it was only possible to uniquely identify and measure I_{Max} of the J=2-1 20.6nm line. All the other lines were either too faint too be detectable or, as in the case of the J=2-1 21.0nm line, were overlapped with other spectral features and could not be resolved. All the lines peak at between 15-20 mrad from the axis with the profiles from the longer 22mm target showing a narrower divergence than the 13.7mm data as expected. Unfortunately, due to the limited angular acceptance of the spectrometer, data at angles greater than 21mrad was not obtained. Therefore, the beam divergences of the 22.0 and 26.3nm lines were not obtained as their emission extended well beyond this range. The 20.6 and 21.0nm lines from the 22mm target both peak at 15 ± 2mrad and have F.W.H.M's of 10.5 ± 2mrad. The 22.0nm line peaks at 18 ± 2mrad and the 26.3 line at 20.0 ± 2mrad. Initial indications are that there is a systematic 2-4mrad extra refractive offset for the higher Z Se system when compared to shots taken under identical conditions but using Ge. This may indicate that the Se slab system is forced to operate in slightly higher density, and density gradient regions of the plasma leading to more significant refractive bending.

The observation of a line's angular peak moving further away from the axis as the wavelength is increased, is similar to results obtained from Ge slab targets. The soft X-ray refractive index η is wavelength dependent[4]. For a plasma with an electron density gradient the deviation of a paraxial ray will depend on the distance travelled, and the refractive index of the medium travelled through[5]. Thus, since $\delta\eta$ / $\delta\lambda$ α -λ an increase in the deviation from axis of the lasing emission at longer wavelengths is reasonable, provided that the rays travel through the same spatial region at similar times.

GAIN MEASUREMENT

The Linford[6] intensity scaling relationship was fitted to graphs of the spectrally integrated maxima I_{Max} against target length L as shown in *figure 3*, to deduce the gain coefficients. This process was possible on the 20.6, 21.0, 22.0 and 26.3nm lines but, in the case of the 18.2nm J=0 - 1 line the overlap problem that was discussed earlier prohibited a gain measurement. No 18.2nm J=0-1 lasing emission could be discerned from the 13.7 and 6.5mm targets. An estimation of the minimum detectable signal which could be present on these shots was made and using this it was possible to place a lower limit on the gain coefficient for this line. The measured gain coefficients for these lines are shown in *table 1* . The magnitudes of the gain coefficients and intensities of all these lines are very similar to the results obtained with Ge slab targets at slightly lower intensity. Again, the two J=2-1 20.6 and 21.0nm B and C transitions (the analogue of the Ge J=2-1 23.2 and 23.6nm lines) show the highest gain. The ratio of their intensities from the 22mm target is $R_{C:B} = 0.8 \pm 0.3$ with the shorter wavelength J =2-1 B line being dominant. For the Ne-like Ge slab targets a lower incident intensity of $1.5 \pm 0.3 \times 10^{13}$ is required to achieve similar gains of 3.0 ± 0.5 cm on the J=2-1 lines.The J=2-1 Ne-like Ge lines at this target intensity are in the ratio of $R_{C:B} \sim 1.2$. The trend for the longer wavelength J=2-1 C line to be dominant at Z < 33 and the shorter wavelength J=2-1 B line to become dominant for Z > 33, is observed for both slab and exploding foil target geometries for targets of Ni[7], Cu[8], Ge[9], Se[10], Y[11], Mo[11] and Ag[12].

For Ge slab targets the J=2-1 B and C transition gain production efficiencies at $I_T = 1.5 \times 10^{13}$ Wcm^{-2} (which gives comparable gain coefficients) are $E_g = 21 \pm 2$ TW^{-1}. For the Se slab targets, gain production efficiencies are still quite high with the average value for the same transitions being $E_g = 15 \pm 5$ TW^{-1}. This figure is much higher than that achieved by the Livermore team[10] using exploding foil targets illuminated in second harmonic of $E_g \sim 4 \pm 1$ TW^{-1}. The typical conversion efficiency into second harmonic is ~ 65% for long pulses at intensities of $\sim 2 \times 10^9$ Wcm^{-2}. If E_g is considered in terms of the driving laser power required, and not the incident power onto target it falls to $E_g = 2.5 \pm 1$ TW^{-1} for the L.L.N.L. results. Thus, by using narrow slab targets, irradiating them without using harmonic conversion and using a 50% longer pulse, an improvement in the gain production efficiency of x6 is achieved. This is significant as it allows experiments at R.A.L. to pump 2.2cm targets with gain length products of $\alpha l > 6$ using only three drive beams of the Vulcan glass laser.

Transition J =	λ nm	α cm^{-1}	E_g TW^{-1}	Ψ L=2.2cm a. u.
1 → 0 A	18.24	2.0± .5(min)	10±7 (min)	4.0±0.5
2 → 1 B	20.64	3.1± 0.3	15±5	66±9
2 → 1 C	20.97	2.9± 0.3	14.5±4	49±7
1 → 1 D	22.03	1.8± 0.3	9.1±4	3.7±0.4
2 → 1 E	26.29	2.7± 0.25	13.3±4	5.3±0.6

Table 1 Table showing the measured gain coefficients from a Ne-like Se slab target lasing system irradiated at 1.9×10^{13} Wcm^{-2}. The alphabetical line labelling used in the text is defined in column 1.

NE-LIKE 3D-3P TRANSITION IN SE

The $[2s_{1/2}2p^53d]_{J=2}$ -$[2s_{1/2}2p^53p]_{J=1}$ Se transition analogous to the 19.9nm 3d-3p (with a 2s inner shell hole) Ne-like Ge transition[13] has been observed from exploding foil type targets. It's wavelength has been accurately measured as 18.195nm. Unfortunately, due to the proximity of this line to the strong carbon Balmer α transition at 18.22nm it was not possible to spectrally resolve it during this experiment. A future experiment is planned where no carbon contamination of the spectrum will occur.

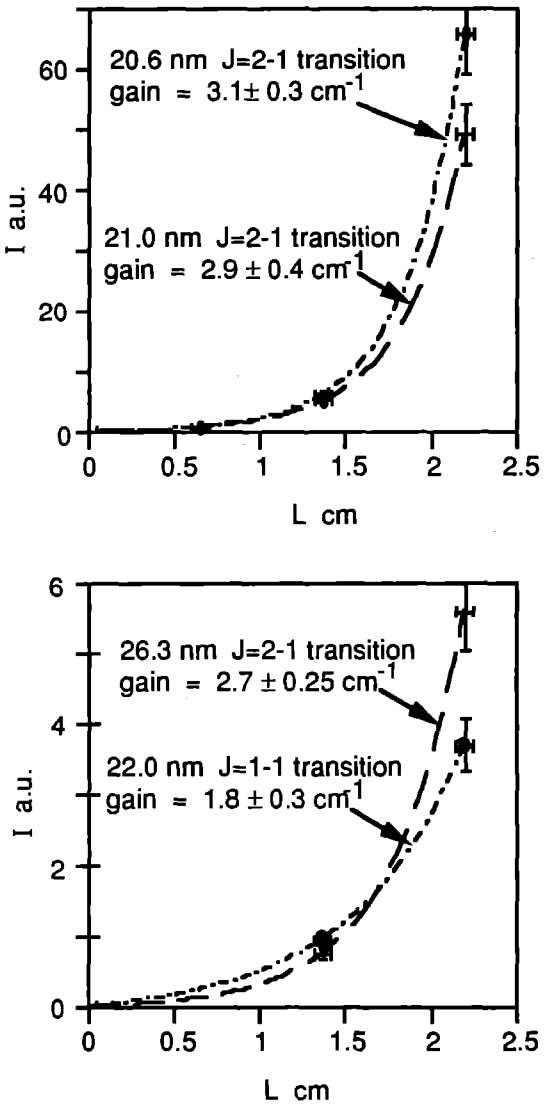

Figure3 a and b Graphs showing the spectrally integrated peak intensity as a function of target length of four 3p-3s Ne like Se transitions observed from 1.06μm driven slab targets.

CONCLUSION

Lasing action in Se slab targets has been demonstrated at $I_T = 1.9 \pm 0.3 \times 10^{13}$ Wcm^{-2} giving $E_g \sim 15TW^{-1}$. This is about 70% as efficient as the Ge system using similar slab targets, and almost a factor of 6 times more efficient than the results achieved at L.L.N.L using second harmonically driven exploding foils. Using a similar double target design as tested with Ge at R.A.L., the expected gain length products for Se is $\alpha l > 12$. With the addition of a normal incidence mirror[14], it should be possible to achieve saturation levels in Se.

Scaling from our experience with Ge and Se slab targets indicates that it should be possible to produce gain length products in the range $4 < \alpha l < 8$ using double slab targets of yttrium Z = 39 at Rutherford. Preliminary shots show that it is possible to heat 1cm, 100μm wide Y slab (Z=39 and lasing at λ=15.5nm) targets to give adequate fractional abundances of Ne and F-like ion stages. A full experiment is planned for the summer of 1992 where the presence of gain on Ne-like Y transitions will be investigated.

1 C. Lewis, D. M. O'Neill, D. Neely, J.O. Uhomoibhi, R. Burge, G. Slark, M. Brown, A. Michette, P. Jeagle, A. Klisnick, A. Carillon, G. Jamelot, J. P. Raucourt, G. J. Tallents, J. Krishnan, L. Dwivedi, H. Z. Chen, M. H. Key, R. Kodama, P. Norrays, S. J. Rose, J. Zhang, G. J. Pert and S. A. Ramsden, Vol 1551, SPIE, July1991, p49-54

2 M. Key et al 1992 Annual report

3 I. N. Ross et al, Appl. Optics 26 9 (1987) p1584

4 R. A. London Phys. Fluids 31 1 (1988)

5 C. L. S. Lewis, Laser Plasma Interactions 4, SUSSP Publications 1989

6 G. J. Linford, E. R. Peressini, W. R. Sooy, and M. L. Spaeth, Appl. Opt 13, 379 (1974)

7 T. Boehly, B. Yaakobi, D. Shvarts, D. Meyerhofer, P. Audebert, J. Wang, M. Russotto, B. Boswell, R. Epstein, R. S. Craxton and J. M. Soures Applied Physics B 50 (1990) P165-172

8 T. N. Lee, E. A. McLean and R. C. Elton Phys. Rev. Lett. 59 11 (1987) p1185-1188

9 D. O'Neill, C. L. S. Lewis, J. Uhomoibhi, M. H. Key, A. MacPhee, G. J. Tallents, S. A. Ramsden, A. Rogoyski and E. A. McLean, Opt. Comm 75406 (1990)

10 D. L. Mattnews et al, Phys. Rav. Lett, 54 2 (1985) p110-113

11 D. Matthews, et al Opt. Soc. Am. B 4 4 (1987) p575-587

12 D. Matthews, et al Inst. Phys. Conf. Ser. No 116 York(1990) p205-215.

13 C. L. S. Lewis , D. Neely, J. Uhomoibhi,, D. M. O'Neill, S. A. Ramsden, G. J. Tallents, Y Al-Hadithi, M. H. Key, S. J. Rose and G. J. Pert, Inst. Phys. Conf. Ser. No 116 York(1990) p231-238.

14 A. Carillon, H. Z. Chen, P. Dhez, L. Dwivedi, J. Jacoby, P. Jaegle, G. Jamelot, J. Zhang, M. H. Key, A. Kidd, A. Klisnick, R. Kodama, J. Krishnan, C. L. S. Lewis, D. Neely, P. Norreys, D O'Neill, G. J. Pert, S. A. Ramsden, J. P. Raucourt, G. J. Tallents and J. Uhomoibhi submitted to Phys. Rev. Lett (1991)

MEASUREMENT OF THE PHOTO-PUMP STRENGTH OF THE 3d-5f TRANSITIONS IN Ni-LIKE Sm^{+34}

P A Norreys[1], J Zhang[2], A Djaoui[1], L Dwivedi[3], M H Key[1,2], R Kodama[1], J Krishnan[3], C L S Lewis[4], D Neely[4], D O'Neill[4], G J Pert[5], S A Ramsden[5], S J Rose[1], G J Tallents[3], J Uhomoibhii[4]

[1]Rutherford Appleton Laboratory
[2]Clarendon Laboratory, University of Oxford
[3]Dept of Physics, University of Essex
[4]Dept of Pure and Applied Physics, Queen's University Belfast
[5]Dept of Computational Physics, Univeristy of York

INTRODUCTION

Collisionally excited Ne-like and Ni-like XUV lasers have been extensively investigated[1,2]. Saturated and near diffraction limited lasing has recently been demonstrated for the Ge XXIII neon-like laser[3] and amplification has been obtained at wavelengths in the water window with the Ni-like collisional excitation scheme at the NOVA facility at the LLNL[4]. Evidence of gain has also been reported for H-like and Li-like recombination X-ray lasers[5-7]. A drawback with the collisionally excited schemes is the large pump power required to create saturated X-ray lasing in the water window region of the spectrum.

Resonant photo-pumping has been proposed as method of overcoming this pump power limitation. However, the major problem to date with the photo-excitation scheme has been the mismatch between wavelengths and line profiles of the pumping and absorbing transitions. This problem can be overcome if the same ion species is used for both the pump and lasing plasmas. This is the "automatic line-matched" scheme[8,9,10].

A major advantage of the photo-excitation scheme is that it is a resonant process, so the upper lasing levels can be selectively populated while avoiding the large pump rate to the lower lasing levels that are inherent in the collisional excitation schemes. This means that the optical pump power needed to create the lasing plasma can be quite moderate and the total optical pump power required to create saturated X-ray lasing in the water window can potentially be achieved with medium sized laser installations.

Another advantage of the photo-excitation scheme is the physical separation of the pump and lasing plasmas, which means that the optimum conditions of each plasma can be investigated independently. In particular, the photo-pump strength of the most prominent photo-pump lines has to be measured, the optimised temperature of the lasing plasma determined, together with the coupling between the pump and lasant plasmas.

In the automatically line-matched photo-pumped Ni-like scheme, the two main 3d-5f absorbing transitions in the lasant plasma are photo-pumped by the same Ni-like ion in the pump plasma, populating the 5f level. The 5f level decays directly to the 4d levels which are the upper lasing states. Lasing then occurs between the 4d and 4p level pairs. These are the $(3d_{3/2}4d_{3/2})_0$-$(3d_{3/2}4p_{1/2})_1$, $(3d_{3/2}4d_{3/2})_0$-$(3d_{5/2}4p_{3/2})_1$ and $(3d_{3/2}4p_{3/2})_1$-$(3d_{5/2}4p_{3/2})_1$ transitions. A simplified energy level diagram of the lasing transitions for the Ni-like Sm^{+34} ion together with some of the more prominent photo-pump lines are shown in Fig 1. The energy levels and radiative rates were calculated by the GRASP code[11].

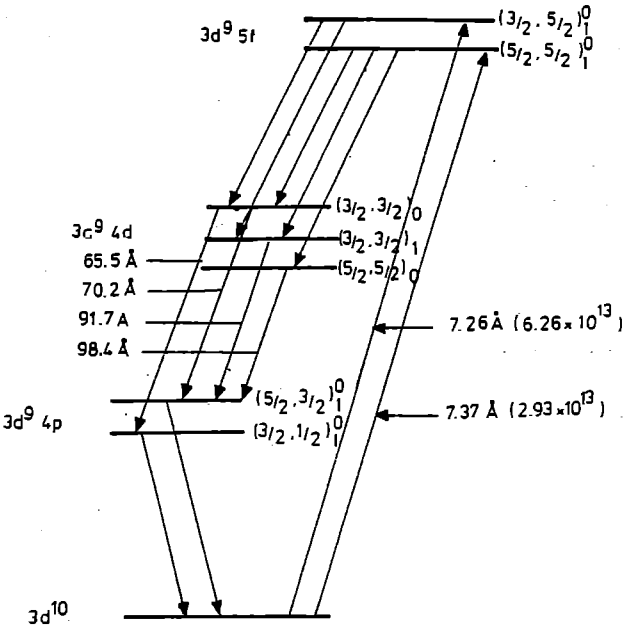

Fig 1 Simplified energy level diagram of the photo-pumped Ni-like Sm^{+34} transitions.

We report here the first measurement of the photo-pump strength of the 3d-5f transition in the Ni-like Sm^{+34} ion . We compare the collisional rates of the 4d-4p transition with the rate of photo excitation of the 3d-5f levels and discuss implications of our measurement.

EXPERIMENT

Three beams from the Neodymium glass laser Vulcan were delivered into the target chamber. These beams were brought into a line focus at the centre of the chamber by using off-axis spherical mirrors. The three $\lambda = 1.06$ μm beams each had an energy of 140 J on target in a pulse length of 510 psec. These beams were overlapped end to end to give a line focus length of 22 mm. Optically polished glass slabs with an evaporated stripe of Al (width 120 μm and thickness 0.5 μm) were overcoated with 0.5 μm of SmF_3 (which is transparent). The pointing of the target and the focusing of the laser beams were adjusted with the aid of the Al stripe and a split field microscope system. The irradiance on target was estimated to be 2.5×10^{13} Wcm^{-2}.

The primary diagnostic was a space resolving TlAP flat crystal spectrometer[12]. The slit was placed perpendicular to the line to observe the uniformity of X-ray emission along the length of the plasma. The distance from the plasma to the source was 4.0 cm, the slit size was 25 μm and the magnification was 1.0. The X-ray emission was recorded on Kodak CX film.

The emission along the axis was monitored by a grazing incidence flat-field grating spectrometer (1200 l/mm average). This instrument was operated in the time integrated mode and the XUV emission was recorded on Kodak 101-07 film.

RESULTS

Fig 2 shows the spectrum recorded from the space resolved crystal spectrometer. The emission lines were identified by comparison to those of Gd^{+36} as measured by Burkhalter et al[13]. The optical densities were converted to intensities using the calibration of Murray[14].

The energy density on the film is related to the total energy emitted the plasma in that line by

$$E_{film} = \frac{E_{plasma}}{4\pi sl} \frac{T R_c}{V} \frac{W}{sin(\vartheta+\varphi)} \quad J\,cm^{-2} \qquad (1)$$

where R_C is the integrated reflectivity of the TlAP crystal, T is the transmission through the filter, W is the slit width, V is the distance from the slit to the plasma, θ is the Bragg angle and ϕ is the angle of the film to the crystal, s is the source size perpendicular to the target, and l is the length of the target. In this spectrometer $\sin(\theta + \phi) \approx 1$, so the intensity of the pump line in the plasma is

$$I_{plasma} = E_{plasma}/\pi sl t_o = \frac{4E_{film}}{T} \left(\frac{V}{W}\right) \frac{1}{R_c} \frac{1}{t_0} \; W\,cm^{-2} \quad (2)$$

In a time integrated measurement determination of the intensity requires knowledge of the pulse length of X-ray emission t_O. We propose that this is approximately equal to the duration of the laser pulse as is well known to be true for high Z materials with emission lines > 1 keV.

The examination was verified using simulations with the one-dimensional hydrodynamic code MEDUSA[15]. The code has recently been modified to include calculation of the coupling of atomic processes to the energy balance in the plasma, allowing the abundance of Ni-like ion in the plasma to be calculated[16]. The irradiance on target in the simulation was 2.0×10^{13} W cm^{-2} in a pulse length of 600 psec. In both LTE and corona models of x-ray emission, the intensity of line emission is directly proportional to the square of ion density. A similar dependence is expected in the collisional-radiative regime (which is the correct description here). Fig 3 shows the peak Ni-like ion density and corresponding electron temperature as a function of time. It can be seen in Fig 3 that the maximum Ni-like ion density is 5.6×10^{18} cm^{-3} at an electron temperature of 750 eV. The density falls to $1/\sqrt{2}$ its maximum value in 600 psec. This is similar to the laser pulse length and gives added confidence to our assumption.

Using the laser pulse length as the value for the x-ray pulse emission, the intensity of the 3d-5f transition is estimated to be 1.5×10^{10} W cm^{-2}.

The intensity of the photo-pump line from the plasma is related to the number of photons per mode by the expression

$$n_\lambda = \frac{I_{plasma}}{8\pi hc^2(\Delta\lambda/\lambda)} \frac{\lambda^4}{} \quad photons/mode \qquad (3)$$

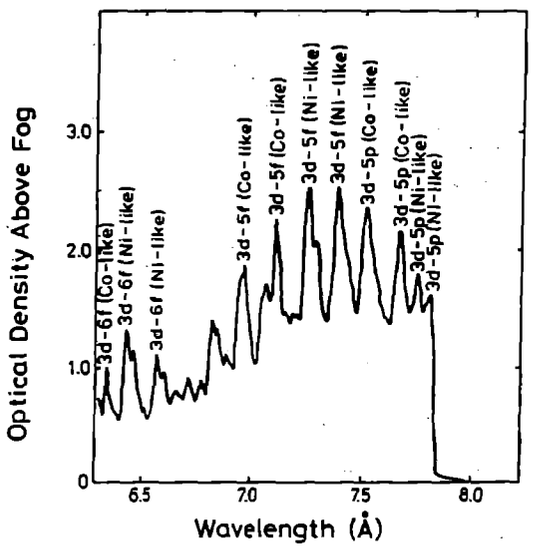

Fig 2 Spectrum recorded from space resolved crystal spectrometer.

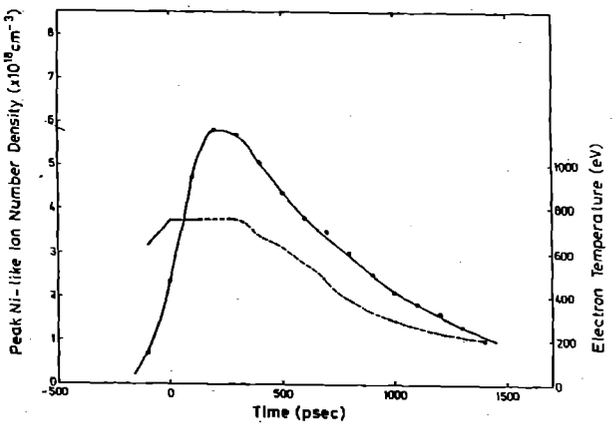

Fig 3 MEDUSA simulation of the peak Ni-like density (solid line) and corresponding electron temperature (dotted line)of a Sm target irradiated at 2.0×10^{13} W cm^{-2} in a pulse length of 600 psec. The peak of the laser pulse was set at 0 psec.

The dominant line broadening in this pump plasma is Doppler broadening. (Stark broadening is estimated to be an order of magnitude smaller[17]). For an irradiance of 2×10^{13} W cm^{-2}, the electron temperature is estimated to be 750 eV from the Fig 3. Hence $\Delta\lambda/\lambda = 1.8 \times 10^{-4}$ and the photo-pump strength is 2.0×10^{-4} photons/mode.

The dominant errors in this estimation are the film calibration (50%) and the X-ray emission pulse length (30%). Taking these into account gives a photo-pump strength of $2\ (\pm 1.2) \times 10^{-4}$ photons/mode.

DISCUSSION

It is useful to compare the rates of collisional excitation for Ni-like Sm and those of photo-excitation. For an electron density of 2.0×10^{20} cm^{-3} and an electron temperature of 600 eV, the maximum monopole excitation rate between 3d and 4d levels is 5×10^{9} sec^{-1}. The rate of photo-excitation through the pumping channel 3d-5f is $n_\lambda .6.0 \times 10^{13}$ sec^{-1}. Hence for our measurement the rate of photo-excitation is twice as high as that of collisional excitation, but in any practical photo-pumping scheme the coupling between the pump and lasant plasmas is never perfect. In addition, for increased efficiency of producing gain from the optical pump energy,

the irradiance of the optical pump plasma should be less than that required for ASE generation from the 4d-4p transitions by collisional excitation. Preliminary investigations of the collisionally pumped Ni-like Sm^{+34} Ni-like X-ray laser indicate that ASE begins for an irradiance of $\geq 2 \times 10^{13}$ Wcm $^{-2}$ [18]. Consequently there is no optical pump energy saving with a two plasma pump lasant configuration. However, it may be advantageous to use the additional photon-excitation pumping of the 4d levels in the collisional excitation scheme. The precise effect of self photo-pumping on the gain in collisional excited Ni-like scheme will be the subject of further investigation.

REFERENCES

1. T Lee, E McLean, R C Elton
Phys Rev Lett **59** 1185 (1987).

2. D Mathews et al
"X-ray Lasers 1990", G Tallents Ed (IOP Bristol) 205 (1991).

3. A Carillon et al,
Phys Rev Lett (submitted).

4. B J MacGowan, S Maxon, L B Da Silva, D J Fields, C J Keane, D L Mathews, A L Osterheld, J H Scofield, G Shimleaveg, G F Stone
Phys Rev Lett **65** (4) 420 (1991).

5. C Chenais-Popovics, R Corbett, C Hooker, M Key, G Kiehn, C Lewis, D Pepler, G Pert, C Regan, S Saadat, R Smith, T Tomie, O Willi
Phys Rev Lett **59** 2161 (1987).

6. Y Kato, P R Herman, T Tachi, K Shihoyana, K Kanei, H Shiraga,
IEEE Trans Plasma Science **16** 520 (1988).

7. P Jaegle, G Jamelot, A Carillon, A Klisnick, A Sureau, H Guennou,
J Opt Soc Am **34** 563 (1987).

8. B N Chichkov, E E Fill
Opt Comm **74** 202 (1990).

9. E E Fill, Th Scheleger, J Steingruber, J Zhang,
"X-ray Lasers 1990", G Tallents Ed (IOP Publishers, Bristol), 110 (1991).

10. T Boehly, M Russotto, R S Craxton, R Epstein, B Yaakobi, L B Da Silva, J Neillsen, E A Chandler, D J Fields, B J MacGowan, D L Mathews, J H Schofield, G Shimkaveg
"X-ray Lasers 1990", G Tallents Ed (IOP Publishers, Bristol), 139 (1991).

11. B L Witton, R A London, R S Walling,
J Opt Soc Am B5, 2537 (1988).

12. Y Al-Hadithi, G Tallents, D Neely
"X-ray Lasers 1990", G Tallents Ed (IOP Publishers, Bristol), 169 (1991).

13. P G Burkhalter, D J Nagel, R R Whitlock
Phys Rev A **9** 2331 (1974).

14. G Murray, C E Bentley
AWE Report EXCAL/IND-C/5/88 (1988) (unpublished).

15. J P Christiansen, D E T F Ashby, K V Roberts
Computer Physics Comm 7 271 (1974).

16. A Djaoui, S Rose
Central Laser Facility Annual Report to the LFC, Rutherford Appleton Laboratory Report RAL-91-025, 53 (1991).

17. M S Dimitrijevic, N Konjevic
Astron Astrophys 172 245 (1987).

18. D O'Neill et al
Central Laser Facility Annual Report to the LFC, Rutherford Appleton Laboratory Report RAL-92-025 (1992).

FILM CALIBRATIONS FOR SOFT X-RAY WAVELENGTHS

J. Krishnan[1], D. Neely[2], C. Danson[3], L. Dwivedi[1], C.L.S. Lewis[2] and G.J. Tallents[1]

[1]University of Essex
[2]Queens University of Belfast
[3]Rutherford Appleton Laboratory

1. INTRODUCTION

Characteristic curves at $\lambda \sim 30\text{Å}$ have been obtained for seven spectroscopic X-ray films widely used in scientific research. The films investigated are Kodak 101-01, 101-07, 104-02, Industrex CX, Russian UF-VR2, UF-SH4 and Ilford Q-plates. The calibrations were obtained using two identical flat-field grazing incidence spectrographs viewing a laser produced CH plasma. Exposures were recorded after transmission through filters of known thickness. The density versus intensity data were fitted by the semi-empirical mathematical model relations given by Henke et al.[1]

A number of papers have been published previously giving calibrations for Kodak 101-01, 101-07, Industrex CX, Russian UF-VR2 and UF-SH4 films[2-8]. The motivation for undertaking new calibrations was to find sensitive replacements for Kodak 101-01 film which is no longer being manufactured. We present direct comparisons of the film response. A calibration for Industrex CX was used to put our calibrations on an absolute scale.[5]

2. EXPERIMENTAL PROCEDURE

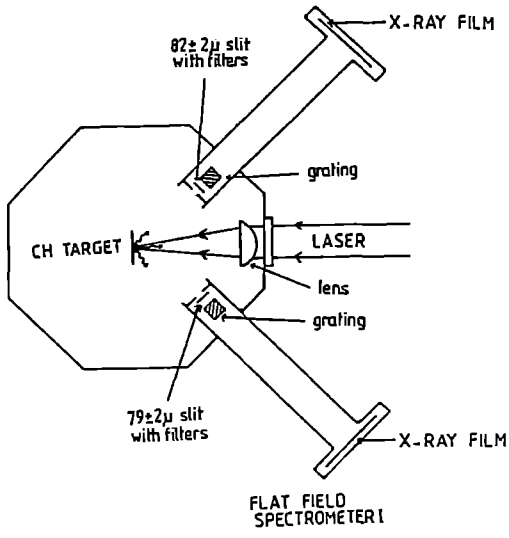

Fig. 1 - Schematic experimental set-up for calibration of soft X-ray films using the filtered transmission from a laser produced plasma at $\lambda \sim 30\text{Å}$.

A single beam of the Nd-glass laser, VULCAN(wavelength 1.06μm, pulse duration 1ns and laser energy 20-100J) was focused onto a CH plastic slab target. Spectra were recorded using two flat-field grazing incidence spectrometers at angles of +45 and -45 ^{0} to the laser axis.(fig. 1)[9].The gratings have an average 1200 lines/mm.Two entrance slits of widths 80μ covered with different filters(.1μ Al, .2μ Formvar and .4μ Formvar) with a section left unfiltered for straight through emission along the slit length were used. The spectrum on the film appears with four exposure levels for each spectral line(fig. 2).

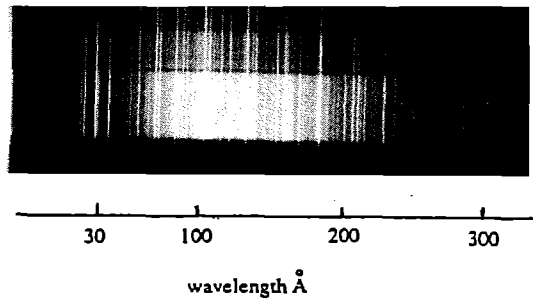

Fig. 2 - Typical spectrogram of soft X-ray line spectra obtained with the grazing incidence flat field spectrometer.

Several spectra were recorded for each film. The films were processed as follows; they were pre-soaked in water for 2 min, developed for 4 min with agitation every 30 sec in 1:1 D-19 developer, washed for 30 sec in water, fixed for 5 min in Amfix and finally washed for 20-40 min in running water. Film processing was carried out at 20 ± 1^0C.

3. INTERPRETATION OF DATA

The optical densities on the developed films were measured using a Joyce-Loebl microdensitometer with matched .25 numerical aperture for both objective and viewing lenses. For a given source brightness, the recorded spectrum yields four measured densities at each wavelength corresponding to four different incidence exposures. If the filter has a transmission T at a given wavelength , then by plotting the corresponding optical density D against T, a comprehensive characteristic curve can be obtained as outlined by Tallents and Shorrock[10] and also by Lewis et al.[3] Essentially, each D versus T curve for different wavelength is scaled along the T axis until a reasonable characteristic curve can be obtained. In order to eliminate the contributions due to the continuum, only the first order H-like and He-like lines at wavelengths 24, 27, 33, 36 and 41.5Å were considered. The absolute intensities were obtained by comparison to the response of the Industrex CX film at 34.7Å(.28 KeV), which is absolutely calibrated. Examples of the calibration curves thus obtained are presented in Fig. 3. Table I gives the intensity of each film at an optical density of 0.5.

Film	Intensity (photons/μm^2)
Kodak	
101-01	1.05
101-07	1.0
104-02	3.2
Industrex CX	2.3
Russian	
UF-VR2	0.42
UF-SH4	0.52
Ilford	
Q-plates	2.4

Table I - Intensity to produce an optical density of 0.5.

Semi-empirical model equations were fitted to the characteristic curves.For monolayer type films (Kodak 101-01, 101-07, 104-02, Russian UF-VR2 and UF-SH4) the model equation according to Henke et al is

$$D=(1-\exp(-CI))\ Dsat \qquad (1)$$

and for thick emulsion type films (Kodak Industrex CX and Ilford Q-plates) the model equation is

$$D=\ln(1+CI)\ Dsat \qquad (2)$$

where Dsat is the saturation density of the films, I is the intensity corresponding to an optical density D and C is a constant dependent on the properties of the particular film such as the grain size, coating thickness etc. Unfortunately the parameters to calculate C are not available from the manufacturers of the different films. The constant C and the saturation densities Dsat were determined by fitting the calibration curves (except for Industrex CX) with equation 1 or 2(see table II). These saturation densities were compared with that of the zeroth order exposure which are heavily over exposed and were found to be identical. It was not possible to fit the curve for Kodak Industrex CX film as there were no points near the saturation. Here we have to determine Dsat from the zeroth order exposure line. The slope of the Industrex CX film characteristic curve was identical to that found previously,[5] so we have used the reported absolute response to put our calibrations on an absolute scale.

Film	Dsat	C
Thin emulsion films: D = (1-exp(-CI)) Dsat		
Kodak		
101-01	1.6	0.37
101-07	2.63	0.22
104-02		0.36
Russian		
UF-VR2	1.51	0.84
UF-SH4	1.85	0.50
Thick emulsion film: D = ln(1+CI) Dsat		
Ilford		
Q-plates	1.27	0.18
Kodak		
Industrex CX	3.0*	0.08

* from zeroth order exposure only.

Table II- Dsat and C from the fitted data.

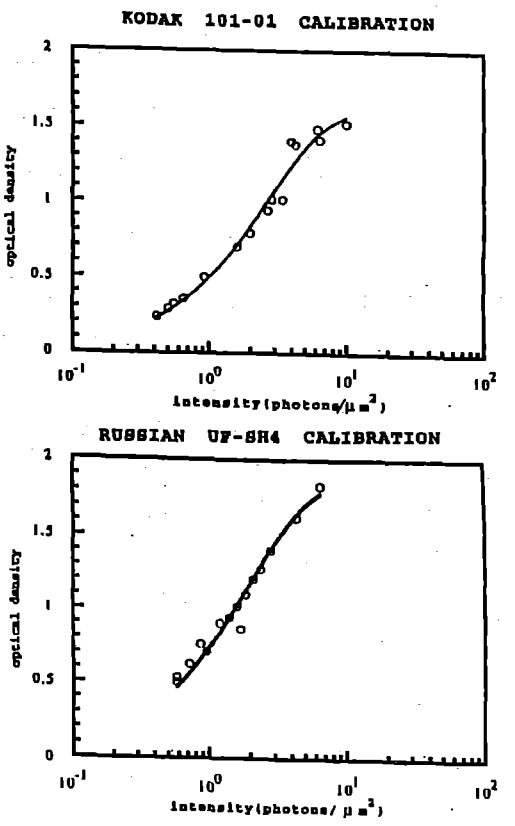

Fig. 3 - Characteristic curves for soft X-ray films (Kodak 101-01 and UF-SH4) at λ~30Å.

4. CONCLUSION

In this work we have presented the absolute intensity calibration for seven soft X-ray films (Kodak 101-01, 101-07, 104-02, Industrex CX, Russian UF-VR2, UF-SH4 and Ilford Q-plates) in the region λ~30Å. The spectral responses of Russian films are similar with a sensitivity approximately twice that of Kodak 101-01. The Q-plates and Kodak 104-02 were found to be very slow at this wavelength region. Our calibrations are probably valid up to 1000Å for the thin emulsion films, but batch variations in the response of these could be great.

5. REFERENCES

1. B.L.Henke, S.L.Kwok, T.Y.Yamanada, G.C.Young and M.H.Palmer. J.Opt.Soc.Am., 1 p818 1984
2. L.N.Koppel. Adv.in X-ray Analysis, 18 p146 1975.
3. C.L.S.Lewis and E.R.Mahoney. J.Phys.E:Sci.Instrum., 17 p744 1984.
4. B.L.Henke, F.G.Fugiwara, M.A.Tester, C.H.Dittmore and M.H.Palmer. J.Opt.Soc.Am., 1 p828 1984.
5. Measurement of the response of Kodak Industrex CX film made at the Excaliber Facility- AWE Aldermaston.
6. Yu.M.Alexadrov et al. "Report on Int. Conf. SR-90", Moscow 1990. (Investigation of sensitometric characteristic of X-ray photoemulsions in the spectral range of 15-80A).
7. M.G.Hobby and N.J.Peacock. J.Phys.E:Sci.Instrum., 6 p854 1973.
8. H.Nishimura et al. J. of X-ray Sci. and Tech., 3 p14 1991.
9. T.Kita, T.Harada. N.Nakano and H.Kuroda. Appl.Opt., 22 p512 1983.
10. G.J.Tallents and L.D.Shorrock. J.Phys.E:Sci.Instrum., 14 p20 1980.

OBSERVATIONS ON THE NI-LIKE COLLISIONAL EXCITATION SCHEME USING SLAB TARGETS

D M O'Neill[#], C L S Lewis[#], D Neely[#], G Cairns[#], A McPhee[#], J Uhomoibhi[#], G J Tallents[§], J Krishnan[§], L Dwivedi[§], H Z Chen[•], M H Key[•¶], R Kodama[•], P Norreys[•], J Zhang[¶], S A Ramsden[¥].

[#]Department of Pure and Applied Physics, The Queen's University of Belfast, N. Ireland.
[§]Department of Physics, University of Essex, Colchester, England.
[•]Central Laser Facility, SERC Rutherford Appleton Laboratory, Chilton, England.
[¥]Department of Physics, University of Hull, England.
[¶]Clarendon Laboratory, University of Oxford, England.

INTRODUCTION

Our initial experimental effort in the area of collisionally excited X-ray laser schemes[1] has concentrated, with some success[2,3,4], on the Ne-like system using massive substrates. However, due to the unfavourable scaling characterisitics of the system, it is clear that significantly shorter wavelength (<10 nm), high-gL lasing based on collisional excitation, will only be achieved with the Ni-like analogue[5] scheme. We describe here some encouraging preliminary data on Ni-like collisional systems, using massive substrate targets.

PRELIMINARY DATA

With the VULCAN laser set up for driving standard Ge stripe targets in the double target[4] configuration, SmF_3-coated targets were substituted. These were irradiated at up to 3×10^{13} W/cm^2 with 1.06 μm, 600 ps pulses. Figure 1 shows a densitometer trace of a time and volume integrated spectrum showing the J = 0-1 4d-4p Ni-like Sm transition at 73 Å in four diffraction orders. This line shows a marked polar distribution (5-10 mrad, FWHM) in its emissivity profile and, furthermore, the peak of the distribution, Ψ_p, relative to the target surface plane ($\Psi = 0$) is seen to change dramatically in going from single targets ($\Psi_p \approx 10$ mrad for 22 mm plasma) to double targets ($\Psi_p \approx 0$ for 22+14 mm plasmas). From our experience with Ge plasmas, both these observations suggest ASE on this transition. This data is preliminary and some points are worth mentioning.

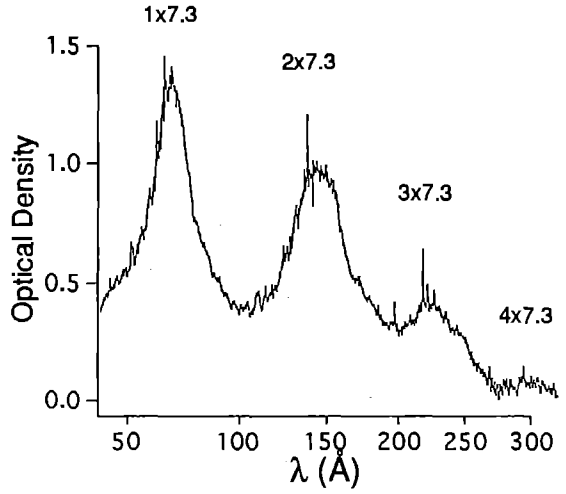

Figure 1 Densitometer trace of time and volume integrated spectrum from a SmF_3 coated slab target, irradiated at $\approx 3 \times 10^{13}$ W/cm^2. The J=0-1 4d-4p transition at 73 Å is clearly visible up to fourth order.

We have ignored data (4 shots) recorded at incident irradiance $\leq 2 \times 10^{13}$ W/cm^2 as this would appear to be a threshold intensity for significant gain to be observed. We have also ignored data (3 shots) where the VULCAN drive laser was mal-functioning and delivering ≈ 50% modulated mode-beating pulses (≈ 100 ps pulses separated by ≈ 100 ps) to target. We do not fully understand why the apparently low gL value on this experiment (gL≤4) gives rise to a narrow polar distribution characteristic of higher gL values.

Figure 2 shoes the peak line brightness at the centre of the polar distribution for targets irradiated in the range $2\text{-}3 \times 10^{13}$ W/cm^2. A least squares fit of the data in figure 2(a) to the Linford formula[6] yields a gain coefficient of $\approx 0.5 \pm 0.2$ cm^{-1}. However, since the data for lengths ≥22 mm correspond to double targets, we can assume that there is a coupling efficiency factor involved. If we assume only 50% of the photons from the 22 mm plasma couple and amplify effectively in the second (9 or 14 mm) plasma, the apparent gain coefficient increases to 0.9 ± 0.3 cm^{-1} as illustrated in figure 2(b). Furthermore, we note that the conditions of irradiation are not optimised in any way, the double target geometry is not optimised in terms of target surface spacing (200 μm as for Ge) and that the ion dilution resulting from the convenient use of SmF_3 reduces the potential gain by a factor of ≈ 0.6x.

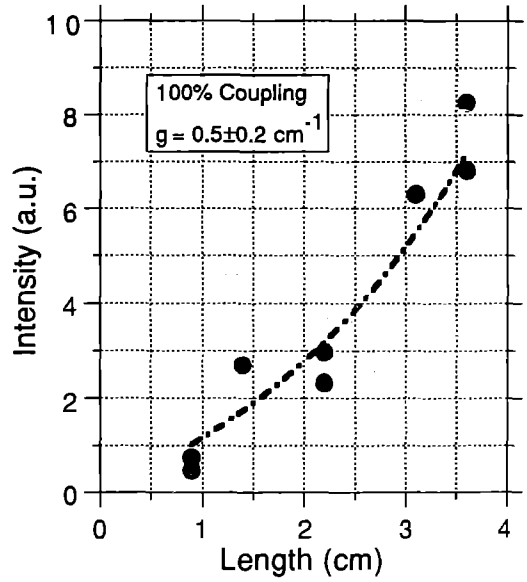

Figure 2 (a) Variation of peak intensity at 73 Å from Ni-like Sm slab target with length, assuming 100% coupling. The dashed line shows the fit to the Linford formula.

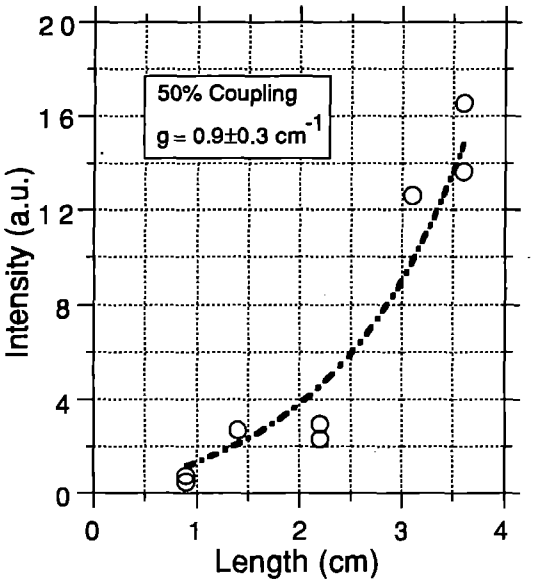

Figure 2 (b) Variation of peak intensity at 73 Å in Ni-like Sm with length, assuming 50% coupling.

ISOELECTRONIC SYSTEMS

Survey spectra of SmF_3, NdF_3, CeF_3 and CsI coated slab targets were taken under the same conditions as described above. Only a limited amount of data was taken, with non-ideal filtering. Densitometer traces of the spectra obtained are shown in figure 3. The data shown is from 22 mm target lengths with the exception of the Sm spectrum. This is from a 14 mm target length and is presented as it was the only Sm data taken at a comparable filtering level to the other survey spectra. The relative wavelength scale is approximate to ±1.5 Å as not all the spectra have been fully identified.

RECENT SM DATA

In a recent experiment, more data has been taken on SmF_3-coated targets up to 15 mm in length at irradiances of 4-5 x 10^{13} W/cm^2. Initial analysis of the output at ~ 73 nm suggests a gain co-efficient of similar magnitude to that deduced above.

In order to more fully diagnose the ionisation balance along the plasma length, a space resolving KAP crystal spectrometer was designed. The crystal was convex curved with a radius of curvature of 30 cm and covered a spectral range from 6.0→10.5 Å. This was sufficient to encompass both the 4-3 and 5-3 transition arrays of Ni-like Sm. Spatial and spectral resolution were ~ 1 mm and ~ 15 mÅ respectively.

Typical spectral details are shown in figure 4. For both the Ni-like and Co-like ion species, the 3d-5f, 3d-5p and 3p-4d transitions are clearly resolved with useful signal levels. The strong unresolved transition arrays observed in the long wavlength region arise from 3d-4f transitions. Initial analysis of the data indicates that the ratio of Ni-:Co-like spectral line intensities along the plasma length fluctuate by ≤ ±15%, at this level of spatial resolution. It is likely therefore that the fall-off in recorded line intensity over the last ~ mm at each end of the plasma image is simply a result of spatial averaging over the resolution length.

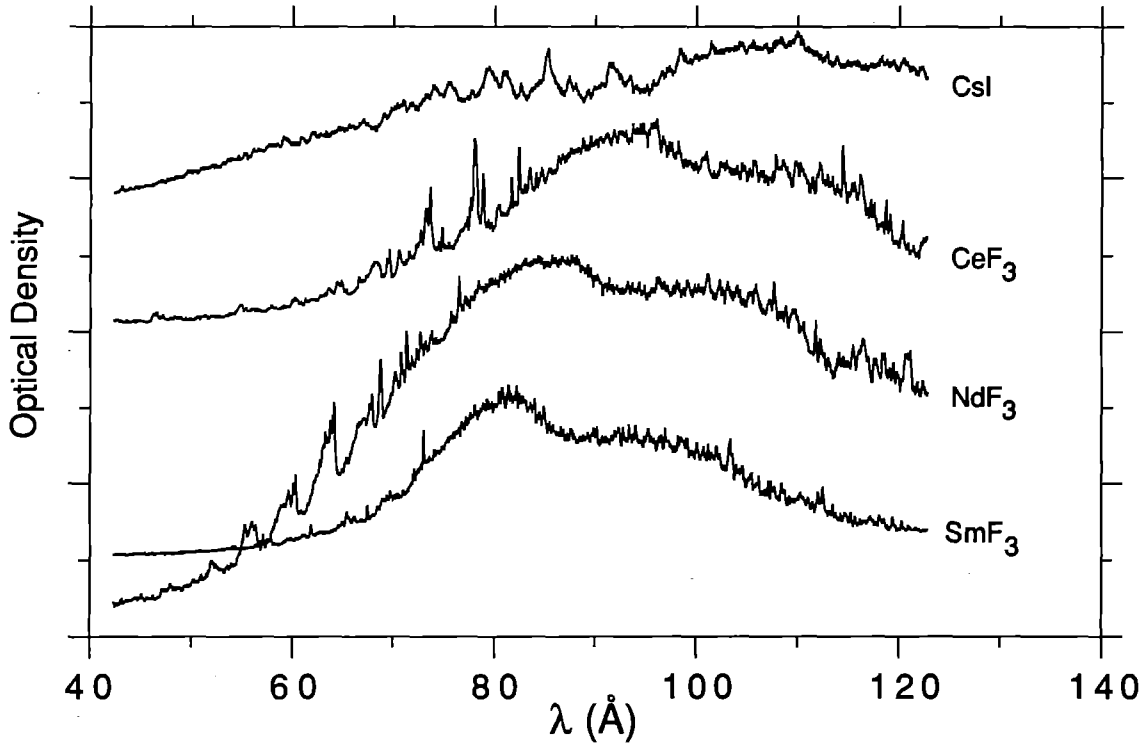

Figure 3 Isoelectronic spectra from SmF_3, NdF_3, CeF_3 and CsI under similar irradiation and filtering conditions. The spectra were all recorded from 22 mm target lengths with the exception of Sm which was from a 14 mm length. The wavelength scale is approximate (±1.5Å) as the spectra have not yet been fully identified.

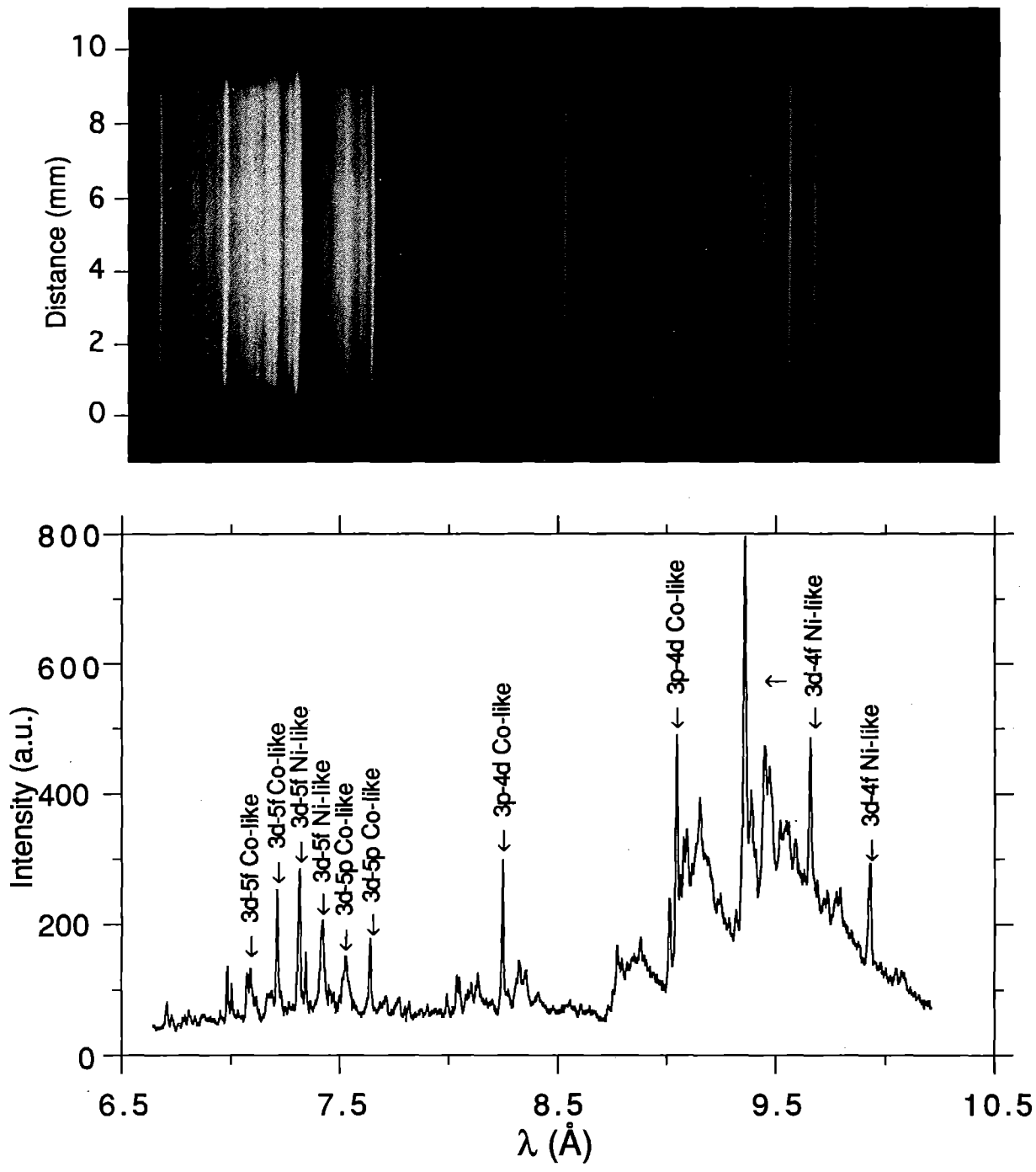

Figure 4 Space-resolved KAP crystal spectrum and densitometer trace from Ni-like Sm showing identified 3-4 and 3-5 lines arising from the Ni-like and Co-like ion species. Spectral emission along the plasma length appears to be fairly constant at this level of spatial resolution (~ 1 mm).

CONCLUSIONS

Encouraging preliminary data has been recorded on the Ni-like collisional excitation XRL system. In particular, a small gain coefficient has been recorded at ~ 73 Å from SmF_3-coated slab targets.

A new curved crystal X-ray spectrometer, designed to simultaneously monitor the 4-3 and 5-3 Ni-like and Co-like emissions along the plasma length, has been successfully implemented. We are now in a position to mount a full scale investigation into the operation of the Ni-like system using slab targets.

[1] eg M A Duguay, Laser Focus **9** 41 (1973); R C Elton Appl Optics **14** 97 (1975); A N Zherikhin et al Sov J Quant Elec **6** 82 (1976)
[2] D M O'Neill et al Opt Comm **75** 406 (1990)
[3] D Neely et al Opt Comm **87** 231 (1992)
[4] C L S Lewis et al Opt Comm (1992) in press
[5] S Maxon et al J Appl Phys **59** 239 (1986)
[6] G J Linford et al Appl Opt **13** 395 (1974)

CHARACTERISATION OF A CAPILLARY PRODUCED PLASMA

W J Blyth ,[1] N C Woolsey,[1] J S Wark,[1] R W W Wyatt[2] P E Young [3]

[1]Department of Physics, Oxford University
[2] Rutherford Appleton Laboratory
[3]Lawrence Livermore National Laboratory

INTRODUCTION

Previous reports have described a capillary device capable of producing plasmas which are 10 mm by 0.5 mm of ion density 10^{19}-10^{21} cm^{-3} using an electrical discharge through an insulating slot. The plasma is produced at about 1 eV. Initial characterization studies have shown that this plasma is very uniform, and might be suitable, when laser heated, for long scale-length plasma studies such as laser scattering instabilities, and x-ray lasers. Further characterization is necessary to measure the uniformity of the laser heated plasma and to ensure that the density and temperature range that can be achieved is suitable for these studies. Another requirement of the device, particularly for x-ray lasers is to be able to control the plasma material by doping the plasma. An experiment to investigate these properties was carried out in TA East in July 1991, during which various design changes were carried out. In order to see the effects of these changes on the unheated plasma, a further experiment using interferometry to measure the plasma density was carried out in TA 4. This report covers both these experiments.

THE LASER HEATED PLASMA

An experiment was carried out in TA East in July 1991 to heat the capillary plasma in a variety of focussing conditions to see what temperature could be achieved. The main diagnostic was spectroscopy, and figures 1 and 2 show two of the spectra which were obtained from the experiment. The first was obtained from the capillary device in its original configuration, with a stainless steel exit slit, while the second spectrum was obtained by lining the walls of the exit slit with PTFE tape. The first spectrum shows lines from the fluorine spectrum as well as many other lines which are presumed to come from material ablated from the slit wall. The second spectrum shows fluorine lines only. It can be seen from these that there is a significant doping of the plasma from the wall material. In previous experiments at LLNL a tapering slit was used so as to increase the amount of plasma emitted.It was found in this experiment however, that the plasma emitted by this type of slit was so large, and came out at such a wide angle that either the plasma could not be heated (except at very high irradiance with a spot focus), or the cool plasma above the heated region blocked the view of the mini-spectrometer. Thus the slits were changed to a parallel sided design which produced a narrower and straighter sided plasma which could then be heated and observed by the mini-spectrometer. The plasma was then heated in line focus from both sides with an irradiance of about 3×10^{12} W/cm^2 with 0.53 μm light. The pin-hole image in figure 3, taken through a 2μm CH filter shows the plasma heated from both sides and producing two regions of X-ray emission. This suggests that the plasma is too dense for the laser to penetrate sufficiently far to give uniform heating. The temperature of the plasma is derived by comparing the intensity of the Lyγ line to the Heγ line which should be optically thin and thus represent the fractions of ions in the H-like and He-like states. The spectra were compared to the spectra produced by RATION, an atomic kinetics code and the temperature was found to be in the range of 100 to 150 eV.

This experiment showed that the plasma material could be changed by changing the material of the walls of the slit. Also it was found that the plasma was much denser than was originally thought and that to achieve uniform high temperatures at these densities, greater beam energies and longer pulse lengths should be used. Alternatively, the plasma could be reduced in density to produce more uniform heating. All the data shown here was taken using high discharge voltages, and the density can easily be reduced by reducing this voltage.

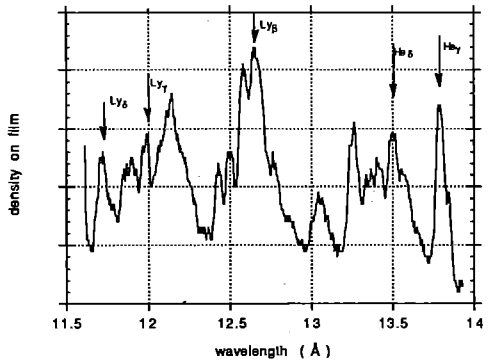

figure 1. Spectrum taken using a stainless steel exit slit. There are many lines other than fluorine.

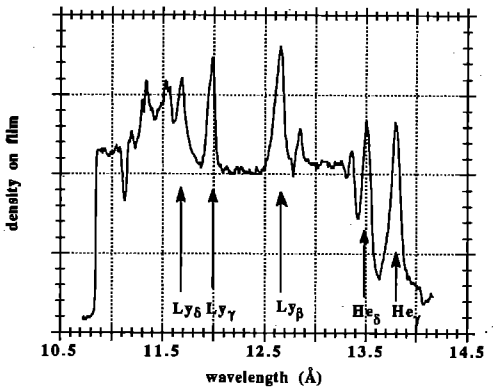

figure 2. Spectrum taken using a PTFE lined exit slit. The spectrum shows mainly fluorine lines.

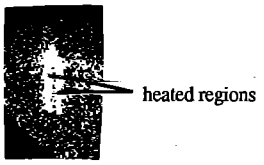

figure 3. X-ray pin-hole image of the heated plasma used to obtain spectrum in fig.2. The plasma is heated on both sides, producing two distinct X-ray emission regions.

THE UNHEATED PLASMA

In order to assess the effects of the changes to the capillary design, an experiment was carried out to measure the density and uniformity of the unheated plasma by interferometry using the laser in TA 4. The interferometry was carried out (separately) with 0.53 μm and with 1.056 μm light. The plasma produces a phase change in the probe beam due to a change in the refractive index of the plasma. The refractive index, and hence the density of the plasma, can be measured by counting the number of fringe shifts which represent the phase change. This is complicated by the fact that an ionized plasma decreases the refractive index, thus giving a positive fringe shift (say) on the interferogram, while an unionized gas increases the refractive index giving a negative fringe shift. Thus the interferometry of the unheated plasma is rather ambiguous when there is a mixture of ionized and un-ionised atoms in the plasma.

However, there are a number of ways that the density of the plasma can be determined using the interferograms. Firstly, the electron density n_e of the plasma can be determined by measuring the number of positive fringe shifts $N_{(+)}$. This is given by

$$n_e = 2.23 \times 10^{21} N_{(+)}/L\lambda \quad \text{with } L,\lambda \text{ in } \mu m.$$

Secondly, the density of the unionised regions of the plasma n_n can be measured by counting the number of negative fringe shifts $N_{(-)}$. This is given by

$$n_n = 1.6 \times 10^{23} N_{(-)} \lambda/L \quad \text{with } L,\lambda \text{ in } \mu m$$

If we take four examples of the different exit slits used on the experiment, we can see how the slit design affects the plasma. These interferograms were all taken looking down the long axis (1cm) of the plasma. Figures 4,5 and 7 were taken with 1.06μm light, while figure 6 was taken with 0.53μm light. It can be seen that the narrow 200μm slits (figures 4 and 5) produce predominantly negative shifts which shows that the neutrals density dominates the refractive index. This means that the plasma is very cool and un-ionized. If we assume that there is no fringe shift due to electrons, the neutrals density for the unlined steel slit (figure-4) is 3.4×10^{19} cm^{-3} while the density for the narrow PTFE-lined slit in figure 5 is higher at 8×10^{19} cm^{-3} due to greater ablation of material from the slit walls. The wider 800μm slits (figures-6 and 7) give predominantly positive shifts which shows that the refractive index is dominated by the electron density, so that the plasma is hotter and more ionized. This is because the plasma loses a smaller fraction of its heat to the walls. The unlined slit (figure 6) shows a positive shift of at least 12. If the effect of neutrals is ignored, this corresponds to an electron density of more than 5.0×10^{18} cm^{-3}. The PTFE -lined slit (figure 7) shows positive shifts in the central region where the temperature is higher, and negative shifts in the outer regions where the plasma is cooled due to the ablation of the PTFE from the slit walls. The positive shifts at the centre, if the shifts due to neutrals in this region are ignored, corresponds to an electron density of 1.1×10^{18} cm^{-3}, while the negative shifts at the outsides, if the shifts due to the electron density are ignored, corresponds to a neutrals density of 6.8×10^{19} cm^{-3}.

These results indicate that there is a large effect on the plasma due to the nature of the slit. The plasma conditions within the capillary body should be very similar in each of the four cases but as the plasma passes through the slit it is subject to cooling due to ablation of the material from the slit walls, and due to heat conduction into the walls. Thus the narrow slits produce a cooler plasma than the wide slits due to a proportionately greater heat loss into the walls, and the PTFE lined slits produce cooler denser plasmas than the steel slits due to greater ablation of the slit walls. Thus the plasma conditions can be controlled within a range of ion densities of 10^{19} - 10^{20} cm^{-3}. The extent of the control over the plasma material has yet to be determined, since this can only be determined spectroscopically.

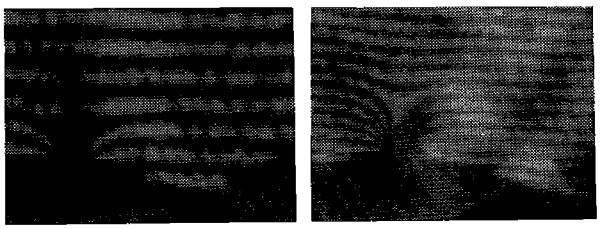

figure 4. 200μm stainless steel slit

figure 5. 200μm PTFE lined slit

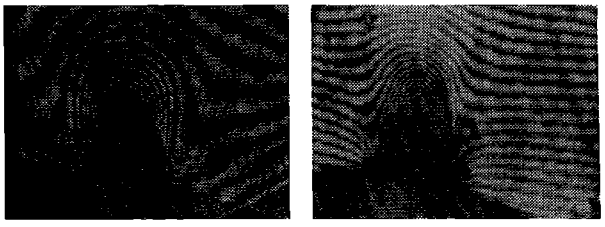

figure 6. 800μm stainless steel slit

figure 7. 800μm PTFE lined slit

CONCLUSIONS

These experiments have shown that the capillary device is capable of producing plasmas with ion density 10^{20} which is denser than was originally thought, and the design has been changed so that the plasma is emitted with a smaller flair angle so that the plasma can be laser heated. It has been shown that doping of the plasma occurs due to ablation of material from the slit walls. Further experiments need to be carried out with larger irradiances and with a lower capillary density to show that the plasma can be heated uniformly and to determine the extent of the plasma doping.

SIMULATIONS OF A LASER HEATED CAPILLARY PLASMA USING MEDUSA

W J Blyth and J S Wark
Department of Physics, Oxford University

INTRODUCTION

Many laser-plasma interaction studies require large uniform plasmas with scale-lengths up to 1cm. They are of interest in the study of parametric instabilities for reactor size targets, and are necessary for the operation of X-ray lasers. The most widely used method for producing these plasmas is to explosively heat very thin foils, or to use the blow-off plasma from massive solid targets. This report compares these plasmas to the laser-heated capillary plasma (described previously in these reports) using MEDUSA code simulations. Particular attention is paid to the efficiency of plasma production, the uniformity of the plasma, and the time-scale over which suitable plasma conditions can be maintained. The requirements for long scale-length plasma experiments will be outlined and it will be shown that the laser-heated capillary plasma offers some significant advantages for studies of this kind.

THE CAPILLARY DEVICE

The capillary device produces a slab of plasma 10mm x 0.6mm of ion density 10^{19}-10^{20} cm^{-3}, and temperature of 1-2 eV so that the plasma is about 10-20 % singly ionized. It is produced by discharging an electrical pulse through an insulator. The density of the plasma can be controlled by varying the energy in the discharge. Interferometry on the unheated plasma shows that it is very uniform and free from local fluctuations. Experiments have shown that doping of the plasma occurs due to ablation of the slit walls, but the extent of this doping has yet to be determined. For the purpose of these simulations, it was assumed that the plasma material could be completely controlled, and an ion density of $3x10^{19}$ cm^{-3} was used throughout.

PARAMETRIC INSTABILITY STUDIES

The successful operation of laser fusion experiments relies on the efficient and stable coupling of the laser power onto the target. There are a number of different ways in which this coupling can be disrupted, one of the most important being parametric instabilities. A great deal of effort has been put into understanding the growth rate of these instabilities, and how they scale with plasma size, but so far there have been discrepancies between the theory and experimental results. Whether these discrepancies are due to experimental conditions or due to basic errors in the modelling is yet to be proven. One possible explanation is that local fluctuations in the plasma could be seeding the growth of the instabilities. Previous experiments have been performed using exploding foil targets to produce a large underdense plasma for interaction studies. This presents three problems.

1) Non-uniformities in the laser beam can imprint themselves on to the plasma density profile. Thus the laser is not interacting with a uniform plasma but with one which has unknown density fluctuations.

2) The conditions in an exploding foil are changing very rapidly due to the expansion. The large velocities make the modelling more complicated and so do the time dependent parameters.

3) Exploding foil targets are surrounded by a mechanical support structure which constricts observation in the plane of the foil. Thus the interaction is usually studied through the plane of the foil after a certain delay to allow the plasma to expand. The maximum size of plasma produced in this way even by Nova is about 1mm.

Thus there is a need for a plasma which has very little local density fluctuations, low expansion velocities and can be produced to scale-lengths up to 10mm which is the size proposed for reactor type targets. These MEDUSA calculations show that the laser heated capillary plasma satisfies all these criteria.

The capillary plasma has some inherent advantages over solid targets for the production of large plasmas. Starting with a large pre-formed underdense plasma, the non-uniformities of the laser beam may not get imprinted on the density profile and so the resulting hot plasma could have less local fluctuations which could seed instabilities. The laser energy is deposited evenly through the plasma and a high proportion of the absorbed energy goes into heating compared to kinetic energy. This makes the plasma production more efficient, and also reduces the ion velocities which complicate the interpretation of the scattering results. Also the required plasma conditions are maintained for longer because the plasma is not expanding nearly as fast as the foil (see fig 1). Finally, the capillary plasma is produced in open geometry so that the whole length of plasma can be heated in line geometry, and can be probed down the axis giving 10mm of interaction length.

MEDUSA SIMULATIONS

For these comparisons, planar geometry was used, and conditions were chosen to give high temperature and good density uniformity so that a low density case was taken. The capillary plasma was assumed to have initially a top-hat density distribution whereas in reality it has a gaussian distribution in the direction parallel to the laser. Thus the spatial uniformity is better then would be expected in practice.

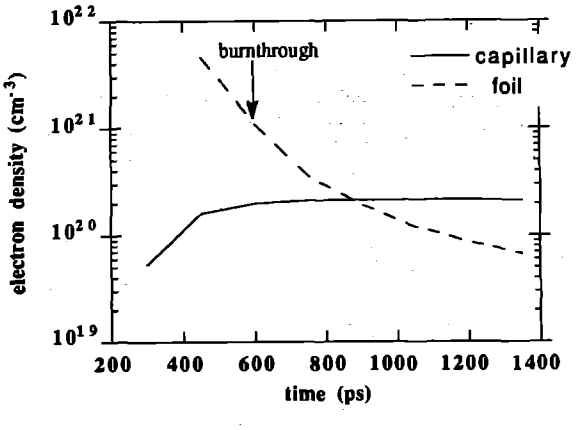

figure 1. Density histories. The values are taken at the plasma centres.

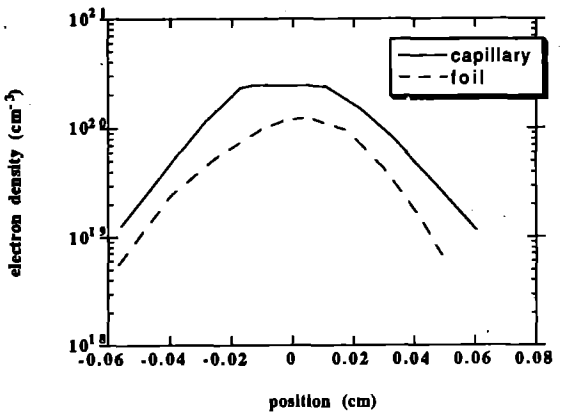

figure 2. Spatial profiles. These are taken at 250 ps after the peak of the pulse. The flat top of the capillary curve is due to starting with a top-hat distribution. This would not occur in practice.

The following table shows a summary of the results. The laser is a 1.06 μm gaussian of pulselength 450ps FWHM. The foil is selenium, of thickness 0.07 mm. The capillary material is PTFE, initial density 0.85 kg/m^{-3}, thickness 0.6mm. Values are taken at 250 ps after the peak of the pulse.

	Te max (eV)	laser energy absorbed	laser energy into thermal	laser energy into kinetic	average velocity cm/s	density weighted mean velocity cm/s
cap	2260	35%	30%	4.8%	2.9×10^7	0.6×10^7
foil	1820	41%	20%	16.8%	6.2×10^7	3.1×10^7

SUMMARY OF RESULTS

It can be seen from these results that the capillary is capable of producing similar plasma temperatures and densities to an exploding foil. More of the energy goes into thermal energy for the capillary making it more efficient in the heating. Hence higher temperatures are reached even though the absorbed fraction is lower. The velocity of the bulk of the plasma is up to 5 times lower than for the foil. The bulk density profiles are both very smooth although the local density fluctuations in the foil due to laser non-uniformities are not accounted for. The capillary thus provides advantages in efficiency, and in producing lower velocities, and possibly a reduction in local density fluctuations although this aspect has to be confirmed experimentally.

COLLISIONAL SCHEME X-RAY LASERS

Current collisional X-ray laser schemes use plasmas produced by explosively heating thin foil targets or massive targets. The main requirement in the design of the targets and laser conditions is to achieve the optimum conditions for gain by synchronising the times at which the required temperatures and densities are produced. For a particular scheme, a certain range of suitable parameters can be identified. For example, in the case studied here, for Ne-like Germanium, the optimum temperature is around 700 eV, and the optimum electron density is around 6 x 10^{20} cm^{-3}. For solid targets, these conditions are achieved in the following ways.

1) Thin foil targets: The foil burns through early on in the pulse, and from this time on the temperature remains roughly constant until the end of the pulse. After burnthrough, the foil expands explosively and after a time of a few hundred ps, it extends over a distance of a few hundred mm. The spatial distribution of the electron density is relatively uniform, but the density is rapidly decreasing due to the expansion of the plasma. Thus a large region of the plasma could match the gain conditions, but only for a short time during the pulse.

2) Massive targets: In this case, the target is not burned through, but a semi steady state situation is developed in which the blow-off plasma has a fairly steep gradient of density but a relatively uniform temperature distribution. This means that gain conditions will always be matched somewhere in the plasma while the laser pulse is on, but only for a small region. Refraction of the X-rays out of the high gain region due to the large density gradients is an important reason why theoretical gains cannot be matched with this system.

The capillary plasma potentially provides the best of both solid target schemes. The gain conditions can be matched over large regions of the plasma due to uniform heating, and because of the low expansion velocities, the conditions can be maintained for the duration of the pulse. The uniformity of the plasma suggests that refraction of the X-rays out of the plasma will be greatly reduced.

Medusa simulations show that suitable temperatures and densities for an X-ray laser can be achieved with the capillary, and if the plasma is taken to be purely germanium, say, high gains can be achieved. More realistic simulations with only partial doping have yet to be carried out. Fig 3 shows the spatial density profile of the capillary plasma compared to the massive target plasma.The capillary is only heated from one side in this simulation, but in practice it could be heated on both sides effectively doubling the heated plasma region.

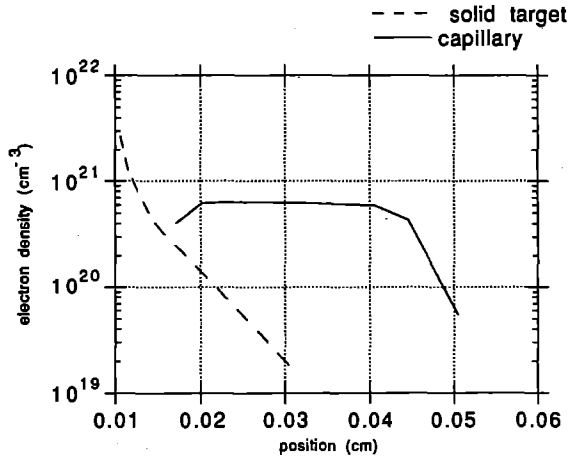

Figure 3 The density profiles of the different schemes

ACKNOWLEDGEMENTS

The authors would like to thank A.Djoui for his extensive and generous help with the Medusa simulations.

ANOMALOUS THOMSON SCATTERING IN A PLASMA GENERATED BY A 1μm LASER BEAM

A.E.Dangor[1], A.K.L.Dymoke-Bradshaw[1], A.E.Dyson[2] and Z.Najmudin[1]

[1] Imperial College of Science, Technology and Medicine
[2] University of California, Los Angeles

ABSTRACT

We describe the most recent of a series of three experiments investigating the scattering of 1μm laser light from a plasma, created by multiphoton ionisation of hydrogen gas by the same beam.

In all three experiments the scattering profiles at 1μm are poor fits to classical Thomson scattering profiles[1].

In particular over a certain range of fill pressures and for scattering at a forward angle of about 15° to the incident beam the scattered spectrum is highly asymmetric showing a blue sideband greatly enhanced in magnitude compared to the red. The peak of this enhanced sideband is found to be upshifted by ω_p and to peak in intensity at electron densities of about 1.4 10^{17} cm^{-3}. The upshifted sideband is also found to be short lived, typically 150ps.

In this latest experiment an attempt was made to scatter off the same plasma wave responsible for the scattering with a $^1/_2$μm beam. In this case there was no sign of anomalous scattering.

INTRODUCTION

The aim of the first experiment had been to investigate the feasibility of using a 1μm laser beam to produce a plasma with sufficient uniformity for use in experiments on the Laser Beat-Wave Accelerator. Earlier work had already shown that such a plasma could be generated with an intense $^1/_2$μm beam, but it was thought that the beat-wave experiments could be considerably simplified without the need for a dedicated $^1/_2$μm ionising beam.

The characteristics of the plasma can be ascertained from the Thomson scattering profiles, which give a measure of the electron density and temperature. Normally this is not considered to be practical with 1μm light, due to the small scattering cross-section (σ=6.6 $10^{-29}m^2$) and low quantum efficiencies of detectors at this wavelength (<0.1%). However in the low temperature/high density regime being considered and with high intensity light it is just feasible. In this experiment scattering was also attempted with a frequency-doubled green beam which would make detection easier. However, this is countered by the need to go to smaller scattering angles with respect to the incident beam in order to scatter off the same plasma wave.

In this experiment longer incident pulse lengths were used (600ps as opposed to 100ps and 200ps previously) to ascertain the time evolution of the enhanced sideband. As in the previous experiment use was made of a fibre optic system for collecting scattered light. This simplifies experimental procedure , and permits the scattering angle probed to be changed easily, over a wide range of values. The scattered signals were time resolved using two Hadland 675 streak cameras, an S1 for infra-red detection an S20 for the green probe.

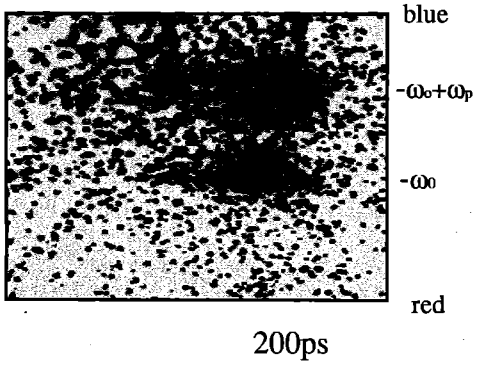

Figure 2 Typical Scattered Spectra

EXPERIMENTAL PARAMETERS

Laser, YLF 1.053μm, beam diameter 100mm, 50-100J in 100 and 200ps, 150-250J in 600ps.
Focussing optics f/20. Spot radius 200μm Rayleigh Length 8mm.
Collecting optics, variable angle, f/4 and f/10, fibre-optic collecting system. Resolution, wavelength, 5Å; time, 100ps.
Plasma, n_e≈0.6 to 3.6 10^{17} cm^{-3} (equivalent to filling pressures from 1 to 6 torr), T_e≈25eV, ω_p≈1.4 to 4.3 10^{13} s^{-1},λ_{di}≈15 to 4.8 10^{-6}cm, v_{osc}/v_{the}≈1.8 to 3.6 (v_{osc} is the quiver velocity of the electrons in the field and v_{the} is the thermal velocity.)

EXPERIMENTAL RESULTS

The anomalous blue sideband was reproduced, as can be seen in figure 2, which shows the very broad blue shifted feature as before. The intensity and spectral profile of the sideband are very dependent on the initial fill pressure and hence electron density (fig3), the scattered intensity is a maximum at a pressure of between 2.5 to 3 torr (i.e. n_e=1.2-1.4 10^{17} cm^{-3}). The sideband becomes more asymmetric as its intensity grows, becoming much broader than the central ω_o feature. However, the peak value for the sideband is upshifted from the central feature by an amount equal to the plasma frequency expected from fully ionising the filling gas (fig.4).

The use of the fibre optic coupled collecting optics enabled scattering at other angles to be investigated. We observed no anomalous

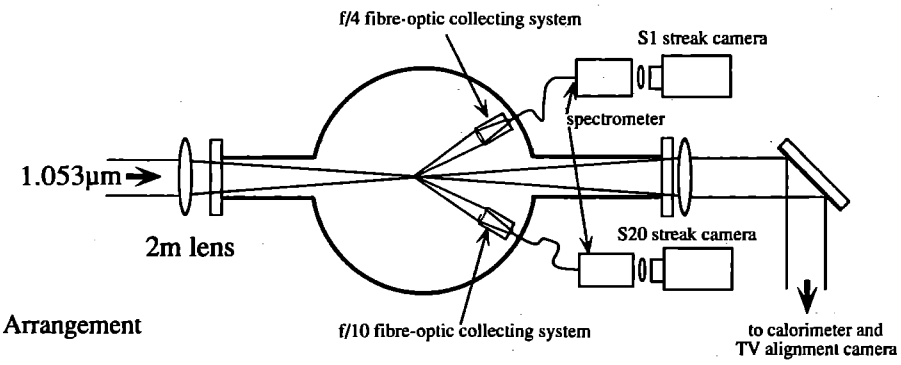

Fig. 1 Experimental Arrangement

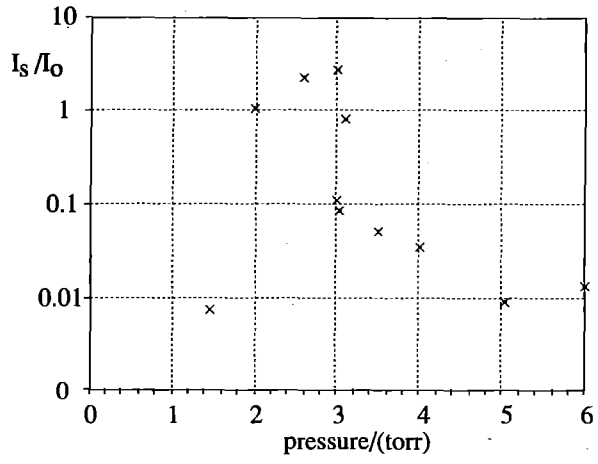

Figure 3 Plot of normalised sideband intensity vs. fill pressure

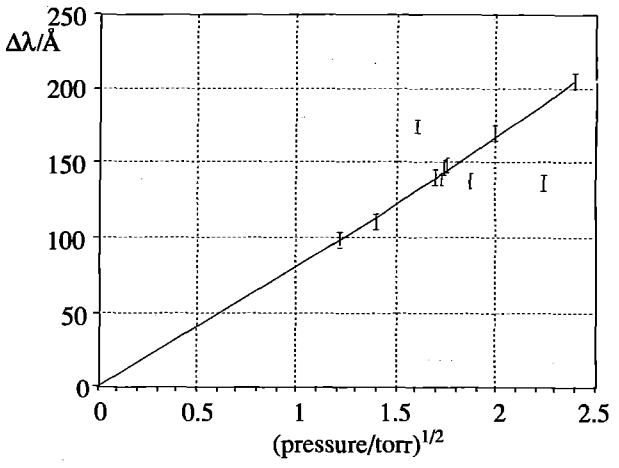

Figure 4 Plot of sideband shift vs. (pressure)$^{1/2}$

scattering at angles away from 15°. The anomalous scattering is associated with a very particular plasma wave which travels close to 90° to the incident beam. The scattering is independent of whether the scattering is done in clockwise or anti-clockwise directions from the incident light and also of the polarisation.

Time resolving the evolution of this sideband (fig.5) shows that the sideband appears 50ps after the central feature and has a lifetime of typically ≈150ps. This is short compared to the time scale for expansion of the plasma driven by either thermal or ponderomotive effects.

CONCLUSION

There is still no explanation for this surprising result and no known mechanism which could provide the required asymmetry between red and blue shifted light. The delay between the onset of the sideband and the start of the ω_0 scattered light rules out a connection with the multi-photon ionisation process. It is unclear why this effect is not seen at smaller scattering angles or at higher pressures as would be expected were the effect to be a result of a plasma wave travelling perpendicular to the incident light. In this case, the contribution from such a wave would be greater.

In the future it is hoped to be able to do this experiment with shorter more intense pulses. At a higher intensity incident light we would expect to drive harder any non-linear processes which might be causing this effect.

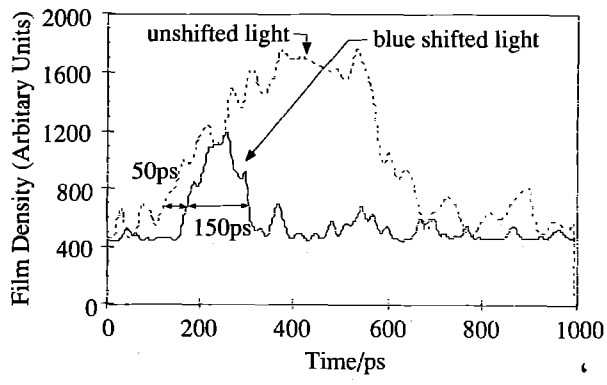

Figure 5 Time Evoloution of sideband and ω_0 feature

REFERENCES

1 A.K.L. Dymoke-Bradshaw, A.E. Dangor and A.E. Dyson. Annual Report of the Central Laser Facility 1990, RAL/90/026, p.26.

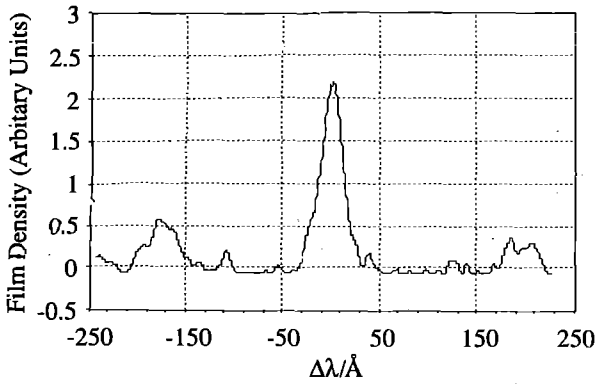

Figure 6 Scattered profile at 25° showing marked fall off of sideband at other angles

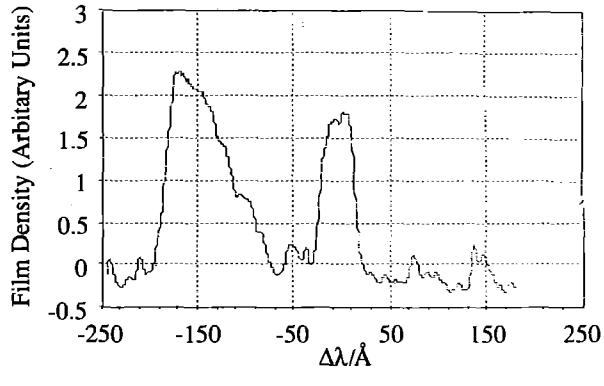

Figure 7 Scattered profile at 15° and 2.6 torr

Time-Resolved Measurement of X-ray Heating in Plastic Foils Irradiated by Intense Soft X-ray Pulses.

J. Edwards, M. Dunne, D. Riley, R. Taylor, O. Willi and S.J. Rose[1]

Blackett Laboratory, Imperial College of Science, Technology and Medicine,
London SW7 2BZ U.K.
[1]Rutherford Appleton Laboratory, Chilton, Didcot, Oxon. OX11 0QX U.K.

INTRODUCTION

With the use of modern high-power laser systems, it is now possible to generate intense, approximately Planckian X-ray sources. These are currently of considerable interest as possible driving power sources for indirect drive Inertial Confinement Fusion. In addition, they may be used for the production of uniform, gradient-free, hot, dense plasmas which cannot be produced by other means in the laboratory and which are ideal for the testing of theoretical calculations of for example opacities, radiative transfer and dense plasma effects which are important for laborartory as well as astrophysics research. Therefore, an understanding of the interaction of intense, soft X-ray pulses with targets is important for the design and interpretation of future experiments. Few experimental studies using X-ray heating of plasmas alone have been reported. The opacity of a radiatively-heated aluminium plasma, close to local thermodynamic equilibrium (LTE), has been measured in the region of the aluminium K-shell transitions[1] and evidence of radiation waves in gold foils has been observed.[2] In this report we summarise the first measurements of X-ray heating as a funtion of time and depth in plastic foils irradiated by intense, approximately Planckian soft X-ray pulses emitted from separate, laser-irradiated, high-Z converters.[3] Plasma temperatures were measured with a novel, time-resolved, XUV absorption spectroscopy technique in the sub-keV photon energy region using L-shell transitions of chlorine ions present in thin tracer layers buried at different depths in the targets.

EXPERIMENTAL

Six frequency doubled (0.53μm wavelength) beams from the VULCAN glass laser at the Rutherford Appleton Laboratory (RAL) were used in a cluster configuration to irradiate a thin gold layer, 1000A thick, supported on a 1μm plastic (CH) substrate, (hereafter the burnthrough or source target). Random phase plates designed and developed in the RAL Laser Division were used to produce a smoothed focal spot which was measured to be 500μm FWHM in diameter by an X-ray pinhole camera filtered for photons in the 1keV energy region. The laser pulse length was typically 800ps in duration. The soft X-rays transmitted through the rear of the burnthrough target were used to heat a separate planar CH foil, 2μm thick, positioned parallel to the burnthrough foil and separated from it by approximately 250μm. A thin chlorinated tracer layer ($C_8H_6Cl_2$), 0.3μm thick, was buried at different depths in the CH foils. The soft X-rays transmitted through the target were analysed using time-resolved, flat-field, XUV spectroscopy in the 50A spectral wavelength region.[4] The temporal and spectral resolutions were approximately 50ps and 0.3A respectively. A pair of parallel, highly polished fused silica mirrors were used in front of the spectrometer to act as a cut-off filter for X-rays with energies above about 600eV to reduce multiple order effects.

MODELLING

The experimental conditions have been simulated with a multi-group radiation transport model coupled to the 1D Lagrangian hydrodynamics code MEDUSA.[4,5] In the calculations, a CH foil was heated with an X-ray pulse whose temporal behaviour was that measured experimentally from the rear of a burnthrough foil when no sample target was present for similar experimental conditions. At the peak of the X-ray pulse, the spectrum was assumed to be Planckian. The introduction of additional spectral features to simulate M, N and O-shell emission was found to have little effect on the results. The X-ray conversion efficiency from the burnthrough target was estimated from time-resolved and time-integrated XUV photodiode measurements taken under similar experimental conditions on VULCAN when a value of 5.5±2% was found.[6,7] The value used in the 1D simulations was adjusted to give best agreement with the experimental measurements to account for the geometrical coupling of the source emission to the target and variations in the conversion efficiency.

In order to perform a detailed spectral analysis of the experimental data we have developed a spectral analysis package (SAP) containing an extensive atomic data base (oscillator strengths, level and transitions energies) generated by a multi-configuration Dirac-Fock (MCDF) atomic physics code.[8] The generation of the atomic data bases is largely automated so that SAP could be used for any LTE plasma of interest. Extensions to the model to allow approximations of absorption/emission by non-LTE plasmas is in progress. Temperature and density gradients are allowed for in the model but velocity gradients and non-LTE line-transfer are not included. Plasma conditions are inferred by comparing the predicted spectra with those observed experimentally. Calculations were performed for the tracer layer only. The remainder of the target introduces no discontinuous absorption features in the energy range of interest and only affects the slope of the underlying continuum as verified when targets with no tracer layers were used. The analysis is based mainly on 2p-3d transitions of F-like to S-like chlorine ions.

RESULTS

Figure 1 shows a comparison between streaked spectra obtained from targets with the 0.3μm tracer layer buried 0.2μm (left) and 1.8μm (right) below the surface of a 2μm CH target. The laser irradiance in these cases was 2×10^{14} Wcm^{-2}. Assuming a 5% conversion efficiency this corresponds to an X-ray flux of approximately $2\text{-}5\times10^{12}Wcm^{-2}$ at the sample. The positions of some 2p-3d transitions of F-like to Na-like chlorine are marked. The broad band of absorption observed at early time is due to 2p-3d transitions in chlorine ions with a partially filled M-shell. The sharp fall in the signal below a wavelength of around 43A is due largely to absorption by a combination of the instrumental filters and the remainder of the target foil.[4,6]

Several distinct differences between the two spectra can be observed. When the chlorinated layer is placed 0.2μm below the front surface of the target (front layer), the band of 2p-3d transitions shifts towards shorter wavelength (higher energy) more rapidly than when the layer is positioned at a depth of 1.8μm (rear layer) indicating a more rapid ionization of the material in the front layer. This can also be seen from the earlier turn on of Na-like and Ne-like absorption features (by ~200-300ps) in the spectrum from the front layer. In addition, the chlorine becomes more highly ionized in the front layer indicating that a higher temperature is attained here. This can be seen from the appearance of F-like absorption features approximately 500ps after the start of the X-ray pulse. In contrast, little evidence is seen for the presence of significant fractions of F-like ions in the rear layer. Also, the 2p-3d Na-like absorption feature remains prominent for the layer at the rear of the target whereas it becomes almost unnoticeable after about 900ps when the layer is positioned near the front surface.

The temperature histories of the tracer layers were inferred as a function of time by comparing the experimental data with detailed, synthetic, absorption spectra calculated by SAP. Figure 2 shows a comparison between the temperature histories inferred from the absorption spectra shown in figure 1 and those predicted by the radiation hydrocode using a "best fit" X-ray conversion efficiency of 2.5%. The solid curves show the range of temperatures predicted by the hydrocode to exist in the tracer layers while the vertical bars show the experimental measurements. The agreement between the experimental results and predictions is reasonably good. These results are discussed in more detail in reference 3.

CONCLUSION

In conclusion, experiments have been performed to investigate the X-ray heating in plastic foils irradiated by intense, approximately Planckian X-ray pulses, generated by separate, laser-irradiated, high-Z converters. The temperature histories of chlorinated tracer layers buried at different depths in the targets were measured with a novel, time-resolved, XUV, absorption spectroscopy technique utilising L-shell transitions of chlorine ions. The temporal temperature profiles were reproduced well by radiation hydrocode simulations. Also, a spectral package for analysing detailed absorption spectra was developed for this work but has much wider applications.

REFERENCES

1. S. J. Davidson, J. M. Foster, S. J. Rose, C. C. Smith and K. A. Warburton, Appl. Phys. Lett. 52, 847 (1988).
2. R. Sigel et. al., Phys. Rev. Lett. 65, 587 (1990).
3. J. Edwards et al., Phys. Rev. Lett. 67, 3780, 1991.
4. J. Edwards et al., Europhys. Lett. 11, 631, 1990.
5. J. P. Christiansen, D. E. T. F. Ashby and K. V. Roberts, Comp. Phys. Commun. 7, 271 (1974). P. A. Rodgers, A. M. Rogoyski and S. J. Rose, MED101: a laser-plasma simulation code. User guide, Rutherford Appleton Laboratory Report RAL-89-127 (1989).
6. J. Edwards et al., Proceedings of the Sarasota Workshop on the Properties of Hot Dense Matter, World Scientific, to be published.
7. C. Back et al., Proceedings of the Sarasota Workshop on the Properties of Hot Dense Matter, World Scientific, to be published.
8. I. P. Grant, B. J. McKenzie, P. H. Norrington, D. F. Mayers and N. C. Pyper, Comp. Phys. Commun. 21, 207 (1980). B. J. McKenzie, I. P. Grant and P. H. Norrington, Comp. Phys. Commun. 21, 233 (1980)

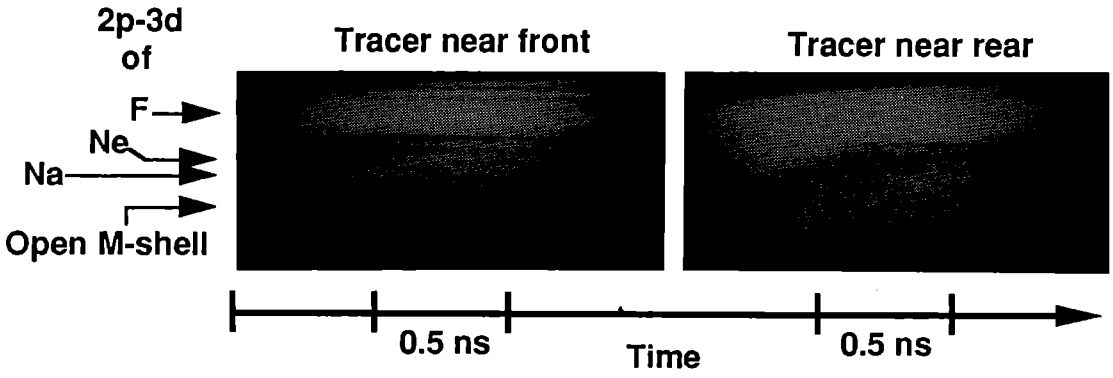

Figure 1. Streaked spectra taken from 2μm plastic targets with chlorinated tracer layers buried 0.2μm (left) and 1.8μm (right) below the surface. Some 2p-3d transitions of F-, Ne- and Na-like chlorine are marked.

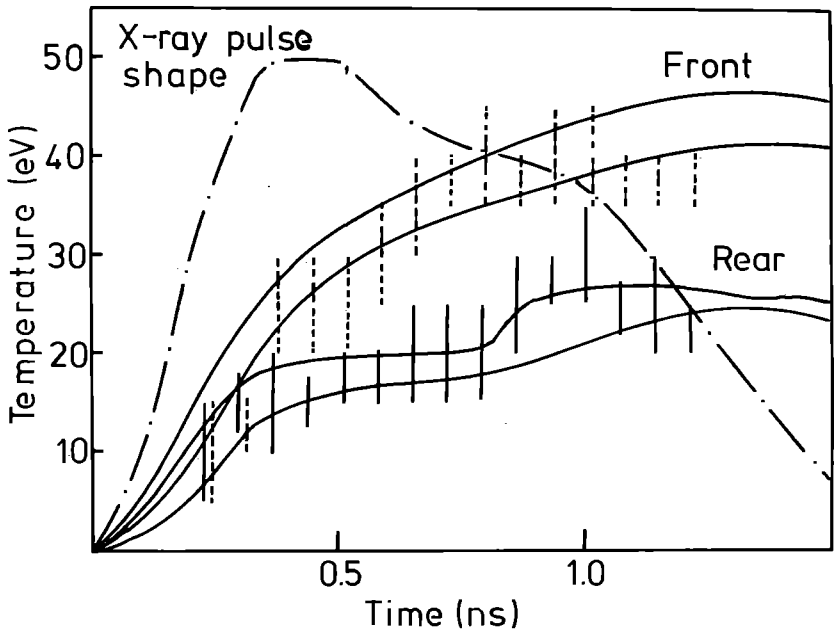

Figure 2. Comparison of experimentally measured temperature histories inferred from the spectra of figure 1 and those predicted by the radiation hydrocode. The X-ray pulse shape is shown.

NONLINEAR LASER INTERACTION WITH LONG SCALELENGTH PREFORMED PLASMAS

M. Desselberger, M. Dunne. F. Y. Khattak, D. Riley and O. Willi

Imperial College of Science, Technology and Medicine, London.

INTRODUCTION

The interaction of intense laser pulses with long scalelength underdense plasmas has been one of the most interesting subjects to plasma physicists due to its relevance to high gain Inertial Confinement Fusion (ICF) targets. The fusion pellet in the envisaged fusion reactor will be surrounded by regions of large underdense plasmas. The interaction of high power pulses with such underdense plasmas gives rise to various instabilities such as the Stimulated Brillouin Scattering (SBS), Stimulated Raman Scattering (SRS), Filamentation and the Whole Beam Self Focusing. These instabilities have deleterious effects on the efficient absorption of the laser energy which is crucial for high gain fusion targets and in the production of very energetic electrons resulting in the preheating of the fusion fuel. In the last few years we have carried out a series of successful experiments[1,2] to study these instabilities under conditions relevant to ICF. Millimeter-sized cylindrical underdense plasmas were generated by irradiating thin foil targets with a number of laser beams in a line focus geometry. A separate laser beam interacted axially with the preformed plasma. In these experiments the plasma generated was relatively cold (about 500 eV) at the time of interaction resulting in some absorption and heating of the plasma due to the interaction beam. In the present set of experiments, the preformed plasma was heated to about one keV by a second set of laser beams which were delayed by about 1ns before the interacting laser pulse was incident on the preformed plasma resulting in a cleaner interaction with less absorption. In addition in the present studies a more energetic interaction beam was used allowing a larger parameter space to be studied.

EXPERIMENTAL ARRANGEMENT

A schematic layout of the experiment is shown in figure 1. Al stripe targets 800μm in length and 400 μm in width having different thicknesses (300nm to 1.5μm) were supported on a 100 nm formvar substrate and irradiated by two opposite pairs of green ($\lambda = 0.53\mu m$) laser beams. These beams smoothed by ISI and RPP systems,

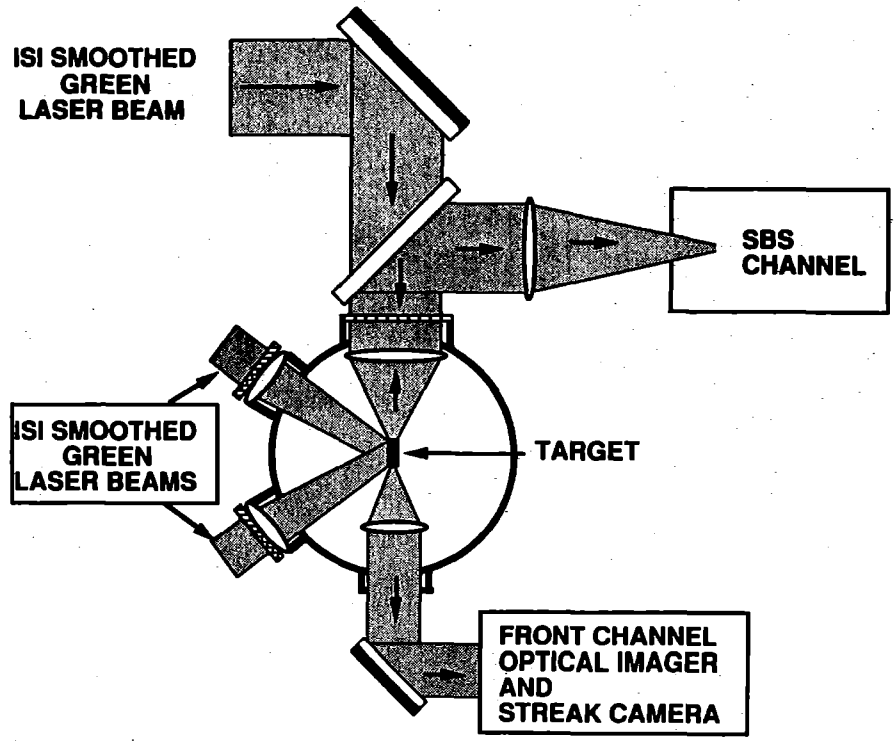

Figure 1: A schematic layout of the experiment.

were focused onto targets, in a line focus configuration, by f/10 lenses resulting in the generation of homogeneous preformed plasmas. Line foci were achieved by tilting the focusing lenses. The length and width of the focal spots were 1mm and 400μm respectively. All the four laser beams were superimposed resulting in a typical irradiance of $5 \times 10^{13} \mathrm{Wcm}^{-2}$ on the target. A pair of beams arriving at the target with various delays from the peak of the plasma generating beams was used to heat the plasma before the interaction beam arrived at the target. The interaction beam, with different time delays from the peak of the heating beams, interacted axially with the expanded and heated plasma. A focal spot of 140μm in diameter was used for the interaction beam. This focal spot was kept constant throughout the experiment. Measurements were made with the broad band, coherent or the ISI and RPP smoothed interaction beam. Irradiance of the interaction beam was varied from $10^{13} \rightarrow 10^{15} \mathrm{Wcm}^{-2}$. By varying the thickness of the target stripe or the interaction beam delay, it was possible to study the interaction physics at different plasma conditions.

DIAGNOSTICS

Beam Characterisation:-

The focal spot of the interaction beam was imaged onto a gated optical imager and an optical streak camera using combination of two lenses. These diagnostics allowed time resolved measurements of the focal spot distribution of the interaction beam to made. The magnification of the image was varied from 40-60 by changing the distance between the two lenses.

Plasma Characterisation:-

Time resolved X-ray spectroscopy was used to measure the plasma conditions. A TLAP crystal spectrometer coupled to an x-ray streak camera was used to find the time history of the hydrogen like (Ly β) and helium like (He β) lines. A spectral and temporal dispersion of 90m$\mathring{A}$/mm and ~100 ps/mm was obtained respectively. The temporally varying intensity ratio of the hydrogen and helium like lines are used in combination with the spectral analysis code (Ration) to obtain the time resolved temperature of the plasma with a temporal resolution of about 100 ps. The density of the plasma was monitored from the Li-like satellites . Our preliminary analysis shows that the temperature and density at the time of interaction were typically 800-900 eV and $10^{20} \rightarrow 10^{21}$. In addition a time integrated crystal spectrometer was also used to observe the x-ray emission.

Stimulated Brillouin Scattering:-

The backscattered light, collected via the focusing optics, propagates back the interaction beam path. A BK7 glass blank was used to split off a small fraction of the backscattered light and was directed towards the SBS diagnostics. A combination of two lenses, a long 5m focal length and a short 1m focal length, was used to focus the SBS signal onto the slit of a 1m Spex spectrograph in order to minimize distortion of the signal due to spherical aberration. A high dispersion (1200 lp/mm) reflection diffraction grating was used in first order giving a spectral dispersion of 5.5 $\mathring{A}$/mm at the spectrometer output. Only time integrated measurements were made. The temperature from the analysis of SBS spectrum is found to be consistent with that obtained from the time integrated spectrometer. The absolute SBS level was measured with a photodiode. Further, a fraction of SBS was split off with a pellicle and directed onto a gentec for comparison. The diode had a sufficient temporal resolution of the scattered light to separate the real signal from reflections off any optical surfaces. An integrated sphere was used in front of the diode as a diffuser to get reproducible output for a given input. The use of calibrated neutral density filters in front of the diode extended its linear range of response. A preliminary analysis shows that the level of SBS does not saturate under the conditions studied.

Whole Beam Self Focusing:-

The interaction beam was imaged out at the output plane of the plasma using the same diagnostics as were used for the beam characterisation. There is some evidence of the WBSF of the ISI smoothed interaction beam but the analysis is still in progress.

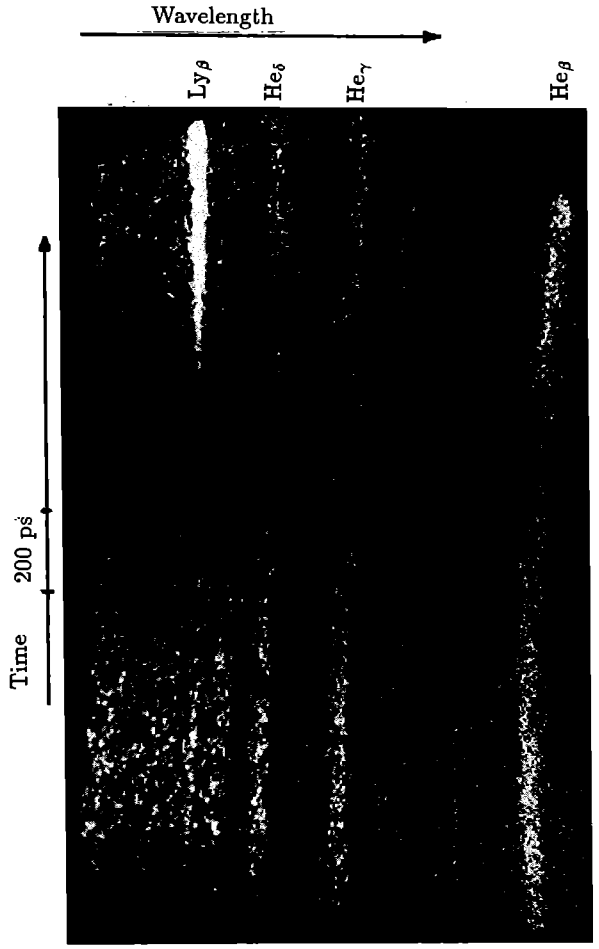

Figure 2: A typical time resolved x-ray spectrum of an Al plasma generated by two opposite pairs of ISI smoothed green laser beams. The interaction beam is timed to arrive 1.5ns after the peak of the plasma generating beams.

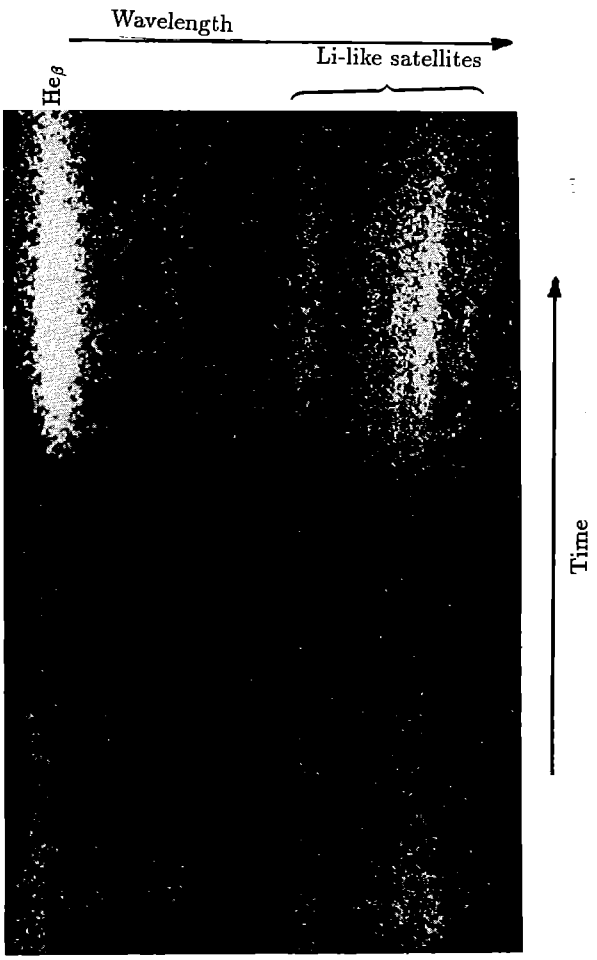

Figure 3: A typical time resolved x-ray spectrum with high spectral resolution, using a Johann crystal spectrometer coupled to an x-ray streak camera. Li-like satellites can be clearly seen to the longer wavelength side of the Heβ transition.

RESULTS

A time resolved x-ray spectrum is shown in figure 2 for a preformed plasma, generated by irradiating an Al stripe target with one set of laser pulses which is interacted axially with an ISI smoothed laser beam. As can be seen the Ly$_\beta$ transition becomes very intense during the interaction implying heating of the plasma during the interaction. In contrast no heating was observed when a plasma was produced and heated with two sets of pulses delayed in time. This shows that no energy is absorbed from the interaction beam with the arrangement used in these experiments. Figure 3 shows an Al spectrum with high spectral resolution which was obtained under similar irradiance conditions. Li-like satellites can be clearly seen. These satellites were used to monitor the plasma density. The analysis is still in progress.

REFERENCES

(1) S.Coe, T. Afshar-rad, M. Desselberger, F. Khattak, O. Willi, A. Giulietti, Z. Q. Lin, W. Yu and C. Danson, "Suppression of instabilities in a long scalelength preformed plasma", Europhys.Lett. 10, 31 (1989).

(2) T. Afshar-rad, L. A. Gizzi, M.Desselbeger, F. Khattak, O. Willi and A. Giulietti, "Evidence of whole-beam self-focusing of induced spatially incoherent (ISI) laser light in large scalelength plasmas", Phys. Rev. Lett., 68, 942, 1992.

MEASUREMENT OF SUPER-CRITICAL DENSITY PROFILES

R.J.Taylor, M.Desselberger and O.Willi
Imperial College of Science, Technology and Medicine

S.Rose
Rutherford Appleton Laboratory

INTRODUCTION

This article describes the implementation of a monochromatic soft X-ray (100eV) imaging system[1] to record time-resolved images of the self-emission from exploding foil plasmas. The level of self-emission can then be related back to the electron density of the plasma with appropriate consideration of the electron temperature and average ionisation state. The X-rays imaged by the system are emitted by the plasma from the high-density, super-critical region, and hence this technique allows us to diagnose density right up to the ablation surface, which is not possible with density diagnostics previously implemented, such as optical probing[2,3] and imaging of optical bremsstrahlung[4]

X-rays are emitted from a hot, dense plasma by three radiative processes: bound-bound electron transitions, free-bound electron recombination and free-free transitions (bremsstrahlung). While bound-bound and free-bound processes are difficult to model because of the many discreet transitions involved, bremsstrahlung emission is related simply to the average ionisation state of the plasma, the electron number density and the electron temperature. (1)

$$\varepsilon_{ff}(\upsilon) = 8.67\text{x}10^{-53}\, n_e n_i\, Z^2\, T_e^{-1/2}\, e^{-(h\upsilon/k_B T_e)}\, G_{ff} \qquad (1)$$

Where $\varepsilon_{ff}(\upsilon)$is the emissivity in watts per cubic meter of plasma per steradian per frequency interval υ, n_e and n_i are the electron and ion number densities in m^{-3}, Z is the average ionisation state, T_e is the electron temperature in degrees Kelvin and G_{ff} is the Gaunt factor, a dimensionless quantity ranging from 1 to about 10, which allows for appropriate cutoffs in the impact parameter and for quantum-mechanical corrections to the classical electron trajectory.

With an appropriate choice of target material and imaging system design, it is possible to record only the bremsstrahlung emission from a plasma. The ionisation state can be predicted by simulations or reference to other work on similar plasmas[5], as can the electron temperature. The dependence of bremsstrahlung on temperature is relatively weak (a factor of 2 error in temperature represents only a factor of 1.5 error in density) and so a reasonable prediction of density can be made by measuring the absolute X-ray flux from the plasma.

EXPERIMENTAL DESIGN

The imaging system's key element is a multi-layer coated spherical mirror, which reflects only a narrow (10eV) band of soft X-rays. Since we wished to record only the bremsstrahlung emission of the exploding foils, we selected a target/mirror combination such that the plasma emitted only bremsstrahlung around the wavelength of the mirror. Prior to the experiment, mirrors were obtained on the basis of predictions made by the opacity code IMP (Ionised Material Package). IMP predicted that a Selenium plasma similar to those we expected to produce would have no bound-bound or bound-free transitions around 97eV, ie the emission would be dominated by bremsstrahlung.

On the basis of these predictions, targets ware obtained in the form of narrow (100μm) stripes of Selenium supported on 0.1μm Formvar for support. The stripes were coated to various thicknesses from 1μm to 0.125μm.

Since the system was being designed to image bremsstrahlung, we knew that our plasmas would be optically thin at the wavelength at which we observed them, and hence we knew that only an insignificant fraction of the self-emission would be re-absorbed over the small depth of the plasma.

Spectral characterisation of both the mirror and the plasma to be imaged was carried out to confirm that the mirror/target combination was correct. In TA4, a flat-field spectrometer fitted with a 1200 lines/mm grating was used to spectrally locate the reflection from the mirror of a gold plasma, which was roughly constant and continuous around the 100eV region. Short wavelength emission from the gold was filtered out using a double gold reflection filter to prevent higher-order reflections from the grating confusing the spectrum. This characterisation confirmed that the mirror's peak reflectivity was at 97eV. The same spectrometer setup was used in TA2 to characterise the Selenium plasma, and this confirmed that the only emission at the wavelength of the mirror was bremsstrahlung. The spectra were recorded on Kodak 10107 film and can be seen in figure 1.

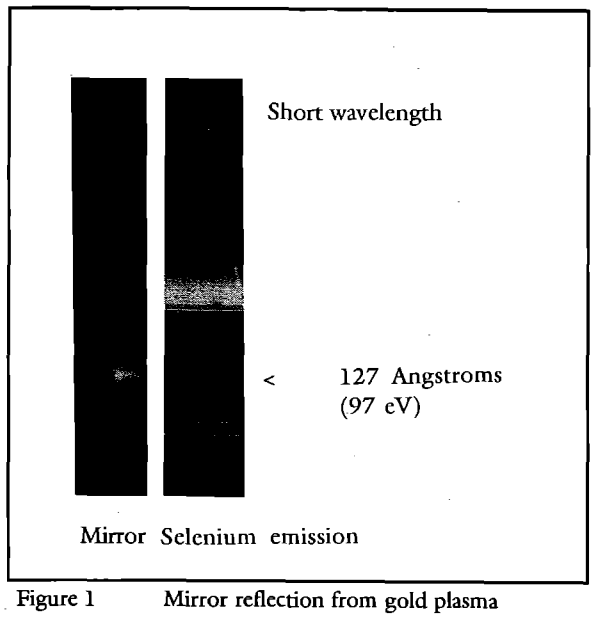

Figure 1 Mirror reflection from gold plasma compared to Selenium emission spectrum.

EXPERIMENTAL APPROACH

The imaging system was set up in TA2 using the backlighter beam of Vulcan at 108mm. The beam was frequency doubled to green (0.53μm) and then split into two, each half focussed with an f2.5 lens onto the foil. The drive was normal to the foil, each side illuminated with equal irradiance (around $5\text{x}10^{13}$ Wcm^{-2}) in 250μm focal spots.

The mirror axis was aligned parallel to the foil, so that it produced an edge-on image at 46x magnification in a plane 2.3m from the target. A 4mm copper disc was placed close to the target on the opposite side from the mirror to prevent direct X-rays from reaching the detector, and the mirror was aligned so that most of the mirror signal passed around the block. When a detector sensitive to optical light was used, a thin aluminium foil (0.1μm thick) was placed in the path of the mirror signal to remove optical scatter.

To record the emission from the plasma, 3 detectors were used. A gated X-ray imager provided 2-D images of the foils (150ps gate time) which showed that the irradiation was uniform. An X-ray streak camera was then used to record temporally resolved (50ps resolution) 1-D images of the width of the foil. Such an image is shown in figure 2 for a 0.125μm Selenium foil. The streak camera records the relative intensity of the X-rays incident on the photocathode, thus providing a relative density profile. In order to extract the absolute density profile, it is necessary to quantify the number of photons emitted by the plasma. To this end, a calibrated X-ray diode was used in place of the streak camera on identical shots, to provide a time-resolved (<50ps resolution) record of the absolute X-ray flux being reflected by the mirror. This, considered with the reflectivity of the mirror (yet to be accurately characterised) will provide an absolute measure of the number of emitters in the plasma.

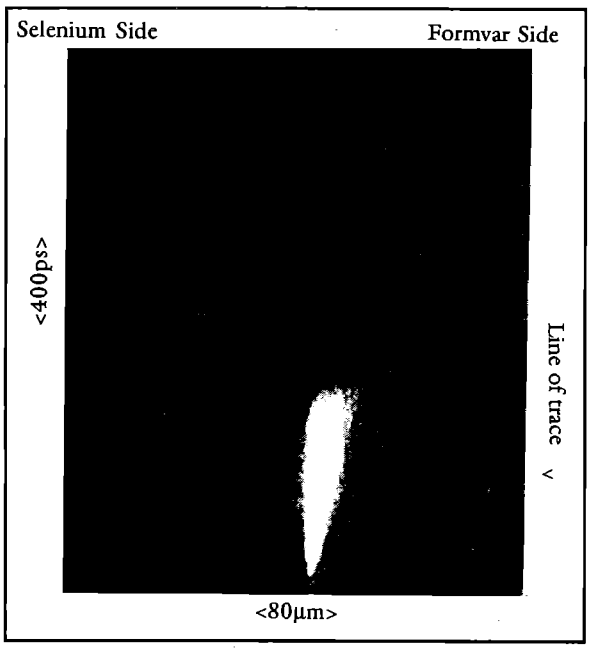

Figure 2 Streak record of 0.125μm Selenium foil irradiated by $5x10^{13}$ Wcm^{-2}

Seperate characterisations of exploding Selenium foils[5] suggest an electron temperature of around 500eV and a roughly Neon-like system for the conditions in our plasmas, and so when the mirror reflectivity has been characterised, an absolute density profile will be avaliable. For now, however it is possible to diagnose the relative profile, as shown in figure 3 for the peak emission from the Selenium streak record.

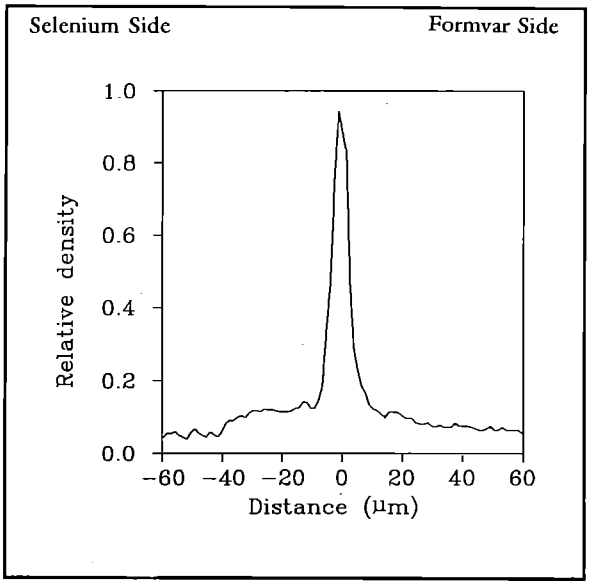

Figure 3 Plot of relative density 300ps after start of emission (taken from a trace along the line shown in figure 2)

REFERENCES

1. M. Desselberger, T. Afshar-Rad, F. Khattak, S. Viana and O. Willi, Appl. Opt. **30**, 2285 (1991).
2. O. Kafri and J. Krasinski, Appl. Opt. **24**, 2746 (1985).
3. M. D. Rosen *et al.*, Bull. Am. Phys. Soc. 27,989 (1982); W. B. Fechner *et al.*, Phys. Fluids **27**, 1552 (1984).
4. D. W. Phillion *et al.*, LLNL Annual Report 1984.
5. M. D. Rosen *et al.*, Phys. Rev. Letts **54**, 106 (1985).

RAYLEIGH-TAYLOR INSTABILITY IN PLANAR FOILS BY ALPHA PARTICLE RADIOGRAPHY

A. P. Fews, M. J. Lamb*, M. Savage*, C. Regan*

H. H. Wills Physics Laboratory, University of Bristol, Tyndall Avenue, Bristol
* Department of Pure and Applied Physics, Queens University Belfast

INTRODUCTION

We have previously described the technique of alpha particle radiography[1,2,3], and how this may be used to determine the mass distribution in laser accelerated planar foil targets. Here we report on progress made in the analysis of alpha radiography data from seeded foils driven by a smoothed laser beam.

Briefly, the experimental technique is as follows. A pulsed source of thermonuclear alpha particles is produced by the 12-beam implosion of a deuterium-tritium filled glass microshell. These alpha particles then pass through a nearby laser accelerated planar foil target and are detected on a sheet of CR-39 plastic nuclear track detector. The position and energy of each alpha particle passing both through and around the foil are then measured. From this data the redistribution of mass in the foil, caused by the Rayleigh-Taylor hydrodynamic instability, may be determined.

CH foils of 550μm diameter and 8μm thickness were driven by a 2ns long smoothed 0.53μm laser beam at irradiances 1-5.10^{13}W.cm^{-2}. Beam smoothing was achieved both by the use of a random phase plate (RPP) and also by the combination of ISI and RPP. RPP smoothing was also used on the implosion drive beams to produce small α-particle cores having narrow energy spectra. Both planar foils, and seeded foils having 1μm deep rectangular grooves with

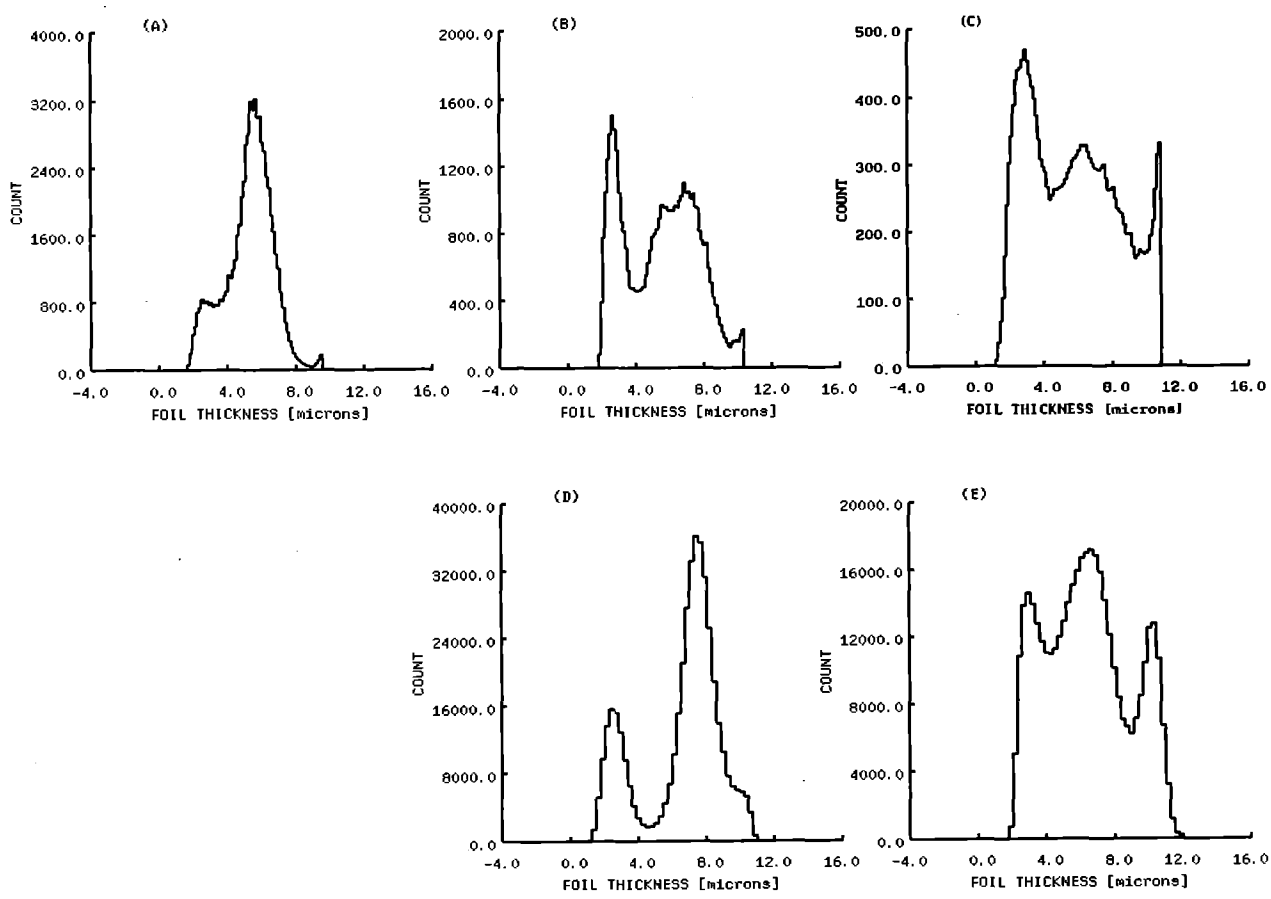

Fig 1. A set of thickness spectra of foils driven by ISI+RPP smoothed beams of irradiance ~2·5.10^{13}W.cm^{-2}, probed at times (a) 0.5,(b) 1.0 and(c) 1.5 ns, for a foil with 20μm wide seed cuts. The POLLUX simulations of (b) and (c) are shown in (d) and (e) respectively.

spatial separations 10μm and 20μm were used. A comprehensive set of α-particle radiographs of such foils was obtained, probed at times 0.5, 1.0, 1.5 and 2.0 ns.

SIMULATIONS

In order to compare the experimental data with the computer simulation we have developed a code RANGER to post process the output from the 2D Eulerian hydrocode POLLUX. POLLUX is used to simulate the hydrodynamic development of a laser accelerated rippled foil corresponding to the conditions of the experiment. The output includes 2D arrays of plasma density and temperature as a function of time. RANGER takes these density and temperature values at the relevant probe time, and using hot matter stopping power data supplied by Dr. S Rose (RAL), determines the energy lost by α-particles having a range of initial energy passing through all points of the plasma. The code takes the experimentally measured source range spectrum from the CR-39 data, and using the energy loss calculated above, determines the predicted range spectrum for particles which have passed through the foil. This predicted spectrum is then unfolded in exactly the same way as the experimental range data to yield a thickness distribution for direct comparison with the experimental results.

RESULTS

Fig 1 shows a set of thickness spectra of foils driven by ISI+RPP smoothed beams of irradiance ~2·5.10^{13}W.cm^{-2}, probed at times (a) 0.5,(b) 1.0 and(c) 1.5 ns, for a foil with 20μm wide seed cuts. The POLLUX simulations of (b) and (c) are shown in (d) and (e) respectively. The measured thickness spectrum stops at ~11μm, corresponding to α-particles being stopped in the foil. The number of particles missing, due to this high foil thickness cutoff (low particle energy) is typically less than 20%, and does not affect the interpretation of the of measured portion of the spectra, as shown. The particles stopped in the foils in the POLLUX simulations are not plotted.

Fig 2 shows a set of thickness spectra of foils driven by ISI+RPP smoothed beams of irradiance ~2·5.10^{13}W.cm^{-2}, probed at times (a) 0.5,(b) 1.0 and(c) 1.5 ns, for a foil with 10μm wide seed cuts. The POLLUX simulations of (b) and

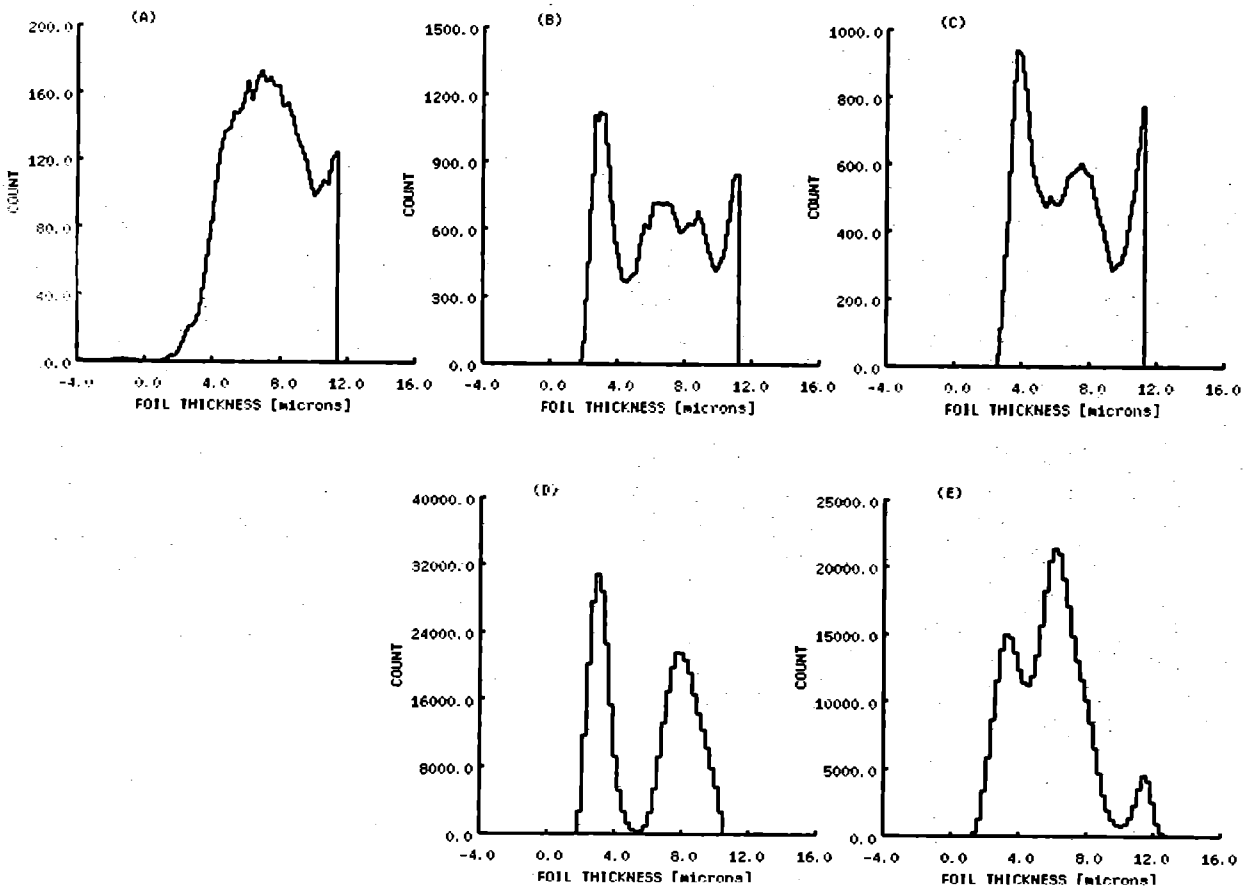

Fig 2. A set of thickness spectra of foils driven by ISI+RPP smoothed beams of irradiance ~2·5.10^{13}W.cm^{-2}, probed at times (a) 0.5,(b) 1.0 and(c) 1.5 ns, for a foil with 10μm wide seed cuts. The POLLUX simulations of (b) and (c) are shown in (d) and (e) respectively.

(c) are shown in (d) and (e) respectively. This corresponds to the data for 20μm spaced modulations shown in Fig 1. This set of data shows a greater modulation than the Fig 1 data, especially at 0.5ns. Both the three measured spectra shown here, and other similar data, all show a sharp cut at ~11μm corresponding to the stopping of the particles, and shows that a greater fraction of the foil has these or greater thicknesses, in comparison to the 20μm spacing data in Fig 1.

The measured and predicted spectra are similar, with the central peak well predicted in all four simulations. The peak at high foil thickness in the measured spectra is close to the low energy cut off of the α-particles, and is within 2μm of stopping the particles altogether. The accuracy of the spectral shape in the ~5 bins approaching this region is therefore likely to be degraded. Thus Fig 1 (d) and (e) are both very close matches to the measurement. Fig 2 (d) and (e) are not as close, with the peak at high foil thickness not predicted by POLLUX. All the measured spectra in Fig 2 show this feature.

Fig 3 shows a set of thickness spectra of unseeded, planar foils driven by ISI+RPP smoothed beams of irradiance ~2·5.10^{13}W.cm^{-2}, probed at times (a) 0.5,(b) 1.0 and(c) 1.5 ns. The results can be compared to the seeded foil thickness spectra shown in Figs 1 and 2. Significant foil modulations can be seen to be induced even for these unseeded foils. Undriven foils typically show a narrower distribution than the 0.5ns example of an unseeded foil in Fig 3(a). These spectra are less structured than those from the seeded foils, and typically show a general broadening at increasing times, with a peak at low thickness only developing at times 1.5ns or later. This smooth broadening of the spectra probably results from the lack of seeding in the foils rather than the use of unsmoothed drive beams, since we found earlier[1,2,3] that seeded foils driven by unsmoothed beams showed structure similar in appearance to the seeded foils driven with smoothed beams shown here in Figs 1 and 2. A greater part of the foil is driven to thicknesses greater than the ~11μm cutoff than for the seed foils. The modulations are probably due to growth from remaining modulations in the irradiance of the drive beam, and as such cannot be modelled.

CONCLUSIONS

It is interesting to observe that the driven foils tend to produce a large modulation at early times. At later times, the number of particles in the satellite peaks increases, but the modulation does not.

In general, the simulations under represent the fractions of the foil thickness at both high and low thicknesses. In particular, the peak at high thickness is not predicted well especially for the data in Fig 2, despite consistently appearing in both the measurements shown here and in other data we have analysed.

At 0.5ns clear features in the measured spectrum are already developing in Figs 1(a) and 2(a), which are well separated from the central peak. We will generate the simulations at this time, and plan experiments to measure the initial growth phase of the Rayleigh-Taylor instability more closely. The α-particle technique is ideal for this because any spatial scale of modulation will be recorded in the thickness spectra, as a direct measure of induced mass modulation, regardless of whether or not it can be spatially resolved.

We wish to thank the staff of the VULCAN laser for their assistance in the conduct of these experiments.

REFERENCES

1. A. P. Fews, M. J. Lamb, M. Savage, Central Laser Facility Annual Report 1990, Rutherford Appleton Laboratory Publication RAL-90-026, pages 31,33 and 36.
2. A. P. Fews, M. J. Lamb, M. Savage, Central Laser Facility Annual Report 1991, Rutherford Appleton Laboratory.
3. A. P. Fews, M. J. Lamb and M. Savage, (1992), "Study of Rayleigh-Taylor Instability by Alpha Particle Backlighting", submitted to Laser and Particle Beams.

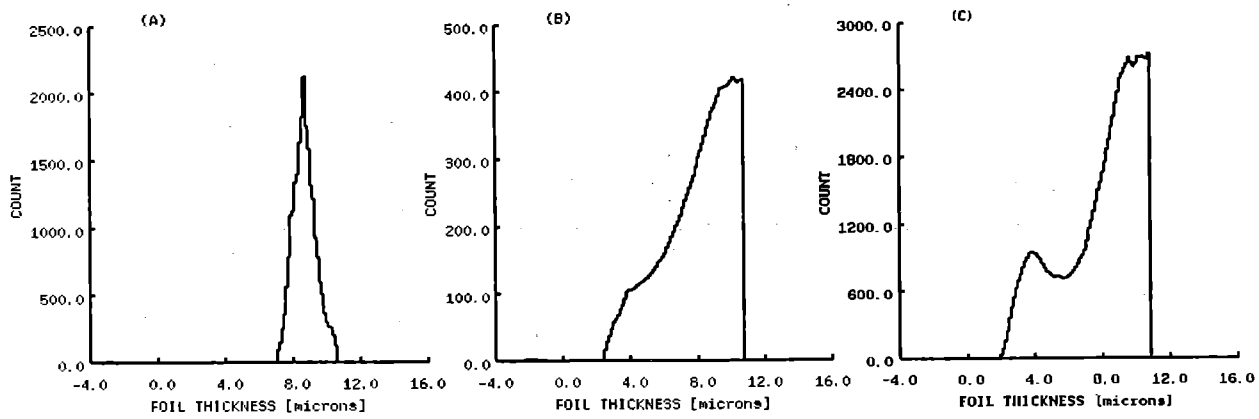

Fig 3. A set of thickness spectra of unseeded, planar foils driven by ISI+RPP smoothed beams of irradiance ~2·5.10^{13}W.cm^{-2}, probed at times (a) 0.5,(b) 1.0 and(c) 1.5 ns. The results can be compared to the seeded foil thickness spectra shown in Figs 1 and 2. Significant foil modulations can be seen to be induced even for these unseeded foils.

THREE DIMENSIONAL IMAGING OF IMPLOSIONS, AND OTHER RECENT DEVELOPMENTS

A. P. Fews, M. J. Lamb*, M. Savage*, C. Regan*

H. H. Wills Physics Laboratory, University of Bristol, Tyndall Avenue, Bristol
* Department of Pure and Applied Physics, Queens University Belfast

INTRODUCTION

We have previously reported[1,2,3] the development of a high yield source of implosions based on DT filled glass shells. These NUHART implosions generated a 20 times enhancement in yield by a deliberately non-uniform laser irradiation pattern generating particle yields of up to 3.10^9. The enhanced yields are produced from the convergence of strong shocks, generated from the localised increases in target irradiance. In this work, we report on recent studies of these implosions and a comparison with high aspect ratio targets uniformly driven by random phase plate smoothed drive beams. Results of direct α-particle and X-ray core images are presented, together with novel results from our recently developed 3D image deconvolution. These give new insight into the emission core structure and particle yield which are not accessible by conventional 2D imaging. These implosions are applied as sources of particles in the study of Rayleigh-Taylor instability and in measurements of plasma stopping power.

The targets used were high aspect ratio glass microballoons of diameter ~550–650μm and wall thickness 0.6-1.6μm filled with 2-5 bar of Deuterium-Tritium (DT) gas. Drive energies of up to 800J, λ=0.53μm, were used in pulse lengths 600-900ps. Two different methods of target illumination were used. In the NUHART mode, the 12 VULCAN laser beams were focused onto the target surface such that ~1/3 of the shell area was illuminated. The second method used a uniform drive, with tangential focusing using drive beams smoothed by random phase plates with a circular zone pattern.

The thermonuclear particle images were recorded in CR-39 plastic track detector and deconvolved by a maximum entropy procedure[2,5]. This technique generates high quality reconstructions containing optimum spatial resolution with low noise, and are safely generated such that the only features present in the reconstruction are those required to maintain statistical consistency between the reconstruction and the measured image.

THREE DIMENSIONAL IMAGING

In order to study the implosion cores in detail, a three dimensional deconvolution of the α-particle emission has been developed. In this procedure, a set of three or four α-particle penumbral cameras are distributed around the target. A tetrahedral arrangement is used in the case of four views. The position of each particle in each image is determined, and used by the analysis in a global maximum entropy treatment, generating a cube of the 3D particle emissions. This is analogous to computed tomography in which sections through the 3D object (rather than just projected views) are obtained.

The 3D images generated give better indications of core structure, since any features will be separated provided they are resolvable with any of the data. All of the data is included in the maximum entropy analysis simultaneously, with correct statistical weighting. In contrast, much of the structure in ordinary 2D images is lost, both because features at different depths tend to be superimposed and due to the fact that constraints on a given view due to data in the other imaged directions can only be applied in the 3D treatment.

Typical results are presented as images, each representing a 2D slice through the 3D result. Summation (projection) of these slices in the viewing direction gives the corresponding result to the 2D analysis. Fig 1 (next page) shows a set of 10μm thick slices through the core of an implosion. This shot was from an RPP driven implosion, and is unusual in containing so much structure, with a bright region of emission to the left, separated from the main core. It is interesting to note that this shot gave the best performance with respect to the model[3], with a correspondingly larger core size and temperature, although the beam balance was no better than for other comparable shots. This is discussed in more detail in the next section. Such structure is only evident from the 3D images.

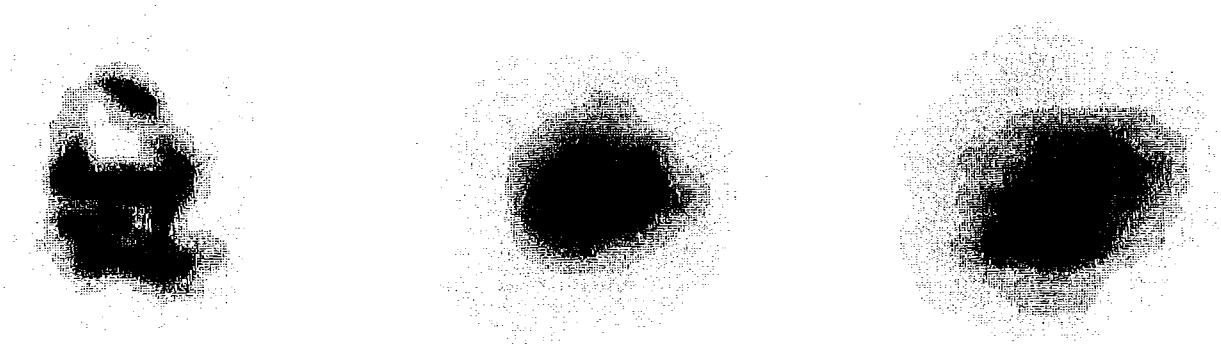

Fig 2. (a) Left. Typical NUHART 2D α-image showing typical core structure. (b) Centre. Typical RPP 2D core. (c) Right. a section through the 3D image of the shot shown in projection in (b). No 3D structure is found, in contrast to the shot shown in section in Fig 1. Scale 20mm to 100μm.

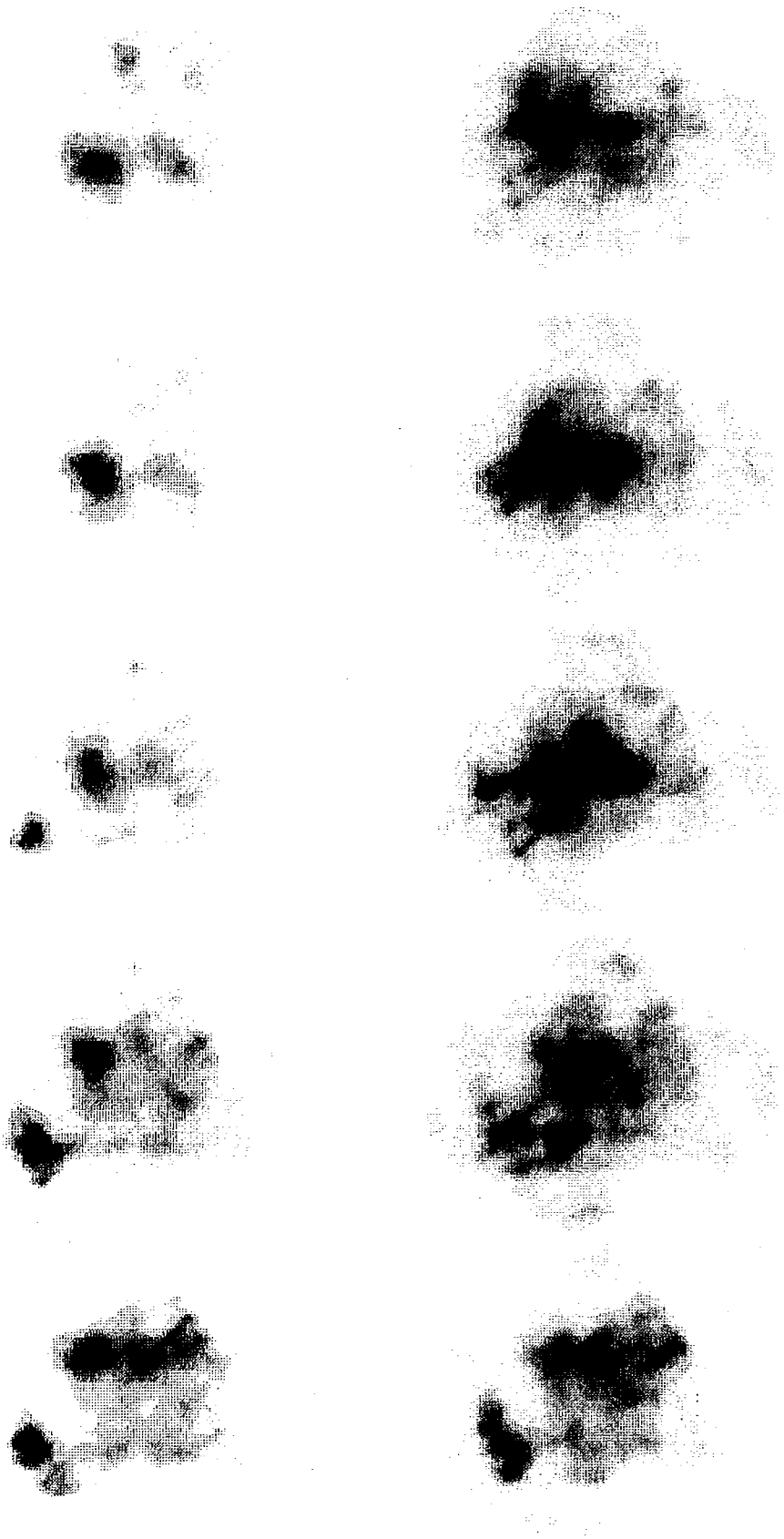

Fig. 1. A 3D α-particle core image. The 3D image is presented as 10 2D slices showing the emission intensity distributed through the core. The slices are 10μm apart. The sequence starts at the top left and finishes at top right, the central sections being at the bottom of the page. Scale 15mm to 100μm.

Fig 2 shows some further image comparisons. Fig 2(a) shows a 2D projection image of a NUHART core, typical in size and structure. Fig 2(b) shows a typical 2D projection image of an RPP core, with significantly less structure. Fig 2(c) shows a section through the 3D core of the projection shown in (b). Little structure is observed. This can be compared to the RPP sections in Fig 1. More structured cores, as in Fig 1, perform better than the less structured cores, in contrast to NUHART implosions where both core size and structure do not correlate with target performance.

ALPHA AND X-RAY IMAGE COMPARISONS

The implosions were studied using 3 near orthogonal X-ray pinhole cameras and 3-near orthogonal alpha particle cameras with 2 alpha-particle cameras diametrically opposing 2 X-ray cameras. The spatial resolution of the X-ray images and the alpha-particle images was 10-15μm and 5-10μm respectively. The α-particle and hard X-ray (>5 KeV) cameras are diametrically opposed and should see an identical mirror image view of the target since both the hard X-rays and α-particles will easily escape from the target since both are isotropically produced.

Fig 3 shows 3 near orthogonal α-particle images and the corresponding set of X-ray images from the same NUHART implosion. The α-particle and X-ray images in (a) and (b) were exactly opposed and in (c) were nearly opposed. Shots driven by random phase plates produced small cores typically ~50μm, while core produced by NUHART implosions are typically a factor ~2 larger than this. As in the X-ray images, α-core sizes vary in shape, many are elongated and they may contain smaller features within them. Images from the same shot but taken from different directions may differ in size, shape and detailed structure. In general less structure occurs in shots driven by random phase plates. X-ray and alpha particle images taken from opposite directions are usually of similar size. The finer structure in the alpha images is often not apparent in the corresponding X-ray image although in some cases, core shapes such as elongated cores occur in both images.

THERMONUCLEAR YIELD DATA

Thermonuclear alpha particle yields of up to 3×10^9 have been obtained from NUHART mode implosions.; and uniform RPP implosions have given yields up to 1×10^9. Many thin walled targets although giving moderate yields have not produced the yields predicted by the model[3] and this was believed to be caused by the total ablation of the shell wall during the laser pulse. Here we give our recent analysis of the results.

The thickness of wall ablated during the laser pulse was calculated using standard mass ablation data[4]:

$$M_a(gcm^{-2}s^{-1}) = 0.77.10^5\,(\lambda/1\mu m)^{-0.82}\,(I_a/10^{13}Wcm^{-2})^{0.48}\,(r/100\mu m)^{-0.11}$$

where I_a is the irradiance on target, λ is the laser wavelength and r is the target radius. Account was taken of the enhanced irradiance achieved in the non-uniform illumination of a target in the NUHART mode.

A figure of merit was awarded to each data point based upon the difference between the actual yield achieved in the implosion and that predicted by the model. Shots with a relatively high figure of merit performed well. The figure of merit is effectively the log of the ratio of the experimental yield to the prediction, with an arbitrary origin. A graph showing how the figure of merit varies with the wall thickness after ablation is shown in Fig 4, indicating that the

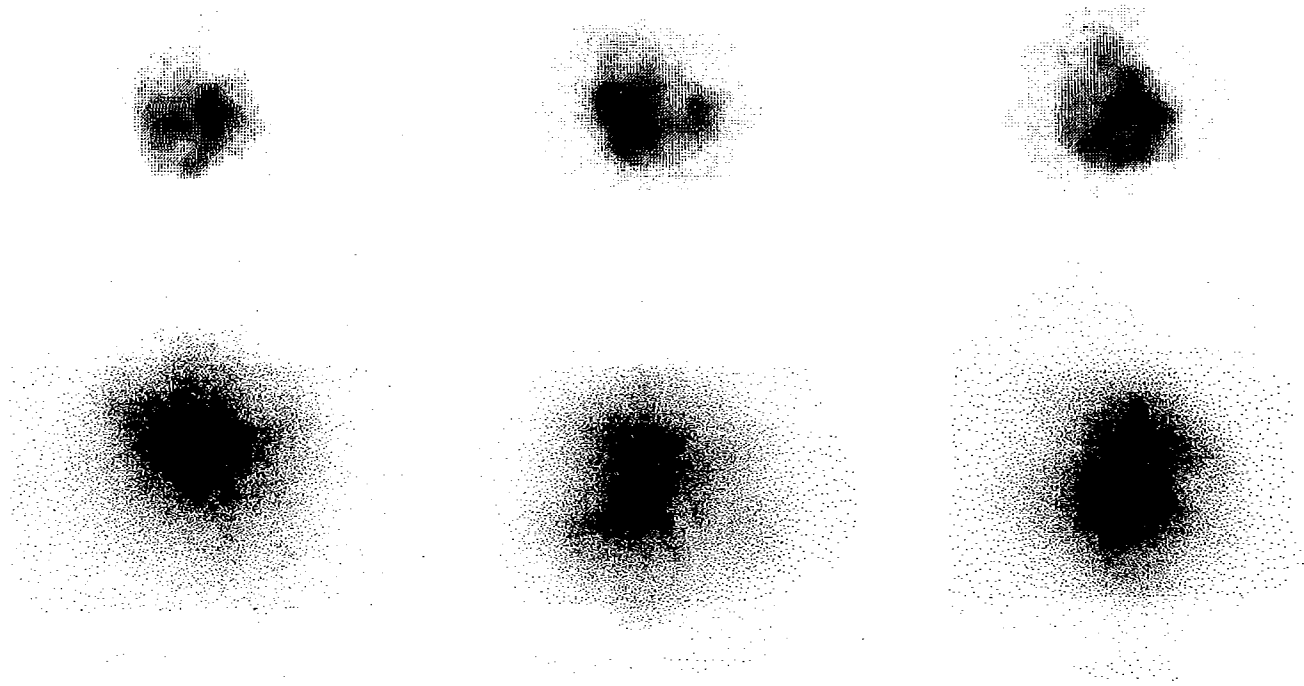

Fig 3. A comparative set of three near orthogonal α-particle (top) and X-ray(bottom) images. The first two α and X images are exactly opposed and should therefore correspond to mirror images of the same view. The third pair is nearly opposed. Scale 10mm to 100μm.

burn through of the shell wall is reflected by poor target performance. It is clear that the NUHART implosions are well predicted by this relationship with the final wall thickness and tightly distributed about the trend line, and that the smooth trend indicates a progressive loss of performance of all the targets and not just the thinnest. However the RPP data are more distributed. This is not due to uncertainties in the amount of energy reaching the target, since the appearance of these data on the plot can be predicted from core size and temperature measurements - as described earlier, RPP shots with wall structure similar to Fig 1 perform better and are at the upper edge of the distribution. Thus, although the aspect ratios are the same in both cases, ~200-400, variations in these targets occur which are not seen in the NUHART case and are not predicted from the shock convergence model.

Also of interest are the different trends that appear within each data set. Fig 5 shows the variation of thermonuclear yield normalised to a target diameter of 550μm and wall thickness of 0.9μm plotted against the average irradiance on target. Shots in which the shell wall is likely to have been burned through are not included in this plot, reducing the scatter in the graph. The random phase plate data points lie below the NUHART line by approximately the factor of 20 that represents the yield enhancement of yields conventional uniform drive.[3] Wall ablation has the effect of increasing the target aspect ratio, improving the yield, but decreasing the amount of light reaching the inner target surface before the target is de-coupled from the drive and reducing the shock strength. This latter effect tends to be

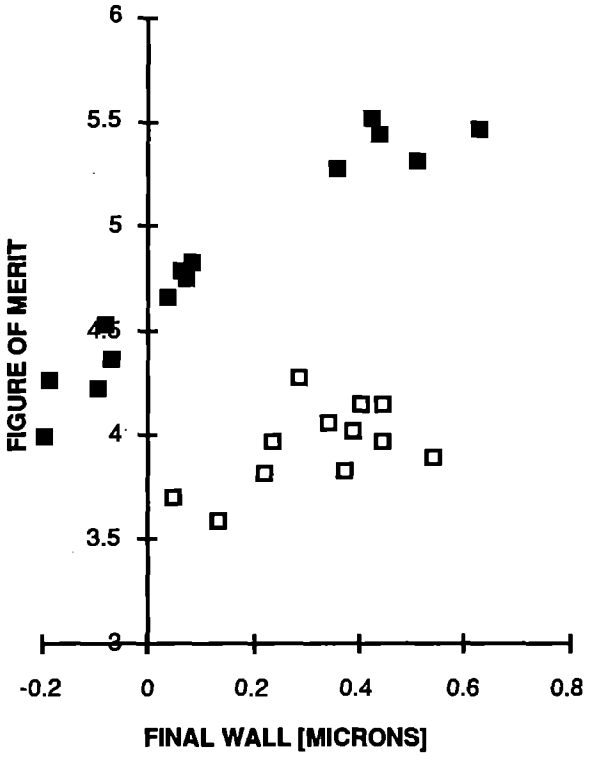

Fig. 4. The variation of Log of yield normalised with respect to NUHART shock model, with the final target wall thickness after ablation. Solid points show NUHART drive, open points show RPP smoothed drive.

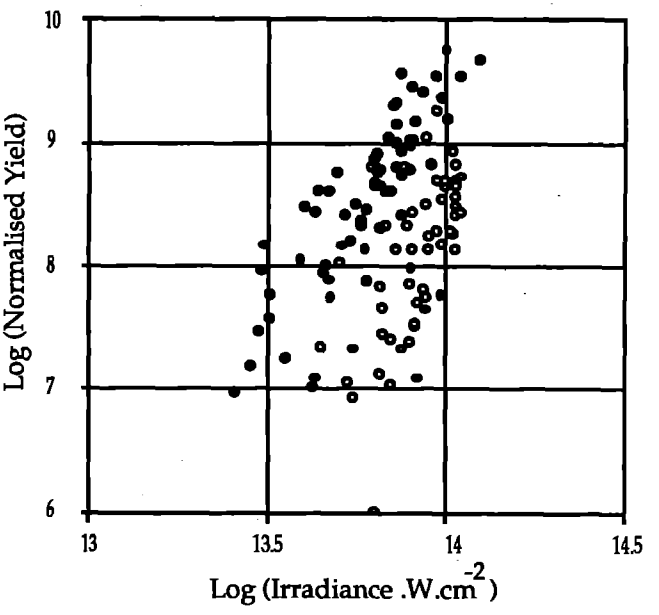

Fig 5 Scaled particle yield versus irradiance for NUHART (solid points) and RPP (open points).

larger and thus although very thin walled targets perform better than thicker targets in absolute terms, they tend to under perform relative to our original model. Optimum yield is obtained when the drive energy is sufficient to ablate most but not all the target wall in a pulse length matched to the implosion time.

It is interesting to note that the small amount of scatter in the NUHART data in Fig 4 demonstrates that particle yield can be totally predicted from target geometry and total drive energy, and that neither beam balance nor core size has any noticeable correlation with performance. However the RPP data do show such a correlation, the better shots all giving larger more structured cores.

Unlike the RPP data, the NUHART shots show a comparatively large $\rho.R$ and $\sigma(r.R)$which indicate as expected that large areas of the shell do not participate in the implosion and that shock convergence does not carry all the shell inwards. The core temperatures, determined from the Doppler broadening of the particle spectra are in the range 1-5KeV for the RPP data, with a mean ~2KeV. The temperatures scale according the predictions of the shock drive model[3]. The $\rho.R$ spectra from the RPP data shows none of the structure evident in the NUHART data.

REFERENCES

1. A. P. Fews, M J Lamb, M Savage, Central Laser Facility Annual Report 1989, Rutherford Appleton Laboratory.
2. A. P. Fews, M J Lamb, M Savage, Central Laser Facility Annual Report 1990, Rutherford Appleton Laboratory Publication RAL-90-026, pages 31,33 and 36.
3. M H Key, M J Lamb, A P Fews et al. Opt. Comm., 71, (89), 184.
4. M H Key, Rutherford Laboratory Report RAL-89-055 (1985) "Energy Transport in Laser Produced Plasmas."
5. A. P. Fews et al, (1992c), Thermonuclear Particle Imaging by Maximum Entropy, submitted to Optics Communications.

ANALYSIS OF NEUTRAL ATOM EMISSION FROM PLANAR TARGETS.

R. Evans, T. A. Hall, Z. Ahmad, Y. A. Zakharenkov.[1]

University of Essex, Colchester

[1]Currently on leave from P. N. Lebedev Physical Institute, Moscow, Russia.

INTRODUCTION

In laser driven ablative implosion studies the production of very uniform pressure is considered to be crucial to the success of the direct drive concept. The degree of target irradiation uniformity required is very difficult to achieve. The development of Random Phase Plates (RPP) and Induced Spatial Incoherence (ISI) have increased considerably the prospects for more uniform implosions even when using a limited number of beams. It was suggested that due to the effects of thermal smoothing the plasma should be insensitive to the speckle spatial frequencies in the focal plane of a laser beam with RPP, produced by the superposition of effectively many independent beams.

In this paper we present the analysis of results from a previous experiment[1] on burn-through measurements of layered plane targets using different RPP's and varying the laser energy and pulse length in the irradiance range 10^{12} - 10^{15} Wcm^{-2} . We have found that at least in the initial stages of the laser-plasma interaction, the ablation process as measured by x-ray time-resolved spectroscopy is very sensitive to the local irradiance, but time averaged characteristics measured with ion and atom diagnostics were in good agreement with predicted RPP focal spot sizes.

EXPERIMENTAL RESULTS

Burnthrough time was measured from streaked x-ray spectra by measuring the delay t_b between Al and Si line emission. The heat front propagation velocity D_{Al}/t_b (where D_{Al} is the Al layer thickness) was calculated as a function of incident irradiance ($I=E_{las}/t.S_{foc}$). For the case when no RPP was present (i.e. spot diameter ~60μm) the heat front velocity is in reasonable agreement with the data[2]. However, introducing any RPP into the beam dramatically changes the observed data: the heat front velocity increased with focal spot diameter at constant irradiance, being higher for long laser pulses than for short ones. One can conclude that for the largest focal spot (where it is possible to neglect lateral losses) the heat front velocity exceeded previous measurements at this irradiance (10^{12}-$10^{13}Wcm^{-2}$) by a factor of 10. Rearrangement of the x-ray data to show the dependence on laser power highlights two obvious sets of data distinguished by the laser pulse length only. Both sets of data overlap when the results of the absorption fraction, obtained from the ion measurements are introduced.

Ion measurements of mass ablation rate were in good relation to the diameter of the overall focal spot produced by RPP, which were much smaller than the size of the neutral particle emission zone (1 - 1.5mm), which was measured with the micro-channel plate pin-hole camera. This gave evidence that energy lost due to lateral transport was not very substantial. In Figure 1 we present the velocity distributions of ions and neutrals for short and long laser pulses. It can be seen that transition from short to long pulses is reflected only by the increases number of of ions within the main velocity region (3 - 6)*10^7 cms^{-1}. Neutral atoms appearing at velocities of (0.5 - 3)*10^7 cms^{-1} are obviously recombined ions and their contribution to the mass and energy balance is negligible.

Effects of lateral energy transport can be inferred from the neutral atom velocity distribution for the range less than 5*10^6 cms^{-1}. The mass of evaporated cold material (10^{-7} g) is around 10 - 50% of the directly heated and ablated mass, the kinetic energy (0.1 - 0.5 J) is only 1% of the absorbed laser energy. The area (A) of the cold emitting zone around the focal spot, calculated on the basis of the mass ablation rate dependence on absorbed energy flux ($m' \sim (E/tA)^{0.33}$)[2], was in the range 0.5 to 4

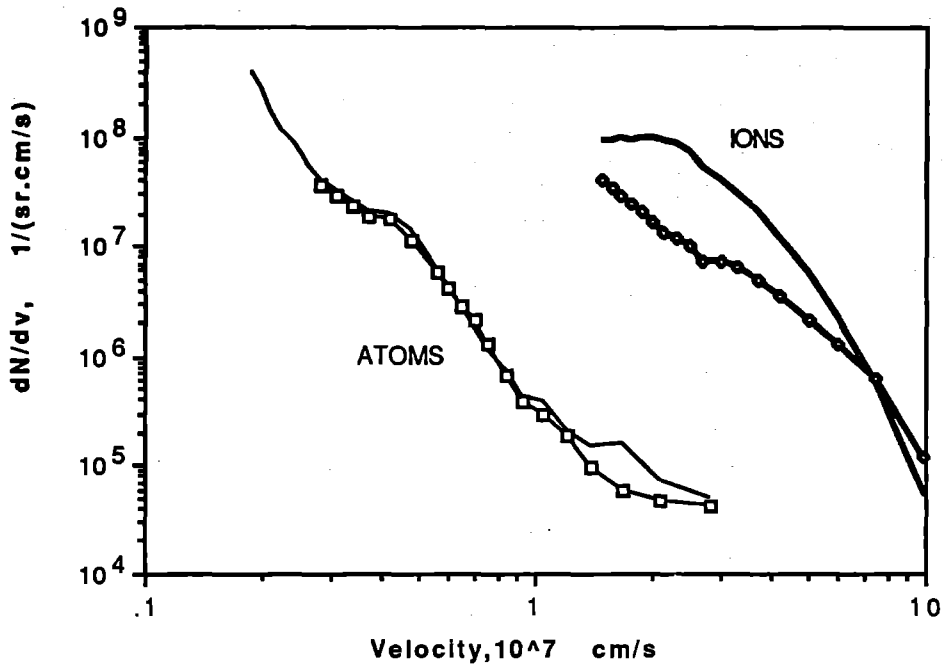

Figure 1 - Ion and neutral atom velocity distributions for short and long laser pulses. Lines with markers are short pulse data.

mm^2. This being larger for shorter laser pulses and in good agreement with particle pin-hole imaging.

DISCUSSION

Figure 2 shows the simulated time evolution of both the critical and ablation surfaces during the initial phase of the laser irradiation obtained using the hydrocode MEDUSA. The separation of the critical and ablation surfaces at the times of burn-through implied from the numerical data are indicated with arrowed lines. The separation is of the order of 15 - 20 μm for both cases although occuring at different times. If we assume a hot spot of around 50μm is present on the plasma critical surface then this separation would be insufficient to allow efficient thermal smoothing[3]. Under these conditions x-ray spectroscopy will provide a measure of the instantaneous and local burn-through rate in the hot spot rather than a time and space averaged rate as measured by ion diagnostics.

The far-field pattern obtained in the focal plane of a laser beam with RPP is characterized with a high spatial frequency interference pattern across the focal spot where the speckle scale length is given by - $L_S \sim f\lambda/D$, (f=focal length of lens in use, λ=wavelength, D=final beam diameter), and the focal spot size is given by - $L_f \sim f\lambda/d$, where: d=RPP element size. In the initial stage of laser interaction some group of speckles may form the hot region inside the focal spot, which results in the increase of local heat front propagation velocity as well as in the outer layer mixing process.

The main conclusion of this consideration is the insensitivity of x-ray measurements of heat front propagation velocity in the presence of Random Phase Plates. Even though this result is contradictory to ion measurements of mass ablation rate, which confirm for different RPP's the well known m'(I) relationship, both approaches fit with a model which includes hot spots at the initial stages of laser irradiation. Due to the increased separation of the critical and ablation surfaces with time (see Figure 2), thermal smoothing becomes more efficient and the hot spots in laser beam become less influential.

Lewis et al[4] observed dependences on focal spot diameter when determining the peak ion velocity. The previous work could be

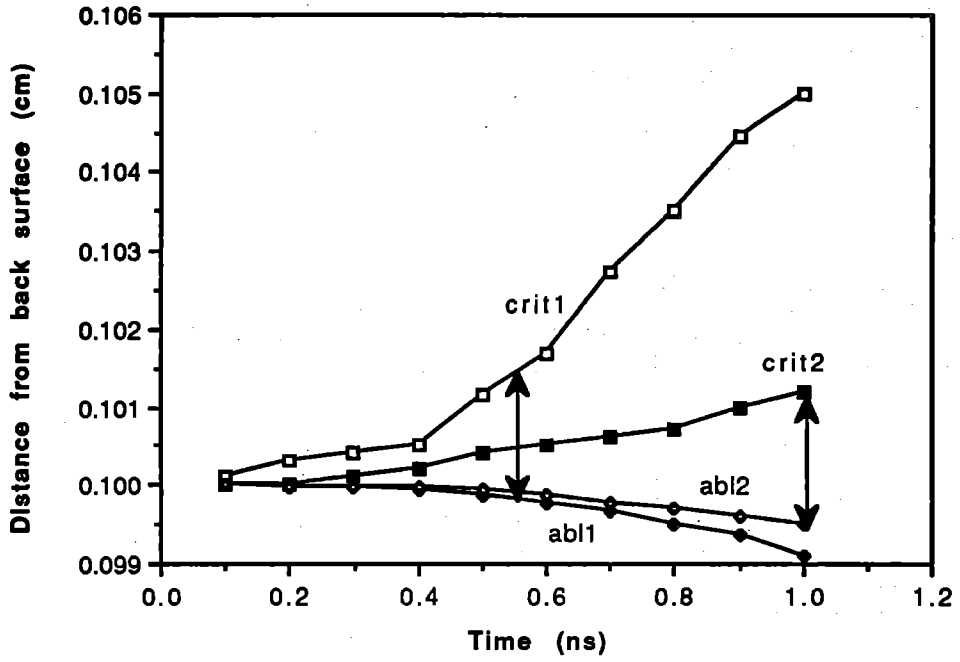

Figure 2 - Evolution of critical and ablation surfaces for two cases of laser irradiance. Curves crit1 and abl1 are data for high irradiance case (Imax= $6.3*10^{14}$ W/cm^2) and crit2 and abl2 are for the low irradiance case (Imax=$2.5*10^{13}$ W/cm^2).

explained in terms of the increase of the emitting area due to considerable lateral energy transport which is in contrast to the present work using RPPs.

CONCLUSION

The application of RPP's to improve the uniformity of target ablation was investigated. It was shown that some hot spots with dimensions of a few microns existed on target, which at least at the initial stage of the laser interaction process produces a local maximum in the ablation pressure. However, the time integrated ion measurements of ablation rate were found to be consistent with the supposed overall focal spot size given by each RPP.

Lateral energy transport according to neutral particle measurements has little influence on absorbed energy redistribution (only 1% of the energy is transported from the laser focal spot to outer region of 2 mm size). Nevertheless, the mass of cold evaporated material (10^{-7}g) emitted from a relatively large area (up to 4mm^2) can contribute to a measurable momentum transferred to the target.

REFERENCES

1. T. A. Hall, R. Evans, Z. Ahmad, Yu. A. Zakharenkov, Annual Report to the LFC. 1991 RAL-91-025, p. 29.
2. M. H. Key, W. T. Toner, T. J. Goldsack et al, Phys Fluids 26, 2011 (1983).
3. S. E. Bodner, J. Fusion Energy 1, 211 (1981).
4. C. L. S. Lewis, P. F. Cunningham, L. P. Pina et al, J. Phys. D. 15, 69 (1982).

SOFT X-RAY CONTACT MICROSCOPY: ADVANCES IN BIOLOGICAL IMAGING IN TA4.

R.A.Cotton[1], M.D.Dooley[2], A.M.Page[1], A.D.Stead[1] & T.W.Ford[1].

[1]Royal Holloway and Bedford New College, University of London,
Egham, Surrey, TW20 0EX, UK.
[2]Rutherford Appleton Laboratory, Chilton, Didcot, Oxon, OX11 0QX, UK.

INTRODUCTION

Soft X-ray contact microscopy (SXCM) is a powerful imaging technique which enables the internal structure of living biological specimens to be imaged at a resolution beyond that of the light microscope. The technique utilises soft X-rays within the so-called "water window" region (0.28-0.53KeV) which lies between the carbon and oxygen K-shell absorption edges. Thus, using water window X-rays, natural contrast is provided between carbon containing structures and the surrounding water or, in the case of biological specimens, between dense carbon-containing organelles and the more carbon-dilute cytoplasm. The principle of SXCM is discussed in more detail elsewhere[1]. Until recently SXCM was little known amongst the life-science community. Now however, as SXCM improves in terms of image resolution and availability of such systems, it is beginning to gain interest.

Target area 4 (TA4), using the "Vulcan" laser to generate X-rays, has been set up to develop SXCM and to provide a facility which is available to biological and medical researchers to image their specimens and so evaluate the potential of the technique. The facility in TA4 has now been operating for over 12 months, with ever increasing success. In addition to imaging a wide variety of organic material, there has been a continued development of the facility and the factors limiting the technique are being investigated.

The actual technique of SXCM involves recording an X-ray image of the living biological material in an X-ray sensitive photoresist. After exposure to X-rays the resist must be developed in a suitable solvent and then magnified by other types of microscopies. Much work over the past year has concentrated on being able to obtain quantitative data on dissolution rates and the development depth of the resist so that the approximate development time for the resist can be predicted from the X-ray fluence which is routinely measured for each shot[2]. In addition, an investigation into the best method of resist examination has been undertaken, which has resulted in collaboration and interest from companies and Universities in the UK and abroad.

FACILITY DEVELOPMENT IN TA4

The alignment of the target relative to laser focus is of critical importance. Different target geometries were investigated and corresponding target mechanisms were constructed. An optimum system is now in routine operation, whereby a fresh portion of target material can be very quickly positioned to within ±30μm relative to laser focus. With this system the reproducibility of the shot to shot X-ray fluence has been substantially improved and the rapid alignment is ideal for imaging experiments.

For SXCM to succeed, it is essential that accurate measurements of X-ray fluence are known for each laser shot. This is necessary, not only to simplify and standardise subsequent resist development of the exposed resist, but precise knowledge of the X-ray conversion efficiencies enables the X-ray production to be optimised. By using a combination of two X-ray diodes, using vanadium and beryllium filters, absolute measurements of the X-ray fluence in the water window (2.3 - 4.4nm) and the hard X-ray component (<2.3nm) can be determined. The two diodes were connected to the Le Croy system at RAL and with the aid of specifically written software, a computer print-out gives data on all parameters of the laser and X-ray emission for each laser shot. This is seen as a major advancement in making the technique "user friendly" for imaging experiments.

Other factors affecting X-ray emission were investigated e.g. position of target material relative to focus and laser pulse length. These measurements were taken for a variety of target materials (gold, tungsten, molybdenum, titanium and carbon) and have therefore extended the work reported previously[2]. The generation of water window X-rays has now been optimised and studies are under way to determine the dependence of X-ray fluence and spectral content on image quality and resolution. In addition preliminary spectra using a transmission grating have been obtained for the above materials, although better resolution is required. Improved gratings are soon to become available, which will give spectra which are an essential part of a comprehensive study of the effect of spectral quality on image resolution and quality.

RESIST DEVELOPMENT

The monitoring of the development of the resist after exposure is performed using a light microscope, although this is far from ideal due to the limited resolution. A more serious limitation however, is that only very limited information about actual development depths can be gained. With the assistance of Leica (UK) we have accurately measured the dissolution rates of the resist for a range of values of X-ray fluence under different conditions. These experiments used a Leitz MPV-SP thickness measurement system, which can determine the thickness of photoresist on the silicon wafer to within ±5nm. Work of this nature is of critical importance for obtaining optimum results since:

1. A greater control over the development depth allows the finest structural details to be obtained, avoiding "over development".
2. The dissolution rates give a second valuable quantitative measurement of the X-ray fluence, giving a direct comparison with other workers[3].
3. The contribution of radiation outside the water window region to image formation can be estimated. In particular the contribution of longer wavelength radiation can be estimated by measuring dissolution rates following exposure in the presence or absence of an aluminium coating on the silicon nitride window (used for protecting the specimen from vacuum). This coating effectively eliminates UV/XUV radiation whilst allowing a high transmission in the water window. Figure 1 shows the dissolution rates using titanium target material, with an incident X-ray flux of approximately 30mJcm^{-2} in the water window . The small difference between the two dissolution rates indicates that with this particular target material, under these specific conditions, the UV/XUV contribution to image formation, which would degrade the image, is low.

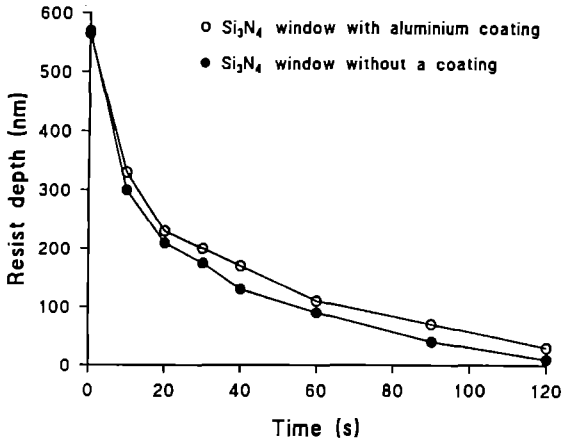

Figure 1. The dissolution rates of PMMA photoresist after exposure to X-rays generated using a titanium target.

EXAMINATION OF RESISTS

Until recently conventional scanning electron microscopy (SEM) has been used to obtain a magnified image of the resist. However, there are several disadvantages with using an SEM for this purpose. Firstly the photoresist must have a metallic coating put on it for electrical conduction. This means that once the resist has been coated, no further development can take place. Furthermore, using conventional light microscopy to estimate when optimum development has been reached is very difficult, due to the poor resolution and relatively low magnification. Therefore when viewed by SEM the development depth is often found to be insufficient. A further potential problem with the use of SEM is the damage that can occur to the resist by the electron beam of the SEM. To avoid such damage it is often necessary to use a low accelerating voltage which in turn reduces the resolution that can be obtained. The ideal situation would therefore be to examine the uncoated resist at high resolution.

Possible alternatives to conventional SEM's have now been investigated, which show that several systems have very exciting prospects for the future.

1. Confocal laser scanning microscopy (CLSM):

CLSM is in effect state-of-the-art light microscopy. Resists can be imaged very quickly and do not require a metallic coating. However the resolution of CLSM is limited to approximately 200nm and hence will limiting factor in the resolution of the SXCM image.

2. Field Emission scanning electron microscopes (FESEM):

Due to the high brightness of the electron source, the FESEM is capable of examining uncoated resists at high resolution (<7nm). In addition, the machine is generally familiar to biologists and the final image is of high quality. However, a slight disadvantage of the FESEM for this purpose is the fact that the electron beam itself does expose the photoresist to some extent, which can degrade the image on further development, although preliminary experiments have not shown this to be a major problem.

3. Atomic Force Microscope (AFM):

The AFM is now becoming widely used in the material science field, although is largely unknown amongst the life science community. An AFM allows the surface of non-conducting materials to be imaged at a resolution approaching atomic dimensions. Experiments have revealed that there is no damage to the resist surface and an accurate height profile of the resist can be obtained.

It is clear that FESEM and AFM are both very well suited to examining the photoresist. The final images with both systems appear to be very comparable and the main factor determining which technology is to be used largely depends on availability. A detailed comparison of the various methods of resist examination will be presented at the forthcoming conference on "soft X-ray microscopy", San Diego 1992.

BIOLOGICAL IMAGING

a) MOSQUITO WINGS

A clear demonstration of the technique of SXCM can be seen in Figures 2a and 2b. This shows two images of a mosquito (*Aeges*) wing, containing numerous hairs that cover this part of the wing surface. Figure 2a shows the wing using a conventional light microscope. Figure 2b shows an X-ray image of a similar portion of the wing recorded in the photoresist. These hairs, normally upright, appear to be pressed onto the surface, since the SXCM image is, in effect, a two-dimensional representation of a three-dimensional structure. The tips of these hairs appear to be extremely fine (of the order of a few hundred nanometres).

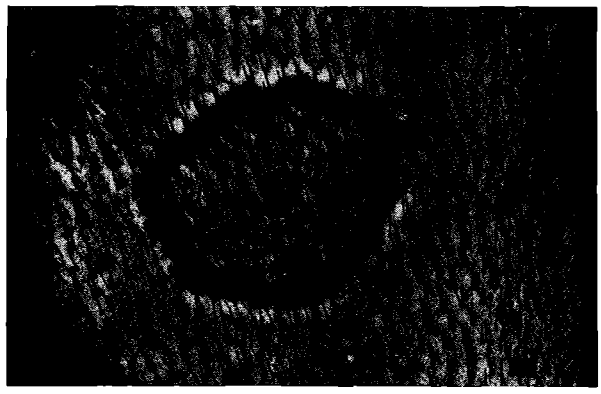

Figure 2a. A light microscope photograph of a portion of a mosquito wing.

Figure 2b. A soft X-ray contact image of same mosquito wing as in figure 2a.

b) EFFECT OF FIXATION ON ULTRASTRUCTURE

In order to examine the ultrastructure of biological specimens by electron microscopy it is necessary to stabilise the highly labile cellular contents before embedding and sectioning the specimens. This is commonly achieved by treating the tissues with various chemical fixatives. The assessment of the

efficiency of these fixatives is usually based upon the appearance of the specimen under the microscope although this is somewhat intuitive as the ultrastructure of the living cell cannot be studied. Previous studies in which the structure of epidermal hairs has been followed under the light microscope as the commonly used fixatives are perfused into the tissue, has shown that the cellular contents are drastically re-arranged by these fixatives. We have studied the effects of some of the commonly used fixatives on cell ultrastructure on tomato epidermal hairs, using firstly electron microscopy and secondly soft X-ray contact microscopy. The latter technique allows not only direct comparisons of the effects of the fixatives, but also allows living, hydrated specimens to be imaged so that the true ultrastructural effects of the fixatives can be seen and compared to the ultrastructure of the living material. Figure 3 shows an X-ray image of a portion of a hydrated epidermal hair, showing a nucleus, various additional organelles, together with intracellular strands. Preliminary work indicates that these strands break up when the tissue undergoes fixation. A detailed paper on this work is currently under preparation and will be presented at the forthcoming SPIE conference on "soft X-ray microscopy", San Diego 1992

Figure 3. Living hair from the stem of a tomato plant imaged by SXCM and the resist viewed by SEM. Internal structures are visible which are cell organelles and protoplasmic strands.

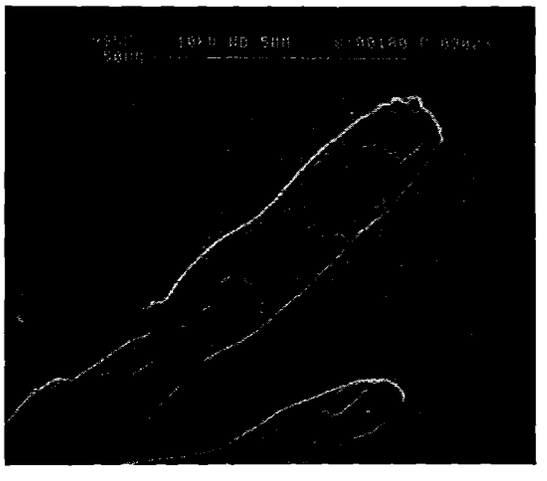

Figure 4. Living moss protonema imaged by SXCM showing the cell wall and intracellular detail.

c) MICROSPORIDIA STUDIES

Spores of a parasite called microsporidia have been imaged. These singled celled organisms have a coil inside their tough exterior. When the spores are taken into the host organism, the coil shoots out like a spring, piercing the gut wall, thus infecting its host. Images obtained using SXCM show for the first time the internal structure of these organisms whilst still alive at this magnification. A detailed paper of this work is currently under preparation.

d) STUDIES OF MOSS PROTONEMA

An SXCM image of protonema of the moss *Rhytidiadelphus loreus* is shown in Figure 4, using a conventional SEM to magnify the resist surface. The specimen was hydrated at the time of exposure with no special preparation whatsoever. The protonema are tip-growing filamentous structures (10-20μm in diameter), produced following spore germination and provide a single row of cells containing features with a range of carbon densities. Delicate structures can be easily distorted or lost during the preparation procedures necessary for transmission electron microscopy. However, for SXCM the protonema have been imaged fully hydrated without any form of pretreatment. The resist image as seen under SEM, clearly shows the cell wall and various intracellular structures.

e) STUDIES OF STARCH MICROSPHERES

When a suspension of water-insoluble materials is injected into an animal body, the location at which they are retained depends on their size, and spheres with a diameter of 1μm are preferentially retained by the lymphatics. Starch microspheres can be used to transport drugs within the body, although it is known that the spheres tend to increase in size when in contact with water. SXCM is an ideal method for obtained detailed information about the change in size of these spheres since these carbon dense structures can be imaged dry and in water. Figures 5a-c, show an SEM image of a real, dry microsphere, an X-ray image of a cluster of dry spheres and an X-ray image of a sphere in water, respectfully.

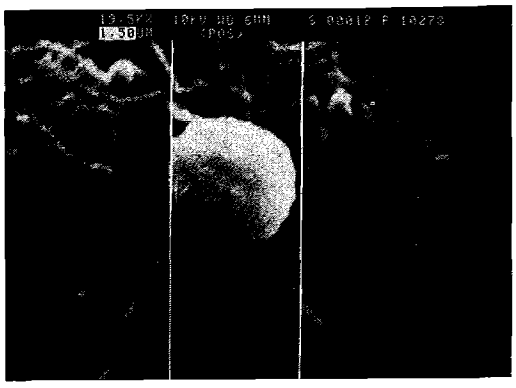

Figure 5a. A starch microsphere viewed under SEM.

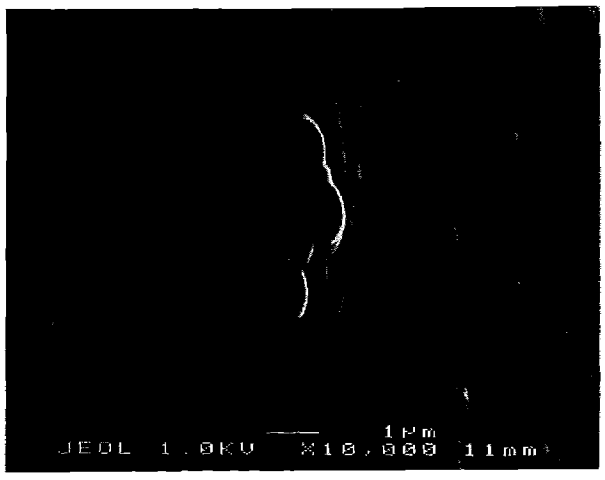

Figure 5b. An SXCM image of a clump of dry microspheres. It should be noted that due to high absorption by the spheres the X-ray image is seen as a "disc", although the diameter of this disc is an accurate measure of the original sphere.

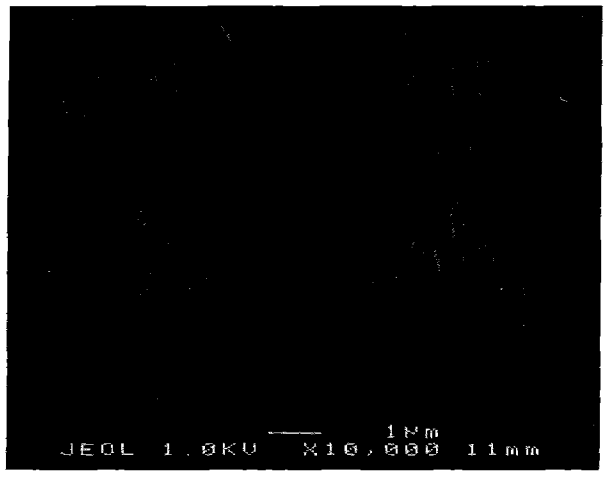

Figure 5c. An SXCM image of a single starch microsphere. The sphere was imaged in water. This image shows that the sphere was of order 4µm, 3-4 times the diameter of a dry sphere.

CONCLUSIONS

Soft X-ray contact microscopy is a technique enabling the internal structure of living biological material to be imaged at sub-optical resolution, and hence has an important role to play in the microscopy of biological specimens. The most suitable X-ray source for this purpose is a pulsed plasma source generated using a high power laser. We have set up a facility in TA4 to develop SXCM, in an attempt to bring SXCM into the biological community.

REFERENCES

1. T.W. Ford et al. Electron Micro.Revs. 4, 269, (1991)
2. R.A.Cotton et al. RAL annual report RAL-91-025, 32, (1991)
3. T. Tomie et al. Science. 252, 691 (1991)

ACKNOWLEDGEMENTS

This work is supported by SERC grant GR/F 81514. We wish to thank the support staff on the "Vulcan" laser at RAL, the staff at the Electron Microscopy unit at RHBNC, Paul Finch of the Chemistry Dept. at RHBNC and Pete Anastasi at Kings College for their help with this work. We would also like to thank Leica (UK), Jeol (UK) and Park Scientific Instruments (USA) for their help and use of instruments.

DOUBLE-CRYSTAL HIGH RESOLUTION X-RAY SPECTROSCOPY OF LASER-PRODUCED-PLASMAS

H. He,[1] J.S. Wark,[1] O.Renner,[3] E. Foerster,[2] M. Kopecky,[3] I. Uschmann,[2] W. Blyth[1]

[1]Department of Physics, Clarendon Laboratory, University of Oxford, Oxford OX1 3PU.
[2]Institute of Optics and Quantum Electronics, Friedrich-Schiller-University, O-6900-Jena, FRG
[3]Institute of Physics, Czechoslovak Academy of Sciences, 18040 Prague, Czechoslovakia.

INTRODUCTION

The development of high-resolution and high-dispersion x-ray spectroscopy of laser-produced-plasmas is important for a whole variety of different applications relevant to high-power laser-plasma interactions. These include the investigation of plasma polarisation shifts[1,2], Doppler shift measurements,[3,4] K-edge shift measurements in laser shocked targets,[5] and the detailed investigation of x-ray line widths.[6,7] In the past conclusive demonstration and measurement of these phenomena, especially plasma polarisation and K-edge shifts, have been severely hampered by the comparatively low resolution of conventional x-ray spectrometers.

In this paper we describe the use of a double crystal spectrometer (DCS)[8] to obtain x-ray spectra emitted from a laser-produced-plasma. The use of such an instrument in such experiments was first suggested by Renner.[9] The instrument has an extremely high-dispersion, similar to that of a conventional flat single crystal spectrometer when used at and around a Bragg angle of $\pi/2$. This high dispersion ensures that the degradation of the resolution due to source broadening is negligible, and in principle the resolution is simply determined by the rocking curve width of the crystals. For the same spectral resolution the x-ray intensity on the detector can be larger than that of a normal flat crystal spectrometer. The instrument also has several other advantageous features, including one dimensional spatial resolution in a direction perpendicular to the spectral dispersion direction, and the fact that two spectra are produced symmetrically disposed about a central wavelength. This last feature makes the instrument especially useful for the study of spectral line shifts.

THE DOUBLE CRYSTAL SPECTROMETER

A schematic diagram of the double crystal spectrometer is shown in Fig. 1. Two flat single crystals are set in the $(n,+n)$ position. We define the primary ray, of wavelength λ_0, to be that which lies in a plane perpendicular to the diffraction planes of both crystals and contains the source. X-rays from the emitting plasma of wavelength λ_0 are incident on the first crystal at the Bragg angle, θ_0. They are thus reflected towards the second crystal. The angle between the two crystals is set to be (π - $2\theta_0$). Thus the x-rays of wavelength λ_0 diffracted from the first crystal are incident on the second crystal at the Bragg angle once again. They are further diffracted and recorded on the detector. Now it can be shown that x-rays with wavelengths slightly shorter than λ_0 are now dispersed in the *vertical* direction at an angle φ such that [8,9]

$$\lambda = \lambda_0 \mathrm{Cos}\varphi \qquad (1)$$

and they satisfy the Bragg condition at angles of incidence θ on the crystal

$$\mathrm{Sin}\,\theta / \mathrm{Sin}\,\theta_0 = \mathrm{Cos}\varphi$$

It is interesting to compare these dispersion characteristics with those obtained for a flat single-crystal spectrometer. In the single crystal case, for rays satisfying the Bragg condition at an angle θ

$$\Delta\theta/\Delta\lambda = \mathrm{Sin}\theta/(\lambda \mathrm{Cos}\theta)$$

whereas for the DCS

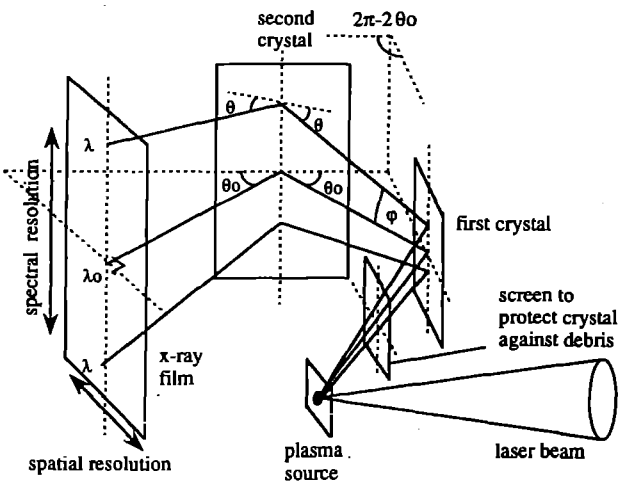

Fig 1. A schematic diagram of the double crystal spectrometer.

$$\Delta\varphi/\Delta\lambda = -\mathrm{Cos}\varphi\,/(\lambda \mathrm{Sin}\,\varphi)$$

Thus we see that the dispersion of the DCS, where is φ small, is identical to that for the single crystal case close to a Bragg angle of $\pi/2$. However, note that it is usually not possible to use single crystal spectrometers in this mode, as they can only then record x-ray wavelengths close to $2d$ (where d is the interplanar spacing). On the other hand, the DCS can be set to record the wavelength of interest at this high dispersion by altering the angle between the two crystals. Furthermore, for a given wavelength λ, reflection occurs at the two angles ($\pm\varphi$) which satisfy equation (1). Thus we record two spectra which are symmetric about λ_0 and the relative wavelength of a given line with respect to λ_0 is simply a function of the distance between the lines recorded in each of the two spectra symmetrically disposed about λ_0. This feature makes the DCS especially useful for measuring shifts in spectral lines.

The DCS also affords a degree of spatial resolution in a direction perpendicular to the spectral dispersion plane. The acceptance angle of the instrument to x-rays is approximately the rocking curve width of the crystals, and thus the x-ray source will be projected at unit magnification onto the detector in a direction perpendicular to the spectral dispersion direction. It follows that the theoretical spatial resolution is approximately the rocking-curve width multiplied by the distance from the source to the detector. The calculated luminosity of the DCS has been investigated[9] and it has been shown that this is independent of the dispersion angle for the small angles of φ used here. Further information about the theory of the instrument can be found in the work of Renner.[9]

The DCS was manufactured at the Institute of Physics of the Academy of Sciences in Prague. In the experiments described here both ADP (Ammonium-Dihydrogen-Phosphate) (101) and silicon (111) crystals were used. The two ADP crystals, each 30 mm wide, 40 mm long, and 2 mm thick, were cut and polished in Carl-Zeiss-Jena, FRG. The deviation angle between the polished surface and the diffraction planes

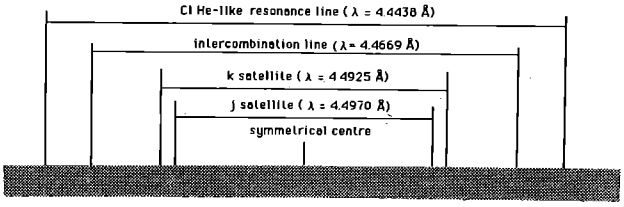

Fig. 2. A spectrum from helium-like chlorine recorded with a Si(111) DCS. The resonance line and intercombination lines are denoted by R and I respectively. The j and k dielectronic satellites are also shown.

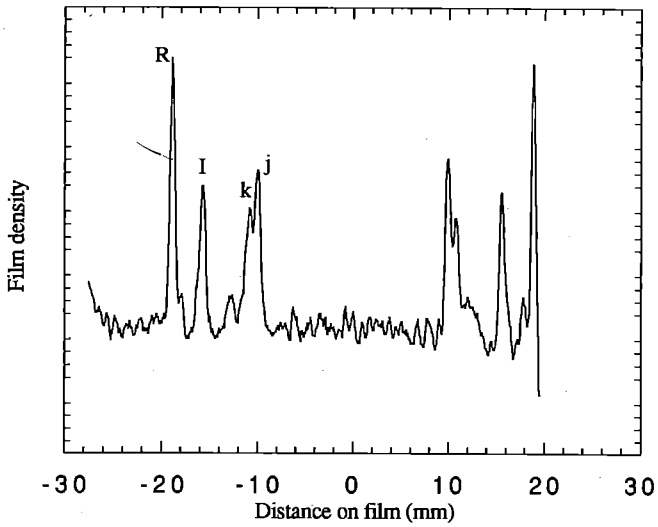

Fig. 3. A lineout of the spectrum shown in Fig.2.

was measured on a x-ray goniometer to be less than 1.0 arc-minute for one crystal, and 6.5 arc-minutes for the other. The silicon (111) crystals, 20 mm wide and 40 mm long, were cut from commercial silicon wafers 250 μm thick. The deviation angle between the polished surface and the diffraction planes was not measured in this case. The angle between the two crystals was set to an accuracy of better than 1 arc-minute by using an optical goniometer. Thus for the ADP crystals the principal ray of wavelength λ_0 was initially set with an accuracy of approximately $|\Delta\lambda/\lambda| \sim 6.0 \times 10^{-4}$. The total spectral range of the instrument, determined by the range in φ ($\pm 12^0$) that can be recorded on the detector where the source to detector distance has been taken to be 10.50 cm, was of order $\Delta\lambda/\lambda$=0.022. Thus the accuracy in setting the angle between the crystals is sufficient to ensure that the x-ray line of interest is recorded somewhere within the spectral range for the ADP crystal. Experience showed that this was also the case for the silicon crystals, indicating that the polished surface and the diffraction planes were also sufficiently parallel. Once the line has been recorded for the first time, further fine adjustment of the angle between the crystals can be made to ensure that the line is recorded close to $\varphi = 0$, i.e. the region of highest dispersion. The spectra were recorded on Kodak DEF X-ray film. The film was protected from visible light using a filter of 8.0 μm polypropylene coated with 3000 Å Al.

EXPERIMENTS

The experiments were performed using the TA4 facility. Laser pulses of 600 psec (FWHM) duration were focussed to a spot approximately 80 μm in diameter on solid targets, the laser energy per shot was approximately 3 J, producing an incident irradiance of order 10^{14} W cm^{-2}. After each laser shot the target was moved laterally a few hundred microns to bring a fresh target surface into line with the laser focus. The DCS was placed such that the total target to film distance was approximately 105 mm. A total of 30 laser shots were needed at this low energy to produce a recordable spectrum on x-ray film. It may therefore be possible to record a spectra in a single laser shot containing several hundred joules.

The instrument was used with ADP crystals ($2d$ = 10.64Å) to study the emission from hydrogenic and helium-like aluminium, and with silicon (111) crystals ($2d$ = 6.27Å) to record spectra from helium-like chlorine (produced by irradiating NaCl pellet targets). A typical recorded spectrum, in this case the resonance, intercombination, and dielectronic satellite lines of helium-like chlorine, is shown in Fig. 2. This figure clearly demonstrates the double spectrum recorded about a central wavelength, and also the one dimensional resolution of the instrument in the direction perpendicular to the spectral direction, which gives rise to the narrow width of the spectrum, and is indicative of the effective source size, which we find to be 150 μm. This is nearly a factor of two larger than the diameter of the laser focal spot, and indicates that there could have been some movement of the focal spot with respect to the detector plane during the integration of the emission from the 30 laser shots necessary to record the spectrum.

A lineout of the density of Fig. 2 in the spectral direction is shown in Fig. 3. The narrowest spectral feature recorded is the resonance line, which gives a value for the resolution ($\lambda/\Delta\lambda$) of a least 2500. In principle the instrument should produce a spectral resolution slightly better than the rocking curve of a single crystal (~7000). However, in this case the effective resolution may have been slightly degraded by the large effective source size; alternatively the actual resolution may indeed be close to the calculated value, but the spectrum itself does not contain sufficiently narrow features to confirm this. Note that for a single crystal spectrometer set at the same source to detector distance and the same source size, the resolution would have been reduced to around 700 by source broadening effects.

SUMMARY AND CONCLUSIONS

We have demonstrated that a DCS can be used to record the x-rays emitted from a laser-produced-plasma with high resolution and dispersion. Spectra have been recorded with a spectral resolution of at around 2500. Two spectra are recorded symmetrically disposed about a central wavelength, this feature, along with its high dispersion and resolution, makes the instrument useful for the study of spectral line shifts. Further work will include using the instrument to obtain spectra from single, higher energy laser shots, and a more detailed investigation of the ultimate spectral and spatial resolutions available.

REFERENCES

1. S Volonté, J. Phys. D, **11**, 1615 (1978).
2. V.S. Marchenko, Sov.Phys. JEPT, **67**, 1111 (1988).
3. F.E. Irons, R.W. McWhirter, and N.J. Peacock, J. Phys. **B**, **5**, 1975 (1972).
4. P. Nicolosi, G. Tondello, and E. Jannitti, Phys. Rev. **A**, **20**, 2574 (1979).
5. D. Riley, O. Willi, S.J. Rose, and T. Afshar-Rad, Europhys. Lett., **53**, 2383 (1989).
6. H.R. Griem, Spectral Line Broadening by Plasmas, Academic Press, New York (1974)
7. For a review of this subject see "High-resolution X-ray spectroscopic diagnostics of laser-heated and ICF plasmas", A.A. Hauer, N.D. Delameter, and Z.M. Koenig, Laser and Particle Beams, **9**, 3 (1991).
8. J. Hrdy, Czech. J. Phys. B, **18**, 532 (1968).
9. O. Renner and M. Kopecky, Laser and Particle Beams (to be published).

X-RAY HEATING OF LASER-PLASMA CRYSTAL SPECTROMETERS

J.S. Wark

Department of Physics, Clarendon Laboratory, University of Oxford,
Parks Road, Oxford, OX1 3PU.

INTRODUCTION

X-Ray spectroscopy is a widely used means of diagnosing conditions within laser-produced plasmas. Densities and temperatures within the plasma are commonly inferred from line widths, line ratios, and recombination slopes.[1] In the quantitative analysis of such data it is necessary to know the response of the film or detector and the wavelength-dependent single-crystal integrated reflectivity of the particular Bragg crystal used.[2] It is assumed that the reflectivity of the crystal, as measured using standard techniques, is valid and constant throughout the laser-plasma experiment. However, owing to the large x-ray fluxes created in such experiments we will show that it is possible to alter the reflectivity of the crystal from its standard response on the nanosecond timescale of data collection, especially if the crystal is insufficiently filtered.[3]

Consider the following situation. X-rays from a laser-produced-plasma pass through an x-ray filter and are then diffracted from a crystal and recorded on a detector. Typically the integrated reflectivity of crystals ranges from 10^{-4} - 10^{-5}. Therefore only a small fraction of the x-rays incident on the crystal are reflected; the vast majority of the x-rays are absorbed within the surface of the crystal by photoelectric absorption. The absorption of this x-ray energy will result in an increase in temperature within a thin layer (thickness of order the typical absorption depth) at the surface of the crystal. Typically the peak temperature increase could range from a few degrees to several hundred degrees with a 1/e depth of 1 to a few microns depending on the x-ray spectrum, the filters used, and the crystal. This exponential temperature-depth profile results in a strain-depth profile being set up within a fraction of a nanosecond. The strain can simply be calculated from the thermal expansion coefficients taking into account its one-dimensional nature. The time taken for the strain profile to be set up is roughly the 1/e depth of the temperature profile within the crystal divided by the crystal sound speed. Typical sound speeds are of order 5 - 10 microns per nanosecond, and thus one could expect that the strain profile is set up on a sub-nanosecond timescale, i.e. within typical data collection times. As soon as the strain in the crystal starts to become larger than of order the natural rocking curve width we can expect that the reflection characteristics of the crystal will be altered. We will show below that this can occur within specific crystals at quite modest increases in temperature. The x-ray induced strain-depth profile will of course decay by diffusion; however, we will show that the decay time is typically greater than ten nanoseconds, and thus is long compared to the data collection time.

A full solution to the time-dependent reflectivity of crystals would require a knowledge of the time-dependent x-ray flux incident on the crystal. The crystal heating and resulting expansion would then need to be modelled using an hydrocode. Such a procedure is outside the scope of this paper, especially since the main aim of the work presented here is simply to encourage spectroscopists working in this field to be aware of the problems that can arise when recording high x-ray fluxes. Instead we will make several simplifying assumptions. Firstly we will assume that the x-ray induced heating of the crystal is instantaneously converted into the corresponding strain-depth profile (as stated above, this should happen on a sub-nanosecond timescale anyway if we compare typical strain depths and crystal sound speeds). Secondly we will ignore the fact that the x-rays are being deposited within the surface of the crystal on a timescale of a nanosecond or so (depending on the pulse length of the laser) and will simply calculate crystal responses assuming all the x-rays have been incident on the crystal - i.e. we will be calculating the reponse of the crystal at the end of the pulse, rather than try to model it in a time-dependent manner. Lastly, the specific changes in crystal reflectivity obviously depend on the particular x-ray spectrum assumed, as well as the crystal used and its angle of diffraction. We thus only model one particular situation for two crystals (silicon (111) and lithium flouride (200) for illustrative purposes).

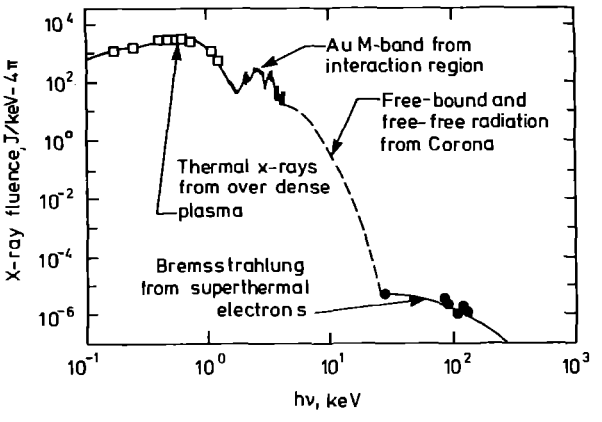

Fig. 1. X-Ray spectrum from a gold disk irradiated with 5KJ of 0.35 μm light in a 1 nsec (FWHM) pulse at an irradiance of 5 x 10^{14} W cm^{-2}.

REFLECTIVITY CALCULATIONS

In Fig. 1 we show a spectrum from a laser-plasma experiment taken at the Nova Laser Facility at Lawrence Livermore National Laboratory.[4] As can be seen from the figure, the spectrum has been measured absolutely. The conditions for this particular shot were 5KJ of 0.35 μm light incident on a gold target in a 1nsec pulse at an irradiance of 5 x 10^{14} W cm^{-2}. We have taken this x-ray spectrum, and calculated the temperature rises in silicon and lithium flouride at various angles and x-ray source crystal distances, assuming that the x-rays pass through a 25 μm beryllium filter before irradiating the crystal. These profiles are shown in Figs. 2 and 3. The strain profiles will decay due to thermal diffusion. However, taking the thermal conductivity of silicon to be 163 W m^{-1}K^{-1} we find that the 1/e decay time of the steepest temperature-profile calculated is about 30 nanoseconds, i.e. far longer than the data collection times. In the case of lithium flouride the timescale is about an order of magnitude longer. Thus, as we are studying the response of the crystal at the end of a nanosecond pulse of x-rays we can treat the strain profile as static once it has been set up.

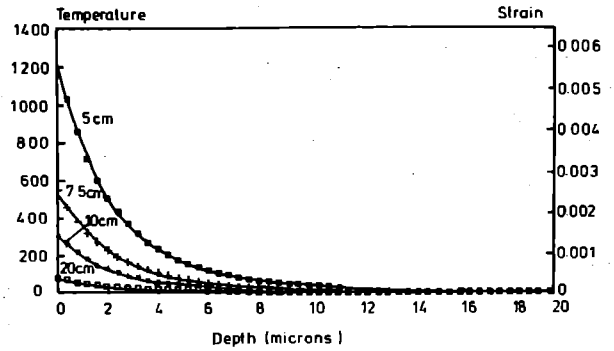

Fig. 2. Temperature rise above ambient and strain profiles in silicon after depositing the filtered spectrum onto the crystal. The crystal is placed at an angle of 45^0 to the line joining the x-ray source to the centre of the crystal. The profiles were calculated for the source to crystal distances shown.

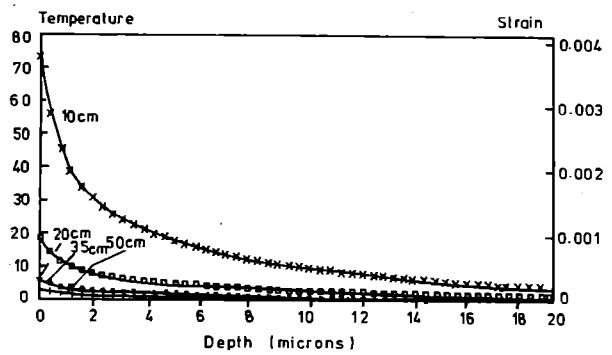

Fig. 3. Temperature rise above ambient and strain profiles in Lithium Flouride under the same conditions as Fig. 2.

For each of the induced strain profiles we have calculated the integrated reflectivity of the crystal by use of the Takagi-Taupin equations.[5-7] A summary of several calculations such as those described above are shown in Fig. 4. In all these cases we have deposited the spectrum shown in Fig. 1 through a 25 μm beryllium filter onto the crystal. We have plotted the normalised reflectivity (i.e. the ratio of the integrated reflectivity of the strained crystal to that of the same unperturbed crystal at the same Bragg angle) as a function of distance between the x-ray source and the crystal. It can be seen that the silicon crystal is not significantly perturbed until it gets very close (<10 cm) to the x-ray source, whereas the lithium flouride has over double the original integrated reflectivity when it is placed 35 cm away from the target. Furthermore, it should be noted that the laser energy used to produce the spectrum shown in Fig.1 is about an order of magnitude less than energies now available, and thus it may be possible to perturb the integrated reflectivity of crystals placed much further from the x-ray target, or alternatively to perturb crystals which are more heavily filtered.

Note that these changes in integrated reflectivity may not be accompanied by an observable loss in spectral resolution. For instance analysis of the rocking curve of silicon (Bragg angle of 45^0) placed 10 cm from the target shows that the intrinsic crystal resolution has decreased from approximately 7000 in the unperturbed case to nearer 2000. However it should be noted that the final resolution of a crystal spectrometer in a laser-plasma experiment is often dominated by other effects such as the source size, and thus the degradation of the intrinsic resolution of the crystal may not be noticed. More important is the change in the integrated reflectivity of the crystals once they have been strained. This change in integrated reflectivity is due to a departure from the purely dynamical nature of the diffraction in the unperturbed case to more kinematic diffraction for the strained crystals.

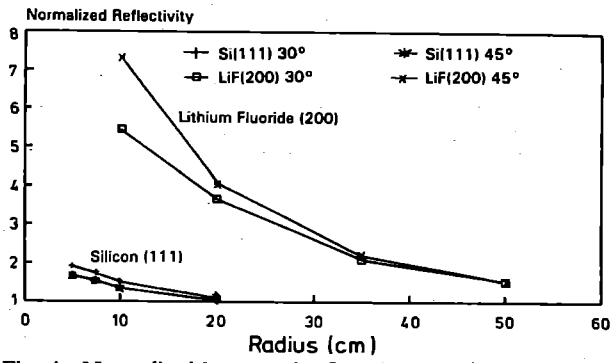

Fig. 4. Normalised integrated reflectivities for the two crystals at 30 and 45 degrees as a function of distance from the x-ray source.

In these calculations we have assumed that the unperturbed crystals can be modelled using dynamical diffraction theory. This assumption is valid in the case of silicon, but generally not true for lithium flouride, which tends to be highly mosaic. The reason we have taken lithium flouride and modelled it in this manner is because we were aware that due to its narrow rocking curve (in the dynamical regime) and relatively high thermal expansion coefficient it would be highly sensitive to the incident x-ray flux, and could be representitive of the worst fractional change in reflectivies that might occur. A confirmation of this will obvioulsy need a study of all the parameters of commonly used crystals, to ascertain those which will be most sensitive to x-ray induced changes in their reflectivity.

The simplest solution to the problem of x-ray induced thermal strain is to filter the crystal more heavily. However, in our experience, spectroscopists sometimes place more importance on filtering the detector rather than the crystal. This most often occurs in time-resolved x-ray spectroscopy where the crystal is usually mounted off a streak-camera up to tens of centimetres from the entrance slit of the streak camera. The main purpose of this paper is to point out that this is not good practice, especially if large x-ray fluxes are being produced, and as much care should be taken in filtering the crystal as in filtering the detector.

CONCLUSIONS

In conclusion we have shown that the x-ray flux from a laser-produced-plasma can be high enough to transiently modify the integrated reflectivity of Bragg reflecting crystals. Values for an illustrative case have been calculated, although a full survey of the commonly used x-ray diffracting crystals is needed before a definitive statement on the extent of the potential problems can be made. The easiest way to overcome this change in reflectivity is to ensure that as much care is taken in filtering the radiation before it diffracts from the crystal, as is taken in filtering the film or detector. Further work will include an experimental study of this phenomenon.

REFERENCES

1. For a review of this subject see "High-resolution X-ray spectroscopic diagnostics of laser-heated and ICF plasmas", A.A. Hauer, N.D. Delameter, and Z.M. Koenig, Laser and Particle Beams, 9, 3 (1991).
2.. B.L. Henke *et al*, Atomic Data and Nuclear Data Tables 27, 1 (1982).
3. J.S. Wark, Laser and Particle Beams 9, 569 (1991).
4. J.D. Kilkenny, R.L. Kaufmann, and R.W. Lee, (Private Communication) (1990).
5. S. Takagi, Acta Crystallogr. 15, 1311 (1962).
6. J. Burgeat and D. Taupin, Acta Crystallogr. 24, 99 (1968).
7. J.S. Wark *et al*, Phys. Rev. B 40, 5705 (1989).

NOVEL MEASUREMENTS OF HIGH DYNAMIC CRYSTAL STRENGTH BY PICOSECOND X-RAY DIFFRACTION

J.S. Wark,[1] N.C. Woolsey,[1] R.R. Whitlock[2]

[1]Department of Physics, Clarendon Laboratory, University of Oxford, Parks Road, Oxford, OX1 3PU, UK.

[2]Naval Research Laboratory, Washington, DC 20375, USA.

INTRODUCTION

In previous annual reports we have shown results of *in situ* picosecond x-ray diffraction from laser-shocked crystals. We outline here how these experiments may constitute a novel method of investigating the ultimate strength of materials.

It has been known for nearly four decades that single crystals with static elastic limits and fracture strengths close to the theoretical limit can be manufactured from micron-scale-diameter defect-free whiskers.[1] As early as 1955 Eisner showed that single crystal whiskers of silicon responded elastically up to tensile stresses of 35kbar.[1] Recent work with highly polished silicon wafers has demonstrated higher static fracture strengths approaching theoretical limits.[2,3] We demonstrate here that such high fracture strengths can also be achieved by pulling a single crystal into tension at ultra-high strain rates.

It has been known for over a decade that the fracture strength of brittle materials increases roughly as the cubed-root of the strain-rate.[4] Grady collated data from several different experiments on brittle materials and plotted the fracture stress as a function of strain rate.[4] An extrapolation of this data to ultra-high strain rates indicates that fracture stresses close to the theoretical limits are reached for strain-rates in the region of 10^8 s^{-1} - 10^9 s^{-1}.

Dynamic tension can be produced within the body of a material by subjecting the front surface of a planar target to impulsive loading. Tensile strain is then induced when the duration of the pressure pulse, τ, is less than cd, where c is the shock velocity within the material, and d it's thickness.[5] In this case two rarefaction waves cross; one is produced at the front surface as the pressure loading falls off, and the other is produced at the rear surface as the incident compression wave is reflected. For sufficiently high tensile stresses a section of the rear portion of the target separates, or 'spalls', from the bulk.[6]

Materials can be subjected to ultra-high strain rates by irradiation with pulsed laser radiation. At irradiances > 10^9 W cm^{-2} absorption of the laser light produces a high pressure plasma at the target surface. As this plasma expands away from the surface momentum balance lauches a compression wave into the bulk of the target. The temporal profile of the compression wave is similar to that of the laser pulse. We present here direct measurements of tensile elastic strain in silicon (111) wafers obtained at strain rates above 10^8 s^{-1}. Tensile elastic strains of 3.4% have been directly observed by *in situ* picosecond x-ray diffraction.[7] We show here that this may constitute a novel method of addressing the ideal strengths of materials.

EXPERIMENT

The experiment was performed using the Neodymium glass laser VULCAN at the Central Laser Facility of the SERC's Rutherford Appleton Laboratory. A schematic diagram of the experiment is shown in Fig. 1. One arm of the laser, containing 100 J of 1.05-μm light in a pulse of 1 ns (FWHM) was focused to a 1.5-cm spot onto a 50-μm-thick silicon (111) single crystal (2d = 6.27Å). The front (irradiated) surface of the silicon is coated with 0.1μm aluminium to ensure abrupt absorption of the laser light, and 18-μm of $(CH)_x$ plastic (which does not break down at these laser irradiances, and is thus transparent) to act as a tamper to ensure increased strength of the applied pressure pulse.[8] Just before the compression wave reaches the rear surface a second laser pulse, synchronous but delayed with respect to the first, was focused to a tight (< 100-μm diameter) spot onto a separate titanium target. This second, frequency-doubled beam contained 25 J of 0.53-μm light in a pulse length of 1 ns (FWHM), thus producing an irradiance on the titanium foil of greater than 10^{14} W cm^{-2}. At these high irradiances a high-temperature plasma is formed, and the titanium atoms are stripped to helium-like and hydrogenic ions, and strongly emit line radiation at the resonance lines of such ions, which lie in the soft x-ray regime. The temporal profile of the x-radiation closely follows that of the laser pulse.[9] The brightest lines produced in these experiments were the resonance line (2.612 Å), intercombination line (2.625 Å), and associated unresolved dielectronic satellites (around 2.635 Å) of helium-like titanium. These x-rays were Bragg diffracted from the rear surface of the laser-shocked crystal during breakout of the compression wave and recorded on a Kentech x-ray streak camera. The temporal resolution of the camera, as determined by the slit width, was 50 ps. Direct measurements of the strain within the crystal during breakout can then be made by observing the shift in Bragg diffraction angle with the changing interatomic spacings within the crystal ($\Delta 2d/(2d) = -\cot\theta\Delta\theta$).

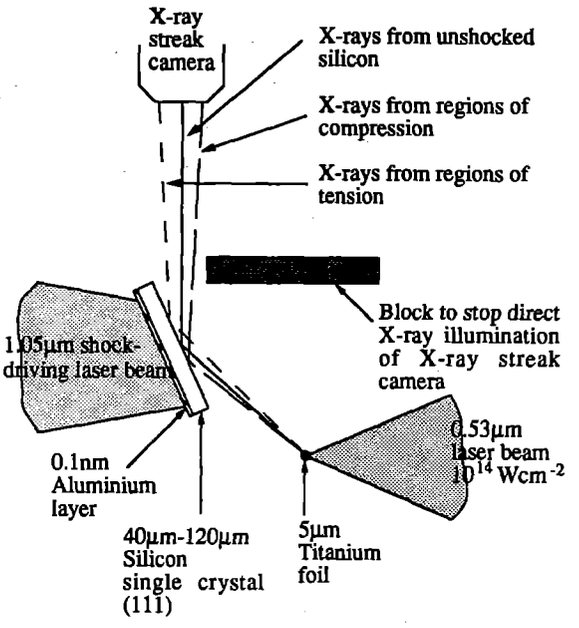

Fig.1 A schematic diagram of the experiment.

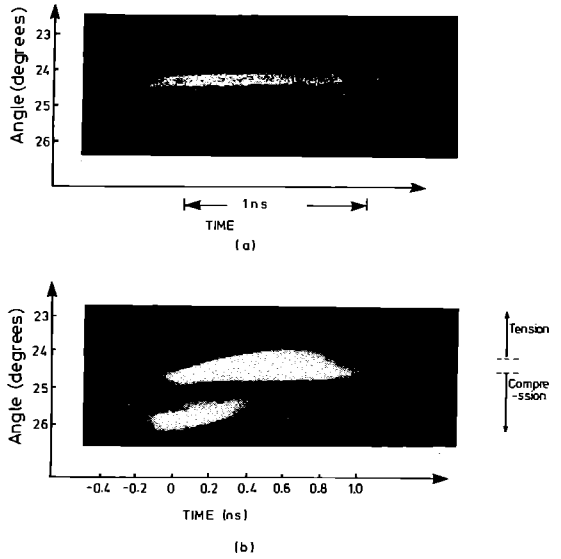

Fig.2 Streak camera record of the diffraction of the x-rays from helium-like titanium from the rear surface of (a) an unshocked silicon crystal (b) a shocked crystal during shock breakout. Zero time is defined as the time when the crystal starts to go into tension.

RESULTS

The experimental results are shown in Fig. 2. Fig. 2(a) shows the unresolved helium-like titanium spectrum diffracted from the rear surface of an unirradiated silicon crystal. Fig. 2(b) shows the spectrum during breakout of the compression wave. In interpreting this data it should be recalled that the x-rays are diffracting from all the varying interatomic spacings in a region of the crystal from the rear surface down to a probe depth several microns below the surface. We have estimated from a simple Beer's law calculation that with x-rays of this wavelength we are obtaining information about the lattice spacings down to a probe depth of order 7-μm below the rear surface of the crystal.

From Fig. 2(b) it can be seen that at -200psec to 0psec the x-rays are probing the crystal in a state of compression, the angular shift in diffraction corresponding to a maximum compression of 6.2±0.2%; later at +200psec the x-rays are being diffracted from both regions of compression and regions of tension; and finally at + 600psec the X-rays are being diffracted from a region of pure tension, with a maximum observed tension of 3.4±0.2%.[7] We have defined time zero to be the point when the crystal first goes into tension. These three regimes correspond to the times when the reflected wave has not yet collided with the rarefaction wave due to release of pressure at the front surface; the time during collision of the rarefaction waves; and the time when the reflected wave has passed the front surface rarefaction wave by at least the probe depth of the x-rays. The spectra from the shocked crystal at 0 and 600psec is compared with that from the unshocked crystal in Fig.3. Thus within the target the strain has changed from 6.2% compression to 3.4% tension within 600 ps, i.e. at a strain rate of 1.6×10^8 s^{-1}. The maximum observed tensile strain 3.4% corresponds to a uniaxial tensile stress of approximately 70 kbar,[10] comparable to the largest fracture stresses observed in static measurements.[2,3]

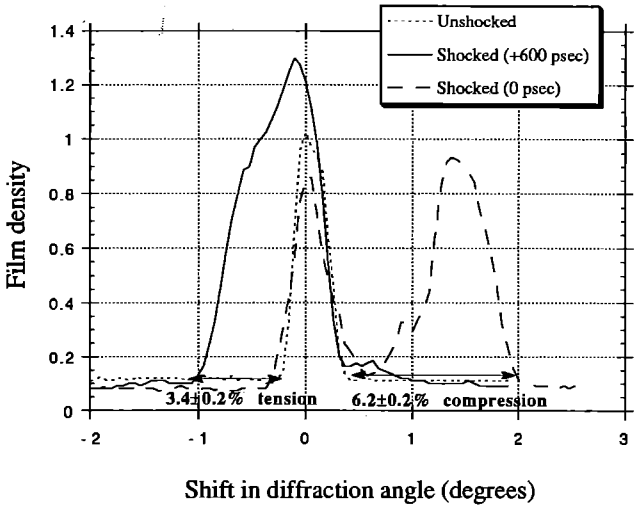

Fig.3 Density lineouts of the data in Fig2(b) at the times indicated, along with the corresponding peak compression and tension.

CONCLUSIONS

Thus by pulling the silicon crystal into tension at ultra-high strain rates. we have observed dynamic tensions comparable to the largest fracture stresses produced by more conventional means. This observation is consistent with the analysis of Grady.[4] He showed that several different models of dynamic fracture in brittle materials all predicted a cubed-root dependence of the strength on the strain rate, and thus at ultra-high strain-rates we may expect ideal strengths to be reached. This increase in strength is simply explained by the fact that there is a terminal growth velocity for crack propagation. Thus this novel method of direct observation of dynamic elastic strains gives rise to the potential of a new method of investigating the ideal strength of solids.

REFERENCES:

1. R.L. Eisner, Acta. Metall. **3**, 414 (1955).
2. S.M. Hu, J. Appl. Phys. **53**, 3576 (1982).
3. Fredric Ericson and Jan-Åke Schweitz, J. Appl. Phys. **68**, 5840 (1990).
4. D.E. Grady and J.Lipkin, J. Geophys. Res. Lett. **7**, 255 (1980).
5. B. Hopkinson, Trans. R. Soc. Lond. **213A**, 437 (1914).
6. B. Hopkinson, *Brittleness and Ductility*, Scientific Papers (Cambridge University Press, London, 1910), p. 64.
7. These results were first presented in the paper by J.S. Wark, D. Riley, N.C. Woolsey, G. Keihn, and R.R. Whitlock, J. Appl. Phys. **68**, 4531 (1990). In this paper the peak compressions and tensions were stated to be 5.9%±0.5% and 3.9%±0.5% respectively. Since that publication a more accurate measurement of the angular dispersion of the x-rays on the streak camera cathode has been extracted from the data. The new, lower value for the maximum tension lies at the lower bound of the error bars of the previously stated value.
8. J.S. Wark, R.R. Whitlock, A.A. Hauer, J.E. Swain, and P.J. Solone, Phys. Rev. B **40**, 5705 (1989).
9. D.W. Phillion and C.J. Hailey, Phys. Rev. A **34**, 4886 (1986).
10. This figure is calculated assuming a linear stress-strain curve, and using the compression data from W.H. Gust and E.B. Royce, J. Appl. Phys. **42**, 1897 (1971).

EXPERIMENTS TO EXAMINE CHANGES IN EUV MULTILAYER STRUCTURES WHEN IRRADIATED BY X-RAYS

B L Evans (1), D S Urch (2), A Ridgeley (3)

(1) Reading University
(2) Queen Mary and Westfield College
(3) RAL

INTRODUCTION

It has been shown independently by Evans et al. (1) and Stearns et al. (2) that multilayer mirrors are subject to annealing effects when heated to temperatures of 200 C or greater. Adjacent layers can react chemically at these temperatures causing extra compound layers to form and changing the effective d-spacing. The x-ray radiation emitted by a laser-produced plasma can be sufficiently intense to heat multilayer coatings momentarily to temperatures in this range, as can also the primary laser radiation scattered by the target. This inter-diffusion is a chemical process which would be expected to occur in the femtosecond timescale of chemical reactions rather than the much longer pico-second timescale of the laser pulse.

Sensitivity to annealing effects is dependent on the materials used in the multilayer coating. Multilayers containing silicon and a heavy metal have been shown to be particularily sensitive to temperature annealing, and would therefore be correspondingly sensitive to x-ray annealing. On the other hand Boher et al (3) have shown that silicon/silicon oxide and silicon/silicon nitride multilayers are resistant to thermal annealing.

Because of the potential damage to the Research Programme of the Facility from x-ray annealing of multilayer mirrors, a programme of work was undertaken in TA4 to try to produce annealing of x-ray mirrors, as has been reported to the High Power Laser Panel (4).

It would be anticipated that annealing by x-rays of multilayer mirrors would cause a sudden fall in the reflectivity of the mirror partway through a laser shot, at the moment the annealing temperature is reached. Since the TA4 programme of work was started we have received reports that just such effects have observed at Osaka and at LLNL.

ANNEALING EXPERIMENTS

The amount of x-rays produced from a laser-produced plasma in TA4 is about 0.5J in total. This is not sufficient to heat a multilayer coating to annealing temperature, but is sufficient to heat a few layers. There exists therefore the possibility of a thermal wave heating a few layers at a time, annealing the entire multilayer structure as it passes through the layers. The primary infra-red laser beam has an intensity around 300MW per sq cm which is sufficient to heat the whole multilayer structure if absorbed.

Two multilayer coatings comprising Si/Pt layers were made on silicon wafers at Reading University. The 18nm d-spacing of these mirrors was confirmed by measurements at Queen Mary and Westfield College using the method described by Urch and Martin (5). One of these mirrors was then selected for a series of experiments in TA4, the d-spacing of the mirror being re-measured after each experiment. The other mirror was kept as a monitor.

In the only x-ray experiment the mirror was exposed to x-radiation produced by a tungsten wire target at a distance of 100mm. The x-ray intensity on the mirror was estimated as 5MW per sq cm. No change in the mirror characteristics was observed as a result of this exposure.

It was then exposed to increasing levels of infra-red radiation by placing it in the main laser beam. No d-spacing changes were observed as a result of these experiments. At the 5J level however the mirror surface was conspicuously damaged and the reflectivity fell by an order of magnitude.

CONCLUSIONS

These experiments indicate:

1. that annealing by stray primary laser radiation is unlikely to occur as physical damage to the mirror occurs before any annealing takes place.

2. X-ray annealing does not occur at the relatively low x-ray fluxes generated in TA4. We have had reports of effects consistent with annealing at Osaka and at LLNL, presumably at much higher x-ray flux levels. It would be interesting to continue investigations at the intermediate flux levels of the other VULCAN or SPRITE target areas.

REFERENCES

1. B L Evans, J Al-Dabbagh, B J Kent, J Mod Opt, 36 471 (1989)

2. D G Stearns, M B Stearns, Y Cheng, J H Stith, N M Ceglio, J Appl Phys. 67, 2415 (1990).

3. P Boher, Ph Houdy, L Hennet, J P Delaboudiniere, M Kuhne, P Muller, Z G Li, D J Smith, Opt Eng, 30, 1049 (1991).

4. A Ridgeley, Report to the High Power Laser Panel on the TA4 Programme, May (1991).

5. D S Urch, E Martins, Central Laser Facility Annual Report, 68, (1991).

CALIBRATION OF A CCD SYSTEM FOR FILM DENSITOMETRY

D. Hardie+, S. Sails+,C. Danson+ D. Neely*.

+ Central Laser Facility, SERC Rutherford Appleton Laboratory, Chilton, England.
* Department of Pure and Applied Physics, Queen's University of Belfast, N.Ireland.

INTRODUCTION

Two dimensional, high spatial resolution (10μm) densitometry of large areas (> 4mm^2) using the available MK3 Joyce Lobel microdensitometer at R.A.L. is a time consuming process. In a recent experiment to quantify focal plane intensity distributions, a fast method of analyzing pin-hole camera images was required. A CCD camera with associated optics and an image grabbing system is shown to be capable of analyzing an image almost instantaneously.

EXPERIMENTAL

A 1.06μm 110mm diameter beam of 600ps duration from the Vulcan glass laser was relayed into target area 2 at R.A.L. A 1m focal length, plano-convex lens was used to generate the focal spot and the random phase plate[1] under test was inserted between the lens and the focal plane. For a R.P.P. of high spatial frequency (100μm structure) it was necessary to ensure that it was the last optical surface in the system, as after passing through the R.P.P. diffraction / interference effects rapidly modulates the energy distribution in the beam line to well above the damage threshold for glass optics. In our case, the R.P.P. was deposited on the inside surface of the vacuum chamber window. The spatial distribution of X-ray emission from the target surface was monitored using two pin-hole cameras, of resolution 25 and 35μm respectively, and the data was recorded on Kodak Industrex C film.

ANALYSIS / RESULTS

Images of the films were obtained using a Bausch & Lamb MonoZoom 7 microscope, a large area (4cm^2) uniformly illuminated white light source, a COHU 4712 CCD camera and an OFA[2] image grabbing/analysis package. The auto gain black level and auto gain setting on the CCD camera were both set to manual. The gamma of the camera can be altered between two settings. It was put to the setting determined to give the largest range of counts for the density range of the results (0 - 2.0 O.D.). Many other cameras were tested but it was found that even with the auto gain switched 'off' some still displayed a detectable degree af automatic gain control.

The OFA frame grabbing system digitized the CCD camera signals to eight bit accuracy i.e. (NC=0-255). The calibration from optical density O.D. to the number of counts NC recorded was carried out using a set of neutral density filters placed at the object plane of the microscope. The O.D. against NC curve was converted to NC against incident photons per square micron N_υ as shown in figure1a, using a film calibration curve for the Industrex C film[3]. In order to monitor the incident energy distribution at the target plane using the pin-hole camera images, it is necessary to know the relationship between the incident energy and the X-ray emission intensity. This was investigated by taking six shots, under nominally identical focal conditions, and varying the incident laser energy E_{laser}. The total number of X-ray photons ΣN_υ recorded as a function of target energy was measured, and is shown in Figure 1b. This graph shows an almost linear relationship, but does not go through the origin. This is believed to be a problem associated with the large uncertainties present in calibrating the CCD camera at low densities (<0.2 O.D.).

CONCLUSION

Using a calibrated CCD densitometry system, pin-hole camera images can be readily examined in terms of the incident energy on target. This allows rapid comparison of the focal intensity distributions generated using random phase plate technology. Although conversion problems do exist at very low image densities, the system is adequate for preliminary analysis purposes.

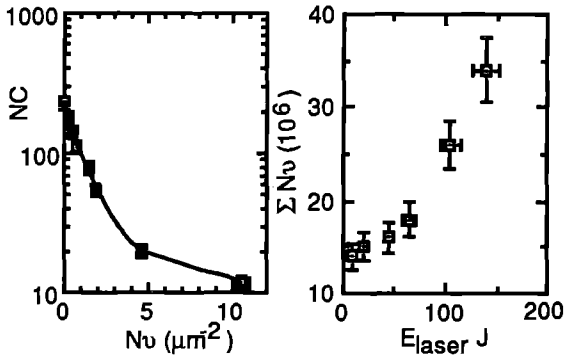

Figure 1a and b Calibration curves obtained for the CCD imaging system as described in the text.

[1] C. Danson et al, Report No RAL-91-025,1991,P62-65

[2] O.F.A. Ltd, Orchard End, Ickleton Road, Wantage, OXON, England, OX12 9JA

[3] A. Ridgely et al SPIE proc 1989

LASING IN X-RAY BEAM INTERACTION WITH PLASMAS.

A. Djaoui

Rutherford Appleton Laboratory

1 INTRODUCTION

Collisional neon-like x-ray laser schemes operating on 3p−3s transitions have shown near saturation[1] and are able to deliver x-ray laser powers in excess of 1 MW at 232Å and 236Å in germanium. Applications in microscopy and holography using the x-ray laser beams have already started [2] and understanding of x-ray laser beam interaction physics with matter is needed. X-ray laser have much shorter wavelength (from approximately 30 to 300 Å) than lasers in the infrared, visible or ultraviolet spectrum. The corresponding photon energies are as high as the ionization potential of many low-Z ions and this results in photoionization and recombination processes playing the dominant role in the interaction. Here we calculate such interaction using an average atom model supplemented with a non-planckian radiation field. The calculation shows that inner shell vacancies, as created by photoionization, followed by tree-body recombination into upper levels leads to population inversion on many resonance transitions. As the x-ray beam intensity increases the inversion proceeds to higher levels and eventually moves to the continuum and results in free-bound stimulated emission gain as suggested first by Kodama [3].

2 THEORY

The average atom model does not take into account fine splitting of atomic levels and can only be used for this study with careful choice of the x-ray photon energy. For example the ionization potential for He I is 24.581 eV and 54.403 eV for He II. These correspond to the removal of the first electron from $n = 1$ shell and the last electron respectively. In this case and at x-ray photon energies above the He I and below He II ionization potentials a detailed collisional radiative model is more appropriate. Despite this limitation, it worth pointing out that the average atom model is easily applied to very complex situation where a detailed model would be too complicated. A description of the average atom model (without the x-ray field) can be found in reference 4. The following atomic processes are included; collisional excitation and deexcitation, collisional ionization and tree body recombination, dielectronic and radiative recombination. In the presence of the x-ray photon field it is necessary to add photoionization and stimulated free-bound recombination. Within the average atom model formalism, the rate of photoionization $P_n R^r_{nc}$ per atom from shell with principal quantum number n corrected for stimulated recombination is given by;

$$P_n R^r_{nc} = 4\pi P_n \int_{\nu_0}^{\infty} \alpha_{nc}(\nu)[1-\frac{Z^* Q_n}{P_n}(\frac{P^0_n}{Z^*_0 Q^0_n})e^{-h\nu/kT}]\frac{J_\nu}{h\nu}d\nu \quad (1)$$

where P_n is the electron population in level n, Z^* the average ionization and $Q_n = 1 - P_n/2n^2$. When used with a 0 subscript or superscript, these quantities refer to the LTE values. $\alpha_{nc}(\nu)$ is the absorption cross section at photon frequency ν. J_ν is the specific radiation intensity which includes both the ambiant photon field and the x-ray beam field J_{ν_x}. By defining a radiation temperature for the x-ray photons T_x, J_{ν_x} can be written as

$$J_{\nu_x} = \frac{2h\nu_x^3}{c^2}\frac{d\nu_x}{e^{h\nu_x/kT_x}-1} \quad (2)$$

This is easily incorporated in equation 1.

3 RESULTS

The average atom rate equations for level populations are solved for a helium plasma at constant mass density (10 mg/cc), temperature (5 eV) and x-ray energy equal to 60 eV at an intensity of $10^{14}\,W/cm^2$, until steady state is reached. The average ionization state is then $Z^* = 0.32$ and the corresponding electron density $4.8\ 10^{20}\ cm^{-3}$. Table 1 compares the rates of ionization and recombination by collisional and radiative processes from different levels. It is seen that photoionization dominates in the low-lying levels. The higher levels on the other hand are populated mainly by three body recombination. The combination of the two processes leads naturally to population inversion.

Table 1: Comparison of contributions to ionization/recombination by collisional and radiative processes

level n	coll. ioniz. (s^{-1})	coll. recomb. (s^{-1})	photo. ioniz. (s^{-1})	photo. recomb. (s^{-1})
1	$4.3\ 10^{05}$	$1.3\ 10^{10}$	$7.9\ 10^{11}$	$1.5\ 10^{11}$
2	$7.9\ 10^{11}$	$9.1\ 10^{11}$	$8.1\ 10^{11}$	$4.7\ 10^{07}$
3	$1.5\ 10^{13}$	$1.5\ 10^{13}$	$2.7\ 10^{10}$	$1.8\ 10^{07}$
4	$1.0\ 10^{14}$	$1.0\ 10^{14}$	$3.6\ 10^{09}$	$9.5\ 10^{06}$
5	$3.3\ 10^{14}$	$3.3\ 10^{14}$	$1.0\ 10^{09}$	$6.1\ 10^{06}$

Figure 1 shows the gains on three lines and on the free-bound transition from the continuum edge in H-like ions. The threshold intensity for gain on the $2p_{3/2} - 1s_{1/2}$ is about 6. $10^{12}\,W/cm^2$. This value increases for transitions from higher levels and reaches $10^{14}\,W/cm^2$ at the edge of the continuum. The drop at higher intensities in the gain on bound-bound transitions is the result of the increased photoionization from the upper levels of the transitions. The rise in the free-bound gain follows the more favourable population inversion on this transition as the fraction of fully stripped ions increases.

A more detailed study, which includes hydrodynamic and thermodynamic effects is in progress and will be presented at the 3rd international colloqium on x-ray lasers in Schliersee.

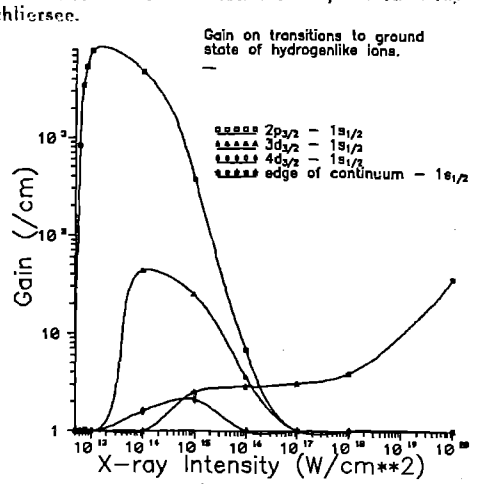

Figure 1. Calculated gain in H-like ions as a function of incident x-ray intensity for $n = 2 \to 1$, $3 \to 1$, $4 \to 1$ and edge of continuum $\to n = 1$ transitions

4 REFERENCES

[1] See for example D Neely et al. Central Laser Facility Annual Report, RAL 91-025 (1991).

[2] RE Burge et al. Central Laser Facility Annual Report, RAL 90-026 (1990).

[3] R. Kodama. 21st ECLIM conference, Warsaw 1991 (to be published in *Laser and Particle Beams*)

[4] A. Djaoui and SJ rose. J. Phys. B: Atomic, Molecular and Optical physics, in print (1992).

SIMULATION STUDY OF X-RAY LASER INTERACTION WITH PLASMAS

R Kodama

Rutherford Appleton Laboratory

I. Introduction

The output power of soft x-ray lasers pumped by optical lasers has increased in recent years [1,2]. By focusing such high power x-ray lasers, we can study x-ray interaction with matter at specific wavelengths and intensities never before achieved in the laboratory.

Non-thermal equilibrium conditions on the ionization balance are expected in the intense monochromatic x-ray interaction with plasmas, which may lead gain on free-bound transitions due to stimulated recombination. One of the criteria to achieve high gain for the application to free-bound lasers is generation of a truly non-thermal equilibrium condition at high particle densities [3]. X-ray lasers can interact with high density plasmas and may create such a non-thermal equilibrium condition on the ionization balance.

In this paper, atomic processes in x-ray laser interaction with plasmas are investigated by using a collisional-radiative model. Population inversions on free-bound transitions are created by photoionization in a strong radiation field. Free-bound lasers pumped by intense x-ray lasers are proposed [4].

II. Photo-absorption

Photoionization and stimulated recombination are most important atomic processes in x-ray laser interaction plasmas (see Fig. 1). In a strong x-ray radiation field I_x, absorption is saturated (saturated absorption) and absorption coefficients $\sigma\Delta N$ on bound-free transitions are given by

$$\sigma\Delta N = \sigma(N_1 - \alpha_0 N_2) = 0 \qquad (1)$$

between upper (N_2) and lower (N_1) ionization stages. N_i is a population of the ionization stage i and α_0 a function due to stimulated recombination for the incident radiation. At the condition of saturated absorption i.e. $N_1=\alpha_0 N_2$ from Eq. 1, bound-free absorption coefficients $\sigma\Delta N_L$ for x ry with photon energyies less than the photon energy of the incident x rays are given by

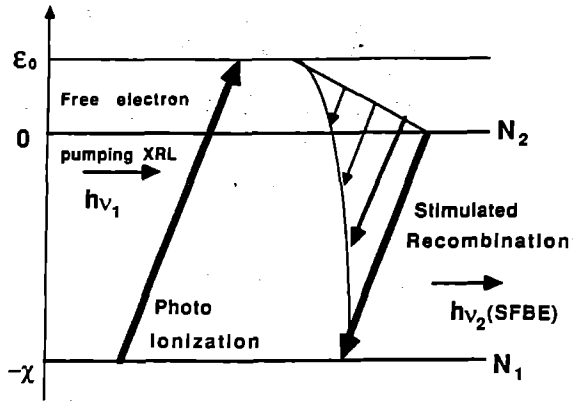

Figure 1
Bound-free transitions between upper (N_2) and lower (N_1) charge states in a radiation field. $h\nu_1$ is a photon energy of the incident x ray and $h\nu_2$ a photon energy of SFBE. $h\nu_1=\chi+\varepsilon_0$ and $h\nu_2=\chi+\varepsilon<h\nu_1(\varepsilon<\varepsilon_0)$ where c is the ionization potential and e a free-electron energy.

$$\sigma\Delta N_L = \sigma[N_1 - \alpha(h\nu)N_2] = \sigma[\alpha_0 - \alpha(h\nu)]N_2 < 0, \qquad (2)$$

$\alpha(h\nu)$ with a smaller ionization energy gap is larger than α_0, i.e. $\alpha(h\nu_2)>\alpha(h\nu_1)$ for $h\nu_2<h\nu_1$ in Fig. 1, resulting that absorption on the bound-free transitions can change to gain in the strong radiation field. The gain on the free-bound transitions due to stimulated recombination is induced by photoionization above a threshold of the incident x-ray laser intensity and leads to stimulated free-bound emission (SFBE).

III. Atomic model

A steady state collisional radiative model [5] is used to investigate the atomic processes in x-ray laser interaction plasmas. The radiation field effect is modeled by considering photoionization and stimulated recombination. All the ionization stages of fully striped to neutral ions are treated and the excited states of H-like to Li-like are included. Total photo-absorption coefficient k is calculated on free-free (k_{ff}) and bound-free (k_{bf}) transitions (i.e., $k=\Sigma(k_{ff}+k_{bf})$). Photon scattering and bound-bound absorption are ignored because of its small cross section and the photon energy coincidence problem, respectively.

Relationship between the cross section of photoionization and radiative recombination is obtained from the principle of detailed balance [6]. Using the Einstein-Milne relation, we obtain

$$\sigma_{vn}(V) = \frac{g_+}{g_n}\frac{m_e^2 V^2 C^2}{(h\nu)^2}\sigma_{cn}(V), \qquad (3)$$

where $\sigma_{vn}(h\nu)$ is the photoionization cross section and $\sigma_{cn}(V)$ the cross section of radiative electron capture. g_i is the statistical weight, V the electron velocity, and C the light speed. Kramers cross section $\sigma_{cn}(V)$ is used for radiative electron capture, which is corrected with a radiative bound-free Gaunt factor g(hν).

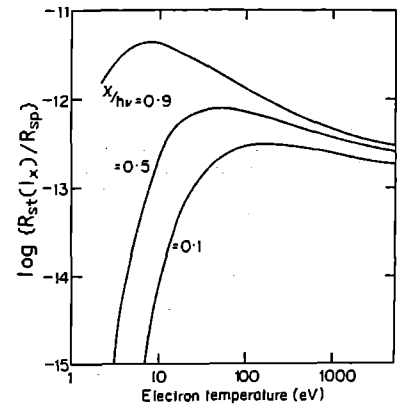

Figure 2
Electron temperature dependence of the ratio of stimulated recombination rate to spontaneous recombination rate as a function of ionization potential ($\chi/h\nu$). χ is the ionization potential an hν the photon energy of the incident radiation.

IV. Results

In the intense x-ray radiation field, stimulated recombination become an important atomic process. Figure 2 shows the electron temperature dependence of the ratio of stimulated recombination rate to spontaneous recombination rate at a unity radiation field ($1W/cm^2$). A Gaussian profile of $\Delta h\nu/h\nu=2.5x10^{-5}$ is assumed for the incident x-ray profile. The stimulated recombination rate has a llinear function of the radiation field, resulting that the stimulated recombination process become larger than the spontaneous recombination rate at intesities above 10^{12}-$10^{13}W/cm^2$ from Fig. 2.

The dependence of photo-absorption or gain coefficient of free-bound transitions for 26nm x rays in the carbon plasmas as a function of the incident x-ray laser intensity is shown in Fig. 3 Above an intensity threshold, absorption of 26nm x rays changes to gain due to stimulated recombination, which is induced by photoionization in the strong radiation field (SFBE). The SFBE gain is saturated at a laser intensity where absorption of the incident x rays (23nm) is saturated because of the saturation of photo-pumping from lower to upper charge state.

V. Application to free-bound x-ray lasers

X-ray laser interaction plasmas may be applicable to free-bound x-ray lasers which have potential of a tunable x-ray laser [3]. The x-ray laser interaction plasmas with SFBE gain are nearly transparent to the pumping x rays due to saturated absorption as shown in Fig. 3. Introducing an end-pumping scheme as shown in Fig. 4, the incident x-ray lasers will pump uniformly the plasmas. Long focal depths l are expected when focusing a short wavelength laser. By using an x-ray focusing optics with f/number, f of 10, an x-ray laser at a wavelength of 23nm with a beam divergence of 4mrad [2] can be focused in a diameter of 4mm, which allows a pumping length l (focal depth) of 0.1cm

A lower electron temperature is necessary to achieve higher gain of the SFBE. Using thin foil targets as shown in Fig. 4, this requirement will be satisfied by the efficient expansion cooling. From the energy equation of hydrodynamic of a thin foil target [4,7], the temperature in a steady state ($dkT_e/dt=0$) is given by

$$kT_e = \frac{\Sigma(\kappa_{ff}+\kappa_{bf})I_x\, b}{2\,U\,(1+Z)N_e}, \qquad (4)$$

where b is a thickness of foil targets and N_e the electron density. U is an expansion speed as equal to the ion thermal speed. The radiation and ionization losses are ignored for a pessimistic estimation. Using a thin foil target with a thickness of 600-700A, the electron temperature of 5eV can be achieved in the carbon plasma with an electron density of $2x10^{21}cm^{-3}$ at 23nm-laser intensities of 1-$3x10^{14}W/cm^2$ from Eq. 4. Assuming an output x-ray laser intensity of 1-$2x10^{11}W/cm^2$ with a Ne-like germanium laser (l=23.6nm), gain product of 5 (SFBE gain coefficient of $50cm^{-1}$) at a wavelength of 26nm will be feasible in the carbon plasmas (T_e=5eV and $N_e=2x10^{21}cm^{-3}$)by using a perfect soft x-ray optics.

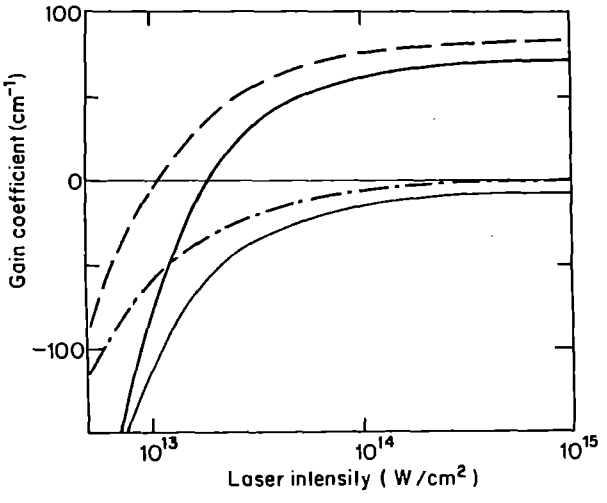

Figure 3
The x-ray laser intensity dependence of SFBE gain at a wavelength of 26nm in the carbon plasma pumped by a 23nm x-ray laser. The effective gain coefficient as shown by a bold-solid line is attributed to all bound-free and free-free transitions. A dotted line shows a gain coefficient on the transition from Li-like to Be-like ions. Solid line is a total gain (absorption) coefficient and dot-dashed line the coefficient of Be-like ions of the pumping x-ray laser.

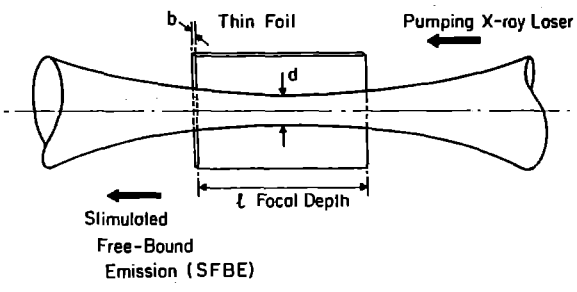

Figure 4
The end-pumping scheme of a free-bound laser using x-ray laser interaction plasmas.

VI. Summary

Bound-free absorption in x-ray laser interaction plasmas is investigated by using a collisional-radiative model. In a strong radiation field, absorption can change to gain due to stimulated recombination, which is induced by photoionization (Stimulated Free-Bound Emission; SFBE).

X-ray laser interaction plasmas will be applicable to free-bound lasers (FBL). An end-pumping scheme using thin foil targets is proposed for the FBL. A simple estimation predicts the feasibility of gain products of 5 at a wavelength of 26nm in carbon plasmas irradiated by a 23nm x-ray laser with a intensity of $10^{14}W/cm^2$. More detail analysis using a time-dependent atomic model coupled with a hydrodynamic code will be necessary to estimate the practicability of FBL using x-ray laser interaction plasmas.

References

[1] D. Matthews et al, 'X-Ray Laser 1990' G. Tallents ed IOP, Bristol (1991) p205.
[2] M. H. Key et al, (to be published 1992).
[3] R. C. Elton, 'X-Ray Laser' Academic Boston(1990), E. E. Fill , Phys. Rev. Lett. 56 (1986) 1687.
[4] R. Kodama, Laser and Part. Beams (in press 1992).
[5] R. W. Lee et al, J. Quant. Spectrosc. Radiat. Transfer 32 (1984) 91.
[6] Ya. B. Zel'dovichi and Yu. P. Raiser 'Physics of Shock Waves and High Temperature Hydrodynamic Phenomena' Academic, New York (1966), D. Mihalas,'Stellar Atmospheres' Freeman San Francisco (1978).
[7] K. M. Dawson, Phys. Fluids 7 (1964) 981.

PLASMAS PRODUCED BY OPTICAL-FIELD-INDUCED IONIZATION: NEW RECOMBINATION X-RAY LASERS?

S. C. Rae and K. Burnett

Clarendon Laboratory, Department of Physics, University of Oxford, Parks Road, Oxford OX1 3PU

In recent years it has been noted that plasmas produced by optical-field-induced ionization (OFI) have certain desirable properties for recombination x-ray laser schemes.[1] The pulse duration produced by the latest generation of intense lasers is sufficiently short to allow the possibility of transient gain on ground-state transitions and, more importantly, the residual plasma temperature may be low enough to allow rapid recombination to commence without the need for additional cooling. By creating a plasma 'instantly' at the optimum conditions for lasing, solid slab or fibre targets could be replaced by atmospheric-density gases.

The ionization in an OFI plasma does not result from collisional processes, but rather from multiphoton absorption due to the intense laser field. Such a mechanism will only be dominant for ultrahigh intensities, typically $I \gg 10^{16}$ W/cm^2. Short laser wavelength and short pulse duration are both important in minimizing the plasma temperature, and the Sprite laser, in conjunction with a chirped-pulse amplification scheme, would provide a very attractive system for performing experiments related to cold-plasma production.

Theoretical studies by Burnett and Enright[2] and Amendt *et al.*[3] have proposed various x-ray laser schemes based on optical-field-induced ionization. The plasma temperature is a crucial parameter in determining the feasibility of such schemes, and in general a residual temperature of less than about 50 eV is needed to achieve a high energy efficiency. Here, we present the outline of a one-dimensional (1D) computer model which we have developed in order to estimate the plasma temperature for the case of an intense femtosecond laser pulse propagating through an atmospheric-density noble gas. The results concentrate on neon, and are thus directly relevant to the proposal by Amendt *et al.* for a recombination x-ray laser in the transient-gain regime in Li-like Ne.

There are a number of mechanisms which are important in determining the final temperature in an OFI plasma, including ATI, collisional heating, space-charge effects and parametric instabilities. As the model developed here is purely one-dimensional, we are unable to address spatial effects directly, but a determination of the contributions from ATI and collisions is nevertheless important, as this sets a lower limit on the achievable temperature.

In our model we solve a coupled set of rate equations at each point in the plasma simultaneously with Maxwell's equations for the propagation of a linearly-polarized laser pulse. Optical-field-induced ionization rates are calculated using the static-field form of the tunneling expression given by Ammosov, Delone and Krainov (ADK).[4] Recent experiments by Augst *et al.*[5] have confirmed that this generalized tunneling formula is in good agreement with observations. Augst *et al.* determine correction factors which can be used with the ADK formula, however, we have not included these in the present model.

The ions are assumed to be in their ground states, and only sequential ionization processes are considered. The rate equations are thus of the form

$$\frac{dN_k}{dt} = -\mathcal{R}_k N_k + \mathcal{R}_{k-1} N_{k-1} \,, \tag{1}$$

where R_k is the ionization rate and N_k the population of the k-th stage.

In 1D, a transverse electromagnetic pulse obeys the time-dependent wave equation

$$\frac{\partial^2 E}{\partial x^2} - \frac{1}{c^2}\frac{\partial^2 E}{\partial t^2} - \mu_0 \frac{\partial J}{\partial t} = 0 \,, \tag{2}$$

where J is the total plasma current. This current is calculated from the electron distribution function, $f_e(x, v, t)$, with the addition of a term to ensure energy conservation during ionization,

$$J = -e \int f_e(x, v, t)\, v \, dv \; + J_{ioniz} \,. \tag{3}$$

The ionization current, J_{ioniz}, is obtained by equating the energy loss through ionization to the Joule heating,

$$E \cdot J_{ioniz} = \sum_k \mathcal{R}_k N_k \mathcal{E}_k \,. \tag{4}$$

where $\mathcal{E}_k$ is the ionization potential of the k-th stage. The equation of motion for the electron distribution function is solved simultaneously with the wave equation. Following the end of the laser pulse, the average ATI energy as a function of distance can be calculated directly from the electron distribution function,

$$\mathcal{E}_{ATI}(x) = \frac{\int \frac{1}{2} m_e v^2 f_e(x, v)\, dv}{\int f_e(x, v)\, dv} \,. \tag{5}$$

Collisional heating is incorporated by modifying the equation of motion for the electron distribution function to include a friction term. The frictional force due to collisions on electrons moving with velocity v is given by $m_e \nu_{ei} v$, and the average power absorption per electron is then

$$P(x) = \frac{\int m_e \nu_{ei} v^2 f_e(x, v)\, dv}{\int f_e(x, v)\, dv} \,. \tag{6}$$

The electron-ion collision frequency, ν_{ei}, is determined using a Spitzer-type expression[6] which includes corrections for the oscillatory motion of the electrons in the laser field and for the change in plasma temperature during the laser pulse. A minimum temperature must be assumed for the Spitzer expression to remain valid, and this is typically taken as 5 eV. As long as the final temperature is significantly greater than this imposed minimum, the actual choice is not critical. Effects due to a non-Maxwellian electron distribution, such as the Langdon correction,[7] have not been included.

The complete system of equations was solved numerically using an explicit finite-difference technique. The laser pulse (with a sine-squared field envelope) was propagated through a relatively short length of neon gas (5 μm), and as the plasma properties are almost constant over such a short distance, the temperatures are plotted simply as averages across the plasma.

Figure 1 shows the plasma temperature and final degree of ionization as functions of the peak laser intensity, for a 100 fs FWHM, 248 nm laser pulse and a Ne gas density of 2.5×10^{18} atoms/cm^3. The intensity required for the production of a Ne^{8+} plasma is approximately 2.5×10^{17} W/cm^2, and further calculations have confirmed that this is independent of the plasma density.

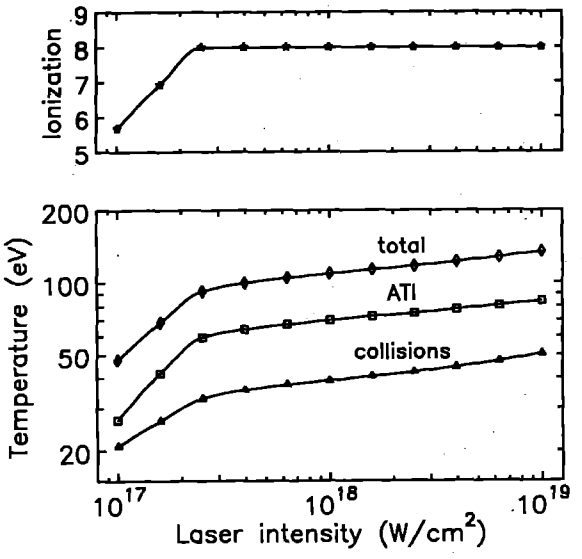

Figure 1. Plasma temperature and final degree of ionization as functions of laser intensity, for a 100 fs, 248 nm laser pulse, and a Ne atom density of 2.5×10^{18} cm^{-3}.

Figure 2 shows the variation in plasma temperature with density, for a 100 fs FWHM, 248 nm laser pulse at the minimum intensity required for producing a Ne^{8+} plasma. The ATI temperature, as expected, is independent of the plasma density. The collisional temperature increases approximately linearly with density, in accordance with the density dependence of the collision frequency.

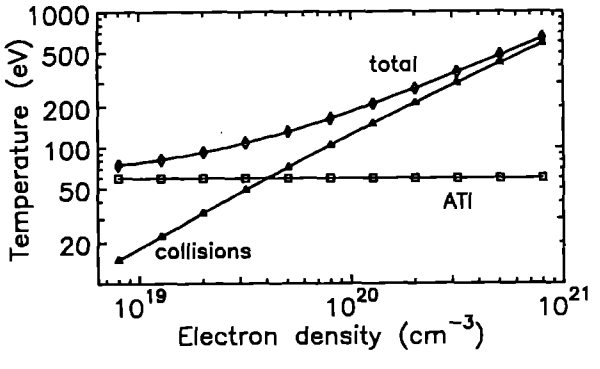

Figure 2. Plasma temperature as a function of density, for a 100 fs, 248 nm laser pulse at a peak intensity of 2.5×10^{17} W/cm^2.

Further calculations have shown that the total plasma temperature decreases for a shorter laser wavelength and for a shorter pulse duration. In the former case, the decrease is predominantly due to the dependence of the ATI temperature on wavelength; in the latter case, the ATI temperature is almost independent of pulse length, but the collisional heating varies linearly with the pulse duration.

The results obtained from the 1D propagation-ionization model for the case of a neon plasma can be summarized as follows:

1. A peak laser intensity of approximately 2.5×10^{17} W/cm^2 is required to produce a Ne^{8+} plasma, independent of the density, and the use of a higher intensity simply raises the plasma temperature.
2. The collisional temperature increases approximately linearly with the density. For a 100 fs, 248 nm laser pulse, the desired ionization stage and a collisional temperature of $\lesssim 50$ eV can only be achieved with an electron density of $\lesssim 3 \times 10^{19}$ cm^{-3}.
3. The ATI temperature is independent of the density. For a 100 fs, 248 nm laser pulse at a peak intensity of 2.5×10^{17} W/cm^2, the ATI temperature is approximately 60 eV.
4. A shorter pulse duration or a shorter laser wavelength would reduce the total plasma temperature.

The proposed recombination x-ray laser scheme of Amendt *et al.* requires an electron density of $\gtrsim 10^{20}$ cm^{-3} and a total plasma temperature of $\lesssim 50$ eV for large gain and high energy efficiency. For a 100 fs FWHM, 248 nm laser pulse at an intensity of 2.5×10^{17} W/cm^2 and an electron density of 10^{20} cm^{-3}, our model predicts a plasma temperature of 185 eV, of which approximately 60 eV is due to ATI and 125 eV due to collisional heating. It should be noted that this does not include any additional contribution due to Raman heating. The x-ray gain is an extremely sensitive function of temperature, and unless some way is found to significantly reduce both the ATI and collisional contributions, this result would suggest that the Li-like Ne scheme is only marginally feasible. Other schemes, based on different transitions or using double-pulse techniques,[2] may still, however, be promising candidates.

There remains a question mark over the importance of space-charge effects, which we are unable to include in our model. Penetrante and Bardsley,[8] in their recent PIC code study of residual energy in OFI plasmas, calculate that for a 200 fs, 248 nm laser pulse at an intensity of 10^{18} W/cm^2 and a Ne^{8+} plasma at an electron density of 10^{20} W/cm^2, the resultant temperature is around 10 eV. The results from our model are not consistent with this, and predict a total plasma temperature under the same conditions of around 200 eV. Preliminary experiments are needed to resolve this issue, and to give an indication of the relative accuracy of the various models.

Another important issue for any recombination x-ray laser scheme based on an OFI plasma is whether a long filament of highly-ionized gas can actually be produced. In the transient-gain regime, where the gain duration is on the order of 1 ps, a traveling-wave pump geometry is necessary. A typical focal spot half-intensity radius of 25 μm corresponds to a confocal parameter of 4.5 cm, and focusing an intense laser pulse through a rapidly ionizing medium over such a long distance is by no means a trivial task. Defocusing caused by the rapid ionization would tend to disrupt the propagation of a Gaussian beam over distances much shorter than the several centimetres required. We are currently working on extending our model to allow the investigation of defocusing effects during the plasma formation process.

REFERENCES

1. N. H. Burnett and P. B. Corkum, J. Opt. Soc. Am. B **6**, 1195 (1989).
2. N. H. Burnett and G. D. Enright, IEEE J. Quantum Electron. **26**, 1797 (1990).
3. P. Amendt, D. C. Eder, and S. C. Wilks, Phys. Rev. Lett. **66**, 2589 (1991).
4. M. V. Ammosov, N. B. Delone, and V. P. Krainov, Zh. Eksp. Teor. Fiz. **91**, 2008 (1986) [Sov. Phys. JETP **64**, 1191 (1987)].
5. S. Augst, D. D. Meyerhofer, D. Strickland, and S. L. Chin, J. Opt. Soc. Am. B **8**, 858 (1991).
6. L. Spitzer, Jr., *Physics of Fully Ionized Gases*, 2nd edn. (Interscience, New York, 1962), Chap. 5.
7. A. B. Langdon, Phys. Rev. Lett. **44**, 575 (1980).
8. B. M. Penetrante and J. N. Bardsley, Phys. Rev. A **43**, 3100 (1991).

CALCULATIONS OF THE RADIATIVE OPACITY OF LASER-PRODUCED PLASMAS - THE OPACITY CODE IMP (IONISED MATERIAL PACKAGE)

S J Rose
Rutherford Appleton Laboratory

The calculations of the radiative opacity of hot dense matter was first of interest in astrophysics and has been of particular importance in the study of stellar structure and evolution. In the last few years the opacity of laboratory (particularly laser-produced) plasmas has been of interest. Experimental measurements of the opacity of near-LTE laser-produced plasmas have recently been made (Davidson et al 1988, 1989 Foster et al 1991). Experiments which measure radiation transport through plastic and doped-plastic foils have also recently been performed (Edwards et al 1991). A numerical model of the radiative opacity of LTE laser-produced plasmas, called IMP (Ionised Material Package) has been developed which involves the use of a Thomas-Fermi mixtures model to provide an average atomic potential for each element of the mixture. Using this potential one-electron wavefunctions are calculated by solution of the Dirac equation and, in turn, these orbitals are used to construct the bound electronic configurations with the largest occurrence in the plasma Bound-bound, bound-free and free-free photoabsorption cross-sections are then calculated and the total photoabsorption cross-section for the plasma is thereby determined.

Comparison of IMP with the experimental transmission of an LTE germanium plasma at 76 eV and 0.01 of solid density is shown in Figure 1. The experimental transmission is shown as a feint line, whereas the IMP calculation is a bold line (a) with and (b) without inclusion of term-splitting in the calculation. Plainly inclusion of term-splitting gives more accurate results.

The good agreement between theory and experiment gives us confidence in the validity of the model and IMP is currently being used to calculate a set of opacities at a range of temperatures and densities for use in radiation transport studies (Edwards et al 1991).

REFERENCES

1. S J Davidson, J M Foster, S J Rose, C C Smith and K Warburton, Appl Phys Letts 60, 2034, (1988).

2. S J Davidson, C L S Lewis, D O'Neill, S J Rose, J M Foster, C C Smith, Laser Interactions with Matter, ed by G Verlarde, E Minguez and J M Perlado (Singapore, World Scientific), (1989).

3. J M Foster, D J Hoarty, C C Smith, P A Rosen, S J Davidson, S J Rose, T S Perry and F J D Surduke, Phys Rev Letts 67, 3255, (1991).

4. J Edwards, M Dunne, D Riley, R Taylor, O Willi and S J Rose, Phys Rev Letts, 67, 3780, (1991).

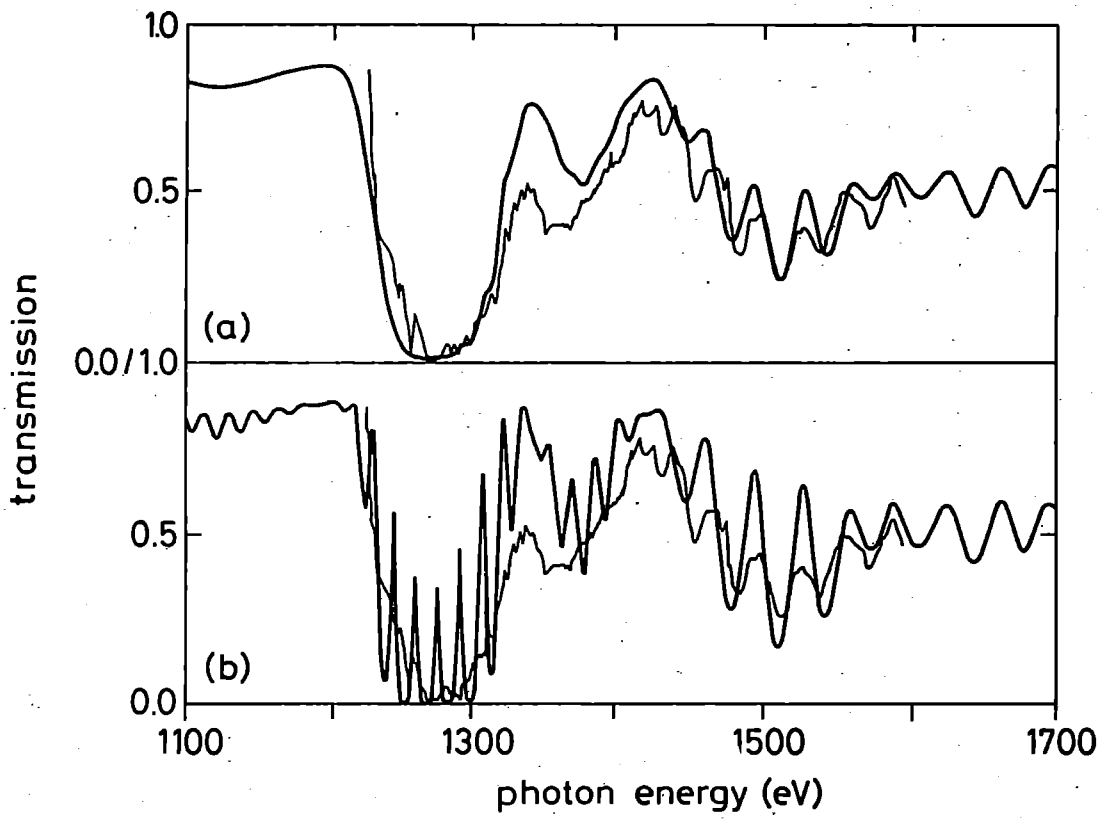

PILOT STUDY INTO SOFT X-RAY EMISSION FROM LASER PRODUCED PLASMAS

P. Fluck[1], A. Djaoui[2] and A.G. Michette[1]

[1]Department of Physics, King's College London.
[2]Rutherford Appleton Laboratory

INTRODUCTION

Preliminary experiments have been carried out, coupling a Scanning Transmission X-ray Microscope (STXM) to a Laser Produced Plasma (LPP) X-ray source[1]. The STXM requires a bright, monochromatic flux[2], since it relies on diffractive optics. At present, the brightness of an LPP X-ray source is between one and two orders of magnitude too faint for a good signal to noise ratio to be obtained. It would therefore be advantageous to conduct a theoretical study into X-ray emission from LPP's to investigate possible (and practical) changes to laser pulse parameters and target parameters to enhance yields of X-rays.

SIMULATION

To investigate the characteristics of frequency integrated radiation from an LPP source, we use computer simulation. The simulations are performed using MED-102, the laser plasma simulation code held at RAL[3]. The target chosen is carbon to closely model the actual target used experimentally, mylar. The laser pulse modelled is that of the KrF eximer laser used in experiments with the STXM. The laser pulse is 22ns in duration, $3.7 \times 10^{12} Wcm^{-2}$ irradiance and 2.48 micron wavelength. The laser-plasma interaction is simulated for 90ns.

To discover the effect of pulse length on radiation emission, we simulate interactions in which the pulse length is varied, keeping target, wavelength and irradiance parameters constant.

RESULTS

The individual contributions of bound-bound, free-bound and free-free radiation are shown in Fig.1., along with their combined output. It can be seen that bound-bound radiation dominates for these conditions. This is in agreement with spectra found experimentally for these conditions[1], where line radiation dominates. The contributions of free-bound and free-free emission are typically factors of 2 and 4 less than the bound-bound contribution, respectively.

Shown in Fig.2. is the conversion efficiency (emitted energy divided by total input energy) as a percentage, plotted versus the logarithm of the pulse length in picoseconds. It is seen that for very short pulses, the conversion efficiency is extremely low, because very little plasma can be formed. There is a sharp maximum corresponding to pulse lengths of 10-15 ns. It would appear that the optimum pulse length needed to produce maximum output of electromagnetic radiation is 15ns.

Fig.1. Time and Frequency Integrated Radiated Energy

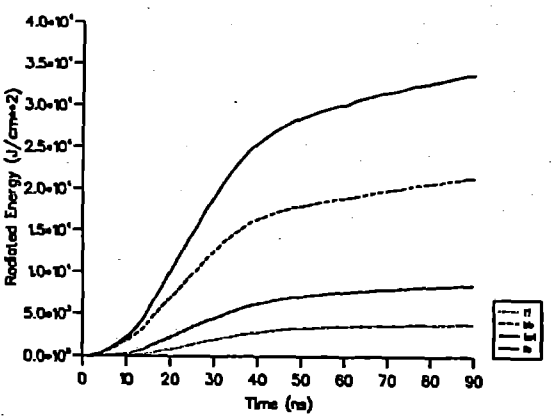

Fig.2. Conversion Efficiency vs log of Pulse Length

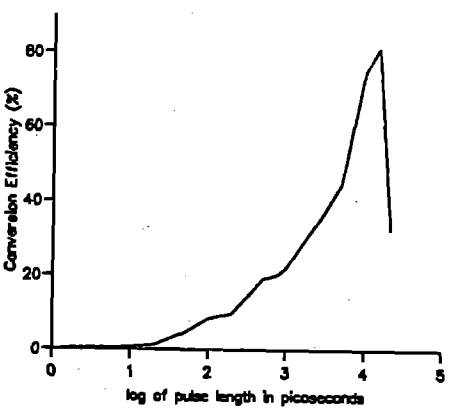

FUTURE WORK

The present simulation code does not incorporate any frequency dependence when calculating emitted radiation. It is hoped that frequency dependence will be written into the model within the next year, along with radiative transport modelling. This would allow spectra to be simulated.

The code at present uses an average atom approximation[3] when dealing with the atomic physics. It remains to be seen whether this will produce sufficiently detailed spectra, or whether a more sophisticated model is needed.

REFERENCES

1. I.C.E. Turcu et al, SPIE, Vol. 1503, 391, (1991).

2. G.R. Morrison and R.E. Burge, 'Synchrotron Radiation X-Ray Microscopy', ch.15, Ellis Horwood Ltd., (1990).

3. A. Djaoui and S.J. Rose, J. Phys. B., (in print) (1992).

INELASTIC ELECTRON SCATTERING IN DENSE PLASMAS

F I Gordon[1] and A Djaoui[2]

[1]Department of Physics, University of Essex
[2]Rutherford Appleton Laboratory

INTRODUCTION

We have calculated the mean-free path of electrons scattering inelastically in a degenerate electron gas at zero temperature, using the formalism of Ritchie[1]. The objective of this work is to obtain an accurate representation of the mean-free path term at all energies for input into the Muller-Schaich EXAFS formula[2] (Extended X-ray Absorption Fine Structure). This is particularly important in situations where only the low-energy part of the EXAFS curve is available. At low photoelectron energies this should provide a more accurate description of energy loss than the complex potential approach used elsewhere[3,4]. The results can be demonstrated by including the loss term in an EXAFS calculation and comparing the resulting spectra with and without the mean-free path term. We fit our results to the 'universal' mean-free path formula of Seah and Dench[5] and obtain a table of best-fit parameters for a range of densities relevant to colliding shock experiments[6] on Al. We note that the more physical formula for high energy electrons given by Szajman and Leckey[7] is a better approximation to our high-energy results.

CALCULATIONS

We follow the treatment of Ritchie[1] for deriving the 'interaction probability per unit path length' via a dielectric function formalism. The quantity of interest to us, the mean-free path λ is simply the reciprocal of this. We require to know λ as a function of electron energy from the Fermi energy upwards. As the mean-free path becomes of the same size as the distances to given shells of atoms/ions these shells contribute less to the interference process giving rise to the EXAFS modulation. Elastic scattering off the ion potentials results in phaseshifts in the photoelectron wavefunction and gives rise to the strong modulation in the absorption coefficient above the absorption edge. We assume T=0 K for the purposes of this exercise - this formalism for the photoelectron is still valid at the moderate temperatures (~ 1 ev) found in shock -compressed solids as these remain strongly degenerate. The effect of temperature on the EXAFS will be treated in a separate publication. Ritchie showed how the interaction probability was related to the imaginary part of a complex dielectric function ε, which was taken to be the Lindhard representation. The problem becomes a double integral over the dimensionless energy and momentum transfers, with different approximations to ε in various regions. The two extreme cases of $E \cong E_F$ and $E >> E_F$ can be treated analytically to give explicit formulae for the mean-free paths, which are:

$$\lambda = A.\alpha^2/(\alpha^2-1)^2 \; for \; E \cong E_F \qquad (1)$$

$$\lambda = B.E/E_P \; ln(E/E_P) \; for \; E >> E_F \qquad (2)$$

where A, B are constants and $\alpha^2 = E/E_F$, and $E_P = \hbar\omega_P/2\pi$, the plasmon energy threshold.

The resulting curve for $\lambda(E)$ is shown in Figure 1 for solid Al. There is a broad minimum around 50 eV and a steep rise to lower energies. The constant A and B have a density dependence, as do both E_F and E_P. Photoelectron energy loss through plasmon emission occurs at all energies above E_P.

Using experimental mean-free path data from several sources Seah and Dench[5] proposed a 'universal' law for all elements of the form

$$\lambda = AE^{-2} + BE^{1/2} \qquad (3)$$

and gave the root-mean-square scatter factor as a measure of the goodness of fit to such a law for their compiled data. We attempted fitting such a law to the Ritchie 'data' but allowed a more general expression, viz.

$$\lambda = AE^{-\alpha} + BE^{\beta} \qquad (4)$$

where now α,β,A and B are to be found. Using a non-linear fitting procedure[8] best-fit values of these parameters were found at a range of densities of interest for EXAFS experiments, namely solid - 5x compressed Al and Na. These results are shown in Table 1. The change in α and β as the density rises suggests that the Seah-Dench law is not really 'universal' in the sense intended.

In fact a different law for high-energies was proposed by Szajman and Leckey[7,9] which is similar to the Ritchie result, ie

$$\lambda = BE/E_P\left(ln(E/\bar{E} + \phi\right) \qquad (5)$$

this result being based on a one-mode approximation to the excitation spectrum, and $\bar{E}$ being a characteristic energy which depends on both Ep and E_F.

They showed[9] how this result could reduce to the Seah-Dench-like result $\lambda \propto E^{0.75}$ under a simple approximation for $\bar{E}$.

We repeated the Ritchie calculation for the high-energy range up to 400 Ryd (= 5.4 keV) and fitted the two formulae

$$\lambda = B_5 E^{\beta} \qquad (6)$$

and

$$\lambda = B_6 E/(ln(\gamma E) + \phi) \qquad (7)$$

The results were as follows:

For formula (6), $B_5 = 0.0083$, $\beta = 0.82$ with a rms scatter factor $f = 1.018$; and for (7) $B_6 = 0.013$, $\gamma = 0.136$ and $\phi = 0.71$ with $f = 1.0016$, showing as expected that the Seah-Dench form is inferior at high energies compared to the Ritchie/Szajman/Leckey version.

APPLICATION OF RESULTS

We applied the mean-free path results for solid Al to an EXAFS calculation similar to that of Djaoui et al[10]. The result is shown in Figure 2, and it can be seen that the amplitude of the EXAFS signal is reduced especially at low energies, showing that the inelastic losses have an important influence on the EXAFS spectra at low energies.

REFERENCES

1. R H Ritchie, Phys Rev 114, 3, 644 (1959).
2. J E Muller and W L Schaich, Phys Rev B27, 10, 6489 (1983).
3. P A Lee and J B Pendry, Phys Rev B11, 8, 2795 (1975).
4. A Djaoui et al, Plasma Physics and Controlled Fusion, **31**, 1, 111(1989).
5. M P Seah and W A Dench, Surface and Interface Analysis, **1**, 1, 2 (1979).
6. T A Hall et al, Phys Rev Lett 60
7. J Szajman and R C G Leckey, Journal of Electron Spectroscopy and Related Phenomena, **23**, 83 (1981).
8. W H Press et al, 'Numerical Recipes', Cambridge University Press (1986).
9. J Szajman and R C G Leckey ibid **23**, 97 (1981).
10. A Djaoui et al, Laser and Particle Beams, **8**, 1, 319 (1990).

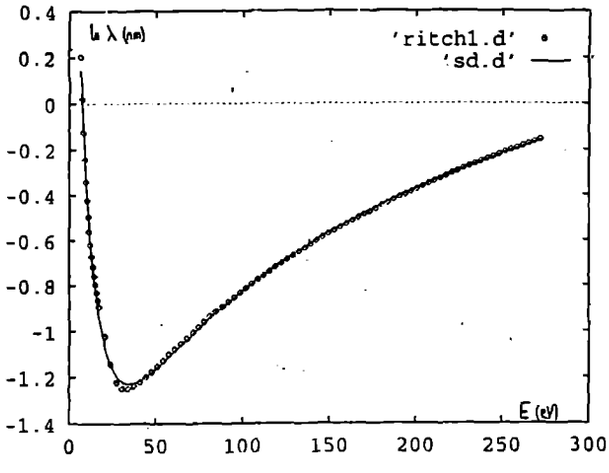

Fig 1 Mean-free path for solid Al calculated by the Ritchie method (the points) and the best-fit curve of the Seah-Dench type with parameters given in the text. The energies are in eV and the mean-free paths in nm.

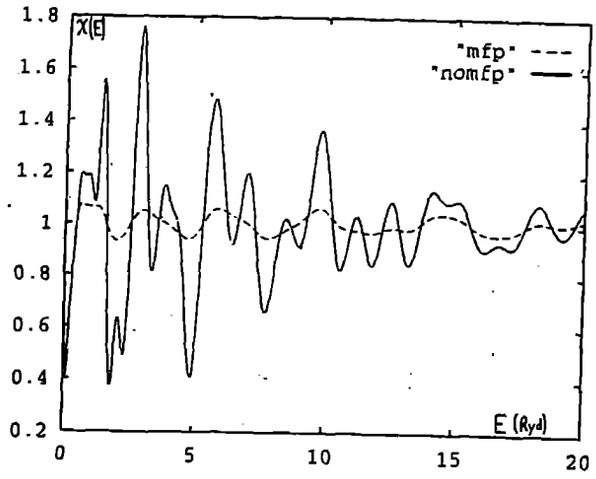

Fig 2 Calculated EXAFS spectrum of Al with and without the mean-free path term.

R_{vs}	α	β	A	B	f_{rms}
3.99	1.30	0.76	3.28	0.026	1.01
3.16	1.57	0.73	9.7	0.023	1.01
2.76	1.84	0.72	12.21	0.02	1.009
2.51	1.55	0.71	15.2	0.019	1.008
2.33	1.54	0.71	17.1	0.018	1.009
2.99	1.51	0.70	19.5	0.016	1.01
2.37	1.32	0.73	18.3	0.011	1.014
2.07	1.18	0.76	15.7	0.008	1.018
1.88	1.11	0.80	14.6	0.006	1.02
1.75	1.04	0.83	13.1	0.004	1.022

Table 1 Seah-Dench parameters for NA, AL.

THE EXAFS SPECTRUM OF COMPRESSED SODIUM

F I Gordon[1], T A HAll[1] and A Djaoui[2]

[1]Department of Physics, University of Essex
[2]Rutherford Appleton Laboratory

INTRODUCTION

Colliding shock experiments at RAL have demonstrated[1,2] the success of the EXAFS (extended X-ray absorption fine structure) technique as a diagnostic for the dense plasmas created in foil targets (eg Al). The density can be reliably obtained from a Fourier transform of the EXAFS spectrum which provides the distance to the first coordination shell of atoms/ions and the temperature can be estimated through the Debye-Waller factor which accounts for thermal vibrations of atoms/ions about their mean positions. This estimate of temperature is however uncertain as no reliable theory for temperatures near 1 eV has yet been found. The EXAFS method however allows the study of matter in a dense plasma state, a condition relevant to the interior of Jovian planets and white dwarfs, for example. We propose an experiment using the well-established techniques on a Na sample, which is of interest as a test of the theory of Meyer-ter-vehn and Zittel[3] (MTVZ) which predicts a significant pressure flattening in the equation of state about 5x compression for both Li and K. This effect is expected in Na at similar densities, and as the k-edge of Na is in the range accessible to X-rays from a Uranium backlighter (1.08 keV) makes it suitable for the proposed method.

Thus we have calculated the EXAFS spectrum for Na at a range of compressions to check if the signal should be detectable and make the experiment viable.

RESULTS AND DICUSSION

We use the method[4] based on the Muller Schaich[6] prescription, and incorporate a self-consistent potential calculated via a semi-relativistic solution of the Dirac equation.

This has been proved successful[5] for the case of Al. The spectra are broadened with a Lorentzian to account for the finite lifetime of the excited core-hole. We can see from the results in Figure 1 that the Na EXAFS spectrum is weaker in amplitude at solid density compared to Al but is relatively stronger at high compressions. In Figure 1 the curve chi-n has the EXAFS spectrum for Wigner-Switz radius =n Bohrs. Energy is in Rydbergs above the k-edge.

These results suggest that Na is a suitable material for a colliding shock experiment, and a test of the MTVZ flattening is feasible by recording a series of EXAFS shots at intervals during and after the shock to allow the density behaviour to be recorded. The theory[3] suggests that the pressure flattening is due to the redistribution of electrons from s,p angular momentum states to d,f states as the atoms are compressed. Such a test would be important as MTVZ provides a model for dense matter equations of state in the regime between solid density and the ultra-high density regime where statistical models such as Thomas-Fermi are expected to be accurate.

REFERENCES

1. T A Hall et al, Phys Rev Lett **60** 20 2034 (1988).
2. A Djaoui et al, Plasma Physics and Controlled Fusion **31** 1 111 (1989).
3. J Meyer-ter-vehn and W Zittel, Phys Rev **B37** 15 8674 (1988).
4. A Djaoui et al, Laser and Particle Beams **8** 319 (1990).
5. A Djaoui et al, Annual Report to the Laser Facility Committee RAL-88-042 105 (1988).
6. J E Muller and W Schaich, Phys Rev **B27** 10 6489.

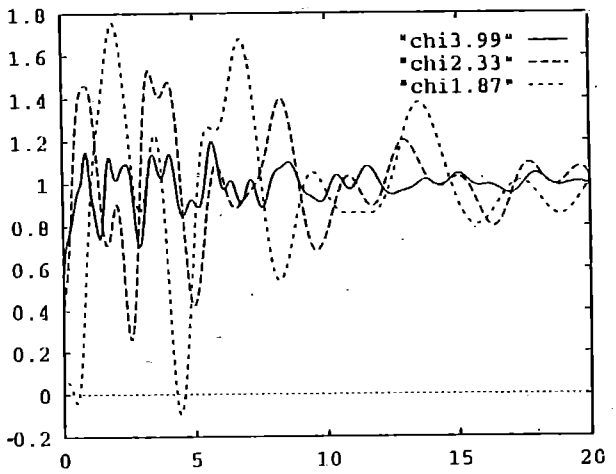

Fig 1 Na EXAFS spectrum for three different densities and zero temperature.

ATOMIC DATA CALCULATIONS FOR X-RAY LASER MODELLING

E Robertson, P H Norrington and A E Kingston

Queen's University of Belfast

The recent tendency at RAL has been for X-ray laser research using laser produced plasmas to look at schemes using increasingly heavier and more highly charged ion systems with the ultimate aim of achieving lasing action at shorter wavelengths ie below the 40 Å water window. This is particularly true of the collisional schemes using Ne-like and Ni-like ions as the lasant in which there is presently a great deal of experimental interest. In parallel to the experimental research, theoretical modelling of these systems is being carried out. For the computational modelling programme to be successful in providing a fully comprehensive simulation of a real plasma, it requires accurate and systematic atomic data such as electron collision rates, energy levels and oscillator strengths for these highly charged systems.

In particular, of major experimental interest at RAL[1] has been the use of a Ne-like Ge plasmas generated using the VULCAN high powered laser system to obtain lasing action by collisional pumping. The laser lines at 232 Å and 236 Å have been used as a source in experiments to obtain X-ray microscopy imaging of biological samples. The results of these experiments are described elsewhere in this year's RAL annual report. Calculations had already been carried out on other Ne-like ions such as Se(Z=34) Fe(Z=26)[2]. As these straddle Ge(Z=32) in the periodic table it was possible to interpolate the Ge electron collisional rates from those calculated for the Fe and Se with a reasonable degree of confidence in their accuracy. The original calculations included all the transitions between the ground state $(1s^2 2s^2 2p^6)\,^1S_0$ and the first 26 excited levels $(1s^2 2s^2 2p^5 3s^1)\,^3P_{0,1,2}\ ^1P_1$; $(..2p^5 3p^1)\,^3S_1\ ^1S_0\ ^3P_{0,1,2}\ ^1P_1\ ^3D_{1,2,3}\ ^1D_2$; $(..2p^5 3d^1)\,^3P_{0,1,2}\ ^1P_1\ ^3D_{1,2,3}\ ^1D_2\ ^3F_{2,3,4}\ ^1F_3$ of the Ne-like ion. The structure calculation was performed first using the configuration interaction code of Hibbert[3]. This used the Hartree-Fock 1s, 2s and 2p orbitals obtained from Tables[4] to then optimise on the 3s, 3p and 3d orbitals. The calculated wavelengths were in reasonably good agreement with the experimentally observed values to well within 1%. In these atomic structure calculations relativistic effects were included in the form of the Breit-Pauli approximation[5]. In the scattering calculations to determine the collisional excitation rates, the relativistic target wavefunctions produced using CIV3 were then used in the R-matrix collisional calculation in the Breit-Pauli approximation[6] for the 27 J levels. This was a large calculation with up to 109 coupled channels for a given total J symmetry.

As a result of the capability of the R-matrix code to determine the effects of resonances, our results for electron collision rates differ significantly from earlier distorted wave calculations at energies near threshold[7] (ie by up to 3 times for transitions between the ground state and the 3p excited levels in Se at T_e = 500 eV). However at higher energies above threshold where there are no resonance effects our collisional results are in good agreement with those earlier calculations.

Oscillator and energy levels were calculated for the first 89 levels of the Ne-like Ge ion using the atomic structure code SUPERSTRUCTURE[8]. This calculation included with full J-splitting the following configurations:

$(1s^2 2s^2 2p^5)3s^1, 3p^1, 3d^1, 4s^1, 4p^1, 4d^1, 4f^1$ and
$(1s^2 2s^1 2p^6)3s^1, 3p^1, 3d^1, 4s^1, 4p^1, 4d^1, 4f^1$

This data has been successfully employed by Professor G Pert and his group from York University in their large scale hydrodynamic X-ray laser codes. The results from this modelling are described elsewhere in this report.

Work is continuing at QUB on a number of other different ion systems in X-ray laser research. These include heavier Ne-like ions such as Y(Z=39) and Ag(Z=47) as well as Ni-like ions (28 electrons) such as those of Sa(Z=62) and Ta(Z=73). The move to more highly charged systems with a correspondingly heavier core results in the greater importance of relativistic effects entering into the calculation. This requires the use of codes which include relativistic effects implicitly in the calculations rather than as an approximation such as the Breit-Pauli approximation. The relativistic codes which we have chosen to employ are the MCDF structure code of Grant et al[9] and the fully relativistic version of the R-matrix code recently developed at QUB[10]. Though calculations of Ni-like Sa are at a preliminary stage, our values for oscillator strengths are comparable with those generated by workers in USA[11] for Ni-like Eu(Z=63). These calculations include the following configurations:

$(1s^2 2s 22p^6)3s^2 3p^6 3d^{10}$
$(\quad)3s^2 3p^6 3d^9 4s^1, 4p^1, 4d^1, 4f^1$
$(\quad)3s^2 3p^5 3d^{10} 4s^1, 4p^1, 4d^1, 4f^1$
$(\quad)3s^1 3p^6 3d^{10} 4s^1, 4p^1, 4d^1, 4f^1$

with full J splitting these amounts to 109 different levels. This is a major calculation and from a scattering point of view this will involve working at the very limit of the present computing power and memory at our disposal.

REFERENCES

1. D Neely et al, Annual Report to the Laser Facility Committee RAL-91 (1991).

2. K Berrington et al, Annual Report to the Laser Facility Committee, A4.8, RAL-87 (1987).

3. A Hibbert, Comput Phys Comm 9 141 (1972).

4. W Clementi and C Roetti, Atomic Data and Nuclear Data Tables, 14 Nos 3-4 (Sept-Oct 1974).

5. R Glass and A Hibbert, Comput Phys Comm 16 177 (1978).

6. K Berrington et al, Comput Phys Comm 14 367 (1978).

7. B Whitten et al, Kinetic Modelling of Neon-like Selenium, LLNL Internal Memo (Apr 1985).

8. W Eissner et al, Comput Phys Comm 8 270 (1974).

9. I P Grant, Comput Phys Comm 21 207 (1980).

10. To be published.

11. Private communication.

PLASMA EFFECTS IN ATI MULTIPHOTON IONISATION

Geoff J Pert

Department of Physics
University of York

INTRODUCTION

Cold dense plasmas can in principle be generated by multi-photon ionisation by intense short pulse radiation. Such plasmas can be used as the gain medium for soft X-ray lasers following recombination. For efficient operation two conditions must be established. Firstly the ions must be fully ionised to a high degree by the multi-photon process, and secondly the electrons must be cold at the end of the ionisation phase. It is the latter question we address in this report.

The underlying concept of this approach is ATI or 'above threshold ionisation' whereby electrons ionised in a linearly polarised electro-magnetic field of sufficiently short duration do not receive additional energy from the field after ionisation[1,2]. This process has a simple classical interpretation in terms of the electronic quiver motion, whereby the electron is introduced with a 'random' plus quiver velocity, the 'random' component remaining when the field is removed. In a linearly polarised field the electron is ionised at the peak of the field, where the quiver velocity is zero; the random velocity is therefore also nearly zero. On the other hand in a circularly polarised field the electron executes a circular motion of constant speed; the random velocity will therefore also have this value. Clearly any departure from linear polarisation will introduce random velocity.

This simple picture is however complicated by several effects, which will give rise to an increased thermal energy at the termination of the laser pulse. These are associated both with the focussing characteristics of the laser, and with the collisional and collective behaviour of the plasma formed.

Finite Focal Spot Effects

It is implicitly assumed that the focussed laser radiation being electro-magnetic, ie transverse, has only one electric field direction. However in the focus there is also a longitudinal component, which is out of phase with the transverse. The field is therefore effectively weakly elliptically polarised, with an attendant additional residual energy. We can estimate the magnitude of this effect for a Guassian beam of 1/e half width x_o where the transverse field varies as

$$E_x = E_o \exp(-x^2/x_o^2), \qquad (1)$$

and the longitudinal as:

$$E_z = 2x/x_o.1/kx_o.\exp(-x^2/x_o^2), \qquad (2)$$

approximately. The residual energy due to this effect is therefore

$$\varepsilon = \frac{1}{(kx_o)^2}\,.\,\varepsilon_q \qquad (3)$$

where ε_q is the electron quiver energy, and may be significant for tight focussed beams.

Plasma Effects

There are a number of effects associated with the collisional and collective behaviour of the plasma. To investigate these we have constructed particle-in-cell codes in one and two dimensions. The codes are relativistic and may be used in a one dimensional planar or two dimensional cylindrical spatial geometry; velocity is calculated in three dimensions, and the full three dimensional electro-magnetic field included. The programme is initialised with a set of fixed ions carrying bound electrons. Electrons are ionised randomly according to probabilities calculated from the tunnelling probability of Ammosov *et al*[3] using the total electric field. The space charge fields are calculated in the appropriate geometry from the net ion and free electron charge using cloud-in-cell differencing.

Elastic collision between ions and electrons scatter the electron quiver energy leading to increased residual energy through inverse bremstrahlung. This effect is included directly in the codes as an option, through a Monte Carlo scattering term. It is, however, expensive computationally, and generally a small

contribution. The effect of ionising inelastic collisions, which produce electrons at the wrong part of the field cycle is not yet incorporated. Co-operative scattering effects, which also heat the electrons, are not included.

The codes are thus somewhat more detailed than those of Penetrante and Bardsley[4], and our initial aim has been to compare results with that work. We have therefore worked mainly with the one dimensional model and will only present results from that simulation here. The gas used is neon which is irradiated with a XeCℓ laser (wavelength 0.308 μm) of 100 fs duration at an irradiance of 10^{18} W/cm^2. We have examined the behaviour at ion densities of 10^{17}, 10^{18} and 10^{19} /cc, and focal spot half-widths of 1, 5 and 10 μm. Our results are broadly in agreement with the behaviour seen by Penetrante and Bardsley. In particular the time history of kinetic and potential energy is very similar, however the residual energy per free electron is markedly greater. Values shown in Table 1 indicate that the lowest energies of about 45 eV per particle occur with wide focus and at high density. These values are about twice those found earlier, the reason for the discrepancy is not known. As the focal spot is narrowed increased residual energy results from the longitudinal component. Equation (3) predicts an energy increase of 20 eV due to this effect at 1 μm width, which is a reasonable estimate in view of the approximate nature of the calculation.

TABLE 1

RESIDUAL ENERGY

r_o \ n_i	10^{17} /cc	10^{18} /cc	10^{19} /cc
1 μm	6.09 keV	0.82 keV	0.088 keV (0.090 keV)*
5 μm	0.55 keV	0.067 keV	0.075 keV
10 μm	0.165 keV	0.045 keV	0.045 keV

*with elastic collisions

As the density is decreased the space charge fields are weakened, and the ponderomotive force associated with the laser field may give rise to significant electron motion during the pulse. Since the ponderomotive force per particle is approximately ε_q/r_o, the distance travelled without restraint by an electron during the laser pulse is $q_o^2\omega_o^2\tau^2/r_o$ where q_o is the amplitude of the quiver motion, ω_o the laser angular frequency and τ the laser pulse duration. On the other hand the space charge restoring force due to an electron displacement d is $m\omega_p^2 d$, where ω_p is the quasi-neutral plasma frequency. If the pulse is sufficiently long this force must roughly balance the ponderomotive term, and the displacement d is $q_o^2\omega_o^2/\omega_p^2 r_o$. Clearly this occurs if $\omega_p\tau \gg 1$, and a significant deflection of the electron density will occur if $d \sim r_o$. This is the condition for the establishment of a density channel.

If significant motion of the electron is induced during the pulse by the ponderomotive force, there is a significant build-up of potential energy in the space charge, which will be returned to the electrons as kinetic energy. In this case the electron may acquire significant residual energy, and show a complex oscillation, bouncing between the limits of the space charge well. In consequence space charge channelling for waveguiding the pump laser may lead to damaging energy gains.

This behaviour is clearly seen at low density in Table 1, where the residual energy is substantially larger than at high energy. Thus at ion density 10^{17} /cc the plasma frequency $\omega_p \sim 6 \times 10^{13}$ Hz, so that $\omega_p\tau \sim 0.6$. Since the electron quiver velocity at 10^{18} W/cm^2 is approximately 8×10^9 cm/s, the electron displacement $d \sim 10^{-4}$ cm. Thus we expect strong well development at focal spot width of 1 μm. Figs 1, 2 and 3 show electron phase space under these conditions. In Figure 1 at the peak of the laser pulse the electrons are moving rapidly from the centre towards the space charge field 'wall'. 50 fs later (Figure 2) at the end of the pulse most electrons have been reflected in the well,

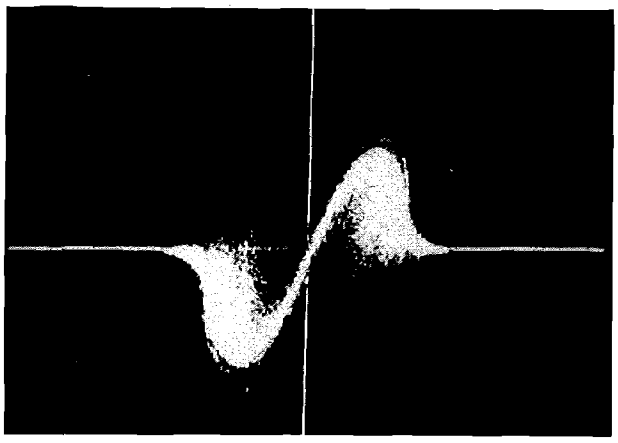

Fig 1 Electron phase space plot at the laser peak (space horizontal, velocity vertical).

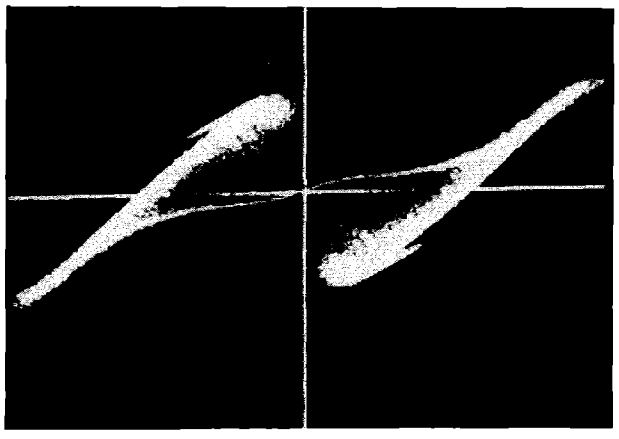

Fig 2 Electron phase space plot at 50 fs after laser peak.

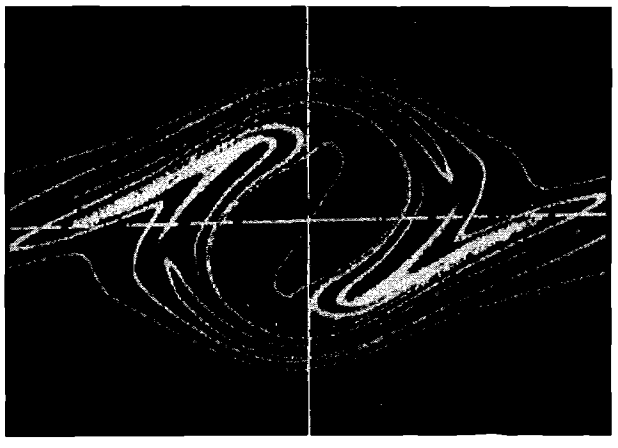

Fig 3 Electron phase space plot at 400 fs after laser peak.

although some pass over the barrier. 400 fs after peak of the pulse (Figure 2) electrons have executed several bounces, and the phase space has a complex vortex structure indicative of chaotic motion.

Conclusions

Although these results are preliminary, we can already draw some qualitative conclusions. At high densities, and short pulses such that electron channelling does not occur, the residual energy is approximately the value given by standard ATI theory. If channelling occurs, the work done by the ponderomotive force is the potential energy of the space charge field and is returned in large part to the electrons as kinetic energy.

References

1. R R Freeman *et al* Phys Rev Lett 59. 1092,1987
2. P B Corkum *et al* Phys Rev Lett 62, 1259, 1989
3. M V Ammosor *et al* Sov Phys JETP 64, 1191, 1986
4. B M Penetrante & J N Bardsley Phys Rev A43, 3100, 1991

THE COLLISIONALLY PUMPED NE-LIKE GE LASER

Phil Holden, Malcolm Lightbody and Geoff Pert

Department of Physics, University of York

INTRODUCTION

Over the past year the effort at York has moved towards concentrating upon developing a greater understanding of the collisionally pumped x-ray laser which is now well known to be significantly more robust than its principal competitor of the recombination laser. We are approaching this problem on two fronts - the understanding of the hydrodynamics and atomic kinetics through detailed models of the plasma development, and the understanding of x-ray beam propagation through the dense medium through ray tracing and wave optics models. The former work is described here, and the latter in the companion report of Lightbody.

THE MODEL

The model is based on the code HYBRID which has been described elsewhere (e.g. Pert 1983). The hydrodynamics use a quasi 2D approach in which the Lagrangian cells are assumed to be isothermal and, as such, the lateral expansion is modelled as a self similar flow.

The atomic kinetics are calculated for the Ne-like ion using the collisional-radiative model with 124 levels. Other ion species are treated using the two level Modified Griem's Model approximation (Davé 1984). Accurate collision rates, calculated using the R matrix approximation (Robertson *et al* 1991), are used between all $n = 2, 3$ levels, the other collision rates assuming the Van Regemorter (1962) form for optically allowed transitions. Dielectronic recombination is included from the three lowest F-like levels assuming Saha populations, and using the rates of Hagelstein (1985).

The dominant line broadening mechanism arises through electron collisions and these are included in a method analogous to the calculation of natural lifetime broadening.

RESULTS

The results compare very favorably with experimental data on all the lasing lines with the exception of the 196Å $J = 0 \rightarrow 1$ transition. Calculations of the gain magnitude and position, the gain length product as a function of target length, and the angular and time dependence of output signal all produce results in close agreement with experiment. Furthermore, we have verified the measured gain dependance upon supplied energy and the reduction of measured gain with 2ω pumping wavelengths. The 196Å line is problematic in that high collision rates into the upper level result in larger calculated gains than on the other transitions, in contrast to experimental findings but in common with all modelling to date. We limit the following description to the behaviour of the 232Å line which has been thoroughly investigated experimentally.

Our findings indicate that simple analytical descriptions are not as appropriate to collisionally pumped lasers as to recombination lasers for a number of reasons;

1) The Ne-like ion cannot be assumed to be the dominant species, and its dependency on T_e and N_i is not straightforward since recombination does not necessarily occur on timescales which are short compared with the problem timescale.

2) Although the fractional inversion is found to be close to that predicted by collisional-radiative equilibrium values, multilevel configurations are required for the calculation to be reasonable. This arises from the fact that pumping from higher levels, especially the 3d levels is significant, in addition to recombination pumping which we find to be less important.

3) Electron collisional broadening is a vital inclusion to the model, since in the region of positive gain we find an increase in the linewidth of a factor typically $2 \rightarrow 10$. Unfortunately, this effect is most significant in regions which exhibit the greatest inversion densities, since increases in both the linewidth and the fractional inversion result from high collision rates.

4) An important factor in the measurement of gain, if not the calculation of the small signal gain coefficient, is that of the electron density gradient. Increased electron densities result in significantly higher refractive index gradients than those found in recombination systems, and the identification of regions which optimise the opposing effects of high refractive index gradients and high gain coefficients is one of the keys to understanding the calculations.

The radial dependencies of the gain, linewidth, electron density and Ne-like ion density at a typical time instant are illustrated in figure 1. The lack of Ne-like ions centrally (due to apparently unavoidable over-ionisation into F-like ions) results in two distinct regions of gain. The large inversion density existing in the inner region does not result in correspondingly large gain on account of the increased broadening in the denser plasma, and the two regions typically exhibit comparable gain. As a result of the reduced refractive index gradient in the outer region, it is here where the dominant contribution to the measured signal arises. At later times, as the inner region moves out in the profile towards lower density gradients, it becomes the dominant source of the signal. The result is that the signal arises from an volume in space between $40 \rightarrow 100\mu m$ from the original target surface, the gain coefficient and refractive index gradient both remaining relatively constant. The details of the behaviour and the calculated signal resulting are described elsewhere in this report (Lightbody *et al* 1992).

The peak gain coefficient is found to increase with pumping power up to an intensity of $\sim 3.0 \times 10^{13} \mathrm{W\ cm^{-1}}$, from which point it remains approximately constant. This results from the need for sufficient power to produce optimum gain conditions, beyond which the gain is relatively insensitive to the supplied energy as the laser functions close to collisional-radiative equilibrium, and the required conditions are always satisfied at some point and time in the plasma expansion. The important effect at large powers is the position of gain on the density profile and the resulting refractive index gradient. HYBRID calculations indicate that the reduced density gradients resulting from greater pumping powers increases the measured signal, although this has not yet been analysed in any detail by raytracing.

A typical time instant for $0.53\mu m$ irradiation is illustrated in figure 2. A shift to greater Ne-like ion abundancies is apparent, resulting from reduced absorption in the underdense plasma, and

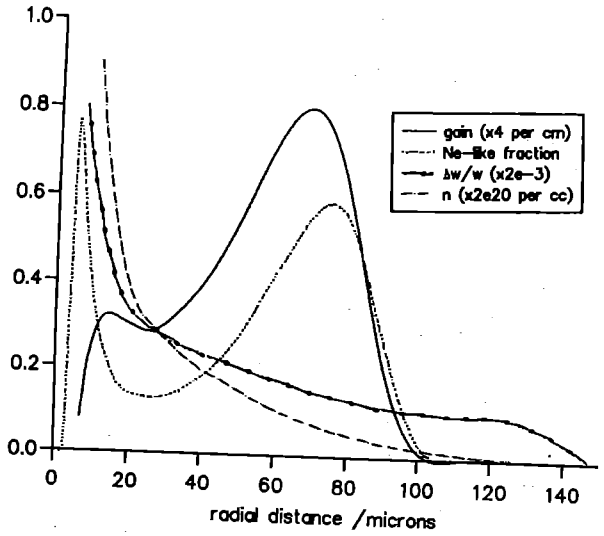

Figure 0.1: The profiles of gain, Ne-like ion abundance, electron density, and linewidth at 300ps for a 1.06μm driving pulse of incident intensity 2.4×10^{13} Wcm^{-2}.

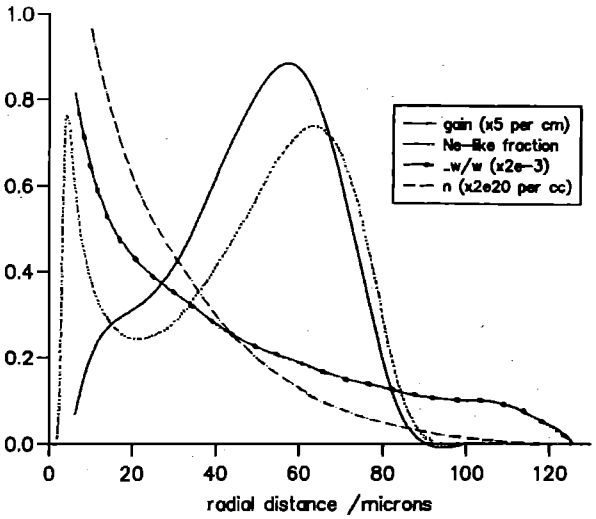

Figure 0.2: The profiles of gain, Ne-like ion abundance, electron density, and linewidth at 300ps for a 0.53μm driving pulse of incident intensity 2.4×10^{13} Wcm^{-2}.

the effect creates a broader outer region of gain with marginally higher values. However, the strong absorption near the ablation front results in the expansion being driven from the heart of the plasma and creates an electron density gradient $\sim$ 2 times greater than the comparable case for 1.06μm irradiation. The x-ray intensity distribution we expect from these calculations is a broader profile, centered at a greater divergence and which peaks later in time resolved measurements. We have no experimental data with which to compare the details of this result, although we note that a reduced gain coefficient is measured for 0.53μm irradiation.

CURRENT WORK

There are two areas in which work on the hydrodynamic aspect of the collisionally pumped laser is currently being conducted within the group. The first of these is the observation by Neely *et al* (1992) that the beam intensity does not only flatten off at longer target lengths (as would be expected on account of refraction limitations), but is actually reduced. Conventional modelling does not predict the existence of negative gain in the region of ablating plasma which can be sampled by the x-rays, even if the laser intensity is reduced at the wings producing a colder plasma.

One possible explanation is absorbtion in an under-stripped ion species, which our limited atomic data does not allow us to analyse. However, it is thought unlikely that such an absorbing ion could exist in sufficient quantities to account for this effect, and the more plausible explanation of resonant line absorption destroying the inversion in the low density plasma is being considered. Early results from calculations which solve the radiative transport problem over the entire plasma indicate that this effect may exist in outer regions of the plasma where resonant absorption of photons emitted within the plasma is significantly greater than emission for populations calculated ignoring this effect. It appears likely that regions of high negative gain will be created at the outer reaches of the plasma, and the reduced expansion in underheated regions of the plasma may locate these regions in the path of the x-ray beam. We expect a conclusion to this possibility in the immediate future.

The second direction of the work is to model systems which may lead to improved operation of the laser. Two possible improvements lie firstly in the well known desire to minimise the refractive index gradients (or their effects) through such methods as double target configurations and secondly in the benefits which could be obtained through reducing the presence of F-like ions. The potential region of peak gain (where the collision rates are optimised) exhibits very low $\sim$ 15% Ne-like abundancies, and an increase of this parameter could lead to gains $\sim$ 10 according to our calculations.

REFERENCES

Davé AK 1984, PhD thesis, University of Hull

Hagelstein PL 1985, UCRL-93811 preprint

Lightbody MTM, Holden PB and Pert GJ 1992, in this report

Neely D 1992, personal communication

Pert GJ 1983, *J. Fluid Mech.* **131** 401

Robertson E 1991, personal communication

Van Regemorter H 1962, *Ap. J* **136** 906

MODELLING OF THE OUTPUT BEAM CHARACTERISTICS IN X-RAY LASER EXPERIMENTS

M.T.M Lightbody, Phil B Holden and Geoff J Pert
Department of Physics,
University of York,
Heslington,
York YO1 5DD.

1 Introduction

We describe the development of a suite of programs designed to model experimentally relevant properties of the x-ray laser output beam. These include the beam pointing angle, the angular divergence, the spatial profile, the frequency profile, saturation characteristics as well as the temporal and spatial coherence properties. The codes have been designed to be used as post processors to existing x-ray laser simulation codes such as EHYBD. The emphasis has been on collisionally pumped systems and one of the objectives was to reproduce recent experimental results, O'Neal et. al. (1990). Another important aim has been to use the codes in both interpretive and predictive roles.

Three different programs have been developed. The first of these, RAYS, is a geometrical optics ray trace of the output beam through the plasma. This code provides the beam pointing angle and divergence, as well as estimates of the spatial profile of the output beam and the peak intensity of the output beam. The ray trace is also used to calculate ray averages of various plasma parameters, such as ray averaged linewidths, saturation intensities and spontaneous emission rates. These quantities are then used as input to SATURATE, which enables the effects of gain saturation on the output intensity to be taken into account. SATURATE will be a useful addition to RAYS after the recent experimental demonstration of saturation in a double amplifier plus mirror configuration, Key et. al. (1992). The third code is based on a wave optics description of the x-ray laser. As well as duplicating some of the results of RAYS, this code will enable prediction of the spatial coherence properties of the output beam. Such calculations will assume greater importance when the emphasis shifts towards holographic applications of x-ray lasers. Figure (1) shows the inter relation between the three codes and existing programs. We will now describe the codes and their results in more detail.

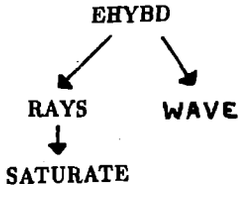

Figure 1: Inter-relation between codes.

2 RAYS

This code runs as a post processor to EHYBD, Holden (1992), which generates the hydrodynamic and ionic data. Angular bunches of rays are emitted at regular intervals throughout the plasma. The initial intensity on each ray is determined from the spontaneous emission rate and source density at that point. The rays are followed in a full refractive raytrace through the mesh defining the plasma. The signal is amplified as it passes through regions of positive gain (or absorbed if the gain is negative). Spontaneous emission, equal to the local value of the source function, is added at the center of each cell. The final intensity and the exit angle are stored on the rays exit from the mesh. This data can then be used to determine the angular profile of the output beam. Ray averages of the Doppler and Lorentz components of the line profile are calculated along each ray path and then averaged over the ensemble of rays to give an intensity weighted average. In the same way, averages of the spontaneous emission rate, saturation intensity, gain-length product and ray path length are calculated. These quantities are used in SATURATE, which is briefly described later.

One of the reasons for the development of RAYS was to model beam propagation in relatively high density collisional systems. The presence of large density gradients in these schemes means that refraction is a potentially limiting factor in a single target experiment. It is useful to be able to model the way in which the output intensity and distribution change with target length. This is particularly relevant in view of the way in which the gain coefficient is calculated from the peak intensity as a function of target length. In the absence of refraction the peak intensity should grow exponentially with target length (neglecting gain saturation). However, refraction limits the maximum useful length over which exponential gain is achieved. It is useful to be able to calculate this maximum target length. RAYS will also be an aid to optimising the coupling distance in multiple target or mirror plus target geometries.

The first objective was to reproduce recent experimental results, O'Neal et. al.(1990), on collisional systems. EHYBD was used to simulate the Ne-like Germanium experiment and RAYS was then used on the output data. Figure (2) shows the temporal development of the output intensity angular distribution on the 236 Angstrom line. It is interesting to note that the beam sweeps through an angle of approximately 7 m rad during the time of peak gain (between 300 and 500 p sec in this example). The reason for this is that the density gradients in the regions of gain change as a function of time, so that the peak signal comes from further out in the plasma at later times. This effect is especially important for longer length plasmas where the longer path length associated with shallower density gradients results in a greater effective gain-length product and hence greater signal from these regions. Figure (3) compares the predicted time integrated beam profile of the 236 A line with experimental results. As can be seen, there is good agreement with both the pointing angle and the angular width of the beam.

One consequence of the presence of refraction is that the experimentally measured gain coefficient will be lower than the actual peak value present in the plasma. This is because the value of the gain coefficient is inferred from the variation of intensity with plasma length. Refraction, coupled with a non uniform gain distribution, means that the rays which experience the greatest αl originate from different depths of the plasma for different length targets, thus sampling different regions of gain. For example, using

RAYS we find that the gain coefficient measured between a 6 mm and a 9 mm target is 2.7 cm^{-1} whereas that between 6 mm and 15 mm is 2.2 cm^{-1} and between 6 mm and 18 mm we get 1.6 cm^{-1}. This point should be taken into account when estimating values of the gain coefficient or spontaneous emission rates from such measurements.

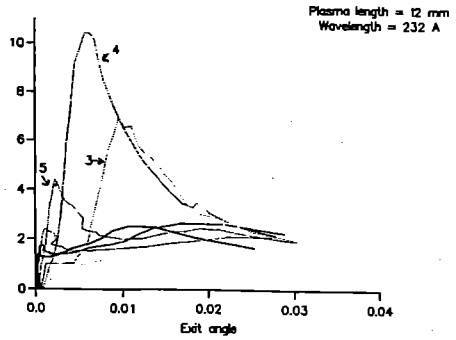

Figure 2: Time development of angular profile.

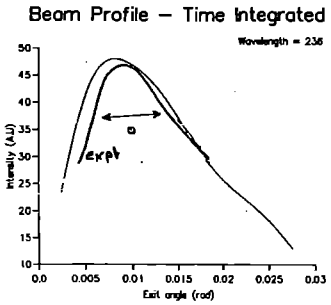

Figure 3: Comparison between predicted and experimental profiles.

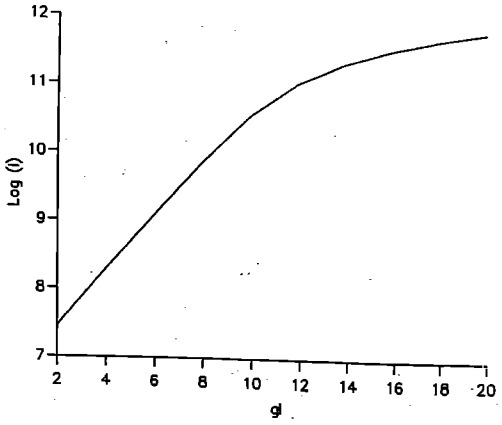

Figure 4: Intensity vs Gain-length product

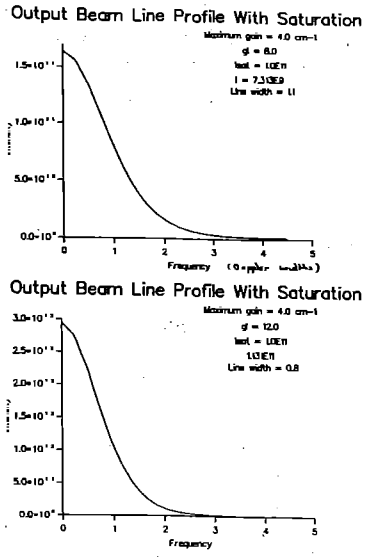

Figure 5: Demonstration of line narrowing.

3 SATURATE

This code is based on an integration of the radiative transfer equation, including gain saturation and using a Voigt line profile, over a solid angle defined by the exit aperture seen by a source point at one end of the plasma. The code is designed to use the average plasma parameters calculated by RAYS as input. It is not claimed to be an accurate description of the radiative transfer through the plasma, though the results of SATURATE are expected to be a good approximation for larger values of αl. SATURATE allows us to correct the results from RAYS for larger αl in order to account for saturation. Besides giving intensity as a function of gain-length, SATURATE also give the line frequency profile. Knowledge of the line width allows an estimation of the temporal, or longditudinal, coherence.

Figure (4) shows the results of using SATURATE to model the results of recent experiments conducted at the Central Laser Facility at RAL, demonstrating the onset of saturation in an experiment involving a double amplifier and mirror, Key et. al. (1992). Figure (5) shows the effect of line narrowing.

4 Conclusions

We have described two of the three codes that have been developed here at York to understand the propagation of the output beam in collisional x-ray laser experiments. The agreement between experiment and modelling is both encouraging from the point of view of the work reported here and from the confidence gained in our hydrodynamic and ion-kinetic codes. The third code is still at a developmental stage and is based on a wave optics description of the problem.

5 References

- Holden P B et.al. This Report
- O'Neal D et. al., (1990), Opt Comm, Vol. 75, No.5,6, pp406-412
- Key M H (1992) To Appear.

RESONANCE LINE RATIO AS A DIAGNOSTIC OF INITIAL CONDITIONS SUITABLE FOR LASER ACTION IN RECOMBINING PLASMAS

J Zhang [1,2], M H Key [1,2], P Norreys [2], G J Tallents [3]

[1]Clarendon Laboratory, University of Oxford, Oxford, OX1 3PU, UK
[2]Rutherford Appleton Laboratory, Chilton, Didcot, Oxon OX11 0QX, UK
[3]Department of Physics, University of Essex, Colchester, CO4 3SQ, UK

Numerical simulations have shown that the gain coefficient for laser action on the Balmer α transition of hydrogenic ions increases for irradiation of fibre targets of smaller diameter by pulse of shorter duration and wavelength [1]. In this scheme, rapid cooling by adiabatic expansion of a plasma of fully stripped ions produces gain on the Balmer α line of H-like ions during a recombination cascade [2]. Preliminary evidence for recombination gain on the H-like carbon and oxygen Balmer α lines at 182 $\AA$ and 102 $\AA$ recently has been obtained using a novel 268 nm KrF pumped Raman laser beam in a line focus as narrow as 8 μm, which can deliver beam energy up to 5 Joules in 12 ps to the target [3].

A large initial abundance of bare nuclei in the plasma is one of the key factors for producing high recombination gain. The ratio of the bare nuclei to hydrogenic ions in a recombining plasma can be assessed from the ratio of Ly β to He β [4]. In this paper, correspondence between the computed line ratio and recombination gain for varying absorbed irradiance is investigated by means of a full hydrocode coupled with an atomic physics code [1]. Some criteria for high recombination gain are obtained by analysis of temporal characteristics of the line ratio and of the gain and their dependences on absorbed irradiance.

Med101 is a 1D hydro/energy transport/atomic physics code, which can calculate population densities of ground states and excited states of H-like ions in recombining plasmas [5]. We have modified this code to include calculation of line intensities of Ly β and He β transitions.

During the heating and early stages of recombination, when LTE is applicable for levels with quantum number $n \geq 3$, population densities of bound levels are then described by the Saha-Boltzmann equation.The resonance line emission from the $n \geq 3$ levels of the He-like ion is proportional then to the population density of the ground state of the H-like ion. For example the intensity of the He β transition is

$$I_\beta^{He} = h\nu^{He} A^{He} \left(\frac{\pi}{2}\right) \left(\frac{g_3^{He}}{g_1^H}\right) \sum_l \left[R^2(l+1) - R^2(l)\right] N_e N_1^H \left(\frac{h^2}{2\pi m_e k T_e}\right)^{\frac{3}{2}} exp\left[\frac{\chi^{He}(3,c)}{kT_e}\right].$$

where g_3^{He}, g_1^H are statistical weights of level 3 and level 1 in He- and H-like ions respectively, $\chi^{He}(3,c)$ is the bound level 3 to continuum c ionization energy of He-like ion, R represents the radius of the plasma, l labels the Lagrangian cells in the code, the other parameters have been used in the conventional sense. Similarly the intensity of the hydrogenic resonance line is proportional to the concentration of bare nuclei and the ratio of the line intensities therefore gives the ratio of the ground state population of the next higher ions. The accuracy of line intensities calculated by this modified code was checked by comparing results with those calculated by a simulation code of Dutson et al [6]. Good agreement between the code results was obtained.

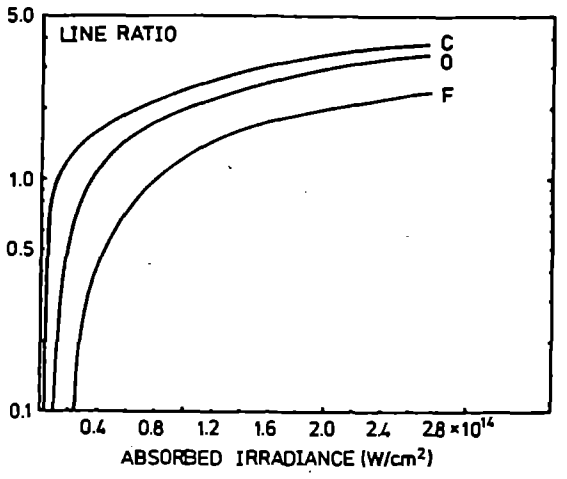

Figure 1: *Resonance line ratios of Ly β and He β in C, O and F plasmas as functions of absorbed irradiance.*

Numerical calculations have been performed with the same parameters as those in a recent experiment with the SPRITE KrF laser facility [3]. The diameter of the fibre target is 7 μm. The pulse duration is 12 ps. The intensity on target was varied between 1.0 × 10^{14} cm^2 and 2.0 × 10^{15} cm^2. We have restricted our discussion to possibility for experimental studies with our current SPRITE KrF laser system [3].

The development of recombination plasma consists of two different phases [5]. During the first phase the fibre target is heated and ionized to a degree determined by the absorbed irradiance. In the second phase expansion leads to adiabatic cooling and to recombina-

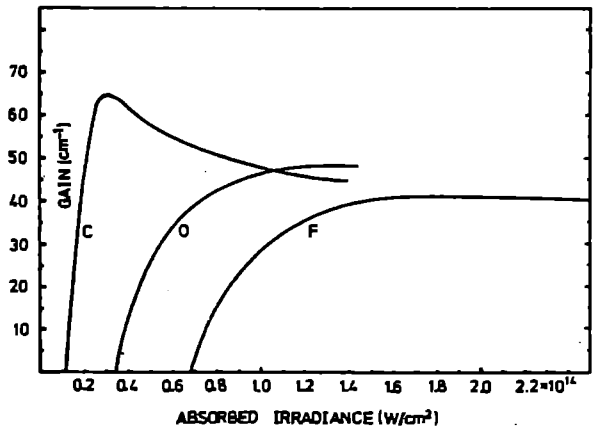

Figure 2: *Recombination gains of C, O and F plasmas as functions of absorbed irradiance.*

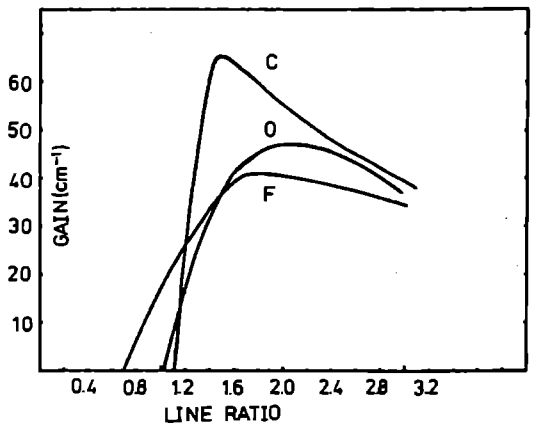

Figure 3: *Peak gain variations against the resonance line ratios.*

tion gain. The cylindrically expanding plasma exhibits a temporal peak of gain occuring soon after the onset of population inversion. The peak intensities of Ly β and He β transitions appear in the first phase. Their ratios are indication of the relative abundance of the bare nuclei and hydrogenic ions, which are determined by the absorbed irradiance from the driving laser. If the absorbed irradiance is varied, the relative abundance and the peak recombination gain will be correspondingly changed. Fig. 1 and Fig. 2 show that the relationship of the line ratios and the peak recombination gains against the absorbed irradiances in C, O and F laser-plasmas.

The determination experimentally of absorbed irradiance is not so easy, but the measurement of peak intensities of Ly β to He β transitions is simple. That has made it interesting to use the line ratio as a method of infering the absorbed irradiances and finding initial conditions optimized for the development of recombination gain. Fitting the experimental line ratios of Ly β to He β transitions of carbon and oxygen plasmas measured in the recent experiment [3] to the calculated data, an absorption of about 10 percent can be inferred.

At small absorbed irradiance, the plasma temperature is not sufficient to give the predominant population of bare nuclei that is the necessary starting point of the recombination laser process. As the absorbed irradiance increases, the abundance of bare nuclei increases. At the absorbed irradiance, which corresponds to the gain onset, the abundance of bare nuclei is about the same as that of H-like ions. When the target absorbs irradiance above the threshold level, the abundance of bare nuclei increases rapidly, but the abundance of H-like ions becomes nearly constant. A large fraction of ions in the plasma are bare nuclei before further cooling starts. The empirical criterion for maximum gain is that the ratio of intensities of Ly β to He β is about 1.5 to 1.7 (Fig. 3). This optimum ratio changes if the fibre diameter or laser duration are varied. Simulation results show that generally larger fibre diameter will lead to a smaller optimum ratio, longer laser duration will lead to a slightly larger optimum ratio.

It may be concluded that measurement of the line ratio of Ly β to He β in the transverse direction is a simple but useful method for infering the absorbed irradiance in the plasma and the production of the plasma which should give maximum laser gain during adiabatic expansion.

REFERENCES

[1] M H Key, N Tragin, S J Rose, 2nd International Colloquium on X-ray Lasers, *X-Ray Lasers 1990*, G Tallents Ed., IOP Publisher, Bristol (1991) 163.

[2] G J Pert, J. Phys. B: Atom. Molec. Phys., **9** (1976) 3301.

[3] P Norreys, A Carillon, H Z Shen, L Dwivedi, J Jacoby, M H Key, R Kodama, J Krishnan, C L S Lewis, G J Pert, I N Ross, G J Tallents, J Uhomoibhi, J Zhang, 21st ECLIM Conference, Warshaw 1991 (to be published in *Laser and particle beams*).

[4] M H Key, E Harvey, G J Hirst, C J Hooker, J Jacoby, R Kodama, J Lister, P Norreys, P Rodgers, S J Rose, I N Ross, M J Shaw, G Tallents, N Tragin, 2nd International Colloquium on X-ray Lasers, *X-Ray Lasers 1990*, G Tallents Ed., IOP Publisher, Bristol (1991) 239.

[5] C Chenais-Popovics, R Corbett, C J Hooker, M H Key, G P Kiehn, C L S Lewis, G J Pert, C Regan, S J Rose, S Sadaat, R Smith, T Tomie, O Willi, Phys. Rev. Lett., **59** (1987) 2161.

[6] D Duston, J Davis, Phys. Rev. A, **21** (1980) 1664.

[7] G J Pert, J. Opt. Soc. Am. B, **4** (1987) 602.

PHYSICAL MODELS FOR OBSERVED INTENSITY RATIOS FROM THE Ge XXIII XUV LASER

M H Key

Rutherford Appleton Laboratory,
and Dept of Atomic and Laser Physics, University of Oxford

INTENSITY RATIO IN THE J = 2-1 DOUBLET 23.2:23.6 nm

The intensity ratio of amplified spontaneous emission for the two lines in the J = 2-1 doublet of the Ge XXIII laser conveys interesting information as the gain length product gl of the amplifying plasma is increased. For a homogeneous medium the brightness can be expressed as

$$B = \frac{2h\nu^3}{c^2}\left(1-\frac{n_e}{n_u}\frac{g_u}{g_e}\right)^{-1}\frac{(exp\ gl-1)^{3/2}}{(gl\ exp\ gl)^{1/2}} \qquad (1)$$

In the limit of small gl, the ratio of two lines (eg 23.2:23.6nm) is

$$\frac{B_2}{B_6} \rightarrow \frac{n_{u2}}{n_{u6}}\frac{A_2}{A_6} \qquad (2)$$

in terms of the upper state population density n_u and spontaneous decay rate A. In the limit of high gain but no saturation and using η to denote the inversion fraction and σ the stimulated emission cross-section.

$$\frac{B_2}{B_6} \rightarrow \frac{\eta_6}{\eta_2} exp\left[g_6 l\left(\frac{n_{u2}}{n_{u6}}\frac{\eta_2}{\eta_6}\frac{\sigma_2}{\sigma_6}-1\right)\right] \qquad (3)$$

Here we see that if the ratio of upper state populations is known and the intensity ratio is measured at high but unsaturated gain, it is possible to deduce η_2/η_6. Finally, at saturation we expect the ratio to become asymptotic to the ratio of the saturation intensities

$$\frac{B_2}{B_6} \rightarrow \frac{\nu_2}{\nu_6}\frac{\sigma_6}{\sigma_2}\frac{\tau_6}{\tau_2} \qquad (4)$$

where τ is the gain recovery time and ν the frequency.

It is interesting to compare these simple considerations with the experimentally observed curve of growth[1]. Knowing that $A_2/A_6 = 0.5$, it follows from equation 2 and the observation that $B_2/B_6 = 0.7$ at small gl that $n_{u2}/n_{u6} = 1.4$.

The observation that the intensity ratio becomes equal to unity for a gl ~ 10 implies from equation 3 that the ratio of population inversion fractions $\eta_6/\eta_2 = 0.7$ since $\sigma_2/\sigma_6 = 0.5$ is known from the atomic physics of Ge XXIII. The ratio of the gain coefficients is given by

$$\frac{g_2}{g_6} = \frac{n_{u2}}{n_{u6}}\frac{\sigma_2}{\sigma_6}\frac{\eta_2}{\eta_6} \qquad (5)$$

and since the ratio n_{u2}/n_{u6} has been deduced from experimental data as has η_2/η_6, we can determine the ratio of the gain coefficients which this analysis suggests is $g_2/g_6 = 1.04$.

Finally the experimentally observed transition from $B_2/B_6 = 1$ at gl = 10 to $B_2/B_6 = 2$ at gl = 21 is consistent with the saturated behaviour of the laser recognising that the 2x larger stimulated emission cross-section of the 23.6 nm line gives a 2x times lower saturation intensity. [We have $I_s = h\nu/\sigma\tau \sim \sigma^{-1}$ since τ, the gain recovery time of the upper levels is the same for both transitions and is linked to the radiative decay time of the 3d levels which have an allowed transition to the ground state and are collisionally coupled to the laser upper levels].

The evolution with increasing gl of the brightness ratio of the 23.2 and 23.6 nm J = 2-1 transitions is therefore a good indicator of the ratio of upper level population, inversion fraction and saturation for a homogeneous plasma.

INTENSITY RATIO FROM OPPOSITE ENDS OF A DOUBLE PLASMA ASE SOURCE

The ratio of intensity emitted from the two ends of the double plasma system has been noted in our earlier work[2] to be significantly different from unity with up to 5x more intensity emitted from the 22 mm plasma relative to the 14 mm plasma in the 22:14 configuration shown in Fig 1.

At first sight this is unexpected but a possible mechanism is illustrated in Fig 1. Refraction in a single 22 mm plasma leads to an experimentally observed maximum intensity emerging from the plasma with a refraction angle of circa 10 mradians. Thus, the propagation of the radiation is closer to the target surface and in denser plasma at the centre of the transit than at the the exit point. Projecting this emission into the 14 mm plasma and considering the effect of reducing the transverse separation between the two plasmas to give optimum gain as studied experimentally[2], a symmetry argument would suggest that optimum gain would be achieved when the entry point into the 14 mm plasma exactly matches the exit point from the 22 mm plasma. This has the consequence that the radiation at the exit from the 14 mm plasma is near to its closest point of approach to the target surface because of the approx 2:1 length ratio. There is thus a systematic difference in that radiation leaving the 22 mm plasma is at its most distant point from the target surface while radiation leaving the 14 mm plasma is close to the target surface. The density at the two points is therefore significantly different. We know from numerical modelling that increased density gives reduced population inversion fraction and this is clear also from simple physics since in the limit high density causes thermalisation .

Equation 1 shows that the brightness of an ASE source depends inversely on the inversion fraction. In a high gain system the radiation which is amplified arises predominantly from one extremity so that the output intensity is inversely proportional to the population inversion fraction at the extremity which is the source region of the ASE. Thus we see that in Fig 1 the source region for radiation emanating from the 22 mm plasma is at high density and therefore low inversion fraction while the source region in the opposite direction is at low density and therefore high inversion fraction.

Equation 1 therefore predicts higher intensity from the 22 mm end of the system and appears to offer a qualitatively satisfactory explanation for the observed difference of intensity leaving the two ends of the plasma system.

It is also interesting to note that when a mirror is introduced to reflect back the radiation emanating from the 22 mm plasma the radiation will reverse its path and saturation of emission will be recorded when the saturation of intensity is reached at the exit from the 14 mm plasma. The relatively high density and low inversion fraction of the radiation source in this configuration will lead to a small reduction in the gain length required to reach saturation which can be expressed as

$$\frac{exp\ gl}{\sqrt{gl}} = 4\pi\ \eta\ (A\tau)^{-1}\left(W^2/L^2\right) \qquad (6)$$

for width to length ratio W/L.

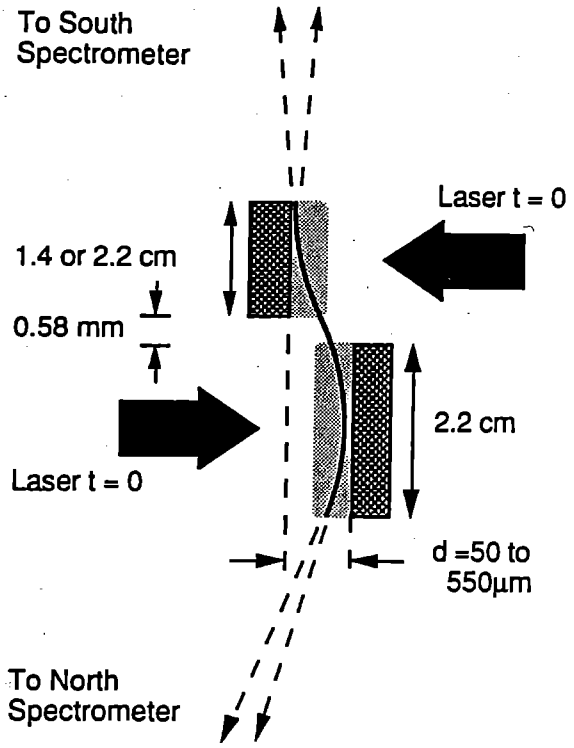

Fig 1 Schematic representation of X-ray paths in the double plasma ASE laser.

The experimental results reported in Section A1.1 show calculations of the saturation based on an inversion fraction of unity. Experimental data show saturation at somewhat lower intensities than those predicted by the model consistent with the above trend. More detailed modelling of the effect using a hydro code and ray tracing is in progress, see Section A5.11.

REFERENCES

1. See Section A1.1 ibid.

2. C L S Lewis et al, Opt Comm (in press).

PROSPECTS FOR REDUCED DRIVER ENERGY IN COLLISIONALLY EXCITED XUV LASERS

M H Key

Rutherford Appleton Laboratory
and Dept of Atomic and Laser Physics, University of Oxford

The gain production efficiency of a collisionally excited laser can be characterised by g/I where I is the intensity on target and g is the gain coefficient produced in the plasma. If a single laser beam of brightness B (W cm^{-2} sterad^{-1}) is used to irradiate a target in a line focus produced by an optical system of convergence ratio f/d (where f is the focal length and d the diameter), and the laser is required to have a gain length product gl, then the power required is

$$P = (f/d)^2 (gl)^2 (g/I)^{-2} B^{-1} \qquad (1)$$

The gl value required for the ideal objective of saturated and diffraction limited output from a single plasma, is given by,

$$\frac{exp\ gl}{(gl)^{1/2}} = 4\pi \left(\frac{W}{\lambda}\right)^2 \left(\frac{\tau_r}{\tau_g}\right) \varepsilon^{-1} \qquad (2)$$

for a plasma of width W, XUV laser wavelength λ, population inversion fraction $1\text{-}n_l g_u / n_u g_l = \varepsilon$, and ratio of laser radiative lifetime to gain recovery time τ_r/τ_g.

For example, in the successful Ni-like Ta laser[1] producing 4.48 nm emission close to the important water window where holography of biological specimens becomes possible, equation 2 indicates a required gl = 26. The experimentally determined optimum driver intensity for the Ta laser is 2.5 x 10^{14} W cm^{-2} and the gain is 3.2 cm^{-1}. The high energy 0.53 μm driver pulse of 0.5 ns duration has a brightness B = 5 x 10^{17} W cm^{-2} sterad^{-1} and practical focusing optics have f/d = 3. Two separated plasmas would be required to achieve diffraction limited performance allowing 2-fold narrower line focus for a given driver brightness. A further 2-fold reduction in the required power is obtained if the intensity is delivered to the targets from two sides by identical optics. The minimum requirement is therefore 17 TW and 8.5 kJ in an 86 μm wide line focus in this example. Experiments to date have actually used line foci of 100 μm or greater and a single 3 cm long plasma irradiated from two sides.

SCALING ARGUMENT

Reduction of the line width below the demonstrated 100 μm value requires not only a driver of higher brightness but also due consideration of other factors.

Self similarity in the hydrodynamics of the exploding foil is desirable in order to avoid increasing 2 dimensional expansion with a narrow line focus. This implies reducing the thickness of the heated plasma at its operating density and temperature in proportion to any reduction of its width. An analytic model of foil heating is useful here[2] and gives the scaling of parameters reached at transparency when the temperature reaches a plateau as follows

$$\begin{aligned} T &\sim I^{1/3} \lambda^{2/3} m^{1/3} \\ n_e &\sim I^{1/2} \lambda^{-1} m^{-1/2} \\ t &\sim I^{-2/3} \lambda^{2/3} m^{4/3} \end{aligned} \qquad (3)$$

for the temperature T, electron number density n_e and time to transparency t, in terms of the intensity I, driver wavelength λ, and foil mass per unit area m.

An interesting possibility is to seek a self-similar scaling which produces a constant temperature at the optimum level for production of gain and conserves other important parameters which will be considered later. Reduced wavelength to the driver laser is the first choice and we can assume a scaling of the form

$$\lambda \rightarrow \lambda_0 / s \qquad (4)$$

with s a scaling factor greater than 1.

Conservation of temperature is then obtained with

$$\begin{aligned} t &\rightarrow t_0 / s^2 \\ I &\rightarrow I_0 s^2 \\ m &\rightarrow m_0 / s^0 \end{aligned} \qquad (5)$$

whence from equations 3, 4 and 5,

$$\begin{aligned} T &\rightarrow T_0 / s^0 \\ n_e &\rightarrow n_{e0} / s \end{aligned} \qquad (6)$$

and it is seen that the thickness z of the expanded plasma scales as

$$z \rightarrow z_0 / s^2 \qquad (7)$$

allowing the choice

$$W \rightarrow W_0 / s^2 \qquad (8)$$

to preserve self similarity. It is also useful that the ratio of the density to the critical density is invariant in this scaling as is the ratio of the product plasma thickness x inverse bremsstrahlung absorption coefficient.

PLASMA DENSITY AND TEMPERATURE AND THE GAIN COEFFICIENT

The gain coefficient in the plasma (in the absence of significant trapping of resonance radiation) is determined by n_e and T and can be expressed as

$$g = n_u \varepsilon \sigma \qquad (9)$$

where n_u is the population number density of the upper level, ε is the inversion fraction and σ is the stimulated emission cross section. σ is a constant for constant temperature provided that Doppler broadening is dominant. The population n_u is governed by an equation of the form

$$\frac{dn_u}{dt} = -\sum_x n_u A_{ux} - n_u n_z \sum_y X_{uy} + n_e \sum_z n_z X_{zu} \qquad (10)$$

(The situation of interest is that equilibrium and with radiative rates weak compared to collisional rates for the laser upper level. The level is therefore in LTE with the next higher ion and we can write

$$n_u \sim \sum_z n_z X_{zu} / \left(\sum_y X_{uy}\right) \qquad (11)$$

so that n_u increases linearly with increasing particle number density provided that the ionisation equilibrium is insensitive to electron number density. This condition is approximately fulfilled for densities is of interest here where the ionisation is close to coronal and more generally described by a collisional radiative model, viz.

$$\frac{dn_z}{dt} = n_{z-1}S - n_e^2 n_z C - n_e n_z(\alpha + D) \qquad (12)$$

and we are concerned with circumstances where radiative (α) and dielectronic (D) recombination predominate over 3-body (C) recombination to give

$$n_z/n_{z-1} \sim S/(\alpha + D) \qquad (13)$$

The temperature is therefore the primary determinant of the ionisation balance and thus also of the collisional excitation rate coefficient which for dipole allowed excitation can be expressed in the form

$$X_{12} \sim T^{-1/2}\Delta E^{-1} f_{12} exp(-\Delta E/kT) \qquad (14)$$

There is therefore an optimum temperature which is approximately density invariant which maximises the collisional rate for producing excited states from the ground state of the laser ion.

The lower level of the laser transition is required to be in non LTE equilibrium with predominance of radiative de-excitation. Its population is small compared to the laser upper state with the inversion fraction ϵ tending towards unity. There is therefore a regime where with increasing density $n_u \sim n_e$ and $\epsilon \sim$ constant which implies $g \sim n_e$. The upper density limit of this gain scaling and specific numerical evidence of it are discussed later.

FURTHER SCALING DISCUSSION

Arising from the previous considerations, it is interesting to note that the approach to ionisation equilibrium is governed by the product $n_e t$ which is invariant under the chosen scaling ensuring invariant ionisation equilibrium. Using the scaling $g \sim n_e$, as discussed previously, leads to a scaling of the gain coefficient which we can express as

$$g \rightarrow g_o s^2 \qquad (15)$$

It is then easy to show that the power and energy efficiency of producing gain, scale respectively as

$$g/P \rightarrow (g/P)_0 s^2$$
$$g/E \rightarrow (g/E)_0 s^4 \qquad (16)$$

with a particularly attractive increase in energy efficiency of gain production.

LATERAL TRANSPORT OF ENERGY FROM THE FOCAL REGION

Experimental studies have shown a correlation between a reduction of effective intensity on the target due to lateral transport of energy and the ratio Z/W where Z is the separation of the critical density and target surface[3]. Empirical fitting to a numerical model suggests the scaling $Z \sim I^{1/3}\lambda^{2/3} t$. The previously chosen scaling for relevant parameters then leads to invariance of Z/W so that lateral transport is expected to be invariant under the chosen scaling whereas it may be a serious problem if longer wavelengths and narrower line foci are used.

REFRACTION

The self similar hydrodynamics assumed here allow a simple assessment of the scaling of the maximum length before refraction of the XUV laser beam from the gain region. This length can be written as

$$l_R^2 = 4XY(n_c/n_e)(1 - n_e/n_c) \qquad (17)$$

assuming that the gain region is of thickness X and that the density gradient scale length is Y with n_c the critical density for the XUV laser radiation. The self similar assumption then gives $XY \sim W^2$ and it follows that

$$l_r \rightarrow l_{r0} s^{-3}$$

so that

$$gl_r \rightarrow (gl_r)_0 s^{-1}$$

thus the chosen scaling leads to a reduction of the maximum gain length due to refraction but only by the relatively weak factor s^{-1}.

FEASIBILITY OF SCALING WITH S = 2

The specific example of scaling with s = 2 is of particular interest since the high brightness KrF Raman laser (λ = 268 nm) can be used instead of the more conventional second harmonic of the neodymium glass laser (λ = 532 nm). The most promising candidates for this scaling are at the high z limit of the neon-like and nickel-like isoelectronic sequences where radiative rates are most dominant over collisions. Table 1 and Table 2 illustrate how the scaling could be applied to neon-like Ag where the dominant J = 2-1 transition is at 9.9 nm and to Ni-like Ta where the dominant J = 0-1 transition is at 4.48 nm. Experimentally observed performance and scaled performance are contrasted in the tables and the main point of interest is that the driver requirement for saturated and diffraction limited operation in the scaled model, (assuming 4 beam irradiation and a double plasma configuration), is reduced to circa 1 kJ in 125 ps with a brightness of 2×10^{18} W cm^{-2} sterad^{-1}. These performance parameters are within the range expected to be achieved with the next generation of KrF Raman laser systems such as the CLF's Titania project.

	(a)	(b)	(a)	(b)
λ, μm	0.53	0.268	0.53	0.268
t, ns	500	125	500	125
I, Wcm^{-2}	5×10^{14}	2×10^{15}	2.5×10^{14}	10^{15}
W, μm	130	30	120	30
P, TW	7	7.8	7.6	5.4
E, kJ	3.5	0.97	3.7	0.68
B, Wcm^{-2}sr^{-1}	5×10^{17}	1.9×10^{18}	5×10^{17}	1.2×10^{18}
g cm^{-1}	4.3	17	3.2	13
gl	4.7	22	8	22
λ_{XUV} nm	9.9	9.9	4.48	4.48

Table 1 Ag XXXVIII Table 2 Ta XLVI
(a) demonstrated in experiments (b) proposal; scaling for saturated and diffraction limited operation.

A crucial question relating to the validity of the scaling is whether the gain will increase linearly with density over the 4-fold range required. Figure 1 shows results from numerical modelling for Ag[4] which show gain increasing more than linearly with density for density up to 3x above the circa 10^{21} cm^{-3} operating electron number density of experiments with the Ag laser. This increase will terminate when the laser lower level becomes thermalised. n_e for thermalisation is computed to be 1.6×10^{22} and well above the level required here. (By comparison the neon-like Ge laser operates at a $n_e \sim 3 \times 10^{20}$ cm^{-3} while its thermal limit is computed to be 7×10^{20}).

The increase of gain with density will also terminate if collisional broadening exceeds Doppler broadening. In that case the stimulated emission cross-section decreases in inverse proportion to the density.

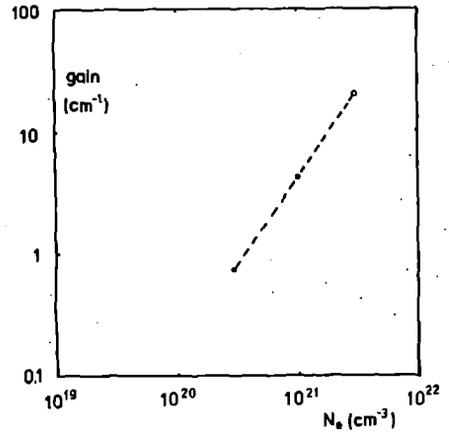

Fig 1 Gain at constant (1800 eV) temperature in for J = 2-1 laser action at 9.9 mm in Ag XXX VIII.

For the example of Ag where T_e = 2 keV and T_i = 1 keV, we have a Doppler width of 6×10^{12} Hz while for collisions to give the same line width would require $n_e \geq 7 \times 10^{22}$. It appears therefore that for Ag thermalisation of population will intervene before collisional broadening in limiting the increase of gain with density.

The situation for Ni-like Ta is similar and Fig 2 shows the density variation of gain computed numerically[5] with thermalisation occuring at about 10^{23} cm^{-3} and a strongly increasing gain up to 10^{22} cm^{-3} .

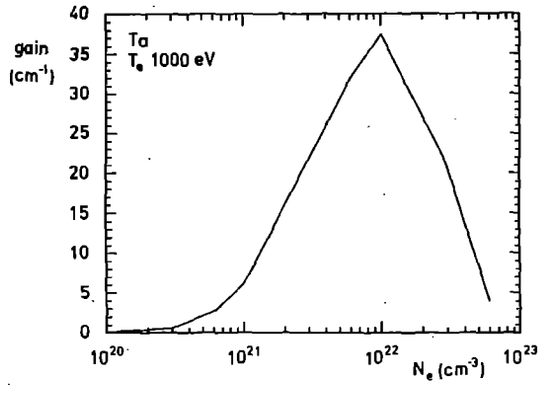

Fig 2 Gain at constant (1000 eV) temperature for J = 0-1 laser action at 9.9 nm in Ta XL VI.

CONCLUSION

This preliminary analysis leads to the conclusion that there is interest both in experimental studies of short wavelength, short pulse irradiation to drive collisional lasers and in further numerical modelling to investigate the suggested scaling in more detail. There appears to be a good possibility of exploiting this scaling to make a significant improvement in the driver energy requirement of saturated and diffraction limited lasers and to realise such a laser at a wavelength close to the water window with circa 1 kJ drive using a KrF/Raman laser.

REFERENCES

1. B J MacGowan et al, Phys Rev Lett 65 420 (1990).
2. R A London and M D Rosen, Phys Fluids 29 3813 (1986).
3. G J Tallents et al, Opt Comm (in press).
4. R S Walling et al in X-ray Lasers 1990, G J Tallents Ed, Publ UK Inst of Physics, p135 (1981).
5. A L Osterheld et al, 8th Topical Conf in Atomic Processes in Plasmas, Portland, Maine (Aug 1991).

NON-UNIFORM LASER ENERGY DEPOSITION CAUSED BY OPTICAL INTERFERENCE

A.M. Azhar & A.R. Bell

Imperial College, London SW7 2AZ

A possible source of non-uniformity in laser energy deposition in a target is the interference between a) laser beams incident from different angles, and b) incoming and outgoing rays from one laser beam. Whereas the former causes non-uniformity on the scale of a laser wavelength, the latter might possibly cause non-uniformity on a larger scale because it is sensitive to the angle of incidence of the incoming ray and this varies relatively slowly across the laser spot due to target curvature or beam convergence. We have examined this latter case with a ray-tracing calculation. We consider the incidence of a converging laser beam onto a spherical target. Ray paths are calculated through a plasma corona of varying thicknesses. The phase of incoming and reflected rays and the interference between the two is calculated. The local energy deposition by inverse bremsstrahlung is then determined from the magnitude of the local oscillating electric field and the total energy deposition is integrated in radius at any particular angle on the target.

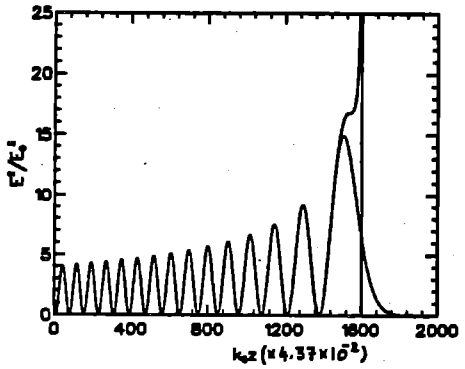

Fig. 1 Comparison of ray tracing solution with the solution to the wave equation. The laser beam comes in from the left.

The ray tracing calculation with interference effects was tested against a full solution of the wave equation for a planar target and found to agree very well except at the critical surface where the ray-tracing calculation produces a singularity and omits the evanescent decay into the overdense plasma (see Fig. 1).

The source of non-uniformity can be most easily understood by considering the idealised case of homogeneous coronal plasma which has a sharp outer edge where the density falls abruptly to zero. If the outer edge coincides with a peak in the interference pattern, then the mean energy absorption is greater within the plasma than if the outer edge coincides with a trough in the interference pattern. The wavelength of the interference pattern is proportional to $1/\cos\theta$ where θ is the angle of incidence. Hence the position of the outer edge relative to the interference pattern and the energy absorption depend on the angle of incidence which in turn varies over the surface of the target.

For more realistic results, we consider a range of coronal density profiles varying from a linear ramp to an inverse square density dependence. Figure 2 is a plot of the absorbed energy against angular distance from the beam axis when a spherical target is irradiated by a single laser beam. L/λ is the ratio of the depth of the plasma corona to the laser wavelength. Interference does not introduce small scale non-uniformity, but instead introduces a gentle variation which produces an absorption profile which differs from that calculated when interference is neglected. Only when $L/\lambda<8.7$ is there an appreciable difference between the absorption calculated with and without interference effects.

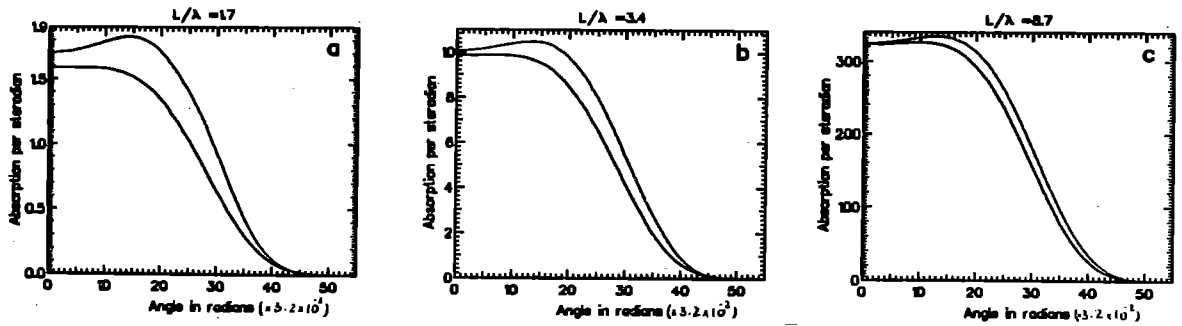

Fig. 2. Comparison of absorbed energy versus angular distance on target surface from the beam axis. In each graph, the upper curve includes the effect of interference, and the lower curve ignores it.

THREE DIMENSIONAL SIMULATIONS OF THE RAYLEIGH-TAYLOR INSTABILITY

R. P. J. Town, B. J. Jones and A. R. Bell

Imperial College, London

The viability of inertial confinement fusion (I.C.F.) depends crucially on implosion symmetry. A spherical three dimensional hydrocode called PLATO has been developed to model the growth in asymmetries during an implosion. The code employs a fixed spherical Eulerian grid. The time dependent equations of mass, momentum and total energy are integrated numerically using the van-Leer algorithm [1] as interpreted by Youngs [2]. The fluid equations are closed using an ideal ($\gamma = 5/3$) equation of state. Currently thermal conduction, laser energy deposition and α particle heating are not included. At present we are employing the symmetry imposed on the target by the Rutherford Appleton Laboratory's twelve-beam Vulcan laser system. The point of intersection of the centre of each laser beam with the target surface defines the symmetry of the target. These points form the vertices of twenty equilateral triangles on the surface. Since the triangles are equilateral the sides can be bisected and six smaller triangles formed for each equilateral one. Hence the smallest self-similar component is 1/120th of the sphere. The symmetric disposition of the lasers prevents the imposition of certain modes. The modes that can be supported start at the sixth order polynomial, followed by the tenth and twelfth order polynomials.

The I.C.F. capsule passes through three phases as it implodes. Initially the shell is accelerated inwards, defects in target manufacture or non-uniform irradiation seed the Rayleigh-Taylor (RT) instability [3] on the outer ablation surface. Simulations from N.R.L. in 2 dimensions (2D) [4] and 3 dimensions (3D) [5] have shown a reduction in the RT linear growth rate to one half the classical value. In the non-linear regime 3D simulations have shown the RT instability growing more rapidly than in 2D.

Provided the shell is still intact the implosion continues into the coasting phase. Although not unstable the large spherical convergence can amplify the distortion further. During this phase the distortion on the outer surface couple to induce distortions on the inner surface. We have previously shown [6] that the growth in the perturbation during this phase scales as $R1^{-1/4}$, where $R1$ is the inner surface of the shell. This scaling is in agreement with the analytic theory of Book and Bodner [7].

As the pressure in the filler gas increases so the shell is decelerated and finally brought to rest. In this final stage the shell is again RT unstable, but this time on the inner fuel-shell interface. Sakagami and Nishihara have performed simulations in 2D [8] and 3D [9] of this phase. They have found a marginally reduced linear growth rate to approximately 90% the classical value. In the non-linear regime they observe an $\eta g t^2$ growth, with an η up to six times larger in 3D compared to similar 2D cylindrical simulations.

Our simulations have concentrated on the growth of the RT instability in the deceleration phase. We have already examined [10] the linear and non-linear growth of the lowest order mode. We found that the linear growth has a growth rate of 90% of the classical value. The reduction is identical to similar 2D cylindrical and spherical simulations.

In the non-linear regime we found that the RT instability evolves in two different geometries: 'bubble-ridge' and 'valley-spike'. In the bubble-ridge arrangement we saw a single well defined bubble rising up, surrounded by a series of interconnecting spikes falling to form ridges. In the valley-spike arrangement thin spikes penetrated into the fuel which were surrounded by a valley of interconnecting bubbles. The distance from the tip of the spike to the head of the bubble was used as a measure of the growth in the non-linear regime. This obeyed an $\eta g t^2$ law with an identical η for both arrangements which was found to be 1.28 times larger than comparable 2D cylindrical simulations. Similar 2D spherical simulations showed similar growth to 3D.

The differences between 2D and 3D and between the two 2D geometries can be explained by considering the nature of the 'bubble' in the different geometries. In the bubble-ridge arrangement we have a truly 3D bubble surrounded by a ridge of interconnecting spikes. Similarly in the 2D spherical case, where a bubble is centred on the pole, the bubble is essentially 3D, surrounded by a ridge around the waist. In the 2D cylindrical case the bubble is in reality a valley running around the sphere. In the 3D case the bubble has a larger boundary to feed mass into the spike than the 2D cylindrical case. Let us assume that the growth can be expressed as the product of the length of the boundary between the bubble and spike and the mass flux flowing across the boundary normalised to the area of the bubble. In 3D the bubble can be thought of as a hemisphere of radius $\lambda/4$ (where λ is the wavelength of the perturbation). The perimeter of the bubble is $2\pi(\lambda/4)$ and the area of the hemisphere is $2\pi(\lambda/4)^2$. In 2D the bubble is a half cylinder of length a and radius $\lambda/4$. The boundary between the bubble and spike is thus $2a$ and the area of the bubble is $a\pi(\lambda/4)$. In order to obtain a in terms of λ we compare the growth of bubbles with the same area, hence $a = \lambda/2$. The boundary in 2D is thus equal to λ. The boundary in 3D is $\pi/2$ larger than 2D allowing mass to pass from the bubble to the spike more easily in 3D, hence giving a faster growth. Sakagami and Nishihara results support this conclusion; faster growth occurs in spherical harmonics which maximise the boundary between bubble and spike.

Figure 1: The inner surface of the shell (defined as the surface of constant density equal to $1/e$ of the maximum density) at 1.3 nsec. This shows the bubble-ridge arrangement when the twelfth mode is excited.

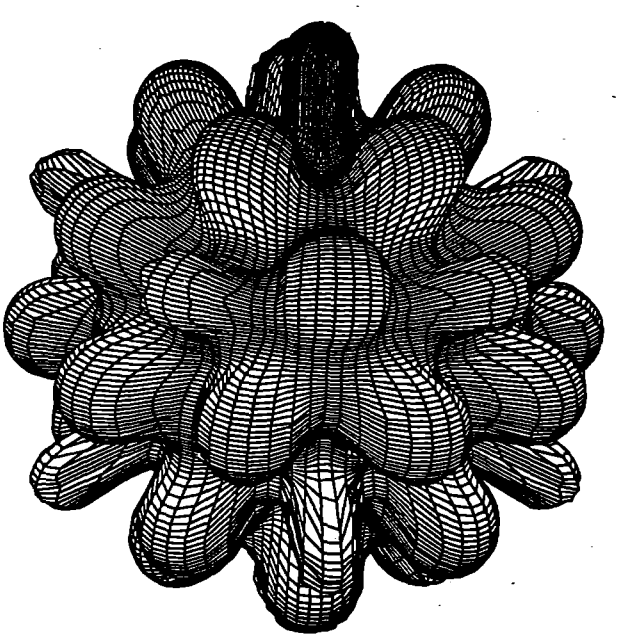

We have extended our study of the linear and non-linear RT growth to modes ten and twelve. We have also examined the effect of thinner shells. In figure 1 we plot the inner fuel-shell interface at 1.3 nsec showing the growth of mode twelve. This clearly show the bubble-ridge arrangement. These higher order modes show ηgt^2 growth with an η similar to that of the sixth order mode.

We examined the mass mode evolution of the bubble-ridge and valley-spike arrangements. When we excited the sixth order mode we found that the bubble-ridge arrangement had a faster sixth order mode evolution than the valley-spike arrangement. However the tenth order mode of the valley-spike grew much faster than in the bubble-ridge arrangement. As the tenth order mode grows so the valley-spike arrangement starts to develop mini-bubbles on its valley. This suggests that the natural evolution of the RT in the non-linear regime is to develop bubbles when we are considering finite width shells.

The bubble-ridge arrangement always has less mass in its minimum radial line ($\sigma_{min}(\theta,\phi)$) than the valley-spike arrangement. Conversely the valley-spike arrangement always has more mass in its maximum radial line ($\sigma_{max}(\theta,\phi)$) than the bubble-ridge arrangement. In figure 2 we have plotted the time rate of change of the minimum mass radial line. We see that the rate at which the bubble-ridge arrangement thins is always greater than in the valley-spike arrangement. The converse, that the rate at which the valley-spike thickens is always greater than in the bubble-ridge arrangement, is also true. The bubble-ridge arrangement is essentially better at bubble development, whereas the valley-spike arrangement is better at spike development. Shell thinning is therefore more rapid in the bubble-ridge arrangement. This shell thinning can cause the shell to breakup, preventing further compression and allowing the fuel to escape. As the bubble increases in size so the mass of the shell at the bubble head is reduced leading to a higher acceleration relative to the rest of the shell. The bubble then sheds mass more quickly. This suggests that thinner shells would have a more rapid evolution of the bubble. The valley-spike geometry has less well developed bubbles so the effect of the shell thinning would not be as important. We performed simulations with a shell of two-thirds the thickness, but with the same mass, to check this hypothesis. We found that the thin shell bubble-ridge arrangement did grow more quickly than the thick and thin shell valley-spike arrangement and the thick bubble-ridge arrangement. Figure 3 shows the contour plot of this thin shell near the end of the simulation showing that the bubble has in fact burst through the back of the shell.

Figure 2: The time evolution of the rate of change of the minimum mass line for the bubble-ridge (A) and valley-spike (B) arrangements.

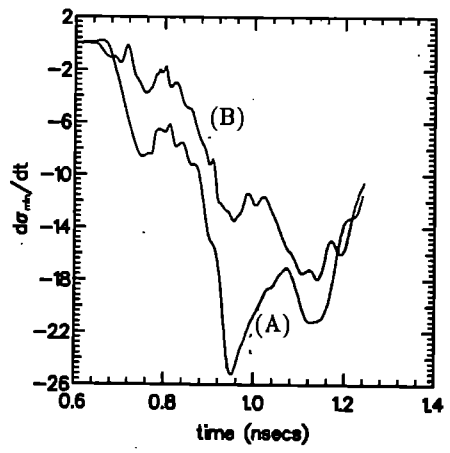

Figure 3: Contour plot of the density of the bubble-ridge arrangement. The bubble has burst through the back of the shell, preventing further compression.

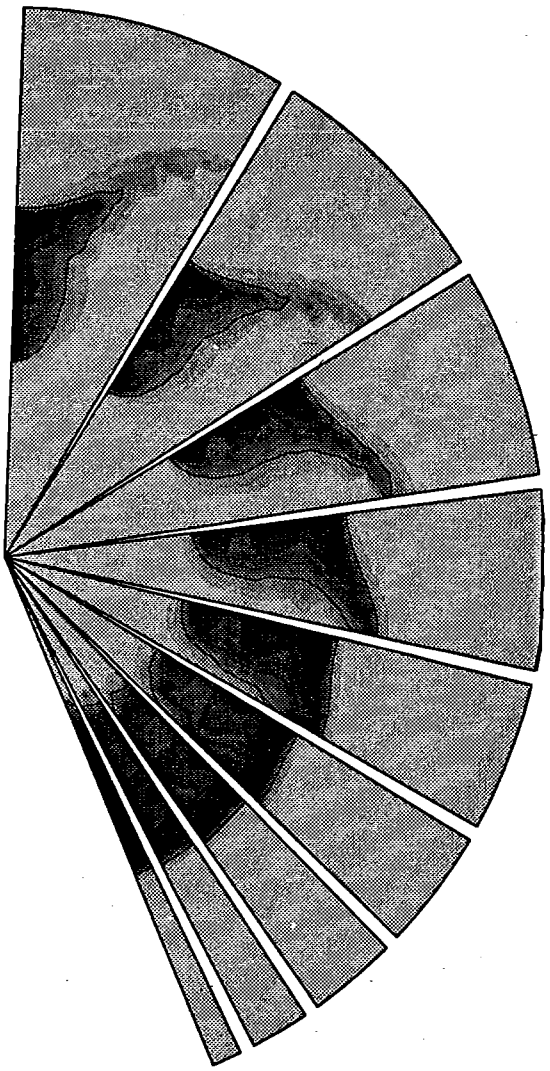

In conclusion, we have reported 3D simulations of the RT instability in the deceleration phase of an I.C.F. target. We have obtained RT linear growth rates which are 90% of the classical value. We have found that in the non-linear regime the growth goes as ηgt^2 with an η approximately 1.28 times similar 2D cylindrical simulations.

REFERENCES

1. B. van Leer, J. Comput. Phys. 23, 276 (1977).
2. D. L. Youngs, Numerical Methods for Fluid Dynamics (Academic, New York, 1982).
3. Lord Rayleigh, Theory of Sound (Dover, New York, 1945) 2nd Edition
   G. I. Taylor, Proc. Roy. Soc. London, Ser A 201, 192 (1950)
4. J. H. Gardner, S. E. Bodner and J. P. Dahlburg, Phys. Fluids B 3, 1070 (1991)
5. J. P. Dahlburg and J. H. Gardner, Phys. Rev A 41, 5695 (1990)
6. R. P. J. Town and A. R. Bell, *Annual Report to the Laser Facility Committee* Rutherford Appleton Laboratory Report RAL-90-026 Sect A4 (1990)
7. D. L. Book and S. E. Bodner, Phys. Fluids 30, 367 (1987)
8. H. Sakagami and K. Nishihara, Phys. Fluids B 2, 2715 (1990)
9. H. Sakagami and K. Nishihara, Phys. Rev. Lett. 65, 432 (1990)
10. R. P. J. Town and A. R. Bell, Phys. Rev. Lett. 67, 1863 (1991)

NONLINEAR EFFECTS IN RESONANCE ABSORPTION

D.A.Johnson and R.A.Cairns
University of St. Andrews

INTRODUCTION

Resonance absorption in laser-plasma interactions has long been an area of interest for plasma physicists. Two main approaches have been adopted in previous investigations; the Vlasov equation models[1] and PIC simulations[2] on high-powered computers. The interaction of a collection of charges with an applied field my be investigated by considering the oscilations of one of the charged particles, driven by the applied field. In the case of a plasma, it is the electrons which oscillate (ions can be considered as immobile due to their relatively high inertia) and the impinging laser beam provides the applied field. As long as the laser pulse is at an oblique angle of incidence, the electric field associated with it will have a component into the plasma. We set out to see what could be learned from such a simple 'forced-oscillator' model of the absorption of a laser pulse by an overdense plasma.

THEORY

The model assumes a simple linear density profile for the plasma and also that the plasma consists purely of electrons and singly-charged ions in equal numbers. The density profile gives solid density for positions to the left of the origin, which is set at the position where the plasma starts to form. To the right of the origin, the density decreases linearly to zero over a scalelength L ($10^{-8}m$). In the construction of a model for the system, we have to represent

1. The damping effect caused by collisions with local ions.
2. The restoring force which is provided by charge separation.
3. The driving force due to the pump wave at oblique incidence.

If we take x_0 to be the position in the profile we wish to examine and ξ to be the displacement from this position, then we can set up the following equation for the motion of an electron .

$$\ddot{\xi} + \upsilon\dot{\xi} = -\frac{e^2}{\varepsilon_0 m}\int_{x_0}^{x_0+\xi} n_0(x)\,dx + \frac{eE_0}{m}cos\omega t \qquad (1)$$

where υ is the (constant) damping coefficient, E_0 is the amplitude of the pump wave, ω is the pump frequency and $n_0(x)$ is a piecewise linear density function with three distinct regions.The integral expression for the restoring force assumes that electron orbits do not cross.

Now if ξ is small, the integral in equation (1) can be approximated by, $\int_{x_0}^{x_0+\xi} n_0(x)dx \approx n_0(x_0)\xi$. This simplifies the equation greatly and allows the displacement ξ to be calculated analytically. The dissipation of energy can also be calculated from the simplified equation to be,

$$\langle eE\dot{\xi}\rangle \propto \frac{\upsilon}{\left(\omega^2-\omega_p^2\right)^2+\upsilon^2} \qquad (2)$$

For larger values of ξ, however, we cannot approximate the integral as before and the equation of motion is that of an anharmonic oscillator.

We can rescale the units of length and time to L and ωt respectively in equation (1) and define the 'solid plasma frequency' $\omega_{0p} = \frac{n_s e^2}{\varepsilon_0 m}$ to get,

$$\ddot{P} + a\dot{P} + b\mathcal{F}(P) = ccosT \qquad (3)$$

where $a = \frac{\upsilon}{\omega}$, $b = \left(\frac{\omega_{0p}}{\omega}\right)^2$ and $c = \frac{eE_0}{m\omega^2 L}$.

The function $\mathcal{F}(P)$ in equation (3) has one of the following forms, depending on the value of the quantity $\frac{x_0}{L} + P$,

$$\mathcal{F}(P) = \begin{cases} P + \frac{1}{2}\left(\frac{x_0}{L}\right)^2 & \frac{x_0}{L}+P<0 \\ P\left(1-\frac{x_0}{L}\right) - \frac{P^2}{2} & 0 \le \frac{x_0}{L}+P \le 1 \\ \frac{1}{2}\left(1-\frac{x_0}{L}\right)^2 & \frac{x_0}{L}+P>1 \end{cases}$$

The model is intended to represent the interaction of a Nd-glass laser produced pulse ($\lambda = 1.06\mu m$) with a target of solid density $n_s = 2.0 \times 10^{29}\ m^{-3}$. A constant collision frequency of $2.0 \times 10^{13}\ s^{-1}$ is assumed as a suitable value. The above fixes the values of the parameters a and b so that $a = 1.13 \times 10^{-2}$ and $b = 2.011 \times 10^2$. The parameter c is a measure of the intensity of the pump wave.

RESULTS

Since the equation (3) is nonlinear, it requires numerical solution on a computer. To establish confidence in the model, the first case examined was that when the parameter c is very small ($\sim 10^{-5}$). Under these circumstances, the results for the solution of the nonlinear equation were found to show very good agreement with predictions made using the linearised form. With c held fixed at 1.0×10^{-5}, the variation of the amplitude of oscillation with the position examined (x_0) showed the expected resonant response at the critical surface. It should be pointed out that the value of the parameter x_0 effectively determines the ratio $\frac{\omega_p}{\omega}$, i.e. the (de)tuning of the plasma frequency to the driving frequency.

When the intensity of the pump wave is increased, we have observed nonlinear effects. In order to study the behaviour of equation (3), Poincaré points are generated at intervals of 2π in the scaled time units. These points are use to construct a Poincaré map. This technique enables the nonlinear effects such as period-doubling and chaos to be identified in a qualitative manner. We have found that these nonlinear effects become apparent for values of c of the order of 1.0×10^{-3}. This corresponds to beam intensities of the order of $1.0 \times 10^9\ W/cm^2$, which is much lower than the 10^{14}–$10^{16}\ W/cm^2$ range expected[3] for such effects to occur. The type of nonlinear behaviour observed depends upon the parameter x_0 for a fixed value of the parameter c. By varying the value of x_0 (principally between the critical point at 0.995 and 1, where the density is zero) we have observed period doubling, trebling, quadrupling and regions of chaos. Figure (1) shows the Poincaré map of a chaotic attractor which exists for the values $c = 1.0 \times 10^{-3}$ and $x_0 = 0.9985$.

In order to verify the periodicity exhibited in the Poincaré maps, Fourier power spectra have been produced. These clearly show the frequency components of the motion of the oscillator and their relative magnitudes. For example, figure (2) shows the power spectrum for $c = 1.0 \times 10^{-3}$ and $x_0 = 0.996$. This falls into the basin of attraction of a period-4 motion and this can be clearly seen from the frequency components at $\frac{\omega_p}{\omega} = \frac{1}{4}, \frac{1}{2}, \frac{3}{4}, 1$. The fourier spectra have

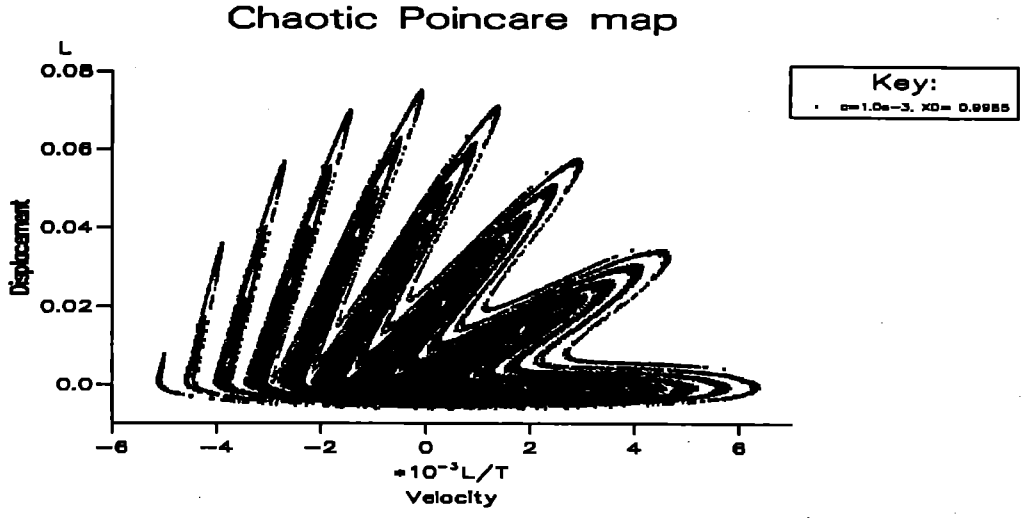

Figure 1: The Poincaré map for $c = 1.0 \times 10^{-3}$ and $x_0 = 0.9985$, illustrates a chaotic attractor

proved most useful in verifying the nature of the chaotic attractors. The power spectrum produced by a chaotic attractor is characterised by its broad-band nature. Figure (3) shows the spectrum for the chaotic attractor of figure (1).

A common feature of nonlinear differential equations is the existence of many different attractors in the phase space of starting values. The results presented thus far have all assumed that the electron was initially at rest at the equilibrium point. So equation (3) was then solved over a mesh of starting values to reveal the structure of the starting value space. The values of c and x_0 were fixed at $c = 1.0 \times 10^{-3}$ and $x_0 = 0.996$ (a known period-4 attractor from earlier results). This revealed the existence of period 1,2,3 and 4 attractors co-existing in the phase space of starting values.

DEVELOPMENT

Setting up a simple model for resonant absorption enables us to examine in detail the nonlinear bifurcations to subharmonics and to chaos which occur, in the hope that these will cast some light on results of experiments and computer simulations.

Work is currently going on into the implications of these nonlinear effects for the absorption of energy into the plasma. The average absorption over a cycle of the system can be calculated numerically and used to show the variation of absorption with the frequency ratio $\frac{\omega_p}{\omega}$.

It is also intended that the model will shortly be improved by making the damping coefficient a dynamic variable in equation (3) and not simply a constant.

REFERENCES

1. Bergmann and Mulser, Darmstadt University.

2. P.Gibbon and A.R.Bell, RAL annual report 1990, pg.61

3. J.Kieffer et al., "Absorption of an ultrashort laser pulse in very steep plasma density gradients", IEEE Journal of Quantum Electronics, vol.25, No.12, p2640 (1989).

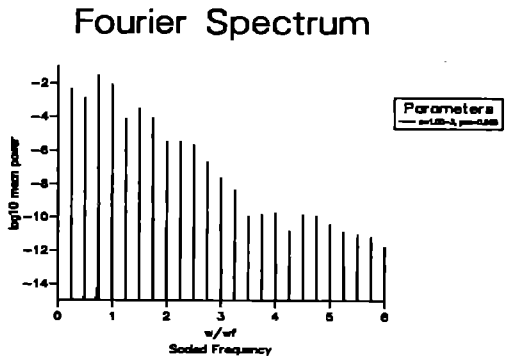

Figure 2: The Fourier spectrum for $c = 1.0 \times 10^{-3}$ and $x_0 = 0.996$.

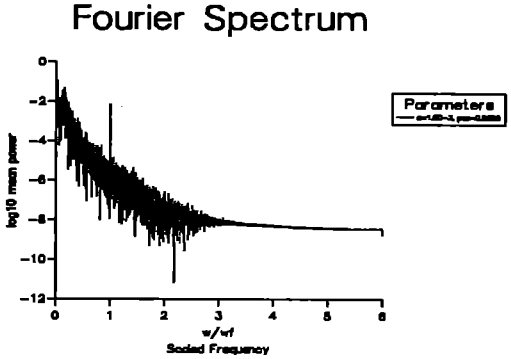

Figure 3: The Fourier spectrum for $c = 1.0 \times 10^{-3}$ and $x_0 = 0.9985$.

ULTRA-SHORT PULSE OPERATION OF THE VULCAN Nd:GLASS LASER FACILITY USING CHIRPED PULSE AMPLIFICATION

Z Chang[1], C N Danson[2], M D Dooley[2], C B Edwards[2], M H R Hutchinson[3], I P Mercer[3], M R G Miller[2], Z Najmudin[3], C E Ollman[2], D A Pepler[2], R A Smith[3], P F Taday[2], W T Toner[2] and T B Winstone[2]

[1]Royal Society Visiting Fellow, Xian Inst. of Optics and Precision Mechanics, People's Republic of China
[2]Central Laser Facility, Rutherford Appleton Laboratory, Chilton, Didcot, OXON OX11 0QX
[3]Blackett Laboratory, Imperial College, Prince Consort Road, London, SW7 2BZ

INTRODUCTION

Ultra-short pulse capability (< 1 ps) is becoming increasingly important in laser/plasma interaction experiments. Applications include: pumping recombination XUV lasers; beat-wave and Wakefield particle acceleration investigations; high order harmonic generation, and solid density interaction experiments. Such pulses can also be used to give improved resolution of diagnostic techniques including X-ray backlighting, and optical probing. The experimental programme at the CLF will benefit greatly from the implementation of ultra-short pulse technology on VULCAN.

Chirped Pulse Amplification[1] (CPA) provides a method of overcoming the non-linear phenomena that limit the maximum energy that can be supplied in ultra-short pulse mode. In high power Nd:glass lasers such as VULCAN, this is a problem due to the high number of optical components which the beam must pass through. In our implementation of the CPA scheme an ultra-short pulse (1 ps) is generated and stretched prior to amplification, and subsequently recompressed at the output of the system. This allows a factor of up to 500 times more energy to be supplied in the short pulse. This report describes a CPA experiment conducted on the VULCAN high power Nd:glass laser system at RAL during December 1991.

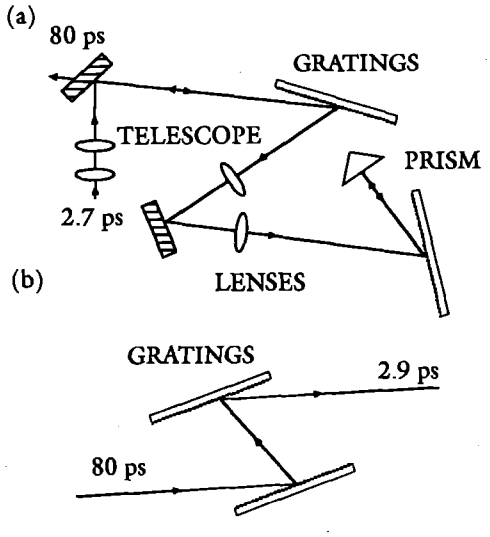

Figure 1. Grating Stretcher and Compressor

PULSE GENERATION, STRETCHING AND PRE-AMPLIFICATION

Ultra-short pulses at 1053 nm were generated using a diode pumped Additive Pulse Mode-locked (APM) oscillator[2] using Nd:YLF. This produced a near transform limited CW pulse train with a pulse-width of 2.7 ps and average power of 100 mW. This gives a single pulse energy of 0.6 nJ. The pulse was stretched to 80 ps using a double passed grating pair, as shown in figure 1(a). The gratings introduce a frequency dependent time delay, producing a pulse with a linear frequency sweep (chirp). A streak camera record of the stretched pulse is shown in figure 2. The two pulses are produced by an etalon which provides a calibration on every shot.

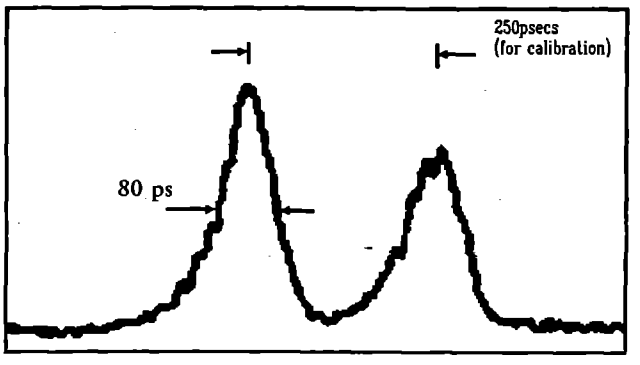

Figure 2. Streak Camera Record of the Stretched Pulse

The pre-amplification and single pulse selector is shown in figure 3. A Faraday rotator provided isolation between the expander and the amplification system to protect the oscillator from back-reflections. A single pulse was selected from the CW pulse train using two Pockel cells in series, one before the pre-amplifier and one after. A double passed 9 mm diameter rod amplifier was used to pre-amplify the pulse before injection into a modified VULCAN system. It was necessary to limit the double pass gain to a factor of 225 to defeat self oscillation. This limitation will be avoided in future experiments.

PULSE AMPLIFICATION

A schematic of the modified VULCAN amplifier configuration is shown in figure 4. The beam passes through a series of rods up to a diameter of 45 mm. The beam was then expanded to 90 mm and passed through two double passed 108 mm diameter disc amplifiers in series, and finally, through a 150 mm clear aperture disc amplifier, without further expansion. The total gross system gain was 10^{15}, with injection and system losses estimated at 10^{4}. This gives a net

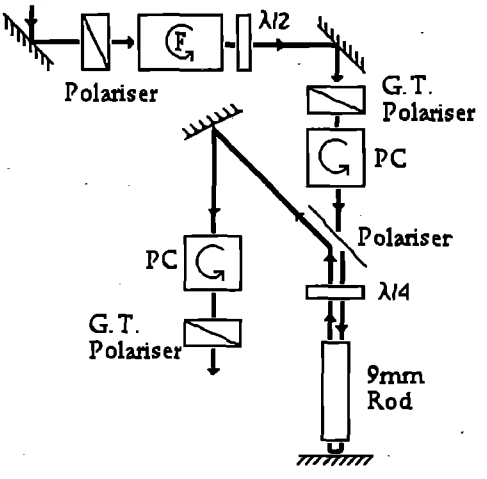

Figure 3. Switchout and Pre-Amplification Scheme

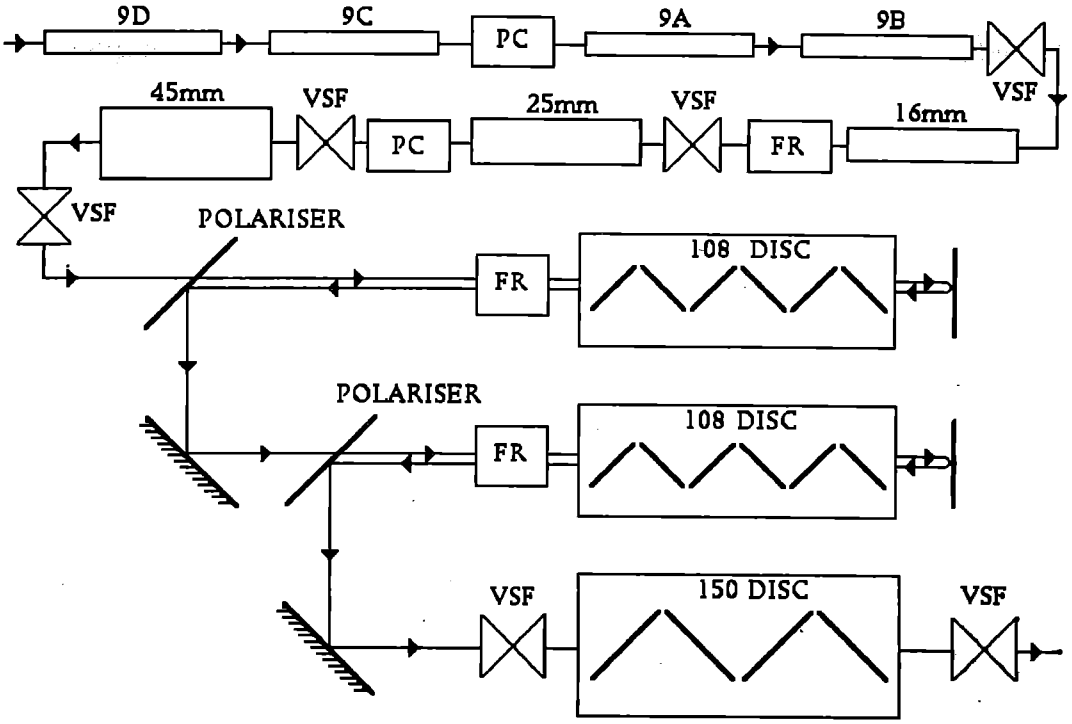

Figure 4. Amplification Schematic of VULCAN for the CPA Experiment

gain of 10^{11}. A series of test shots were fired to establish safe operating limits of the system. A maximum of 39 J was obtained, limited by B-integral effects.

PULSE COMPRESSION

The amplified pulse was propagated to Target Area West, where it was compressed using a pair of large aperture (220x165 mm) diffraction gratings, in single pass. The configuration is shown in figure 1(b). With this grating configuration, the chirp imposed on the beam by the stretcher was compensated. The total incident beam energy on the gratings was limited to 10 J, to ensure the damage limit was not exceeded.

The compressed pulse was diagnosed using a single shot auto-correlator[3]. The pulse length dependence on grating separation is shown in figure 5. This shows a minimum pulse duration at a grating separation of 2.68 m. The maximum energy off the gratings was 4.9 J, giving a grating efficiency of 70%. This energy in a compressed pulse of 2.9 ps converts to system output power of 1.7 TW.

BEAM FOCUSING

An equivalent-plane monitor was used to measure the far-field intensity distribution of the compressed pulse. The beam was focused through a 10 m lens, then passed through two etalons to produce a 3x3 array of foci. Figure 6 shows the beam at best focus, equivalent to 5x diffraction performance. This is similar to the value measured for standard system operation, demonstrating that the gratings do not significantly degrade the beam focussing.

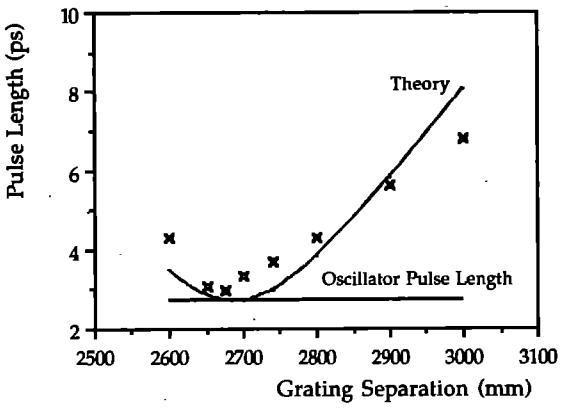

Figure 5. Experimental and Theoretical Pulse Length Dependence on Grating Seperation

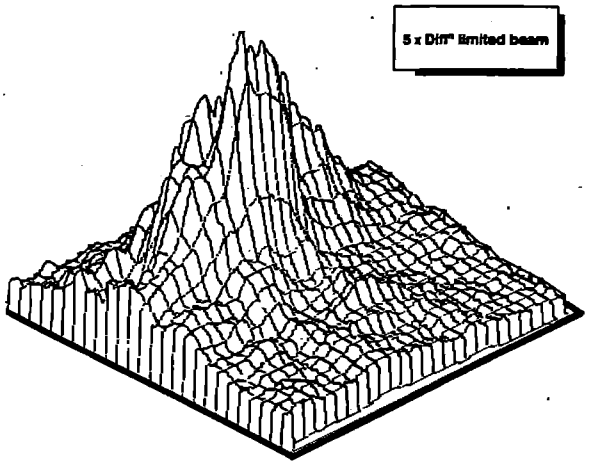

Figure 6. Far Field Intensity Distribution

CONCLUSION

It has been shown that the VULCAN laser in CPA mode can be used to amplify a stretched pulse from 0.6 nJ to 39 J. 7.8 J of this output was then recompressed to 2.9 ps with an efficiency of 70%. It was also shown that the beam suffered no significant distortion in passing through the gratings and could be focussed to about 5x diffraction limit. It is planned to conduct further experiments starting in the autumn of 1992 to increase the total power generated, and to propagate these pulses to target for laser-plasma interactions studies.

REFERENCES

1. P Maine et al. SPIE Vol 913 (1988) pp 140-146.
2. Z Chang et al. CLF annual report 1992.
3. Z Chang et al. CLF annual report 1992.

AN ULTRA-SHORT PULSE DIODE PUMPED Nd:YLF OSCILLATOR OPERATING AT 1053 nm

Z Chang[1], C N Danson[2], C B Edwards[2], M H R Hutchinson[3], I P Mercer[3], M R G Miller[2]

[1]Royal Society Visiting Fellow, Xian Inst. of Optics and Precision Mechanics, People's Republic of China
[2]Central Laser Facility, Rutherford Appleton Laboratory, Chilton, Didcot, OXON OX11 0QX
[3]Blackett Laboratory, Imperial College, Prince Consort Road, London, SW7 2BZ

INTRODUCTION

This report describes the development of an Additive Pulse Modelocked (APM) oscillator[1,2] using Nd:YLF as the active medium and delivering a CW modelocked train of pulses of 1.6 - 2.7 ps duration at 1053 nm. The oscillator was used as the pulse generator for the Chirped Pulse Amplification (CPA) experiments on VULCAN during December 1991.

APM OSCILLATOR

A schematic of the coupled cavity oscillator is shown in figure 1. The primary cavity consists of a Nd:YLF rod which is cut at Brewsters angle at the output to minimise cavity losses and to provide polarisation discrimination between the 1053 nm and 1047 nm lasing lines in Nd:YLF. Nd:YLF was chosen as it provides a good wavelength match for the peak gain in phosphate glass amplifiers used in high power glass laser systems. Pumping of the Nd:YLF rod is provided by means of a 3W laser diode. The pumping system is described elsewhere[3]. A 500 mm radius of curvature reflecting mirror is used to control the mode size and angled at 14 degrees from the normal to compensate for astigmatism generated in the Brewster cut rod. An 80% output coupler provides a pulse which is fed into the secondary cavity via a beam splitter with 70% reflectivity.

The secondary cavity induces a chirp on the pulse by self-phase modulation caused by the intensity dependent refractive index in an optical fibre. The pulse double passes a 1m length fibre, and is then fed back into the primary cavity. The two cavities are interferometrically matched by means of a piezo-electric transducer, which drives the mirror reflecting the pulse back into the fibre. This is controlled by a feedback circuit monitoring the average power in the cavity. The pulse is coupled to the optical fibre using index matching of 40x microscope objectives.

The chirped pulse is fed back from the secondary cavity and interferes with the non-chirped pulse of the primary cavity at the output coupler. The peak of the pulse interferes constructively, while the pedestal of the pulse interferes destructively as the phase of the pedestal of the chirped pulse differs significantly from the phase of the non-chirped pulse. This reduces the pulse duration progressively on each trip around the cavity and hence modelocks the laser.

FIBRE COUPLING

Index matching of the optical fibre to the microscope objectives minimises the losses in the secondary cavity and eliminates stray reflections which cause relaxation oscillations and disrupts the modelocking process. Several different techniques were tried, the most successful being a cell which fitted over the end of the microscope objective into which the fibre was inserted. The cell was filled with either parafin or glycerol as an index matching fluid. It was found that glycerol could not be used at the higher operating fluences. Fibre coupling efficiences in excess of 50% have been achieved using a 600µm thick glass slide coated with index matching fluid, between the fibre and the microscope objective.

OSCILLATOR PERFORMANCE

The output of the oscillator consists of a CW train of optical pulses separated by the cavity round trip time of 7.2 ns. Figure 2 shows a diode signal of the oscillator output displayed on a Tektronix 7104 oscilloscope. The output pulse train was stable for many hours but it was susceptable to vibration of the optical table which would interrupt the feedback signal to the piezo-electric drive, disrupting the mode-locking process. Tapping the optical bench was found to restart the mode-locking. The mode-locking process starts from optical noise within the cavity, and tapping the table changes the phase of the modes within the cavity, producing beating which allows short pulses to be generated.

Figure 3 shows a graph of the average power output of the primary and mode-locked cavities with variation in the diode drive current. The maximum oscillator output power was 1.0

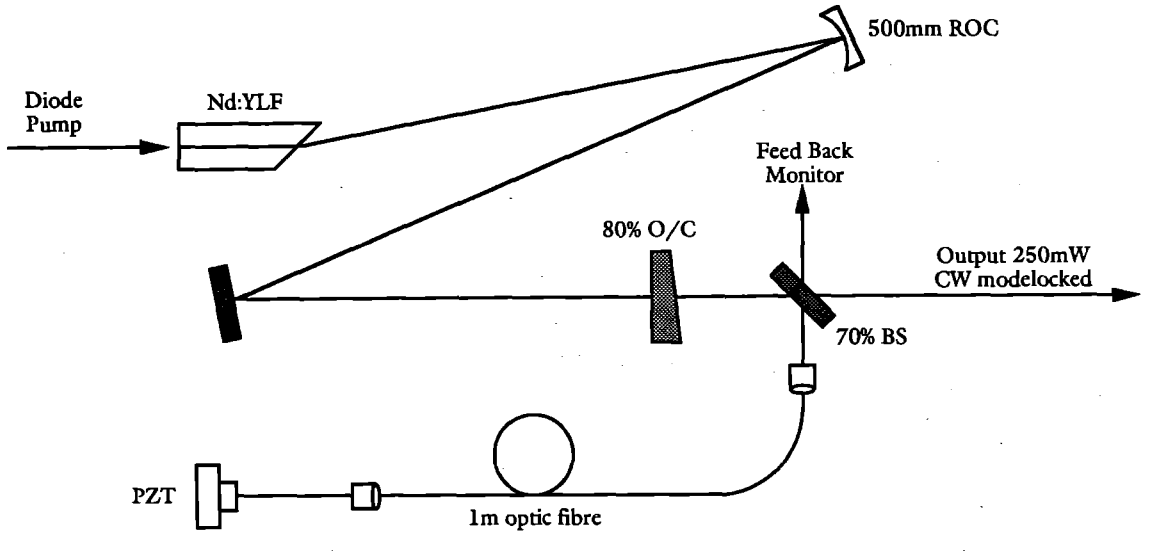

Figure 1. Schematic of the APM oscillator.

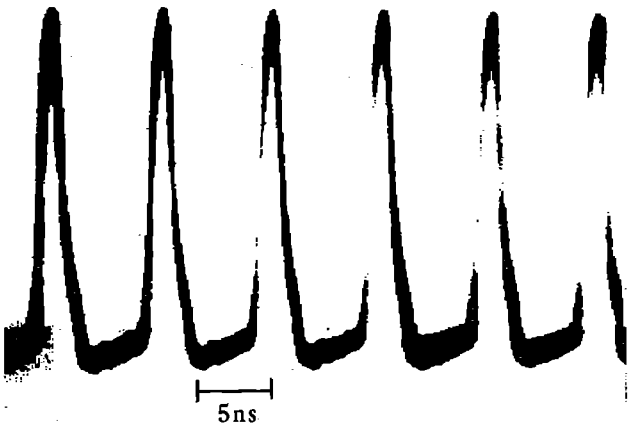

Figure 2. CW mode-locked pulse train from the APM oscillator.

W, using a drive current of 4.5 A and a 90% output coupler. This drive current corresponds to a pump power of 3.0 W, giving an efficiency of 33%. The graph clearly shows the clamping of mode-locked output at higher pumping currents, due to a change in the cavity mode structure as the pump power increases. This clamping of the output resulted in a reduction in the energy that could be coupled into the optical fibre and hence a reduction in the overall output power.

The maximum single pulse energy extracted from this cavity was 1.6 nJ, recorded with a CW pulse train of 139 MHz and an average power of 220 mW. For the December experiment the oscillator was configured for maximum stability, operating with a single pulse energy of 0.6 nJ.

The bandwidth and pulse-width of the oscillator output was measured using a grating spectrometer and a scanning auto-correlator[4] respectively. Typical outputs are shown in figure 4. For this example the output pulse-width was 2.7 ps and the bandwidth measured at 0.576 nm, giving a time X bandwidth product of

$$\Delta\tau.\Delta\upsilon = 0.411$$

corresponding to an approximately bandwidth limited Gaussian pulse.

The oscillator was found to be extremely reliable during the commissioning phase of the CPA experiment in December 1991. Problems arose during full system shots on VULCAN when the mode-locking would be interrupted for a few

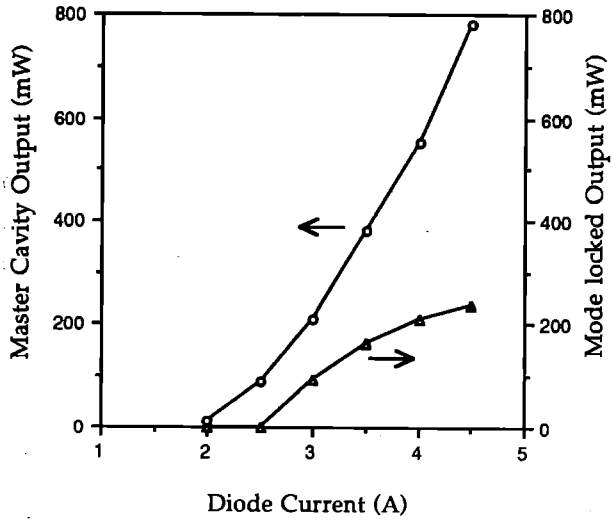

Figure 3. Average power output of the primary cavity and of the APM oscillaor.

milliseconds, with the oscillator giving nothing out at the peak of the amplifier gain. Monitoring the oscillator output showed that the mode-locking stopped when the ignitrons fired the disc amplifier flashlamps. It was inferred that electrical noise, either air bourne or via the earthing system in the laser room, was effecting the feedback circuitry, interrupting the mode-locking process. Efforts are now being made to harden the circuitry to electrical noise to prevent these problems from reoccurring.

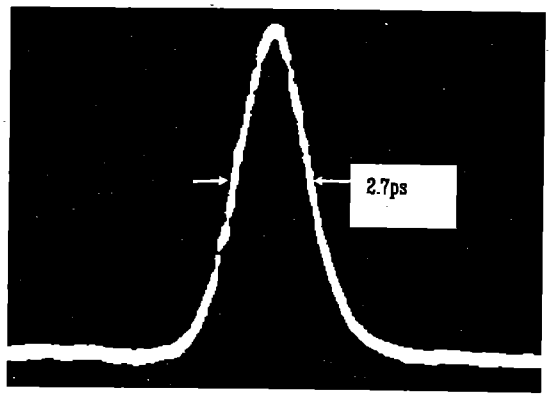

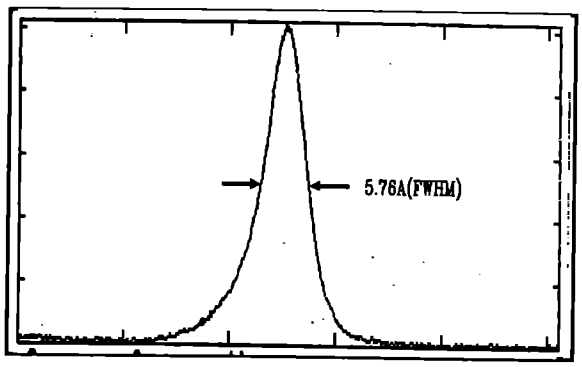

Figure 4. APM oscillator pulse measurements from the scanning auto-correlator and the grating spectrometer.

CONCLUSION

We have developed a stable, diode-pumped modelocked oscillator, operating on the 1053 nm transition in Nd:YLF. Bandwidth limited pulses of 1.6 - 2.7 ps duration were observed. This is the first time that a diode pumped APM oscillator has been operated at this wavelength. This oscillator was used sucessfully as a driver for CPA experiments on the VULCAN high power Nd:glass laser system in December 1991.

ACKNOWLEDGEMENTS

The authors acknowledge the valuable assistance of the staff at the Optoelectronics Research Centre at Southampton University during the course of this work, and in particular that of Dr John Barr and Matthew McCarthy.

REFERENCES

1. J.M.Liu and J.K.Chee; Opt Lett 15, 685 (1990).
2. G.P.A.Malcolm, P.F.Curley and A.I.Ferguson; Opt Lett 15, 1303 (1990).
3. Z.Chang et al; CLF Annual Report 1992.
4. Z.Chang et al; CLF Annual Report 1992.

CHARACTERISATION OF A 3 W LASER DIODE FOR Nd:YLF CAVITY PUMPING

Z Chang[1], C N Danson[2], C B Edwards[2], M H R Hutchinson[3], I P Mercer[3], M R G Miller[2]

[1]Royal Society Visiting Fellow, Xian Inst. of Optics and Precision Mechanics, People's Republic of China
[2]Central Laser Facility, Rutherford Appleton Laboratory, Chilton, Didcot, OXON OX11 0QX
[3]Blackett Laboratory, Imperial College, Prince Consort Road, London, SW7 2BZ

INTRODUCTION

A picosecond oscillator has been developed to provide seed pulses for the CPA programme on VULCAN[1]. This oscillator was based on a Nd:YLF laser, pumped by a 3W laser diode. Nd:YLF has been predominantly used as the gain medium for oscillators with phosphate glass amplifiers because of its wavelength (1053 nm), high gain, large bandwidth and good thermal properties. The large bandwidth (1.2 nm) enables 1 ps pulses to be generated. It has strong absorption lines at 800 nm and so can be pumped efficiently by a GaAlAs diode laser.

Diode pumping of solid state lasers has many advantages over the convential flashlamp pumped lasers. In particular, the high pumping efficiency makes forced cooling unnecessary and with the low power consumption makes the system easy to maintain, compact, and simple to operate. This report describes investigations into efficient pumping of the cavity using a diode laser, and the optimisation of the output mode from the laser cavity.

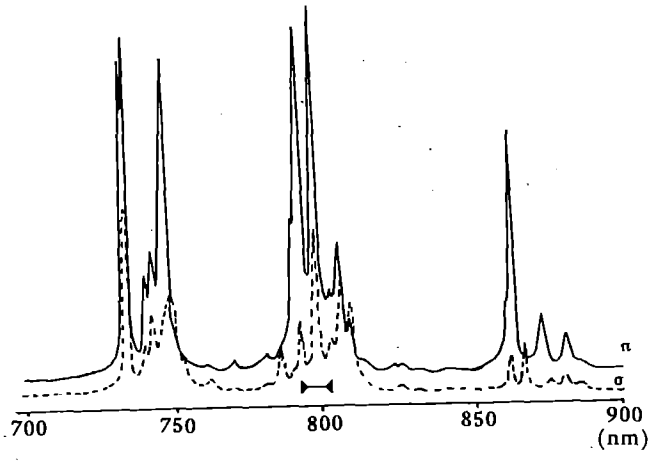

Figure 1 Absorption lines of Nd:YLF

DIODE PUMPING CONFIGURATION

The laser diode (SDL-2482-PI) was a 3W gain guided, partially coherent, phase coupled, GaAlAs multi-stripe device. This type of diode operates in the 780 to 870 nm wavelength region with a bandwidth of approximately 2 nm. The wavelength can be tuned by adjusting the temperature of the diode using a thermoelectric cooler contacted to the device. Figure 1 shows the absorption lines of Nd:YLF[2], the practical tuning range of the specific diode used is shown by the solid bar. The dimensions of the multi-stripe laser are 500 microns (H) by 1.0 micron (V), with a beam divergence of 10 degrees and 40 degrees respectively (H being the plane parallel and V the plane perpendicular to the junction plane).

The pumping configuration is shown schematically in figure 2. The diode output was coupled to a Nd:YLF rod through a dichroic multi-layer dielectric coating, <5% R at 800 nm and >95% R at 1053 nm. The coupling optics consisted of a high numeric aperture (0.65) multi-element collimator, a 100 mm focal length cylindrical lens to correct for the astigmatic output mode pattern of the diode array, a half-wave plate and a 25 mm focal length plano-aspheric focusing lens.

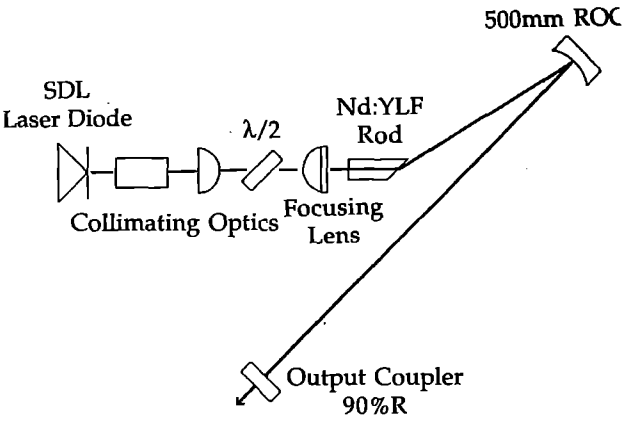

Figure 2 Diode Pumping Schematic

The pumping mode near the focus point in air is shown in figure 3. The mode size of the pump in the Nd:YLF rod is smaller than that in air due to refraction. It is clear from figure 3 that the pump mode is not axially symmetric and that the minimum focal point, in the two directions are not the same due to the astigmatic diode output. The mode in the vertical plane is transform limited, but not in the horizontal plane because the beamlets from the multi-stripes are incoherent. It is therefore the divergence in the horizontal plane that limits the pumping efficiency. The spatial intensity distribution of the pumping beam is shown in figure 4. Note that the interference pattern in the horizontal plane changes before and after focus.

PUMPING EFFICIENCY

The Nd:YLF rod used in these experiments was 10 mm in length and 4 mm in diameter with a plano-Brewster cut. The c-axis of the crystal was orientated perpendicular to the beam propagation axis and the Brewster angle plane to reduce the loss for the ordinary light (1053 nm transition). The absorption of Nd:YLF to the pump light is larger in the π (E parallel to c) plane than the σ (E perpendicular to c) plane, so a half wave plate was used to rotate the polarisation of the pumping beam.

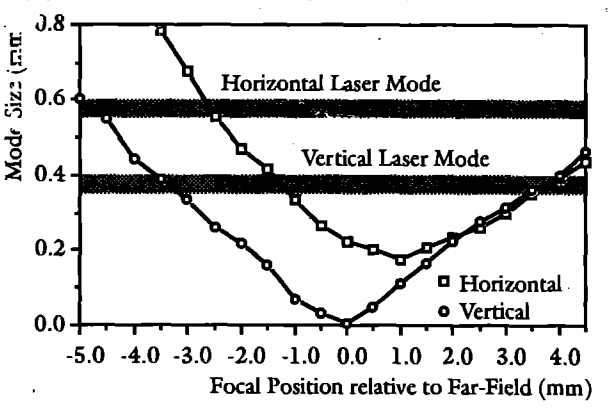

Figure 3 Pump and Laser Modes

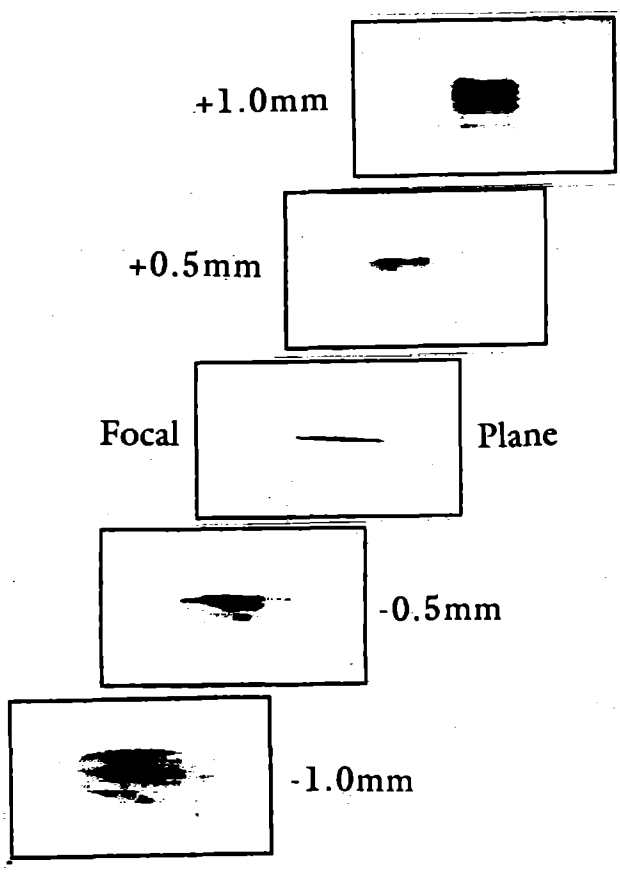

Figure 4 Laser Diode pump beam uniformity
(Showing Position from focal plane)

LASER MODE

To achieve good pumping efficiency the pumping mode in the rod must overlap with the laser mode. The laser mode is determined by the cavity configuration, shown in figure 2. The resonator consisted of three mirrors: the plano end of the rod, the 500 mm ROC spherical mirror and the output coupler. The spherical mirror is used to keep the cavity stable and to compensate the astigmatism introduced by the Brewster angle of the rod. The size of the laser mode in the rod is dependent on the separation between the rod and the spherical mirror, while the output mode shape is dependent on the folding angle of the spherical mirror. In the configuration used the separation was 290 mm and the angle 30 degrees. The separation between the folding mirror and the output coupler was approximately 1m. The size of the laser mode, obtained by calculation, is shown on the dotted line in figure 3, demonstrating good overlap with the pumping mode.

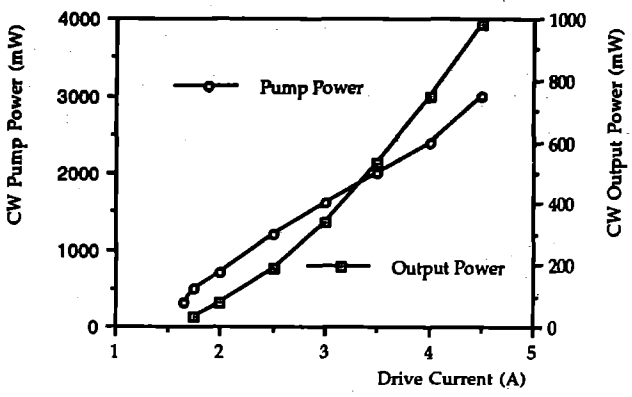

Figure 5 Average Power Output of the Diode Pump and the Main Cavity

Typical output power characteristics are shown in figure 5, for a cavity with a 90% R output coupler. The maximum output power was 1W when the pumping power was 3W, corresponding to an optical efficiency of 33% and a slope efficiency of 57%. This is the highest output power from a single diode end pumped Neodymium doped laser. The lasing threshold was approximately 400 mW.

The spatial mode of the beam is shown in figure 6. A TEM_{00} mode structure is maintained from just above threshold to full output power. This is important when the laser is coupled to a single mode fibre for mode-locking.

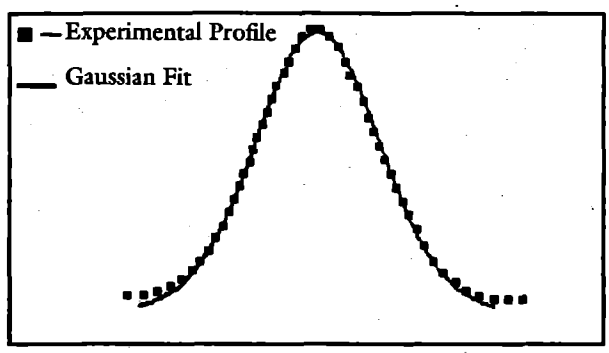

Figure 6 Spatial Mode of Oscillator Output

CONCLUSION

An efficient diode pumped Nd:YLF laser has been developed which generates 1 W in a single spatial output at 1053nm with a high optical and slope efficiency.

ACKNOWLEDGEMENTS

The authors acknowledge the valuable assistance of the Optoelectronics Research Centre at Southampton University during the course of this work, in particular that of Dr John Barr and Matthew McCarthty.

REFERENCES

1. Z Chang et al. CLF Annual Report 1992.
2. M Thomas et al;
IEEE J of QE Vol QE18 No 2 Feb 1982 p159

AN APM Nd:YLF OSCILLATOR WITH MICHELSON CONFIGURATION OPERATING AT 1053 nm

Z Chang[1], M R G Miller[2], C N Danson[2] and C B Edwards[2]

[1]Royal Society Visiting Fellow, Xian Inst. of Optics and Precision Mechanics, People's Republic of China
[2]Central Laser Facility, Rutherford Appleton Laboratory, Chilton, Didcot, OXON OX11 0QX

INTRODUCTION

A new Additive Pulse Mode-locked (APM) oscillator based on a Michelson configuration[1], has been developed for CPA experiments on VULCAN. We have demonstrated shorter pulse durations, improved stability, and higher powers than the Fabry-Perot based oscillator used in the previous CPA experiment[2] during December 1991.

CONFIGURATION AND PERFORMANCE

A schematic of the oscillator is shown in Figure 1. The oscillator comprised of two coupled cavities, corresponding to the two arms of a Michelson interferometer. A 1 m length of optical fibre was inserted into the nonlinear cavity to generate chirp on the pulse, and the linear cavity could be left empty, or could contain a pair of Brewster-angled SF10 prisms. The prisms have a negative group velocity dispersion to compensate for the positive dispersion of the chirped pulse from the nonlinear cavity. The nonlinear cavity length was an integral multiple of the length of the linear cavity. When the two pulses from the two cavities interfere at the beamsplitter, the pulse duration is progressively reduced. This is due to phase differences between the leading and trailing edges which when summed, reduce their intensity. This APM process is very similar to that operating in a Fabry-Perot configuration.

The gain medium chosen was Nd:YLF, pumped by a 3 W GaAlAs diode laser at 798 nm, (described in detail elsewhere[3]). The oscillator has important advantages over the Fabry-Perot configuration in that : the fibre coupling optics do not need to move when changing the prism configuration; and higher output powers can be generated because all the output from the laser is used.

The reflectivity of the beamsplitter was 90%, a compromise between high output power and low modelocking threshold. The output power and pulse duration from the oscillator is shown in Figure 2. This was measured with a 1 meter fibre in the nonlinear cavity but without a prism pair in the linear cavity. The maximum stable modelocked output was 440 mW, and the shortest pulse duration was 1.68 ps (for a $sech^2$ pulse shape). It was found that the pulse duration changed with the pumping power and there was always an optimum pumping power to get the shortest pulse. For a fixed pumping power, the pulse duration changes with the phase of the pulse from the nonlinear cavity. This was adjusted by changing the offset of the feedback electronics to change the position of the mirror on the piezoelectric transducer (PZT).

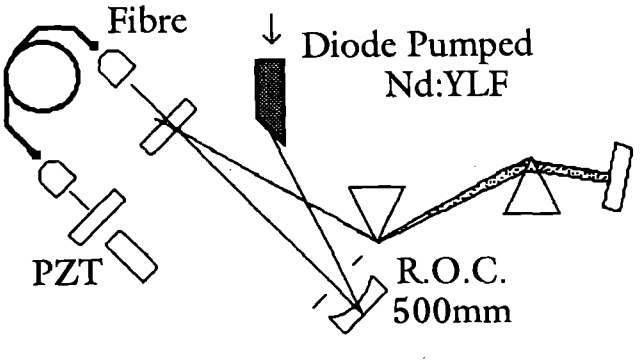

Figure 1 Schematic of the APM oscillator based on the Michelson configuration

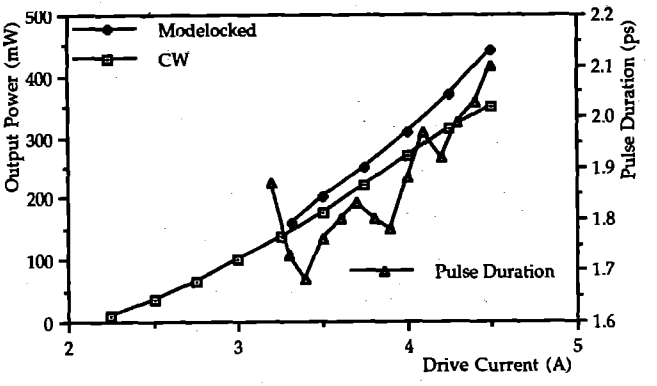

Figure 2. Output Characteristics of the Michelson APM Oscillator

The output power also changed with the phase, with the highest peak power corresponding to the shortest pulse duration for a given pumping power. This did not correspond to the highest average power of the pulse train, which was monitored by a fast PIN diode. The shortest pulse duration which could be produced ranges from 1.68 ps - 1.9 ps for a given length of fibre. The pulse width was very sensitive to the fibre coupling efficiency, but insensitive to the absolute fibre length so long as it introduces sufficient self-phase modulation to the pulse.

Investigations have commenced using prism pairs in the Michelson cavity. A significant reduction in pulse length is anticipated using Nd:glass, which has a substantially broader bandwidth than Nd:YLF.

With the Michelson cavity configuration, output pulse stability was maintained throughout the entire pumping range. As a measure of this stability, the oscillator remained modelocked for tens of seconds even after the electronic feedback to the PZT was switched off.

CONCLUSION

A Nd:YLF APM oscillator, operating at 1053 nm, has been developed using a Michelson cavity configuration. This oscillator was found to be simple to operate, produced shorter (1.7 ps), more stable pulses and had a higher output (440 mW, 3.2 nJ) than the Fabry-Perot design used in previous experiments.

REFERENCES

1. RS Grant and W Sibbet;
Opts Comm, Vol 86, No 2, 177 (1991)
2. Z Chang et al; CLF Annual Report Report 1992
3. Z Chang et al; CLF Annual Report Report 1992

SIMULATION OF AN ADDITIVE PULSE MODELOCKED OSCILLATOR

Z Chang[1], C N Danson[2] and C B Edwards[2]

[1]Royal Society Visiting Fellow, Xian Inst. of Optics and Precision Mechanics, People's Republic of China
[2]Central Laser Facility, Rutherford Appleton Laboratory, Chilton, Didcot, OXON OX11 0QX

INTRODUCTION

Laser oscillators modelocked by coupling an external nonlinear cavity started from the concept of a 'soliton laser'[1], and have become very important as ultra-short pulse generators. Near bandwidth limited pulses have been obtained from various gain media using this additive pulse modelocking (APM)[2] technique, or "coupled cavity modelocking"[3]. The published APM theory explains the pulse shortening process qualitatively, but it cannot predict the pulse duration. In this report, we describe a computer simulation method based on the time-domain matrix formalism[4], which shows the quantitative evolution of pulse formation. Using this simulation it is now possible to design and optimise oscillator performance.

TIME-DOMAIN MATRIX FORMALISM

In the slow varying envelope and parabolic approximation[5], the electric field, E (η,z), in the cavity is given by:

$$E(\eta,z) = \Re \{ A(z) \exp[\frac{i\eta^2}{P(z)}] \exp[i(\omega t - kz)] \} \qquad [1]$$

Where:

E is the electric field; $\Re$ is the real part; A is amplitude;
k is the wave vector amplitude; z is the space coordinate;
ω is frequency; t is time;
η is a local temporal coordinate ($\eta = t - \frac{z}{v_g}$);
v_g is the group velocity;
and P is a complex parameter defined by,

$$\frac{1}{P} = \beta + \frac{i}{\tau^2} \qquad [2]$$

where τ is the pulse duration. The real part of [2] gives the chirp (β) and the imaginary part is equal to the inverse square of the pulse duration (τ). Various transformations on the laser field can be performed to model propagation through dispersive elements, nonlinear (Kerr) elements and amplification by bandwidth limited media, etc. Each can be represented as a transformation of the complex parameter P, of the form

$$\frac{1}{P'} = \frac{\frac{D}{P} + C}{\frac{B}{P} + A} \quad <------> \quad \begin{bmatrix} AB \\ CD \end{bmatrix} \qquad [3]$$

where the coeffiecients for this transform A,B,C, & D, can be found in reference 4. For the pulse chirping in the fibre, a more accurate formula was derived than that used in reference 4. The pulse is chirped by the nonlinear refractive index of the fibre.

Since $n = n_o + n_2 I$

then $kz = k_o n z = k_o n_o z + k_o n_2 I z$

and for a Gaussian pulse $I = I_o \exp[-2 \frac{t^2}{\tau^2}]$,

$$k_o n_2 I z = k_o n_2 I_o z \exp[-2 \frac{t^2}{\tau^2}]$$

$$\approx k_o n_2 I_o z (1 - 2\alpha \frac{t^2}{\tau^2})$$

where α is an adjustable parameter. When $t << \tau$, $\alpha = 1$ is the result of ref 4. This is not a good approximation. To find a reasonable value of α it is better to use the least squares method. That is, from

$$f(\alpha) = \int_0^{\tau/\sqrt{2}} [1 - 2\alpha \frac{t^2}{\tau^2} - \exp(-2\frac{t^2}{\tau^2})]^2 dt$$

$$\frac{df}{d\alpha} = 0$$

we get $\alpha = 0.7193$.

Hence in [1], the phase produced by spatial motion becomes:

$$\exp[-ikz] = \exp[-ik_o n_o z] \exp[-ik_o n_2 I_o z] \exp[i2\alpha \frac{k_o I_o z n_2 t^2}{\tau^2}]$$

ie. the chirp introduced by the fibre is

$$\beta = \frac{2\alpha k_o I_o z n_2}{\tau^2}$$

The phase shift introduced by n_2, ($\varphi = k_o n_2 I_o z$) cannot be neglected to simulate the APM oscillator.

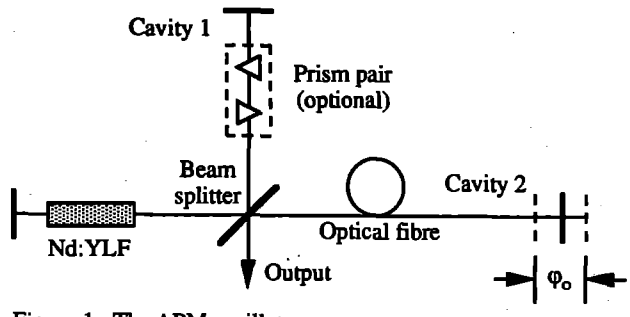

Figure 1. The APM oscillator

CHIRPED PULSE ADDITION

To apply the time-domain matrix formalism on the APM oscillator, we have to find out the parameter P and the amplitude for the pulse after the addition (interference). The oscillator considered is shown in figure 1, which is a Michelson for simplicity. At the beamsplitter, the pulses before and after addition can be expressed in the following way:

$$\begin{cases} E_1(\eta) = \{A_1 \exp[\frac{i\eta^2}{P_1}] \exp[i\varphi_1] \exp[i\omega\eta]\} \\ E_2(\eta) = \{A_2 \exp[\frac{i\eta^2}{P_2}] \exp[i\varphi_2] \exp[i\omega\eta]\} \\ E_a(\eta) = \{A_a \exp[\frac{i\eta^2}{P_a}] \exp[i\varphi_a] \exp[i\omega\eta]\} \end{cases} \qquad [4]$$

Where

A_1, φ_1, A_2, φ_2,

and $\frac{1}{P_1} = \beta_1 + \frac{i}{\tau_1^2}$; $\frac{1}{P_2} = \beta_2 + \frac{i}{\tau_2^2}$ are known

and P_a is defined as $\frac{1}{P_a} = \beta_a + \frac{i}{\tau_a^2}$

$E_a (A_a, P_a, \varphi_a)$ describes the pulse after addition.

Since $E_a(\eta) = E_1(\eta) + E_2(\eta)$ [5]

that is,

$$A_a \exp[\frac{i\eta^2}{P_a}] \exp[i\varphi_a] = A_1 \exp[\frac{i\eta^2}{P_1}] \exp[i\varphi_1] + A_2 \exp[\frac{i\eta^2}{P_2}] \exp[i\varphi_2] \qquad [6]$$

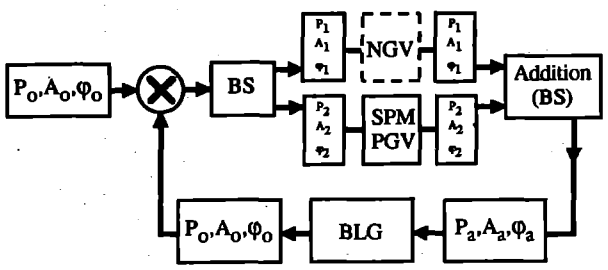

Figure 2. The APM oscillator feedback loop

by separating the real and imaginary parts of [6], we get

$$\varphi_a = \arctan\left(\frac{A_1\sin\varphi_1+A_2\sin\varphi_2}{A_1\cos\varphi_1+A_2\cos\varphi_2}\right) \quad [7]$$

$$A_a = \frac{1}{\cos\varphi}(A_1\cos\varphi_1 + A_2\cos\varphi_2) \quad [8]$$

$$\tan(\beta_a\eta^2+\varphi_a) = \frac{[A_1\exp[-\frac{\eta^2}{\tau_1^2}]\sin(\beta_1\eta^2+\varphi_1)+A_2\exp[\frac{\eta^2}{\tau_2^2}]\sin(\beta_2\eta^2+\varphi_2)]}{[A_1\exp[-\frac{\eta^2}{\tau_1^2}]\cos(\beta_1\eta^2+\varphi_1)+A_2\exp[-\frac{\eta^2}{\tau_2^2}]\cos(\beta_2\eta^2+\varphi_2)]} \quad [9]$$

$$A_a\exp[-\frac{\eta^2}{\tau_a^2}]\cos(\beta_a\tau^2+\varphi) = A_1\exp[-\frac{\eta^2}{\tau_1^2}]\cos(\beta_1\eta^2+\varphi_1)+A_2\exp[-\frac{\eta^2}{\tau_2^2}]\cos(\beta_2\eta^2+\varphi_2) \quad [10]$$

The β_a in [9] and τ_a in [10] can be calculated by parametric least squares fitting. By substituting the results of [7] - [10] in the last expression in [4] we get the pulse after addition represented by a Gaussian pulse.

MODELOCKING SIMULATION

When a noise pulse is generated (which can be produced by mode-beating in a real cavity), the evolution of the pulse can be simulated by the equations given above. It is important to take the phase of the pulse into account when the transformation is applied to the pulse, especially the phase shift by the Kerr effect in the optical fibre. The simulation iteration, which corresponds to the round trip in the oscillator is shown in figure 1. We have used this method to simulate a APM Nd:YLF oscillator with Michelson configuration as shown in figure 1. A typical pulse evolution in the cavity is shown in figure 3. From the simulation we find :

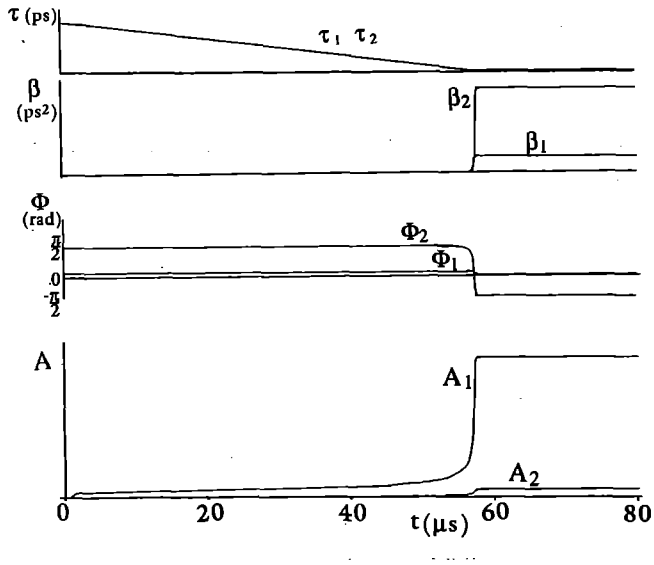

Figure 3. Simulation of the modelocking process in a APM Nd:YLF laser.

a) Modelocking can only take place when the phase offset φ_o is in the range $\varphi_1 < \varphi_o < \varphi_2$, φ_1 and φ_2 are related to g_o the small signal gain and also to the cavity parameters, which have been described by the earlier APM theory[1].
b) Modelocking can only take place when g_o is large enough for a given set of cavity parameters which represent the modelocking threshold.
c) The pulse duration is related to the phase offset for a given g_o, as shown in figure 4, which was discovered experimentally[6].

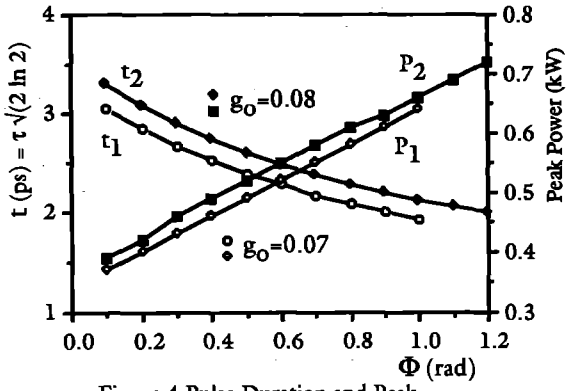

Figure 4 Pulse Duration and Peak Power vs Phase Offset

d) The pulse duration is related to the g_o when φ_o is fixed. The greater the value of g_o the longer the pulse, this relationship was also discovered experimentally
e) The pulse duration is always longer than the bandwidth limit of the gain medium. For Nd:YLF, the theoretical pulse duration is typically ~2 ps (see figure 3), which fits the experimental results, although the bandwidth limit is 1.3 ps.
f) Group velocity dispersion compensation, in the cavity, by using a pair of SF10 prisms shows the pulse duration can only be reduced by about 0.1 ps. This also fits the experimental results.

Oscillators with other gain media, fibre length, cavity parameter, or cavity configuration can be simulated. This is very interesting from both physical understanding and practical designing points of view. On a 486 based PC it takes only about 10 minutes to simulate a given cavity. This makes the cavity optimisation practically possible and shows the advantage of the matrix method.

CONCLUSION

An APM oscillator was simulated with parabolic and Gaussian approximations. The results obtained can well explain the most important experimental features of an APM oscillator. This package can also be used to design new laser configurations.

REFERENCES

1. LF Mollenauer & RH Stolen; Opt Lett 9, 13-15 (1984)
2. EP Ippen, HA Hans & LY Liu; J Opt Soc Am B Vol 6 No 9 1736 (1989).
3. X Zhu, PN Kean and W Sibbett; IEEE J QE, QE-25, 2445 (1989)
4. A Caprara; SPIE Vol 1229, 48 (1990)
5. SA Akhmanov et al; Soviet Physics JETP, Vol 28, 748 (1969)
6. Z Chang et al; CLF Annual Report 1992.

AUTO-CORRELATOR DEVELOPMENT FOR THE CPA PROGRAMME ON VULCAN

Z Chang[1], C N Danson[2], M D Dooley[2], C B Edwards[2], M H R Hutchinson[3], S Luan[3], I P Mercer[3], M R G Miller[2], Z Najmudin[3], C E Ollman[2], D A Pepler[2], R A Smith[3], P F Taday[2], W T Toner[2] and T B Winstone[2]

[1]Royal Society Visiting Fellow, Xian Inst. of Optics and Precision Mechanics, People's Republic of China
[2]Central Laser Facility, Rutherford Appleton Laboratory, Chilton, Didcot, OXON OX11 0QX
[3]Blackett Laboratory, Imperial College, Prince Consort Road, London, SW7 2BZ

INTRODUCTION

During 1991 a comprehensive suite of diagnostics was developed and commissioned for the CPA experiment[1] on VULCAN. This report describes the development of two auto-correlators used to measure the ultra-short pulse oscillator and the recompressed amplified system output.

SCANNING AUTO-CORRELATOR

A scanning auto-correlator[2] was used to measure the pulse-length of the CW mode-locked 139 MHz ultra-short pulse oscillator. A schematic of the auto-correlator is shown in figure 1. The correlator construction used a double arm delay line with the polarisation in one arm being rotated by 90°, produced by a double-pass through a quarter-wave plate. This enabled the two beams to be recombined and focused into a type II non-colinear KTP crystal. This produced a background free second harmonic ($2\omega_0$) signal. The correlator operated with approximately 6 pJ per pulse, ~1% of the oscillator output. The $2\omega_0$ from the KTP crystal was analysed using a photomultiplier tube, the output of which was displayed on a digital oscilloscope. The photomultiplier was operated at low level (~350V), virtually eliminating thermal noise.

Both arms of the correlator incorporated corner-cube reflectors used "off-axis" to eliminate back reflections, which could interact with the oscillator. One of the corner-cubes was mounted on a mechanical shaker and driven by a triangular wave generator operating at 20 Hz. Two auto-correlations were detected within each cycle.

The device was calibrated by adjusting the position of the shaker on its translation stage. The delay of each half-cycle of the triangular wave gives a 30 ps double pass delay window within which the pulse-length could be measured. The temporal resolution of this instrument was ~0.1 ps, limited by the digitising resolution of the oscilloscope. The pulse-length was measured from the auto-correlation trace of the two recombined pulses, as the full width half maximum (FWHM), calculated assuming a sech^2 intensity profile.

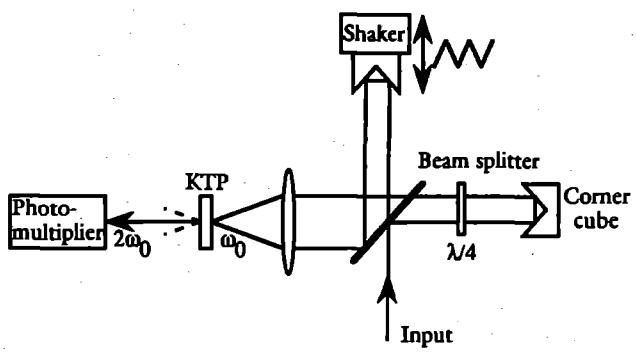

Figure 1. Scanning auto-correlator.

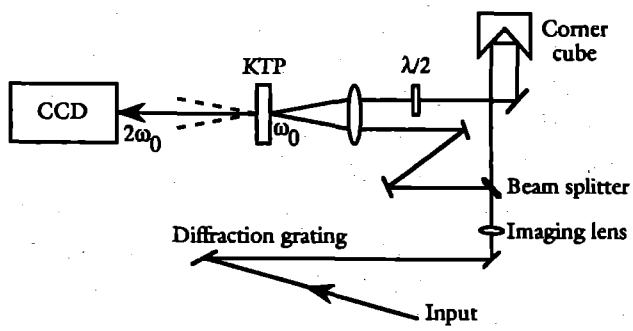

Figure 2. Single shot auto-correlator.

SINGLE-SHOT AUTO-CORRELATOR

A single-shot auto-correlator was used to measure pulse lengths at the output of the system of CPA laser shots. A schematic of the correlator is shown in figure 2. A diffraction grating[3] was used to introduce a time gradient across the width of the beam, followed by a double arm delay with one arm having the time gradient inverted by means of a corner-cube. Both arms were tuned to have the same optical path length. The grating was imaged onto the crystal by means of a cylindrical lens. Another cylindrical lens, orthoganal to the first was used to focus both beams into the crystal.

In order to generate a background free signal one arm of the auto-correlator had its polarisation rotated by 90° and then the two beams were recombined and focused into a non-colinear type II KTP crystal. The second harmonic signal was monitored using a CCD camera and readout system. The grating spacing and the angle at which the beams recombined through the crystal determined the range of the pulse lengths that could be measured. Using a 5° angular beam separation and a grating with 1200 lines mm^{-1} gave a measurement window of 50 ps, and a temporal resolution of 0.5 ps limited by the pixel size in the CCD camera.

The instrument was calibrated by altering the time delay in one arm of the correlator to produce a known shift on the readout system. As a further check it was cross-calibrated with the scanning auto-correlator. In future experiments this instrument will be used to measure the contrast ratio between the compressed pulse intensity and the pedestal intensity level.

CONCLUSION

Two auto-correlators were developed and commissioned for the CPA experiment on VULCAN in December 1991. They provided reliable pulse-width measurements of both the APM oscillator and the system output.

REFERENCES

1. Z.Chang et al; CLF Annual Report 1992.
2. EP Ippen & CV Shank; App Phys Lett 27, 488 (1975)
3. R Wyatt & EE Marinero; Appl Phys 25, 297-301 (1981)

VULCAN OPERATIONAL STATISTICS

CB Edwards and CN Danson

Rutherford Appleton Laboratory

1991/92 saw a full year of VULCAN operations with 13 full experiments and two experiments part completed by year end. In addition TA4 was used intensively.

Shot statistics for the period are summarised in Table 1. All target areas have been operational with 1442 full disc shots being delivered to scheduled experiments. The shot failure rate continues at a level below 3%.

TA4 continues to be an area which is in constant demand with a total of 1253 shots being delivered to target. It is now used as a routine facility for X-ray microscopy following detailed source characterisation at the beginning of the period. Other experiments included XUV mirror testing and absolute X-ray wavelength spectroscopy. During the year the scheduling of this area has become more formalised to minimise conflict due to the increasing demand for beam time. Bids for the use of TA4 must now be directed through the established high power laser scheduling procedures. However some flexibility will be maintained to cater for the type of experiments this area attracts.

The main facility development during the past year was an intensive programme to develop further short pulse operation of VULCAN using Chirped Pulse Amplification. The experiment, which was highly successful, was carried out in collaboration with Imperial College, London and with technical assistance from Southampton University. The details of this development are summarised in section A6.

Focal spot smoothing continues to be an important area of development. This year has seen the use of circular RPP's for routine operations and significant progress towards large top-hat profiles. These will be introduced during the coming year.

Total number of shots	6215
Total number of disc shots to target areas	1442
Total number of disc shots to TA West	139
Total number of disc shots to TA East	729
Total number of disc shots to TA 2	574
Total number of target shots to TA 4	1253

EXPERIMENTAL PERIOD	EXPERIMENT (No. of disc shots)		
	TA WEST	TA EAST	TA 2
25 March - 5 May	Implosions (57)	XUV Laser (140)	
6 May - 23 June		Self-focussing (107)	Mono-Imaging (171)
24 June - 30 June	AIR	CONDITIONING	MAINTENANCE
1 July - 18 August		Capilliary Plasma (70)	
19 Aug - 6 Oct		XUV Lasers (137)	MP Ionisation (63)
7 Oct - 24 Nov		Radiation Trans. (102)	EOS Meas. (129)
25 Nov - 22 Dec	Short-Pulse	(CPA)	Development
6 Jan - 16 Feb		XUV Laser Imag. (113)	Crystal Plasticity (146)
17 Feb - 22 March	High Res Spect (77)	Thermal Smoothing (60)	

Table 1. VULCAN shot statistics for the year to March 1992

KrF LASER DEVELOPMENT & EXPERIMENTS

M J Shaw

Rutherford Appleton Laboratory

INTRODUCTION

This has been a year of transition for the Sprite KrF laser system from a predominantly R & D role to that of an operational facility. This has been reflected in a divisional reorganisation in which the Sprite system will, from April 92 belong to Operations Division. The further development of KrF, however, continues with the Science Board approval of two joint university projects for the development of the Raman system in conjunction with Imperial College and the provision for femtosecond pulses on Sprite in conjunction with St Andrews University. In addition, an in-house development programme called "Titania" has begun with a view to provide a substantial upgrade to the existing KrF capabilities on a two-to-three year time scale.

TARGET EXPERIMENTS

Recombination X-Ray lasers were the subject of two experimental runs during the year culminating in a very well diagnosed experiment on carbon VI in February. The absorbed irradiance was inferred from measurements of line intensity ratios. The initial results reported here were rather disappointing, with the hoped for improvement in gain due to short wavelength irradiation not being observed.

In the other target experiment, the prepulse-free nature of the Sprite Raman beam was exploited to produce hot plasmas at extremely high density. Temperatures up to 700 eV were recorded at densities of up to 10^{23} cm^{-3}.

LASER DEVELOPMENT

The laser development work reported here splits into two main topics which reflect the joint university projects. A considerable amount of data has been gathered on the Sprite Raman system with a primary view to understanding the determinants of beam quality. The highlights of this work are the revelation that the near field of the beam is strongly dependent on pump beam position and that the highly divergent light which was found to accompany the Raman beam was due to higher order Raman generation both in methane and air.

An experimental run on Sprite demonstrated the possibility of high contrast ratio short pulse amplification. Furthermore, collaboration with the University of Gottingen has shown that chirped pulse amplification is applicable to a saturating gain medium such as KrF which opens up the possibility of femtosecond amplification to Joule level in the Sprite system. The effects of ASE in multi-pass short pulse amplifiers has also been investigated in detail. The collaboration with the University of Loughborough continues to provide us with much useful data on the damage levels and scattering properties of UV coatings.

PULSED POWER DEVELOPMENT

The pulsed power development programme in R7 has made significant progress during the year. Two pulse forming lines have been installed and the operation of the two PFL diaphragm switches has been tested up to full operating voltage. A full suite of diagnostic probes have been developed and tested against one another. The system is now ready to test a single "Oberon" diode.

The instigation of the "Titania" upgrade programme has resulted in a major change in the direction of the pulsed power development programme. The priority is now the construction of the Titania amplifier module which will utilise a major part of the hardware installed for the Oberon diode tests. Some of the key pulsed power components for Titania have already been designed and will be tested in the coming year.

One interesting small off-line investigation has been the pressure cycling of the electron beam window foils as used on the Goblin amplifier. Contrary to expectation, it was found that repeated pressure stress was not the cause of foil failure. Further work needs to be done to understand the mechanism of foil failure.

OPERATIONS

Operationally it has been another record year for Sprite. A total of 2176 system shots were fired. Shot number 12,000 was passed in February. There has been a significant increase in the energy available to target using the Raman beam with an average of 5J in 12 ps pulses being recorded during target experiments towards the end of the year. Measurements of the Raman beam brightness at the target chamber show that peak intensities at the focus of the off-axis parabaloid of well in excess of 10^{18} W cm^{-2} can be achieved.

The Sprite system has also been characterised for amplification of 3 ps KrF pulses. Although the brightness is about an order of magnitude less than the Raman beam, up to 1.8 J was recorded with a contrast ratio between the short pulse and ASE brightness of greater than 10^{7}.

Finally, it is a pleasure to record that the computerised interlock system "Cerberus" is now fully operational maintaining its silent vigil on the safety of the whole of the Sprite system.

X-RAY RECOMBINATION LASER EXPERIMENTS PUMPED WITH 12 PS KrF PUMPED RAMAN PULSES

L Dwivedi[1], Y Kato[2], M H Key[3,4], R Kodama[3], J Krishnan[1], C L S Lewis[5], K Murai[2], P A Norreys[3], G J Pert[6], S A Ramsden[6], H Shiraga[2], C Smith[4], G J Tallents[1], J Uhomoibhi[5], G Yuan[2], and J Zhang[4].

[1]Department of Physics, University of Essex, Colchester, C04 3SQ, UK
[2]Institute of Laser Engineering, Osaka University, Suita, Osaka 565, Japan
[3]Central Laser Facility, SERC, Rutherford Appleton Laboratory, Didcot, OX11 0QX, UK
[4]Clarendon Laboratory, University of Oxford, Oxford, OX1 3PU, UK
[5]Department of Pure and Applied Physics, Queen's University Belfast, Belfast, BT7 1NN
[6]Department of Computational Physics, University of York, York, Y01 5DD, UK

INTRODUCTION

KrF pumped Raman lasers are well-suited as recombination X-ray laser drivers because the combination of short wavelength (268 nm) with low beam divergence and high beam intensity allows very high focussed intensities to be produced in very narrow line foci. In previous work, an ~8μm wide line focus has been produced and narrow line plasmas formed from slab targets containing a buried layer of NaF overcoated by CH. Lateral transport from the line focus was found to be small[1,2]. Mylar coated fibre targets were also irradiated with line foci of 3mm length and tentative measurements of CVI and OVIII Balmer alpha gain have been made[3].

Computer modelling using the MEDUSA one-dimensional hydrodynamic code has predicted high gains (up to 60 cm^{-1}) on the CVI Balmer alpha line at 182 Å from 8μm diameter carbon fibre targets irradiated by focussed pulses of 12 ps duration, intensity $\simeq 3 \times 10^{14}$ Wcm^{-2} at 0.268 μm wavelength. Experiments with these irradiation conditions have been undertaken using the KrF pumped Raman laser SPRITE which produces 12 ps, pre-pulse free pulses with a brightness of $2 \times 10^{19} Wcm^{-2} sr^{-1}$. We report here preliminary results of a carefully diagnosed UK-Osaka University experimental programme undertaken to measure X-ray gain by recording the carbon Balmer alpha intensity emitted along the fibre axis for fibre lengths in the range 2-7 mm.

EXPERIMENT

The KrF pumped Raman laser generated 12 ps pulses of typically 5 Joules with a 20 μradian divergence for this experiment. A line focus was produced using reflective optics to minimise transmission losses due to two photon absorption as outlined by Ross[4]. A tilted off-axis paraboloid reflector produced a spot focus and the laser pulse after passing through the spot was focussed to a $\simeq$ 7mm x 8μm line by a tilted off-axis spherical reflector. A CaF_2 window to the target chamber was employed. This window transmitted 70% of the laser energy. Intensities $\simeq$ $3 \times 10^{14} Wcm^{-2}$ were produced along the line focus.

A flat-field grating spectrometer and streak camera were used to record the Balmer alpha intensity emitted along the irradiated carbon fibre lengths. The pointing of the carbon fibre targets was aligned to an accuracy better than ±1 mrad relative to the spectrometer axis and the positioning of the targets and focal line to better than ±2 μm using a split field microscope system[5]. To increase the X-ray flux into the spectrometer, a toroidally shaped grazing incidence mirror was used to image the fibre end onto the entrance slit of the spectrometer. With this arrangement, the angular detection range from the fibre ends was ~ ±1 mrad. Separate measurements have been made at angles directly in line with the fibre and at 4 mrad to the fibre axis (in the horizontal plane towards the irradiating laser).

Ionisation balance and X-ray emission along the fibre length were monitored with a flat field grating spectrometer recording the CVI and CV resonance spectra and with a filtered X-ray slit camera. Only shots with good uniformity (<30% variation) and ionisation balance in the correct computed regime[6] for gain were considered in the deduction of gain.

RESULTS

Laser shots for different target lengths with very similar laser energies, uniform X-ray emission along the plasmas lines and with the theoretically optimal CV to CVI resonance line ratios were selected to deduce the CVI Balmer alpha gain (Figure 1). The gain increases with time, peaking at about 200 ps after the laser pulse and then decreases (Figure 2). Similar behaviour is seen for observations at both 0 and 4 mrad to the fibre axis.

The magnitude of the observed gains are much smaller than the theoretically calculated values, but are broadly in agreement with our previous measurements[3] with carbon fibre targets of up to 3mm length. The reasons for the discrepancies with the code predictions are not yet clear. The gain length products of peak value $\simeq$3 are also too low to unequivocally demonstrate the presence of gain or to use the laser emission for applications. However, longer lengths should enable gain x length products of, say, 10 for 2 cm irradiation, which should be possible with the SPRITE laser in the near future. Further analysis of this recently obtained data is in progress.

Figure 1 Intensity of CVI Balmer alpha emitted axially as a function of target length at different times. Deduced gains are shown.

(a)

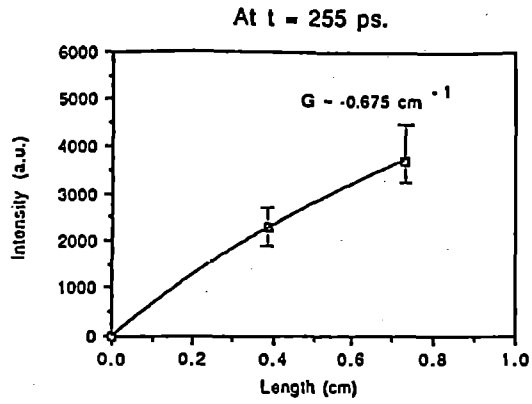

(b)

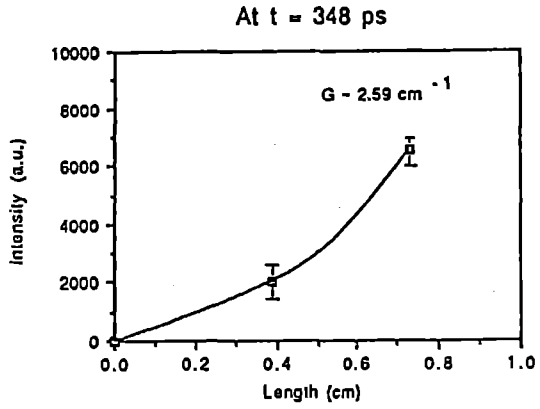

(c)

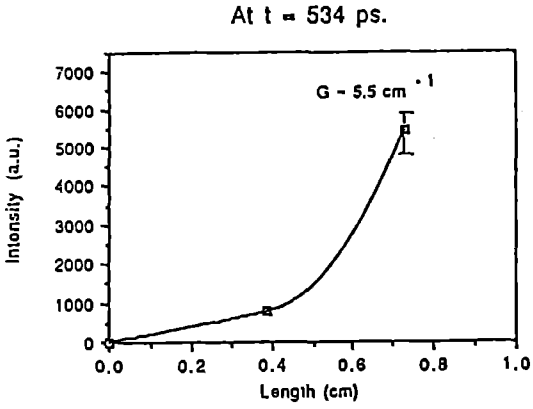

Figure 2 Time variation of deduced gains.

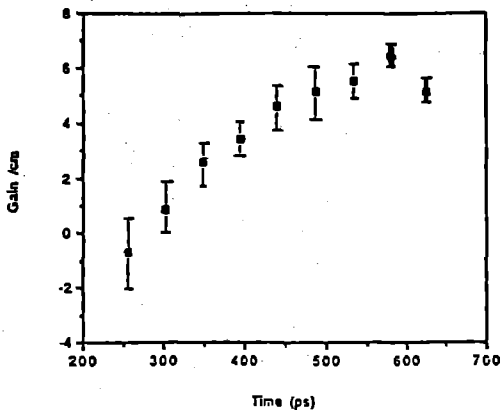

REFERENCES

1. G J Tallents, M H Key, P Norreys, J Jacoby, R Kodama, N Tragin, H Baldis, J Dunn and D Brown, Proc SPIE 1413, 70 (1991).

2. G J Tallents, M H Key, P Norreys, J Jacoby, R Kodama, N Tragin, H Baldis, J Dunn and D Brown, Ann Rep Fac Comm (RAL-91-025) P104 (1991).

3. P Norreys, A Carillon, H Z Chen, L Dwivedi, J Jacoby, M H Key, R Kodama, J Krishnan, C L S Lewis, G J Pert, I N Ross, G J Tallents, J Uhomoibhi and J Zhang, ECLIM Conference, Warsaw (to be published) (1991).

4. I N Ross, Ann Rep Fac Comm (RAL-91-025) P106 (1991).

5. I N Ross, O Willi, G P Kiehn, R Corbett, C L S Lewis, L D Shorrock, M H Key and C J Hooker, Appl Optics 26, 1584 (1987).

6. J Zhang, M H Key, P Norreys and G J Tallents, 3rd International Colloquium on X-ray Lasers, Schliersee (to be published) (1992).

EXPERIMENTAL STUDIES OF LINE INTENSITY RATIO AS A DIAGNOSTIC OF RECOMBINING PLASMAS

J Zhang[1], L Dwivedi[2], Y Kato[3], M H Key[1,4], R Kodama[4],
J Krishnan[2], C L S Lewis[5], K Murai[3], P Norreys[4], G J Pert[6],
S A Ramsden[6], H Shiraga[3], C Smith[1], G J Tallents[2], J Uhomoibhi[5], G Yuan[3]

[1]Clarendon Laboratory, University of Oxford, Oxford, OX1 3PU, UK
[2]Department of Physics, University of Essex, Colchester, CO4 3SQ, UK
[3]Institute of Laser Engineering, Osaka University, Suita, Osaka 565, Japan
[4]Rutherford Appleton Laboratory, Chilton, Didcot, Oxon OX11 0QX, UK
[5]Department of Physics, Queen's University of Belfast, Belfast BT7 1NN, UK
[6]Department of Computational Physics, University of York, York Y01 5DD, UK

1. INTRODUCTION

Measurement of the line intensity ratio of Ly β to He β is an effective diagnostic method for infering absorbed irradiance in plasmas and for monitoring the production of the plasma which could give maximum soft x-ray laser gain during adiabatic expansion [1]. Simulation studies have shown correspondences between the ratio, which is determined by the absorbed irradiance from the driving laser, and gain on the Balmer α transition in expanding adiabatically cooling plasmas [2]. It is of great interest to investigate experimentlly this method of monitoring initial conditions optimized for laser action in recombining plasmas.

2. EXPERIMENT

The 12 ps - 268 nm SPRITE laser pulse with up to 6 J was focussed onto 7 μm diameter carbon fibre targets. With the low laser beam divergence and use of CaF_2 window, the intensity on target could vary between 1.0×10^{14} W/cm^2 and 2.0×10^{15} W/cm^2 for line focus length in the range of 4 - 7 mm. A grazing incidence spectrometer, incorporating an aperiodic (2400 grooves/mm average) flat field grating of 5 m radius curvature, viewed the plasma in a transverse direction to record the spectrum in the range of 20 $\AA$ - 100 $\AA$. In order to get spatially resolved and integrated spectra simultaneously, a special type of slit was used. One part was horizontal with width of 100 μm to provide a spatially integrated spectrum. The other part was vertical with a width of 200 μm to spatially resolve the spectrum. The two parts of the slit were separated by 2 mm to avoid overlap of the spectra. The magnification of the experimental configuration was 2.8 and the spatial resolution was about 300 μm. The spectra were recorded either by 10107 film or with a streak camera to give respectively time integrated or temporal resolved information. A timing slit of 500 μm determined the minimum temporal resolution of about 200 ps when using a streak speed of 262 ps/mm.

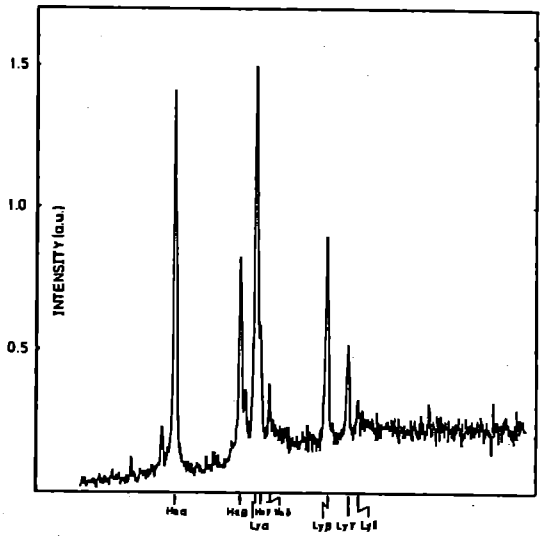

Figure 1: *Integrated soft x-ray spectrum of C fibre plasma (shot 11887)*

3. RESULTS AND DISCUSSION

An example of a spatially integrated spectrum is shown in Fig. 1. Almost all of the strong resonance emission lines and satellite lines of hydrogenic-like and helium-like ions appear in the spectrum. In-

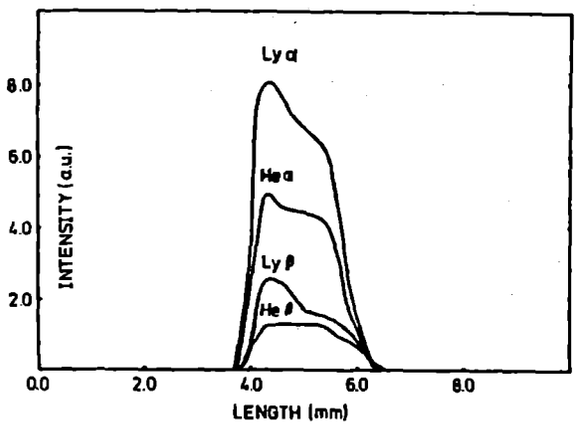

Figure 2: *Variation of resonace line emissions of shot 12013 along the C fibre plasma.*

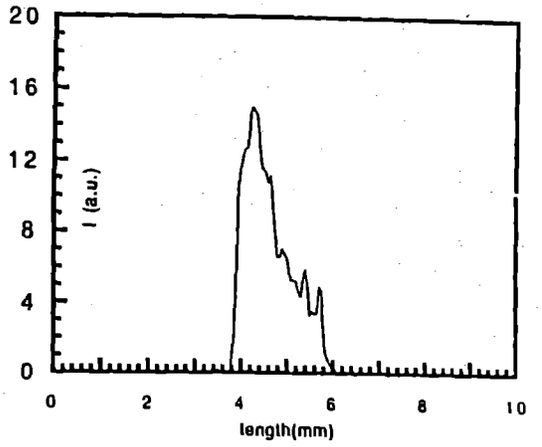

Figure 3: *Spatial resolved x-ray image of C fibre plasma (Shot 12013) by a slit camera.*

formation about the absorbed irradiance, ionisation stage and laser gain could be inferred for shots with good uniformity. Unfortunately, the problem of nonuniformity along the fibre plasma was rather serious, which made it difficult to interpret the spectrum, because the radiation from high emission regions tends to dominate the spectrum. The spatial resolved measurements avoided this problem.

Table 1.*Spatial resolved C VI Lyβ to C V $1s^2$ - 1s3p line ratio and relevant absorbed irradiance along the fibre plasma deduced from model calculations* [2]

Pos.(mm)	Line Ratio	Abs. Irrad.(W/cm^2)
4.00	1.25	1.8×10^{13}
4.33	2.03	7.0×10^{13}
4.66	1.82	5.6×10^{13}
5.00	1.30	2.0×10^{13}
5.33	1.22	1.5×10^{13}
5.66	1.35	2.2×10^{13}
6.00	1.39	2.4×10^{13}

A typical result of such measurements is shown in Fig. 2. The general behavior agrees with that obtained by a slit camera (Fig. 3). A slit camera are often used for monitoring uniformity of the plasma. However, only spectrally integrated data can be recorded and consequently, it is not possible to monitor the variation of a specific ionization stage. The spatially resolved spectrum provides much more information. It is possible to quantitatively measure effects due to the nonuniformity along the plasma and to estimate the absorbed irradiances locally by comparing the experimental ratios of the resonance line intensities with the simulation results [2]. Table 1 shows measured C VI Lyman β to C V $1s^2$ - 1s3p line ratios and the deduced absorbed irradiance along a fibre plasma. The line ratio from the corresponding spatially integrated spectrum is 1.74, giving a spatially integrated absorbed irradiance of 5×10^{13} W/cm^2 which is much higher than the real average along the plasma length. The integrated absorbed irradiance deviates significantly from the real experimental values due to the nonuniformity of the plasma. This is critical for laser gain. Moreover, for the shot 12013, the lower emission part of the plasma faced toward the axial spectrometer, which used to measure laser gain [3]. This configuration could destroy the laser gain produced by the higher emission plasma before it reached the axial spectrometer. In order to get high recombination gain performance, the formation of a colder plasma, specially in the axial spectrometer side, must be avoided.

According to our previous study [2], resonance line emission from the $n \geq 3$ of the helium-like ion is proportional to the population density of the ground state of the H-like ion. Similarly, the intensity of the hydrogenic resonance line is proportional to the concentration of bare nuclei. It can be seen from comparison between Fig. 2 and Fig. 3 that the concentration of the bare nuclei is much more sensitive to the variation of the absorbed irradiance along the target than that of hydrogenic ions, while the intensity of He β line emission remains almost constant for the variation of the absorbed irradiance above a certain threshold. It is for this reason that the ratio of the line intensities of Ly β to He β effectively reflects variation of the absorbed irradiance, which is of great importance for generation of laser gain in the plasma. Thus

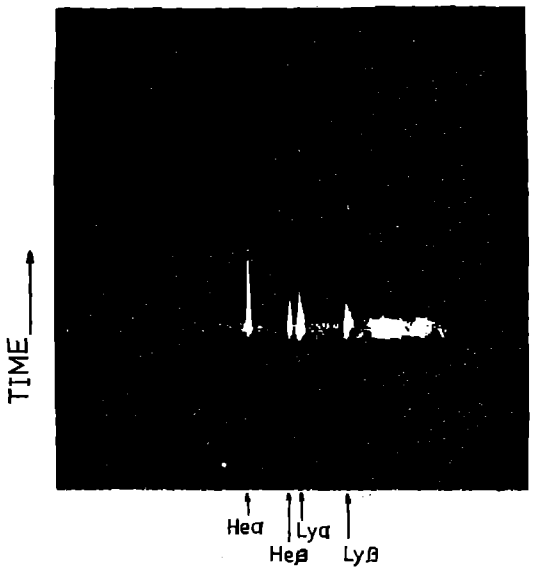

Figure 4: *Time resolved soft x-ray spectrum of C fibre plasma.*

it is another advantage to use space-resolved soft x-ray spectroscopy as a monitor to quantify the deviation of the absorbed irradiance along the line focus from the optimum condition for high recombination gain.

The spacially resolved line ratio measurement can be used as an effective diagnostic for inferring the absorbed irradiance along the fibre plasma and for monitoring the production of the plasma with good uniformity which should give maximum laser gain during adiabatic expansion. The observed signal in Fig. 2 is the convolution of the real signal with a wide (200 μm) slit. This explains why the shape of the curve is blurred and the edge of the emission is not so steep as with the slit camera (Fig. 3).

Fig. 4 shows a streaked soft x-ray spectrum from the C fibre plasma. The spectrum indicates the temporal characteristic of H-like C^{+5} resonance lines (Ly α, Ly β), He-like C^{+4} resonance lines (He α, He β) and continuum. The continuum decays rapidly in less than the 200 ps resolution, while the He α line radiation persists for 500 ps. The duration of the other line emissions are about 300 ps. The intensities of line emissions from the Lyman series are stronger than those from corresponding helium like series lines. That give us a rough estimation of the temporal development of the plasma expansion. The time scales agree with the prediction of the simulation [2]. This work is still in progress and more detailed analysis will be possible.

4. CONCLUSION

In conclusion, a double slit has been incorporated in a flat field spectrometer to record spatially resolved and integrated spectra simultaneously. Variation of the absorbed irradiance and ionisation stage along the fibre plasma has been monitored with this instrument. By comparison of the spatially resolved and integrated resonance line ratios, it is found that the spatially integrated value deviates significantly from the real experimental circumstance due to nonuniformity along the plasma. Spatially resolved measurements of line intensity ratios of H-like to He-like resonance emission are an effective diagnostic for infering the absorbed irradiance in the plasma and for monitoring the production of the plasma suitable for laser action during adiabatic expansion.

ACKNOWLEDGEMENTS

We are grateful to the SPRITE laser operations team and the target preparation group of the SERC Central Laser Facility for their effective cooperation.

References

[1] M H Key, N Tragin, S J Rose, 2nd International Colloquium on X-ray Lasers, *X-Ray Lasers 1990*, G Tallents Ed., IOP Publisher, Bristol (1991) 163.

[2] J Zhang, M H Key, P Norreys, G J Tallents, RAL Annual Report (1992).

[3] L Dwivedi, Y Kato, M H Key, R Kodama, J Krishnan, C L S Lewis, K Murai, P A Norreys, G J Pert, S A Ramsden, H Shiraga, C Smith, G J Tallents, J Uhomoibhi, G Yuan, J Zhang, RAL Annual Report (1992).

PLASMA CONDITIONS GENERATED BY INTERACTION OF A HIGH BRIGHTNESS, PRE-PULSE FREE RAMAN AMPLIFIED KrF LASER PULSE WITH SOLID TARGETS

D. RILEY, L.A. GIZZI, F.Y. KHATTAK, S.M. VIANA and O. WILLI

The Blackett Laboratory, Imperial College of Science, Technology and Medicine, Prince Consort Road, London SW7 2BZ

Interest in the production of dense, hot plasmas by irradiation of solids with short pulse high power lasers is motivated by the applications to X-ray laser research where rapid heating at high density is required. Several workers have already published experiments in which spectroscopy is used to diagnose dense plasmas created by irradiation of solid targets with laser pulses of sub-picosecond to a few tens of picoseconds duration [1-5].

We have carried out an experiment in which the interaction of the 12ps Raman amplified SPRITE pulse was interacted with solid targets. The Amplified spontaneous emission (ASE) pre-pulse level was not detectable at the threshold of measurement, implying that it is $<10^{-10}$ of the power and 10^{-8} of the energy in the main pulse. For the irradiances of up to 10^{17} W/cm^2 used, no pre-formed plasma should be present during the pulse interaction. The laser was directed onto planar (25μm thick) aluminium foils by an off axis paraboloid, with f/4 effective focussing of about 4J on target.

The main diagnostic of the plasma conditions was a time resolving X-ray spectrometer which consisted of a Tlap crystal coupled to a streak camera which was fitted with a KBr photocathode and viewed the plasma at an angle of approximately 35 degrees to the normal. The temporal and spectral resolutions achieved were approximately 10ps and 350 respectively. Using this instrument, the aluminium K-shell emission between 6 and 7 Angstroms was recorded on film.

For the streak data, the focal spot was monitored via the X-ray emission with a time integrating pinhole camera which was fitted with four separately filtered pinholes of 10μm diameter and had a x15 magnification. The pinhole used to define irradiance was filtered with 25μm Be + 3μm Al, and had greater than 1/e transmission for photon energies above 2.5keV, and so was mainly sensitive to the bremsstrahlung and radiative recombination X-rays generated during the laser pulse. Approximately 90% of the X-ray emission was contained within the FWHM intensity, which was similar to the nominal focal spot set by focussing onto a wire of known thickness. The X-ray emission in several energy bands was monitored with *p-i-n* diodes and the velocity of the ions in the blow-off plasma was monitored with ion cups.

The absorption of the laser pulse was measured as a function of incident angle and intensity by monitoring the energy on target and measuring the scattered light via an Ulbricht sphere and a calibrated diode on a backscatter collection channel. A detailed description of the data collected on the interaction and absorption of the beam with solid targets will be presented at a later date. In this report we concentrate on the plasma conditions generated with this pre-pulse free high brightness laser at normal incidence and irradiances of a few times 10^{15} Wcm^{-2}.

Figure 1 shows a graph of the reflected light versus irradiance for normal incidence on aluminium foils. In the absorption data, the focal spot was defined by moving the target a fixed distance from the smallest focus as observed on a T.V alignment system which viewed the target through a small hole in the Ulbricht sphere. As can be seen, efficient coupling of the laser energy is achieved for irradiances up to 10^{17} Wcm^{-2}. This is understandable in terms of classical absorption arguments in which the moderate Z of the targets and the short wavelength tend to favour inverse bremsstrahlung.

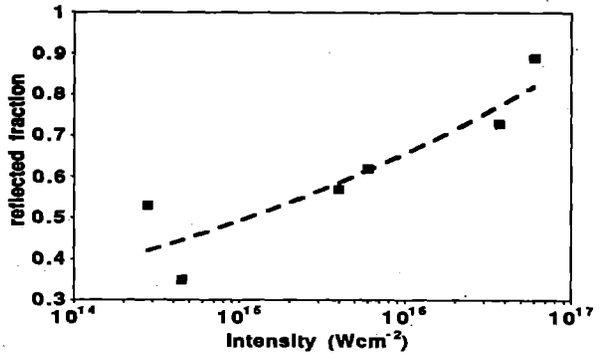

Figure 1. Measured total reflectivity versus incident irradiance for Al foil targets.

Figure 2a shows streak data taken from an aluminium target irradiated at approximately 10^{16} Wcm^{-2}. Note the temporal evolution of the He-like line series from a broad emission band into distinct emission lines, indicating high electron density at the start of the emission. This can be seen clearly in the film density line outs

of figure 2b, which shows a band of emission well above the bremsstrahlung continuum at early time which evolves into distinct Al XII $1s^2$-1s4p (Heγ) and $1s^2$-1s5p (Heδ) transitions. The curvature of the image due to electron path differences in the camera introduces a timing difference across the spectrum of the order of the temporal resolution due to the cathode slit. The width of the AlXII $1s^2$-1s3p (Heβ) line was modelled as described below and indicates an electron density of approximately $1.4x10^{23}$ cm^{-3} for scan(i) in figure 2b. The continuum lowering model of Stewart and Pyatt [7] suggests that for temperatures of a few hundred electronvolts, when He-like emission is strong, the He-like n=5 level is still bound at this electron density. If we assume the plasma to be fully or almost fully ionised, the merging of the Heγ and Heδ lines is consistent with the Inglis-Teller model [8] of line series merging at high electron density.

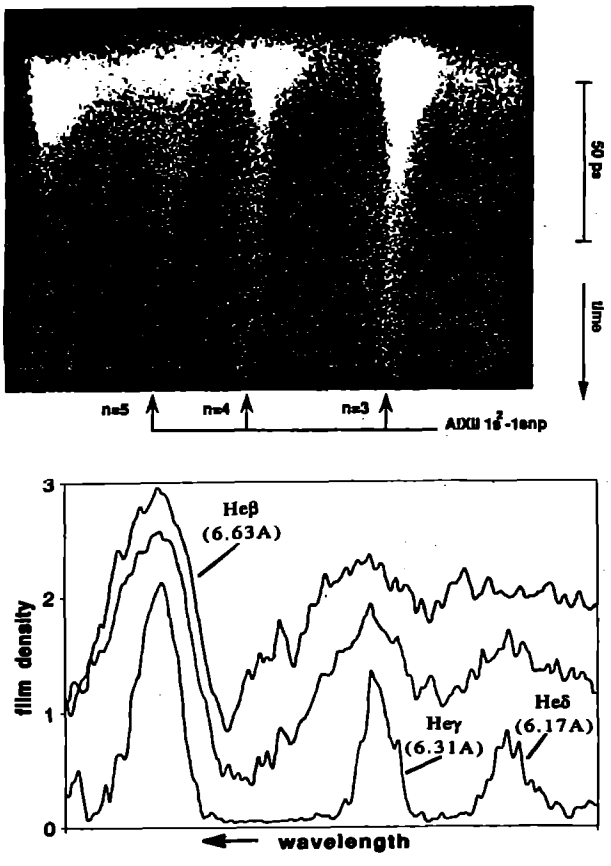

Figure 2. (a) Streaked X-ray spectrum of He-like line series (b) Film density line-outs. Timing is (i) 10ps before peak Lyβ emission, (ii) 10ps later and (iii) 50ps later. Note that scan (i) is displaced in density by 0.3 for ease of viewing.

In order to assess the plasma conditions more closely, we have analysed data on aluminium foils taken with lower dispersion. This means that the AlXIII 1s-3p (Lyβ) transition is included in the spectrum, and the temperature is indicated by the ratio of He-like to H-like emission. The evolution of the Heγ and Heδ lines from a broad band into separate emission lines was also seen for these data shots. The electron density was determined from the Stark width of the Heβ and Lyβ transitions. The variation of linewidth with density for these two lines was calculated using the spectral simulation code SPECTRA [9] which includes detailed Stark profiles for H, He and Li-like lines as well as continuum lowering, opacity, Doppler broadening and instrument width. The temperature was assumed to be 400eV for Heβ and 600eV for Lyβ, but to account for uncertainty in opacity, was varied from 200 to 800 eV and 300 to 900eV for Heβ and Lyβ respectively, with the plasma ρR being varied up to $1.2x10^{-4}$ gcm^{-2}: these conditions span the expected values for the emission region with the foil targets. The variations in predicted density for a given linewidth were then used to set the error bars. A fit of the full line profile was carried out on a few scans; the results obtained were the same as for the FWHM comparison to within the error bars generated. Due to instrument broadening, the linewidth ceased to be sensitive to density below about $3x10^{22}$ cm^{-3}.

The experiment was simulated with a 1-dimensional hydrocode, MEDUSA [10]. The heat flow is given by the smaller of the Spitzer value and a flux limited free streaming limit. From the work of Rickard et al [11], we decided on a flux limit of 0.1. The energy is absorbed by inverse bremsstrahlung and resonance absorption. The amount of resonance absorption is varied with the scalelength [12] at critical density in conjunction with the averaged angle of incidence due to the f/4 focussing. Some of the resonantly absorbed energy is dumped at critical density, with the rest being put into hot electrons which are transported in 10 energy groups with an initial temperature at the critical density surface which is calculated from the expression derived from experiments, by Giovanielli [13]. The fraction of resonantly absorbed energy put into the hot electron population was not found to significantly alter the hydrodynamic behaviour, because the high density and relatively low suprathermal electron temperature, (4.5keV for $I=4.0x10^{15}$ $Wcm-2$), due to the short laser wavelength meant that the hot electron energy was dumped spatially quite close to the critical density surface anyway. A value of 50% was used for simulations presented here. The ionisation balance is calculated with a time dependent non-LTE average atom, (AA) model similar to XSN [14], which includes reabsorption of the resonance line by use of an escape factor which is determined by the Doppler width. Because the AA model treats ions in a hydrogenic approximation it might be expected to give reasonable results as the plasma is dominated by the He-like to bare ions. A

comparison of the AA model and a detailed ionisation model [7,15] has been made for the steady state case. For electron temperatures between 200 and 900eV and electron density from 10^{22} to 10^{23} cm^{-3} , the two models were found to give the ratio of bare to Hydrogenic ions to within at most a factor of two with differences less than 20% for most of the conditions of interest. The emission intensity of the AlXII $1s^2$-1s3p and AlXIII 1s-3p lines was calculated by assuming that the n=3 levels of H and He-like ions were in local thermodynamic equilibrium (LTE) with the bare and Hydrogenic ground states respectively. Using the usual criterion [16], this should be a reasonable assumption at above critical electron density ($1.6x10^{22}cm^{-3}$). The predicted electron density and temperature was calculated as an emission weighted average over the simulation cells for the H-like and He-like lines separately The effect of hot electrons on the ionisation balance early in time (i.e during the laser pulse) is not included in our ionisation modelling; however, the simulations suggest that few hot electrons will reach the high density plasma from which the early time emission originates and are not expected to significantly alter our conclusions about the plasma conditions.

Figure 3 shows the experimentally inferred electron density compared to predicted averages for an aluminium foil irradiated at $4x10^{15}$ Wcm^{-2}. In order to make the comparison, the time of peak Lyβ emission in the simulation was equated to the experimental peak (timing differences due to image curvature are accounted for). In both simulation and experiment the peaks of the Heβ and Lyβ were separated by less than the experimental temporal resolution. The predicted absorption was 41% which is consistent with the data in figure 1. We can see that the peak electron density and general fall of in density is reasonably well reproduced by the hydrocode but is slightly better for the Lyβ than for for the Heβ line. The agreement of experiment and simulation is better at early time if the escape factors are not used, but is better at late time if they are included. This is possibly due to the invalidity of assuming a Doppler width dominated line profile at early time when the electron density is high. This explanation has to be treated with care as the error bars on the data are larger than the difference in predicted histories.

Figure 4a shows the predicted Heβ/Lyβ line ratio compared to experimental measurement for times when the electron density of the emiting region is above the limit for LTE to apply. The measured ratio generally agrees with the predicted ratio, at the average irradiance, to within a factor of two. In order to

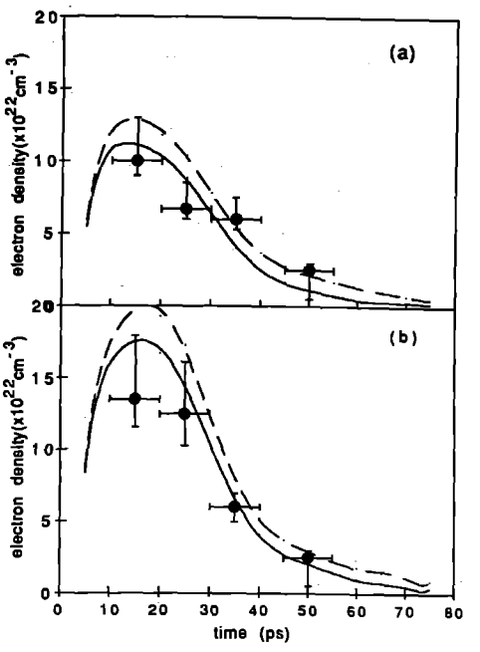

Figure 3. Time history of the electron density inferred by the Lyβ and Heβ linewidths, compared with the simulation, without(——), and with (----) reabsorption of the resonance line. Note that a 10ps window has been folded into the predicted data to simulate temporal resolution.

show the sensitivity to temperature, the simulated ratio is shown for irradiances 50% above and below the average. The predicted typical temperature is taken by finding the emission weighted average temperature in the simulation cells for the He-like and H-like lines separately and taking the mean of these. For the

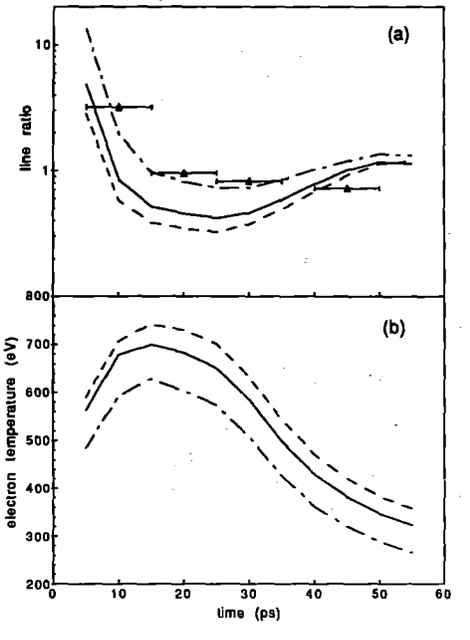

Figure 4. (a) measured Heβ/Lyβ line ratio vs. simulation for irradiances of $6x10^{15}Wcm^{-2}$ (broken line), $4x10^{15}Wcm^{-2}$ (solid line) and $2x10^{15}Wcm^{-2}$ (dot-dashed line). (b) Predicted average plasma emission temperature for the same irradiances, with same line styles as (a). Again a 10ps window is folded into predicted data.

irradiances considered, the predicted temperatures for H-like and He-like emission differ by less than 20% of their average. Figure 4b shows simulated typical plasma temperature for the conditions in figure 4a. As can be seen, the variation in temperature that would bring the predicted and measured line ratios into agreement is generally less than 100eV.

The simulated FWHM duration of emission is 20ps and 25ps for the Heβ and Lyβ lines respectively, which compares well with the value of 25-30ps for both lines from the data. However, the streak data shows a strong tail of emission which lasts for about 100ps. The approximations made in our ionisation model are not appropriate for modelling the coronal plasma late in time, and as the density is below our resolution limit we do not address this phase of the plasma expansion here. This longevity of emission is probably responsible for the fact that time integrated data, taken with this laser [15], indicates electron densities of only a few times 10^{22} cm^{-3}, when it is predicted that most emission will come from substantially higher density. This may also help to explain the smaller linewidths measured by other workers from time-integrated spectroscopy of plasmas created with short pulses.

In order to further reduce the effects of opacity on the linewidth we have also taken data with layered targets. These consisted of a 10μm plastic subtstate onto which was coated a 0.2μm layer of Al and a 0.1μm layer of CH facing the laser. Figure 5 shows spectra taken fomr a layered target irradiated at $6.4x10^{15}$ Wcm^{-2}. Again, we can clearly see the evolution of the He-like series from a broad emission band into distinct transitions. The peak densities for this shot were $2.1x10^{23}$ cm^{-3} and $1.0x10^{23}cm^{-3}$ for the Heβ and Lyβ lines respectively. This was in reasonable agreement with the hydrocode simulations. However, at later times the density inferred from the line widths did not fall below around $5x10^{22}cm^{-3}$. This was not in agreement with the hydrocode which predicted that the density should fall of in a similar manner to the solid targets. The reason for this discrepancy is not clear as the irradiation conditions were similar and the crystal set-up identical to that for solid targets. The line ratios predicted are also in worse agreement than for solid aluminium, and indicate a colder plasma, than predicted by simulation. However, if the absorbed irradiance were much lower than predicted, we would not expect the K-shell emission observed to come from such high density plasma as indicated by the linewidths. Clearly more work on the hydrodynamic modelling of layered targets is needed.

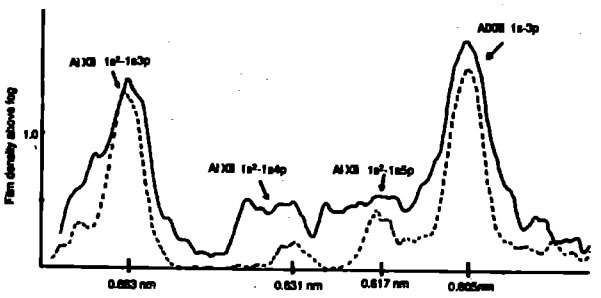

Figure 5. Film density line outs at (a) peak Lyβ emission and (b) 40ps later for a layered target at $6.4x10^{15}$ Wcm^{-2}

In conclusion, we have demonstrated the production of a rapidly heated plasma with a high brightness, pre-pulse free, Raman amplified KrF laser. The absence of a pre-formed plasma means that the plasma heating occurs at high density, with observed spectral features that differ markedly from previous observations with time integrated spectroscopy. In support of the measurement of high electron density from the Stark linewidths, we have clearly observed the time evolution of line series merging for the He-like aluminium lines. We consider that the fair agreement between the predicted and experimentally inferred electron density and temperature indicates that the plasma conditions are quite well modelled by the hydrocode, although more work is needed to understand our layered target data. In future, we intend to gain a fuller understanding of the ionisation dynamics, especially late in time, by developing time dependent detailed level accounting models.

The authors would like to thank the staff of the Central Laser Facility at the Rutherford Appleton Laboratory. We would also like to thank Dr J. Edwards for helpful discusions. This work was funded by a SERC research grant.

1. C.H. Nam, et. al Rev. Lett. **59**, 2427 (1987)
2. J.A. Cobble, et al. Phys. Rev. A. **39**, 454 (1989)
3. M.M. Murnane et al Phys. Rev. Lett. **62**, 155, (1989)
4. G.J. Tallents, M.H. Key, P. Norreys, D. Brown, J. Dunne and H. Baldis, Phys. Rev. A. **40**, 2857 (1989)
5. O. Willi, et. al Europhys. Lett., **10**, 141 (1989)
6. I.N. Ross, M.J. Shaw, C.J. Hooker, M.H. Key, E.C. Harvey, J.M.D. Lister J.E. Andrew, G.J. Hirst and P.A. Rodgers, Optics Communications, **78**, 263 , (1990) : E.C. Harvey, C.J. Hooker, J.R. Houliston, M.H. Key, A.K. Kidd, J.M.D. Lister, I.N. Ross, and M.J. Shaw, Rutherford-Appleton Laboratory Report RAL-91-025, 77
7. J. Stewart and K. Pyatt, Astrophysics J. **144**,1203(1966)
8. D.R. Inglis and E. Teller, Astrophysics J. ,**90**,439 (1939)
9. R.W. Lee, B.L. Whitten and R.E Stout II, J. Quant. Spectrosc. Radiat. Transfer, **32**, 91, (1984)
10. J.P. Christiansen, D.E.T.F. Ashby and K.V. Roberts, Computer Phys. Comm. **7**, 271, (1974)
11. G.J. Rickard, A.R. Bell, and E.M. Epperlein, Phys. Rev. Lett. **62**, 2687 (1989)
12. T.P Hughes *Proceedings of the XXth Scottish Summer School in Physics* eds. R.A. Cairns and J.J. Sanderson (SUSSP Publications Univ. Edinburgh 1979)
13. D.N. Giovanielli, Bull.Amer.Phys.Soc. SeriesII **9**, 1047
14. W.A. Lokke and W.H. Grasberger, Lawrence Livermore National Laboratory Report UCRL-52276 (1977): J. Edwards and S.J. Rose RAL report 91-025 (1991)
15 V.A. Barrow, Phd Thesis, University of London 1991
16. H.R. Griem *Plasma Spectroscopy*, McGraw-Hill, New York 1964

CHARACTERISTICS OF THE SPRITE RAMAN AMPLIFIER SYSTEM

G Bialolenker[1], J M D Lister, G J Hirst, J R Houliston and M J Shaw

Rutherford Appleton Laboratory
[1]on sabbatical from the Laser Department, NRCN, Beer-Sheva, ISRAEL

INTRODUCTION

Between 9/91 and 2/92 the two Raman amplifiers RA2 & RA3, in the SPRITE system were operated and over 1000 shots were fired to study their characteristics. The experimental objective was to obtain a better understanding of the effects which determine the beam quality and efficiency in the SPRITE Raman system.

THE EXPERIMENTAL DETAILS

Pulses at the Stokes wavelength of 268 nm and at the KrF wavelength of 248 nm were generated in the oscillator room and sent to the Raman amplifier room via a multi-pass optical delay line in helium. In all the work reported here the pulse duration was 12 ps. The performance of the Raman generator and Raman pre-amplifier has been discussed elsewhere[1].

The KrF beam is amplified in the two electron-beam pumped amplifiers Goblin and Sprite. Angular multiplexing with 8 beams is used to send pulses at 4 ns intervals through the amplifiers.

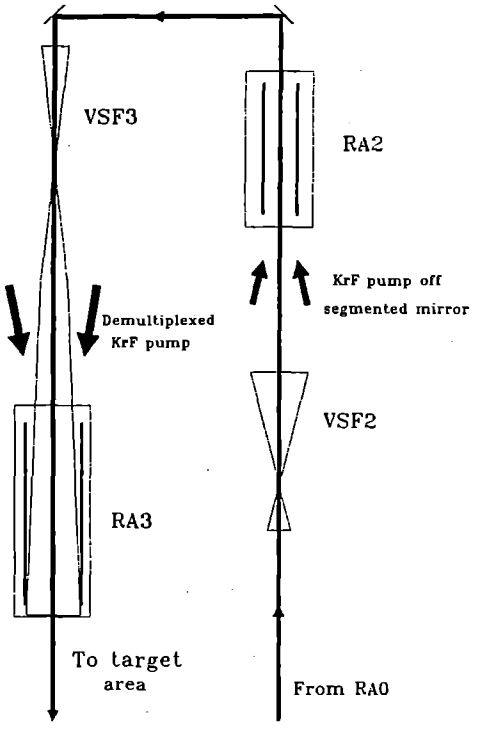

Figure 1. Raman amplifier chain

The layout of the two Raman amplifiers under study is shown in Fig. 1. A Stokes beam of 2.5 cm diameter was amplified in a 1 metre long reflective waveguide amplifier, operating at 0-2 bar methane pressure (RA2), and pumped by 4 or 6 beamlets at 3^0 to the axis. The beamlets were produced by a segmented mirror reflecting one of the KrF beams extracted from Sprite. CaF_2 windows were used on RA2 to reduce the high losses in silica due to two photon absorption The performance of the segmented mirror will be discussed later.

The final stage, RA3 was a 8 cm x 8 cm x 1 m reflecting waveguide amplifier operating at 1 bar pressure of methane with pump beams at 3^0 to the axis. RA3 was pumped by 7 of the main output beams from the Sprite laser. In this amplifier two-photon effects are reduced by using an ultra-thin (0.625mm) fused silica plate for the entrance window.

The chain also incorporated two beam-expanding spatial filters in vacuum, located before RA2 and between RA2 and RA3.

The behaviour of the output Stokes beam was checked as a function of the energy of the input Stokes beam, and the energy of the KrF pump beam. During all the work we optimized the relative timing of the Stokes and pump pulses in both amplifiers, and also the relative timing of the seven pump beams to RA3.

RESULTS AND DISCUSSION

The major part of the measurements were done in RA2 because it was planned in advance to change the pump mirror array to RA2, and we can easily change the methane pressure in this amplifier.

IMPROVEMENT OF OUTPUT BEAM HOMOGENEITY

The near field pattern of the amplified Stokes beam is affected by the uniformity and by the division of the pump beam. In this work we changed the pump beam division of RA2 to improve the homogeneity of the Stokes beam. The change was made in two steps, first we changed from 8 rectangular mirror segments on the pump mirror array to 6 circular mirror segments equally spaced about the axis.

The initial position of the 6 circular mirror segments produced a very non uniform near field output pattern (Fig. 2a). Rotation of the pump mirror array around the Stokes axis of 15^o improved the near field pattern considerably, but still left dark lines due to loss of reflections of the pump beam from the waveguide corners as seem in Fig. 2b.

To study the effect of the pump division on the near field pattern a computer simulation was written. This simulation assumes uniform circular pump beams and computes the pump intensity averaged along the length of the lightguide as a function of transverse position. In the limit of amplifier saturation the output Stokes intensity will be proportional to the pump intensity. The code is run for different rotation angles of the pump mirror array and different numbers of the mirror segments. The simulation is in good agreement with the experimental results as shown in Fig. 2.

In order to avoid the "tramlines" which resulted from reflections in the lightguide corners, it was decided to use the 4-mirror array shown in Fig. 2c in which the beam only reflects from opposite faces of the guide. In this case the simulation shows a radially uniform pump distribution and the measured output (Fig. 2c) was in good agreement.

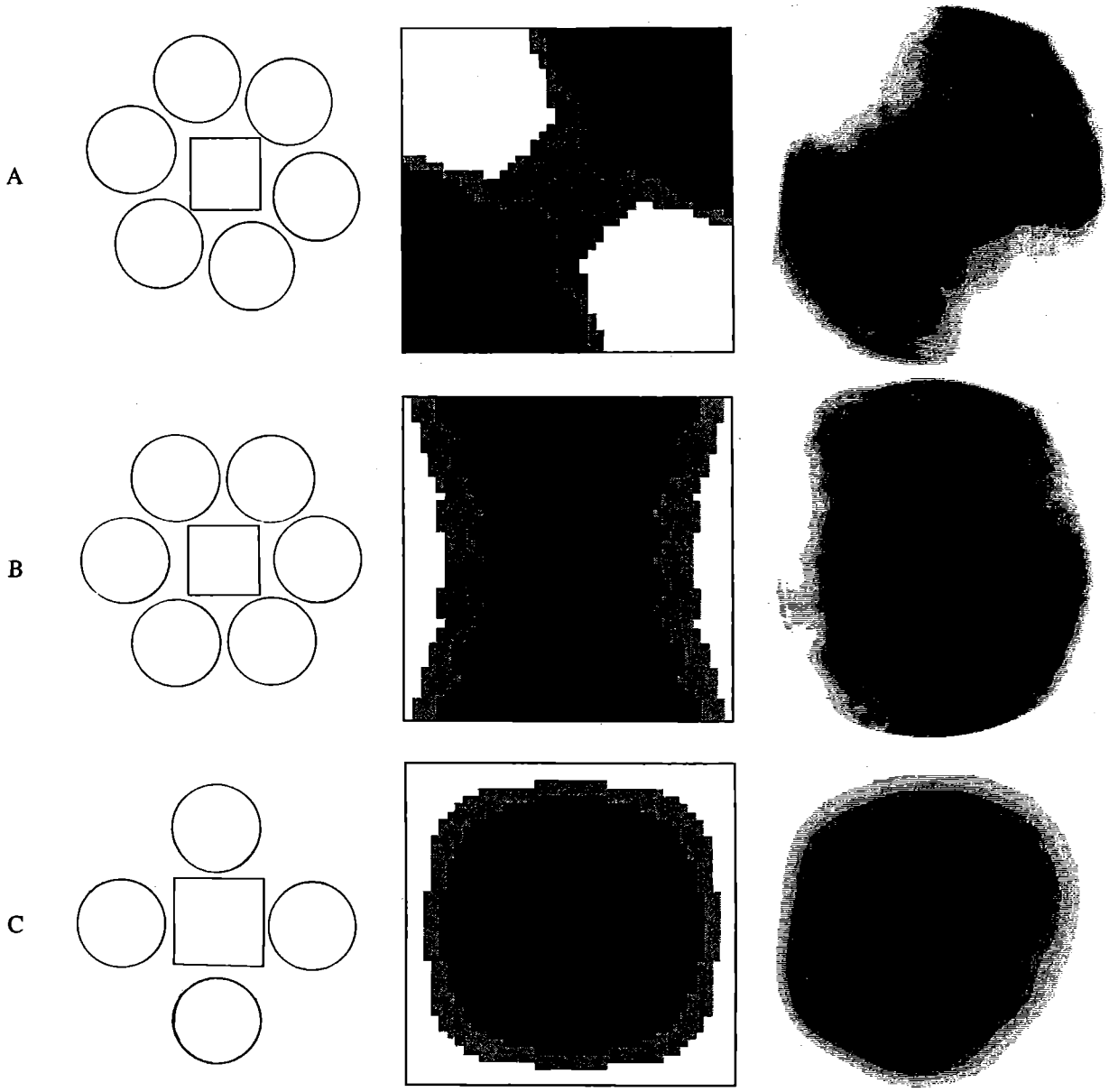

Figure 2. Simulation and experimental plots of the Stokes output near field pattern of RA2 for different rotation angles between the mirror array and the light guide. (a)- 6 segment mirror array at 0°, (b)- 6 segment mirror array at 15°, (c)- 4 segment mirror array.

From the initial 8 square mirrors, to the 4 mirror array the pump area was reduced by 50% and the pump energy by 33%, however the homogeneity of the pump beam in RA2 was improved significantly as we can see from Fig. 2c. The following results were obtained with the 4 circular mirror segments.

MEASURMENT OF INPUT/OUTPUT CHARACTERISTICS

To measure the performance of RA2 and RA3 a set of energy monitoring diagnostics were installed to measure three quantities for each shot: the input Stokes energy E_i, the output Stokes energy E_o and the energy of the KrF pump beam E_p. All three energies were monitored by calibrated photodiodes or calorimeters and corrected for losses in the amplifier windows.

Results plotted in Fig. 3 show the internal conversion efficiency ($\eta=E_o/E_p$) vs the steady state gain factor $\gamma I_p L$ were $\gamma=2.4 \times 10^{-10}$ cm/W for methane at 1 bar pressure. The input energy for these results was varied between 10 and 40 mJ. It is clear from Fig. 4 that RA2 reaches saturation with a $\gamma I_p L > 200$, which gives a conversion efficiency of 30%. In the saturation region, changes of $\gamma I_p L$ do not effect the efficiency, so we can suppose that E_o varies linearly with E_p. Thus the imprinting of transverse spatial variation in the pump to the Stokes will be no worse than a linear effect in this region. For $\gamma I_p L > 600$ the efficiency drops. This could be explained by generation of second Stokes in the system or self generation of Stokes along the pump beam axes that reduce the total output.

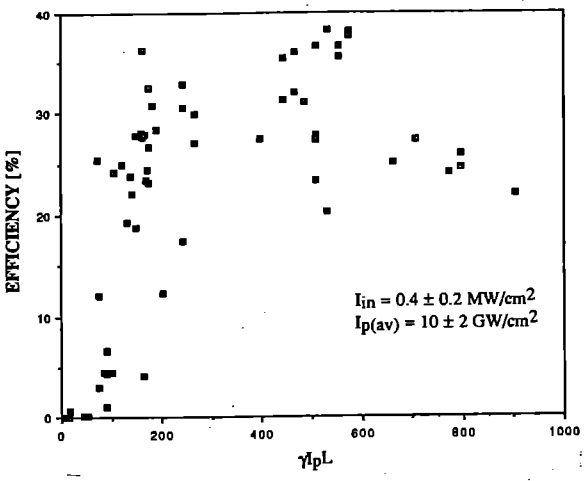

Figure 3. Efficiency of RA2 (E_o/E_p) vs $\gamma I_p L$ at nominally constant input intensity and pump intensity. $\gamma I_p L$ varied by varying pressure

Results plotted in Fig. 4 show the stage gain (E_o/E_i=gain) vs $\gamma I_p L$. The pump energy for these results changed between 0.5 and 0.9 J.

For the highest values of $\gamma I_p L$, RA2 reaches saturation with a stage gain of 8000. In the non-saturated region ($\gamma I_p L$ < 150) the gain increases in a quasi-exponential manner. For comparison we plot the gain predicted by the transient limit analytical expresion[2] $G = (1/2\pi u^2)e^{2u}$ were $u^2 = 2\gamma I_p L t_p/T_2$. The general data trend indicates that the "effective" gain coefficient is reduced to about 50% of the value it would have for transform limited pulses.

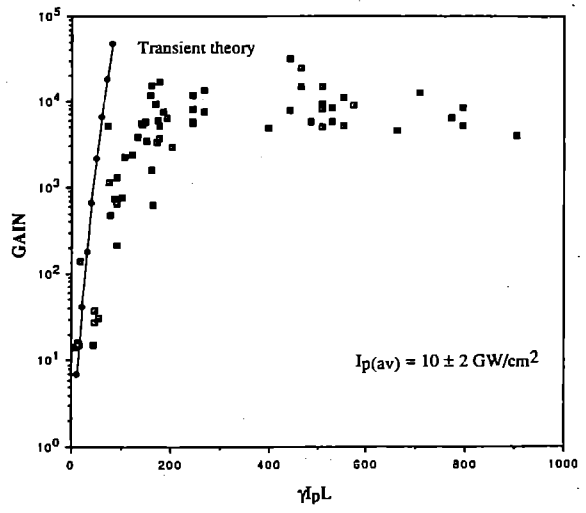

Figure 4. Stokes gain in RA2 vs $\gamma I_p L$ at nominally constant pump intensity. $\gamma I_p L$ varied by varying pressure. Also shown gain as predicted by transient theory in the non-depletion limit[2].

Results plotted in Fig. 5 show the internal convertion efficiency ($\eta = E_o/E_p$) vs E_n/E_p for both RA2 and RA3 which were operated at the same average $\gamma I_p L$ of 240.

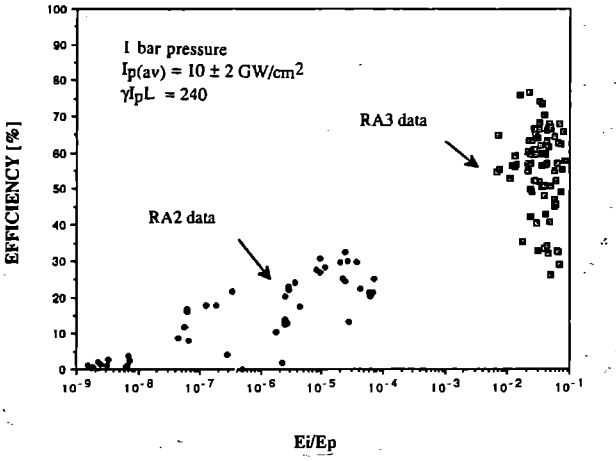

Figure 5. Efficiency (E_o/E_p) of RA2 and RA3 vs Stokes input relative to pump at constant pressure 1 bar and nominal constant pump intensity. Both amplifiers at the same value of $\gamma I_p L$.

The "best" results for the external characteristics of the two amplifiers are given in Table 1.

	Max. Pump Energy	Max. Output Energy	Typical Stage Gain	External Efiiciency
RA2	1.0J	320 mJ	8000	32%
RA3	14J	7J	24	53%

Table 1.

DISCUSSION

The pulses in the experiment are close to transform limited in the generator but there is some deterioration of the quality of the pump pulse and possibly of the Stokes pulse due to nonlinear interaction as they propagate in the air and through the KrF amplifiers. Measurements indicate that the pump pulse at RA3 is between 1-4 x transform limited. Raman gain is known to be reduced for non transform limited pulses.

The pump radiation to RA3 is delivered in 7 beams at 3° to the guide axis with each beam separated from the others in angle. This effect is not included in the theoretical calculation and it leads to a relative transverse shift of the interacting parts of the Stokes and pump wavefronts because of the short duration of the pulses, making the amplification dependent on the transverse coherence.

REFERENCES:

1. C J Hooker, J M D Lister and P A Rodgers, Opt Comm 82, 497 (1989).

2. M D Duncan, R Mahon, L L Tankersley and J Reintjes, JOSA B5, 37-52, (1988).

MODELLING THE RAMAN CONVERSION PROCESS

Karen E Hill and G H C New

Laser Optics & Spectroscopy Group
Imperial College London SW7 2BZ
United Kingdom.

INTRODUCTION

Over the last year, we have continued to develop and improve the computer modelling of the Raman conversion process that plays a central role in the Sprite laser system. Two aspects of the problem that have received particular attention in the past concern stochastic effects in the non-transform-limited pump and Stokes pulses ("noise") and angular effects associated with the non-colinear beam geometry. While we have not attempted to simulate the complicated three-dimensional beam configuration used in the laboratory, we do take account of a key consequence of the geometry by making the pump and Stokes pulses propagate at different effective speeds; we refer to this feature as "angular dispersion". Noise and angular dispersion interact in a complex way because the latter process interferes with the process of "phase pulling"[1] in which the Stokes pulse tries to compensate for its imperfect phase relationship with the pump. A description of this part of the work has recently appeared in the literature[2].

RESULTS

In the present report, we highlight another important aspect of the problem, the way in which, under high gain conditions, a long pump can amplify and even compress a short Stokes pulse. We consider the case of transform-limited pump and Stokes pulses of 30 ps and 3 ps duration respectively. The Stokes pulse is assumed to have an initial delay of 15 ps with respect to the pump, and to travel faster than the pump by an amount corresponding to the 7.5^{o} angle between the beams.

Results are presented in fig. 1 for three values of $G = \gamma I_p L$ and three values of the initial pump to Stokes energy ratio E_p/E_s. Here, the interaction constant for the Raman medium (methane) is $\gamma = 2.4 \times 10^{-10}$ cm/W, I_p is the peak intensity of the pump, and L is the interaction length (= 1 m). The parameter G is the small signal gain coefficient in the long pulse limit.; since the relaxation time of methane is 27.9 ps, the present case is in the transient regime, and the gains recorded will be substantially lower.

These definitions imply that for G = 30, the pump energy E_p is 39.76 mJ; the value for the energy clearly scales with the value of G. Under high gain conditions, the Stokes pulse evolution can be expected to be strongly dependent on the signal structure in the wings of the pulse. To investigate this property, the computer code allows for the inclusion of a weak background on the initial Stokes signal. This was taken to be 10^{-10} of the pump pulse profile in the present simulations.

Three different values of G (30, 100, 300) are used in the simulations presented in fig. 1. In each case, the left hand frame charts the Stokes energy gain factor $E_s(L)/E_s(0)$ through the interaction cell, while the right hand frame shows the corresponding Stokes pulse duration, normalised to its initial 3 ps value. The three curves in each frame are for different initial values of E_p/E_s (20, 60, 100), the arrow in each case indicating the direction of increase. The dotted lines in the frames for G = 300 refer to the case where the low level background is included. For the lower values of G, the background has no significant effect on the results.

DISCUSSION

For the low gain case (G = 30), the Raman interaction is not sufficiently strong to deplete the pump and as a result the tail of the Stokes pulse is amplified and the pulse width increases; the effect is particularly marked for the lower initial Stokes energies (corresponding to the higher values of E_p/E_s). When G is increased to 100, saturation begins to have a significant effect, and the output Stokes pulse duration is similar to that of the input. The development of multiple pulse structure is just starting to be apparent, although this cannot be discerned from fig. 1 Finally, for G = 300, significant Stokes pulse compression occurs in the absence of the low level background. However, while inclusion of the background has a relatively minor effect on the Stokes pulse energies, it has a major impact on the pulse shape, as evidenced by the rapidly rising dotted lines in the bottom right hand frame in fig. 1. This is associated with the appearance of multiple peaks in the Stokes profile and highlights the importance of background radiation effects under high gain conditions.

FUTURE WORK

More work along these lines is planned for the coming year. We particularly want to look at the properties of frequency-swept Stokes pulses to see to what extent it is possible to preserve chirp structure in the Raman interaction. This has an important bearing on the viability of some of the CPA schemes being considered for future application in the Sprite system.

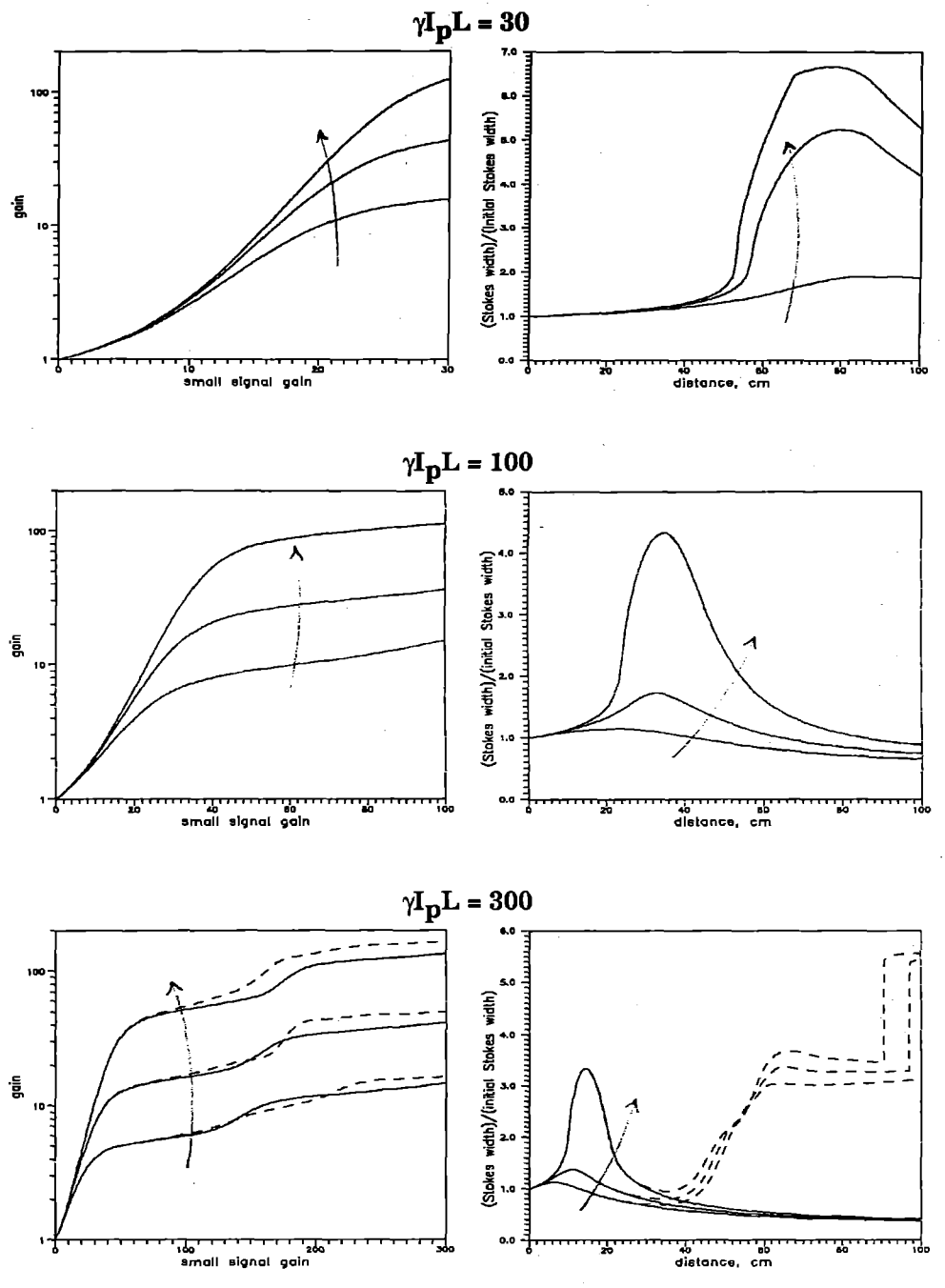

Fig. 1 Stokes pulse energy gain and pulse duration as a function of propagation distance in the Raman medium for three different values of G and for E_p/E_s = 20, 60 and 100; the arrows incicate the direction of increasing E_p/E_s. Other parameters are detailed in the text.

REFERENCES

1. M D Duncan, R Mahon, L L Tankersley, G Hilfer and J Reintjes, J Opt Soc Am B **7** (1990) 202.

2. K E Hill, G H C New, P A Rodgers and K Burnett, Opt Commun **87** (1992) 315.

STABILITY OF A RAMAN BEAM IN A CHAIN OF RAMAN AMPLIFIERS

M H Key

Rutherford Appleton Laboratory
and Dept of Atomic and Laser Physics, University of Oxford

INTRODUCTION

The KrF pumped Raman laser system in use and under development at the CLF has, at its core, a chain of CH_4 Raman amplifiers fed by a beam generated from amplification of Raman scattering in a focused KrF beam in a CH_4 gas cell. The source is spatially filtered to produce a near-diffraction limited beam and the amplifiers are pumped by typically 30x diffraction limited KrF beams from the multiplexed pulsed amplification system[1].

Ideally the major fraction of the pump energy is transferred to the Raman beam which maintains its near diffraction limited quality. In practice there are limitations to the ideal behaviour and two of these are considered here. Firstly, non-uniformity on the pump beams can be imprinted onto the Raman beam with consequent deterioration of the Raman beam quality. Secondly, with high gain in the Raman amplifiers, needed to obtain maximum conversion efficiency, the pump beams in the Raman medium, the Raman beam in the Raman medium or the Raman beam in its air path in the laboratory may become unstable to amplification of diffuse Raman scattering. The resulting wide angle emission that can in turn trigger a cascade of four-wave mixing processes. An important consideration in the design of a large system is to minimise these deleterious effects.

STABILITY AGAINST AMPLIFIED DIFFUSE RAMAN SCATTERING (ADRS)

The focused beam source of the Raman beam exhibits an abrupt threshold when the exponent of the amplification reaches a value which brings the Raman intensity to the level of the pump. The gain exponent in steady state amplification through a focus can be expressed in the form $2\gamma P/\lambda$ where γ is the gain coefficient of the Raman medium and P the pump power. The threshold gain is readily shown to be approximately exp (25) and the threshold power for steady state gain is circa 2 MW in CH_4. Pulses with duration $t \leq T_2$ have an energy dependent threshold at about 15 μJ[2]. Recollimation of the emission from the focused generator provides the input for the Raman amplifier chain.

An amplifier can be characterised by its pump dependent small signal gain which, in the steady state, is $\gamma I_p L$ for pump intensity I_p. The intensity of amplified diffuse scattering at the exit face of an amplifier of length L and cross-sectional area A, can be written as

$$I_s/I_p = n_a \frac{d\sigma}{d\Omega} \frac{A}{L^2} \frac{1}{\gamma I_p} (exp(\gamma I_p L) - 1) \qquad (1)$$

in the steady state approximation where n_a is the density of scattering molecules and $d\sigma/d\Omega$ is the differential scattering cross-section. A similar result can be derived for transient gain replacing the gain factor exp ($\gamma I_p L$) by the corresponding transient gain which is a function of the pulse energy density[3]. Equation 1 shows that when the gain exponent reaches 20-25 the amplified diffuse scattering will reach the level of the pump for geometrical aspect ratios in the amplifier in the range 10-100.

Another way to view this is in terms of an effective injected signal for spontaneous scattering at a level exp (- 20) to exp (- 25) of the pump. This can be contrasted with the magnitude of the injected signal from the generator which is typically six orders of magnitude higher. The amplifier is therefore dominated by the injected signal (provided there is no time interval when the pump is present without injected signal). Instability of the system to conversion of pump to diffuse Stokes is therefore not a problem. If the small signal gain in the system were sufficient to reach the threshold for ADRS to become comparable with the pump there would be heavy depletion of the pump by saturated amplification of the injected signal and the gain for ADRS would be quenched.

A related problem is ADRS from the Raman beam itself. Here there is no injected signal and generation from diffuse scattering is not quenched. There are two interesting limiting cases. In the limit of a heavily saturated amplifier the intensity of the Raman beam is approximately uniform throughout the amplifier at its output level. In this case equation 1 describes the generation from noise with the intensity of the Raman beam being the constant pump intensity. At the other extreme, an amplifier in a small signal regime has an exponentially varying intensity of the Raman beam and the effective amplification of diffuse Raman scattering is confined to the last 'e' folding length in the amplifier.

The threshold condition for strong conversion to ADRS is evidently more easily reached under conditions of saturated amplification. It becomes crucial in the Raman chain for the final amplifier where heavy saturation is required to obtain high efficiency. The angular distribution of the ADRS is uniform over the solid angle A/L^2 defined by the geometrical aspect ratio of the amplifier. [If it is produced in hot spots of the beam where the hot spot area $A_s < A$ then A_s defines the solid angle].

Where the gain in a single amplifier is insufficient to reach the threshold for significant ADRS, then the combined gain of amplifiers in series may exceed the threshold. Spatial filters separating amplifier stages restrict the solid angle of the ADRS and therefore raise the threshold gain, see (Equation 1 where A/L^2 is the solid angle to be replaced by a lower value $d\Omega$ defined by the VSF). Inter-stage spectral filtering can limit this type of instability which is generally not as problematic as instability of a single amplifier. It does not, for example, trigger four-wave mixing because the parasitic radiation co-propagates within the angle of the main Raman beam.

FOUR WAVE MIXING

The generation of Stokes shifted radiation from ADRS triggers four wave mixing as illustrated in Fig 1. Two frequencies combine to produce a third with the parametric generation giving an intensity of the third frequency proportional to $I_1^2 I_2 L$. The first anti Stokes frequency of the Raman beam is produced in a cone of angle determined by the dispersion of the Raman medium. The main Raman beam acts as the strong pump signal and the ADRS as the second frequency. Second anti Stokes is generated at a wider cone angle with the first anti Stokes as the strong pump and the Raman beam as the weak partner. Second Stokes generation occurs with first Stokes as the strong pump and the Raman beam as the weak partner. Four wave mixing processes can convert a significant fraction of primary radiation if they are strongly excited[4].

EXPERIMENTAL EVIDENCE

Experimental evidence of the above processes has been observed[5] in the emission from the final Raman amplifier of Sprite operating with 12 ps pulses, 1 bar CH_4 in a 100 cm amplifier with a Raman output intensity of 5 GW cm^2 and saturated gain of 25x. The Raman beam

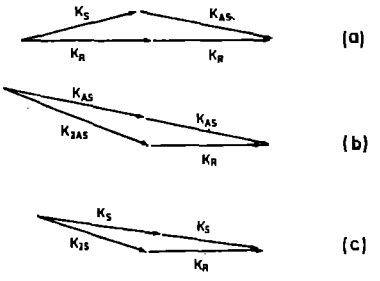

Fig 1 Matching of K vectors in 4 wave mixing (a) Anti Stokes generation, (b) 2nd Anti Stokes (c) 2nd Stokes assuming a primary Raman beam K_R and diffuse Stokes (ADRS) K_S.

was focused onto the input slit of a spectrometer to display the angular and spectral distribution of the emission. CH_4 first Stokes of the Raman beam was observed to be angularly diffuse. First anti-Stokes formed a well defined cone of angle 3 mrad. Second anti Stokes was observed more weakly at a cone angle of 5.5 mrad consistent with the previous description. Second Stokes was angularly diffuse suggesting a diffuse source at the main Raman beam frequency perhaps from scattering at the input window to the amplifier.

Similar behaviour was observed for N_2 Raman lines. This was attributed to the circa 10 metres of air path following the 1 metre Raman cell. Comparison of the values of Raman cross-section, T_2 and line width for CH_4 and N_2 (13.3×10^{-29} cm^2, 28 ps, 0.38 cm^{-1}, cf 1.5×10^{-29} cm^2, 7.1 ps, 1.5 cm^{-1}) indicates an approximately 10:1 ratio of gain coefficient for 12 ps pulses consistent with a similar threshold for both processes since the CH_4 path is 1 m and the air path 10 m.

The fraction of total energy converted into these undesired subsidiary Raman frequencies was $\leq 15\%$[6], but the effect is undesirable and is expected to have adverse consequences on beam quality. It can be reduced in the Raman amplifier by reducing the degree of saturation using reduced CH_4 pressure. It can be reduced in the air path by eliminating nitrogen or expanding the beam to reduce its intensity. Further study of the process and its control is in preparation.

SMOOTHING OF PUMP FLUCTUATIONS

A simple model can give a useful indication as to the smoothing of intensity fluctuations in the pump beams and their imprinting onto the Raman beam.

If the pump beam is n x diffraction limited it will have approximately n cycles of intensity variation across its aperture and therefore n^2 aperture elements each of which we can regard as having a randomly varying intensity. Representing the intensity in each cell as $m \pm \sqrt{m}$ to give the random variation and, considering the possibility of super position of p multiple pump beams at different angles in a reflecting waveguide system, the resultant intensity in each element can be represented as $pm \pm (pm)^{1/2}$.

The effect of angling of the pump beams in the reflecting waveguide creates a sampling of all the cells across the pump beam by the Raman beam, as illustrated in Fig 2.

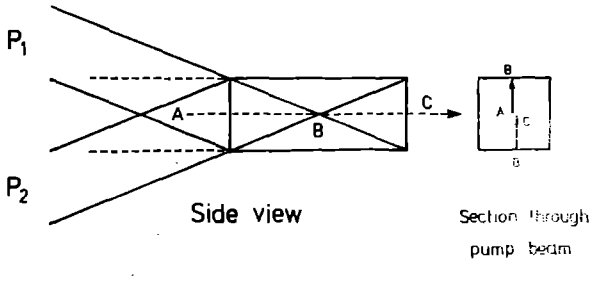

Fig 2 Angled pump beams P_1 and P_2 in a Raman amplifier with reflecting walls. ABC denotes the centre ray of the Raman beam. The cross-section through pump beam P_1 shows how it is sampled along a line by ray ABC.

This gives a resultant line averaged intensity for the Raman beam which we can represent as $(npm \pm (npm)^{1/2})/n$. The fluctuation fraction can therefore be represented as a fraction $m^{-1/2}$ for one beam $(pm)^{-1/2}$ for p superimposed beams and $(npm)^{-1/2}$ for line averaging through angled pump beams through the waveguide. The previous argument assumes negligible diffraction spreading from one element of the wavefront to another. This will be valid where $n^2\lambda L/D^2 < 1$ where L is the length of the waveguide, D is the diameter and n the number of fluctuations across the beam. For a typical case of L = 100 cm, D = 10 cm this criterion suggests that pump beams better than 200x diffraction limited will not be significantly influenced by diffraction spreading of the pump fluctuations in the transit through the waveguide.

MODULATION TRANSFER FUNCTION FOR PUMP FLUCTUATIONS ONTO THE STOKES BEAM

Pump fluctuations will be amplified in the exponentiation of Stokes intensity if the amplifier operates in the small signal regime. This is easy to see for a steady state gain representation where $I_s = I_{so} \exp(\gamma I p l)$. For a pump $Ip(1 \pm \Delta Ip/Ip) = Ip(1 \pm \varepsilon)$ the Stokes intensity is

$$I_s \pm \frac{(dI_s/dI_p)\Delta I_p}{I_s} = I_s(1 \pm A\varepsilon)$$

where A is the amplification of the fluctuation. It is readily shown then for small signal gain that $A = \gamma I p L$. Thus amplifiers operating in the small signal regime have a deleterious effect on the intensity pattern and therefore on the beam divergence of the Stokes beam through the amplification of fluctuations from the pump. Saturation of gain reduces this effect since the fluctuations on the Stokes beam are proportional to dI_s/dI_p. In the limit of full saturation $dI_s/dI_p \rightarrow 0$ and fluctuations are eliminated. When $dI_s/dI_p < I_s/I_p$ there is attenuation in the transfer of fluctuations.

This simple analysis illustrates, first, how the use of multiple angled pump beams in the waveguide Raman amplifier reduces the effect of imprinting of pump fluctuations onto the Raman beam and, secondly, that operation with gain saturation is highly desirable for maintenance of high quality in the Raman beam. The degree of gain saturation which can be used is limited by the previously discussed tendency towards instability of the Stokes beam and also by the need to provide significant total amplification of the initial Stokes pulse which would require a very large number of amplifier stages if each one were heavily saturated.

REFERENCES

1. I N Ross et al, Opt Comm 78 263 (1990).
2. N J Everall et al, Opt Comm 64 393 (1987).
3. R L Carman et al, Phys Rev A2 60 (1970).
4. C Risser et al, J Opt Soc Am B 6 1859 (1989).
5. Unpublished results CLF KrF R&D Programme.
6. See J Lister and G Bialolenker ibid.

SPRITE RAMAN SYSTEM UPGRADES

S Hancock, C J Hooker, M H Key, A K Kidd, G New* and M J Shaw

Rutherford Appleton Laboratory
* Imperial College

INTRODUCTION

During the past year a number of design studies have been undertaken to consider future development of the Sprite Raman system. These studies have now gelled into a two-phase programme which has been approved by Science Board. The first phase, entitled "Enhanced Raman beams on Sprite", has university collaborators and will involve an approximate threefold increase in energy of the present system and a doubling of beams to the target area. The second phase, to be known as "Titania", will involve a major upgrade to the existing facilities in R2 with a more than 10-fold increase in energy to target. This report outlines the main features of the proposed upgrades.

ENHANCED RAMAN BEAMS ON SPRITE

The Sprite Raman system is the only high power Raman laser in the world. Its advantages are that it produces short wavelength (268 nm), prepulse-free beams of extreme brightness (approaching 10^{20} W cm^{-2} sterad^{-1}). It does not, however, make efficient use of the capabilities of the Sprite pump laser. A two-stage upgrade is planned to improve the overall efficiency of the system and provide more energy on target.

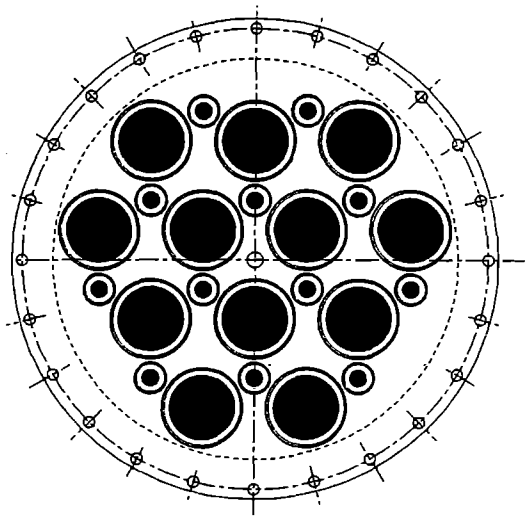

Fig 1. Sprite beam pipe showing 12 input and output beams

In the first stage the number of beams multiplexing Sprite will be increased from 8 to 12. The beam size will stay the same at 80 mm. Change of beam pipe will not be necessary since 12 beams can fit into the existing pipe as shown in Fig.1. This 12-fold multiplicity is consistent with the Titania upgrade (see below). A single Raman beam would be enhanced by having an enlarged spatial filter between RA2 and RA3.

In stage 2 it is proposed to multiplex RA3 with two beams. This would involve double-pulsing the KrF beams to provide a total of 24 pulses at 1.5 ns separation to extract energy from Sprite. Operation at higher pressure and pump rate will be necessary in order to maintain high pulse energy. This effect has been modelled using the RAL extraction code[1] and the result is shown in Fig 2.

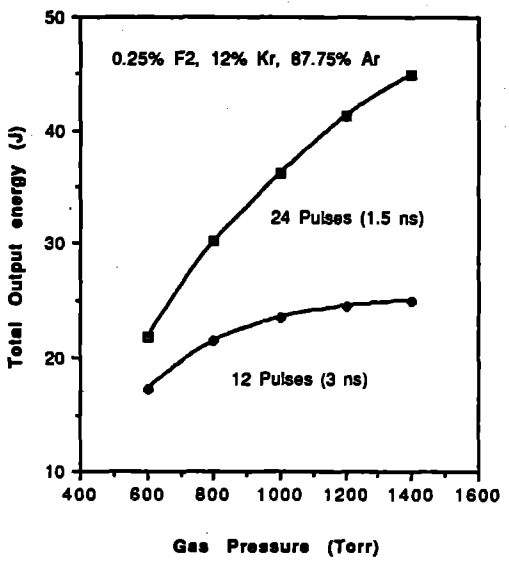

Fig. 2. Predicted output energy per beam from Sprite for pulse separations of 1.5 and 3 ns as a function of pressure. Pump rate assumed to be given by: W(MW cm^{-3}) = 7.5 x 10^{-4} p(Torr).

	Existing	Phase 1 Enhanced	Phase 2 Titania
On Target Power (t =10 ps)	0.5 TW	1.5 TW	20 TW
On Target Energy (t > 100 ps)	10 J	30 J	400 J
Number of Beams	1	2	4
Beam Diameter	80 mm	80 mm	120 mm
Beam Brightness (W cm^{-2} StR^{-1})	6 x 10^{19}	10^{20}	10^{21}

Table 1. Expected performance of the Raman upgrades

The Raman beam would be multiplexed into two after RA2 and after spatial filtering the two beams extract RA3 sequentially. To avoid

deterioration in beam quality the two Raman beams would be piped to target in helium gas.

Pulse lengths up to 100 ps will be relatively easy to provide using the new TiS front end (with extra GTI's). Operating the lightguides in compression mode could produce much shorter pulses. Durations down to 2 - 3 ps may be possible. Table 1 gives expected performance parameters at 10 ps and 100 ps.

THE TITANIA UPGRADE

The existing R2 complex offers good possibilities for a low cost option to upgrade the Sprite facility. Cranage is good and the 1 m thick level concrete floor excellent for optical stability. All necessary services already exist. The overall size, however, limits the optical path length available for multiplexing and the total beam numbers involved and this in turn limits the beam energy available to target. Sufficient floor area is available however to effect a sizeable upgrade to the present Sprite performance.

The most logical upgrade is to incorporate the intermediate 40 cm aperture module "Titania" into the existing system using "Goblin" and a modified "Sprite" as drivers. The new amplifier (discussed elsewhere in this report) would be constructed off-line in R7 whilst Sprite is still operational in phase one. The incorporation of the intermediate system into the R2 building would require the enlargement of the multiplexer room by using the existing target area space and the relocation of the target area. Sufficient floor area exists if the development labs are also relocated. The present oscillator room, pulsed power area and control room would not need to be moved. Fig 3 shows the proposed new layout.

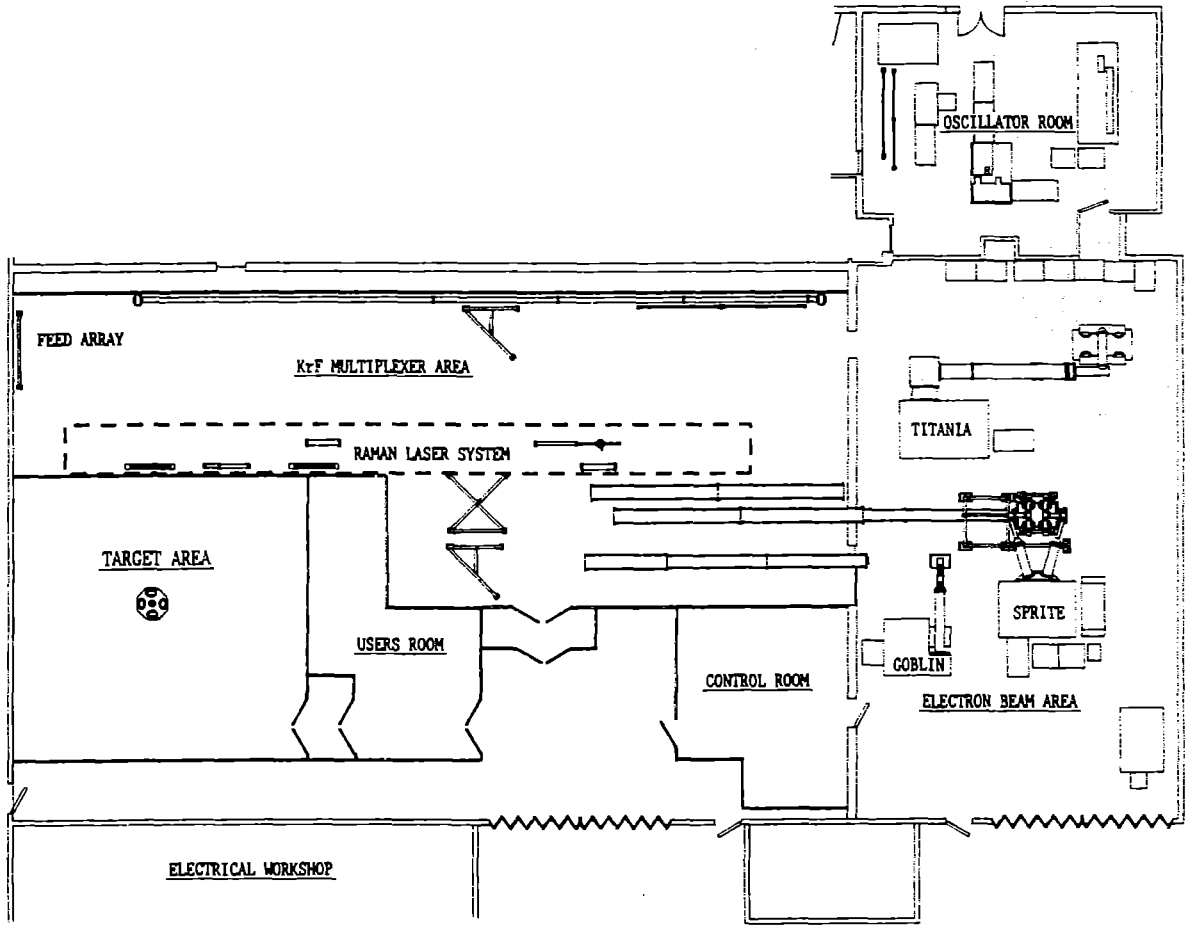

Fig. 3. Proposed layout of the Titania Laser System in R2.

The KrF optical chain is shown in Fig 4. Goblin and Sprite are Optically multiplexed with 12 beams. Each beam consists of a train of 4 pulses thus a total of 48 pulses extract energy from these two amplifiers. After Sprite each beam is split into 2 to give a total of 24 beams (96 pulses) extracting energy from Titania. The RAL extraction code[1] has been used to predict the output energies from the various KrF amplifiers. Results are shown in table 2.

Figure 5 shows a schematic of the proposed Raman chain. A 1 mJ input from the existing RA1 is assumed. The amplifiers RA2 and RA3 are also the existing amplifiers. The beam is assumed to be multiplexed before RA3 into 4 beams. RA3 is pumped by two of the 24 KrF beams from Titania. A new 150 mm aperture amplifier RA4 will be installed and will be pumped by the remaining 22 KrF beams. It will be extracted by the 4 preamplified Stokes beams. Output energies per beam are shown in table 2 and are based on the assumption of a maximum 50% conversion efficiency, a figure which has already been exceeded in practise on the Sprite system.

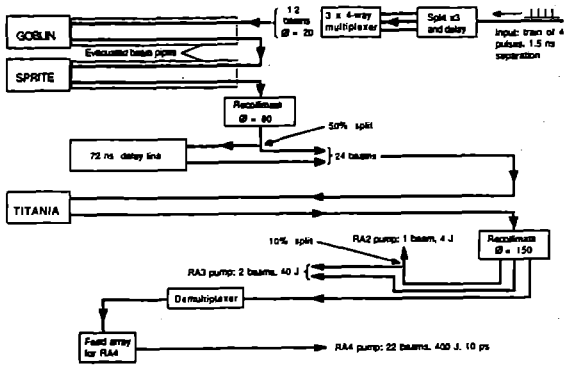

Fig 4. Schematic diagram of the Titania KrF chain.

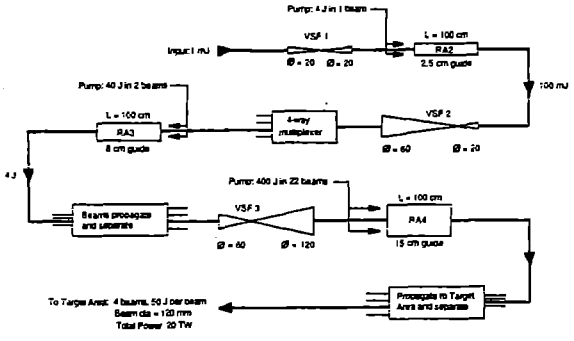

Fig 5. Schematic diagram of the Titania Raman chain.

OTHER FEATURES

In addition to the Raman mode of operation the phase 2 system would also be expected to be capable of delivering sub-picosecond KrF pulses to target and also a single mirror composited ISI beam. The expected performance would be:-

- Factor of 2 increase in power of femtosec pulse over phase 1.

- 50 J / 0.5 ns broadband (60 cm^{-1}) ISI beam at 100x DL. Target intensity = 10^{15} W cm^{-2} with f/3 focusing.

The femtosec option would probably not be compatible with simultaneous Raman operation. On the other hand, the ISI beam could be used with Raman beams for backlighters. In this case, the Raman power would be reduced by about 25%. If demand for ISI beams warrants, a fully flexible system providing a total of four beams any of which could be either ISI or short pulse Raman would be possible. In this case the ISI beams would be restricted to 50 J per beam as above and the Raman beams to 5 TW per beam. This option has not yet been costed.

	Aperture	No of beams	Pulses per beam	Total output energy
Goblin	80 mm	12	4	470 mJ
Sprite	270 mm	12	4	55J
Titania	400mm	24	4	430 J
RA2	25 mm	1	1	100 mJ
RA3	80 mm	4	1	4 J
RA4	150 mm	4	1	200 J

Table 2. KrF and Raman amplifier parameters for the Titania system

CONCLUSION

These upgrades provide a continuous sequence of improvements to the existing Sprite laser system. By using the existing site and retaining a very large number of phase 1 components in phase 2, the development costs have been significantly reduced.They will ensure that RAL continues to possess a world lead in high brightness UV laser systems.

REFERENCE

1. E C Harvey et al J. Appl. Phys. **70**, 5238 (1991)

SPRITE AS AN ULTRA-SHORT PULSE KrF LASER - MODELLING AND INITIAL TESTS AT 3 PSEC

J M D Lister[1], G Bialolenker[2], G J Hirst[1], M H Key[1,3], G Brady[3] and A K Kidd[1]

[1]Rutherford Appleton Laboratory
[2]On sabbatical from Laser Dept., NRCN, Beer-Sheva, Israel
[3]Dept. of Atomic & Laser Physics, University of Oxford

INTRODUCTION

Technical evaluations, modelling studies and consultations with users during the year have led to a new project to exploit the Sprite system as a generator of high energy ultra-short pulses at 249nm. The eventual goal is to produce 100fs pulses of energy exceeding 1J. This will require chirped pulse amplification and compression which is discussed in another section.

We report here on the performance of the Sprite system in direct amplification of short pulses including the important issue of the background intensity due to amplified spontaneous emission (ASE). Calculations indicate the possibility of single pulse energies of up to 1.8J with a contrast ratio relative to the ASE of 3×10^8. In the experiment described here, pulses of 3ps duration were amplified to energies exceeding 1.7J. Contrast ratios (in terms of brightness) of over 10^8 were achieved with a slightly lower output energy. Future work with shorter pulses will use a new titanium sapphire (Ti:S) oscillator due to be installed in June.

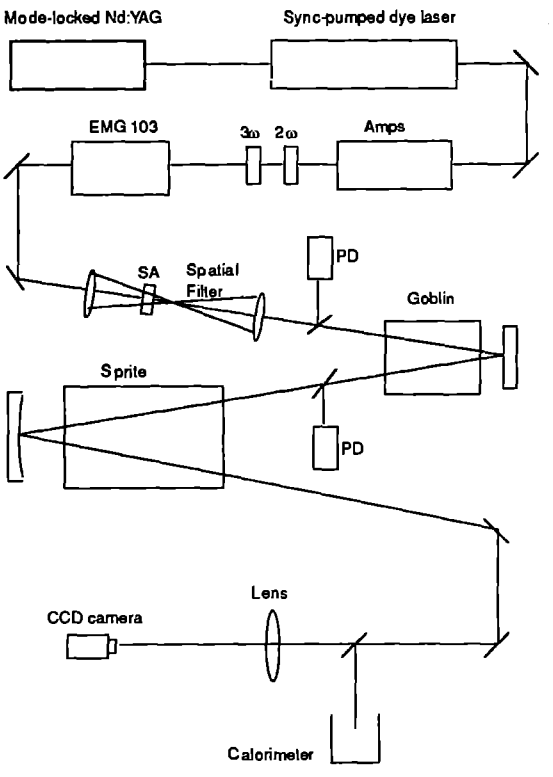

Figure 1: Layout of short pulse KrF experiment

EXPERIMENTAL

The present system consists of a frequency-doubled mode-locked Nd:YAG laser pumping a feedback stabilised sync-pumped dye laser to produce transform limited pulses of 3ps duration at 746nm[2]. The output is amplified in two dye cells to an energy of about 100μJ and then frequency tripled to produce about 15μJ at 249nm (the KrF wavelength). In order to keep the amplified spontaneous emission to a minimum, and hence maximise the contrast ratio, it is necessary to minimise the gain of the KrF chain. A Ti:S amplifier stage was used after the dye amplifiers to increase the 746nm output pulse energy to 0.8mJ and the input to the KrF chain to over 100μJ.

The Ti:S amplifier initially delivered an output energy of 100μJ at 249nm. However, passive losses between the amplifiers, and a steady decline in the performance and stability of the Ti:S stage, necessitated the reintroduction of the discharge laser (EMG 103) into the amplifier chain. The experimental layout is shown in Figure 1. The Goblin input and output energies were measured by calibrated photodiodes, and the Sprite output by a UV calorimeter. To reduce the coupling of ASE between the amplifiers, a saturable absorber dye was introduced after the EMG 103. The dye cell was positioned close to the focus of the spatial filter before Goblin. A solution of 1 mg of Acridine in 40ml of ethanol had a small signal transmission (for the ASE) of about 1%, and a saturated transmission for the signal of 25-30% at a fluence of 1.1mJ cm^{-2}. Losses in the dye cell windows (and possibly also the solvent) reduced the short pulse transmission to below the expected value of 50%.

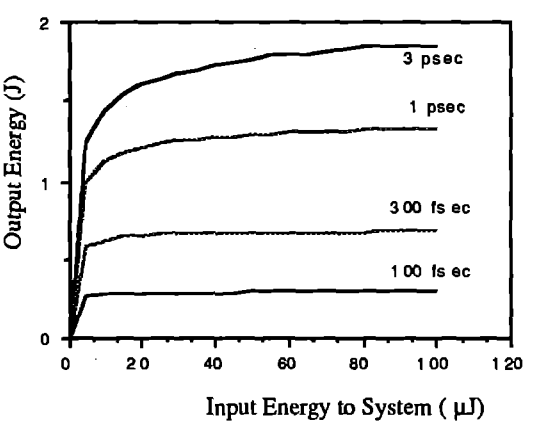

Figure 2: Code predictions for Sprite output as a function of Goblin input

	Goblin Input (μJ)	Sprite Input (mJ)	Sprite Output (J)	ASE Output (mJ)	Brightness ($W\ cm^{-2}\ st^{-1}$)	Contrast ratio
Code - Goblin + Sprite	100	24	1.8	3.0	1.4×10^{18}	2.0×10^{8}
Ti:S + Goblin + Sprite	5.0	1.5	0.55	0.8	5.0×10^{17}	3.0×10^{8}
Ti:S + EMG + Goblin + Sprite	250	14	1.5	20	1.5×10^{18}	2.0×10^{6}
Ti:S + EMG + Sat. Abs. + Goblin + Sprite	150	12	1.4	1.2	1.4×10^{18}	3.5×10^{7}

Table 1: Experimental results and code predictions for output energies and beam brightness

Table 1 summarises the results for three operating conditions; with and without the discharge amplifier, and with the saturable absorber. A simulation code was used to model the effects of ASE depumping on amplifier gain[3]. The results of the simulation are included in Table 1 for the case of amplification in Goblin and Sprite only. The graph in Figure 2 shows the predicted output from Sprite as a function of input energy to Goblin for pulse durations from 100fs to 3ps. For a pulse energy input to Goblin of 100μJ, the predicted pulse energy from Sprite is 1.8J and the predicted brightness is 1.4×10^{18} $W\ cm^{-2}st^{-1}$. The energy is close to that measured for a similar input to Goblin, but because the discharge amplifier was required to achieve this input energy, the contrast ratio was lower than predicted. The output pulse energy is limited by saturation of the gain in Sprite. The predicted ASE output is 3.0mJ, predominantly from Goblin.

The far-field pattern of the beam was monitored by a UV sensitive CCD camera placed at the focus of an 8m focal length lens. The beam was attenuated by an NO_2 absorber cell. The far field patterns were generally non-uniform with large intensity fluctuations, as is expected for a coherent beam in an optically imperfect amplifier chain. However, most of the energy was contained within a divergence of 80μrad (25 x DL). The figures for the brightness of the output beam are averaged over this area. The average intensity on target using the current target chamber optics would be about 7×10^{16} $W\ cm^{-2}$, although the peak intensity could be much greater. The divergence of the ASE was measured using the same set-up but with much less attenuation. The ASE divergence for amplification in Goblin and Sprite only was about 400μrad, compared with 100μrad with the EMG103 included in the amplifier chain. The saturable absorber greatly reduced the ASE energy introduced by the discharge amplifier, but the lower divergence of the additional energy reduced the contrast ratio in terms of brightness by an order of magnitude.

SUMMARY

When the discharge amplifier was used without the saturable absorber, the ASE energy at the output of the system was increased from less than 1mJ to over 20mJ, giving a reduced contrast ratio of 2×10^{6}. Including the absorber reduced the final output energy slightly but improved the contrast ratio by over an order of magnitude. It is likely that this figure could be further improved by better use of the saturable absorber, by using different concentrations of the dye, using a dye jet instead of a cell, or by using different solvents. The best contrast ratio (3×10^{8}) was achieved without the discharge amplifier. It is expected that the maximum brightness measured in this experiment (1.5×10^{18}) can be achieved without using the discharge amplifier. This would require the performance of the Ti:S stage to be significantly improved, and the losses between the Ti:S amplifier and Goblin to be reduced. This should result in a contrast ratio for the brightness approaching 10^{9}.

REFERENCES

1. I N Ross et al, "A high performance excimer pumped Raman laser" Optics Communications **78**, 263,(1990)
2. C J Hooker et al, "Variable-length transform-limited pulses from a stabilized synchronously pumped mode-locked laser" Optics Communications **80**, 375, (1991)
3. E C Harvey et al, "Picosecond gain and saturation measurements in a KrF laser amplifier depumped by amplified spontaneous emission" J. Appl. Phys. **70** (10), 5238 (1991)

CHIRPED PULSE AMPLIFICATION WITH SHORT-PULSE KrF

J R Houliston[1,2], I N Ross[2], M H Key[1,2], S Szatmari[3], P Simon[4]

[1]Rutherford Appleton Laboratory
[2]Clarendon Laboratory, University of Oxford
[3]Max Planck Institut für Biophysikalische Chemie, Albeilung laserphysik, Göttingen, Germany
[4]Laser Laboratorium Göttingen eV, Göttingen, Germany

The purpose of the UV Chirped Pulse Amplification (CPA) programme[1] is to maximise the power and brightness of the large-aperture electron beam-pumped KrF amplifier, SPRITE, by employing a CPA technique for pulses limited in duration by the gain bandwidth of the amplifier as opposed to direct amplification of the initial short pulses[2-4].

In order to overcome the power limit imposed by two-photon absorption in the output window of large-aperture KrF amplifiers (5 GW/cm^2 for 2 cm thick silica SPRITE output window) and self phase modulation in the air paths, 100 fs input pulses must be stretched by a factor of approximately 30 in order that they may be amplified to several times the saturation fluence (2 mJ/cm^2).

The criticality of recompression parameters, particular compressor grating separation and symmetry between stretcher and compressor diffraction geometries, is in proportion to the stretch factor. In comparison to solid state CPA lasers[5] for which a stretch factor of order 1000 is required for efficient energy extraction at 100 fs, the principal advantage of the modest stretch factor of 30 for a KrF system is that higher recompression fidelity and hence a higher contrast ratio in the recompressed pulse is possible. The brightness of the recompressed pulse is dependent on the diffraction efficiency of the compressor gratings and the focusability of the recompressed beam.

CPA experiments[6] using 5 ps, 249 nm pulses with saturated amplification in a discharge-pumped KrF amplifier of 80 ps stretched pulses before recompression to the original duration have established confidence in the design of a subpicosecond CPA system based on autoaligning stretcher and compressor diffraction geometries. In particular it was shown that spectral profile distortion due to saturated amplification of the chirped pulses did not affect recompression fidelity, within the measurement sensitivity.

We report here on a CPA experiment conducted in collaboration with Max Planck Institut fur Biophysikalische Chemie, Göttingen, in which subpicosecond, 249 nm CPA performance was investigated.

Fig 1 illustrates the Laser Laboratorium Göttingen femtosecond laser[7] used for generation and amplification of 249 nm pulses. The system is based on a Lambda Physik EMG 150 discharge-pumped excimer laser which is used as a pump for a subpicosecond dye generator-amplifier operating at 497 nm and as an amplifier for the frequency doubled output of the dye system at 249 nm. The single-pass amplified pulses (300-500 fs, 8 mJ, up to 20 Hz) exhibit a chirp and can be directly compressed by a factor of approximately 3. The asymmetrical spectrum is broadened and the chirp increased under further amplification resulting in recompressibility to an even shorter duration (Fig 2).

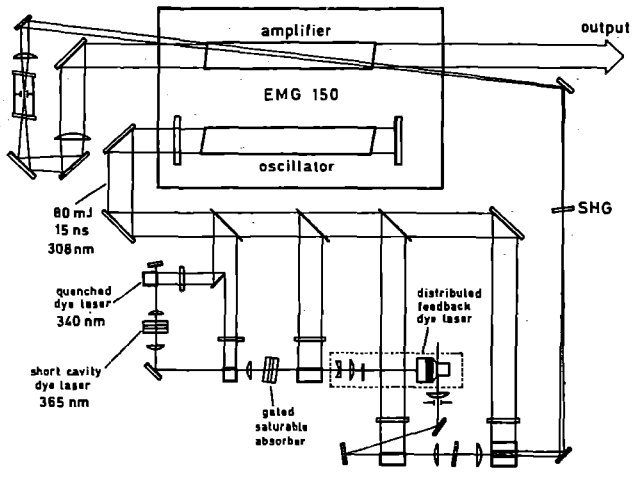

Fig 1 Laser Laboratorium Göttingen femtosecond KrF laser

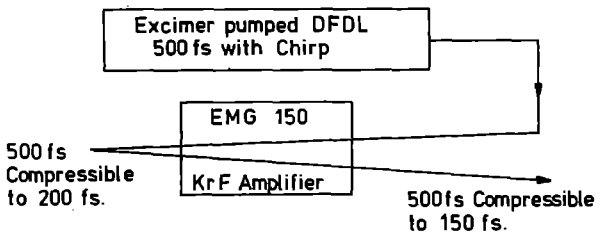

Fig 2 Compressibility of femtosecond pulses.

Temporal measurements were made using a Michelson interferometer moving-arm autocorrelator using, as nonlinear process, two-photon ionisation in NO gas[8]. Spectral measurements were made using a spectrometer based on a 3050 1/mm diffraction grating with the spectral plane imaged on to a diode array.

The experimental arrangement is shown in Fig 3. The diverging single-pass amplified beam is collimated using a Galilean telescope, with further adjustment using an iris. The stretcher operates in a folded geometry with a 3600 1/mm diffraction grating placed 20 cm from a 72 cm focal length silica lens. The beam undergoes a slight vertical tilt at the mirror at the focal plane of the stretcher lens in order to separate the input and output beams. The grating is used in first order near-Littrow diffraction geometry (angles of incidence and diffraction 39° and 15° respectively) with a diffraction efficiency of 40%. The stretched beam is amplified in a second pass of the amplifier chamber of the EMG 150 laser to several times the KrF saturation fluence before recompression.

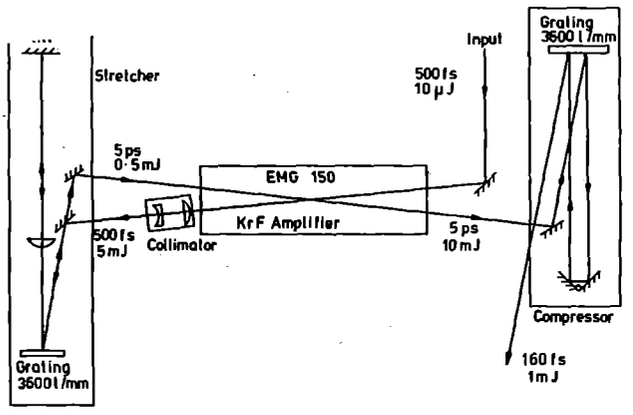

Fig 3 248 nm subpicosecond CPA arrangement.

The compressor operates in a folded geometry with a 3600 1/mm grating used in a similar diffraction geometry to the stretcher grating. A 90° quartz prism placed 55 cm from the compressor grating with the prism back edge perpendicular to the dispersion plane is used to retro-reflect the diffracted beam to the grating for recollimation.

Fig 4 shows autocorrelation measurements of the input, stretched and optimally recompressed pulses for which an autocorrelation coefficient of 0.71 (Gaussian) is used. The measured stretched pulse duration is in agreement with the theoretically predicted value which is determined from the pulse bandwidth (7 Å) and the stretcher geometry. The compressor distance was larger than the effective stretcher distance (the stretcher lens focal length minus the grating-lens separation) in order to additionally compress the chirp on the input pulse.

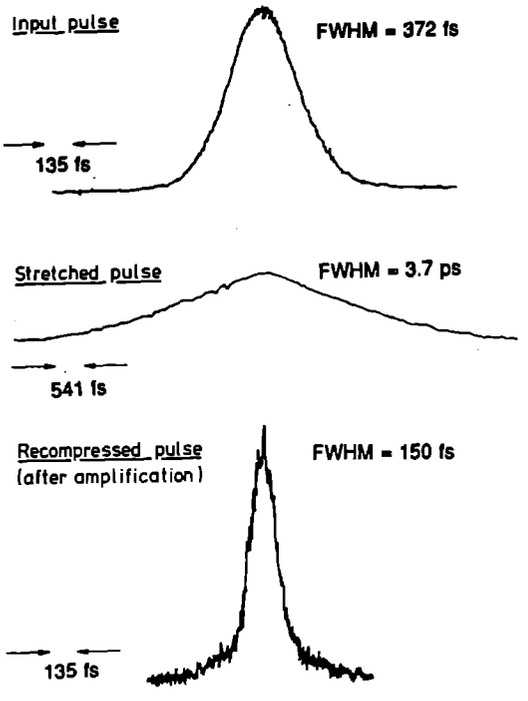

Fig 4 CPA autocorrelations.

The input pulse was also directly compressed after 2-pass amplification in a parallel 3600 1/mm grating geometry and the minimum recompressed duration was found to be the same as the minimum recompressed duration obtained in the stretch/recompress configuration, within the limits of spectral stability of the system. The spectral characteristics of pulses were dependent on dye laser alignment and on dye and KrF amplification and were regularly monitored.

Spectral measurements of the stretched pulse before and after saturated amplification showed that there was significant spectral profile and pulse shape distortion under amplification. The stretcher introduces additional linear positive chirp and under homogeneous saturated amplification the long wavelength leading edge of the pulse is amplified preferentially with respect to the short wavelength trailing edge. Relative suppression of the short wavelength components was seen to be strongest in the most intense parts of the amplified stretched beam. Assuming a Gaussian time-bandwidth product, the recompressed pulse duration was approximately transform-limited (Fig 5).

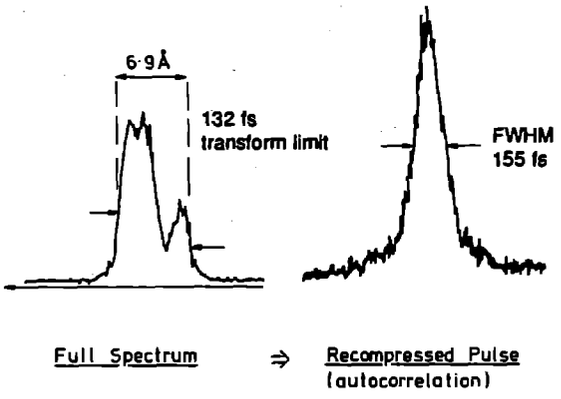

Fig 5 Spectral and temporal profiles of recompressed pulses.

Studies involving spectral filtering at the spectral plane of the stretcher were conducted. Blocking portions of the long and short wavelength ends of the spectrum led to an increase in the recompressed pulse duration (Fig 6) with these lower intensity components contributing strongly to the effective time-bandwidth product of the recompressed pulses. The shortest recompressed pulse durations were obtained by spectrally filtering out a proportion of the centre of the spectrum without attenuating the longer wavelength components resulting in reduced suppression of the short wavelength components in the second amplification pass. The principal conclusion of the spectral filtering study is that the recompressed pulse duration is critically dependent on the full bandwidth of the recompressed pulse and that the relative spectral intensities in the recompressed pulse do not significantly affect recompressed pulse duration. It is expected however that spectral profile distortion under amplification has a stronger effect on the contrast ratio of the recompressed pulse. Saturated amplification of certain pulse shapes leads to a spectral shift resulting in off-peak gain amplification which in turn results in reduced energy extraction efficiency from the amplifier.

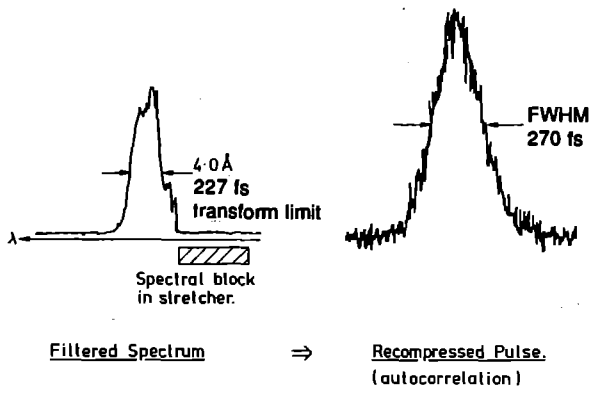

Fig 6 CPA with spectral filtering

A study of the independent and interrelated effects of the input beam collimation, stretcher collimation due to stretcher back mirror positioning and compressor distance on recompressed pulse duration was carried out. It was found that there is no critical dependence on input or stretcher collimation for faithful recompression and it was observed that a non-collimated beam can be optimally recompressed by marginal adjustment of the compressor distance with respect to the collimated beam compression distance. The system showed considerable geometrical tolerance both for diffraction geometry symmetry between the stretcher and the compressor and for the criticality of compressor distance. It should be noted that the geometry was designed to be tolerant to wavefront distortion[1].

The recompressed pulse focusability was investigated using a 5 m focal length lens arrangement. The recompressed pulse was found to be 1.5 times diffraction limited. This represented only a small deterioration in focusability with respect to the 500 fs input pulse.

A new technique for investigating pulse contrast characteristics was used (Fig 7). The pulse was focused into a long (25 cm) rod of silica which acts as a strong nonlinear attenuator due to two-photon absorption. The output was focused through a spatial filter pinhole onto an energy monitor. By varying the input energy and measuring the energy with and without the rod, the intensity dependent suppression of the main pulse relative to the low intensity pedestal was calibrated and an estimation could be made of the intensity in the pedestal of the recompressed pulses. This gave a value of about 0.1% of the peak intensity.

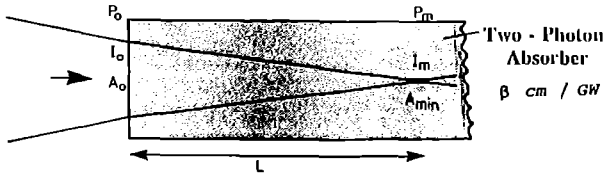

PEAK POWER SUPPRESSION RATIO:

$$\frac{P_0}{P_m} = \frac{\pi}{2} \times \sqrt{\frac{A_0}{A_{min}}} \times (\beta \times I_0 \times L)$$

Eg. $\beta \times I_0 \times L = 50$, $\frac{A_0}{A_{min}} = 10^6$ $\Rightarrow$ $\frac{P_0}{P_m} = 8 \times 10^4$

Fig 7 Pre-pulse enhancement for measurement.

The subpicosecond CPA experiment reported here, in conjunction with picosecond CPA experiments reported elsewhere[1,6] has provided verification and insight into CPA operation at 249 nm. This has enabled us to design a full 100 fs CPA experiment for the SPRITE laser with expected recompressed pulse energy 1-2 J.

REFERENCES

1. Central Laser Facility Annual Report 1991, 112. (1991).

   J R Houliston et al, Technical Digest European Quantum Electronics Conference, Edinburgh, 70, 1991.

2. F Kannari, J Appl Phys, 67, 3954 (1990).

3. T R Gosnell et al, Opt Lett, 16, 1686 (1991).

4. S Szatmari et al, Opt Comm, 79, 64 (1990).

5. P Maine et al, IEEE JQE, QE25, 61 (1989).

6. Central Laser Facility Annual Report 1992, Section 3.2 (1992).

7. S Szatmari, F P Schäfer, Opt Comm 68, 196 (1988).

8. P Simon et al, Opt and Quantum Electronics 23, 73 (1991).

GAIN DEPLETION DUE TO AMPLIFIED SPONTANEOUS EMISSION IN MULTI-PASS LASER AMPLIFIERS.

I Okuda* and M J Shaw

Rutherford Appleton Laboratory
*Electro-Technical Laboratory, Ibaraki, Japan.

INTRODUCTION

The multi-passing of laser amplifiers is frequently used to boost stage gain in laser media of low gain coefficient. For example, a 4-pass telescopic system was recently used by Hofmann et al[1] to amplify sub-picosecond pulses to TW level in an XeF (C-A) laser. Also a similar system has been proposed by Hirst and Shaw[2] for large-aperture KrF amplifiers designed to amplify pulses up to PW level.

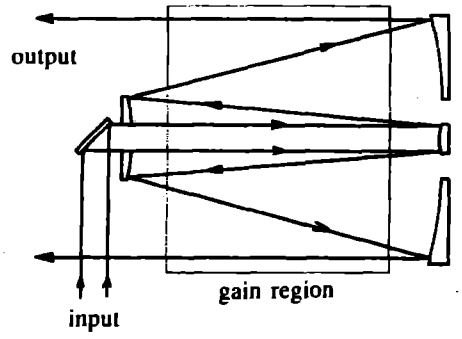

Fig. 1. Conceptual design for a 4-pass beam expanding amplifier for sub-picosecond pulse amplification.

In this paper we discuss the effects of ASE in multi-pass amplifiers. In particular we are interested in the 4-pass Cassagrainian-type scheme depicted in Fig. 1 which is similar to that used in[1]. Such amplifiers are particularly useful in that the optics provide the dual function of multi-passing and beam expansion at the same time. The expanding beam is useful in helping avoid saturation in the early stages of amplification.

RESULTS

Because of the complexity of the multi-pass amplifiers we require to model, we rule out the use of a 3-D ASE code. Instead we have developed a 1-D code which caters for an extended ASE source in cylindrical symmetry by simple approximations.[3] The pumping of the medium is assumed to be axially and radially uniform. The ASE depletion of the telescopic 4-pass scheme is compared with the case of two double-pass amplifiers in series and a long single-pass amplifier having four equal gain regions. These three types are shown unfolded in Fig 2.

The total small-signal gain-length products for the ASE depleted amplifiers are shown in Fig 3. The telescopic 4-pass system is shown to be less depleted than either the equivalent single-pass amplifier or the two double-pass amplifiers in series. For an undepleted total gain-length product $g_0L = 12$, the total depleted gain for the type A amplifier $g_dL = 10.7$ and so the effect of ASE at this total gain value is small.

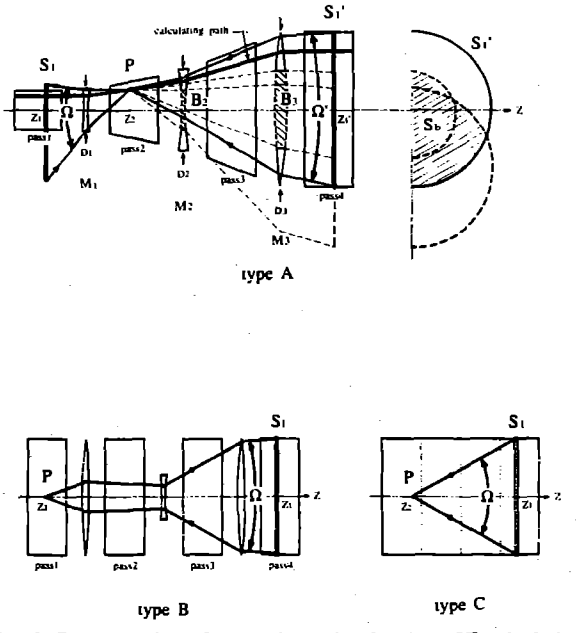

Fig. 2. Determination of the solid angles for the ASE calculation in 4-pass amplifiers. Amplifiers are shown with the 4 passes unfolded. Type A is a beam expanding amplifier where the signal beam expands in passes 2 and 3. Type B is two coupled double-pass amplifiers having full aperture input and output signal beams. Type C represents 4 single-pass amplifiers coupled together with a parallel signal beam.

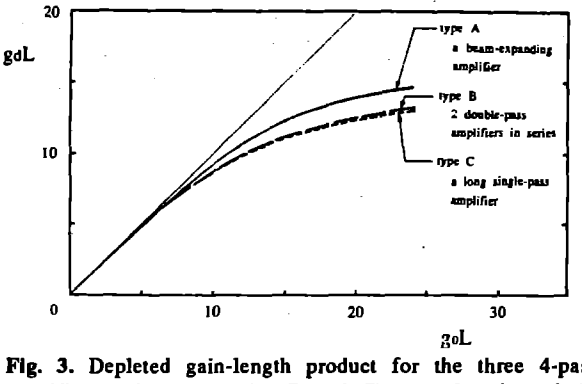

Fig. 3. Depleted gain-length product for the three 4-pass amplifier configurations (A, B and C) as a function of the undepleted total gain-length product.

REFERENCES

1.T. Hofmann, T.E. Sharp, C.B. Dane, P.J. Wisoff, W.L.Wilson, F.K. Tittel, and G. Szabó: Proc SPIE, **1412**, 84 (1991)
2. G.J. Hirst and M.J. Shaw: Appl. Phys. B, **52**, 331 (1991)
3. I Okuda and M J Shaw: Appl. Phys. B accepted for publication

SCATTER AND UV DAMAGE THRESHOLD MEASUREMENTS

David T Sheerin and David C Emmony

Loughborough University of Technology

INTRODUCTION

Scatter from optical components can considerably impair the efficiency of multiplexed systems especially when the interbeam angle is very small (of the order of mR)[1]. Problems arising from crosstalk due to scatter from laser windows lead to loss of resolution, loss of energy, introduce secondary pulses and markedly reduce the final peak power delivered at the focus. Knowledge of the near angle scatter characteristics of all components used to deliver the beams to the impact area is therefore clearly desirable.

This report describes the progress to date of the scatterometer built in the Physics Department at Loughborough. This instrument was designed to investigate the progressive growth of near angle scatter on a variety of dielectric thin film combinations when exposed to fluorine environments.

Also presented are results from the damage testing of dielectric thin films to establish their UV damage threshold at 248 nm. It has been reported that laser annealing of fluoride dielectric multilayers has led to a significant improvement in the damage threshold and data is presented that supports this hypothesis although it does not seem to hold for all materials.

EXPERIMENTAL ARRANGEMENT

A diagrammatic representation of the apparatus is shown in Fig. 1 below:

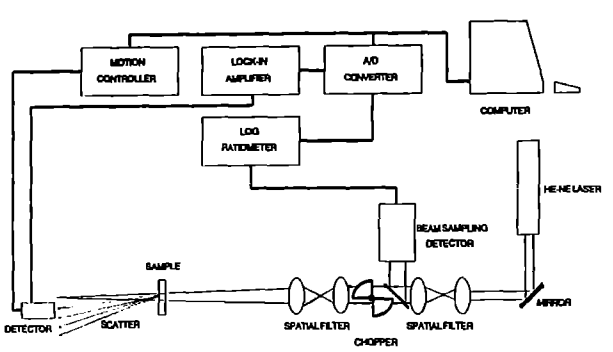

Fig. 1

A number of changes to the instrument described previously[2] has led to improved efficiency in terms of reduction of the signature (the instrument's own scatter profile when no sample was present) by using less focusing elements, and by reducing the number of sensing elements (photodiodes) to just one has allowed problems associated with electrical noise when switching between elements to be minimised. Angle resolved scatter data thus relies upon the translation of one photodiode.

RESULTS

The results are divided into two main sections, namely the results from scatter measurements and those from the damage testing.

(a) *Effect of Fluorine Exposure on the Near Angle Scatter Properties of Optical Components:*

Scatter data is presented in BTDF format. This may simply be stated as the ratio of scattered radiance (dP), normalised by the incident irradiance (P), and divided by the solid angle subtended at the surface by the detecting aperture $d\omega \cos(\theta)$:

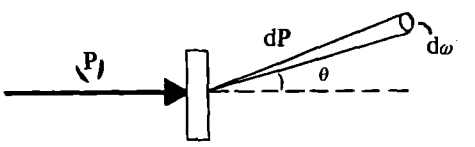

$$\text{BTDF} = \frac{dP/d\omega}{P \cos(\theta)}$$

Differences between the instrumental signature and the recorded scattered intensity can differ by several orders of magnitude. BTDF data is therefore presented in logarithmic format with BTDF vs. angle from specular (in mR).

Windows exposed to fluorine can degrade with time due to etching effects of hydrofluoric acid and it is of interest to know how each component is able to resist such chemical attack and what the effect is on its scattering characteristics over a period of time.

Before any dielectric thin film combinations were exposed to fluorine however, it was decided to look at how uncoated silica windows degraded at differing fluorine concentrations to see what fluorine concentrations would be needed to produce any effect on the dielectric coatings. Fig. 2 shows the scatter on three separate silica windows after a period of 45 minutes exposure. As expected the sample exposed to the highest concentration etched very badly very quickly whilst it was found that the sample exposed to the weakest concentration hardly changed at all, even over a period of days. It was therefore decided that future investigations would use a fluorine concentration of 0.7% fluorine diluted in helium by volume.

Closer inspection of the surface of the samples revealed what appeared to be a periodic etch pattern which was verified by diffraction patterns formed by passing a HeNe beam through the samples[3]. This would seem to indicate that fluorine attack takes place along lines in the fused silica surface which may be associated with the polishing stages or the final chemical cleaning of the silica.

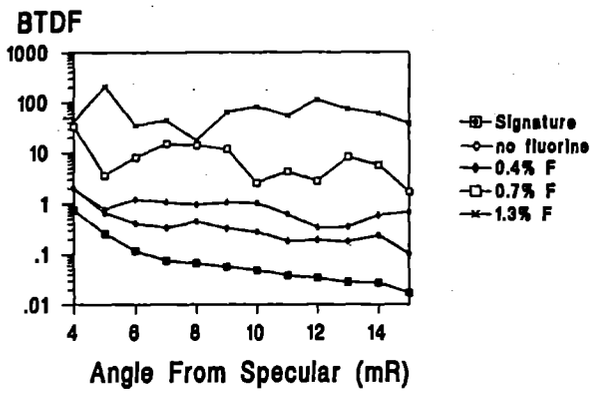

Fig. 2

The next stage was to investigate the fluorine compatibility of dielectric multilayers. Among the samples tested were dysprosium fluoride / cryolite, thorium fluoride / cryolite, and gadolinium fluoride / cryolite. Each sample was exposed to a 0.7% fluorine atmosphere.

Little change was observed in all cases apart from the gadolinium fluoride / cryolite sample. Fig. 3 shows the increase in scatter as a function of time.

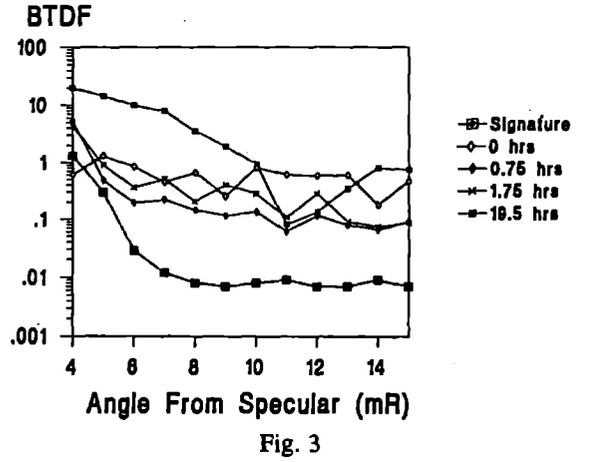

Fig. 3

(b) *Effect of Laser Annealing on the Damage Threshold of Dielectric Multilayers:*

Izawa et al[4] have found that the single shot damage threshold of various fluoride multilayers increased, in some cases by a factor of more than two, by irradiating the sampling site to a steadily ramped fluence, it was decided to use the same technique on the selected coatings mentioned above. Among the first samples to be studied were a gadolinium fluoride / cryolite HR composing of approximately 20 HI/LI layers. The single shot damage threshold gave a 100% probability of damage after 1 shot at around 11 J/cm^2, which agreed with Izawa's results for the same material. Fig. 4 shows the damage threshold graph together with the results from irradiating the sample with multiple low fluence shots. Each vertical tick represents 10 shots at that fluence. No significant improvement was seen unlike the samples tested by Izawa who reported an increase in the damage threshold by a factor of 2.7.

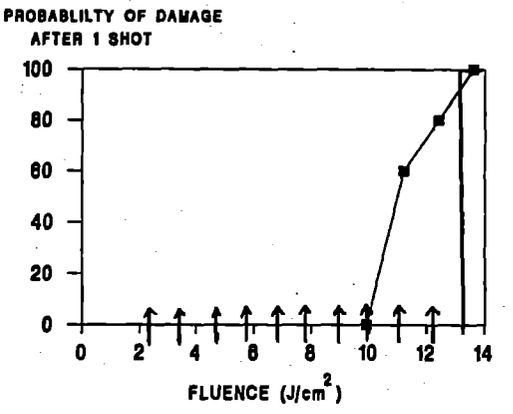

Fig. 4

The same technique was applied to a dysprosium fluoride / cryolite combination and as can be seen from Fig. 5, a significant improvement was observed - the 100% damage threshold increasing from 3 J/cm^2 to around 8 J/cm^2.

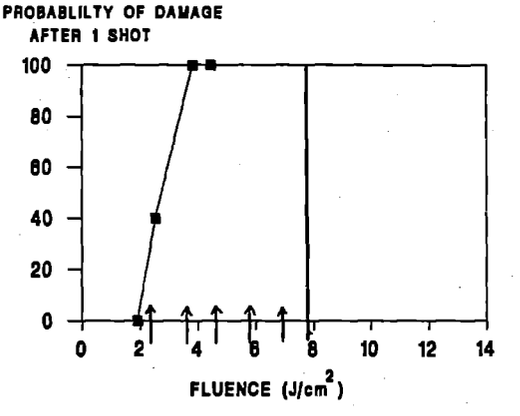

Fig. 5

These results indicate that the method of laser annealing when applied to certain thin film multilayers could be a viable method of improving damage thresholds, although it remains to be seen whether the technique is applicable in every situation.

REFERENCES

1. M.H. Key, M.J. Shaw, I.N. Ross, P.A. Rodgers and M.C. Gower, Analysis of High Power KrF Laser Systems Report RAL-89-133, 1989.

2. D.T. Sheerin and D.C. Emmony, RAL Annual Report RAL-91-025, p. 122, 1991.

3. D.T. Sheerin, D.C. Emmony, C.J. Hooker, I.N. Ross and M.J. Shaw, Proc. SPIE., 1991, to be published.

4. T. Izawa, N. Yamamura, R. Uchimura, I. Hashimoto, T. Yakuoh, Y. Owadano, Y. Matsumoto and M. Yano, Proc. SPIE, 1441, p. 339, 1990.

PERFORMANCE OF THE OBERON LASER-TRIGGERED OUTPUT SWITCHES

G J Hirst, R Bailly-Salins and M J Shaw

Rutherford Appleton Laboratory

INTRODUCTION

The design and preliminary testing of an Oberon output switch was described in the 1990 and 1991 Annual Reports[1]. Since then the switch has been tested up to full voltage and its laser-triggered performance has been investigated. A second switch has been constructed, using insulators made from alumina-loaded epoxy, and the results of initial tests on this are now becoming available.

SELF-BREAK CHARACTERISTICS

The switch was designed to operate at an SF_6 pressure of 60 psia, where a brief literature survey[2] suggested the cathode breakdown field would be 320 kV/cm. Electrostatic analysis showed that this field would be reached at a switch voltage between 2.05 and 2.10 MV. The operating voltage would be 1.7 MV so the switch would be running at slightly more than 80% of self-break. This would be comfortable if the self-break voltage was reasonably reproducible.

Figure 1 shows the self-break voltage measured for both switches. Each point represents a single shot, the data being taken over a period of approximately 1 year. Switch 1 was the older switch, switch 2 the more recent version with the loaded-epoxy insulators. The Marx voltage was adjusted so that the gaps always broke at the same point on the PFL charging curve. This eliminated any dependence of the self-break on the charging time, which was about 0.8 μs.

It is clear from figure 1 that the self-break voltage is very reproducible, both for each individual switch and also between the two switches. The mean measured self-break voltage at 60 psia was 2.07 MV, in very good agrement with

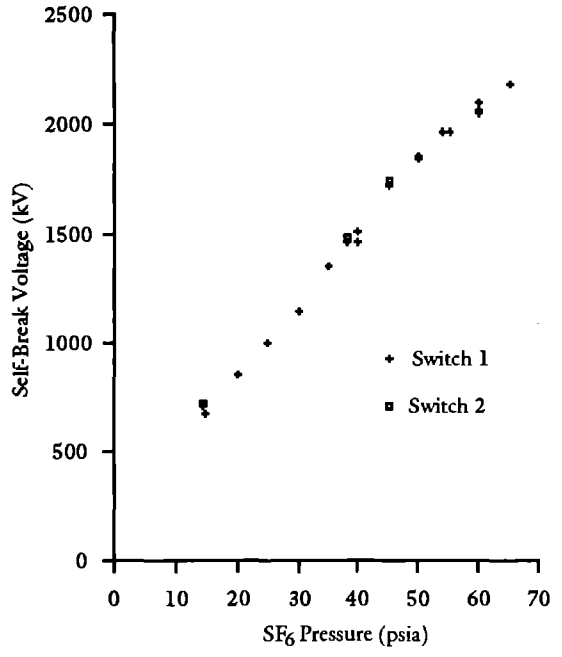

Figure 1: Switch self-break voltage as a function of pressure.

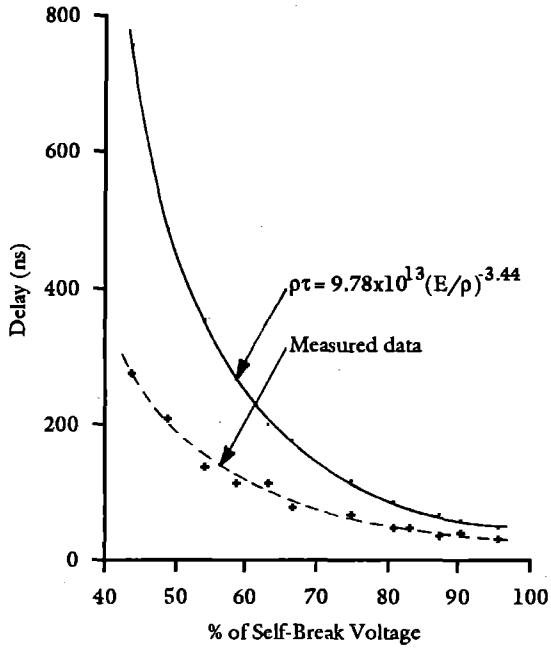

Figure 2: Switch triggering delay as a function of percentage of self-break.

the design figure. Above 50 psia the dependence of the self-break on pressure seems to become slightly sublinear. This effect has been reported elsewhere[3].

LASER-TRIGGERED PERFORMANCE

The switches have been laser-triggered using both the three-channel optics described elsewhere[1] and a simpler set of single-channel optics, consisting of a 45° prism and an 85 mm focal-length lens. In both cases the laser energy used was far in excess of that needed to produce a spark in the SF_6. Despite changes to the output line impedance and an increase in the switch operating pressure it has still been difficult to achieve three-channel operation. The benefit from the reduced switch inductance was also relatively small so three-channel operation has not been pursued.

The switch performance was assessed by measuring the delay between the start of the laser pulse in the spark gap and the start of the switch's voltage collapse. Switching is most reliable when this delay is shortest and the timing jitter is then at a minimum. Figure 2 shows the delay as a function of the voltage at which the switch was triggered. These results were taken with 60 psia of SF_6 in the gap, using the three-channel optics. The shortest delays were 30-50 ns, achieved at voltages between 80% and 96% of self-break. At 80% the timing jitter was 3.9 ns (1σ) taken over 11 shots.

Also shown in figure 2 is the delay curve predicted using the formula of Martin[3]. This relates the delay, τ, to the gas density, ρ, and the mean electric field in the gap, E. The discrepancy between the formula and the measured results is explained by Martin in terms of the ionisation produced

by the trigger laser "shorting out" part of the gap. This increases the effective E-field in the remainder, thus reducing the delay. If the delay is measured then the enhanced E can be deduced and in the mean-field approximation the shorted length, X, can be calculated in terms of the gap spacing, D. This has been carried out for the data of figure 2 and the results are shown in figure 3.

The calculated values of X/D vary between 0.1 and 0.26. Photographs of the switch arcs[1] suggest that a slightly larger fraction, perhaps 0.3-0.4, of the arc length is influenced by the trigger laser. The discrepancy can be explained by recalling that the arcs are not straight. The unshorted length is therefore greater than D minus X and the effective field is less than the simple mean-field approximation would suggest. It is also likely that the fraction of the arc influenced by the trigger laser is not completely shorted out, so again the field in the remainder will be less than the deduced value.

The only assertion in Martin's paper which is not supported by our data is that "X ... disappears rapidly when the laser is turned off". Figure 3 shows that X survives for at least 250 ns and earlier data show that kinked arcs are produced for up to a microsecond after the laser pulse. (The apparent tendency for X/D to *increase* with delay in figure 3 may be due in part to a slow fall in the laser pulse energy, which was lower for the short-delay data.)

The present machine configuration has two PFLs connected to separate 5.5 Ω dummy loads via separate switches. Because the switch triggering has been so reliable it has been possible to fire one switch without the other, connecting the PFLs in series to one load. The resulting 685 ns waveform (FWHM) is shown in figure 4, the central dip being caused by the transfer tank inductance which isolates the two PFLs. The waveform is obviously not ideal but it should allow some basic diode testing with extended pulse durations.

SWITCH RELIABILITY

Over the last year the switches have, between them, been pulsed up to volts a total of 254 times. 112 of these reached

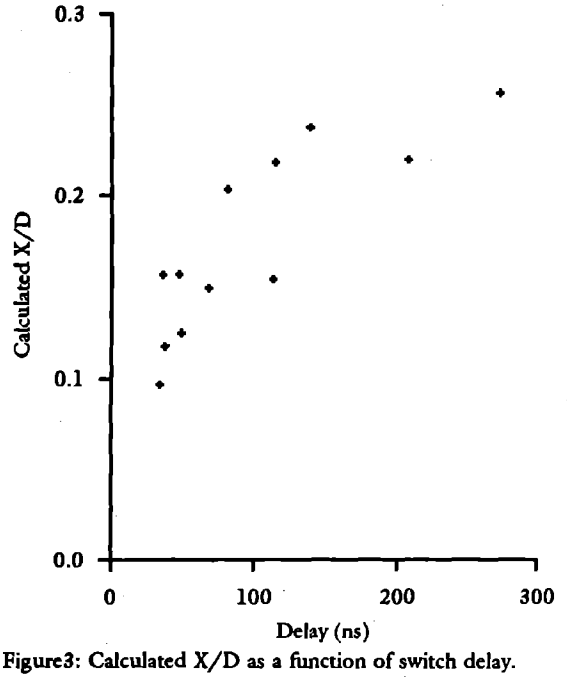

Figure3: Calculated X/D as a function of switch delay.

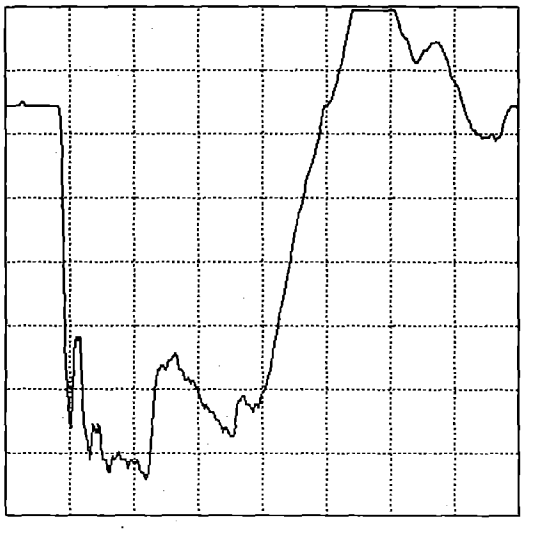

Figure 4: Output voltage when only one switch is fired (200 ns/div, 52.7 kV/div).

or exceeded the 1.7 MV design voltage. The maximum voltage (on switch 1) was nearly 2.2 MV. There were no cases of unplanned self-breaking. The switch optics, which were fused silica, were checked several times in this period but showed no sign of dust contamination or etching.

There were only three cases of the switches tracking, all on 1.7 MV shots and all on the PFL insulator. In the first 80 shots there were two tracks on switch 1. Both occurred long after the switch had closed. There was evidence to suggest that water had leaked through from the PFL and had run down the insulator, causing a track on the next shot. The water seal was cleaned and reassembled and the tracking has not recurred. The third track, on switch 2, happened at peak volts, just as the switch should have closed. Afterwards the lens which had been mounted inside the anode was found to have shattered, possibly on the previous shot. One of the sharp fragments had fallen to the bottom of the PFL insulator and could then have initiated the track. The reason for the lens failure is not clear, but its proximity to the arc may have exposed it to excessive blast when the switch closed. It has been replaced by a sapphire lens and tests are continuing.

REFERENCES

1. E M Madraszek and R Bailly-Salins, *Annual Report to the Laser Facility Committee,* Rutherford Appleton Laboratory RAL-90-026 Section B3.3, p.107, (1990).
   G J Hirst, R Bailly-Salins, S Hancock and M J Shaw, *Annual Report to the Laser Facility Committee,* Rutherford Appleton Laboratory RAL-91-025 Section B2.4, p.99, (1991).

2. D Craddock, C B Edwards, F O'Neill and M J Shaw, *Annual Report to the Laser Facility Committee,* Rutherford Appleton Laboratory RL-82-039 Section 2.2, p.2.09, (1982).
   W K Tucker, Report No. SC-DR-72 0506, Sandia Laboratories, Albuquerque NM (1972).
   J R Woodworth, R G Adams and C A Frost, IEEE Transactions on Plasma Science, PS-10 p.257 (1982).

3. T H Martin, Proc. 7th IEEE Pulsed Power Conference, p.73 (1989).

ELECTRICAL MONITORING FOR THE OBERON PULSED POWER SYSTEM

G J Hirst

Rutherford Appleton Laboratory

INTRODUCTION

The Oberon Test Module is an R & D system being used to develop pulsed power components for a proposed operational laser. This paper describes the testing of monitors which measure the machine's pulsed voltages and currents. Pulse lengths are of the order of 1 μs, voltages are typically 1 MV and currents can exceed 100 kA. The characteristics required of the monitors are:

i) Accuracy: particularly important during machine development, when absolute performance levels need to be assessed over wide parameter ranges,
ii) Long-term stability: more important once the machine becomes operational, since monitor degradation then leads to reduced confidence in machine performance and shortened service intervals,
iii) Noise immunity: the pulsed power environment is intrinsically noisy so large signals (hundreds of volts) make good signal-to-noise ratios easier to achieve,
iv) Compactness: monitors need to be physically and electrically unobtrusive, particularly in the machine's highly-stressed "fast" sections.

CURRENT MONITORS

The simplest current monitor is the resistive shunt, usually placed in the outer earth return of a coaxial transmission line. The Oberon Test Module shunt consists of 200 1 Ω carbon resistors in parallel. Its sensitivity, 5 mV/A, is easily calculated and is accurate provided that voltage-dependent resistance changes do not become significant. Shunts are very stable and can give more than adequate signal levels. They suffer, however, from the drawback that in a complex machine there may be many earth returns and the shunt may be partially shorted out.

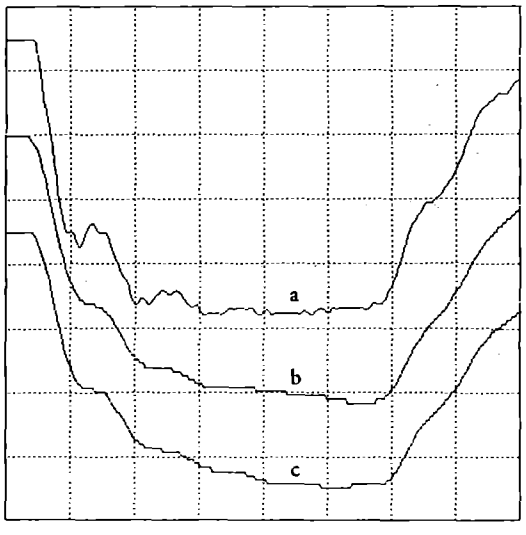

Figure 1: Current traces in the Oberon dummy-load section a) 12.5 kA/div, b) 1.25 x 10^{-5} Vs/div, c) 5.0 x 10^{-6} Vs/div, timebase 50 ns/div.

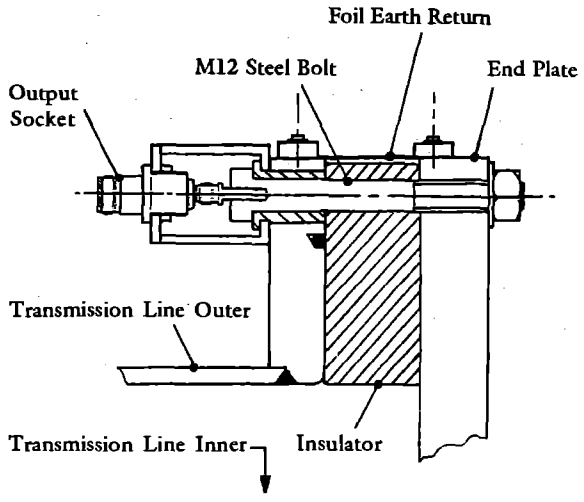

Figure 2: Design of the B-dot loop using the end plate bolt.

An alternative current monitor is the B-dot loop. In its simplest form this is a loop of wire mounted *within* a transmission line in such a way that it is threaded by the B-field associated with the current in the HV conductor. The induced voltage, which is proportional to the derivative of the current, can be digitised and then integrated numerically. A loop of area A, placed a distance r from the axis of a coaxial line, has a sensitivity of $\mu A/2\pi r$ Vs/A, where μ is the magnetic permeability. This is accurate if the field is locally undistorted and if the external circuit imposes no load.

Figure 1 shows three current traces measured in the Oberon dummy-load section, using the resistive shunt (*a*) and two kinds of B-dot loop (*b* and *c*). Trace *a* reaches a peak value of 53 kA, based on the above shunt sensitivity. Trace *b* comes from a simple loop of RG 405 50 Ω microwave cable. Its area is 13.5 cm^2 and it is mounted 27.9 cm from the line axis. The calculated sensitivity of 9.7 x 10^{-10} Vs/A agrees very well with the measured value, given the peak signal of 5.15 x 10^{-5} Vs. Trace *c* was produced using the loop shown in figure 2. This is formed from one of the securing bolts for the dummy-load section's end plate. One end of each bolt is insulated, resulting in an open loop made up of the bolt and the earth return. The loop area is difficult to estimate because the current-flow is distributed across the bolt section and the magnetic field is also locally distorted, but as a simple estimate the loop edge is assumed to pass through the centre of the bolt. The resulting area is 6.15 cm^2, centred 37.8 cm from the line axis. This gives a sensitivity of 3.26 x 10^{-10} Vs/A. The peak measured signal is 2 x 10^{-5} Vs, yielding a sensitivity of 3.77 x 10^{-10} Vs/A, which is in reasonable agreement with the calculation.

The B-dot loops are simple, stable and noise-immune. The design using the bolt is also compact. Their sensitivity cannot be calculated sufficiently accurately to dispense with independent calibration, but there is no substantial disagreement with the basic theory. The only outstanding problem with both loops is their apparently slow response time (see figure 1). This is being investigated further.

VOLTAGE MONITORS

The three different sorts of voltage monitors presently in use are resistive dividers, capacitative dividers and D-dot probes.

The resistive dividers use dishwasher powder solution as the electrolyte[1] contained in flexible PVC tubing with stainless steel electrodes. Typical resistances are a few kΩ in series with a few Ω. They have worked well, remaining stable over 1-2 years and needing no maintenance so far. Experience elsewhere, however, has shown that PVC eventually loses its plasticity in transformer oil and that fluid leaks then arise. They are also relatively complicated to assemble and they are limited to electric fields of <100 kV/cm. Although it is possible to calculate a sensitivity based on the resistors' geometry, the flexibility of the PVC usually makes this too unreliable so calibration is necessary.

Measurements of the voltage in the water-filled transmission lines have routinely been made using compact capacitative dividers. These are very similar in design to those used on Sprite[2], with the circuit shown in figure 3. R_1 and R_2 represent the resistance of the deionised water which is the dielectric in C_1 and C_2. They do not affect the division ratio since R_1C_1 is equal to R_2C_2. R_3 must be sufficiently large that it does not divert a significant fraction of the C_1 current away from C_2, thus leading to "droop" of the monitor waveform. This is equivalent to the constraint that R_3C_2 is much longer than the duration of the pulse being measured. In the Oberon PFL the estimated value of C_2 is 1780 pF and R_3 is 56.7 kΩ so the RC time is 101 μs, which is indeed much longer than the 1-2 μs PFL charge time.

The calculated division ratio of the whole monitor is $(C_2+C_1)(50+R_3(1+50/R_4))/50C_1 : 1$. C_1 is estimated to be 11.3 pF and R_4 is 470 Ω giving a ratio of 199300:1. The measured division ratios of two such monitors were 192000:1 and 196000:1. The small discrepancies between these figures and the predicted value are almost certainly due to inaccuracies in the estimated capacitances. The monitor risetime should be limited only by the size of the metal cylinder which forms the lower electrode of C_1 and the upper electrode of C_2. As a voltage wave propagates down the PFL it passes across the flat end of this cylinder and part of it is diverted into the monitor. The risetime of the resulting signal cannot be shorter than the transit time across the flat face, which in the Oberon PFL is a little over 2 ns. Keeping the risetime short imposes a second constraint, now on the maximum size of C_1.

The major limitation of the capacitative divider is the low signal level it delivers, with the constraints on C_1 and R_3C_2 preventing the division ratio from being reduced substantially. In the Oberon PFL the peak signal is 5-10 V, which is acceptable, but attempts to use the same monitor in the oil section beyond the switch were not successful. The much lower dielectric constant of oil, compared with water, led to lower values of C_1 and C_2. This required a corresponding increase in R_3 with a resultant increase in the division ratio. The signal then became swamped by noise.

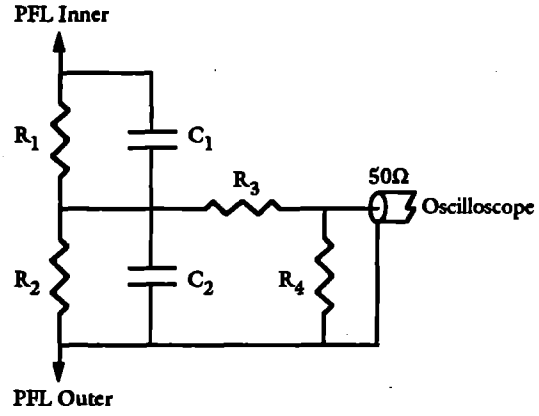

Figure 3: Circuit of the capacitative divider.

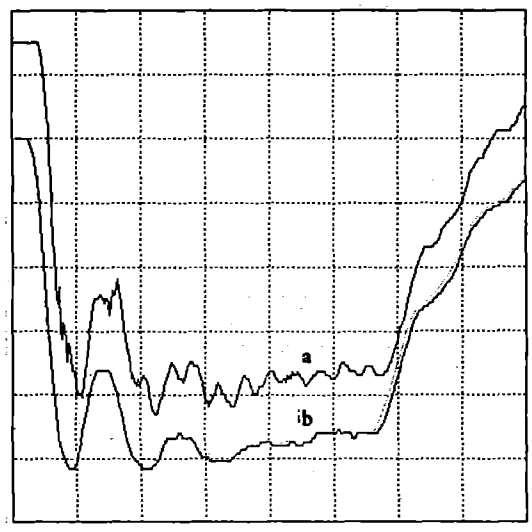

Figure 4: Voltage traces in the Oberon diode feed section a) 50 kV/div, b) 1.25×10^{-6} Vs/div, timebase 50 ns/div.

The solution to this problem was to reconfigure the monitor as a D-dot probe. R_3 was set to zero and R_4 was reduced to 33 Ω. Almost all of the C_1 current now flows through R_4 in parallel with the 50 Ω cable, whose combined resistance shorts C_2 on timescales longer than a nanosecond or so. The voltage across R_4 is proportional to the C_1 current and is small by comparison with the C_1 voltage. In this approximation the C_1 current is proportional to the derivative of the C_1 voltage i.e. the output signal is proportional to the derivative of the voltage being measured. The constant of proportionality is $50R_4C_1/(50+R_4)$ Vs/V. The estimated value of C_1 is 0.889 pF which gives a calculated monitor sensitivity of 1.77×10^{-11} Vs/V.

Figure 4 shows voltage traces measured in the Oberon diode feed, using a resistive load in place of the vacuum diode. Trace *a* comes from a separately calibrated resistive divider. The average voltage towards the end of the trace is 256 kV. Trace *b* is from the D-dot probe. The signal level which corresponds to 256 kV is 5.84×10^{-6} Vs so the measured sensitivity is 2.28×10^{-11} Vs/V. There is thus a 30% discrepancy between the resistive and D-dot monitors. As with the B-dot loops the D-dot probe also seems to have a longer risteime than its non-derivative counterpart. These matters are again still under investigation.

REFERENCES

1. G J Hirst, *Annual Report to the Laser Facility Committee,* Rutherford Appleton Laboratory Report RAL-90-026, Section B3.3, p109 (1990).

2. M J Shaw and C B Edwards, *Annual Report to the Laser Facility Committee,* Rutherford Appleton Laboratory Report RL-82-039, Section 2.2.1(d), p2.06 (1982).

MEASUREMENT OF TITANIUM FOIL LIFETIME UNDER REPEATED PRESSURE CYCLING

C.Hylton*, W.Bowsher, S.Hancock, G.J.Hirst, G.Pullinger and M.J.Shaw

Rutherford - Appleton Laboratory
*Newcastle-upon-Tyne Polytechnic

INTRODUCTION

In an electron-beam-pumped KrF laser a thin foil (usually of titanium) is used to separate the diode vacuum where the electrons are accelerated, from the high pressure (~1 bar) laser gas mix. Ideally, for maximum transmission of electrons into the laser cavity, the foil should be as thin as possible. In order to support the thin foil, a grid support structure, commonly known as a hibachi, is used. The open area of the hibachi should be as large as possible, requiring the minimum number of support ribs and those ribs to be as narrow as possible. Constraints on these ideals are determined by the maximum allowable stresses in foil and hibachi materials. Below 25μm thickness the foil is less likely, and is certainly not guarranteed, to be pinhole free and the window area is limited by the ultimate tensile strength of the foil. Likewise, the number and width of ribs is dependent on the need to withstand the total force on the structure (up to 7500N in this test).

The physical effects on the foil and its support grid which occur during and immediately after an electron beam pulse can be divided into four main categories:

1.Transport of charge through the foil (~10μC/cm^2)

2.Flash heating of the foil (typically 10°C-100°C depending on charge density).

3.Chemical reaction of the fluorine in the KrF laser gas with the hot foil.

4. A pressure jump within the laser cell (typically 0.1 - 0.5 bar) due to heating of the laser gas.

Although a combination of these effects could be a factor in any failure, the sudden pressure jump was seen as the most likely major single factor, as reported previously by McGeoch et al [1]. There has been some suspicion, based on experience with the existing e-beam-pumped laser Goblin, that the durability of foils was also related to the aspect ratio of the foil windows, determined by the aperture design of the supporting grid. Those windows which were approximately square suffered a failure mode thought to be caused by sonic effects within the foil at the centre of such windows, showing itself as a stress 'pip' with a pinhole at its peak. Typical foil lifetimes were ~300 shots on Goblin and ~3000 shots on Sprite.

Since the pressure jump on the proposed Titania / Oberon upgrade to the Sprite system was predicted at several times larger than on Sprite and a thinner foil (25μm c.f. 37μm currently in use) for better e-beam transportation is also proposed, an off-line experiment was devised to test the effect of repeated pressure jumps on different foil and hibachi combinations.

EXPERIMENT

Two hibachi grids (~0.5m x 0.1m) with very different aspect ratio windows were made as shown in Fig.1, one 'long', (100mm x 29mm), and one 'square', (57mm x 47.5mm). Real laser pressure and vacuum conditions were simulated by inserting the foil and grid assembly into a test chamber (see Fig.2) where it became the separator between an evacuated section and the pulsed pressure section. The

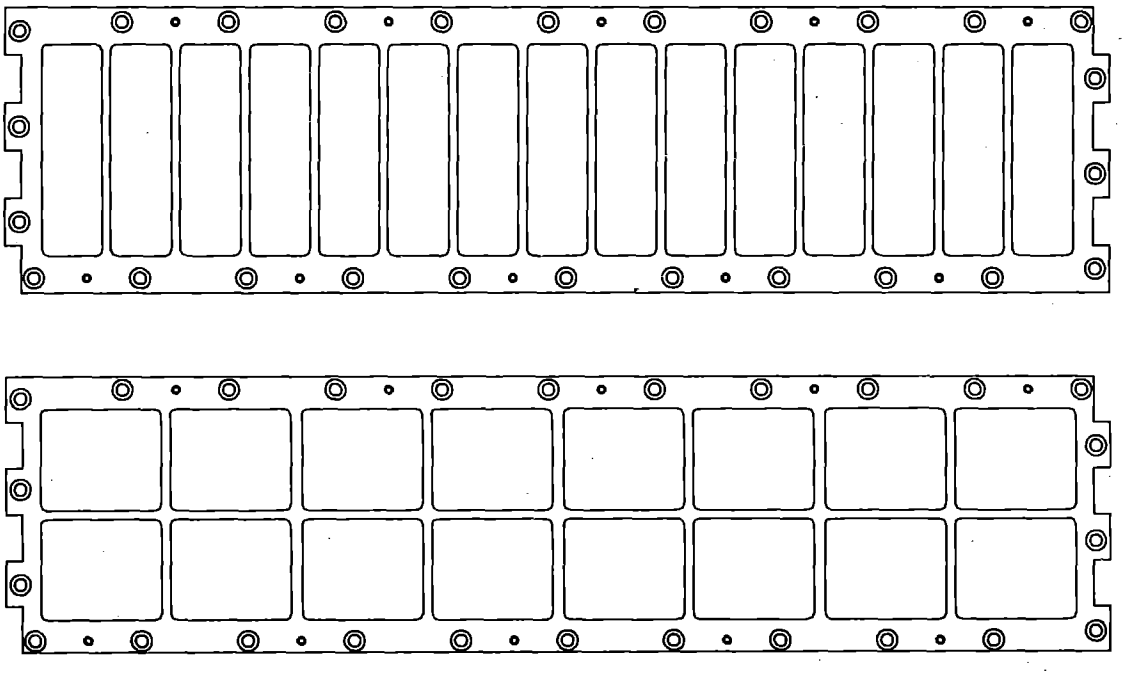

Fig.1 Long and 'square' window hibachis (~0.5m x 0.1m)

vacuum side was pumped down to ~0.05mbar. The pressure pulse was applied to the foil by first pressurising an ante-chamber of ~20ml volume to 6 - 9 bar with helium via valve V1 from a cylinder. The gas was expanded into the main chamber (~120ml) volume via a fast acting solenoid valve V2(RS439-060). The resultant pressure jump was in the region of 0.6 - 0.9 bar. Helium was used to give a rapid pressure rise (due to its low mass).

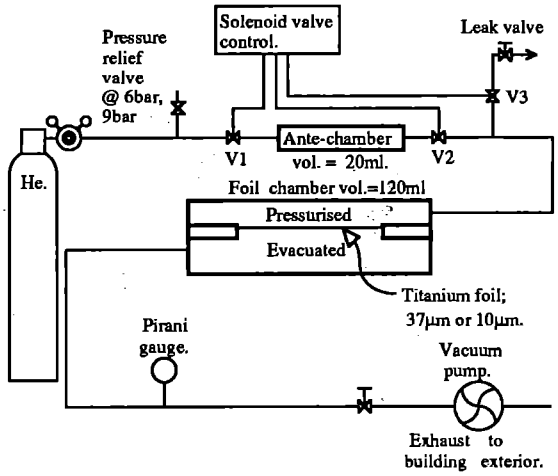

Fig.2 Schematic diagram of testing equipment

Fig.3 shows the pressure jump as recorded by a fast pressure transducer (Bell+Howell 4-366-0001-01M0). The 10% to 90% rise time of pressure was 5ms. After pausing at the peak pressure for 1.75s valve V3 was opened to exhaust the system to atmospheric pressure. The complete pressure cycle time was 12s.

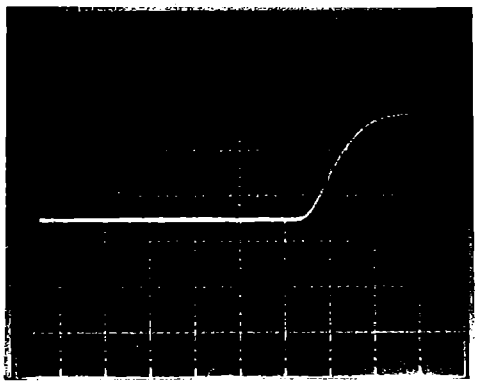

Fig.3 Typical pressure jump, 5ms/div., 0.8bar

The cycling of the valves was controlled by a motor driven cam-switched assembly. A Pirani gauge was connected to the evacuated side in order to detect the increase in pressure resulting from foil pinholes and the Pirani gauge's trip contacts were interlocked with the cam-switch motor. A cycle counter was incorporated in the control box.

RESULTS

The two different designs of hibachi were initially tested with 0.6 and 0.8 bar pulses with foil of 37μm thickness as currently used on Goblin and Sprite and this was followed by tests with 10μm foil, previously only used as a pre-foil for Goblin and Sprite, also at 0.6 and 0.8 bar. The results obtained are shown in Table 1.

Table 1.

Hibachi type	Foil thickness/ mm	No. of cycles	Pressure pulse/bar	Result
Long(29 x 100)mm	37	6370 +1359	0.6 0.8	no failure
Square (57x47.5) mm	37	11000	0.6	no failure
Square	10	~8700	0.6	failure*
Long	10	10000	0.8	no failure

* Pinhole failure occurred ~1mm away from a window due to pitting in the hibachi frame surface.

DISCUSSION

The 'lifetime' of these foil samples, (not less than 7500 'shots' and up to 11000 shots with no sign of failure), is far in excess of that experienced with those in service. The amplitude of the pressure pulse was much greater than that expected in service although the speed was not quite as sudden.

We are left with the conclusion that either the rise time of the pulse is very important to foil failure or that foil heating or charge transport is the main problem. In previous work[1], the thermal effects were thought to be unimportant. However, it is worth considering the greatly differing lengths of heat path to the ribs (which act as the heat sink). In the example quoted in [1] this was ~3 - 5 mm compared with that on Goblin which is ~25mm. The effect would be that the foil would remain hot for much longer in our case and the thermal effect may well be more important. An experiment to stress the foil with repetitive heat pulses as well as combined heat - pressure pulses would clearly be informative.

REFERENCE

1.M McGeoch, AJ DeFuria, CT Pike,"Pulsed Electric Laser Technology - Electron Beam Window Foil Material" Avco Everett Research Lab. Everett MA 02149, Tech Report No.RH-CR-84-13, US ARMY MISSILE COMMAND, Redstone Arsenal, Alabama 35898 (Jan. 1984).

DESIGN OF THE TITANIA AMPLIFIER MODULE

S Angood, R Bailly-Salins*, G J Hirst and M J Shaw

Rutherford Appleton Laboratory
* On leave from CEA, Is-sur-Tille, France

INTRODUCTION

In the Titania upgrade to the Sprite Laser System (section B2) a new KrF amplifier module will be installed in R2. The pulsed power design of this module is the subject of this paper. The optical parameters of the amplifier call for an aperture of 400 mm and a gain length of 1.5 m. The module will amplify a total of 96 pulses of 1.5 ns separation and so the required gain window is 144 ns. Allowance for gain risetime and amplifier fill time increased this duration to 168 ns for the pumping pulse duration. The required total energy from the KrF system was 600J (for 300 ps pulses) which implies a module capability of more than 1.5 kJ for CW extraction over the pumping time.

PUMPING REQUIREMENTS

The gas mix and operating pressure determine the electron beam voltage. A 50 % Ar/Kr mix was chosen at a pressure of 1000 Torr so that a relatively high e-beam voltage of 600 kV could be used. Use of the simple kinetics code[1] predicts the following parameters assuming a gain length of 150 cm and an overall length of 210 cm:

Assumed gas mix	500/500/3 : Ar/Kr/F2
Assumed pump rate	0.65 MW/cm^3
Saturation Intensity	2.3 MW/cm^2
Gain-length product (g_0L)	8.3
Gain-to-loss ratio	10.0
Output Intensity	8.4 MW/cm^2
Fluorine burn time	300 ns

Table 1. Predicted steady-state laser parameters for the Titania amplifier module.

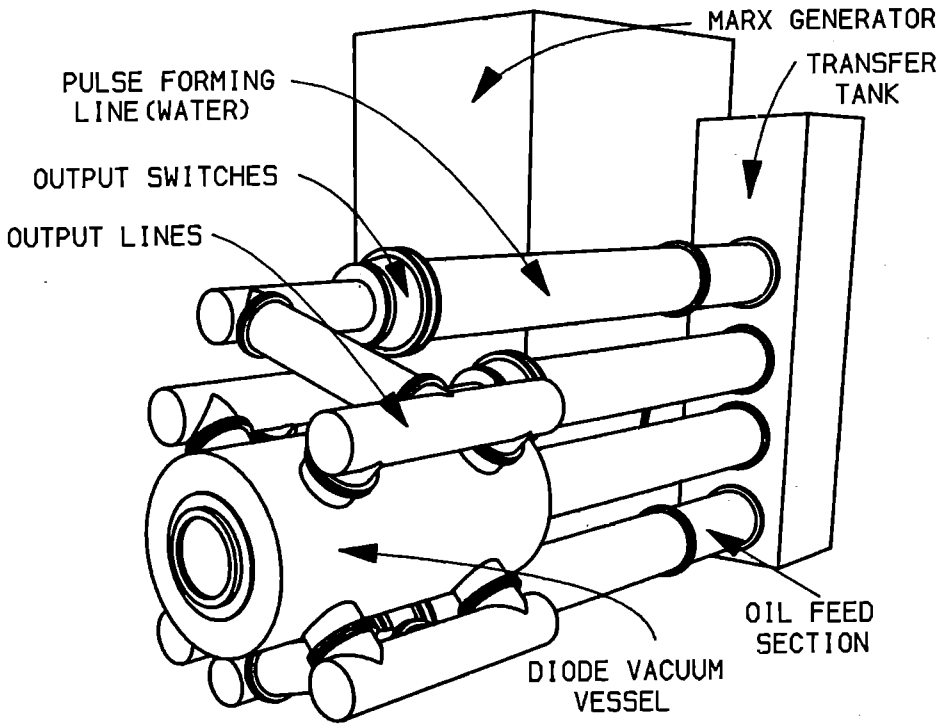

Fig.1. Layout of the Titania laser module showing main pulsed power components

The predicted long pulse output energy is thus 1.7 kJ for a deposited energy of 20 kJ. Assuming a transmission efficiency from diode to gas of 35%, the required diode energy is 57 kJ which at 600 kV and 168 ns implies a machine impedance of exactly 1 ohm. Titania will thus be yet another verification of Martin's Law[2].

PULSE FORMING LINES AND MARX GENERATOR

Four 4 Ω diodes are proposed (see below) each diode being powered by its own matched pulse forming line. For the pulse duration of 168 ns the line length is 2.8 m using water as the dielectric medium. The diameter of the lines is determined by

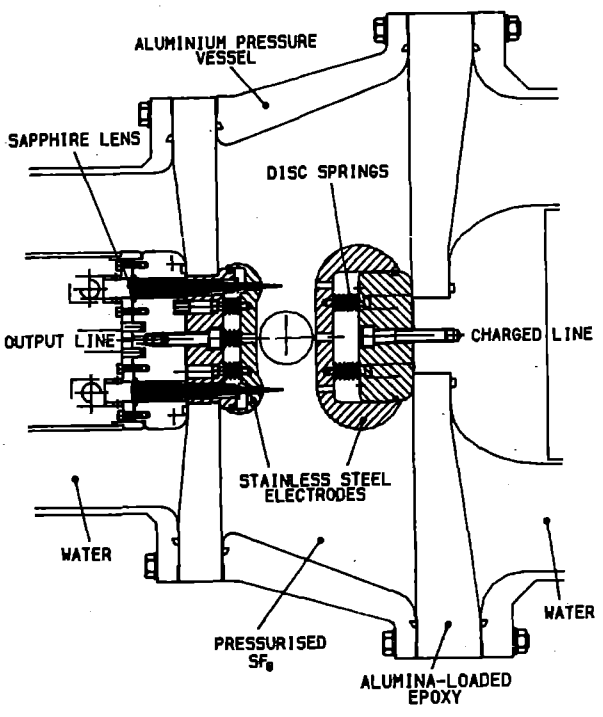

Fig.2. Cross section through the PFL output switch

breakdown at the positive electrode given by the formula $F\,t^{1/3}A^{1/10} = 0.3$ where F is in MV/cm, t is in μs and A, the stressed area, in cm^2. Using standard tube sizes of 448 mm i/d for the outer and 240 mm o/d for the inner, the field at the outer is 86 kV/cm for a 1200 kV charge and the breakdown field (calculated for a single line) is 133 kV/cm. The peak working field is thus 64% of the breakdown field, a suitable safety margin.

The capacitance of the four lines is 84 nF which is exactly matched to a Marx generator of 8 stages (16 capacitors of 1.35 μF) of the Hermes type[3]. Calculation suggests that the 1200 kV line charge should be reached with 87 kV charge on the Marx at a transfer efficiency of 75%. The overall energy flow in the system is given in table 2.

	Voltage	Energy	Transfer Effy
Marx generator	87 kV per stage	82 kJ	
Pulse forming lines	1200 kV	61 kJ	75%
Diodes	590 kV	58 kJ	95%
Gas		20 kJ	35%
Laser Output		1.7 kJ	8.5%
Overall Efficiency			2.0%

Table 2. Energy flow in the Titania Pulsed Power System.

To save costs it was decided to use the existing Marx and transfer tanks so a geometry capable of feeding the 4 radial diodes from 4 in-line PFLs was necessary. It was also required that the output lines between the diodes and the switches have the same length as the PFLs. This latter requirement results from test runs with the Bertha transmission line code[3] which showed that a much cleaner pulse resulted due to the reflections from the diode returning after the main pulse terminates.

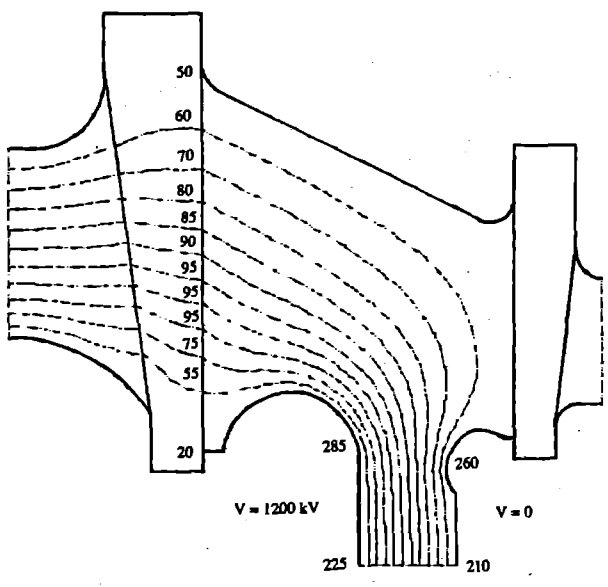

Fig.3. Equipotentials in the PFL output switch at peak charge volts. Numbers give the field magnitude in kV/cm.

The solution arrived at is shown in Fig.1. Two of the lines are connected directly to the transfer tank and the other two are extended forward by extra oil sections. The extra inductance is negligible. The result is that the laser output beam can be taken in the direction of the PFLs and Marx, easily clearing the transfer tank, and resulting in a considerable saving of floor area.

PFL SWITCHES

The most important pulsed power components are the PFL switches. For Titania it has been decided to stay with the radial diaphragm design that has been successfully tested at larger size on the Oberon system (see elsewhere in this section). However, due to the lower line impedance and shorter pulse duration, a much lower inductance is required without increasing the electrical stress on the insulator surfaces.

The design arrived at is shown in Fig.2. The operating pressure is 4 bar of SF_6 and the minimum anode/cathode spacing is 50 mm. Two alumina-loaded epoxy diaphragms support the pressure load. The electric field distribution is shown in Fig.3. The peak cathode field is 285 kV/cm and the peak field on the insulator on the gas side is 95 kV/cm. The cathode breakdown field at 4 bar and 1.5 μs charge time is 320 kV/cm. Shock isolation from the electrodes is obtained by spring washer stacks.

Two laser triggering channels are provided since significant improvement in risetime can be obtained this way. It is calculated that the effective insertion inductance of the switch is 110 nH for a single channel and 60 nH for two channels. A single EMG 150 laser should be able to trigger all 8 spark channels with energy to spare.

DIODE

The four 4 Ω output lines each bifurcate into two 8 Ω sections to feed through into the vacuum diode. The proposed vacuum insulator is a single piece epoxy cone at an angle of 45^{o} in a coaxial feed section. Fig.4 shows the equipotential distribution on the vacuum side obtained using the "MagNet"[3] code. Over the bulk of the insulator the working field is less than 40 kV/cm. The breakdown field is given by $F = 80/ t^{1/6} d^{1/10}$ kV/cm, where t is in μs and d, the distance along the insulator, is in cm. this formula gives F = 80 kV/cm and so the insulator should be very safe even without segmentation and grading rings.

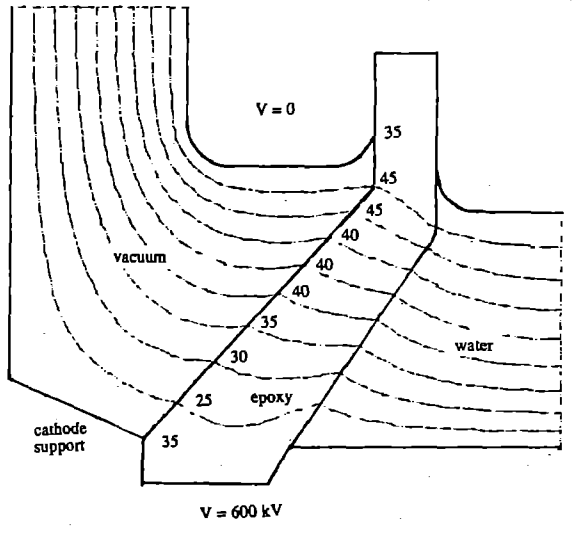

Fig.4. Equipotential plot of the diode vacuum feedthrough. Numbers give the electric field along the vacuum interface in kV/cm.

Within the diode vacuum region it is proposed to divide the emitting region into two parts with separate foil windows so that the laser gas is pumped from eight sides like the ETL Ashura[4] machine. Two cylindrical emitting surfaces will be used so that the pinch effect can be countered by electrostatic defocussing to give a near normal electron trajectory at the anode foil. Fig. 5 shows a calculation from the "e-gun"[5] code of the expected electron trajectories.

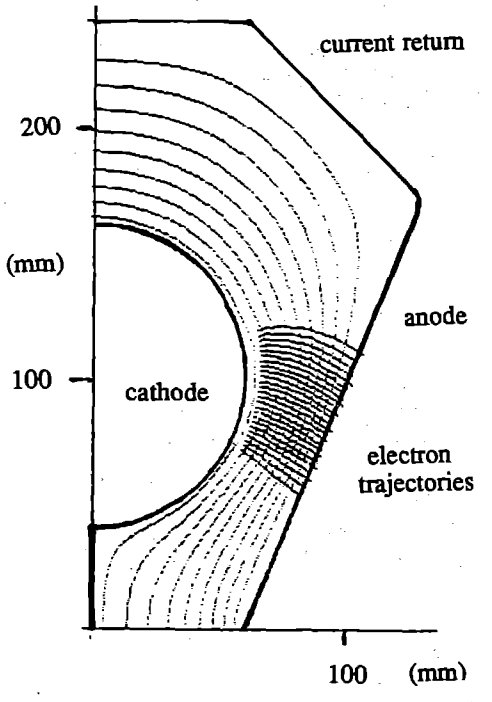

Fig. 5. Electron trajectories in the Titania diode as calculated using the e-gun code.

TIMESCALES

The first component to be tested will be the PFL switch. These tests will be done using the Sprite Marx generator while the Oberon diode tests will test diode components common to both Oberon and Titania. These tests will be completed in the Summer of 92. The new Marx configuration and transfer tank will be installed in the winter 92/93 and the full system should be operational in the summer of 1993.

REFERENCES

1. E C Harvey and M J Shaw, Laser and Part Beams 9, 659 (1991)

2. J C Martin, Public communication on numerous occasions " All large pulsed power machines end up having an impedance of one ohm, thus proving that the ohm is a God-given unit".

3. G J Hirst R Bailly-Salins and M J Shaw, Proc 8th IEEE Pulsed Power Conf p306 (1991)

4. Y Owadano et al, Laser & Part Beams, 7, 383, (1989)

5. W B Hermansfeldt, SLAC Rept. 331 (1988)

SPRITE SHOT STATISTICS

J M D Lister
Rutherford Appleton Laboratory

INTRODUCTION

In the year ending March '92, a total number of 2176 shots were fired on the Sprite KrF laser system. Of these, 492 were target shots and over 500 shots were fired during a Raman characterisation experiment.

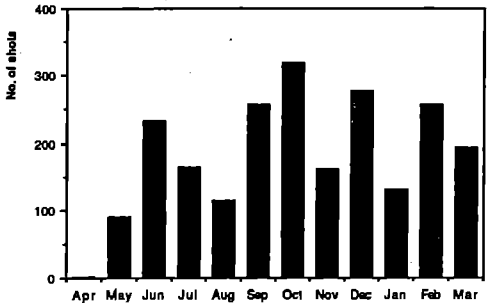

Figure 1: Sprite shot record 1991/92

TARGET SHOOTING

Three target experiments were conducted during the period. In June/July, the X-ray laser consortium used a single Raman beam in line focus geometry using an off-axis parabola/off-axis spheric mirror combination in the target chamber. 114 target shots were fired, the pulse duration was 12ps, and the average energy from the final Raman amplifier was 3.5J.

In December, a total of 210 shots were delivered to target for the Imperial College group. The pulse duration was the same at 12ps, but a spot focus geometry was used. The average output energy was about 4J and the maximum was 6.4J, at a conversion efficiency in the final Raman amplifier of 65%. The divergence of the output beam was below 7μrad.

The X-ray laser consortium returned in February '92 to use the Raman line focus set-up again. For this experiment the average output energy for target shots was 5J, with a maximum 6.9J. During the experiment, broad band spectra were recorded which indicated the presence of spectral lines away from the first Stokes wavelength. An experiment was conducted (see Section B2) to investigate any effect this would have on the fraction of the laser output energy incident on the target. The results indicated that about 40% of the energy measured at the output of the final amplifier was incident on the target, i.e. within a divergence of 20μrad. This suggests a value for the brightness of 1.5×10^{19} W cm^{-2} st^{-1}. The peak brightness, however, is almost 1×10^{20} W cm^{-2} st^{-1}. Equivalent plane spot focus measurements were made which suggest that up to 40% of the energy reaching the target is contained within the central spot, which has a divergence of 5 μrad (1.4 x diffraction limit). This gives a peak brightness of 2×10^{20} W cm^{-2} st^{-1}, and a peak intensity on target of 8×10^{18} W cm^{-2}. Figure 2 shows typical far-field spot focus images for the Raman and KrF beams, and a 3D plot of the Raman far-field.

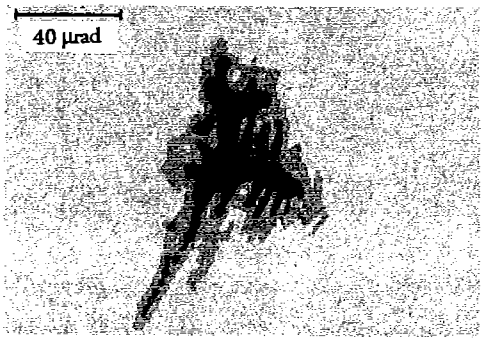

(a)

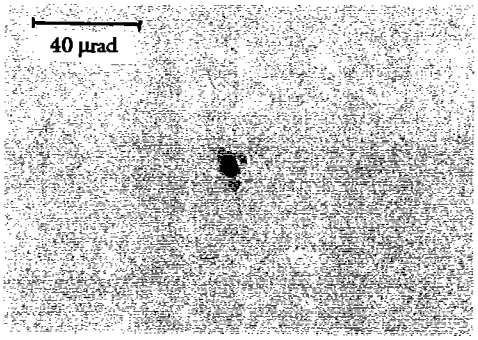

(b)

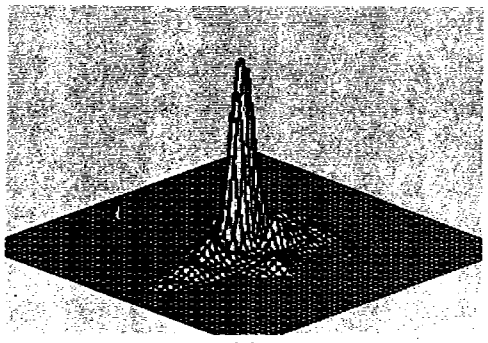

(c)

Figure 2: (a) KrF and (b) Raman far-field images
(c) expanded Raman far-field 3D plot

LASER CHARACTERISATION

In August/September the system was reconfigured to amplify single KrF pulses of 3ps duration. Over 300 shots were fired, the maximum energy was 1.8J, the brightness was over 10^{18} W cm^{-2} st^{-1}, and the contrast ratio between the brightness of the short pulse and that of the ASE was greater than 10^{7}.

A detailed characterisation of the Raman system was carried out in October/November concentrating on measurements of beam uniformity and divergence. Over 500 shots were fired, with energies from RA3 exceeding 7J at a conversion efficiency of about 67%.

Detailed results from these characterisation experiments are presented elsewhere in this report.

LINE FOCUS CHARACTERISATION

J M D Lister and G Bialolenker

Rutherford Appleton Laboratory

INTRODUCTION

During the X-ray laser target run on Sprite in February, measurements were made of the broad band spectrum of the Stokes output beam which showed the presence of a number of lines above and below the first Stokes wavelength of 268nm. Analysis of the spectra indicated that these lines were due to Raman scattering in air, and also to generation of other Stokes orders in the final Raman amplifier. There was clearly a need to ascertain the amount of energy being lost to other wavelengths, and also the effect of the scattering on the distribution of energy near the focal spot.

Since little time was available, at the request of the experimenters we concentrated on measuring the fraction of the total energy incident on the target. During the experiment the far-field pattern of the beam had been routinely measured, and indicated a focal spot of less than twice the diffraction limit. The camera used for this purpose, however, is not calibrated and does not have a high enough dynamic range to enable us to measure the fraction of the total energy contained within the central maximum.

MEASUREMENTS

The transmission from the multiplexer room window to the outside of the target chamber was measured on a full energy shot, using a calibrated calorimeter with an aperture the same size as the target chamber window. The observed transmission of 72% compares with an expected 82% calculated from Fresnel losses and mirror reflectivities measured at 268nm. The additional loss can be explained either by highly divergent components of the beam being apertured by the calorimeter, or by the presence of wavelengths outside the reflectivity bandwidth of the turning mirrors. When the losses due to the target chamber window and internal mirrors are included the overall transmission from the final Raman amplifier to the target is 66%.

The contrast ratio between the peak intensity and the background in the far-field is less for a line focus than a spot focus, so we made our measurements using a line focus geometry equivalent to that in the target chamber, but with a much longer focal length, and hence a wider line focus. An uncoated concave/convex mirror pair was used to attenuate the beam by a known factor and to reduce its diameter. It was then reflected by an off-axis spherical mirror to produce a line focus 6 mm long. An adjustable slit was placed at the focus with a calorimeter behind it to measure the transmitted energy, and some images of the line focus were recorded with a heavily attenuated CCD camera. The images were analysed to determine the amount of energy, as a proportion of the total, lying within regions of different width centred on the geometric line focus. Figure 1 shows data from both sets of measurements.

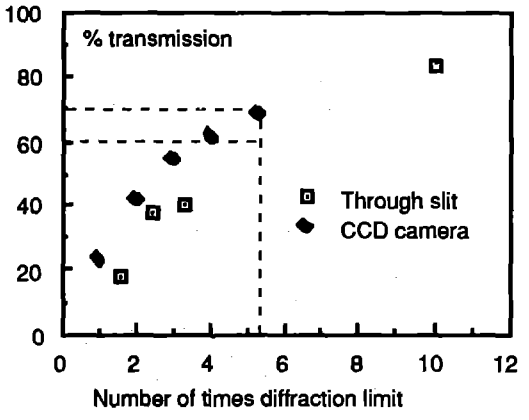

Figure 1. Line focus energy distribution data.
10 x diffraction limit = 31 μrad

Although the two sets of data might be expected to agree, in fact the transmission values obtained from the line focus images are higher than those from the measurements through the slit. This could be due to some of the energy not falling on the camera (which has an aperture of only 4.6mm perpendicular to the line focus). The lost energy does not contribute to the total as integrated over the CCD, so the amount in the line focus is apparently increased.

CONCLUSIONS

The dashed line in Figure 1 at 5.3 times diffraction limit corresponds to the equivalent size of the target used for the X-ray laser experiment (~6μm), and it can be seen that between 60 and 70% of the energy falls within this region. From these data we would estimate that between 39% and 45% of the total output energy of RA3 is incident on the target. However, the optical system used to generate the test line focus undoubtedly had some aberrations of its own which would degrade the focal distribution, so the above figure should be considered a worst-case estimate. Further investigation is required to determine where the losses are occurring. The spectral measurements suggest that the strongest effect is Raman scattering in air, which would occur mainly in the high-power beam leaving RA3 as it propagates to the target chamber. Some improvement can probably be made by minimising the path length of the beam, but if this is not sufficient it may be necessary to install a helium-filled beam pipe.

CERBERUS, A COMPUTERISED INTERLOCK SYSTEM FOR THE SPRITE LASER.

C J Reason, C J Hooker, P Gottfeldt and W L Lester

Rutherford Appleton Laboratory

INTRODUCTION

The proposal to install a computer controlled interlock system on the Sprite laser was briefly described in last year's Annual Report[1]. During the year the system has been installed, tested and is now fully operational, although we intend to develop further diagnostic displays in the future.

HARDWARE

The system is based on an IBM PC clone running at 16 MHz with a VGA colour display and a floppy disk. It was decided not to install a hard disk in order to keep the computer system as simple as possible and discourage its use as a general purpose computer. A keyboard is currently connected, but is not used for normal running and will be replaced by a keyboard eliminator to prevent unauthorised changes to the system.

The computer contains an Amplicon digital I/O board to interface with signals in the control room and a Arcom card interfacing to an Arcnet token bus network giving access to the rest of the facility. The PC card is electrically connected to an active hub which is connected by a ribbon cable to a fibre optic hub, all in the same rack. This has four fibre inputs and outputs giving access to the STE crates in the four main areas of Sprite: the oscillator room, the e-beam area, the multiplexer room and the target area. The STE crates in each area are identical and contain a 80186 processor card, a CGA display card, a fibre optic Arcnet interface card, digital I/O cards and signal conditioning cards. See Fig 1.

Each area has a monochrome monitor, driven by the CGA interface, which shows the state of all the areas covered by the system. Vacuum Fluorescent displays outside the doors show the state of the area inside, and indicate the precautions to be taken before entering. These displays are driven by the RS232 port on the 80188 cards, using fibre optic links for noise immunity.

THE SPECIFICATION.

Considerable effort was spent on writing a detailed specification for the system in English and refining it to a stage where it mapped reasonably well onto a structure that could be used in coding the system. It was hoped that the central logic of the specification could have been written in a formal specification language (e.g. Z) so that it could be rigorously verified. On investigation this turned out to be a major exercise and there was not enough time for it. The specification may be formally verified retrospectively.

The underlying principle of the system is that actions which increase the level of laser hazard, such as opening a laser beam stop, can be carried out only by authorised operators who are fully aware of the hazards. In the Cerberus system, key switches are used to control such actions, and only authorised operators hold keys. Actions which decrease the laser hazard, such as closing a laser beam stop, can be performed by anyone without the need for a key. There are different keys for the oscillator room, the e-beam area and multiplexer room, and the target area, so that a person can be authorised for target area only.

With the system as currently specified, it is possible to defeat the interlocks but it takes two people, at least one of whom is an authorised person. This means that the system has to be backed by a number of administrative rules, e.g. no authorised person may lend their key to another person.

The specification is designed around a number of entities such as rooms, doors, shutters and beam stops, each of which can be in a number of states. The states vary from entity to entity but

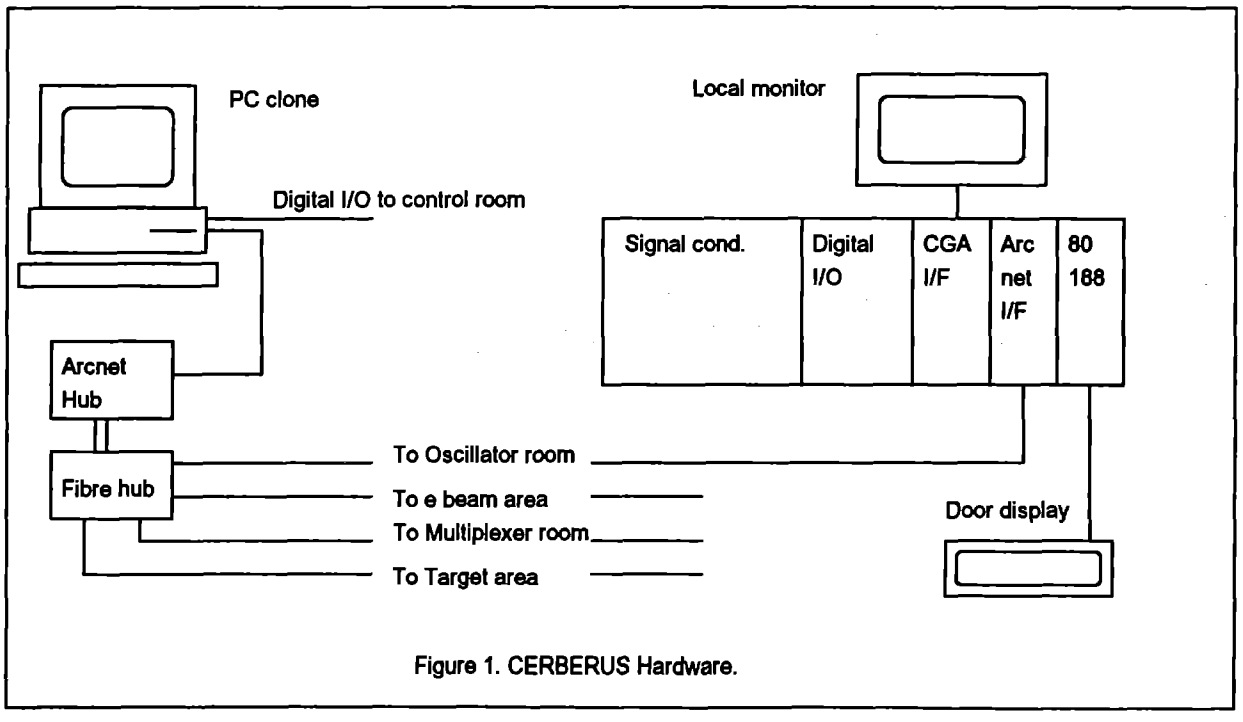

Figure 1. CERBERUS Hardware.

include Hazardous, Occupied, Searching etc. for rooms, Overridden, Open for doors. The specification defines how the entities can change from one state to another and what actions are allowed in any given state. A few examples will illustrate how this operates.

The state of a particular Room is Hazardous if there is a Laser in that Room with a Beam stop that has the state of Open. If there is a Shutter which has the state of Open between that Room and another Room then the second Room must also have the state of Hazardous. This is called the Propagation Rule.

An interesting part of the specification was the mechanism of changing the state of a room from occupied to unoccupied. To make this change the room must be searched, which requires a defined sequence of actions to be performed by an authorised person, using the appropriate key. The room starts the sequence as occupied with all doors closed. The person makes a key switch (one or more) in parts of the room remote from the exit door thus forcing him to visit all parts of the room. The exit door must then open and close and the person must make the key switch on the outside of the exit door. This series of actions must occur within a defined time (typically between 30 sec. and 1 min.). If it is successfully completed then the room is declared unoccupied and remains so until a door into it is opened. During this sequence the state of the room takes a number of values to force the order of the actions.

THE SOFTWARE.

The code was written in Turbo Pascal and the structure of the main logic is, as far as possible, a direct mapping from the specification to statements in Pascal. The central logic is a few hundred lines but the overall program is some 2000 lines, most of this taken up by handling the colour display on the PC, receiving and transmitting the data on the network etc. The code operates in a fixed loop with no interrupts in order to make the structure as simple as possible. It was hoped to read all signals at 10 Hz although in practice 8 Hz was achieved.

The code was written from the specification in abstract, in that it had information about how entities such as rooms, doors, shutters and beam stops interact within the system, but no information about the specific configuration of Sprite. The software is driven from a table which contains all the information about a particular system, including the graphical information to draw the layout diagram on the colour display, the number of rooms, door, shutters, etc., the location of all the signals in the array of data assembled from the network, systems timing etc. An editor was written to allow the LRO (Laser Responsible Officer) to enter or change these details, which would be done on an off-line computer and reloaded onto the interlock computer. This proved its worth when the doors to the target area were moved. In principle the same code can be used to provide an interlock system for another laser of a similar type with only the table being changed. Some tests were done and this proved to be the case.

The code running on the 80186 computer card in each STE crate was also written in Turbo Pascal. It was developed on a system with a PC and STE crate and down line loaded via a RS232 link to the card in the crate. It was then tested with the PC controlling the traffic on the network. This synchronous mode, with the PC requesting data over the network and waiting for a reply, is also the way the final system is configured. The STE code was blown onto ROM and mounted on the processor card when it was fully debugged.

THE IMPLEMENTATION

The software was largely written off-line on a computer with a hard disk but the central logic was written and tested in sections after the hardware had been installed. As each section was tested it was largely left unchanged. In some cases the coding raised questions about the specification and this had to be formally revised. Cases included the way a door was specified when it led from one potentially hazardous area to another (rather than from an area to the outside), and also the conditions set on start-up.

The operation of the system is governed by a watchdog signal that is sent from the PC to the STE crates each time round the loop. It operates in such a way that if a remote STE crate does not see a signal within a pre-determined time then it will close any beam stops in the area and render that area safe. If the PC does not receive an acknowledgement from an STE crate that the watchdog is OK then the PC will shut down the rest of the system rendering it safe. For both hardware and software failures, the system will fail safe because the watchdog transmission will cease. The watchdog time was set in the light of operating experience to allow for some fluctuation in the loop time, but shorter than it takes to get into a hazardous situation (estimated at 1 second). The setting is currently about 0.5 sec.

Some problems were experienced with the Arcnet token bus network. A few times each day the token became corrupt and one crate would be lost from the network. Sometimes this was co-incident with known noise (e.g. Sprite firing) but other times there was no known cause. Left to itself the network would re-configure automatically in just under 1 second. With software intervention it could have been done in about 600 to 700 mSec. Both of these times are longer than the watchdog time-out period and the watchdog would cause the system to shut down. The system was 'hardened' by improving the screening on the crates and computer, but the problem was solved by designing a circuit that detected the short (70 microsec) gap when the token is first lost and issuing a 'reconfigure burst' which causes the network to reconfigure in less then 100 mSec. This operation is transparent to the software.

TESTING

The system was tested on the laboratory bench and also as it was installed and the code written. Once it was running an exhaustive test was carried out by the LRO and a colleague who had not been involved in the project. This tested not only for the normal operating modes and trip modes but also for illegal operations (e.g. a shutter between areas being manually lifted) and failure modes (e.g. cables being disconnected). It was found to be working correctly and was later examined by an external assessor.

CONCLUSION

Cerberus works well and is safe. It is easy to change in a formal way when the laser system changes and can give good diagnostics as to what is happening while running. A similar system will be considered for any interlock systems that may be designed in the future.

REFERENCES

1) A R Damerell and C J Hooker. The Central Laser Facility Annual Report 1991. RAL-91-025, p 120.

C: LASER SUPPORT FACILITY

W T Toner

INTRODUCTION

This section contains scientific and technical reports from 34 user groups covering many different fields of chemistry (C1), Biology (C2) and Physics (C3). The facilities used at RAL and in the Loan Pool are summarised in Table I. The systematic work on improving performance reported in C4 has led to significant improvements in scientific output. In particular, the psec Raman system is now capable of yielding useful spectra with integration times as short as two seconds and with a stability good enough to determine kinetic data on transient species identified by their structure. Studies of carotenoids and of trans-stilbene are reported. In the latter, excited state electron transfer has been observed from trans-stilbene to tetranitromethane in micellar solution resulting in the decay and conversion of the excited singlet state to the radical cation.

A notable feature of the work this year is the increased application by users of a battery of techniques to round out their work. The psec Raman work on carotenoids are an extension of the nanosecond work. Raman studies of Vitamin E are built on preparatory experiments using the laser-flash-photolysis equipment. Nanosecond LIF measurements of matrix isolated metallocenes have been complemented by picosecond transient absorbance and SPC fluorescence measurements.

Other highlights include:

In Raman spectroscopy, a demonstration of a semiquinone-like structure of the Vitamin E radical whose extensively delocalised nature can explain the effectiveness of Vitamin E as a chain breaking antioxidant; the first Raman spectrum of solvated Buckminster Fullerene; the first direct observation in solution of the separation of geminate ion pairs. In chemical reaction dynamics, correlations between reagent velocity and the velocity and angular momentum of the product in the reaction $O+CS \rightarrow CO+S$ have been obtained for the first time and studies of the photodissociation spectrum of SiH_2^+ have revealed a case where fragmentation is competitive between two chemically distinct channels and therefore give information on the reaction surfaces for $Si^+ + H_2 \rightarrow SiH^+ + H$.

In Biology, Raman studies of a single 4-thio-thymidine base incorporated in an oligonucleotide chain show that binding of the chain to the restriction endonuclease Eco RV results in the loss of the H-bonding of the base.

In physics, the first experimental determination of the phase boundary of the solidification of a 2-D electron fluid in a GaAs-Al GaAs heterojunction has shown an unexpected result of the competition between the quantum fluid and the electron solid.

TABLE I

LASER SUPPORT FACILITY EQUIPMENT

Picosecond Systems at RAL

2 cw modelocked pump lasers; sub-picosecond oscillator; 2 cavity dumped oscillators; injection-locked YAG pump and dye amplifier (10 Hz); copper vapour pump and dye amplifier (4.5 KHz). Pump-probe absorption system; single photon counting; streak camera. Wavelengths from the UV to the far infrared are available, with further amplification at the excimer wavelengths.

Nanosecond Systems at RAL

2 high repetition rate fluoride excimer lasers; laser-plasma X-ray source;
2 high repetition rate XeCl excimer lasers pumping dye lasers; BBO and Raman wavelength conversion. 5 watt ion laser. Raman spectrometer. Laser-flash-photolysis system.

Loan Pool

4 YAG-pumped tunable dye lasers with frequency doubling and mixing; Excimer-pumped dye laser; fluoride excimer laser; 5 watt cw Ar ion laser with dye laser or Ti-sapphire laser; streak camera; gated integrators.

TIME RESOLVED SPECTROSCOPIC STUDIES OF PHTHALOCYANINE TRIPLET STATES

A.Beeby, S.M. Bishop, A.J. MacRobert, A.W. Parker*, M.S.C. Simpson, D.Phillips

Department of Chemistry, Imperial College, London SW7 2AY
*Laser Support Facility, Rutherford Appleton Laboratory, Didcot, Oxon.

INTRODUCTION

The water soluble sulphonated derivatives of aluminium phthalocyanine AlS_nPc (n=1,2,3 & 4) are of considerable interest as photosensitisers for Photodynamic therapy, PDT. The degree of sulphonation affects the lipid solubility and aggregation properties both of which are known to influence cellular uptake and phototoxicity with the lesser sulphonated, more lipophilic components exhibiting higher in vitro photoactivities. Sulphonated aluminium phthalocyanines have a high photodynamic efficiency and like the porphyrin sensitisers show preferential localization and retention in malignant tumours. Fractions of defined sulphonation of AlS_nPc (n=1,2,3,4) can be reproducibly isolated and exhibit an intense Q band absorption in the 670-675nm region ($\varepsilon \sim 10^5\ M^{-1}cm^{-1}$). The phototoxicity of AlSPc is believed to be mediated by the triplet state of the dye which can either react directly with another chemical entity by hydrogen or electron transfer to yield transient radicals, which is classified as the Type I mechanism; or more commonly, the triplet state can interact with oxygen, to generate the reactive and cytotoxic species singlet oxygen, O_2 ($^1\Delta_g$), defined as the Type II mechanism. The singlet oxygen quantum yield, Φ_Δ, is often determined for convenience in deuterated solvents because singlet oxygen is deactivated more rapidly in protiated solvents, in particular H_2O[1]. In this work we have used nanosecond laser flash photolysis to compare the triplet lifetime τ_T and triplet quantum yield Φ_T of AlS_nPc (n=1,2,3,4) and sulphonated zinc phthalocyanines in a range of solvents and deuterated solvents. In particular, anomalous effects are observed upon deuteration of the solvent and addition of fluoride ions.

EXPERIMENTAL

Triplet state studies were carried out using the Laser Support Facility's ns laser flash photolysis apparatus and is fully described elsewhere. The system utilises an excimer pumped dye laser at either 355nm or 660-680nm, atypical pulse duration of 10ns and energy of 10-2000μJ, which is delivered to the sample by a 5mm liquid light guide.Transient species are probed using the output of a quartz halogen lamp. Using either a mirror, or a 5° wedge the transmitted light is reflected onto an EG&G OMA III gateable diode array detector which allows the rapid acquisition of transient absorption spectra from 1-256 laser shots. Where necessary degassing was achieved by Ar bubbling or by vacuum line freeze pump thaw technique. The relative triplet quantum yields were determined by plotting the intensity of the triplet-triplet absorption at time t=0 as a function of the absorbed laser energy. The relative gradients in the linear, low power region of the graphs were then compared.

RESULTS AND DISCUSSION

Under the conditions used the triplet lifetime of sulphonated aluminium phthalocyanines, AlS_nPc (n=1,2,3,4) decays by a first order process in aqueous and organic solutions. At low pump energies the triplet lifetimes in degassed solution were independent of light dose but did vary with sensitiser concentration and the observed lifetimes fitted an equation of the form :

$$\tau_T = 1/k_R\ k_Q[Pc]$$

where k_R is the rate coefficient of the triplet decay at zero concentration, k_Q is the rate coefficient of quenching by the ground state and [Pc] is the concentration of the sensitiser.
In H_2O $k_R = 1670 \pm 120 s^{-1}$ and $k_Q = 1.1 \pm 0.1 \times 10^8$ $mol^{-1}dm^3s^{-1}$; in D_2O $k_R = 630 \pm 30 s^{-1}$ and $k_Q = 1.0 \pm 0.2 \times 10^8 mol^{-1}dm^{-3}\ s^{-1}$. The triplet-triplet absorption spectra in the two solvents were identical as were the triplet extinction coefficients at 490nm. Figure 1 shows the ratio of the triplet quantum yields determined from the power dependence of the triplet state absorption at 490nm and were measured as $\Phi_T(H_2O) : \Phi_T(D_2O):\Phi_T(\text{Methanol}) = 1: 1.3: 1.8$. The triplet lifetime data in Table 1 show that excited triplet lifetime of AlS_nPc exhibits no significant variation with the degree of sulphonation in either aqueous or methanolic solutions. Fluorescence data show the same result.

Figure 1. Excited state triplet quantum yields, Φ_T in H_2O and D_2O.

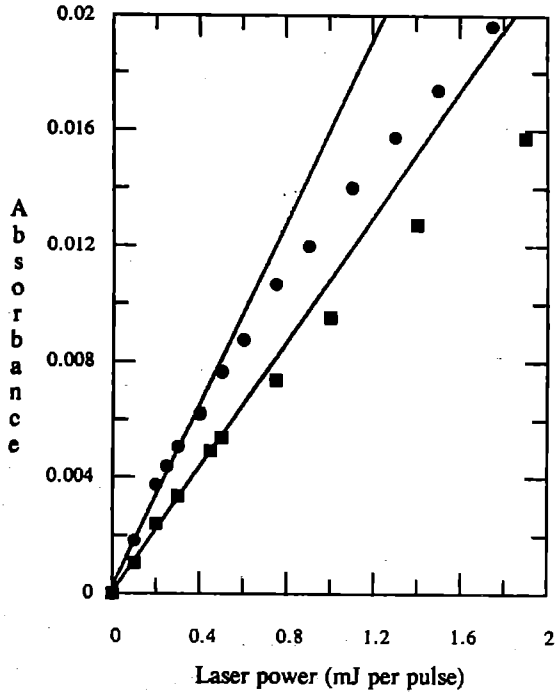

Table 1. Excited State Triplet Lifetimes (τ_T/ μs) of Sulphonated Aluminium Phthalocyanine (2.5μM) in various solvents.

Solvent	AlS_1Pc τ_T/μs	AlS_2Pc τ_T/μs	AlS_3Pc τ_T/μs	AlS_4Pc τ_T/μs
H_2O	400±20	550±10	520±20	560±30
PBS	390±25	520±15	490±30	530±20
D_2O	990±30	1130±30	1150±30	1140±40
D_2O/PBS	960±40	980±30	1000±40	1050±40
Methanol	620±20	640±15	630±20	635±10

Figure 2. Transient spectra of AlS2Pc in H2O on addition of ascorbic acid showing the quenching of the triplet state at 490nm and the grow in of the radical anion at 610nm

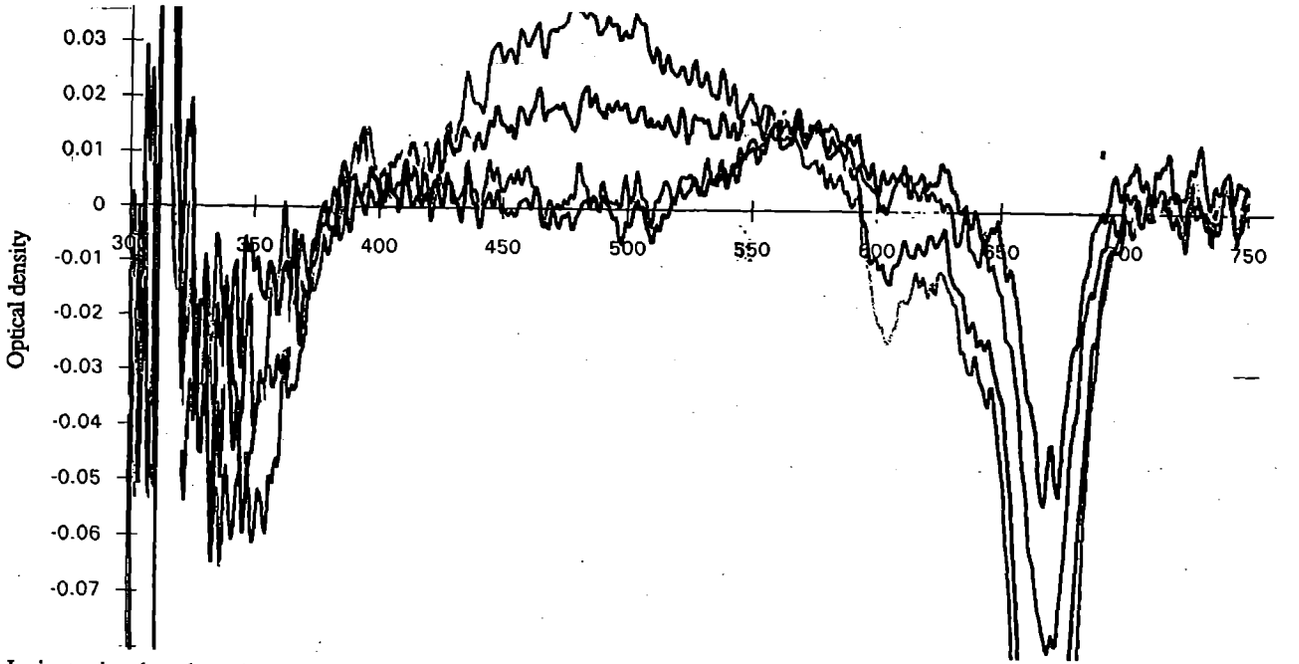

In isotonic phosphate buffered saline solutions the triplet lifetime is constant within the range of pH of 5.5 - 8.0 indicating that the differences in triplet lifetimes and quantum yields are not caused by differing degrees of phthalocyanine ionisation[2]. The addition of fluoride ions (20mM) to a solution of AlS_2Pc in H_2O at pH 7.4 and containing 120mM NaCl caused a hypsochromic shift of 6nm in the absorption spectrum indicating that F^- is interacting with the metal by displacement of the coordinated solvent. An accompanying increase in both the triplet lifetime and triplet quantum yield was observed.

Table 2. Excited State Triplet Lifetimes τ_T ,and Ratio of Triplet Quantum Yields Φ_T of AlS_2Pc (2.5μM) in Various Solvents.

Solvent	τ_T /μs	$\Phi_T(D) / \Phi_T(H)$
H_2O	520±10	
D_2O	1130±20	1.3
CH_3OH	670±10	
CH_3OD	700±15	1.0
CD_3OD	1400±30	
Pyridine	650±20	
Pyridine-d_5	1200±15	1.0
Isopropanol	800±15	-
Triton X 100	630±20	-
Glycerol	360±30	-
Ethoxy ethanol	990±15	-
Ethylene glycol	630±20	-

In methanol and higher alcohols the triplet lifetime and triplet quantum yield is increased relative to that in H_2O, however no increase in triplet lifetime or triplet quantum yield is observed between CH_3OH and CH_3OD. One difference between water and methanol is the almost complete absence of the >O-H ($2\upsilon_{OH}$) stretching overtone (@1418nm) of water in methanol, possibly indicating that the rate of relaxation of the excited state is increased by the coupling or perturbation of this vibration[3]. In CD_3OD a dramatic increase in triplet lifetime is observed, τ_T=1400 ± 50μs, presumably due to coordination of CD_3O- to the metal. Previously, Gradyushko *et al* have reported that deuteration of alcohol ligands bound to magnesium porphyrin cause an increase in triplet lifetime[4]. A similar effect is obtained with pyridine and pyridine-d_5 as the solvent. Pyridine is known to facilitate in the disaggregation of zinc phthalocyanine by coordinating to the metal, The observed excited state triplet lifetime of zinc tetra-sulphonated phthalocyanine (ZnTSPc) also displays a solvent dependent effect, albeit a less dramatic Addition of pyridine (120μl) to ZnTSPc dissolved in D_2O results in a disaggregation of the phthalocyanine, but also a decrease in the triplet lifetime from $\tau_T(D_2O)$ = 366 ± 10μs to τ_T 230 ± 10μs coincident with the triplet lifetime of ZnTSPc in pyridine, τ_T = 235 ±10μs. In pyridine-d_5 the triplet lifetime is 370 ± 15μs and no increase in triplet quantum yield is observed. The triplet lifetime of AlSPc is quenched by ascorbic acid with a rate of 1.1±0.2 x10^{-8} $mol^{-1}dm^3s^{-1}$ generting the radical anion. The time resolved transient spectra of AlS_2Pc in degassed water are shown in Figure 2, and were recorded using the a time gated optical multichannel analyser (OMA III). These time gated spectra illustrate the quenching of the triplet state at 490nm by ascorbic acid (5 x 10^{-6}M) and the grow in of the long lived phthalocyanine radical anion at 610nm[5].

CONCLUSION

The excited state triplet lifetime and triplet quantum yield of sulphonated aluminium phthalocyanine are sensitive to solvents or substrates e.g F^- OH^-, capable of coordinating to the central metal of the macrocycle. In particular, any coordinating species which do not possess the $2\upsilon_{OH}$ vibrational stretching frequency of H_2O result in increased triplet lifetimes and quantum yields relative to those in water.

REFERENCES

1 P.B. Merkel, D.R. Kearns. *JACS.* **94** (1972) 7244-7253

2 J. McVie, R.S. Sinclair, T.G. Truscott. *J. Chem. Soc. Faraday* **2**, 1978) 1870

3 P.C. Martin, M. Gouterman, B.V. Pepich, G.E. Renzoni. *Inorg. Chem.* **30** (1991) 3305-3309

4 M.C.R. Symons. *Acc. Chem. Res.* **14** (1981) 179-187

INTERACTIONS OF FREE RADICALS OF DRUGS AND ANTIOXIDANTS

Roger H Bisby[1] and Anthony W Parker[2]

[1]University of Salford
[2]Rutherford Appleton Laboratory

INTRODUCTION

This project is concerned with free radical reactions involved in both xenobiotic-induced oxidative stress in cellular systems and the protection afforded against free radical damage by low molecular weight antioxidants such as vitamins E and C. Nanosecond laser flash photolysis is being used to generate free radicals involved in these processes and to measure the kinetics of their reactions. In addition resonance Raman spectroscopy of the transient intermediates is being used to provide information concerning structure and interaction of the free radical with its environment.

In the previous report it was shown that the flash photolysis was capable of producing the required intermediates both from a drug (minocycline) and an antioxidant (α-tocopherol). A principal objective was to study the regeneration of α-tocopherol from the tocopheroxyl radical by ascorbate and other intracellular reductants. The reaction with ascorbate has been reported in homogenous solution, but a recent study on turnover of α-tocopherol in an animal model has cast doubt on the importance of this reaction in cellular systems where the reaction must occur across a membrane interface[1]. Initial flash photolysis studies at RAL showed that this reaction occurred readily with the tocopheroxyl radical located in a micellar environment[1]. A more detailed study of this reaction has been undertaken and extended to work in model bilayer membrane systems.

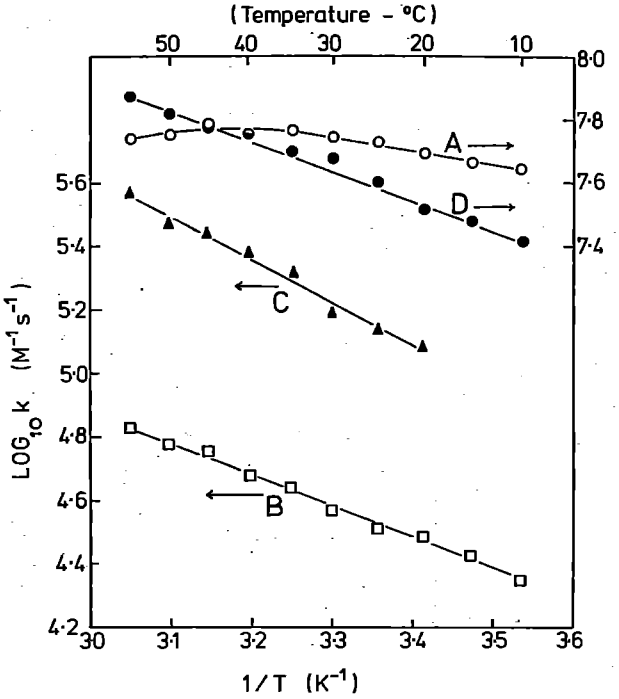

Figure 1. Arrhenius plots for the reaction of ascorbate with the α-tocopheroxyl radical located in micelles of hexadecyltrimethyl ammonium chloride (A); sodium dodecyl sulphate (B); bilayers of dipalmitoylphosphatidylcholine(DMPC) (C); or mixed bilayers of DMPC and didodecyldimethylammonium bromide (25:75 mole%) (D).

RESULTS AND DISCUSSION

Reaction of the α-radical with ascorbate

Laser flash photolysis of α-tocopherol in bilayer membranes of phospholipids produced the same characteristic spectrum of the α-tocopheroxyl radical as had been observed previously in detergent solutions. The rate of decay of the radical was found to be first order in ascorbate concentration giving a value of 2×10^3 M^{-1} s^{-1} for the second order rate constant in membranes of dipalmitoylphosphatidylcholine (DMPC). Quite clearly the "repair" of membrane bound α-tocopheroxyl radical by ascorbate is not restricted by the membrane interface and the only obstacle to this reaction *in vivo* may be a high negative potential at the membrane surface, as discussed below.

Arrhenius plots for the reaction of α-tocopheroxyl radical with ascorbate in a number of systems are shown in Figure 1. In sodium dodecyl sulphate (SDS) micelles and in bilayers of DMPC or DMPC + didodecyldimethyl ammonium bromide (75:25 mole ratio), the plots are linear with activation energies in the range 18-26 kJ mol^{-1}. These plots show the strong effect of micellar or membrane charge on the rate of reaction. The result obtained in bilayers containing the positively charged DDAB show the same enhancement in rate as in HTAC micelles. Additional data (not shown) indicates that addition of a negatively charged lipid (dipalmitoyl phosphatidic acid) to DMPC bilayers lowers the rate constant by a factor of approximately 10. The Arrhenius plot for hexadecyltrimethyl ammonium chloride (HTAC) micelles is anomalous and is probably explained by the reaction being preceded by reversible binding of the negatively charged ascorbate anion to the positively charged micelles. The rate of reaction in these systems may also depend on the ionic strength of the medium, as shown in Figure 2. When the α-tocopheroxyl radical is located in positively charged HTAC micelles the reaction with the ascorbate anion decreases with increasing salt concentration, whereas in the negatively charged SDS micelles the opposite effect is seen. In the bilayers of zwitterionic DMPC there is very little effect of salt concentration. These data provide additional support to show that the reaction occurs at the interface rather than by the radical exiting from the micelle prior to reaction in the bulk aqueous phase.

Resonance Raman Spectroscopy The resonance Raman spectrum of the α-tocopheroxyl radical in SDS micelles shown in Figure 3 was obtained using a 430nm dye laser probe pulse, corresponding to the maximum in the tocopheroxyl radical absorption spectrum. The spectrum obtained before formation of the radical by pumping at 308 nm contains bands attributable to SDS and phosphate buffer. After formation of the radical by photolysis at 308nm, the radical spectrum is dominated to two strong lines at 1501 cm^{-1} and 1600 cm^{-1}. The 1501 cm^{-1} band is assigned to the phenoxyl C-O stretch (Wilson 7a mode) and the wavelength indicates that the bond has near double bond character. The 1600 cm^{-1} band is assigned to the ring C-C stretch (Wilson 8a mode). This mode is not resonantly enhanced in the spectrum of the phenoxyl radical, but is a strong feature in the spectrum of the p-benzosemiquinone (1613 cm^{-1}) and p-methoxy-phenoxyl (1607 cm^{-1}) radicals[3]. The spectrum contains other much weaker bands which remain to be assigned. The two weak features at 1672 and 1700 cm^{-1} are due to a decay product, possibly tocopheroquinone. The relative intensities of the two most intense bands indicate that the α-tocopheroxyl radical has a semiquinone-like structure in both ground and excited states, indicating that the radical site on the phenoxy group is extensively delocalised. The involvement of the chromanol oxygen atom in sharing the unpaired spin, as so clearly demonstrated by the Raman spectrum, is one important factor[4] in contributing to the stability of the tocopheroxyl radical and is the major reason why α-tocopherol is such a good chain-breaking antioxidant.

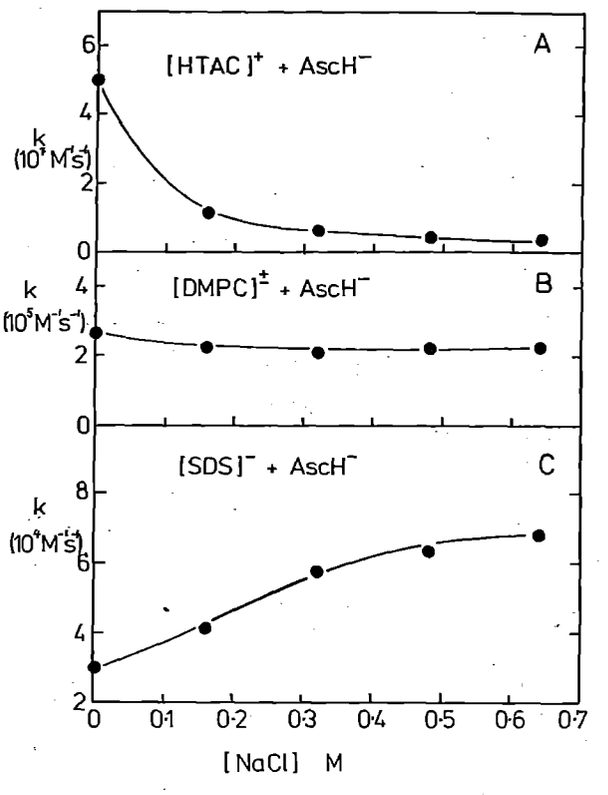

Figure 2. Effect of salt concentration of the second order rate of reaction of ascorbate with the α-tocopheroxyl radical in A:- HTAC micelles; B:- DMPC bilayers; and C:- SDS micelles.

REFERENCES

1. GW Burton et al Lipids 25 199 (1990)
2. RH Bisby and AW Parker FEBS Lett 290 205 (1991)
3. GNR Tripathi and RH Schuler J Phys Chem 92 5129 (1988)
4. GW Burton et al JACS 107 7053 (1985)

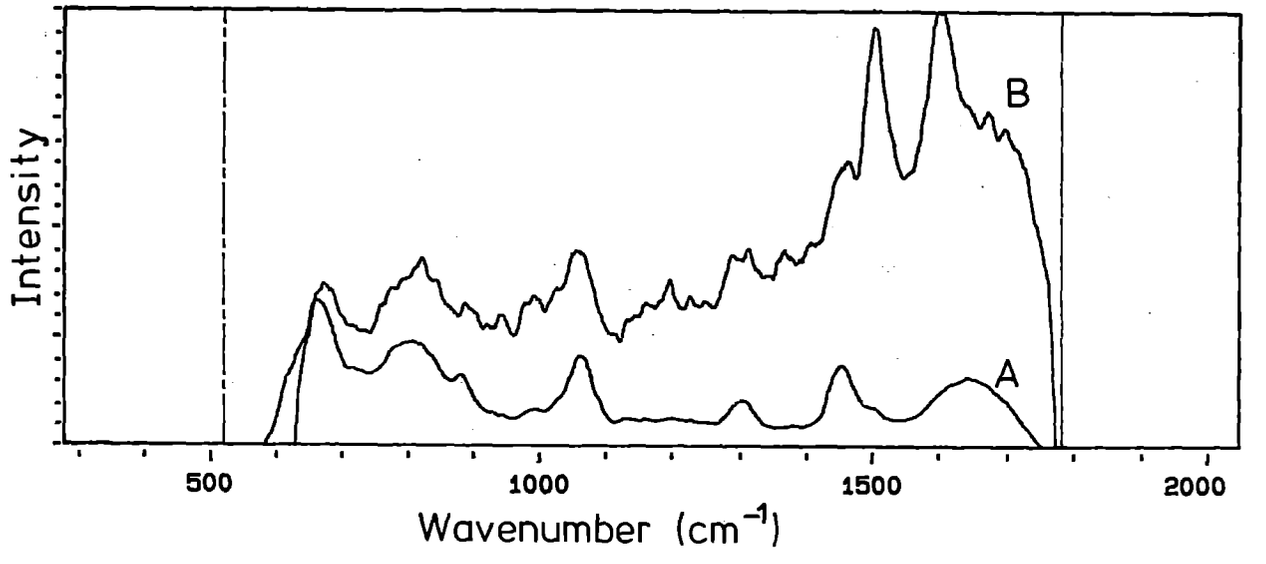

Figure 3. Resonance Raman spectrum of α-tocopheroxyl radical in SDS micelles. A:- SDS micelles and α-tocopherol before irradiation at 308 nm; B:- after photolysis and formation of the α-tocopheroxyl radical.

LASER-INDUCED FLUORESCENCE OF REACTIVE METALLOCENES

Jeremy N. Hill and Robin N. Perutz

University of York

INTRODUCTION

The metallocenes of molybdenum, tungsten and rhenium are highly reactive open shell molecules which act as short-lived intermediates in solution chemistry. They may be generated in low temperature matrices by photolysis of the corresponding hydride complexes, Cp_2MH_n ($Cp = \eta^5$-C_5H_5).[1]

In previous reports, we have outlined Laser-Induced Fluorescence studies of these metallocenes and the related substituted metallocene Cp^*_2Re ($Cp^* = \eta^5$-C_5Me_5) in both dinitrogen and argon matrices.[2,3] The overall aim has been threefold: i) to record sharp fluorescence spectra, ii) to measure excitation profiles and iii) to determine excited state lifetimes, where possible. Much of this work was completed previously, except for a detailed study of Cp_2W in argon and dinitrogen, which is the subject of this report. In preceding visits to the LSF, we found that it is more problematical to obtain a consistent energy output from the dye laser with UV than with visible dyes. As this was of crucial importance for good excitation spectra, a different method for attenuating the output was devised and is described below.

RESULTS

The method devised for getting a more constant energy at the sample involved using two hollow wedge prisms, fixed to independently movable mounts, such that the pathlength through the prisms could be changed without any deviation of the laser beam through them. The prisms were filled with an appropriately absorbing solution (in our case, a standard mixture of $CoSO_4$ and $NiSO_4$). The resulting variable density filter worked well and was a considerable improvement on previous methods employed.

Cp_2W in dinitrogen

The absorption spectrum reveals partially resolved bands complicated by fine structure caused by matrix trapping sites and/or conformers of the metallocene. Warming the matrix to 30 K allows some thermal reorganisation of these sites and results in a more highly resolved spectrum. Several vibrational progressions in ν'_4, the symmetric ring-metal-ring stretch, are clearly visible. Laser irradiation into the absorption band leads to intense fluorescence. Careful choice of the laser wavelength leads to sharp, well defined vibrational progressions from which it is possible to assign ν''_4 and ν''_3, the symmetric breathing mode of the Cp rings (figure 1). However, measurement of a point by point excitation profile of the fluorescence showed no improvement in resolution over the absorption spectrum. The excited state lifetime of all sites/conformers was found to be within the duration of the laser pulse. Hence it is only possible to put an upper limit to the lifetime of 10 ns.

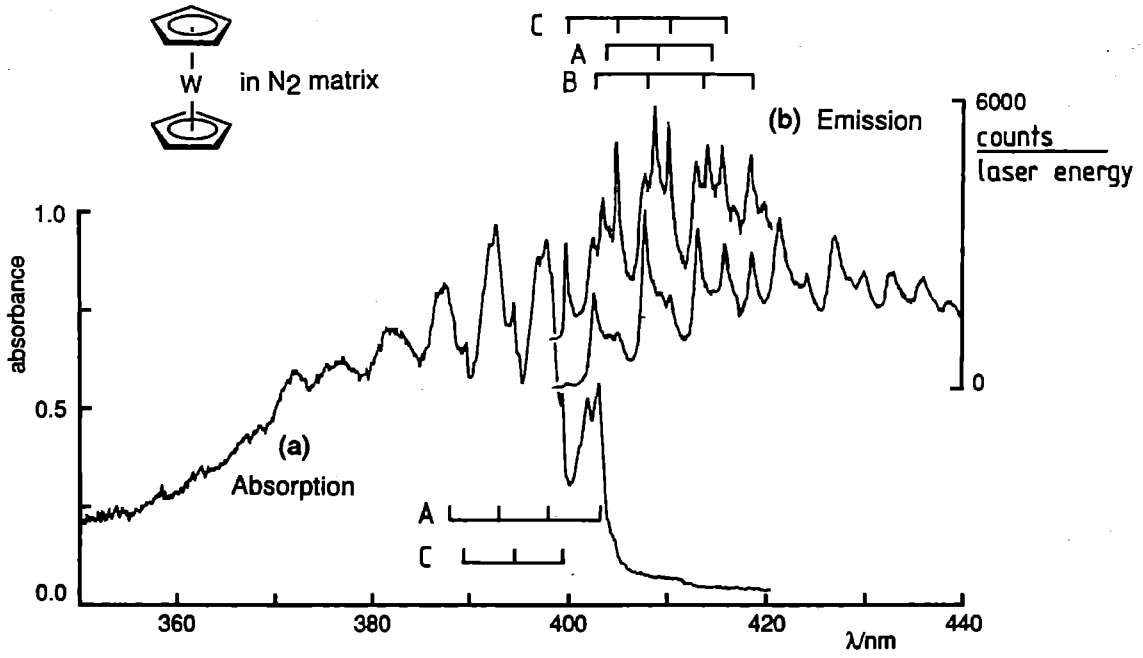

Figure 1. Spectra of Cp_2W generated by UV photolysis of Cp_2WH_2 isolated in a dinitrogen matrix at 12 K. (a) Absorption spectrum before annealing.. (b) Emission spectra: upper λ_{ex} = 385.4 nm before annealing, lower λ_{ex} = 385.4 nm after annealing to 30 K for 1 minute.

Cp_2W in argon

The absorption spectrum of Cp_2W in argon matrices is of comparable resolution to that in dinitrogen, although the site/conformer effects are not so pronounced. Laser irradiation into the absorption band leads to intense emission, showing a high dependence on the laser wavelength. Judicious selection of the laser wavelength leads to highly resolved spectra (figure 2). Recording the intensity of the A2 peak in emission as a function of the laser wavelength enables a site selective excitation profile to be recorded. This is clearly much sharper than in absorption: the ν'_4 are precisely determined, although ν'_3 still remains elusive. In agreement with what was found in dinitrogen, the lifetime was less than 10 ns.

CONCLUSIONS

The principal features of the LIF spectra of Cp_2W are in agreement with those obtained from the other metallocenes. Emission spectra reveal a (0,0) transition coincident with the absorption spectra, and show well resolved progressions in ν''_4 and (ν''_3 + ν''_4). The spectra in emission are much sharper than in absorption, due to the site/conformer selectivity of the laser. However, the emission spectrum in dinitrogen is broader than in argon. The excitation spectrum obtained in dinitrogen shows no more vibrational detail than is seen in the absorption spectrum. This implies that a requirement for a detailed excitation profile is that the emission is sharp. A further point to consider is the change in ν_4 between the ground and excited states, as this reflect changes in bonding. There is a small, but significant decrease in ν_4 on going to the excited state. This is quite unlike what is seen in Cp_2Re and Cp_2Mo, which show an increase, and conform to the simple ligand field model in which an electron is removed from a ligand π-bonding orbital and placed in a metal-ligand bonding orbital, resulting in an increase in the metal-ring bonding and ν_4. The intensity distribution in fluorescence is dictated by Franck-Condon factors, which in turn can be used to calculate bond distortions that occur in the excited state. Much of the data for this calculation is derived from the emission and excitation spectra measured at the LSF. These are ν'_4, ν''_4, the emission intensities and E(0), the energy of the (0,0) transition for a given site/conformer. For Cp_2W in argon, initial calculations suggest that a distortion of 0.003 Å can account for the intensity of the first four transitions in emission. A more complex model which takes account of perturbation of the intensities by other vibrational modes is under development.

REFERENCES

1. P. Grebenik, R. Grinter and R. N. Perutz, Chem. Soc. Rev., **17**, 453 (1988)
2. S. E. J. Bell, J. N. Hill, A. McCamley and R. N. Perutz, *Annual Report to the Laser Facility Committee*, Rutherford Appleton Laboratory RAL-91-025, 134 (1991)
3. S. E. J. Bell, J. N. Hill, A. McCamley and R. N. Perutz, J. Phys. Chem., **94**, 3876 (1990)

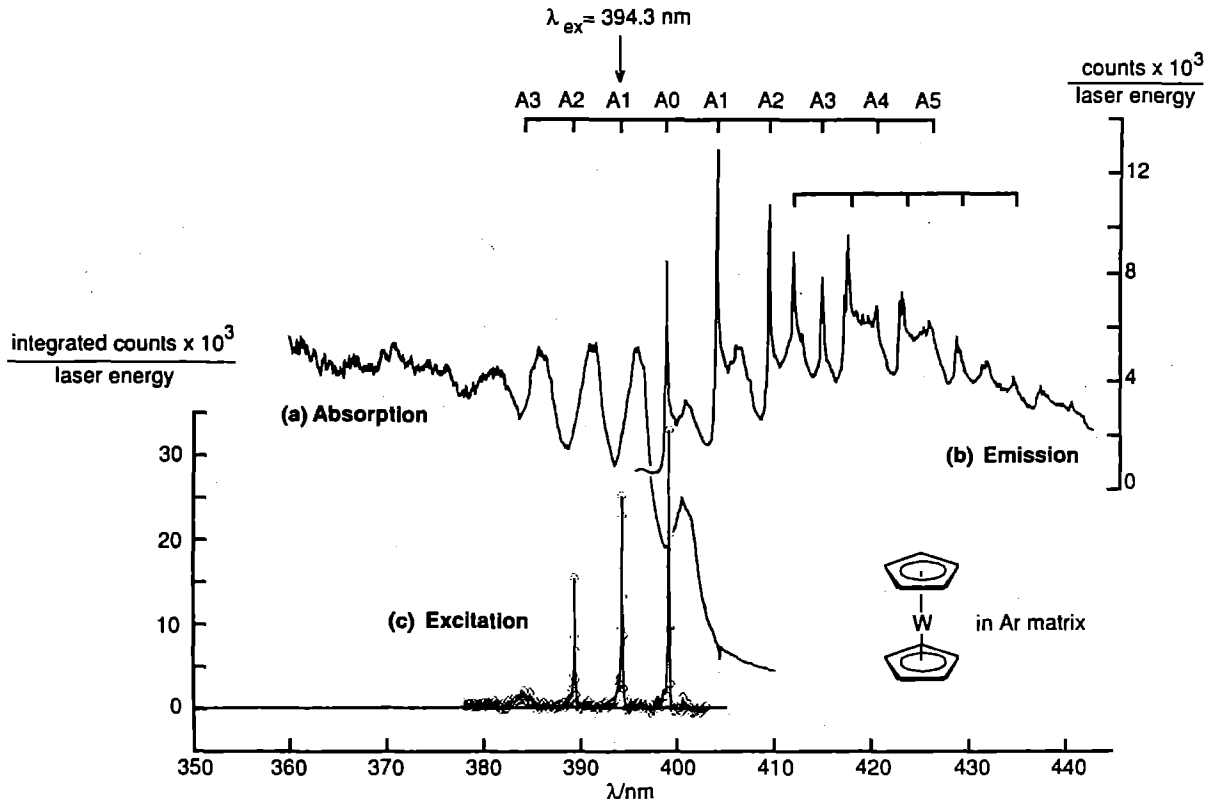

Figure 2. Spectra of Cp_2W isolated in an argon matrix at 12 K. (a) absorption spectrum, (b) emission spectrum, λ_{ex}= 394.3 nm, with ν''_4 and ν''_3 shown, (c) corresponding excitation spectrum for the A2 emission band. The emission and excitation spectra are shown for one site only.

PICOSECOND TRANSIENT ABSORBANCE DIFFERENCE SPECTROSCOPY OF MONO- AND POLYNUCLEAR Cu(I) COMPLEXES.

Ditanya I C Martin[1], Stephanie J Rigby[1], Steven E J Bell[1], John J McGarvey[1], Jean-Marie Lehn[2], Annie Marquis-Rigault[2],Andrew Langley[3] and Waseem Shaikh[3].

[1]School of Chemistry, Queen's University of Belfast, Belfast BT9 5AG.
[2]Institut Le Bel, Universite Louis Pasteur, Strasbourg.
[3]Rutherford Appleton Laboratory.

INTRODUCTION

The excited state properties of polypyridyl complexes of Cu(I) have been quite extensively investigated in recent years by luminescence and time-resolved resonance Raman techniques[1,2]. One of the interesting features of copper(I) complexes is that the preferred coordination geometry of the metal centre changes from tetrahedral to planar upon excitation and the coordination number may also change from 4 to 5 or 6. This tendency of the excited complexes to form entities with higher coordination numbers results in exciplex formation[3] which in nucleophilic solvents reduces the lifetime of the charge-transfer states if the metal centre is not protected by sterically bulky ligands.

The present report concerns the excited states of complexes of Cu(I) with ligands based on 2,2'-bipyridine (**BPY**). The ligands investigated are shown below. Compounds with ligands (**1**) and (**2**) were chosen to allow us to investigate the effect of ligand rigidity, rather than steric hindrance, on the quenching process. Those with ligands (**3**) and (**4**) are of interest because of their demonstrated[4] ability to self-assemble in solution, making helical structures (see (**5**) with repeating units similar to the monomeric systems described above. The ligands and complexes shown in (**3-5**) below were synthesized in Strasbourg. Structures like (**5**) are of particular interest in the context of supramolecular chemistry since they are in effect photoactive arrays with DNA-like spatial organization.

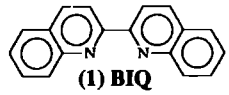

(1) BIQ

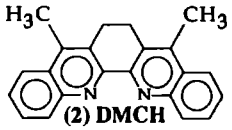

(2) DMCH

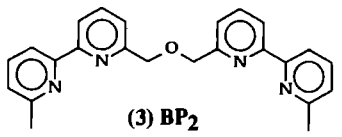

(3) BP_2

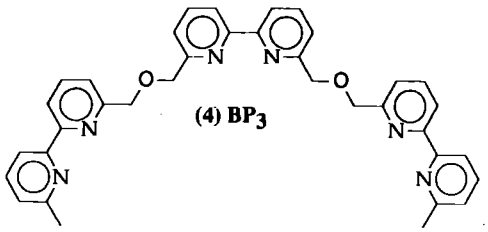

(4) BP_3

(5)

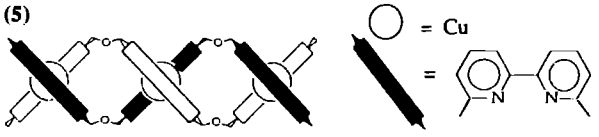

EXPERIMENTAL

Two-colour pump and probe measurements were carried out using a 585 nm photolysis beam and probe wavelengths in the range 620 - 690 nm. A schematic diagram of the experimental layout is shown in Figure 1 (overleaf). Solutions of the complexes (ca. 10^{-3} mol dm^{-3}) were prepared in dichloromethane (Aldrich spectroscopic grade solvent). UV-visible spectra of the test solutions were run before and after experiments to check that no decomposition had occurred.

RESULTS AND DISCUSSION

The lifetimes measured for several complexes are summarised in Table I. Some examples of the decay traces recorded are shown in Figure 2 and demonstrate the excellent signal:noise ratios obtainable. The lifetimes recorded for the complexes with the ligands DMCH and BIQ are virtually identical within the experimental uncertainties and suggest that ligand rigidity has little effect on the excited state dynamics of these systems. This implies that solvent ingress to the photoexcited metal centre is not decreased even if the ligands are constrained from twisting about the central C-C bond. Estimates of the rotational correlation times from preliminary polarisation anisotropy studies give similar values of ca. 80 ps for both complexes which seem reasonable for molecules of this type in dichloromethane.

Table 1. Excited state lifetimes of mono- and polynuclear Cu^{I} complexes in dichloromethane at room temperature.

Complex	Lifetime/ps
$[Cu(BIQ)_2]^+$	1050 ± 50
$[Cu(DMCH)_2]^+$	1100 ± 150
$[Cu_3(BP_3)_2]^{3+}$	360 ± 40
$[Cu_2(BP_2)_2]^{2+}$	>2500
$[Cu(BPY)_2]^+$	<50

The lifetime measurements for the polynuclear Cu(I) helicate complexes are surprisingly disparate. The monomeric precursor has a lifetime shorter than the response time of the apparatus used while that of the dimer is longer than 2.5 ns which is the upper limit set by the optical delay line of the ps apparatus. We have subsequently measured[5]the lifetime of the dimer to be 25±2 ns. There is much more torsional rigidity in the dimer but the results on complexes with ligands (**1**) and (**2**) suggest that this is not a significant factor in determining the lifetime. Surprisingly, the trimer lifetime (360 ps) falls between those of the monomer and dimer. Evidently the effect

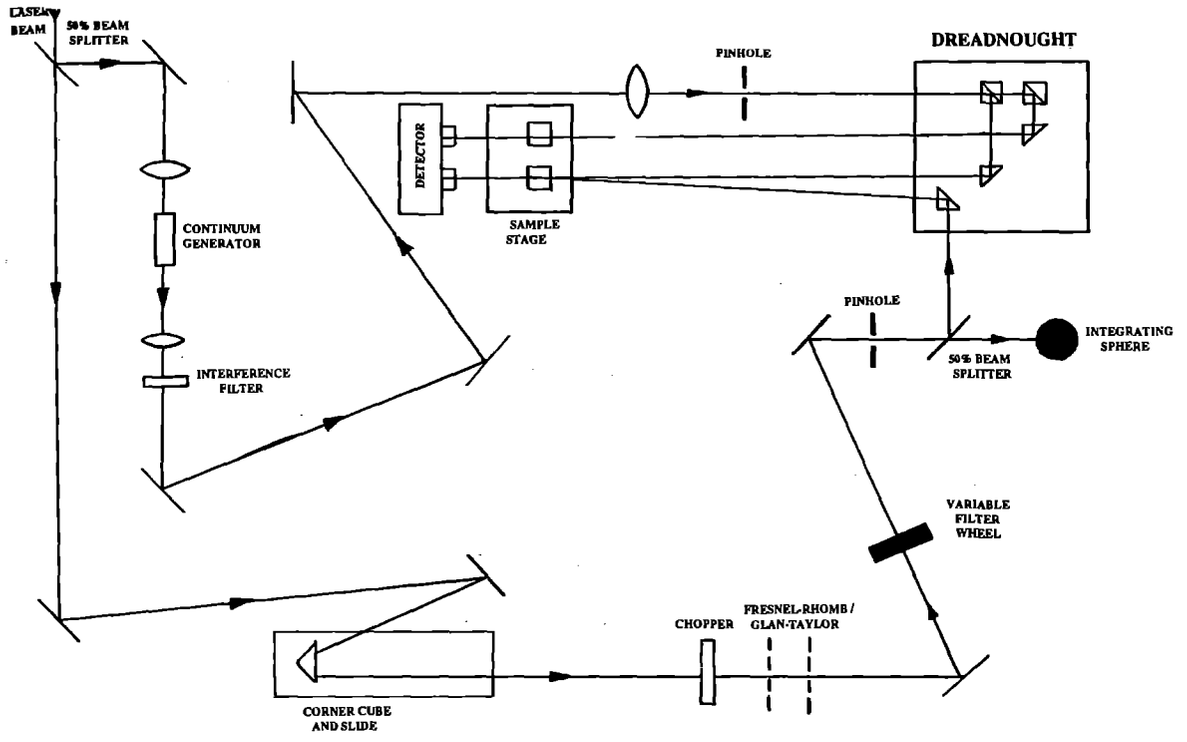

Figure 1. Schematic layout of the apparatus for excited state absorbance decay studies in the picosecond range. The Glan-Taylor and Fresnel rhomb combination was used to vary the relative polarization between pump and probe beams for the anisotropy studies.

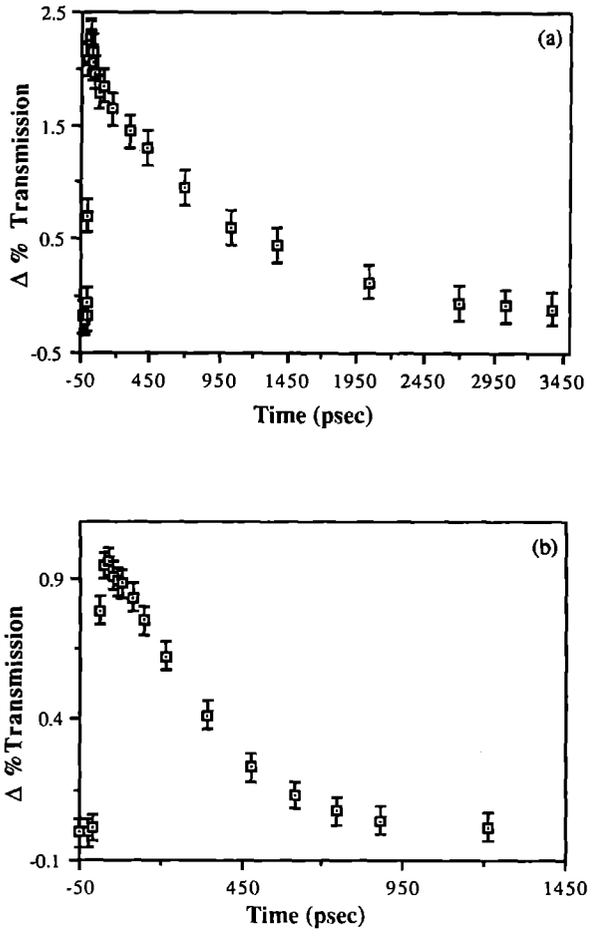

Figure 2. Excited state decays of Cu(I) complexes in dichloromethane at room temperature: (a) $[Cu(BIQ)_2]^+$; (b) $[Cu_3(BP_3)_2]^{3+}$

of chain length on the photophysical decay pathways is critical but is difficult to rationalize on the basis of such a limited data set. We are hoping to investigate samples of the higher members of this helicate series when they become available. This will allow us to determine if the lifetimes continue to fluctuate with chain length or if they reach a more stable plateau implying that it is the dimer which is exhibiting anomalous behaviour. Initial polarization anisotropy measurements on the helicates have been relatively unhelpful, showing only that the signal risetime is independent of the relative polarization angle of the pump and probe beams. In any case the long (25 ns) lifetime of the dimer makes it a good candidate for time-resolved Raman studies which may probe the degree of interaction between the monomer units in the dimeric complex.

REFERENCES

1. D R McMillin, J R Kirchoff and K V Goodwin. Coord. Chem. Rev., **64**, 83 (1985).

2. J J McGarvey, S E J Bell and K C Gordon. Inorg. Chem., **27**, 4003 (1988).

3. E M Stacey and D R McMillin. Inorg. Chem., **29**, 393 (1990).

4. J-M Lehn, A Rigault, J Siegel, J Harrowfield, B. Chevrier and D Moras. Proc. Natl. Acad. Sci. USA, **84**, 2565 (1987).

5. R.A. McNicholl, studies in progress.

ACKNOWLEDGEMENTS

We are grateful to SERC for support (GR/ F 42980) and the award of an earmarked studentship to SJR. We wish to thank the Department of Education (N Ireland) for a Distinction Award to DM. We thank Dr R.A. McNicholl for lifetime data on $[Cu_2(BP_2)_2]^{2+}$.

HOW FAST IS REDUCTIVE ELIMINATION OF DIHYDROGEN? PICOSECOND PHOTOLYSIS OF $Ru(dmpe)_2H_2$.

R. Osman, R. N. Perutz, A. D. Rooney
Department of Chemistry, University of York

INTRODUCTION

It is now well established that photodissociation of carbon monoxide from a metal carbonyl takes place in well under 1 ps, and is followed by vibrational relaxation processes which occur in 1 - 100 ps. There is another fundamental ligand dissociation process (reductive elimination) in which two metal ligand bonds are broken and a bond between the ligand atoms is made. The prototype example is the reductive elimination of dihydrogen:

Equation 1

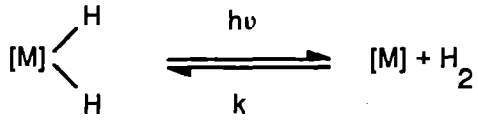

As far as is known, both this process and its reverse, oxidative addition, are concerted. Alternatively expressed, what does the word concerted mean quantitatively? Our own experiments (in York) set an upper limit to the time for reductive elimination of hydrogen of ca. 50 - 100 ns. We undertook preliminary experiments at RAL designed to probe on a much faster timescale. They hold out the exciting prospect of establishing the timescale of a reaction involving bond-breaking and bond making.

We have recently completed a set of laser flash photolysis experiments on $Ru(dmpe)_2H_2$ (dmpe is a chelating diphosphine, $Me_2PCH_2CH_2PMe_2$, see eq. 2). We have shown by nanosecond flash photolysis that this molecule loses H_2 photochemically to generate $Ru(dmpe)_2$, which has a singlet ground state and probably possesses a square planar structure. The resulting $Ru(dmpe)_2$ intermediate has a very characteristic three band optical spectrum. It reacts back with H_2 to regenerate starting material at a diffusion-controlled rate (7×10^9 dm^3 mol^{-1} s^{-1}). Proof that the transient is a reaction intermediate rather than an excited state is obtained by photolysis of the starting material in an argon matrix which gives the same spectrum (a matrix stabilises a ground state and not an excited state). We, therefore, have a reversible system for probing the reductive elimination - oxidative addition process. This is particularly well suited to picosecond absorption spectroscopy.

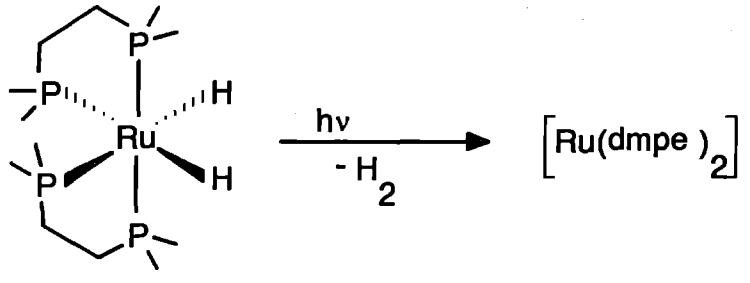

Equation 2

RESULTS

We irradiated solutions of $Ru(dmpe)_2H_2$ under one atmosphere of hydrogen in cyclohexane solution with a picosecond laser pulse at 300 nm (ca 2 μJ at the sample, 10 Hz repetition rate) and probed the transient species at a series of wavelengths between 470 nm and 720 nm. The experiments showed that a product with absorption at the characteristic wavelengths of $Ru(dmpe)_2$ (720, 540, 470 nm), figure 1 and 2, is formed with a risetime of < 16 ps, figure 3. The absorbance of product increased linearly with laser energy, indicating that we were examining a single photon process. The product does not decay over 4 ns. Its formation is independent of the relative polarization of the probe and pump beams confirming the absence of rotational effects. Unfortunately, we were not able to obtain kinetic data with different probe wavelengths sufficiently reproducibly to obtain an absorbance spectrum of the photoproduct. Here we were limited by the difficulty in ensuring consistency in the overlap of the pump and probe beams while changing monitoring wavelength, and by the small change in transmission of ca 1 - 2 %.

CONCLUSION

The ps transient absorption results obtained are very promising indicating that the upper limit for loss of dihydrogen from $Ru(dmpe)_2H_2$ is 16 ps. However, until we obtain an absorbance spectrum for the transient it is not possible to identify the picosecond photoproduct positively as the square planar species $Ru(dmpe)_2$.

ACKNOWLEDGEMENTS

We would like to express our gratitude to Dr. A. Langley and Mr. W. Shaikh for their considerable assistance.

Figure 1 $Ru(dmpe)_2H_2 + h\upsilon$

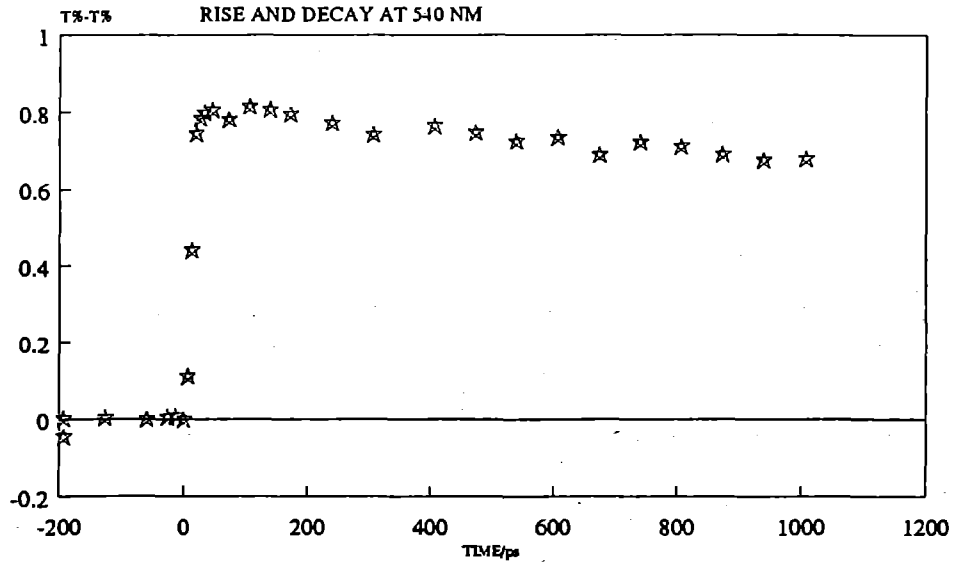

Figure 2 $Ru(dmpe)_2H_2 + h\upsilon$

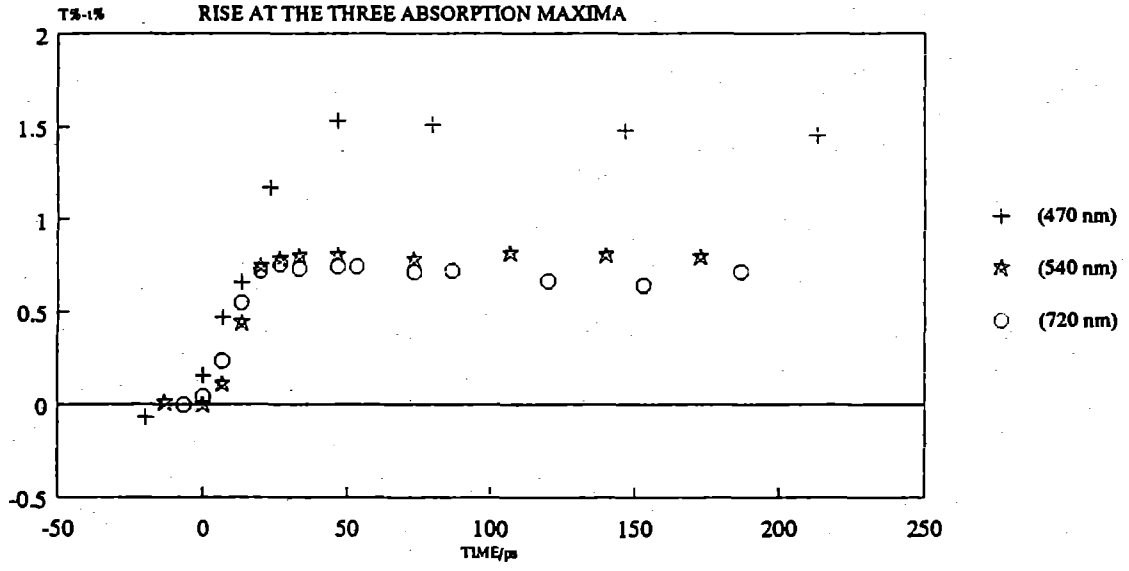

Figure 3 $Ru(dmpe)_2H_2 + h\upsilon$

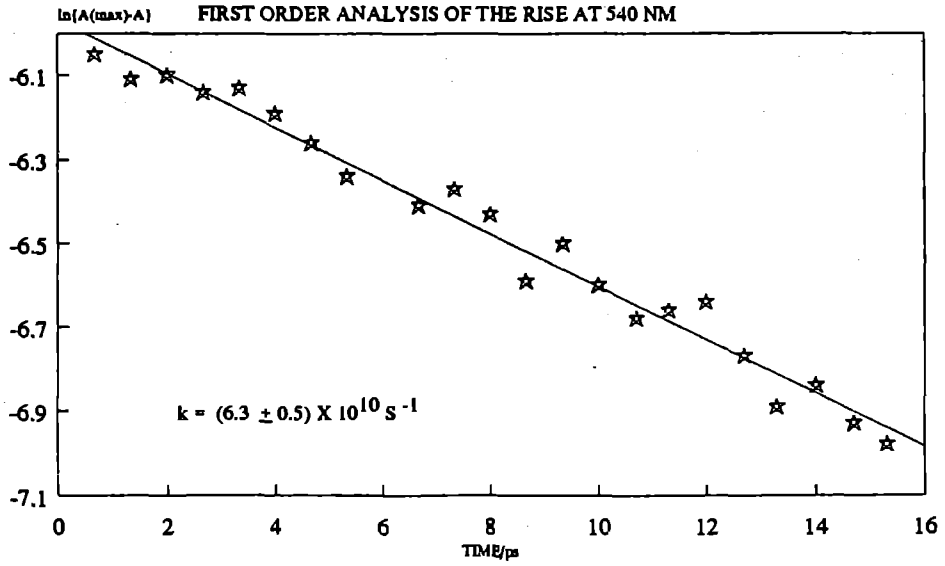

PICOSECOND TRANSIENT ABSORPTION IN PYRAZOLOTRIAZOLE AZOMETHINE DYES

F. Wilkinson[a], D.R. Worrall[a], D.J. McGarvey[a], A. Goodwin[a], J. Hobley[a], A. Langley[b] and W. Shaikh[b]
[a]Loughborough University Of Technology [b]Rutherford-Appleton Laboratory

Introduction

Pyrazolotriazole azomethine dyes (figure 1) are important compounds in the colour photographic industry. Subtractive colour photography relies on combinations of three dyes known as subtractive primaries to selectively absorb parts of the spectrum and thus give rise to all possible colours through suitable combinations[1]. The dyes used are in colour yellow, magenta and cyan, and each absorbs approximately one third and transmits approximately two thirds of the visible spectru. The pyrazolotriazole class are the principal dyes used as magenta image formers, and of the three subtractive primaries they are the most susceptible to light induced fade. Since this differential susceptibility to photochemical fade causes changes in the colour balance of a photographic print, it is desirable to reduce the fade rate of the magenta dyes. That the magenta dye should be the most susceptible to fade is somewhat unfortunate, since we are most likely to notice fade of this image component as it will result in a yellow or blue cast to flesh tones. Since the chemistry involved in the colour photographic development process places severe restrictions on the dye classes which may be used, attention has focussed on elucidating the degradation pathways of pyrazolotriazole azomethine dyes with a view to inhibiting fade either through structural modifications to the dyes or by the addition of suitable quenching agents to the product formulation.

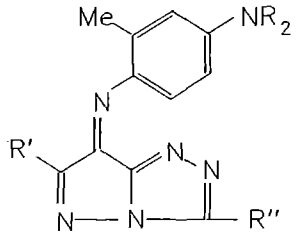

Figure 1: General structure of pyrazolotriazole azomethine dyes

From an academic point of view, these dyes represent an opportunity to add to the understanding of the processes involved in the dissipation of excitation energy in flexible dye systems, and to probe the effects of solvent parameters on the frequency of large amplitude motions. With this in mind, research has been carried out by us into the characterisation of the excited states of the pyrazolotriazole azomethine dyes. Both the singlet and triplet states of these compounds are too short lived to be studied using nanosecond flash photolysis techniques, and as a consequence the desired information can only be obtained using picosecond spectroscopy. In addition, the quantum yield of fluorescence from these dyes is very low at room temperature and consequently pump-probe laser flash photolysis to study photoinduced absorption changes has been employed in these investigations. Using nanosecond flash photolysis, only syn-anti isomerisation about the C=N azomethine linkage is observed. In dyes not symmetrical about the azomethine linkage, the anti isomer absorption spectrum is shifted bathochromically relative to the ground state absorption spectrum.

Results

We have reported previously on some initial results obtained using picosecond spectroscopy to investigate the photophysical properties of these dyes[2], which could only be explained on the basis of at least two short lived transient species being formed following pulsed excitation, which decay within fifty picoseconds of the arrival of the excitation pulse to give a species which does not decay on nanosecond timescales. The magnitude of the residual absorbance change associated with this long-lived component varies with solvent in the same manner as does that associated with the anti isomer observed using nanosecond techniques. Comparison of data from nanosecond and picosecond flash photolysis experiments leads therefore to the assignment of this component as the anti isomer of the dye. We report here an extension of these studies to include a range of solvent systems and dye substitution patterns, which have allowed tentative assignment of the two short lived transients leading to isomerisation.

The principal absorption band in the magenta product dyes is centred at approximately 530nm, and hence excitation of these dyes with the wavelengths easily accessible from the synchronously pumped dye laser is limited to the long wavelength edge of this band owing to the pumping wavelength being the second harmonic of the mode-locked Nd:YAG laser; however, appropriate substitution leads to a bathochromic shift in the maximum of this absorption band, R'=CO_2Et shifting the peak to around 600nm, allowing pumping of the dye at its absorption maximum and probing in the trailing edge of the band. Hence many studies were carried out using this model dye, and much of the information upon which state assignments have been made has come from these. However, there is evidence that the behaviour seen for this dye is general for the class, since data obtained for the dye with R'=CN demonstrates similar behaviour. The data obtained from flash excitation of this dye in a range of solvents at a range of analysing wavelengths has clearly demonstrated that at least two transient species are required to explain the observed behaviour; this is illustrated for the R'=CO_2Et dye in di-n-butylphthalate solution in figure 2. It is evident that at wavelengths shorter than 620nm, both transients absorb less than the ground state. At longer wavelengths, however, the second, longer lived transient species absorbs more than the ground state while the shorter component still absorbs less. At wavelengths greater than 660nm, where the ground state absorbs very little, the first short lived species still has some absorption.

The data has been interpreted in terms of two transients

formed sequentially, since such a model is simple to rationalise and has precedent in other flexible dye systems such as the stilbenes[3] and cyanines[4]. The first, shorter lived transient is characterised by a lifetime of between one and three picoseconds which is, to within the error of the experiment, solvent independent. There is also no evidence for a dependency of the lifetime of this state on the dye substitution patterns, although small changes may be masked by convolution with the excitation and probing pulses which are of a duration similar to the lifetime of the state. No stimulated emission can be detected from this state, and hence it is not assigned as the fluorescent singlet state. The fluorescent state is known to exist, and indeed has an appreciable lifetime at low temperature. However, the proposal is advanced that while this is the initially populated state, the barrier to isomerisation is so small that evolution to the configuration where the two ring systems are approximately orthogonally opposed is very rapid and the population of the fluorescent singlet at room temperature is extremely small. The first transient, then, is assigned as a combination of evolution of the population towards the orthogonal conformation and possible quasi-equilibrium in the potential well, if internal conversion therefrom is rate limiting. This is illustrated schematically in figure 3.

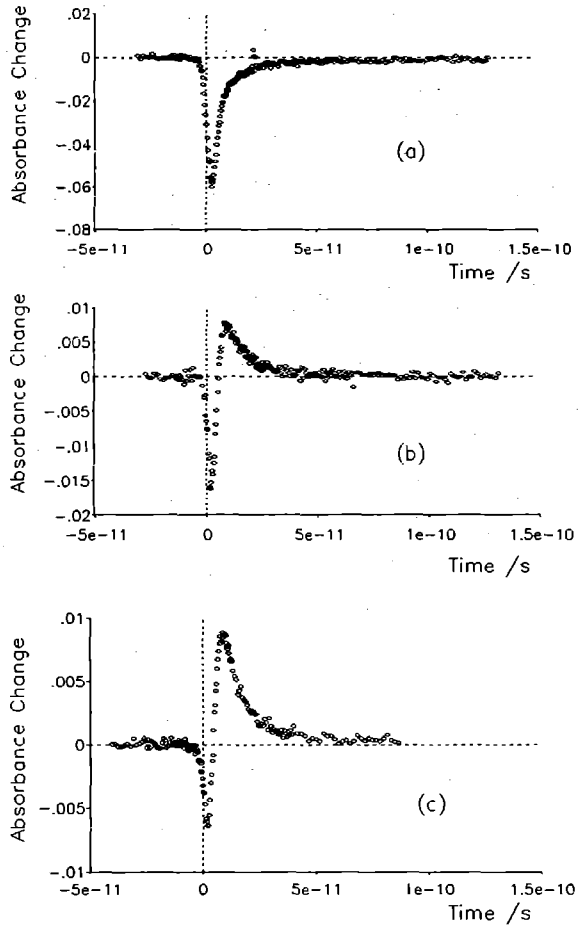

Figure 2: Transient absorption changes induced in a di-n-butylphthalate solution of the R' = CO_2Et dye exciting at 585nm and probing at (a) 600nm (b) 640nm and (c) 650nm

The second transient is characterised by a somewhat longer lifetime, of some 5 to 15ps, which shows a much greater dependency on solvent and dye structure. The solvent dependency is illustrated for the R' = CO_2Et dye in table 1. The proposal is advanced that this second transient is evolution of the population along the ground state potential surface to the two possible isomeric configurations. This again is illustrated in figure 3, evolution to the two isomeric forms being characterised by rate constants k_2 and k_3.

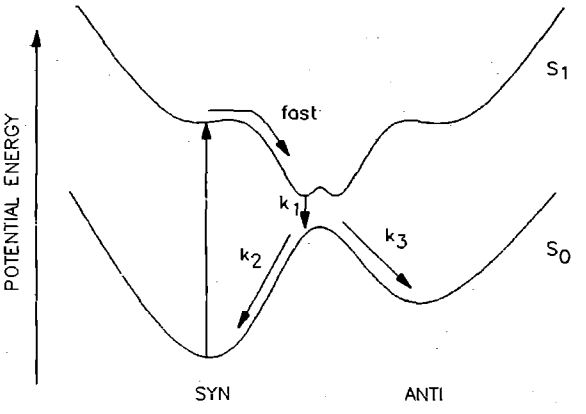

Figure 3: Potential surface diagram to explain the photophysical behaviour of azomethine dyes

Solvent	Lifetime /ps
Methanol	4.4±0.9
Di-n-butylpthalate	6.3±1.1
Benzene	8.1±1.0
Acetonitrile	9.5±0.7

Table 1: Second transient lifetime as a function of solvent

Hence the frequency of the motion on the ground state surface demonstrates an appreciable solvent dependency, which does not correlate with the standard physical solvent properties such as viscosity and dielectric constant. This is evidently due to specific solvent-solute interactions, the nature of which have not been elucidated to date.

References

1. T.H. James (Ed.), "The theory of the photographic process", fourth ed., Collier-Macmillan (1988)

2. F. Wilkinson, D.R. Worrall and R.S. Chittock, Chem. Phys. Lett., 174(5), 416 (1990)

3. S. Abrash, S. Repinec and R.M. Hochstrasser, J. Chem. Phys., 93(2), 1041 (1990)

4. V. Sundstrom and T. Gillbro, J. Phys. Chem., 88, 1788 (1982)

PICOSECOND ABSORPTION STUDIES ON THE ROLE OF CHARGE TRANSFER INTERACTIONS IN THE MECHANISM OF QUENCHING OF TRIPLET STATES BY MOLECULAR OXYGEN

F. Wilkinson[1], D.J. McGarvey[1], D.R. Worrall[1], A. Goodwin[1] and J. Hobley[1]

A. Langley[2] and W. Shaikh[2]

[1]University of Technology, Loughborough, Leicestershire LE11 3TU

[2]Rutherford-Appleton Laboratory, Chilton, Oxfordshire

ABSTRACT

This report descibes the first picosecond pump-probe studies following direct excitation into the charge transfer absorption bands of oxygenated hydrocarbon solutions.

INTRODUCTION

In 1953 Evans (1) reported the observation of additional absorption features in the UV/visible absorption spectra of oxygenated organic liquids. The origin of these absorption bands was attributed to a charge transfer (CT) transition involving a contact complex between the organic molecule (M) and molecular oxygen (O_2).

$$^1M_0 + O_2\ ^3\Sigma_g^- \leftrightarrow {}^3(M..O_2) \xrightarrow{h\nu} {}^3(M^+..O_2^-)^* \qquad (1)$$

In 1960 Mulliken (2) published a detailed discussion of these phenomena including a brief section on diffusional quenching of excited states by molecular oxygen and how these quenching processes may be related to the type of complexes described above.

In recent years attention has once more been directed towards these organic molecule-molecular oxygen complexes following a report (3) that excitation into the benzene-O_2 CT band produced singlet oxygen ($O_2\ ^1\Delta_g$). Ogilby et. al. have subsequently published several papers in which singlet oxygen yields following CT state population of different molecules have been measured (4,5). The main objective of these investigations is to shed light on the mechanism of excited state quenching by oxygen and, in particular the quenching of triplet excited states.

Charge transfer interactions during oxygen quenching of excited states have been implicated by numerous authors in the past. But perhaps the most cited work is that by Garner and Wilkinson in 1977 (6) in which they proposed the participation of charge transfer interactions (scheme 1) when triplet states of organic molecules are quenched by oxygen.

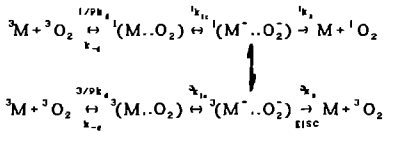

SCHEME 1

In Garner and Wilkinson's work the higher oxygen quenching rate constants observed for certain aromatic ketones and amines in comparison with aromatic hydrocarbons were interpreted as being due to the presence of low lying triplet CT states which facilitate quenching through the enhanced-intersystem crossing (EISC) pathway.

The importance of the EISC channel for aromatic ketone triplets is supported by numerous measurements showing that the efficiency of singlet oxygen production(f_Δ^T) is ~0.3 (7,8) which is close to the value of 0.25 expected from spin_statistical arguments (6). In contrast (f_Δ^T) values for aromatic hydrocarbons are generally substantially higher and often close to unity which would suggest that, for these molecules, quenching by the triplet pathway (EISC) is less important.

However a recent report by Ogilby et. al. (5) insists that these CT interactions are solvent dependent as well as sensitiser dependent. Although their reported singlet oxygen yields (Φ_Δ^T) include contributions from excited singlet state quenching they conclude that f_Δ^T values for aromatic hydrocarbons are ~0.3 in a polar solvent (acetonitrile) but in a non-polar solvent (cyclohexane) f_Δ^T values are substantially larger.

The recent literature concerning excited state interactions with oxygen is conflicting and methodically inconsistent (5,7,8,9,10). It is apparent that a unified approach is required which will aid the reporting of unambiguous and directly comparable data.

Thus, we have recently initiated a project investigating all aspects of excited state quenching by oxygen including the role of the solvent, the nature of the sensitiser and the participation of CT interactions. This involves the use of nanosecond and picosecond laser photolysis techniques particularly time-resolved absorption and time-resolved near infra-red luminescence.

We are interested in ascertaining:

(i) Whether the CT state can be detected on picosecond timescales and which are the main deactivation channels.

(ii) Whether there is any relationship between $^3(M^+..O_2^-)^*$ and the CT state postulated in scheme 1.

In these experiments we have used concentrated (1-3M) solutions of naphthalene (N) and 1-ethylnaphthalene (EN) in various solvents. The recent nanosecond investigation of the 1-methylnaphthalene(MN)-O_2 complex by Ogilby et. al. (5) invites comparison with some of the data reported here.

EXPERIMENTAL

(i) Sample preparation: solutions of 1.5M EN and 3M N in various solvents (benzene, DMF, ACN) were degassed using the freeze-pump-thaw technique. The solutions were subsequently equilibrated with 2-4 atmospheres of oxygen yielding absorbances of ~0.3 compared with < 0.05 for air-equilibrated solutions. For comparison of CT state singlet oxygen yields with the yield from a triplet sensitised process benzophenone (BZP) (or p-methoxyacetophenone (p-MAP)) was added to air-equilibrated 1.5M EN or 3M N solutions such that these solutions were optically matched to the samples under high pressures of oxygen.

(ii) Picosecond pump-probe conditions: the operating conditions of the picosecond apparatus were as follows: pump wavelength = 353nm, pump energy = 4μJ probe wavelength = 424nm and 706nm, pulse duration = 5ps, irradiation area = 0.008 cm^2. The probe wavelengths are convenient for detection of N and EN triplet states (424nm) and radical cations (706nm) which are possible products of CT state deactivation.

(iii) Nanosecond experiments: the near infra-red singlet oxygen luminescence detector was identical to a detector described previously (9).

PICOSECOND RESULTS

Typical picosecond absorption traces at 424nm for naphthalene-saturated acetonitrile (ACN) are given in Figure 1.

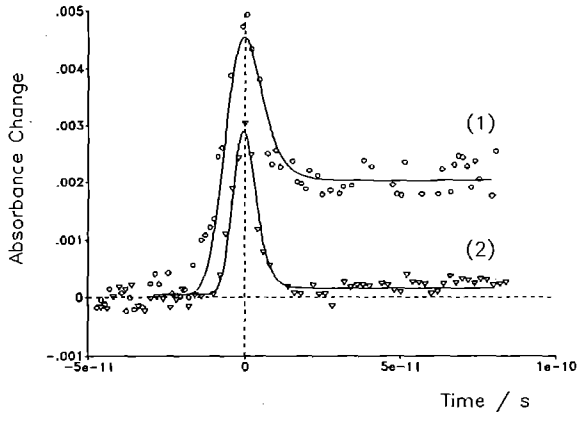

Figure 1: Typical picosecond absorption traces obtained from (1) naphthalene-saturated ACN equilibrated with 3 atmospheres O_2, (2) naphthalene-saturated ACN-nitrogen purged.

The absorption is described by a symmetrical temporally unresolved rapid rise and decay superimposed on a rapidly formed long-lived absorption which we attribute to the triplet state of N (or EN). The rapid symmetrical component observed upon excitation of N, EN in all solvents with and without oxygen is also observed for benzene(BZ) alone and is attributed by us to biphotonic excitation resulting in solvent aromatic hydrocarbon ion-pairs which rapidly undergo geminate recombination. This component has been observed previously (11) in studies of multiphoton absorption by neat aromatic liquids as a rapid component absorbing around 420nm. In this previous report the rapid component is reputed to be followed by a long-lived absorption identified as being due to biphotonically produced excimers. Richards and Thomas (12) estimate the number of biphotonic excitations per unit volume per second is given by:

$$N = (e^2/mc^2)^2(\lambda^2/n^2\Delta\nu)N_0F^2 \qquad (2)$$

Where N_0 is the number of ground state molecules per unit volume, F is the photon flux, λ is the excitation wavelength (353nm), Δν is the width of the $^1E_{2g}$ band in benzene ($4*10^{14}$ s^{-1}) and n is the refractive index.

Using this equation we calculate that the excimer absorbance under our conditions would be $< 10^{-4}$, well below our detection limit of 10^{-3}. This is consistent with the fact that we do not observe the benzene excimer at 424nm nor any long-lived component in oxygen-free N or EN solutions.

We therefore assign the type of long-lived absorption shown in Figure 1 to the triplet state of N or EN. We have compared the magnitude of these absorptions with the BZP triplet absorption from an optically matched solution of BZP in benzene. Although accurate values of the triplet absorption coefficients for N and EN are not available at present we estimate that quantum yields of triplet formation upon exciting into the CT bands exceeds 0.5 in all the solvents studied. Furthermore, the triplet state is produced very rapidly in all solvents suggesting a sub-picosecond lifetime for the initially prepared CT state. Using a probe wavelength of 706nm we searched for evidence of N^+ and EN^+ but found no absorption at this wavelength. This agrees with our findings using nanosecond flash photolysis where we were also unable to detect any radical cations. However, these observations conflict with the claims of Ogilby et. al. (5) that CT excitation of N or EN in a polar solvent (ACN) produced the radical cations N^+ and MN^+. Unfortunately, Ogilby et. al. (5) do not give specific details concerning the amount of the radicals they say they detected. Also, they do not provide any information on the radical lifetimes. These discrepancies obviously have to be resolved, so we are currently making more nanosecond and picosecond measurements to determine the product channel distributions of these CT states in a variety of solvents.

NANOSECOND RESULTS

Recently, Ogilby et. al. (5) reported singlet oxygen yields for the MN-O_2 complex in different solvents relative to the singlet oxygen yield of MN when sensitised by an aromatic ketone ($\Phi_\Delta^{MN}/\Phi_\Delta^{CT}$). We have carried out some similar experiments and, in this case, our data are in reasonable agreement with Ogilby's data. The results are given in Table 1.

Sensitiser/Solvent	ACN	DMF	BZ	CHX
Naphthalene	1.30	1.12	1.20	
1-Ethylnaphthalene	1.43	1.34	1.15	1.11
1-Methylnaphthalene (5)	1.52		1.00	1.00

Table 1: Ratio of $\Phi_\Delta^{MN}/\Phi_\Delta^{CT}$ for naphthalenes in different solvents.

REFERENCES

(1) Evans D.F., J. Chem. Soc., 345 (1953).

(2) Tsubomura H., and R.S. Mulliken, J. Amer. Chem. Soc., 82, 5966 (1960).

(3) Scurlock R.D., and P.R. Ogilby, J. Amer. Chem. Soc., 110, 640 (1988).

(4) Scurlock R.D., and P.R. Ogilby, J. Phys. Chem., 93, 5493 (1989).

(5) Kristiansen M., Scurlock R.D., Iu K-K., and P.R. Ogilby, J. Phys.Chem. 95, 5190 (1991).

(6) Garner A., and F. Wilkinson, Chem. Phys. Letts., 45, 432 (1977).

(7) Redmond R.W., and S.E. Braslavsky, Chem. Phys. Letts., 148, 523 (1988)

(8) Gorman A.A., Hamblett I., Lambert C., Prescott A.L., Rodgers M.A.J., and H.M. Spence, J. Amer. Chem. Soc., 109, 3091 (1987).

(9) McLean A.J., McGarvey D.J., Truscott T.G., Lambert C., and E.J Land, J. Chem. Soc. Far. Trans., 86, 3075 (1990).

(10) McLean A.J., and T.G. Truscott, J. Chem. Soc. Far. Trans., 86, 2671 (1990).

(11) Miyasaka H., Masuhara H., and N. Mataga, J. Phys. Chem., 89, 1631 (1985).

(12) Richards J.T., and J.K. Thomas, Chem. Phys. Letts., 5, 527 (1970).

EXCITED STATE LIFETIME OF DECAMETHYLRHENOCENE MEASURED BY SINGLE PHOTON COUNTING

Jeremy N. Hill, Robin N. Perutz and Susan M. Tavender[1]

University of York

[1]Rutherford Appleton Laboratory

INTRODUCTION

Decamethylrhenocene, Cp^*_2Re (Cp^*= η^5-C_5Me_5), has been studied by absorption and emission spectroscopies in dinitrogen matrices. The LMCT transition in the absorption spectrum exhibits almost completely resolved vibrational fine structure. Within this, there are two predominant progressions, A and B, separated by 130 cm^{-1} (B is higher energy). The A progression is further subdivided into A_α and A_β, which are separated by only ca. 20 cm^{-1} . Laser-Induced Fluorescence experiments using the nanosecond excimer pumped dye laser system at the LSF have shown that Cp^*_2Re exhibits intense structured fluorescence with the same progressions, A and B that are seen in the absorption spectrum.[1,2] Both progressions originate in the symmetric ring-metal-ring stretch, ν_4. These emission experiments revealed that the A progression was subdivided into three components; A_α, A_β, and A_γ. A_α and A_β could be excited selectively from their corresponding bands in the absorption spectrum. B band excitation not only leads to B emission, but also to emission from another site, A_γ, implying that energy transfer is occurring between these two sites/conformers. This process, as well as the decay of the excited state proved to be too fast for the nanosecond system to detect (10 ns laser pulse). Fortunately, the LMCT absorption band occurs in a region where it is possible to apply the technique of Single Photon Counting (SPC), now available at the LSF. SPC is a technique that can measure fluorescence lifetimes directly. The temporal resolution depends on the excitation source and the speed with which the electronics can respond to the light pulse. The set up at the LSF has been described previously.[3] Since a picosecond laser system is used, it is possible to measure subnanosecond lifetimes. The purpose of these experiments was to determine the emission lifetime of the various sites/conformers. If any difference between A and B emission lifetimes was observed, the rate of energy transfer between B and A_γ could be obtained.

EXPERIMENTAL SET UP

The output from the cavity dumped dye laser (570-600 nm) was used directly to irradiate a sample of Cp^*_2Re isolated in a dinitrogen matrix at 12 K. These wavelengths fall within the range of the LMCT absorption band. Laser wavelengths were determined by observing the beam through a hand held monochromator. Emission wavelengths were selected using a an interference filter. (625-635 nm). Instrument response was measured by scattered light from a ludox solution. Correct functioning of the electronics was checked by comparing the lifetimes obtained from the laser dye Rhodamine B with known literature values.[4]

RESULTS

Instrument response times were typically 400 ps. Observation of scatered light from ludox revealed that there was a small peak every 12 ns. This was found to be from the YAG pump laser. Measurement of the lifetime of a standard sample of Rhodamine B agreed with literature values.[4]

Irradiation into absorption maxima of Cp^*_2Re resulted in observable fluorescence decays. Selective excitation to induce emission from A_α and A_β was achieved and found to give a lifetime of 3.646 ± 0.015 ns, χ^2 = 1.48 (figure 1). Emission from B and A_γ was monitored and also found to have a lifetime of 3.6 ns. All experimental data could be fitted to first order decays indicating that the energy transfer step must be extremely rapid.

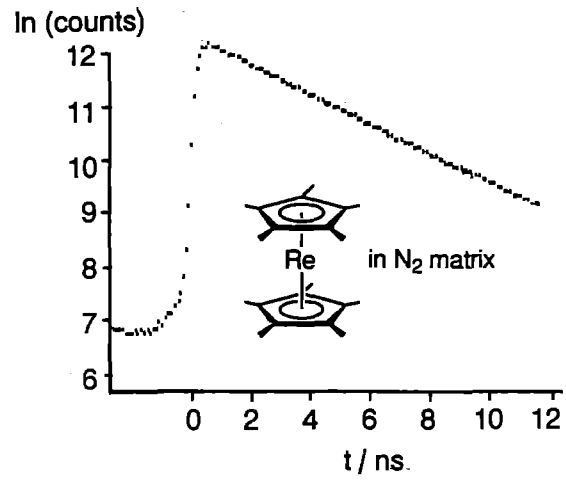

Figure 1. Logarithmic plot of fluorescence decay of Cp^*_2Re in a dinitrogen matrix at 12 K, measured using Single Photon Counting. This gives an excited state lifetime of 3.646±0.015 ns (χ^2= 1.48). Emission is observed between 625-235 nm, λ_{ex}= 588 nm.

Several problems were encountered with this experiment. The residual pump laser interfered with the fluorescence decay and caused some problems with the fitting procedure. The method of selecting the fluorescence with an interference filter appeared inadequate as the emission bands are so sharp. Better discrimination would be achieved using a monochromator. Nevertheless, they have enabled us to compare the fluorescence lifetime of Cp^*_2Re (3.6 ns) with that of Cp_2Re (72 ns) and establish that the energy transfer processes are fast compared to the rate of decay of the excited state of Cp^*_2Re.

REFERENCES

1. S. E. J. Bell, J. N. Hill, A. McCamley and R. N. Perutz, J. Phys. Chem., 94, 3876 (1990)

2. S. E. J. Bell, J. N. Hill, A. McCamley and R. N. Perutz, *Annual Report to the Laser Facility Committee*, Rutherford Appleton Laboratory Report RAL-91-025, 134 (1991).

3. S. M. Tavender, *Annual Report to the Laser Facility Committee*, Rutherford Appleton Laboratory Report RAL-91-025, 202,(1991).

4. L. A. Chewter, R. A. Lampert, S. R. Meech, D. V. O'Connor, D. Phillips and A. J. Roberts, Anal. Chem., 55, 68 (1983).

Time-Resolved Raman Spectroscopy of an Electron Transfer Reaction

E Vauthey[1], D. Phillips[2] and A. W. Parker[3]

[1]ETH, Zurich, Switzerland
[2]Department of Chemistry, Imperial College
[3]Laser Support Facility, Rutherford Appleton Laboratory

Introduction

There is still controversy over the nature of the intermediates resulting from electron transfer between a donor acceptor pair, Figure 1. Specifically the state arising from energy transfer between a triplet state acceptor and donor ground-state is sometimes referred to as a triplet exciplex [1,2], but could be a geminate radical ion pair [3]. In addition, the distinction by transient absorption spectroscopy between a geminate ion pair and free ions is difficult. We present here time-resolved resonance Raman spectral data on the electron transfer reaction between triplet 9,10-anthraquinone (AQ) and 1,2,4-trimethoxybenzene (TMB) in solvents of different polarity, which clarifies the situation for this donor-acceptor pair. The apparatus has been described fully elsewhere [4].

Results and discussion

Figure 2 shows typical high-frequency results in three solvents, and at different delays. Table 1 gives frequencies of transient species in acetonitrile and in benzene for the AQ/TMB pair, and Table 2 gives tentative assignments of the various bands. In acetonitrile, the rate of separation of the geminate ion pair into free ions is expected to be much faster than spin conversion, and Raman spectra are very similar to that of the anthraquinone radical anion, $AQ^{-\cdot}$. Raman spectra are very similar to that of the anthraquinone -2,6-disulphonate radical anion [5] when probed at 460nm, bands at 1516cm^{-1} and 1336cm^{-1} were assigned to AQ-., and those at 1608 and 1140cm^{-1} to $TMB^{+\cdot}$.

In benzene, dissociation into free ions cannot occur. With the exception of the 1570cm^{-1} band, all bands in benzene are at the same frequencies as in acetonitrile, thus whatever the transient, the vibrational frequencies are similar to those of the free radical ions. The most likely candidate is the geminate ion pair. There is no good evidence in any solvent of triplet exciplex formation.

The 1607cm^{-1} band in acetonitrile assigned to the aromatic C-C stretch of $TMB^{+\cdot}$ is solvent dependent, occurring at 1590cm^{-1} in CCl_4 (Figure 1), 1602cm^{-1} in hexafluorobenzene, and 1607cm^{-1} in cyclohexane. This environmental dependence can be used to study separation of the geminate ion pair into free ions, since the environment of the $TMB^{+\cdot}$ in the geminate ion pair consists of both solvent molecules and the counter ion $AQ^{-\cdot}$, whereas in the solvated free ion it is solvent molecules only. The time-dependence of the TR^3 spectra in Figure 1 shows this clearly. Thus in acetonitrile, at Δt=0ns, the $TMB^{+\cdot}$ band has maxima at 1618cm^{-1} and 1607cm^{-1}, attributable to geminate ion pair and free ion respectively. At longer delays, the 1618cm^{-1} band disappears, but accurate measurements of the rate of disappearance in this solvent are beyond the resolving power of the instrument. In 1,1,2,2-tetrachloroethane, TCE, the band positions are at 1607 and 1590cm^{-1} respectively, and the shift is slower, and thus more easily measured. Estimated rate constants (K^{exc}_{diss}) for separation of geminate ion pair to solvated ions based upon the Weller equation (2)[6] is 7×10^8s^{-1} in acetonitrile, and 2.5×10^5s^{-1} in TCE in good agreement with experiments here.

$$k^{exc}_{diss} = \frac{2.3\cdot10^9}{\eta}(cPs^{-1})\exp\left(-\frac{e^2}{\varepsilon_s kT}\left(\frac{1}{d}-\frac{1}{a}\right)\right)$$

e.g. Where η is the solvent viscosity, ε_s the static dielectric constant, a and d, the acceptor-donor distance in the exciplex and geminate ion pair respectively.

FIGURE 1: Reaction scheme of a photoinduced e.t. reaction involving an excited state including the various possible transients.

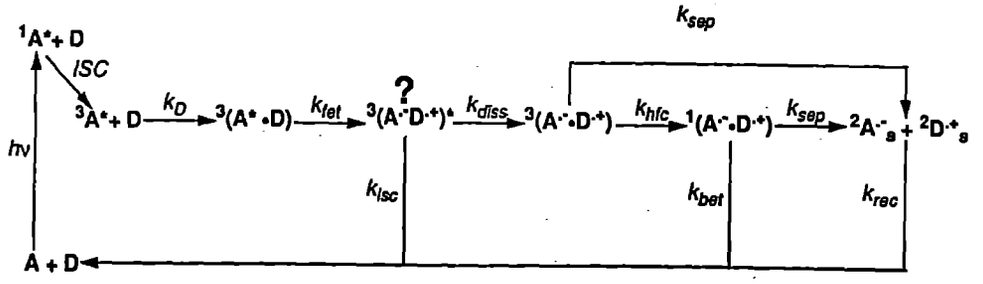

TABLE 1: Frequencies (in cm^{-1}) of the Raman bands observed for the AQ/TMB couple in MeCN and benzene when pumped at 351 nm and probed at 460 and 540nm.

probed at 540 nm		probed at 460 nm	
in MeCN	In benzene	In MeCN	In benzene
1516	1510	1608	---
1336	1337	1516	1511
1171	-----	1337	1337
1016	-----	1140	1135
961	-----	-----	1014
747	747	546	545
679	678	532	536
492	-----	493	-----
373	373		

TABLE 2: Observed high frequencies (in cm^{-1}) and tentative assignments by comparison with AQ26DS of QA and $AQ^{\cdot-}$, $^3AQ^*$, TMB and $TMB^{\cdot+}$.

AQ	$AQ^{\cdot-}$	$^3AQ^*$	TMB	$TMB^{\cdot+}$	assignment[a]
1666	1336	1322			(C=O) str
			1612	1607	(C-C) str
1595	1513	1540			(C-C) str
1178	1171	1141?			(C-H) ip bend
			1156?	1140	
1030	1016	1016			

a) str=stretch; ip=in plane.

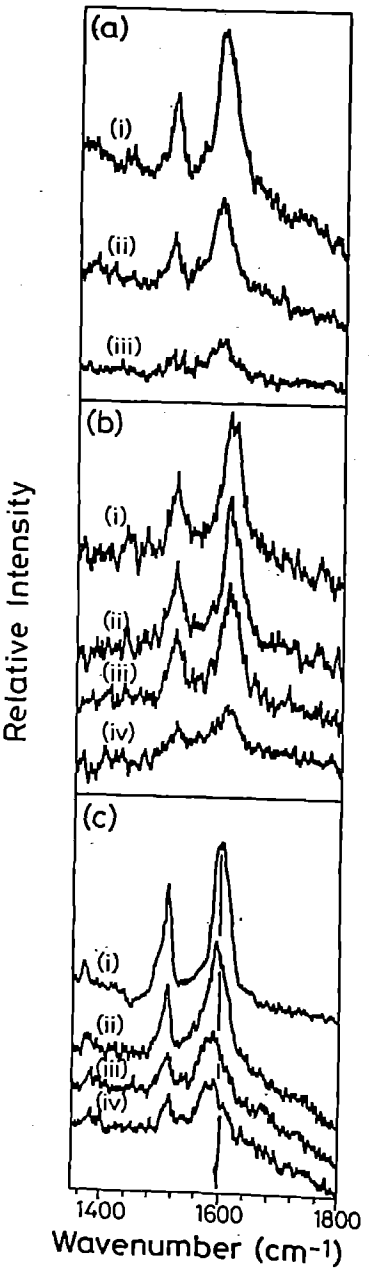

FIGURE 2: Corrected TR^3 spectra of AQ in the presence of TMB pumped at 351 nm and probed at 460 nm in:

a) CCl_4 with time delays of 45 ns (i), 300 ns (ii) and 1000 ns (iii);

b) MeCN with time delays of 0 ns (i), 100 ns (ii), 100 ns (iii) and 500 ns (iv)

c) TCE with time delays of 5 ns (i), 1 μs (ii) 5 μs (iii) and 15 μs (iv)

References

[1] U. Steiner and G. Winter Chem. Phys. Letters 55, 364, (1978)

[2] V.A. Kuzmin, A.P. Darmangan, and P.P. Levin Chem. Phys. Letters 63, 509, (1979)

[3] T. Asahi, and N. Mataga J. Phys. Chem. 93, 6575, 1989)

[4] 'Time-resolved resonance Raman Spectroscopic investigations on the photochemistry of ubiquinone'A.W.Parker, R.E. Hester,D.Phillips and S. Umapathy JCS Faraday Transactions (submitted).

[5] J.N. Moore, D. Phillips and R.E. Hester J. Phys. Chem. 92, 5619, (1988)

[6] A. Weller Pure Applied Chem. 54, 1885, 1982

PS-TR^3 STUDIES OF THE EXCITED SINGLET STATE OF TRANS-STILBENE IN MICELLES

R. E. Hester[1], I. K. Lednev[1], P. Matousek[2], J. N. Moore[1], A. W. Parker[2], D. Phillips[3], W. T. Toner[2], M. Towrie[2] and S. Umapathy[1].

[1]Chemistry Department, University of York
[2]Laser Division, RAL
[3]Chemistry Department, ICSTM, London

INTRODUCTION

The photoisomerization of trans-stilbene (*t*S) and its simple derivatives have been studied for almost 50 years [1]. This reaction serves as a model for the important class of unimolecular isomerizations. Its study continues to yield valuable mechanistic insights and is helping to provide a good understanding of solvent effects. The generally accepted potential energy profile for the *trans/cis* interconversion involves an electronic ground state (S_0) characterized by a high barrier peaking at the 90° twisted geometry and an excited state (S_1) having a potential well at this geometry. A small potential barrier inhibits twisting from the *trans*-planar geometry in the S_1 state but not from the *cis*-planar side. In the 90° twisted geometry the transition from the S_1 to the S_0 potential surface occurs in less than a picosecond, but the overall reaction dynamics result in an S_1-*t*S lifetime of some tens of picoseconds in alkane solvents.

A detailed vibrational mode assignment has been reported, based on the C_{2h} symmetry point group [2]. This helps to interpret the vibronic spectra from *t*S in jets which, together with a rotational analysis, indicate weakening (elongation) of the ethylenic C_e=C_e bond and strengthening (shortening) of the bonds to the phenyl groups, C_e-C_p [1], in going from S_0 to S_1. In its turn, this is consistent with the most intense bands in the resonance Raman spectra of S_1-*t*S being due to the C_e=C_e and C_e=C_p bond stretching modes.

EXPERIMENTAL

We have used picosecond time-resolved resonance Raman (ps-TR^3) studies to determine the vibrational spectra of the excited singlet state of *t*S. The apparatus used for this work employs a copper-vapour-laser (CVL)-pumped multipass dye cell to amplify the output of a cavity-dumped dye laser and has been described in previous reports [3]. Approx. 5 ps pulses at 4.5 kHz were used to pump the ground state of *t*S at 305-310 nm and synchronous probing with pulses at 610-620 nm, controlled by an optical delay line, gave good quality vibrational spectra of the species (see Fig. 1). Average probe powers in the range 30-60 mW were used, with pump-probe time delays ranging from -150 ps to +1200 ps.

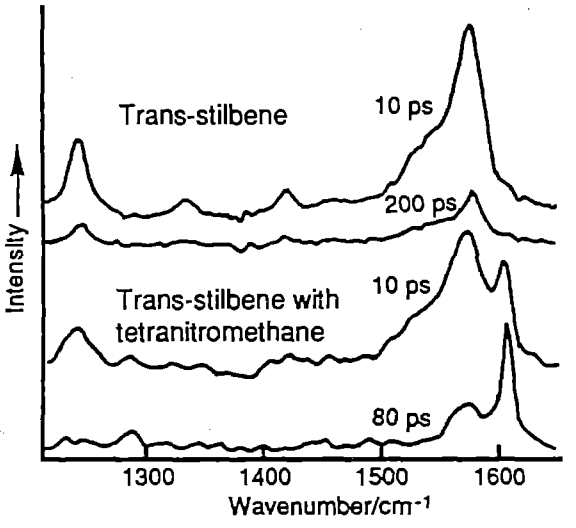

Fig. 1. ps-TR^3 spectra of *trans*-stilbene (*t*S) in aqueous Triton X-100 micelles, showing the effects of added tetranitromethane (TNM) quenching agent. Time delays between the 305 nm pump and 610 nm probe pulses are shown. [*t*S] = 1 x 10^{-3} M; [TX-100] = 5 x 10^{-2} M; [TNM] = 2 x 10^{-2} M.

Millimolar solutions of *t*S in n-hexane and in acetonitrile were used to calibrate and standardize the experimental conditions. These then were compared with *t*S in aqueous solutions containing the surfactant Triton X-100 (a neutral molecule) or SDS (anionic) at levels in excess of their critical micelle concentrations (CMCs). Micellar solutions of *t*S were then modified by the addition of various concentrations of the powerful electron acceptor tetranitromethane (TNM), which functions as a quenching agent in the presence of S_1-*t*S. The resonance Raman bands of S_1-*t*S were monitored (wavenumbers and bandwidths) as a function of the changing solution conditions (all at ambient room temperature) and their intensities were measured as a function of pump-probe delay time.

RESULTS AND DISCUSSION

Figure 1 shows representative ps-TR^3 spectra obtained with both short and long time delays for S_1-*t*S in aqueous Triton X-100 micelles, with and

without added TNM. The TX-100 concentration here was 5 x 10^{-2} M, TNM 2 x 10^{-3} M, and *t*S 1 x 10^{-3} M. The strong Raman band at 1573 cm^{-1} for *t*S in TX-100 without added TNM is attributed to C_e=C_e bond stretching, while the low wavenumber shoulder (*ca.* 1530 cm^{-1}) arises from a phenyl ring breathing mode. The Figure shows that the $\nu(C_e=C_e)$ band is still readily measurable at a time delay of 200 ps, although it has diminished greatly in intensity. Careful examination of many spectra taken over a wide range of time delays indicates a small shift in the $\nu(C_e=C_e)$ band maximum to higher wavenumber and also a narrowing of the bandwidth with increasing time delay.

The illustrative data given in Fig. 1 show quite striking effects resulting from the addition of TNM. The 1573 cm^{-1} band is shifted down to *ca.* 1570 cm^{-1} and becomes broader. Similarly the 1242 cm^{-1} band (attributed to C_e-C_p vibration coupled with a phenyl ring mode) shifts down to 1238 cm^{-1} and broadens on addition of TNM. A new, sharp band appears at *ca.* 1605 cm^{-1}. Fig. 1 shows the lifetime of the S_1 species to be much shorter in the presence of TNM and also shows that the species responsible for the 1605 cm^{-1} band has a much longer lifetime. This 1605 cm^{-1} band has been attributed to the tS^+ free radical cation [4].

A typical plot of the S_1 Raman band intensity against time is shown in Fig. 2, this being determined for 1 x 10^{-3} M *t*S with 4.7 x 10^{-2} M TX-100 and 2 x 10^{-2} M TNM. The curves fitted to the experimental points are derived on the basis of (1) a well established mathematical model for photoinduced bimolecular redox processes in micellar systems [5] and (2) a simple monoexponential function. The two approaches are consistent in giving a lifetime of τ = 74 ± 12 ps for S_1-*t*S in TX-100 micelles quenched by TNM. This compares with τ = 383 ± 19 ps in the absence of TNM. This latter lifetime is substantially longer than that found for S_1-*t*S in n-hexane solution (74 ± 5 ps, in agreement with previously published work [6]). Our analysis yields a rate constant for the intramicellar TNM quenching reaction of 2 x 10^8 s^{-1} in TX-100, which is consistent with the analysis of fluoresence quenching data in similar systems [7].

These new data reveal the effectiveness and subtlety of the ps-TR^3 spectra of *t*S as a probe of solvent-solute interactions. We have reproduced the recently reported transient Raman data on *t*S in n-hexane and acetonitrile which revealed how mode-specific, solvent-dependent dynamics relate to the mechanism of intra-molecular vibrational relaxation and energy transfer [8]. We then have extended the study to the important topic of micellar systems. A more detailed report of these results and their interpretation is in preparation.

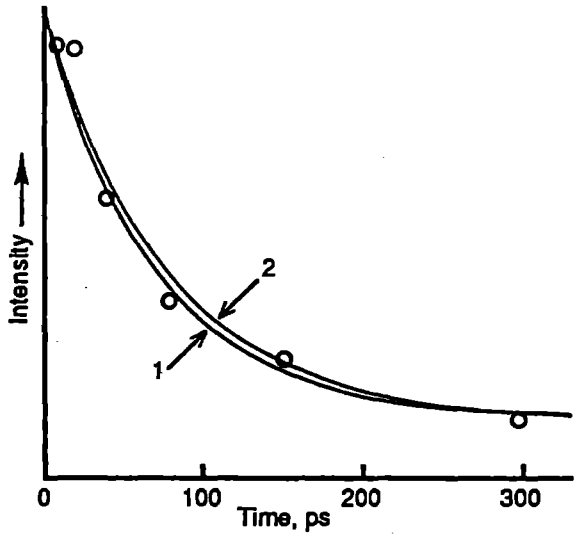

Fig. 2. Decay kinetics of the *trans*-stilbene excited singlet state after photoexcitation of a 1 x 10^{-3} M solution in aqueous Triton X-100 (4.7 x 10^{-2} M) micelles, with 2 x 10^{-2} M tetranitromethane added as a quenching agent. Points marked (o) show Raman band intensities at various pump-probe delay times. (1) and (2) are theoretical fits (see text).

REFERENCES

1. D.H. Waldock, *Chem. Rev.* **91**, 415 (1991).
2. T. Urano, H. Hamaguchi, M. Tasumi, S. Tsuchiya and T.L. Gustafson, *J. Chem. Phys.* **91**, 3884 (1989).
3. S. Umapathy, E. Turan, J.N. Moore, S.E.J. Bell and R.E. Hester, RAL (CLF) Ann. Rep., 189 (1990); G.J. Hirst, P. Matousek, P. Mawson, W. Toner, M. Towrie, A. Parker and R. Williams, RAL (CLF) Ann. Rep., 201 (1991).
4. H. Hamaguchi, *J. Phys. Chem.* **89**, 2587 (1988).
5. M. Maestri, P.P. Infelta and M. Grätzel, *J. Chem. Phys.* **69**, 1522 (1978).
6. T.L. Gustafson, D.M. Roberts and D.A. Chernoff, *J. Chem. Phys.* **79**, 1559 (1983); *ibid* **81**, 3438 (1984).
7. M. van der Auweraer, D. Dederen, C. Palmans-Windels and F.C. de Schryver, *J. Am. Chem. Soc.* **104**, 1800 (1982).
8. T.L. Gustafson, K. Iwata, L.A. Huston and W.L. Weaver, *Proc. 5th Internat. Conf. on Time-resolved Vibrational Spectroscopy* (ed. H. Takahashi), Tokyo, Japan, 1991, p90.

PICOSECOND TIME-RESOLVED RESONANCE RAMAN SPECTROSCOPY OF CAROTENOIDS.

P.F.Conn [a], P.Matousek [b], A.W Parker [b], M.Towrie [b] and T.G.Truscott [a].
[a] Department of Chemistry, Keele University, Staffs. ST5 5BG, UK.
[b] Laser Support Facility, Rutherford Appleton Laboratory, Oxon. OX11 OQX, UK.

Introduction

In photosynthesis, carotenoids assume two roles, that of accessory light harvesting pigments and photoprotective agents [1]. Both functions involve energy transfer ; in the former, the lowest excited singlet state of the carotenoid transfers energy to the chlorophyll/ bacteriochlorophyll singlet state, while in the latter, the carotenoid intercepts the chlorophyll/ bacteriochlorophyll triplet state and/or singlet oxygen thereby preventing harmful photo-oxidative damage.

Excitation of *all-trans* β-carotene results in population of the $1\,^1Bu$ (S_2) state which within 300fs internally converts to the 2^1Ag (S_1) state [2]. The intense absorption in the visible region, 400-500nm, arises from the allowed 1^1Bu-1^1Ag (S_2-S_0) transition, electronic transitions between the 1^1Ag and 2^1Ag states are symmetry forbidden. The lifetime of the 2^1Ag state of *all-trans* β-carotene has been determined as 8.4ps [3] using picosecond ground state recovery techniques. So far, the determination of the exact mechanism whereby carotenoids act as light harvesting agents has been hampered by the short lifetimes of the excited states involved and the very low fluorescence quantum yield of these molecules. Raman spectroscopy is particularly suited to the study of non-fluorescent or weakly fluorescent molecules and since $\Phi_f \sim 10^{-5}$ [2,4] carotenoids are ideal candidates for this technique. Time-resolved resonance Raman spectroscopy (TR^3) has been used extensively to probe the lowest excited singlet state of carotenoids. The position of the C=C stretch of *all-trans* β-apo-8′-carotenal (ATBA) in the 2^1Ag state was first reported in 1989 [5], its unusually high frequency is ascribed to vibronic coupling between S_0 and S_1 [6].

In this work, picosecond resonance Raman spectroscopy was used to generate spectra of ATBA, lycopene and decapreno-β-carotene in their lowest excited singlet states. Time-resolved measurements yielded a lifetime for the 2^1Ag state of ATBA in cyclohexane.

Experimental

Carotenoids were generously supplied by Hoffmann-la Roche. Solutions were prepared in either cyclohexane (8×10^{-4}M) or in tetrahydrofuran (10^{-3}M). Spectrograde solvents were employed throughout. Samples were nitrogen saturated and maintained at constant temperature, 17+/-2°C, by immersing the sample reservoir in an ice bath.
The TR^3 apparatus is described elsewhere [7].

Results and Discussion

The lifetime of the 2^1Ag state of all-t β-apo-8'-carotenal

Fig. 1 shows a set of time-resolved resonance Raman spectra for ATBA in cyclohexane. The peak corresponding to the 2^1Ag C=C stretch is clearly seen to rise and fall with increasing delay times. Each spectrum corresponds to an accumulation time of 600s and spectra are corrected for any variation in pump and/or probe intensity throughout the run. Each spectrum was normalised to ground state Raman bands assuming linear dependence of the transient intensity on the product of pump and probe intensities, after the ground state Raman band subtraction.

Figure 1 *Resonance Raman spectra of ATBA in cyclohexane using 306nm pump (0.4μJ) and 612nm (1.8 μJ) probe. The data are presented as subtracted spectra, obtained by subtraction of a negative delay (-100ps) spectrum. Pulse Width 10+/-2ps.*

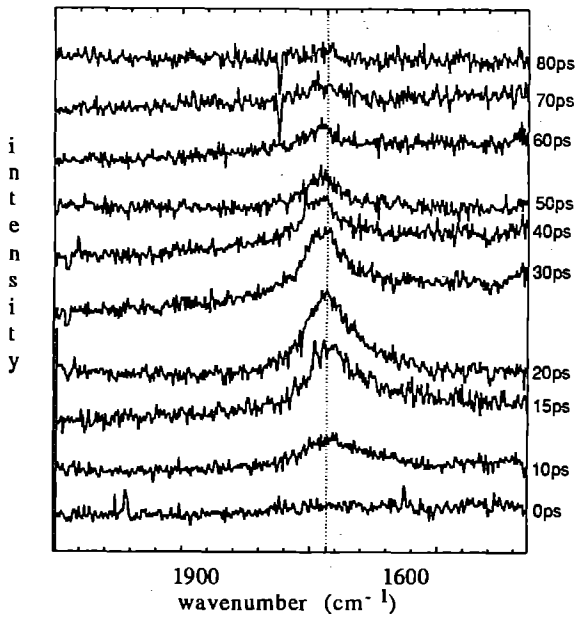

The rise time of the transient Raman, peak between 0 and 20ps delay, is fully explained by pump / probe pulse width giving a minimal response time of the apparatus of the order of 20ps. The lifetime of the 2^1Ag state of ATBA was determined to be 22+/-4ps by deconvolution from the response function. This value compares favourably to an earlier estimate of 25ps [3] which was determined using picosecond excitation and following the kinetics of the recovery of the ground state. Some asymmetry of the resonance Raman peak was observed at short time delays, 10-15ps, and this

effect will be examined further. Similar observations have been reported for ground state carotenoids [8] and for the excited singlet state of *t*-stilbene [9,10]. In the first case, the broadening was assigned to the population of excited vibrational levels in the 1^1Ag state by the decay of the 2^1Ag state. For *t*-stilbene, this was assigned to a distribution of conformations in the S_1 state with differing degrees of twist, while Hamaguchi [10] attributed this effect in part to power broadening. Furthermore, at long time delays the position of this transient band is seen to shift by ~23cm^{-1} to a higher wavenumber. These effects may be due to the C=C stretching vibration within the 1^1Bu state prior to conversion to the 1^1Ag.

Assignment of the 2^1Ag C=C stretching frequency in lycopene and decapreno-β-carotene

Fig. 2a is the resultant resonance Raman difference spectrum, high power minus low power, of lycopene in tetrahydrofuran with excitation at 578nm. The resonance Raman peak is assigned to the 2^1Ag C=C stretch in lycopene based on previous TR^3 studies of the 2^1Ag state of carotenoids and on its lifetime.

Figure 2a *High power probe (578nm) minus low power resonance Raman spectrum of lycopene in tetrahydrofuran.*
Figure 2b *Probe-only (597nm) spectrum of decapreno-β-carotene in cyclohexane. Raman intensities are not comparable.*

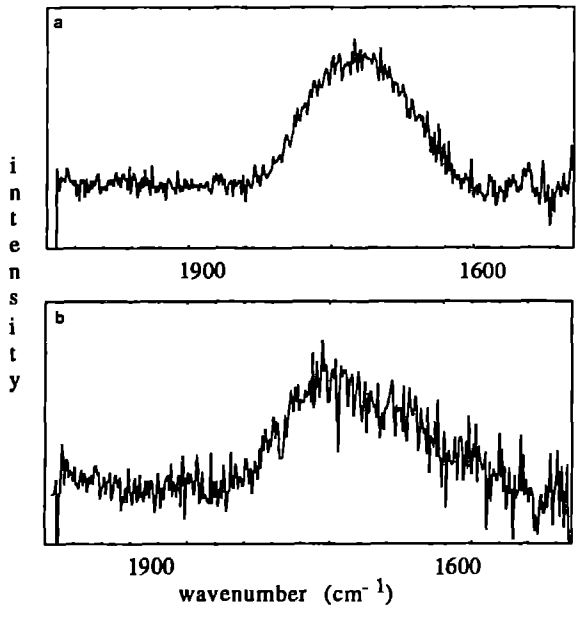

In cyclohexane, (spectrum not shown), with excitation at 597nm, the band is shifted to higher wavenumbers following the solvent dependent behaviour of ATBA, although the increase in bandwidth (156cm^{-1} to 202cm^{-1}) is much less marked for lycopene than for the apo-carotenoid. The resonance Raman profile shown in Fig. 2a was generated using probe-only excitation, in fact, pump excitation in the UV (298nm) did not result in the population of the 2^1Ag state. This suggests that a mechanism other than that outlined in the introduction occurs on excitation in this low wavelength region.

Again, using probe-only excitation at 597nm, the resonance Raman spectrum of decapreno-β-carotene in cyclohexane, Fig. 2b, was obtained. Previously only the ground and excited triplet state of this molecule has been studied by TR^3 [11]. The band at 1760cm^{-1} is assigned to the C=C stretching frequency in the 2^1Ag state, for the same reasons stated above for lycopene, and is, within our error limits of +/-5cm^{-1}, at the same position as the C=C stretch of lycopene, a significantly shorter carotenoid. This supports previous work [12] which demonstrated convergence of the position of the C=C stretch in the 2^1Ag state of carotenoid with increasing chain length.

The results from this work can be used to determine both kinetic and structural data on the carotenoids.This will lead to a better understanding of the energy transfer mechanism *in vivo*.

Acknowledgements

We thank Professor R E Hester, Professor D Phillips and Mr W T Toner for access to the ps-TR^3 system.

Dr. C. Lambert is thanked for many useful discussions. We are grateful to Hoffmann-La Roche for the generously donating the carotenoids.

References

[1] R.J.Cogdell and H.A.Frank, Biochim. Biophys. Acta **895** (1987) 63
[2] T.Gillbro and R.J.Cogdell, Chem. Phys. Lett. **158** (1989) 312
[3] M.R.Wasielewski and L.D.Kispert, Chem. Phys. Lett. **128** (1986) 238
[4] S.L.Bondarev, S.M.Bachilo, S.S.Dvornikov and S.A.Tikhomirov, J.Photochem. Photobiol. A : Chem. **46** (1989) 315
[5] H.Hashimoto and Y.Koyama, Chem. Phys. Lett. **162** (1989) 523
[6] T.Noguchi, H.Hayashi, M.Tasumi and G.H.Atkinson, J. Phys. Chem. **95** (1991) 3167
[7] In SERC Laser Support Facility Annual Report, (1992). Picosecond Time-Resolved Resonane Raman Spectroscopy Apparatus - A Progress Report, Section C4.
[8] H.Hayashi, T.L.Brack, T.Noguchi, M.Tasumi and G.H.Atkinson, J. Phys. Chem. **95** (1991) 6797
[9] T.L.Gustafson, D.M.Roberts and D.A.Chernoff, J. Chem. Phys. **79** (1983) 1559
[10] H.Hamaguchi, J. Chem. Phys. **89** (1988) 2587
[11] R.F.Dallinger, S.Farquharson, W.H.Woodruff and M.A.J.Rodgers, J. Am. Chem. Soc. **103** (1981) 7433
[12] T.Noguchi, H.Hayashi, M.Tasumi and G.H.Atkinson, Chem. Phys. Lett. **175** (1990) 163

TIME RESOLVED RESONANCE RAMAN STUDIES OF CAROTENOIDS IN HOMOGENEOUS AND MICELLAR SOLUTIONS

P.F. Conn[1], J. Haley[1], C. Lambert[1], A.W. Parker[2] and T.G. Truscott[1].

[1]Department of Chemistry, Keele University, Staffs. ST5 5BG
[2]Laser Support Facility, Rutherford Appleton Laboratory, Oxon. OX11 OQX

INTRODUCTION

Carotenoids are ubiquitous pigments which function as light harvesting pigments, antioxidants and colourants. They are currently of great interest being suggested as possible anti-cancer agents [1]. Of prime importance in their photophysical behaviour is their ability to undergo energy transfer and it is this mechanism which is the subject of the present work. Time resolved resonance Raman spectroscopy (TR^3) has in the past provided critical structural information on both the excited singlet and triplet states of carotenoids, *in-vitro* and more recently *in-vivo* [2].

For this work we have studied the lowest excited triplet state of all-t β-carotene, lycopene, γ-carotene, zeaxanthin and canthaxanthin. The results obtained for all these carotenoids were similar and for the purposes of this report only β-carotene and γ-carotene will be considered. To our knowledge, the Raman profile of γ-carotene has not been reported as has not the resonance Raman spectra of any carotenoids in micellar solutions. Previous photophysical studies of β-carotene in micellar solutions have been concerned with charge transfer processes [3], triplet-triplet energy transfer from chlorophyll [4] and singlet oxygen quenching [5]. Chauvet *et al.*, using the model of Robson and Dennis [6] for Triton X 100 (TX100) proposed that β-carotene is localised in the hydrophobic core of the micelle.

MATERIALS AND METHODS

Carotenoids were generously supplied by Hoffmann- La Roche and used without further purification. Anthracene (Fluka 99%+), was recrystallised from benzene prior to use. TX100, (Fluka) and spectrograde solvents were used as supplied.

Raman spectra of the carotenoid triplet states were obtained using nitrogen saturated solutions at ambient temperature which were maintained at a steady flow through the Raman cell by a peristaltic pump. Micellar solutions were prepared by adding stock solutions of anthracene and carotenoid in chloroform or carbon tetrachloride, to TX100 followed by rotary evaporation to remove the organic solvent. The resultant film was resuspended by addition of the appropriate volume of water. Solutions of 2% of TX100 (w/v) were used to solubilise the carotenoid. Working solutions were $5x10^{-5}M$ in anthracene and $1x10^{-4}M$ in carotenoid.

The resonance Raman apparatus has been described previously [7]. The exact wavelength of the probe beam depended on the triplet absorption spectrum ; β-carotene, γ-carotene and zeaxanthin were probed at 527nm while the remaining carotenoids were probed at 550nm. The pulse width is of the order of 9ns. TR^3 spectra were obtained at laser powers where the Raman signal was linearly dependant on pump and probe laser powers. The carotenoid triplet states were generated by energy transfer from anthracene. Care was taken that the flow rate was sufficient to present a fresh sample to the pump and probe beams for every shot, but slow enough that there was negligible movement of the sample, in the overlapped beams over the time of the pump-probe. The maximum delay time was 50μs.

RESULTS AND DISCUSSION

The results obtained in homogeneous solution are similar to those reported previously by Dallinger *et al.* [8] The Raman spectrum of γ-carotene has not been previously reported and is shown in figure 1.

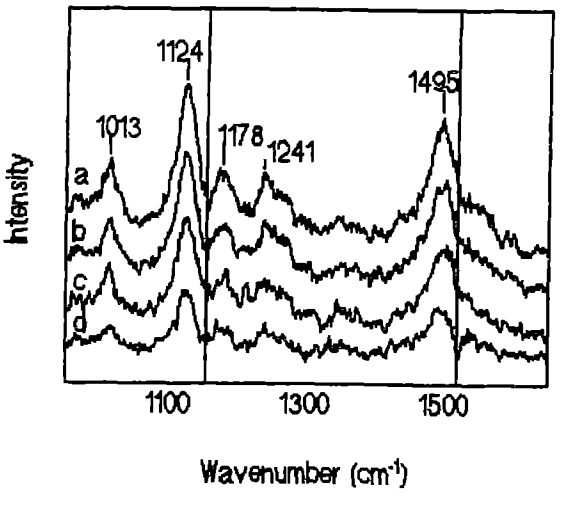

Figure 1. TR^3 spectra of triplet γ-carotene in $CHCl_3$ with pump-probe delays of a) 3μs b) 2μs c) 1μs d) 10μs. Pump 359nm, probe 527nm. Spectra are corrected for both solvent and ground state bands. The cursors mark the position of the carotene ground state Raman.

The spectrum recorded in TX100 micelles for β-carotene, with 3μs delay is shown in figure 2b. This spectrum is almost identical to that seen in homogeneous media, figure 2a.

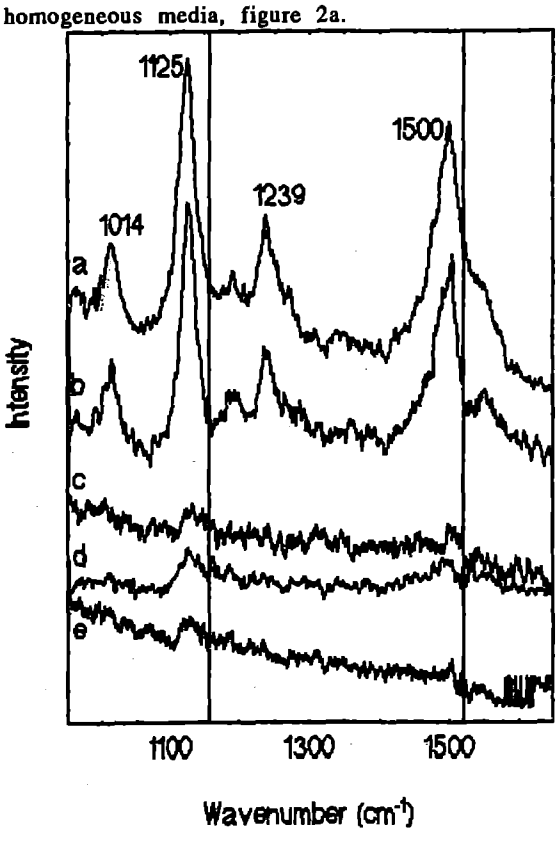

Figure 2. TR^3 spectra of triplet β-carotene in a) benzene at 3μs delay, b)TX100 at 3μs delay and c) at overlap, d) TX100 / AOT at 3μs delay, and e) at overlap. Pump 359nm, probe 527nm. Spectra are corrected for solvent and ground state bands. The cursors mark the position of the carotene ground state Raman.

The observation that the TR^3 spectra were unchanged in micellar solutions implies two possibilities. The first is that carotene triplet state Raman spectra are insensitive to environment, or secondly, that the environment within the micelle is strongly hydrophobic.

Of particular interest is that the resonance Raman spectrum of the carotenoid triplet could be observed within the pump pulse (at overlap) for all the carotenoids used. Control experiments were run using micelle only and carotene-micelle only solutions. Under these conditions Raman was not observed. It should be noted that we failed to observe this phenomenon using laser flash photolysis. Despite the sensitivity of the two techniques being comparable, under the conditions of our experiments, with higher anthracene concentration and higher laser (pump) intensity,,the TR^3 experiment is expected to produce an order of magnitude higher concentration of triplet carotene.

The ground state spectra (not shown) obtained using a c.w. argon ion laser were comparable with those generated with the pulsed, probe only system. This confirmed that there was no distortion of the ground state Raman spectrum at the powers used.

The slow growth of carotene triplet observed over several microseconds is attributed to micellar-micellar interaction. This mechanism was tested by making mixed micelles of TX100 with Aerosol-OT (AOT). Incorporation of AOT gives a net negative charge to the micelle. The micelles so produced electrostatically repel each other, thus preventing intermicellar energy transfer.

The results of these experiments, figure 2d and 2e, showed "immediate" carotene triplet formation with no subsequent growth of further TR^3 spectra. Based on Poisson statistics, the probability of finding a micelle with both anthracene and carotenoid is approximately 0.06. Therefore it is almost certainly possible that the "immediate" Raman signal arises from this population of micelles.

CONCLUSIONS

The main conclusions of this work have been:
i) The biphasic nature of the observed kinetics in heterogeneous solution is the result of inter- and intra micellar energy transfer.
ii) The carotenoid triplet Raman spectra are insensitive to solubilisation in TX100 micelles as compared to homogeneous solution.
The second observation will be investigated further by using mixed micelles in which the core environment is varied. This work is already in progress.

REFERENCES

[1] Mathews-Roth, M.M. and Krinsky, N.I., Photochem. Photobiol. **40** 471 (1984)
[2] Koyama, Y. Kito, M., Takii, T., Saiki, K., Tsukida, K. and Yamashita, J., Biochim. Biophys. Acta **680** 109 (1982)
[3] Chauvet, J-P., Viovy, R., Land, E.J., Santus, R. and Truscott, T.G., J. Phys. Chem. **87** 592 (1983)
[4] Chauvet, J-P., Bazin, M. and Santus, R., Photochem. Photobiol. **41** 83 (1985)
[5] Lindig, B.A. and Rodgers, M.A.J., Photochem. Photobiol. **33** 327 (1973)
[6] Robson, R.J. and Dennis, E.A., J. Phys. Chem. **81** 1075 (1977)
[7] See for example Central Laser Facility, RAL Annual Report (1990)
[8] Dallinger, R.F., Farquharson, S., Woodruff, W.H. and Rodgers, M.A.J., J. Am. Chem. Soc. **103** 7433 (1981)

TIME RESOLVED RESONANCE RAMAN STUDIES OF THE OXIDATION OF DIHYDROXYPHENYLALANINE

P.F. Conn,[1] C. Lambert[1], A.W. Parker[2] and T.G. Truscott[1]

[1]Department of Chemistry, Keele University, Staffs. ST5 5BG
[2]Laser Support Facility, Rutherford Appleton Laboratory, Oxon. OX11 OQX.

INTRODUCTION

Of prime importance in the polymerisation of tyrosine, *via* the amino acid dihydroxyphenylalanine (dopa), to melanin is the intermediacy of the metastable species, dopachrome, shown in scheme 1.

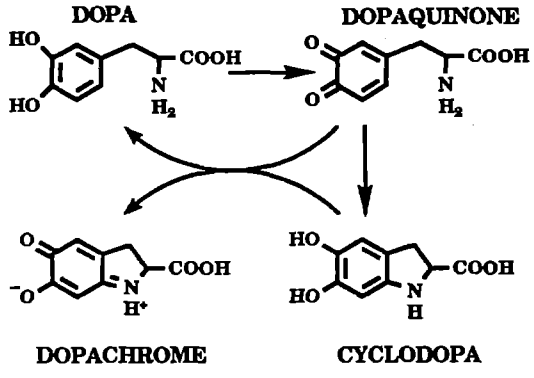

Scheme 1. Oxidation of dopa

This species is the 4 electron oxidation product of dopa and thought to be the immediate precursor of 5,6-dihydroxyindole in melanogenesis.

The oxidation mechanism of dopa has previously been described [1]. The process was studied by pulse radiolysis using one electron oxidation to generate the dopasemiquinone. The reaction mechanism is summarised in scheme 1.

To our knowledge the definitive structure of the compound has not been ascertained and indeed there is some debate in the literature as to whether it exists as a zwitterion in solution. In the present paper we describe some time resolved resonance Raman (TR[3]) results on the oxidation of dopa and the steady state Raman spectrum of dopachrome.

MATERIALS AND METHODS

The apparatus has been described previously [2]. The pump (267nm) and probe (317nm) beams were obtained by frequency doubling the output of two excimer pumped dye lasers.
For the steady state experiment a solution of dopachrome was prepared by chemical oxidation of dopa using chloranil.
Dopa was dissolved in 100ml of 10-3M phosphate buffer pH7. Chloranil was dissolved in diethyl ether and poured onto the dopa solution and the two phases were agitated by bubbling the lower layer with nitrogen gas. This technique also served to prevent autooxidation of the dopachrome once formed. After thirty minutes the two layers were seperated and the N_2 saturated dopachrome solution used for steady state Raman.

The Raman spectrum was obtained using 351nm radiation from an argon ion cw laser. This line was chosen because of the ability of resonance Raman to selectively probe only the dopachrome, the dopa being off resonance at this wavelength.

RESULTS AND DISCUSSION

i)*Steady State.* The spectrum obtained from the steady state Raman experiments of dopachrome is shown in figure 1. It is apparent that there are three bands centred around 1650cm^{-1}, more specifically 1612cm^{-1}, 1670cm^{-1} and 1704cm^{-1}.

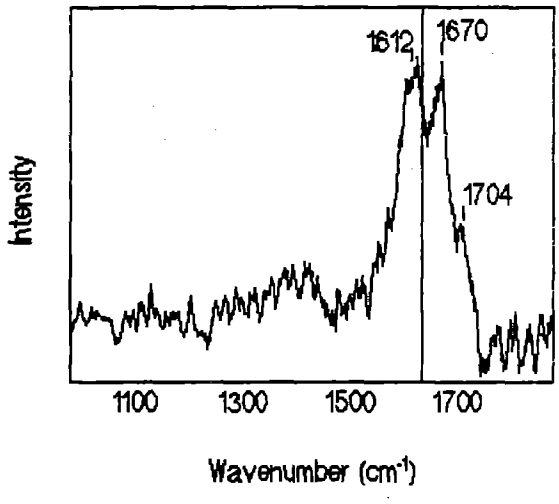

Figure 1. Fluorescence and solvent corrected, steady state Raman spectrum of dopachrome in phosphate buffer pH7. Laser wavelength 351nm. Cursor marks the position of the solvent band.

The spectra observed for the C=O stretch of mono-amino substituted p-quinones are discussed in reference [3] This reference cites the work of Dähne *et al* who suggested that these molecules could be considered to be composed of two ir functional groups. By analogy, similar conclusions can be reached for dopachrome as shown by the broken lines in scheme 2.

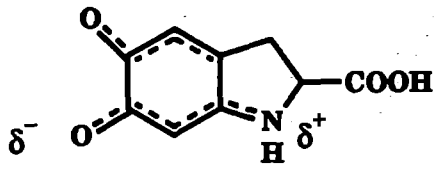

Scheme 2 Zwitterionic structure of dopachrome.

Given the poor signal to noise ratio of the spectrum a fuller interpretation of the data will wait until further data have been obtained for other analogous compounds such as adrenochrome which is more stable.

ii)*Time Resolved.* The data presented in figure 2 are the result of averaging over 20,000 laser shots for each spectrum. Clearly the Raman intensity associated with dopa and its oxidation products is very low however the following discussion of these results is put forward.

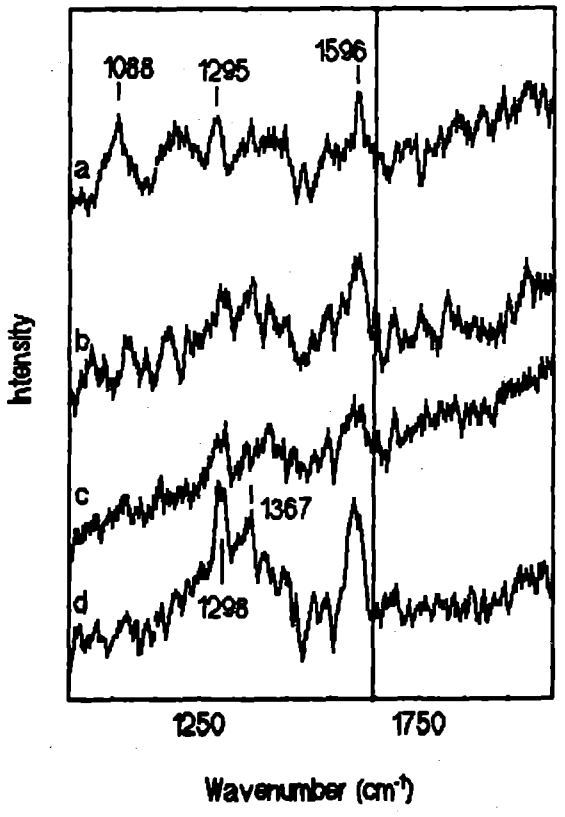

Figure 2. Solvent corrected TR^3 spectra obtained for the oxidation of dopa. Pump (267nm) and probe (317nm) delays were a) 10μs b) 1μs c) 50ns d) probe only. Cursor marks the position of the solvent band.

The major feature is the growth of a band centred around $1088cm^{-1}$ after 10μs and the depletion of the $1596cm^{-1}$ band prominant in the probe only spectrum. There is bleaching of the $1298cm^{-1}$ band after 50ns and the appearance of a more structured spectrum after 1μs. Despite the poor signal to noise ratio we find it difficult to dismiss the apparent reproducible structure in the baseline.

It is not at all understood at present why the Raman bands observed for this system are so weak compared with the data obtained for other quinones in water.

CONCLUSIONS

Our results can be summarised as follows:-

i) The data are consistent, and support the zwitterionic nature of dopachrome.

ii) The time resolved data do not contradict previous pulse radiolysis results. The apparent change in kinetics of the TR^3 spectra compared with that obtained using pulse radiolysis is a consequence of the much higher concentrations of intermediates generated by the TR^3 technique.

Finally, the medical importance of melanogenesis and related biochemistry demands that the mechanism of phenol and catechol oxidation is clearly understood.

In theory TR^3 should provide a powerful tool to make significant progress in this field. However, as is apparent from this report, there are serious experimental problems with this methodology which as yet are not clearly understood.

ACKNOWLEDGEMENTS

Many thanks to all the staff at the LSF for their kind hospitality.

REFERENCES

1. M.R. Chedekel, E.J. Land, A. Thompson and T.G. Truscott. J. Chem. Soc. Commun., 1170, (1984)
2. See for example Central Laser Facility, RAL Annual Report (1990).
3. In "The Chemistry of the quinonoid compounds" Eds S. Patai and Z. Rappoport. Vol. 2, Part 1, 35-43, (1988). J. Wiley and sons

Resonance Raman Investigations on Solvated C_{60}

A W Parker[1], A Beeby[2], S Tavender[1] and D Phillips[2]
[1]Laser Support Facility, Rutherford Appleton Laboratory
[2]Department of Chemistry, Imperial College

Introduction

Following the discovery of the fullerenes some six years ago this exciting new form of carbon, C_{60}, has been the subject of much attention. It is now available commercially, prepared by the method of Krätschmer *et al*[1] making it readily accessible for a wide range of chemical and spectroscopic studies. Structurally C_{60} has an unusually high symmetry with all 60 carbon atoms occupying equivalent sites[2]. To date vibrational spectroscopy studies have centred on the C_{60} solid state and many theoretical studies have been made to calculate the vibrational spectrum of C_{60}. The findings predict 10 Raman active, 2 non-degenerate A_g and 8 fivefold degenerate H_g modes and 4 infrared active modes[3]. The observed solid state C_{60} spectra agree with the theoretical predictions with all the bands being observed. However, the theoretical calculations differ somewhat from each other (by as much as 150 cm^{-1} for some bands) and from the observed values. We report here for the first time the resonance Raman spectrum of C_{60} in solution. The very nature of C_{60} limits the choice of possible solvent that it will freely dissolve in to produce a solutions with high enough concentration for resonance Raman spectroscopy (*ca.* 1 x 10^{-3} mol dm^{-3}).We have chosen benzene. Commercially available C_{60} samples were purified by column chromatography using hexane/alumina.

Results and Discussion

Resonance Raman spectra of C_{60} (0.8 x 10^{-3} mol dm^{-3}) have been obtained using an argon ion (Coherent Inova 90K) 363.8 nm (10 mW at sample) excitation source, Spex Triplemate 1877 spectrograph (with a 600 grooves/mm grating in the final spectrograph stage) and Wright Instruments liquid nitrogen cooled CCD detector, Model 2. Figure 1a shows the Raman spectrum of benzene and figure 1b shows C_{60}/benzene solution. The low concentrations of C_{60} in conjunction with the high solvent Raman scatter has made the C_{60} spectrum particularly weak. Our attempts to fully remove the solvent bands from the C_{60}/benzene spectrum have failed because of an apparent shift of these bands from the benzene only spectrum. This effect is highlighted in figure 2 which shows the result of subtracting the two spectra in figure 1 the lower wavenumber solvent bands being shaped as a 'second derivative'. This shift is the subject of further investigations as we are uncertain of its cause. Some possibilities are that is due to absorption of the Raman bands by the solute or due to a change in refractive index of the sample. It seems unlikely to be the former as attempts to correct using the absorption profile of ground-state C_{60} have failed.

The table compares the observed Raman frequencies of solvated C_{60} with those obtained from the solid state.

Conclusions

The values listed in the table show that there is little difference between the solvated and solid state spectra. It is proposed that the 1467 cm^{-1} band results from the A_g cage breathing mode and the 494 cm^{-1} band as the cage squashing mode[5]. From these assignments any solute solvent interaction would be expected to perturb these modes. As we see no effect on these modes our results tend to indicate that the C_{60} is unperturbed by its solvating molecules and seems to be

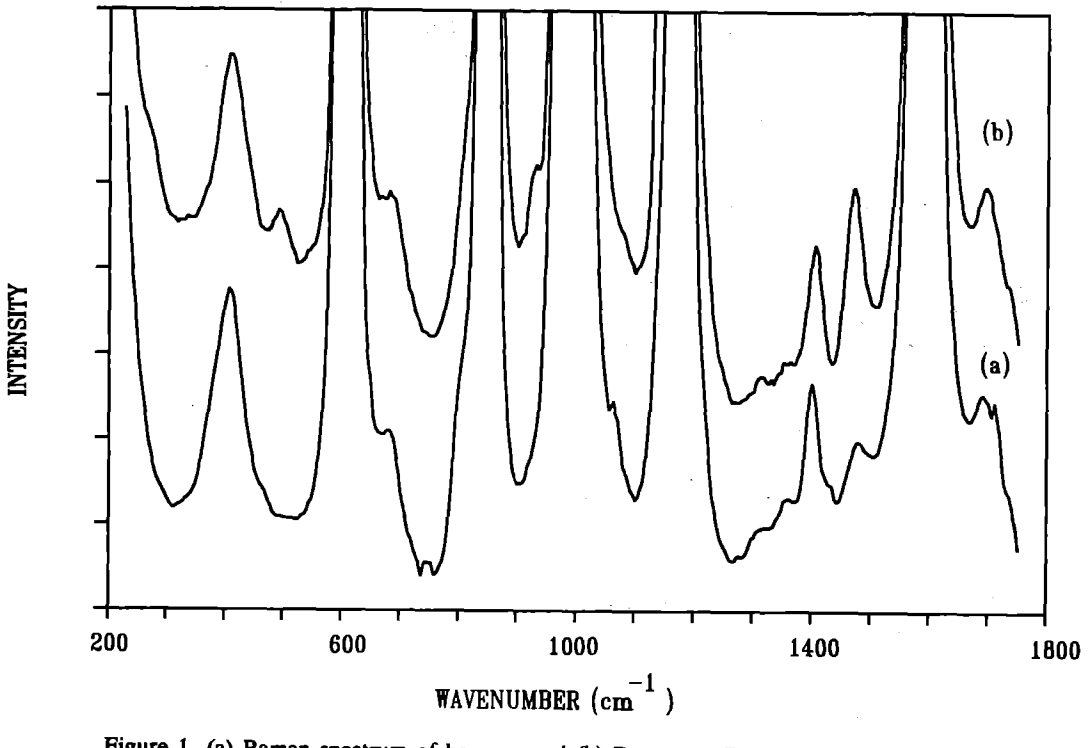

Figure 1. (a) Raman spectrum of benzene and (b) Resonance Raman spectrum C_{60} (0.5 mol dm^{-3}) in benzene. Each spectrum is an accumulation of 5 x 20 min runs.

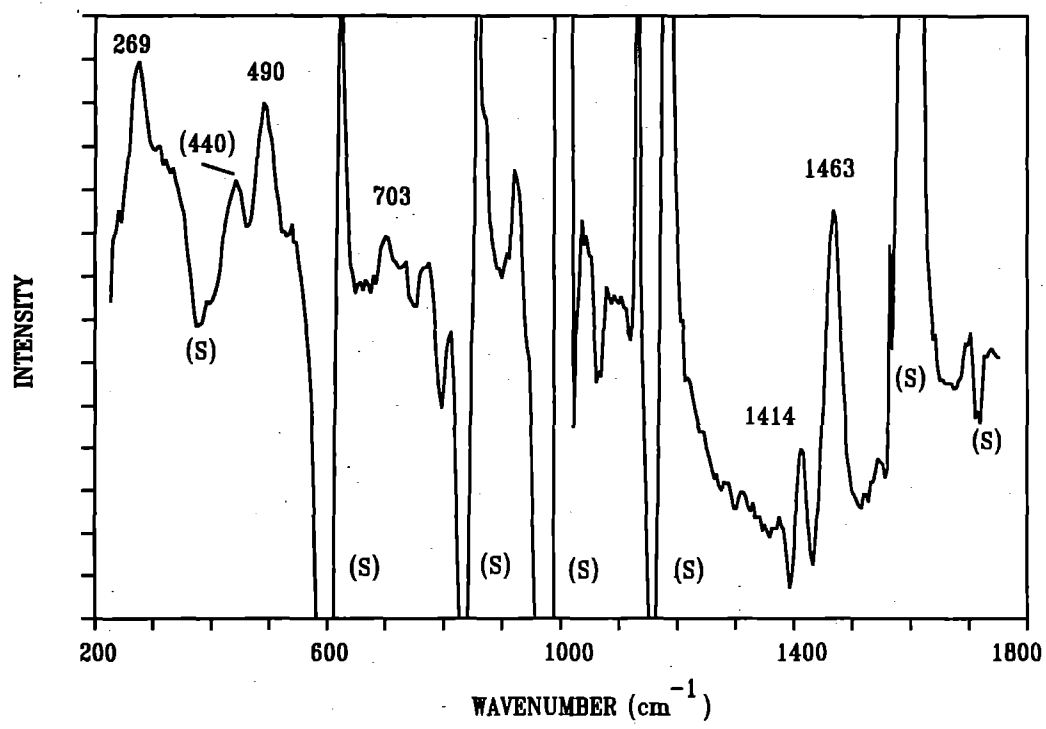

Figure 2. Result of subtracting benzene only spectrum(Fig 1(a)) from C_{60}/benzene spectrum (Fig 1(b)). (S) represents solvent bands.

independent of its environment. That is to say, in solid state the C_{60} to C_{60} interactions are equivalent to the C_{60} to benzene interactions within the solution system.

Table: Comparison of Raman frequencies (cm^{-1}) observed for solvated C_{60} and solid state C_{60} bands.

Solvated C_{60}*	Solid State C_{60}**	Mode#
269	258 (273)	H_g squashing
440	429 (437)	H_g
490	495 (496)	A_g breathing
-	570	
703	772 (710,774)	H_g
-	1099 (1099)	H_g
-	1250 (1250)	H_g
1414	1422 (1428)	H_g
1463	1467 (1470)	A_g pent.pinch
-	1573 (1575)	H_g

*Present work. Values quoted are to an accuracy of $\pm$ 5 cm^{-1}
**Values taken from reference 4, values in parentheses are taken from reference 5
#Assignments are from reference 5

References

1 W Krätschmer K Fostiropoulos and D R Huffman, Nature, **354**, 347 (1990).
2 H W Kato, J R Heath, S C O'Brian, R F Curl and R E Smalley, Nature, **162**, 318 (1985).
3 F Negri, G Orlandi and F Zerbetto, Chem. Phys. Lett., **144**, 31 (1988).
4 T J Dennis, J P Hare, H W Kroto, R Taylor, D R M Walton and P J Hendra, Spectrochim. Acta, **47A**, 1289 (1991).
5 D S Bethiune, G Meijer, W C Tang, H J Rosen, W G Golden, H Seki, C A Brown and M S de Vries, Chem. Phys. Lett., **179**, 181 (1991).

TWO-COLOUR THRESHOLD PHOTOIONISATION SPECTROSCOPY OF JET-COOLED Ag_2

A.M.James, J.F.Miller, J.W.Macdonald, G.W.Lemire, P.F.Brevet and P.R.R.Langridge-Smith

Department of Chemistry, The University of Edinburgh

1. INTRODUCTION.

The electronic structure of small transition metal clusters is currently an area of intense research interest, both from the theoretical and experimental viewpoint. The Group IB, "coinage", dimers are in many ways the simplest of the transition metal dimers, being formed from atoms with filled *d* subshells. Consequently, they have become benchmark species for calibration of both *ab-initio* and core pseudopotential electronic structure calculations **[1]**.

One of the most fundamental molecular properties is the first ionisation potential (IP). The magnitude of the IP provides a direct measure of the strength with which the valence electrons are bound to the molecular core, and of the stability of the molecular ion. The relatively high value of the IP's of the "coinage" metal dimers , makes direct one-photon measurements with tunable lasers somewhat difficult. Moreover, this approach often enables only the*vertical* ionisation potential to be accessed due to Franck-Condon restrictions. We report here the results of two-colour threshold photoionisation spectroscopic measurements on jet-cooled Ag_2, complementing our earlier studies on Cu_2 and CuAg **[2]**.

In these experiments one laser is tuned into resonance to excite some specific intermediate electronic state of the molecule, whilst a second laser is scanned across the ionisation threshold, ionising molecules out of this chosen excited state. By monitoring the photoion signal as a fuction of the wavelength of the ionising laser, a photoionisation efficiency (PIE) curve can be generated. Isotopically specific, rovibronic state selective excitation can be achieved, and additionally, the use of jet-cooling removes any complicating contributions from vibrationally excited ground state molecules, thereby sharpening the threshold of the PIE curve and allowing a more accurate determination of the ionisation potential.The accuracy with which the IP may be measured is limited by the width of the threshold, which may be <2 cm^{-1} when field ionisation effects have been completely eliminated. However, the technique can provide more than simply a means of extracting accurate adiabatic ionisation potentials, since processes such as autoionisation may be probed by investigating the shape of the PIE curve in the post-threshold region yielding information on the electronic configurations involved in the ionisation process. Depending on the chosen vibrational level v' in the intermediate state, we are able to record threshold spectra (via v'=0) or high lying Rydberg state spectra (via v'=1). In both cases, we can measure IP's and access information on the molecular electronic structure, such as configuration mixing.

2. EXPERIMENTAL.

The experimental apparatus used in the present studies is shown schematically in Figure 1. A pulsed supersonic beam of silver clusters was produced by laser vaporisation of a silver rod (5mm dia.), located within the throat of a pulsed supersonic nozzle, using the second harmonic output from a Q-switched Nd:YAG laser (532 nm, 20 mj/pulse, focussed to a diameter of approximately 1 mm). The ejected atoms were entrained in a channel 2 mm in diameter and 3.5 cm in length. The resulting molecular beam was then skimmed (5 mm skimmer) prior to its entrance into the ionistion region of a high resolution reflecting geometry time-of-flight mass spectrometer (RETOFMS). There the molecular beam was crossed perpendicularly by counterpropagating, superimposed beams from two pulsed dye lasers. The first, Nd:YAG pumped dye laser (JK HY750/Quanta Ray PDL-2) was used to populate levels (v',J') in the A (O_u^+) state of Ag_2. The tunable ultraviolet radiation for the second, ionising step was generated by frequency doubling the output of an excimer pumped dye laser (Lambda Physik EMG 201MSC/FL23002EC) in a beta barium borate crystal. Since the molecular constants of the A and X states of Ag_2 had already been determined to high accuracy **[3]**, there was no need to perform another calibration of the position of the A-X bandheads. It was sufficient to carry out a short R2PI scan before each threshold scan to ensure that the exciting laser was tuned correctly to the appropriate bandhead. Calibration of the photon energy in the second ionising step was achieved by recording monitor etalon fringes together with neon optogalvanic lines, using the fundamental visible laser output. Laser powers were monitored using photodiodes in order to enable the PIE curves to be power-normalised.

Atomic and molecular ionisation potentials are depressed in the presence of static electric fields due to the occurrence of field ionisation **[4]**. The static field opposes the coulombic core-electron attraction and facilitates escape of the outgoing electron at a lower ionisation energy than in the zero-field case. To circumvent this problem pulsed, rather than static extraction fields were used to enable the measurement of PIE spectra under field-free conditions. The Ag_2 molecules were ionised with the ion extraction optics of the time-of-flight mass spectrometer held at ground potential. After a short, variable delay, the newly created photoions were accelerated in to the RETOFMS by switching on the extraction voltages using a custom built fast risetime high voltage pulser.

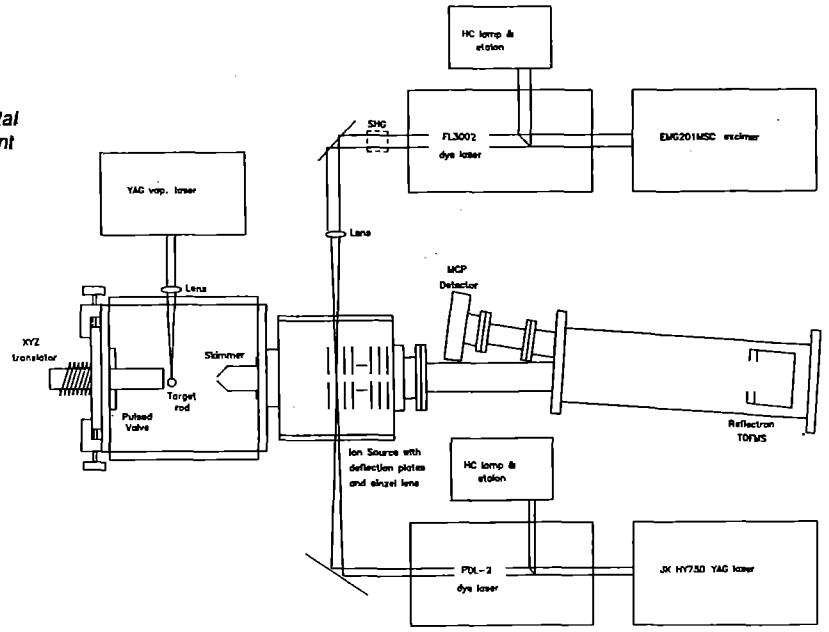

Figure 1: Schematic of the experimental apparatus used in the present studies.

3. RESULTS AND DISCUSSION

Figure 2 shows the PIE spectrum for two-colour photoionisation of $^{107}Ag_2$ under zero-field conditions. Here the exciting dye laser was tuned to the A - X (0-0) band at 22987 cm^{-1} while the ionising laser was scanned over the threshold. The time delay between the synchronised laser pulses and application of the high voltage extraction pulse was 150 ns. During this delay period, the nascent photoions drift along the molecular beam axis by only 0.3 mm, so that they are still well within the ion source when the accelerating potential is applied.

The observed field-free threshold is somewhat broader than we have observed previously for Cu_2 and CuAg. Consequently the ionisation potential for Ag_2 is somewhat more poorly determined. Summing the laser photon energies at threshold yields the value 61725 (30) cm^{-1};
(cf. Cu_2, IP= 63752(3) cm^{-1}; CuAg, IP= 62754(4) cm^{-1}) [2]. This value may be compared with the adiabatic ionisation potential recently reported by Beutel et al. [5], 61747(4) cm^{-1}, from the convergence limits of Rydberg series converging towards vibrational levels v^+ in the ground state of the cation Ag_2^+.

One slightly suprising feature of the PIE spectrum is the almost complete absence of features lying to the red of the ionisation threshold. By analogy with atomic spectroscopy, one might have expected to see sharp features due to long-lived molecular Rydberg states being field ionised by the pulsed extraction field before they decay. We apply approximately 1000 V across the repeller-draw out region in the RETOFMS, creating an extraction field of approximately 330 Vcm^{-1}. This should permit the observation, by field ionisation, of all molecular Rydberg states as far as 110 cm^{-1} below threshold, provided that they do not decay during the time delay between laser excitation and pulsed extraction. The unexpectedly short lifetimes of the Rydberg states remains a puzzle. One possible explanation is that they may be heavily predissociated by repulsive states correlating with excited neutral atomic limits. However, there is clearly scope for further work to elucidate the dynamical processes responsible.

Figure 3 shows the PIE spectrum following excitation via the (1-0) band of the A-X system, at 23181 cm^{-1}. Within experimental error, the ionisation threshold was found at the same two-laser energy as for the determination via the (0-0) band above. Qualitatively, however, the PIE spectrum in the post-threshold region is very different to that obtained when the vibrationless level of the A state was excited. The initial rise in ion signal as the first threshold is crossed is somewhat diminished compared to that observed for excitation via the origin band. More noticeably, there is considerably more post-threshold structure which we assign to vibrationally excited states that autoionise into the first ionisation limit. A detailed analysis of this post-threshold structure is currently in progress.

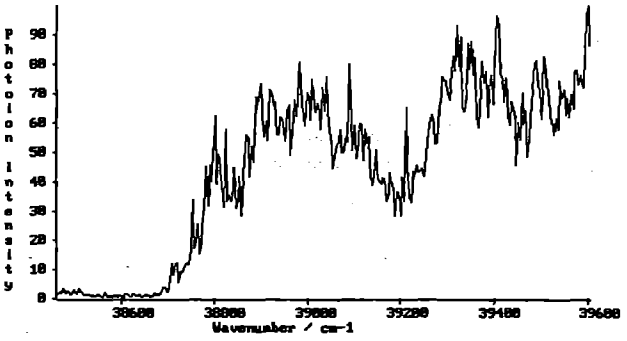

Figure 2: PIE curve for $^{107}Ag_2$. Excitation via the A - X (0-0) band.

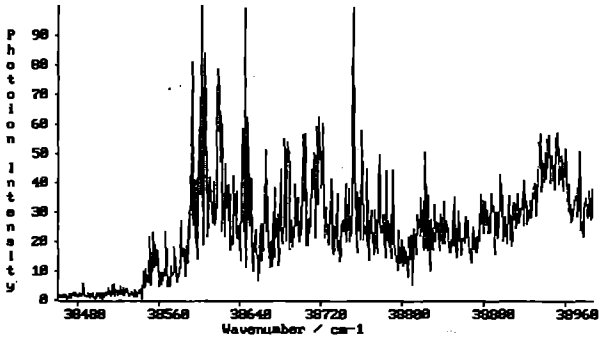

Figure 3: PIE curve for $^{107}Ag_2$. Excitation via the A - X (1-0) band.

4. REFERENCES

1. C.W.Bauschlicher, Jr., S.R.Langhoff, H.Partridge and S.P.Walch, J.Chem.Phys., **86**, 5603, 5603 (1987); E.Miyoshi, H.Tatewaki andT.Nakamura,J.Chem.Phys.,**78**,815(1983);H.Stoll, P.Fuentealba, M.Dolg, J.Flad, L.V.Szentpaly and H.Preuss, J .Chem.Phys., **79**, 5532 (1983).
2. A.M.James, *Ph.D. Thesis*, The University of Edinburgh (1990); A.M.James, J.F.Miller, G.W.Lemire and P.R.R.Langridge-Smith (unpublished work).
3. B.Simard, P.A.Hackett, A.M.James and P.R.R.Langridge-Smith, Chem.Phys.Lett., **186**, 415 (1991).
4. M.Broyer, J.Chevaleyre, G.Delacetaz, S.Martin and L.Woste, Chem.Phys.Lett., **99**, 266 (1983).
5. V.Beutel, G.L.Bhale, M.Kuhn and W.Demtroder, Chem.Phys.Lett., **185**, 313 (1991).

DETERMINATON OF THE CF_3 TORSIONAL POTENTIAL FUNCTION IN THE S_0 AND S_1 ELECTRONIC STATES OF 3- AND 4-AMINOBENZOTRIFLUORIDE

Robert G Gordon and J Michael Hollas
University of Reading, U.K.
Paulo J A Ribeiro-Claro and Jose J C Teixeira-Dias
University of Coimbra, Portugal

1. INTRODUCTION

There has been much interest in recent years in the internal torsional or rotational motion of the methyl group attached to the benzene ring, in both the ground (So) and first excited singlet (S1) electronic states. Much less attention has been paid to the CF3 group in otherwise similar molecules. Before the present work, all that was known was that, from the microwave spectrum, the CF3 torsional barrier in the So state of benzotrifluoride ($C_6H_5CF_3$)[1] is 3.57 ± 0.11 cm^{-1}, very similar to that of 4.875 ± 0.007 cm^{-1} in toluene ($C_6H_5CH_3$)[2].

In the present work we have used the techniques of fluorescence excitation (FE) and dispersed fluorescence (DF) to obtain the CF3 torsional potential functions in the So and S1 electronic states of 3-aminobenzotrifluoride (3ABTF) and 4-aminobenzotrifluoride (4ABTF).

2. EXPERIMENTAL

Both FE and DF spectra were obtained with the molecules (3ABTF or 4ABTF) seeded into a supersonic jet of helium, at a stagnation pressure of 1.4 atm, by flowing the helium over the surface of the liquid sample. The gases passed through a 100 μm diameter pinhole and the resulting rotational and vibrational temperatures were about 10 K and 100 K, respectively.

The molecular beam was crossed by the beam from the frequency doubled dye laser pumped by a Nd:YAG laser, the Quantel Datachrom system from the Laser Support Facility loan pool.

Fluorescence was detected by a photomultiplier and integrated by a boxcar.

3. RESULTS

(a) 3-Aminobenzotrifluoride

Figure 1 shows a part of the FE spectrum of 3ABTF close to the 0_0^0 band. There are remarkably long progressions in the CF3 torsional vibration ν_τ. The most intense one is from v_τ = 0 in So but, even in the supersonic jet, levels with v_τ = 1, 2, and 3 are sufficiently populated for progressions from these levels to be observed.

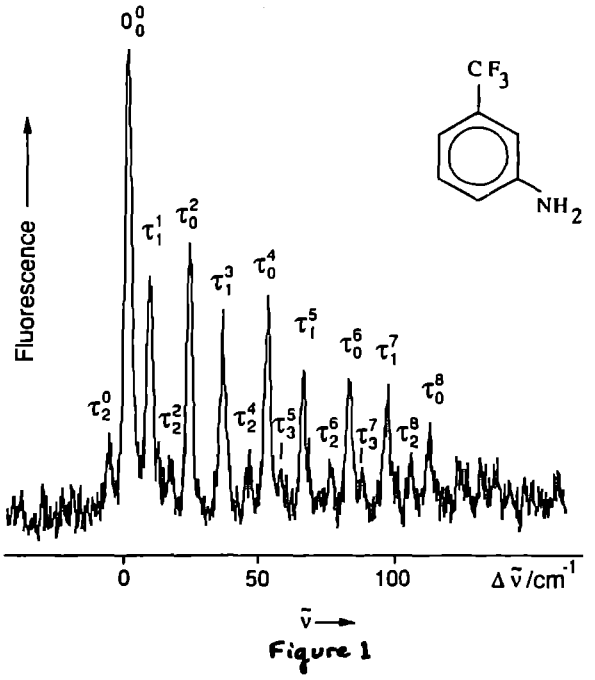

Figure 1

In figure 2 are shown parts of DF spectra from levels with v_τ = 0, 1, 2, and 3 in S1.

The progressions in ν_τ in these spectra are much more crowded than in the FE spectrum due to the much lower torsional barrier (see later).

The torsional levels in each electronic state have been fitted[3] to a potential of the form

$$2V(\phi) = V_3(1 - \cos 3\phi) + V_6(1 - \cos 6\phi) \qquad (1)$$

with the following results:-

So: $V_3'' = 9 \pm 5$ cm^{-1}, $V_6'' = -10 \pm 2$ cm^{-1}

S1: $V_3' = 155 \pm 5$ cm^{-1}, $V_6' = -40 \pm 2$ cm^{-1}

These potentials are plotted in figure 3.

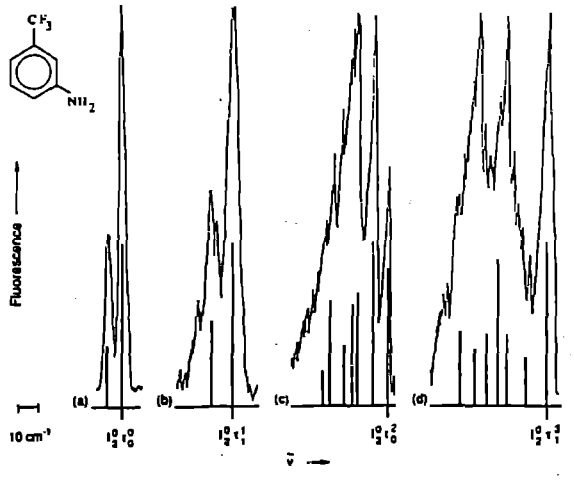

Figure 2

(b) 4-Aminobenzotrifluoride

Figure 4 shows parts of the FE spectrum and of the 0_0^0 DF spectrum of 4ABTF. The torsional potential is expected to involve only the V_6 term of eqn. (1) when substitution is in the 4-position.

The torsional structure in the FE spectrum can be reproduced[4] with

So: $|V_6''| < 5$ cm^{-1}; S1: $|V_6'| = 33 \pm 4$ cm^{-1}.

A positive or negative value of V_6 corresponds to an eclipsed or staggered CF3 group, respectively[5]. It is not possible to determine the sign from the torsional structure in the FE spectrum but the observation of the out-of-plane C-CF3 bending mode, ν_{28}, in both spectra in figure 4 shows that the equilibrium configuration must be staggered in both electronic states and that V_6'' and V_6' are both negative.

The potentials are illustrated in figure 5.

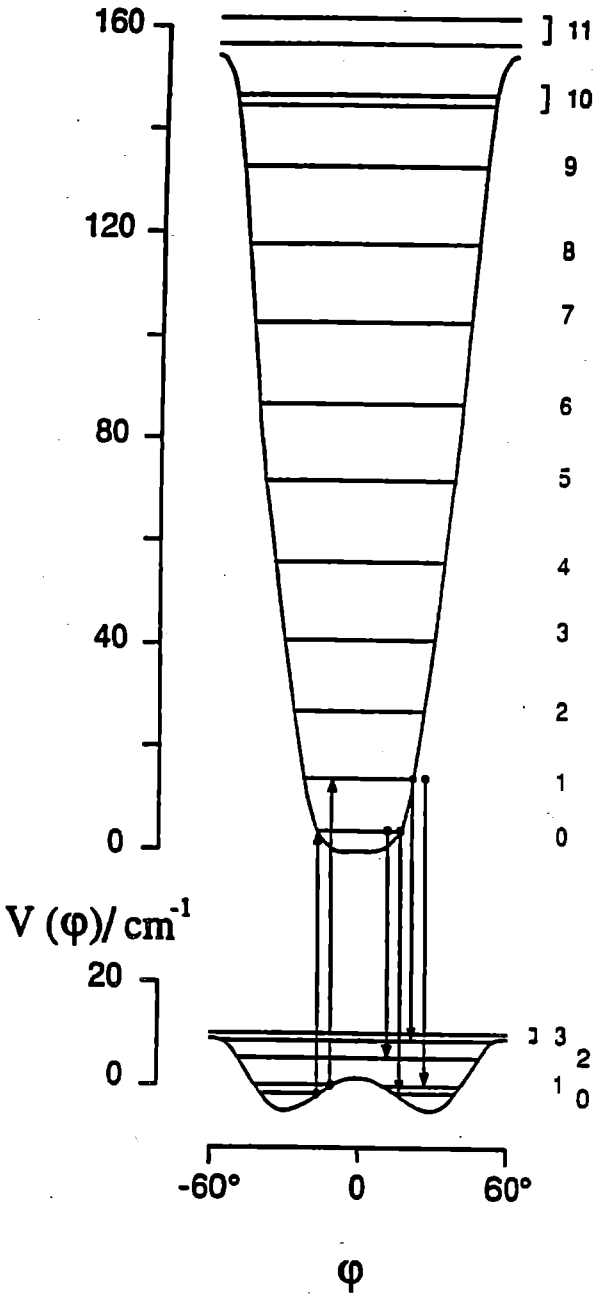

Figure 3

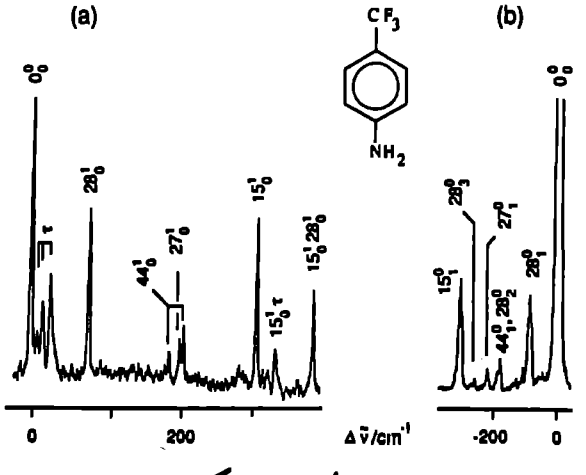

Figure 4

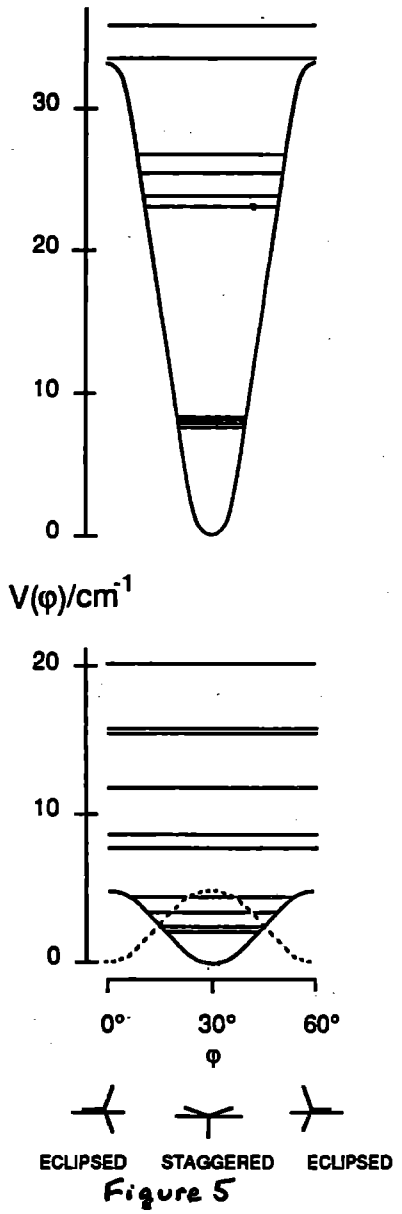

Figure 5

4. CONCLUSIONS

In the So state of 3ABTF the values of V_3'' and V_6'' in the CF_3 torsional potential correspond to an equilibrium configuration in which the CF_3 group is rotated by 25° relative to an eclipsed configuration. The height of the main barrier, at $\phi = 60°$, is 17 cm^{-1}. Contrasting with this is the equilibrium configuration in S_1 which is eclipsed with a much higher barrier, at $\phi = 60°$, of 155 cm^{-1}.

In 4ABTF, the potential contains only the V_6 term and the equilibrium configuration is staggered, but with the barrier increasing from $\leq$ 5 cm^{-1} in So to 33 cm^{-1} in S_1.

The CF_3 torsional potentials of 3ABTF and 4ABTF are quite similar to the CH_3 torsional potentials in both electronic states of 3-toluidine and 4-toluidine, respectively. This similar behaviour of the CF_3 and CH_3 groups is very surprising and awaits an explanation.

REFERENCES

1. T.Ogata and A.P.Cox, J. Mol. Spectrosc., 61, 265(1976).
2. H.Rudolph, H.Dreizler, A.Jaescke and P.Wendling, Z. Naturforsch., A22, 940(1967).
3. R.D.Gordon, J.M.Hollas, P.J.A.Ribeiro-Claro and J.J.C.Teixeira-Dias, Chem. Phys. Lett., 183, 377(1991).
4. R.D.Gordon, J.M.Hollas, P.J.A.Ribeiro-Claro and J.J.C.Teixeira-Dias, Chem. Phys. Lett., 182, 649(1991).
5. R.D.Gordon and J.M.Hollas, Chem. Phys. Lett., 164, 255(1989).

ELECTRONIC SPECTROSCOPY OF INVOLATILE HEAVIER ELEMENT COMPOUNDS FORMED IN A FREE JET EXPANSION

J.M.Brown[1], I.R.Beattie[2], S.H.Ashworth[1], N.M.Lakin[1], M.P.Barnes[1]
[1]OxfordUniversity
[2]SouthamptonUniversity

With involatile solids, high temperatures are required to obtain adequate vapour pressures. This, however, causes problems with gas phase spectroscopy since the spectra obtained are broad and structureless and yield little information. In our experiment molecules formed in the heated region of an alumina nozzle are seeded into a high pressure inert gas stream (usually argon). They undergo a free expansion through a small orifice ($250\mu m$ diameter) into a rapidly pumped vacuum chamber. This causes the rotational, and to a lesser extent vibrational, energy to be converted into translational energy. In consequence, greatly simplified spectra which correspond to a rotational temperature of about 10K are obtained. The beam from a narrow band tunable dye laser is used to irradiate the jet and the resultant fluorescence is recorded (laser excitation spectroscopy). The excimer-pumped dye laser at the LSF has been used in this way to record the spectra of a number of interesting molecules.

In three separate visits to the LSF we have been able to extend our observations of the spectra of $NiCl_2$ and InOH, and also started work on recording the spectra of $CuCl_2$.

i Experimental Improvements

During this time the main improvement was to the recording of dispersed fluorescence. The laser wavelength is set on a particular signal and the fluorescence is dispersed using a 1m monochromator. The separations of dispersed signals corresponds to the vibrational and spin-orbit splittings in the ground state of the molecule. Both resolution and signal-to-noise were improved by positioning two lenses between the collection optics and the monochromator in order to focus as much of the fluorescence as possible into the monochromator. The signal gain was increased by 100× preamplification.

For very weak signals, the signal-to-noise was increased by putting two integrator gates on the fluorescence decay using an analogue processor. This enhances the discrimination between signal and random noise since the latter is not sampled by both gates. Using this method, good dispersed signals for $NiCl_2$ and InOH were recorded for the first time.

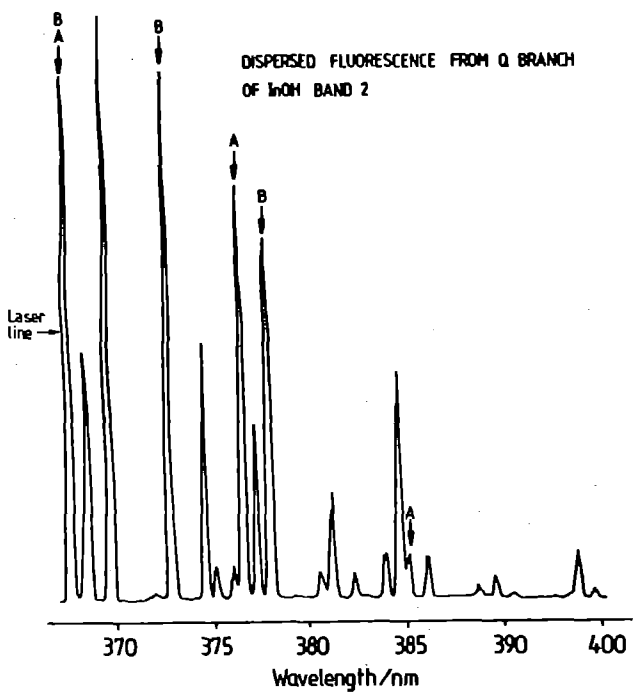

Figure 1: Dispersed fluorescence from Q branch of InOH with an excitation frequency of 27208.52cm^{-1}.

ii Results for InOH

Improvements were also made in the production of InOH. Better signals were obtained by replacing the quartz crucible used to hold the indium sample with an open stainless steel crucible so that a larger surface area was exposed to reaction. The signal was also increased by extending the needle of the motor driven syringe so that water was introduced directly into the hottest region of the nozzle. Consequently we were able to use water in the syringe instead of the more reactive hydrogen peroxide for all further measurements of InOH. This reduced the frequency of nozzle blockage which had plagued the experiment in the past. The fluorescence from the main absorption bands of both InOH and InOD was dispersed to help in the analysis of the spectra. Figure 1 shows the spectra obtained from the Q branch of one band of InOH with an excitation frequency of 27208.52 cm^{-1}. No signals were observed to higher frequency of the laser line (anti-Stokes signals), which implies that the transition is originating from a ground state in which the vibrational excitation has been cooled out by the free expansion. A progression of bands with a separation of around 630.6 cm^{-1} starting at the laser frequency can be seen. The same separation also occurred between bands which were removed from the laser frequency. In the dispersed signals of InOD a separation of about 630.0 cm^{-1} was also observed starting from the laser frequency and amongst some of the other bands. This separation has been tentatively assigned as the In-O stretching frequency (which should be only slightly smaller in InOD than InOH) and is shown by the bands denoted A in figure 1. For InOH a second progression (denoted B in figure 1) starting at the laser frequency is seen which has a separation around 388.5cm^{-1}. For InOD the corresponding progression has a separation of around 305.0cm^{-1}. The ratio of these separations is roughly $\sqrt{2}$ supporting the assignment of these separations as the bending frequencies of the two isotopomers. The small separations of about 60 and 100cm^{-1} from the laser line have yet to be explained. Furthermore these signals were found to have a more lengthy decay curve that the other signals. This phenomena has not been seen before and further work is needed.

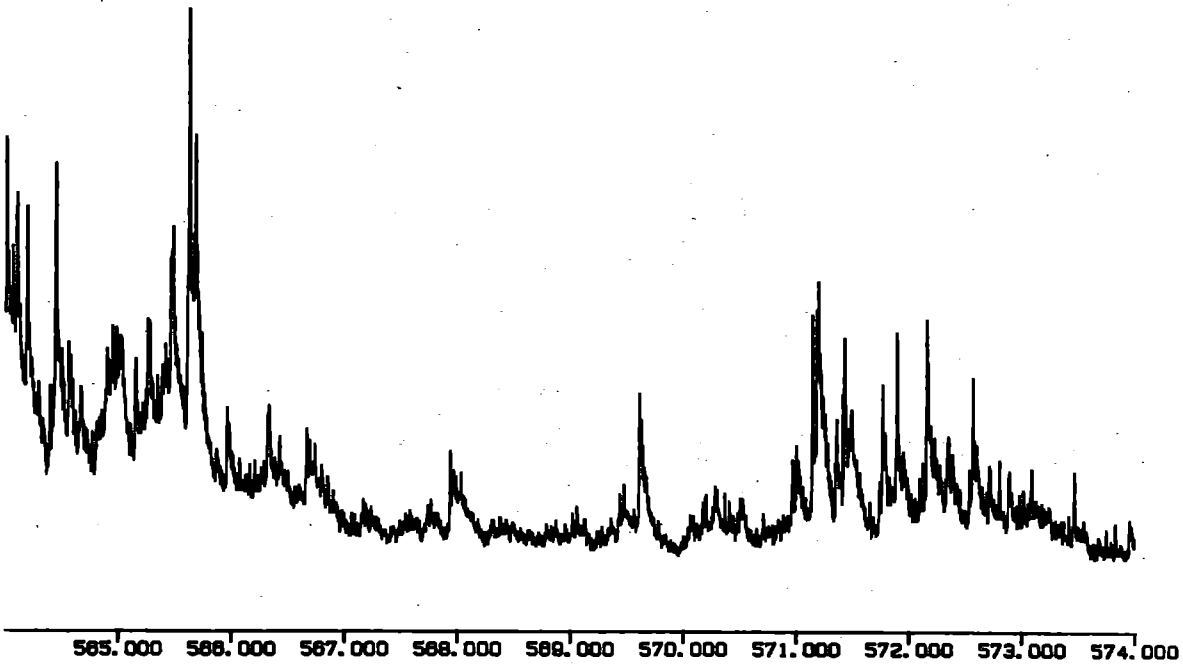

Figure 2: A portion of the spectrum of $CuCl_2$. None of the signals are as yet assigned.

iii Results for $CuCl_2$

Preliminary work has been carried out on the spectrum of $CuCl_2$, which shows a strong absorption band in the 530-600nm region of the electromagnetic spectrum. The reaction between hot Cu and CCl_4 did not prove to be an efficient source of $CuCl_2$. Successful methods found were the use of either copper (in a finely precipitated form), CuCl or $CuCl_2$ heated to about 800°C and passing about 2atm of 5% chlorine in argon over the sample. The best signals were obtained using anhydrous $CuCl_2$ but the sample was used up too quickly for this method to be convenient. The method of production used was the reaction of heated copper with 5% chlorine in argon.

The excitation spectrum was recorded from 530-610nm; a portion is shown in figure 2. There appears to be no absorption at wavelengths greater than 600nm. The rotational structure of the vibronic bands is not resolved. Recently published dispersed fluorescence for this system [1] suggests that the transition involved is $^2\Pi_u \leftarrow {}^2\Pi_g$. Very little is known about the upper state involved in this transition and analysis of the results is proving difficult. In an attempt to aid assignment, the fluorescence from some of the stronger absorption bands was dispersed. These show a progression of bands with a separation of $370cm^{-1}$ starting at the laser frequency, which is likely to correspond to the symmetric stretching frequency of the ground state. Bands were also seen $170cm^{-1}$ from the laser frequency which may be the spin-orbit splitting in the ground state. Both these values agree with the published values [1]. Furthermore, a third separation of about $250cm^{-1}$ was observed which may be twice the ground state bending frequency. This mode has not been observed previously. Further experiments, however, are needed in order to help with the analysis of this system, including an extension of the measurements to longer wavelength.

References

[1] A.J.Bouvier, R.Bacis, J.Bonnet, S.Churassy, P.Crozet, B.Erba, J.B.Koffend, J.Lamarre, M.Lamrini, D.Pigache and A.J.Ross. *Chem. Phys. Lett.* in press.

ENERGY TRANSFER BETWEEN ADSORBED MOLECULES ON A DIELECTRIC SURFACE FOLLOWING ULTRAVIOLET EXCITATION

C.J.S.M. Simpson[1], A. Takami[1], K.R. Yoxall[1], A.S. Solodukhin[1] and A.W. Parker[2]

[1] Physical Chemistry Laboratory, Oxford University
[2] Rutherford Appleton Laboratory

INTRODUCTION

There is great interest in laser induced processes for molecules adsorbed on surfaces using both infrared and ultraviolet lasers [1]. At least three processes are responsible for laser induced desorption and subsequent molecular dissociation. In thermal desorption the species are desorbed with temperatures of a few hundred Kelvin, or even lower [2]. It may occur from surfaces which are transparent to the laser radiation if high fluences are used [3–5] and also if energy is released from an optically pumped molecule giving rise to local heating [3–6].

Dissociation and desorption processes can be initiated following the ejection of electrons from the surface. Examples are the dissociation and desorption of NO_2 from a NO coated Pd(111) surface [6] and for CO desorbed from epitaxially grown NiO [7].

Ultraviolet excitation may cause a molecule to dissociate [4–6,8]. Alternatively fluorescence, or curve crossing may occur to give vibrationally excited ground electronic state molecules which may then be desorbed intact [3].

Before desorption of the excited molecule occurs, energy may be transferred to a co–adsorbed molecule, provided that this molecule has suitable energy levels to accept the energy and that there is a means of coupling these energy levels. Results in the gas and liquid phases [9] make it likely that near–resonant energy transfer between infrared active modes may be very fast between co–adsorbed molecules. If this occurs faster than the rate of desorption of the pumped molecule, then non–thermal desorption of the acceptor molecule is expected to occur. There is also expected to be some thermal desorption of weakly bound species caused by the energy released when the excited molecule relaxes from the upper to the ground electronic state.

We report the use of non–thermal desorption as a probe of energy transfer between adsorbates.

THE NECESSARY EXPERIMENTAL CONDITIONS

In order to avoid thermal desorption it is necessary to employ a surface which is transparent to the ultraviolet light and from which electrons will not be ejected. Furthermore, the surface must not cause rapid vibrational deactivation of the excited molecules. We selected single crystal MgF_2.

If a tunable frequency doubled dye laser is used, the frequency of the ultraviolet light may be chosen to match the maximum of the molecular absorption. We have used this technique successfully [3] and have also shown that when the laser is tuned off the molecular absorption band no desorption occurs. However, the desorption process is very dependent on the laser fluence [4,5] and the beam profile from a frequency doubled dye laser is very uneven. For this reason this means of excitation is not satisfactory. Much more uniform beam profiles can be obtained from a modern excimer laser, operating at one of a few fixed frequencies.

We have selected 1,3–cycloheptadiene (1,3–CHD) for two reasons. The first is that it has the extremely large absorption coefficient of 8000 $dm^3\ mol^{-1}\ cm^{-1}$ at 248 nm and a very small absorption coefficient at 351 nm. The second is that like 1,3–cyclohexadiene it is desorbed intact and can act as an energy store before it is desorbed.

RESULTS

THE ADSORBATE TO SURFACE BINDING ENERGIES

These were determined using temperature programmed desorption (T.P.D.). The T.P.D. spectra are given in Figure 1. The binding energies were calculated using the Redhead model [10]. The results are given in Table 1.

1,3–CYCLOHEPTADIENE:XE AS A 4:1 MIXTURE

Xe is very weakly bound to the surface and the energy released from the decay of the upper electronic state causes local heating resulting in the thermal desorption of Xe. The time of flight spectrum is very broad, corresponding to a temperature of 200 K, whereas that of 1,3–cycloheptadiene is a single Boltzmann corresponding to 1200 K, shown in Figure 2. The relative yield of Xe:1,3–cycloheptadiene normalized for mixture composition is 2.0:1.0 as given in Table 2.

1,3–CYCLOHEPTADIENE:CS_2 AS A 4:1 MIXTURE

CS_2 is bound much more strongly than Xe, as shown in Table 1, and hence thermal desorption is expected to be less important than for Xe. The CS_2 is not optically excited at 248 nm. If the CS_2 can accept energy before the 1,3–cycloheptadiene is desorbed then some higher temperature non–thermal desorption is expected. This is found to be the case as shown in Figure 3 and Table 2. The normalized relative yield of CS_2 to 1,3–cycloheptadiene for the non–thermal component of the desorption is slightly greater than expected from the mixture composition.

1,3–CYCLOHEPTADIENE:CYCLOHEXANE AS A 4:1 MIXTURE

Cyclohexane (CH) is bound more strongly than CS_2, as shown in Figure 1 and Table 1. It is not optically pumped at 248 nm. However, the normalized non–thermal yield is 4.8 which is much greater than for CS_2. Since the binding energy for cyclohexane is greater than for CS_2, this cannot be the result of local heating. From Figure 4 it is clear that there is a thermal component of the TOF distribution with a temperature of about 200 K and a non–thermal component with a temperature of 800 K. These results establish that energy transfer has taken place from 1,3–cycloheptadiene to cyclohexane before the 1,3–cycloheptadiene has been desorbed.

TABLE 1
TEMPERATURE PROGRAMMED DESORPTION

System	Desorption Temperature /K	Binding Energy /kJ mol^{-1}
1,3–CHD	175	46
CH	150	40
CS_2	140	35
Xe	70	16

[1] Results are accurate to 5%

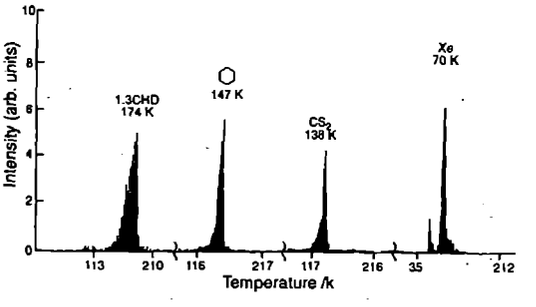

Figure 1: TPD Spectra of Adsorbed Molecules

TABLE 2
TIME OF FLIGHT

System	Temp /K	Yield[2] $\times 10^{-11}$	Ratio[3]	Fluence /mJ cm^{-2}	Figure
1,3–CYCLOHEPTADIENE:Xe = 4:1					
1,3–CHD	1200	7.1	1.0	8.0	2(a)
Xe	200	3.6	2.0	6.5	2(b)
1,3–CYCLOHEPTADIENE:CS_2 = 4:1					
1,3–CHD	1100	4.2	1.0	8.0	3(a)
CS_2	600 NT	1.5	1.4	8.0	3(b)
	200 T	0.3	0.28		
1,3–CYCLOHEPTADIENE:CYCLOHEXANE = 4:1					
1,3–CHD	1200	2.4	1.0	7.5	4(a)
CH	800 NT	2.9	4.8	8.5	4(b)
	200 T	1.2	2.0		
1,3–CYCLOHEPTADIENE					
1,3–CHD	1500	14		8.6	

2 The yield is given in molecules.
3 The ratio is calculated as: yield of co–adsorbate/yield of 1,3–cycloheptadiene.
4 NT stands for the non–thermal part and T for the thermal part.
5 Results are accurate to ± 10%

CONCLUSION

We have shown that laser induced desorption can be used as a probe to prove that energy transfer between co–adsorbed molecules occurs; provided that the acceptor molecule has near–resonant, infrared active modes and a low temperature heat capacity comparable with that of the pumped molecule.

REFERENCES

1 G.E. Ewing, Int. Rev. Phys. Chem. 10 (1991) 391.
2 J.P. Hardy and C.J.S.M. Simpson, Chem. Phys. Lett. 130 (1986) 175.
3 S.J. Clemmet, A.W. Parker, K. v. Puttkamer, A. Takami and C.J.S.M. Simpson, J. Electron Spectrosc. Rel. Phen. 54/55 (1990) 211.
4 K. Domen and T.J. Chuang, J. Chem. Phys. 90 (1989) 3318.
5 K. Domen and T.J. Chuang, J. Chem. Phys. 90 (1989) 3332.
6 E. Hasselbrink, S. Jakubith, S. Nettersheim, M. Wolf, A. Cassato and G. Ertl, J. Chem. Phys. 92 (1990) 3154.
7 Z. Ying and W. Ho, Phys. Rev. Lett. 60 (1988) 57.
8 I. Harrison, J.C. Polanyi and P.A. Young, J. Chem. Phys. 89 (1988) 1498.
9 J.J. Andrew, A.P. Harriss, D.C. McDermott, H.T. Williams, P.A. Madden and C.J.S.M. Simpson, Chem Phys. 139 (1989) 369.
10 P.A. Redhead, Vacuum 12 (1962) 203.

TALKS

C.J.S.M. Simpson
University of Canberra
University of Brisbane

THESIS

S.D. Hooke Part II Thesis, Oxford University, 1991.

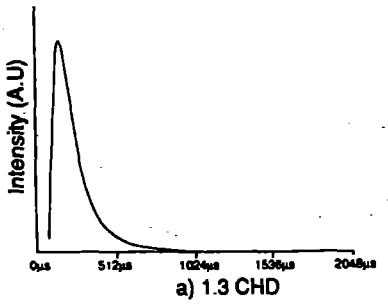

Figure 2: Desorption Traces for a 4:1 1,3–cycloheptadiene: Xe Mixture.

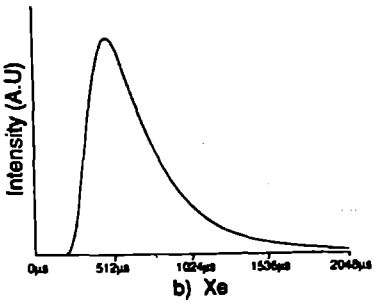

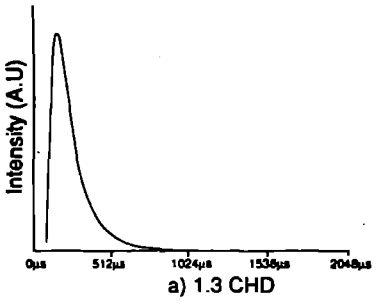

Figure 3: Desorption Traces for a 4:1 1,3–cycloheptadiene: CS_2 Mixture.

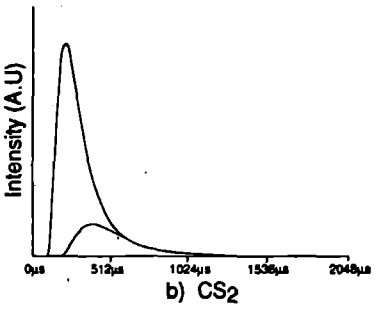

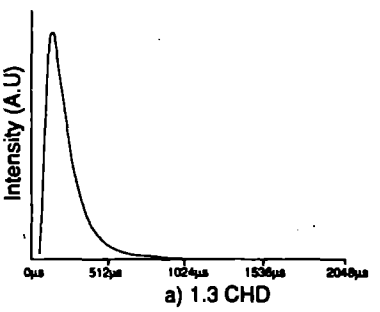

Figure 4: Desorption Traces for a 4:1 1,3–cycloheptadiene: cyclohexane mixture.

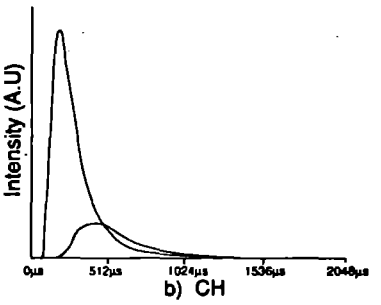

INTERFACIAL SECOND HARMONIC GENERATION: INVESTIGATION OF p-NITROPHENOL AT WATER/AIR AND HEPTANE/WATER INTERFACES.

Christopher G. Hickman[1], Andy J. Bell[1,2], Ted J. Vandernoot[3], Andrew Langley[4] and Jeremy G. Frey[1]

[1]Department of Chemistry, University of Southampton, Southampton, SO9 5NH, UK.
[2]SPAM, CEA, Saclay, France.
[3]Department of Chemistry, QMW, Mile End Road, London, UK.
[4]Rutherford Appleton Laboratory

Introduction

The non-linear spectroscopic technique of second harmonic generation provides a method of probing the structure of interfaces and the concentration and orientation of molecules adsorbed at these interfaces[1]. The technique obtains its surface specificity because at least to first order centro-symmetric regions give do not generate any second harmonic radiation[2]. A molecule such has p-nitrophenol which has a high non-linear coefficient, will not give rise to any second harmonic signal in a bulk solution. At an interface the molecules where the molecules become aligned to some extent, a second harmonic signal can be generated[3].

Experimental

As in the previous work at the LSF we used the amplified picosecond laser facility[4]. The introduction of a feedback system in the sync-pumped dye laser by the LSF staff produced a significant improvement in the quality of the picosecond output. The polarisation of the visible radiation at 600nm was selected using a Fresnel rhomb and the light focused on to the liquid surface. The reflected radiation was collected using a second lens and passed through filters to block the fundamental radiation and then a monochromator. Any SHG signal was detected using a PMT. An iris was used to select the required reflection when more than one surface was present.

A half-wave plate and polariser were used to detect the polarisation of the SHG wave. Thus while the monochromator always received the same polarisation rotating the half-wave plate allowed us to determine the polarisation of the SHG signal.

The majority of the optical system was moved from Southampton to RAL together with a computerised data collection system capable of recording the SHG signal and a calibration signal for each laser shot. The majority of the laser pulses have a reasonably constant energy (fluctuation of about 10-15%) but on many occasions a significant number of the pulses have almost no energy. The calibration arm of the experiment can detect these rogue pulses and they can be eliminated in the subsequent data analysis.

Results

Measurements of the polarisation of the SHG signal generated from p-nitrophenol at air/water and heptane/water interfaces, were made for different polarisations of the fundamental radiation. The intensity of the SHG signal was also monitored as the solutions were titrated with NaOH[5].

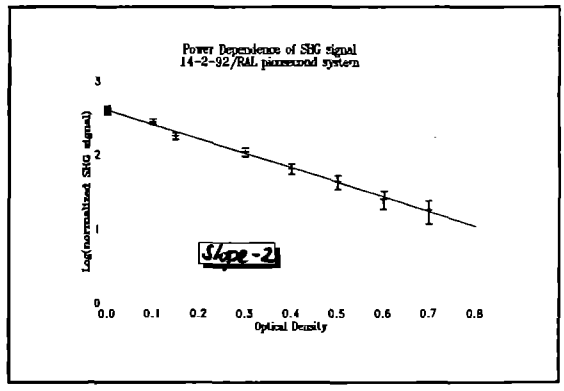

Figure 1 Power dependence of the SHG signal from p-nitrophenol at the air/water interface. The slope of -2 confirms the expected quadratic power dependence.

The power dependence of the SHG signal was measured to ensure that we were really observing a second harmonic process. The expected quadratic dependence is confirmed by the slope of -2 in the plot (figure 1) of the Ln(SHG signal) vs. the optical density of the filter (in this plot the error bars are 3 standard deviations).

The polarisation of the SHG signal is a complex function of the polarisation of the incident radiation. The dependence for both s- and p-polarised fundamental radiation has been fit by expressions given by Mazeley and Hetherington[6]. The quality of the data is much better than in our previous work, and our preliminary analysis indicates that in addition to the zzz, zxx, and xzx components of the susceptibility tensor the xyz component may also be non-zero. However, at this stage we are not sure if the small non-zero xyz component we determine simply indicates some unforseen systematic problem with our experiments. If it is a real observation then it indicates that the p-nitrophenol molecules are not as symmetrically placed around the water surface as we had previously thought.

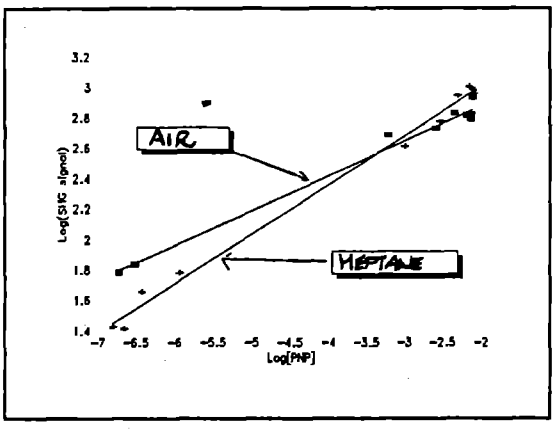

Figure 2 The concentration dependence of the SHG signal at both air/water and heptane/water interfaces.

Figure 2 shows the dependence of the SHG signal on the concentration of p-nitrophenol in the bulk solution for both air/water and heptane/water solutions. These experiments were performed by adding NaOH to the bulk solution, converting the p-nitrophenol to the phenolate. The data points fall on a straight line but with slightly different slopes for the two types of interface. We are investigating how this may reflect upon the different environment of the p-nitrophenol in the two systems.

Acknowledgments

CGH would like to thank the SERC for the award of a studentship. This work was supported in part by the SERC under grant GR/G24293 and the European Community under grant EEC/SCI-0146-C.

References

1.Y.R. Shen, Nature (London), **337**, 519, (1989)

2.J.E. Sipe, V. Mizrahi, and G.I. Stegeman, Phys. Rev. B, **35**, 9091, (1987); D.L. Andrews and N.P. Blake, Phys. Rev. A, **38**, 3133, (1988).

3.Y.R. Shen, Annu. Rev. Phys. Chem., **40**, 327, (1989).

4.A.J. Bell, J.G. Frey and T.J. Vandernoot, J. Chem. Soc. Faraday Trans. to be published.

5.X-D. Xiao, V. Vogel and Y.R. Shen, Chem. Phys. Lett. **163**, 555, (1990); X. Zhao, S. Subrahmanyan and K.B. Eisenthal, Chem. Phys. Lett., **171**, 558, (1990).

6.T.L. Mazeley and W.M. Hetherington, J. Chem. Phys., **86**, 3640, (1987).

TIME RESOLVED KINETIC STUDIES OF THE REACTIONS OF GAS-PHASE METHYLSILYLENE

R. Becerra[a], H.M. Frey[b], B. Mason[b], and R. Walsh[b]

[a] C.S.I.C., Madrid,
[b] University of Reading

INTRODUCTION

Silylenes are ubiquitous intermediates in both thermal and photochemical decompositions of silanes and organosilanes. We have studied by means of laser flash photolysis/laser absorption the kinetics of reactions of $SiMe_2$[1-3], SiH_2,[4,5] and PhSiH[6]. In several of these studies the silylenes were detected for the first time in the gas-phase[1,6]. Moreover a number of these investigations were carried out using lasers supplied by the Laser Support Facility[2,6]. Accounts of these studies have appeared in previous annual reports[7]. Measured rate constants (at ca 298 K) are relatively high with many reactions occurring faster than 1 in 10^3 collisions. Mechanisms are of the acid/base type and appear to depend on a delicate balance between the electrophilic and nucleophilic character of the silylenes and substrate molecules.

Last year[8] we reported the first ever study of MeSiH. Rate data was obtained for its reactions with SiH_4 and Me_3SiH. The data indicated a reactivity close to that of SiH_2 and PhSiH, but much greater than that of $SiMe_2$. Evidently replacement of a single H (by Me) in a silylene has a less marked effect than replacement of both Hs. During the most recent loan period we have extended the studies of MeSiH to reaction with $MeSiH_3$ and Me_2SiH_2 in order to gain further insight into the nature of the Si-H insertion process.

EXPERIMENTAL

The apparatus and equipment used for these studies was similar to that employed in earlier studies of $SiMe_2$ and is described in detail elsewhere[1-3]. Briefly, transients from the decomposition of 1,2-dimethyldisilane were generated by pulsed 193 nm photolysis (Oxford KX2 ArF exciplex laser). Transient absorptions were detected and monitored in the wavelength range 460-520 nm using the Spectra Physics 2025 Argon Ion Laser provided by the Laser Facility loan scheme. A multipass arrangement gave total path detection lengths of up to 4.8 m although usually ca 1.4 m was employed in our high temperature cell. Absorption signals were detected using a dual photodiode/differential amplifier combination and stored in a transient recorder interfaced to a BBC micro computer used as a signal averager. The precursor substance, 1,2-dimethyldisilane (DMDS), was kindly supplied by E. Hengge (University of Graz) and was ca 95% pure.

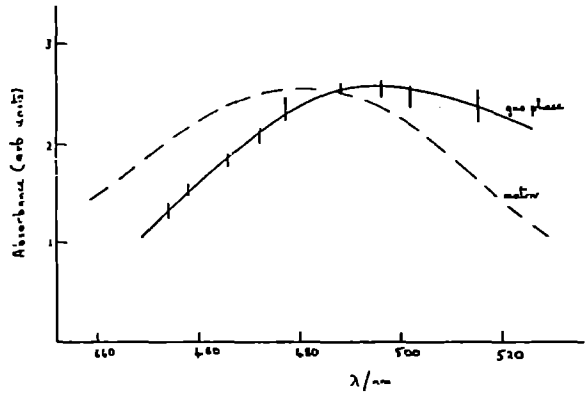

Figure 1 Absorbance spectrum of MeSiH

RESULTS

With the experience gained last year[8] we were able to repeat our early attempts to obtain a spectrum of the MeSiH transient under more favourable conditions. 25 mTorr samples of DMDS diluted in SF_6 (total pressure, 5 Torr) were flash photolysed at 357 K, at a constant exciplex laser pulse energy of 83 ± 5 mJ. Absorption signals were monitored at each of the available nine wavelengths of argon ion probe laser. Signals decayed exponentially (with a rate constant of (2.0 ± 0.3) x 10^5 s^{-1}) independent of wavelength. Averaged signal absorbances (at a time delay of 15 μs) are shown in figure 1 as a function of wavelength. This effective gas-phase spectrum is compared with the known argon matrix spectrum[9]. The broad band appearances of the two spectra encourage belief that they are the same species. The small bathochromic shift of the gas phase spectrum is similar to that obtained for $SiMe_2$ [1]. Further support for the formation of MeSiH comes from end-product studies[10] of Si-H insertion reactions using g.c.analysis.

Kinetic experiments were carried out with mixtures containing 20-100 mTorr of DMDS with partial pressures of substrate up to 600 mTorr and total pressures 6 Torr (made up with Ar or SF_6). Experiments were made difficult by erratic amounts of dust formation. This tended to vary from experiment to experiment. For data processing purposes only runs with little or no dust were used. Signal decays (averaged for 20-30 laser shots) were single exponential and second order rate constants were determined by measuring the pseudo-first order decay constants as a function of added substrate. Reasonable linear dependencies were found. The reactions investigated in the past year were with $MeSiH_3$ and Me_2SiH_2. Experiments were carried out at five different temperatures in the range 370 - 586 K for both reactants. The measured rate constants were fitted to the Arrhenius equation by least means-squares analysis. The resulting parameters together with those obtained earlier for SiH_4 and Me_3SiH are shown in table 1. Error limits (two standard deviations) are ca ± 0.4 (log A) and ±3.6 kJ mol^{-1} (E_a). These rate data for MeSiH were more difficult to obtain than those for $SiMe_2$, as a result of a combination of relatively inefficient MeSiH production combined with high decay rates.

Table 1 Arrhenius Parameters for MeSiH insertion reactions

Substrate	log A[a]	E_a[b]
SiH_4	-11.4	-7.5
$MeSiH_3$	-12.1	-14.5
Me_2SiH_2	-11.8	-11.5
Me_3SiH	-12.9	-18.9

a. Units: cm^3 $molecule^{-1}$ s^{-1} b. Units: kJ mol^{-1}

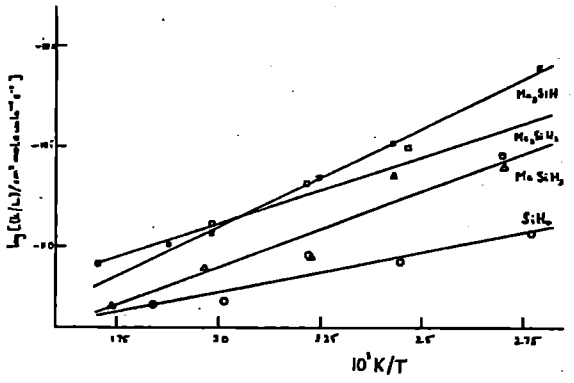

Figure 2 Arrhenius plots for the insertion reactions of MeSiH

DISCUSSION

The measurements reported here represent the first experimentally determined rate constants for MeSiH. Three features of the data emerge clearly from these results. (i) The rate constants are all very high ($\geq 10^{-11}$ cm^3 molecule^{-1} s^{-1}). (ii) There is a clear trend towards lower values with increasing temperature, i.e. activation energies are all negative. (iii) There is a rate enhancement effect of methyl substituents in the substrate silane. The last point is brought out in figure 2 which shows the Arrhenius plots for the statistically corrected rate constants, k/L. The fact that the Me_2SiH_2 and Me_3SiH plots cross should be taken as a reflection of scatter in the data, rather than contradiction of the general trend. Plots similar to figure 2 were obtained previously for $SiMe_2$ [3] and PhSiH[6].

These results confirm last year's findings[8], viz. that the rate constants for MeSiH are much closer to those of SiH_2 and PhSiH than to those of $SiMe_2$ (which is relatively much less reactive).

An explanation for these findings is necessarily fairly complicated. We are currently in the process of elaborating the details[11]. In summary this is as follows.

We believe these results offer further support for the operation of a mechanism involving an intermediate complex. This process is as shown in the following equation:

$$MeSiH + RH \underset{-1}{\overset{1}{\rightleftharpoons}} Complex \xrightarrow{2} MeSiH_2R$$

The rate constant observed depends on the balance between redissociation of the complex (back to reactants), step (-1), or reaction to products, step (2). The nature of the complex is not known but recent ab-initio calculations show the complex for SiH_2 + SiH_4 to involve a Si-H bridged structure[12]. This is shown in figure 3, as adapted for MeSiH + Me_3SiH, together with a schematic potential surface.

Our interpretation is then that the initial interaction, step (1), is fast for all silylenes, probably approaching the collision rate. The reactive outcome depends on magnitude of k_2/k_{-1}. This depends on both the silylene and substrate molecule, but as a generalisation, k_2/k_{-1} is large for SiH_2, intermediate in value for MeSiH and small for $SiMe_2$. It obviously varies from substrate to substrate but tends to increase with methyl substituents in the substrate silane. Thus the magnitude of these silylene rate constants is determined by a subtle blend of the stability of these complexes and the magnitude of their barriers to rearrangement (H-shift). These factors can be further related to the deep-seated operation of electrophilic and nucleophilic interactions between silylene and silane.[11]

REFERENCES

1. J.E. Baggott, M.A. Blitz, H.M. Frey, P.D. Lightfoot and R. Walsh, Chem. Phys. Lett. 135 39 (1987).
2. J.E. Baggott et al, J. Chem. Soc., Faraday Trans. 2 84 515 (1988).
3. J.E. Baggott et al, J. Am. Chem. Soc. 112 8337 (1990).
4. J.E. Baggott et al, J. Phys. Chem. 92 4025 (1988).
5. J.E. Baggott et al, J. Chem. Soc., Faraday Trans. 86 27 (1990).
6. M.A. Blitz, H.M. Frey, F.D. Tabbutt and R. Walsh, J. Phys. Chem. 94 3294 (1990).
7. SERC Central Laser Facility; Annual Report 1988, p 172; Annual Report 1989, p 240; Annual Report 1990, p.115.
8. SERC Central Laser Facility; Annual Report 1991, p.146.
9. G. Maier et al, Chem. Ber. 117 2369 (1984).
10. N. Al-Rubaiey and R. Walsh, unpublished results.
11. R. Becerra, H.M. Frey, B.P. Mason and R. Walsh, article in preparation.
12. R. Becerra et al, J. Am. Chem. Soc. 114 2751 (1992).

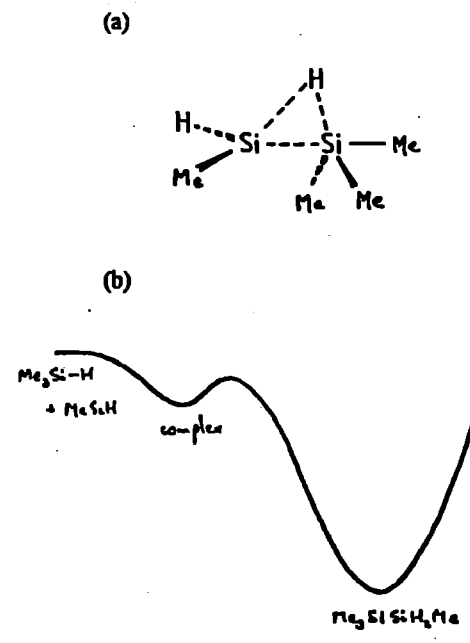

Figure 3 (a) Structure of MeSiH + Me_3SiH complex
(b) Potential energy surface (qualitative)

SPECTROSCOPIC AND DYNAMICAL STUDIES OF SiH_2^+

D.I. Hall and P.J. Sarre

Department of Chemistry, University of Nottingham, University Park, Nottingham NG7 2RD

INTRODUCTION

The photodissociation spectrum of SiH_2^+ is proving to be a spectacular example of how insight can be gained into scattering, and in this special case, reactive collisional processes via spectroscopically based experiments. In general a photodissociation event can be considered to be a half-collision between the dissociating fragments; in SiH_2^+ we have discovered a case where the fragmentation is competitive between two chemically distinct dissociation channels, namely $SiH^+ + H$ and Si^+ and H_2.[1] This can therefore be considered to be a spectroscopic study of part of the reaction surface for the $Si^+ + H_2 \rightarrow SiH^+ + H$ chemical reaction.

EXPERIMENTAL

The principles of fast-ion-beam laser photofragment spectroscopy have been described in detail elsewhere.[2] In brief, a mass-selected fast ion beam of SiH_2^+ is generated by electron impact ionisation of silane gas and is irradiated with a tunable laser. Excitation to a predissociating state results in the formation of fragment ions (Si^+ and/or SiH^+) which are separated from the parent beam and detected with an electron multiplier. In this case the laser radiation was provided by an argon-ion-pumped Spectraphysics 3900 broad-band Ti-Sapphire tunable laser system with an approximate linewidth of one reciprocal centimetre. The laser was modulated at 3 kHz and the photofragment signal recovered by phase sensitive detection. The spectra were recorded simultaneously with etalon fringes and calibrated using optogalvanic lines.

RESULTS AND DISCUSSION

A rich spectrum was recorded in the Si^+ channel, part of which is shown in figure 1. However, no corresponding spectrum was found in the SiH^+ channel, showing that all of the levels accessed by irradiation with wavelengths between 700 and 850 nm lie between the two dissociation limits, in contrast to the previous data for excitation at shorter wavelengths. Figure 1 shows a Σ sub-band with an origin near 778 nm from which a set of rotational constants for the ground and excited states has been derived. A second Σ sub-band near 710 nm exhibits a perturbation at N = 4 in the excited electronic state. Also shown in figure 1. is an $^rR(\Delta K = +1)$ sub-band with K' = 5(v'=1). The rotational structure is markedly different from that of the Σ sub-band and a large spin-splitting is observed. Only in the case of electronic emission spectra of NH_2 have similar transitions been found, although there is no predissociation in the case of NH_2.[3] The appearance of predissociated levels involving high values of K, even up to K = 25, is surprising as it had been generally thought that the predissociation mechanism involves coupling of the excited and lower electronic surfaces by a-axis rotation which would result in an increasing predissociation rate with increase in K value. However, for high values of K a centrifugal barrier arises which prevents the molecule from accessing the linear configuration where the potential surfaces touch, and hence the predissociation rate is actually rather slow for high values of K. The predissociation rates are being modelled and the results will be discussed in detail elsewhere.[4]

REFERENCES

1. P J Sarre, Farad. Discuss. Chem. Soc. No. 91, 414 (1991)
2. C P Edwards, C S Maclean and P J Sarre, Molec. Phys. **52**, 1453 (1984)
3. R N Dixon, S J Irving, J R Nightingale and M Vervloet, J. Chem. Soc. Farad. Trans. **87**, 2121 (1991)
4. D I Hall and P J Sarre, in preparation.

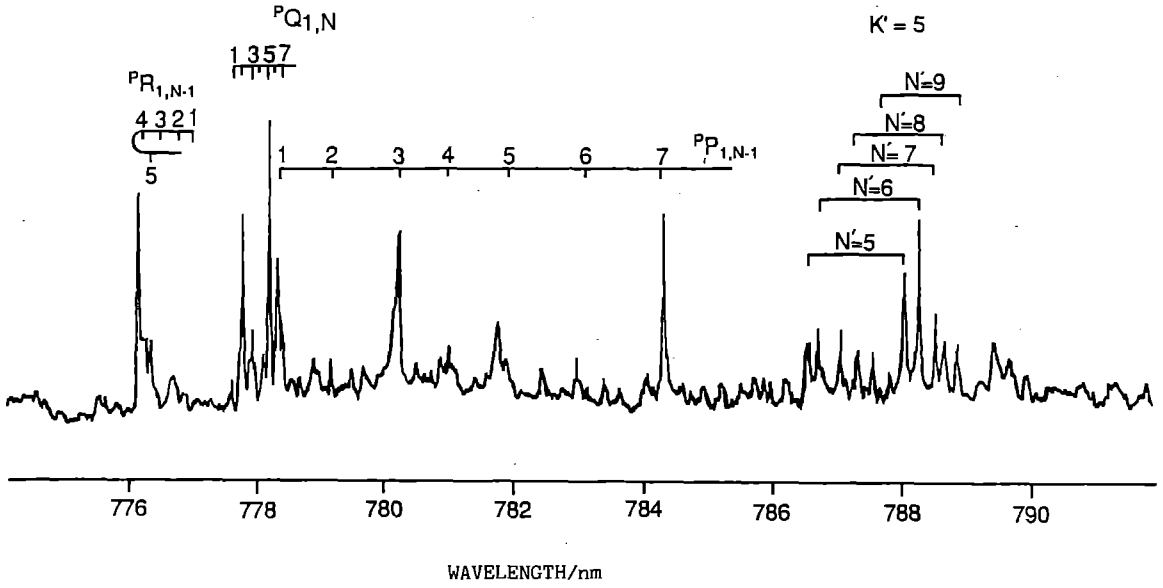

Fig. 1 Laser photofragment spectrum of SiH_2^+ recorded by the detection of Si^+ ions.

STUDIES IN COMBUSTION AND ATMOSPHERIC CHEMISTRY

D.L. Baulch and Helen D. Black

School of Chemistry
University of Leeds

INTRODUCTION

An excimer pumped dye-laser system has been used recently in this laboratory in two experimental studies, one concerned with time resolved measurements of free radical concentration changes in oscillating combustion systems, the other being an investigation of the rates and mechanisms of a number of rapid gas phase reactions of importance in atmospheric chemistry. The former study, on combustion processes, has led to a number of publications and much of the work is summarized in reference 1. In this report we describe the more recent work on atmospheric reactions for which the EMG 101 Excimer Laser on loan from the Rutherford Laboratory was used. This work, which is being prepared for publication, was the subject, in part, of a successful Ph.D. submission by Dr. Helen Black (available through the Brotherton Library, University of Leeds) and was carried out in collaboration with Dr. A.J. Hynes, Georgia Institute of Technology, who was able to participate in the work in Leeds by virtue of receiving a grant from the U.S. National Science Foundation.

The atmospheric reactions studied all involved the hydroxyl radical which plays a key role in most combustion processes and in the chemistry of the polluted and unpolluted atmosphere. In one part of the work the rates of reaction of OH with acetonitrile and deuterated acetonitrile was studied with the intention of clarifying ambiguities in the current evidence for the mechanism of these reactions. The other part of the work involved measuring rates of reaction of OH with furan and tetrahydrofuran. This was part of a broader study aimed at characterizing the atmospheric chemistry of heterocyclic compounds which are often present in substantial amounts in the troposphere.

EXPERIMENTAL

The rate constant measurements were carried out using a discharge-flow system of conventional design consisting of a 25 mm diameter flow tube the interior walls of which were coated with halocarbon wax. Reagents were introduced into the flow tube by means of a sliding double injector. Hydroxyl radicals were produced by titration of H atoms, produced by means of a microwave discharge in a He/H_2 mixture, introduced into the flow tube through a side arm, and titrated with nitrogen dioxide. The compounds to be studied were added downstream of the OH production point in concentrations greatly exceeding that of the OH, ensuring that all measurements of [OH] decay were made under pseudo first order conditions. The OH radicals were detected by laser induced fluorescence. 308 nm radiation generated by the excimer laser was used to pump a dye laser (Lambda Physik FL 3002) containing a solution of coumarin in methanol as the lasing medium. The radiation from the dye laser was frequency doubled using a KDP crystal and used to excite the three overlapping rotational lines (Q', Q" and R_2^3) of the OH ($A^2\Sigma \rightarrow X^2\Pi$) 1-0 band at 281.915 nm. Fluorescence in the 0-0 and 1-1 bands was detected after passing through a pyridine filter and a band pass filter centred on 312 nm. Rate constants were determined at ambient temperatures by measuring the pseudo first order rate constant for OH removal and plotting these rate constant values against substrate concentration. In all cases, excellent linear plots were obtained yielding values of the bimolecular rate constant for the OH reaction with the compound under study. Helium was used as the carrier gas throughout.

RATES OF REACTION OF HYDROXYL RADICALS WITH ACETONITRILE

Acetonitrile plays an important role in the formation of stratospheric ions and is present in ppbv levels in the lower troposphere. This has generated a number of studies aimed at characterizing its sources, emission rates and oxidation mechanism in the atmosphere. Its lifetime in the atmosphere is largely controlled by its rate of reaction with the OH radical. Most previous studies of this reaction, OH + $CH_3CN \rightarrow$ products, assumed that it proceeded entirely by hydrogen abstraction but a recent study by Hynes and Wine suggested a pressure dependence of the rate constant implying a more complex mechanism. The effect was small, barely outside the error limits of their work, and with the technique they were using they could not study the reaction at pressures below 50 Torr where the effect was expected to be more pronounced. The discharge flow system used in the present study is well suited to low pressure work particularly in the 1-10 Torr region.

Values obtained in the present work for the rate constant of the reaction OH + $CH_3CN \rightarrow$ products are shown in Table 1.

Table 1. Values of k at 295 K for the reaction OH + CH_3CN

Pressure/Torr.	10^{14} k/cm^3 molecule^{-1} s^{-1}
1.4	1.52±0.08
5.2	2.01±0.04
7.5	2.57±0.10

A pressure effect is clearly evident. However, when compared with measurements by others over the whole pressure range it is more difficult to quantify the pressure effect because of the scatter in the data obtained by others at higher pressures.

The pressure effect is expected to be more marked for the reaction of OH with deuterated acetonitrile which was therefore studied by the same technique. Measurements were only made at a pressure of 1.0 Torr. The result is compared in Figure 1 with the results obtained by others at higher pressures. In this case, the pressure dependence of the rate constant is very evident.

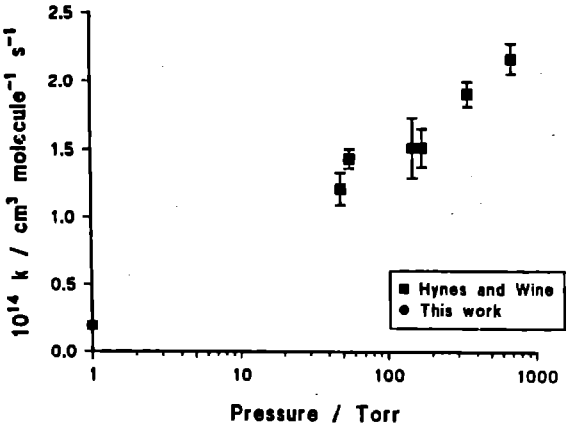

Figure 1. Pressure Dependent of k(OH + CD_3CN). (T = 295 K)

The implication for the reaction mechanism is that it occurs, in part, by adduct formation, via $(OH)CH_3CN$. Formation of such species has parallels in the observed pressure dependence of the reaction of OH with the related compounds HCN and $(CN)_2$.

REACTIONS OF HYDROXYL RADICALS WITH TETRAHYDROFURAN AND FURAN

Semiempirical schemes relating the chemical structures of a series of related compounds to the rate constant for their reaction with the OH radical have been derived for a wide range of aliphatic and aromatic hydrocarbons. Such schemes are widely used and are essential for modelling tropospheric chemistry where measured data are still relatively sparse. It is important to extend them to a wider range of compounds.

In the work described here, rates of attack on the compounds, furan and tetrahydrofuran, are reported. Both of these compounds are emitted into the atmosphere in significant amounts from a number of anthropogenic sources. It is important to know their lifetimes, governed by their rate of reaction with OH, but as well, this is part of a broader study aimed at extending empirical prediction schemes for OH reactivity to heterocyclic compounds containing O, S and N.

The value of the rate constant found in the present work for the reaction of OH with tetrahydrofuran is $(1.47 \pm 0.15) \times 10^{-11}$ cm^3 molecule^{-1} s^{-1} compared with an average value of $(1.61 \pm 0.22) \times 10^{-11}$ cm^3 molecule^{-1} s^{-1} from three other studies performed at much higher pressures (up to 760 Torr) confirming the absence of a pressure effect.

The results for the reaction of OH with furan (Figure 2) on the other hand show that the rate constant is pressure dependent.

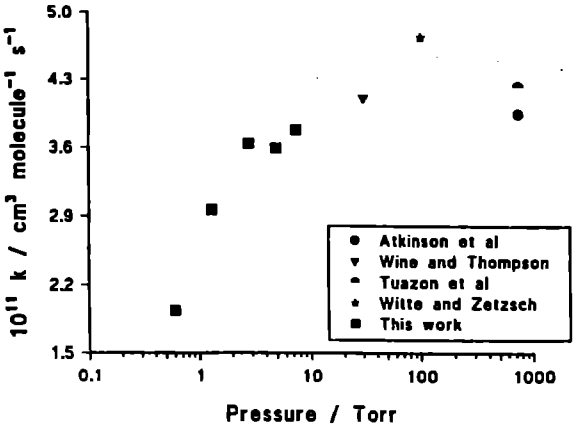

Figure 2. Pressure Dependence of the Rate Constant k(OH + furan). (T = 295 K)

In principle, it should be possible to derive from these results values of the limiting high pressure (k_∞) and low pressure (k_0) constants for the reaction. When this was attempted, using Troe's method, it was only partially successful because of the scatter in the results. A value of $k_\infty = (4.5 \pm 0.4) \times 10^{-11}$ cm^3 molecule^{-1} s^{-1} was obtained, which is sufficiently larger than most values measured at atmospheric pressure to suggest that the reaction is still significantly affected by fall-off at 1 atmosphere.

These results can be used to derive values of atmospheric lifetimes for furan and tetrahydrofuran, and useful comparisons of these results can be made with reaction rates of analogous hydrocarbons and N and S containing heterocyclic compounds. It is intended to extend these studies to reactions of polycyclic compounds containing a hetero atom and for this reason preliminary studies were made on the corresponding heterocyclic compounds benzofuran and 2-3-dihydrobenzofuran. The measured OH decays in the presence of these species was found to be complex and difficult to reproduce, suggestive of a heterogeneous contribution to the reactions which will need to be characterized before the homogeneous reaction can be studied by the discharge-flow technique.

REFERENCES

1. D.L. Baulch, J.F. Griffiths, W. Kordylewski and R. Richter. Phil. Trans. R. Soc. London A **333**, 199 (1991).

VECTOR CORRELATIONS IN REACTION DYNAMICS

G. Hancock and A.J. Orr–Ewing

Physical Chemistry Laboratory, Oxford University.

For a full understanding of the dynamics of simple bimolecular reactions what is required are detailed measurements of the ways in which vector as well as scalar attributes of the reactants are converted into the equivalent quantities in the products. We have studied the reaction

$$O(^3P) + CS(^1\Sigma^+) \longrightarrow CO(^1\Sigma^+) + S(^3P) \qquad (1)$$

and obtained, for the first time, correlations between the pairs of vectors $\underline{k}$, $\underline{k}'$ and $\underline{J}'$, representing the reagent velocity, the product velocity and the product angular momentum respectively. Such correlations, as shown by trajectory calculations, are extremely sensitive to details of the potential energy surface controlling the reaction, and together with the scalar observations of partitioning of vibrational, rotational and translational energy in the products, provide a wealth of information on the reaction dynamics.

Oxygen atoms in their ground electronic state are formed with a known distribution of velocities (and hence vectors $\underline{k}$) by the 355 nm photolysis of NO_2 [1]. These react with CS radicals, formed from a weak microwave discharge in CS_2, at low pressures inside the reaction chamber, and the resultant CO molecules are detected by laser induced fluorescence (LIF) of the $A^1\Pi - X^1\Sigma^+$ transition at wavelengths between 200 – 230 nm. Measurements of the variation of the LIF signals as a function of relative polarisations of the photolysis and probe beams allow the correlation between $\underline{k}$ and $\underline{J}'$ to be found, and sub–Doppler linewidth techniques enable the products velocity vector $\underline{k}'$ to be correlated with both these quantities[2]. LIF measurements over a range of vibrational and rotational levels have also allowed the rotational distributions in the CO product to be found.

Figure 1 shows the data for the correlation of $\underline{k}$ with $\underline{J}'$, both in terms of the measured laboratory frame alignment parameter and the centre of mass equivalent A_0^2 (cm), obtained with knowledge of the translational anisotropy of the O^3P product from NO_2 photolysis. The major point is that for all rotational levels of $v' = 12$ and 14 in CO studied, the value of A_0^2 (cm) is close to zero, and far from its limiting values of 2 and –1 corresponding to $\underline{k}//\underline{J}'$ and $\underline{k} \perp \underline{J}'$ respectively. $\underline{k}$ and $\underline{J}'$ thus appear to be uncorrelated. In Figure 2, Doppler profiles of the Q(17) line of the (6,14) CO band are given for different geometries of the pump–probe lasers, together with functional forms fitted to the data. Such experiments probe the $\underline{k}$, $\underline{k}'$ correlations, and indicate

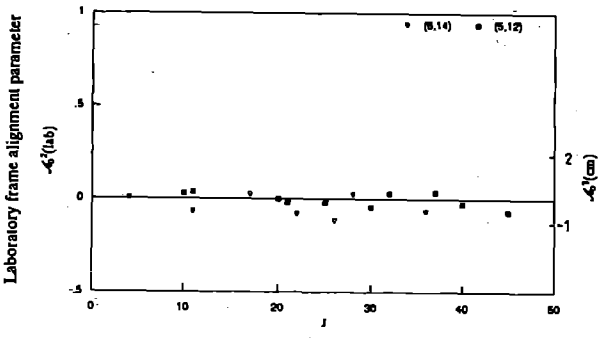

Figure 1. Values of measured laboratory frame alignment parameters and the corresponding centre–of–mass parameters for different (v J) levels. No marked $\underline{k}\,\underline{J}'$ correlation is observed.

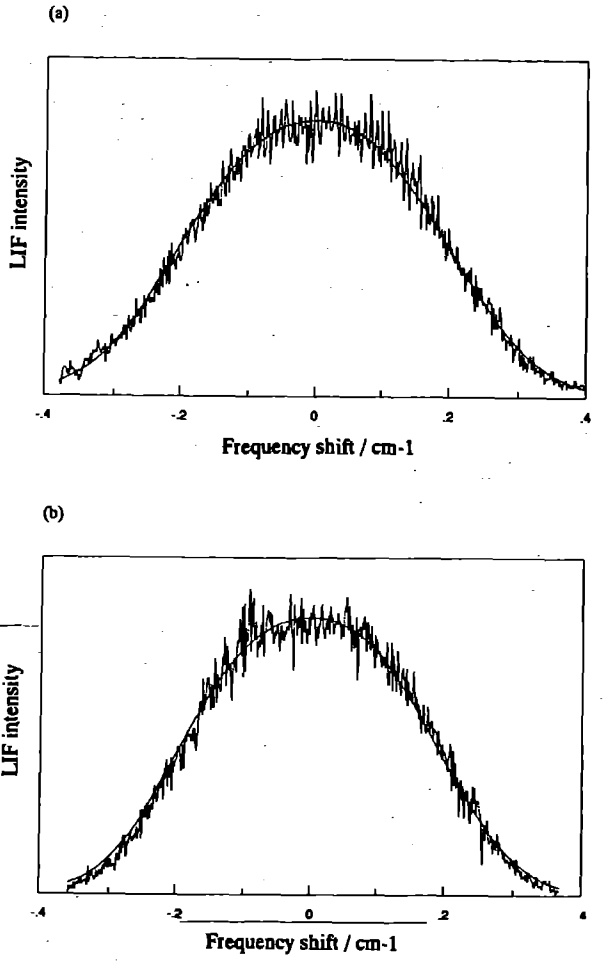

Figure 2. Doppler profiles for the Q(17) line of the (6,14) band recorded with the angle between the electric vector of the photolysis laser and the probe laser direction of (a) 30° and (b) 90° , together with fitted lineshape functions. The slightly narrower profile observed in (b) shows a slight preference for $\underline{k}//\underline{k}'$.

again that these are not strong, but show some preference for forward or backward scattering (the Doppler widths are slightly smaller when the probe beam propagates perpendicular to $\underline{k}$). Figure 3 shows some marked structure in the profile of the Q(20) line of the (5,12) band, with the fitted function consistent with there being a marked correlation between $\underline{k}'$ and $\underline{J}'$, these being mutually perpendicular.

We believe that our results demonstrate the influence of the initial angular momentum of the CS radical on the reaction dynamics, and that they are consistent with a preference for trajectories which sample a bent transition state for the 'hot' oxygen atom reagents. Quasi-classical trajectory calculations on a LEPS surface which reproduces the scalar attributes of the reaction (rate constant, vibrational and rotational distributions) clearly show the influence of this, and predict low $\underline{k}\ \underline{J}'$ and $\underline{k}\ \underline{k}'$ correlations, with $\underline{k}' \perp \underline{J}'$ as experimentally seen. Our next aims are to cool the CS reagent to J=0 by nozzle expansion, and to produce O atoms with a higher value of their translational anisotropy by photolysis of jet cooled NO_2. The experiment will then edge towards being a completely state selective study on both scalar and vector properties of reactants and products.

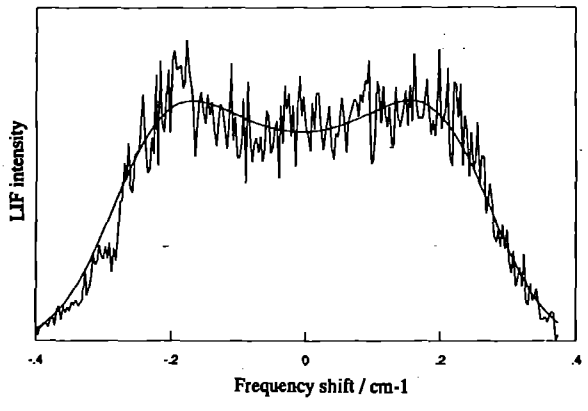

Figure 3. Doppler profile of the Q(20) line of the (5,12) band, together with a fit to the data. The dip in the line centre is consistent with a marked $\underline{k}'\ \underline{J}'$ correlation, with these vectors perpendicular to each other.

Equation (1) is not the only process amenable to study by this technique, as demonstrated by Simons and co-workers in their measurements on the $O(^1D) + N_2O$ reaction[2,3]. We have also observed $OH(X^2\Pi)$ radicals formed when NO_2 is photolysed in the presence of H_2S. One possibility for their origin is in the reaction

$$O(^3P) + H_2S(X^1A_1) \longrightarrow OH(X^2\Pi) + SH(X^2\Pi) \quad (2)$$

although we have yet to eliminate conclusively their formation from photolysis of HONO, known to be formed slowly by heterogeneous reactions between NO_2 and H_2S [4].

The distribution of rotational, spin orbit and lambda doublet populations show differences from those formed in HONO photolysis, but the most compelling evidence for formation of the radical by (2) comes from the observation that the OH LIF signal rises from a zero value when the time separation between photolysis and probe lasers is small, to a maximum after a few μs, consistent with chemical reaction and not laser photolysis being the radical source. If this is confirmed, we have measurements of all scalar and all vector correlations for process (2), including an additional parameter which does not feature in (1) namely the correlations between 'nuclear coordinate' vectors $\underline{k}$, $\underline{k}'$ and $\underline{J}'$ and an electronic vector, namely the alignment of the unpaired Π electron with the nuclear framework as measured via lambda doublet propensities. More studies are in progress.

References

1. F. Green, G. Hancock and A.J. Orr-Ewing, Faraday Discuss. Chem. Soc. 91, 79 (1991).
2. F. Green, G. Hancock, A.J. Orr-Ewing, M. Brouard, S.P. Duxon, P.A. Enriquez, R. Sayos and J.P. Simons, Chem. Phys. Letters 182, 568 (1991).
3. M. Brouard, S.P. Duxon, P.A. Enriquez, R. Sayos and J.P. Simons, J. Phys. Chem. 95, 8169 (1991).
4. C.P. Cantrell, J.A. Davidson, R.E. Shelter, B.A. Anderson and J.G. Calvert, J. Phys. Chem. 91, 6017 (1987).

AN EPR STUDY OF PHOTOIONISED DNA BASES

Mark Malone,* Anthony Parker* and Martyn Symons*

* *Department of Chemistry, The University, Leicester LE1 7RH*
* *Central Laser Facility, Rutherford Appleton Laboratory, Chilton, Didcot, Oxon OX11 0QX*

INTRODUCTION

It is commonly thought that cell death on exposure to ionizing radiation arises primarily as a result of DNA damage. It is, therefore, important to try to understand the mechanism of radiation damage to DNA. There are two limiting overall mechanisms for γ-irradiation damage to DNA. One being direct interaction between the radiation quanta and DNA giving rise to single (SSB) and double (DSB) strand breaks (direct damage). The other being indirect damage *via* attack by water radicals (e.g. ·OH) which predominantly give rise to SSB. In the cellular environment the "direct damage" mechanism is believed to be of greater importance due to the tightly packed nature of the cell nucleus which leaves little room for the water necessary to induce indirect damage. Also SSB are more readily repaired than DSB by enzymatic pathways.

The study of the direct damage mechanism in DNA by conventional pulse radiolysis techniques is not feasible because of the overriding influence of the indirect mechanism. Consequently, the study of strand break formation in DNA and polynucleotides induced by pulsed, high intensity, photoionising laser light is of increasing interest as a means of mimicking direct radiation damage to DNA. RT photoionisation studies of DNA have lead to the conclusion that $G^{\cdot+}$, the most stable cation, gives rise to a significant number of strand breaks.[1] Also the electrons are totally ejected from the DNA to form solvated electrons and do not play a significant role in strand breakage.[2,3] We and others have studied the effect of ^{60}Co γ-radiation damage to DNA between 77 K and RT using EPR spectroscopy.[4] Under these conditions the major electron-loss centre is $G^{\cdot+}$ and the major electron-gain sites are $T^{\cdot-}$ and $C^{\cdot-}$. Strand break studies of annealed samples suggest that both centres can lead to strand breaks. Hence there is some disagreement between solid state γ-radiolysis of DNA and liquid phase photoionisation studies.

To bridge the gap between the two methods we have undertaken an EPR study of photoionised DNA and its constituents between 77 K and RT. We have detected a number of pristine radical cations and/or their deprotonated or hydroxylated radical products trapped in the matrices. Also we have shown that there are considerable differences between γ-radiolysis and high intensity UV laser photolysis of DNA at 77 K. In this article we report on our initial results obtained for the nucleotides, nucleosides and free bases using perchlorate glasses.

EXPERIMENTAL

The DNA base π radical cations were generated by laser photolysis in 3M $Mg(ClO_4)_2$ or 8.5M $NaClO_4$ glasses. Typically the solute (0.05M) is dissolved in the perchlorate solution (H_2O or D_2O), frozen, irradiated at 77 K and then analysed by X-band EPR at 77 K. Photolysis was done using a KrF eximer laser at 248 nm. The laser energy varied between 250 and 350 mJ, the pulse duration was 20 ns, the area of beam cross section 2.5 cm^2, the repetition rate was 5 Hz and the total irradiation time was varied between 30 seconds and 2 minutes.

The process has been found to be biphotonic involving an initial excitation to the triplet state. Absorption of a second quantum drives the electron through the ionisation threshold thereby generating a radical cation and a photoejected electron. The perchlorate scavenges the electron (1) producing ClO_3^- and $O^{\cdot-}$.

$$X + ClO_4^- \xrightarrow{2\,h\nu} X^{\cdot+} + O^{\cdot-} + ClO_3^- \quad (1)$$

The signal due to $O^{\cdot-}$ shows characteristic anisotropic g-values, $g_{\parallel} \equiv 2.002$ and $g_{\perp} \equiv 2.0053$. The perpendicular feature overlays those of the π radical cations, however it may be efficiently subtracted to reveal the radical cation. Also annealing the sample to 155 K for $Mg(ClO_4)_2$ or 180 K for $NaClO_4$ removes the $O^{\cdot-}$.

RESULTS AND DISCUSSION

Thymine and N1 Substituted Thymine Cation Radicals

Thymine yields a π radical cation with a large methyl hyperfine splitting (hfs) of ~20 G and an anisotropic nitrogen coupling arising from N1 with $A_{\parallel} \equiv 12$ G (Fig. 1a). It is assigned to radical (I) with an unpaired electron density of 0.5 at C-5 and is presumably deprotonated at N1.[5]

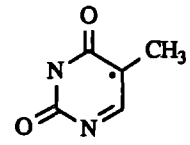

(I)

For the N1 substituted thymine derivatives the expected primary cations were not detected. Also, they do not appear to deprotonate from N3 but undergo deprotonation from the C-5 methyl group to form the $TCH_2^{\cdot}$ radical (II). The hyperfine spectrum of this radical (Fig. 1b) originates from the interaction of the unpaired electron with the two remaining α protons of the methyl group and *via* resonance delocalisation with the proton attached to carbon atom C_6.[6] Computer simulation of the spectrum for radical (II) using the g and hyperfine tensors reported by Hüttermann[6] provides reasonable agreement with the experimental spectrum.

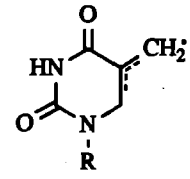

(II)

Upon thermal annealing of photoionised frozen aqueous TMP to *ca.* 250 K the $TCH_2^{\cdot}$ radical is quantitatively converted into a 1,4,6,4,1 quintet (Fig. 1c). This has been tentatively assigned as the hydrolysis product of $TCH_2^{\cdot}$ namely $TOH^{\cdot}$ (III) with a methyl and C-6 proton hfs of *ca.* 20.5 G. However, the quintet may also arise from $TCH_2^{\cdot}$ attack at the C-6 position of a nearly or adjacent TMP molecule.

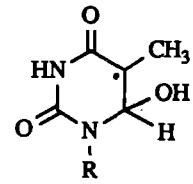

(III)

In situ RT photolysis of H_2O_2 added to single stranded DNA

solutions in the absence of oxygen gives rise to both $TCH_2^{\cdot}$ and $TOH^{\cdot}$.[8] They produce strand breaks presumably *via* hydrogen abstraction by $TOH^{\cdot}$ from an adjacent deoxyribose. However, their overall contribution to SSB in this system is minor with the major component of strand breaks being from short-lived non-EPR observable species.

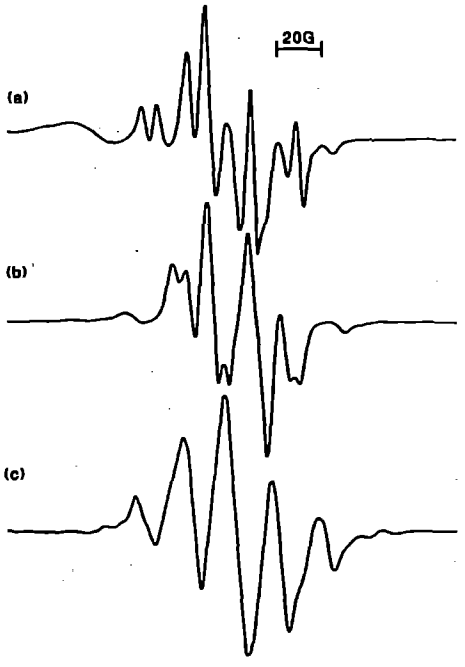

Figure 1. The X-band EPR spectra of:
(a) the thymine π radical cation and $O^{\cdot-}$;
(b) $TCH_2^{\cdot}$ formed by deprotonation at the C-5 methyl group [note the outermost two features are due to an impurity and may be ignored];
(c) $TOH^{\cdot}$ formed by hydrolysis of $TCH_2^{\cdot}$ on annealing.

Cytosine and N1 substituted cytosine π-radical cations

The cytosine π-radical cation produced by one-electron oxidation with $Cl_2^{\cdot-}$ in γ-irradiated alkaline LiCl glasses shows coupling to the C-5 proton and two ^{14}N nuclei; one being the exocyclic NH_2 nitrogen and the other N1[5] in radical (IV).

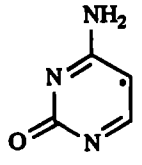

(IV)

In this study photoionisation of cytosine in $Mg(ClO_4)_2$ glasses (pD ≅ 5.5) produces a radical with a slightly different EPR pattern to radical (IV) (Fig. 2a). These differences are probably due to the influence of pH *via* protonation or deprotonation of the parent and radical cation molecules. The 5-methyl cytosine π-radical cation has a characteristic 1,3,3,1 EPR quartet indicative of a 20 G methyl hfs (Fig. 2b). In addition, there are two anisotropic nitrogen couplings with ($A_{||}$ = 11, $A_{\perp}$ = 0) and ($A_{||}$ = 6, $A_{\perp}$ = 0).[9] Upon warming in neutral glasses the $O^{\cdot-}$ decays leaving the initial radical cation unaltered. However, in alkaline glasses ($NaClO_4$, pD 11.5) deprotonation from the C-5 methyl group occurs to produce $CCH_2^{\cdot}$ radical (V), probably deprotonated at N1, (Fig. 2c).

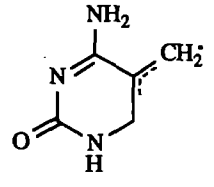

(V)

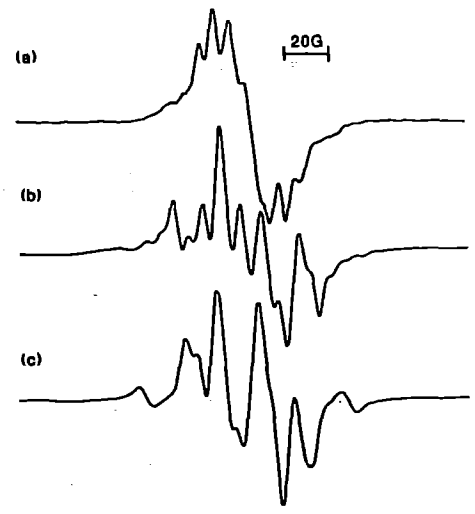

Figure 2. The X-band EPR spectra of:
(a) the cytosine π radical cation;
(b) the 5-methyl cytosine π radical cation;
(c) $CCH_2^{\cdot}$ formed by deprotonation of 5-methyl cytosine and 5-methyl dCMP at the methyl group [note the outermost two features are due to an impurity and may be ignored].

N1 substitution greatly reduces the quantum yield of π-radical cation formation for both thymine and cytosine. Photoionisation of 2′ deoxycytidine-5′-monophosphate (dCMP) at 77 K yields a quartet (approx. 1,1,1,1) extending *ca.* 54 G with a peak-to-peak width of 16 G (Fig. 3a). The identical line splittings of the quartet indicate couplings to two non-equivalent proton, one being approximately twice the magnitude of the other. The EPR spectra were identical in both H_2O and D_2O although, as expected, the linewidths are narrowed in the latter. This indicated that the unpaired electron is not strongly coupled to a hydroxyl or amino proton thus eliminating a number of possible radicals and, in particular, the aminyl radical.[10,11] Deoxycytidine (dCytd) yields an identical quartet to dCMP thereby excluding any possibility of the radical being associated with the phosphate group.

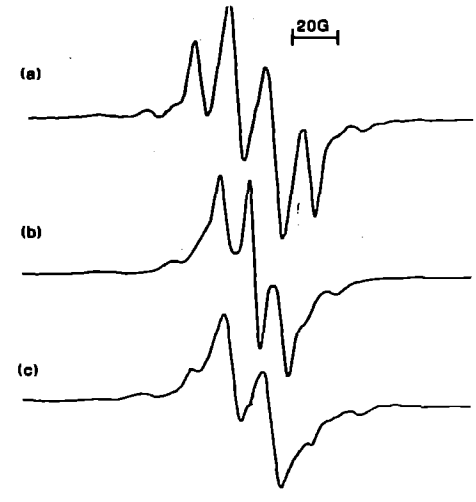

Figure 3. The X-band EPR spectra of photoionised:
(a) 2′-deoxycytidine-5′-monophosphate (dCMP);
(b) cytidine-5′- monophosphate (CMP);
(c) 2′,3′-dideoxycytidine (ddCytd).

If the quartet to arise from the base π radical it would have to involve coupling to the H_5 and H_6 protons. Substitution of the H_5 with a methyl group should give rise to a quintet whilst substitution of either of the hydrogens with deuterium should collapse the quartet since the hfs of a deuterium is $\cong$ 1/6.5 that of a hydrogen. 5-Methyl dCMP, 5-methyl dCytd and 5,6-dideutero-2′-deoxycytidine all gave the 16 G quartet. This clearly indicates that this species is not a base-centred π-radical but rather a sugar-centred radical. The most compelling evidence for this is indicated by the different radicals obtained for cytidine monophosphate (CMP) and 2′,3′-dideoxycytidine (ddCytd) shown in Fig. 3.

The extinction coefficient of cytosine is orders of magnitude larger than those of the sugars at 248 nm, therefore photoionisation must occur exclusively from the base. Also Close *et al.*[12] have observed the base π-radical cation of dCMP at 6 K which has considerable spin centred at C-5 and N1. We suggest that the radicals observed dCMP, CMP and ddCytd in this study are produced by an initial electron-loss from the base followed by a single or multi-step hydrogen abstraction (even at 77 K) thereby forming carbon-centred sugar radicals. There are a number of possible sugar radicals (VI → XI) and without detailed knowledge of their conformation and possible covalent bond breakages, identification is rather difficult. A number of possibilities can be eliminated by considering which radical (VI → XI) would be the same for two or more of the three sugars. In this manner all but two possible species (C_2'· and C_3'·) can be eliminated since they should yield different EPR patterns for each of the sugars.

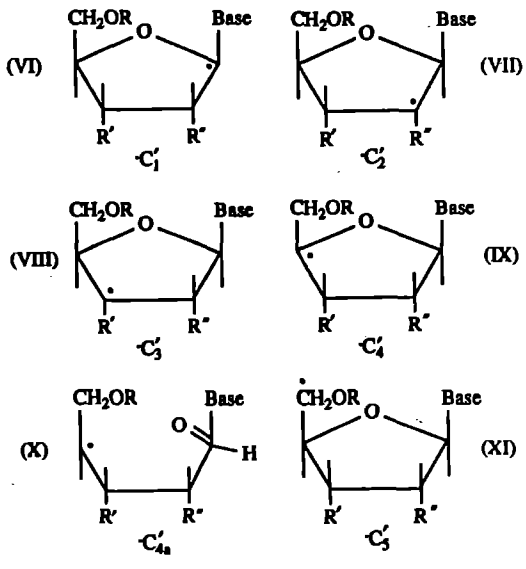

R = H or Phosphate

ribose	R′ = R″ = OH
2′-deoxyribose	R′ = OH; R″ = OH
2′,3′-dideoxyribose	R′ = R″ = H

Cullis *et al.*[13] have predicted the EPR patterns of a number of deoxyribose radicals arising from hydrogen abstraction. They report three radicals which approximate equidistant 1,1,1,1 quartets namely C_1'· ($\cong$ 23 G), C_2'· ($\cong$ 25 G) and C_4'· ($\cong$ 16 G). Although the theoretical prediction of the C_4'· radical most closely matches our results it can be dismissed as a possibility since CMP would clearly yield an identical radical, which it does not. For similar resons C_1'· can be eliminated thus leaving the C_2'· radical as the most likely candidate. Predicting hyperfine couplings theoretically is by no means fullproof and the fact that the C_2'· hfs are rather large could be due to unaccounted conformational changes in the sugar. We therefore tentatively assign the dCMP quartet (Fig. 3a) to the C_2'· radical.

On warming dCMP to 155 K very little change occurs in the EPR pattern other than a gradual loss of signal intensity. On annealing 5-methyl dCMP to 155 K the quartet is replaced by an EPR pattern characteristic of the CCH_2· radical (V). Presumably this arises by back hydrogen abstraction from the quartet or by hydrogen abstraction by O^-.

Deoxyadenosine-5′-monophosphate and Deoxyguanosine-5′-monophosphate π radical cations

Photoionisation of dGMP and dAMP readily produces π radical cations ($G^{\cdot+}$ and $A^{\cdot+}$) with very similar singlet EPR spectra. They both rapidly deprotonate to form the uncharged radical $G(-H^+)$· and $A(-H^+)$· but predicting the actual site of deprotonation is difficult since the unpaired electron density is distributed diffusely about the purine ring.[11] The guanine radical cation has a pK_a = 3.9 at RT and can deprotonate between 10 K and 77 K,[11,14,15] therefore under our conditions the guanine radical is likely to be of the form $G(-H^+)$·. The adenine radical cation is a broad unresolved singlet with unpaired spin delocalised throughout the ring system. The properties of the adenine radical are similar to those of guanine and it readily deprotonates (pK_a < 1) at RT.[11] Under these conditions it is likely that the radical cation is of the form $A(-H^+)$· although the site of deprotonation is uncertain.

Competition studies - dinucleotides

Preliminary results on the mononucleotides and dinucleotides indicate that the ease of photoionisation has the order dCMP < TMP ≡ dAMP << dGMP which confirms the expectation that $G^{\cdot+}$ should be the predominant radical cation in DNA. Although $G^{\cdot+}$ dominates, this does not provide clear evidence that hole transfer to G occurs following radical cation formation on the other bases. The comparative ease of photoionisation of dGMP compared with the other mononucleotides suggests that its large quantum yield for intersystem crossing ($\phi_{isc} \equiv 0.15$) and the 1.3 sec lifetime of the triplet state results in a high quantum yield for $G^{\cdot+}$ compared to the other bases. Consequently the predominance of $G^{\cdot+}$ in nanosecond photolysed DNA may, in fact, be due to photochemical factors.

REFERENCES

1. D T Croke, W Blau, C Ohlligin, J M Kelly and D J McConnell. *Photochem. Photobiol.*, **47**, 527 (1988).
2. D Schulte-Frohlinde, M G Simic and H Gorner. *Photochem. Photobiol.*, **52**, 1137 (1990).
3. E Bothe, H. Gorner, J O Pitz and D Schulte-Frohlinde. *Photochem. Photobiol.*, **52**, 949 (1990).
4. M C R Symons. *J. Chem. Soc., Faraday Trans.*, **83**, 1 (1987).
5. M D Sevilla, D Suryanarayama and K M Morehouse. *J. Phys. Chem.*, **85**, 1027 (1981).
6. J Hüttermann. *Int. J. Radiat. Biol.*, **17**, 249 (1970).
7. M D Sevilla. *J. Phys. Chem.*, **80**, 1898 (1976).
8. K Hildenbrand and D Schulte-Frohlinde. *Free Rad. Res. Comms.*, **11**, 193 (1990).
9. M D Sevilla, C Van Paemel and C Nichols. *J. Phys. Chem.*, **76**, 3571 (1972).
10. C Decarroz, J R Wagner and J Cadet. *Free Rad. Res. Comms.*, **2**, 295 (1987).
11. S Steenken. *Chem. Rev.*, **89**, 503 (1989).
12. D M Close and W A Bernhard. *J. Chem. Phys.*, **70**, 210 (1979).
13. P M Cullis, S Langman, I D Podmore and M C R Symons. *J. Chem. Soc., Faraday Trans.*, **86**, 3267 (1990).
14. B Rakvin, J N Herak, K Voit and J Hüttermann. *J. Radiat. Environ. Biophys.*, **26**, 1 (1987).
15. E O Hole, W H Nelson, D M Close and E J Sagstuen. *Chem. Phys.*, **86**, 5218 (1987).

RESONANCE RAMAN SPECTROSCOPY OF OLIGODEOXYNUCLEOTIDES CONTAINING 4-THIOTHYMIDINE

Timothy R .Waters[1], Bernard A. Connolly[2], Christopher W.Wharton[3] and Anthony W. Parker[4]

[1]Department of Biochemistry, University of Southampton, Southampton, S09 3TU
[2]Department of Biochemistry and Genetics, The University, Newcastle-upon-Tyne, NE2 4HH
[3]Department of Biochemistry, The University of Birmingham, Birmingham B15 2TT
[4]Laser Support Facility, Rutherford Appleton Laboratory, Chilton, Didcot, Oxon, OX11 0QX

The structure of 4-thiothymidine is shown in Figure 1. This base analogue has the 4-keto oxygen atom replaced by sulphur. One consequence of this is that the absorbance maximum is shifted from 270 nm to 340 nm as shown in Figure 1. Recently our laboratory has developed methods for the incorporation of 4-thiothymidine into oligodeoxynucleotides. As is shown in Figure 1 these oligodeoxynucleotides show two absorbance peaks in the UV region. One centered on 260 nm is due to the four normal bases and the other at 340 nm is caused by the 4-thiothymidine.

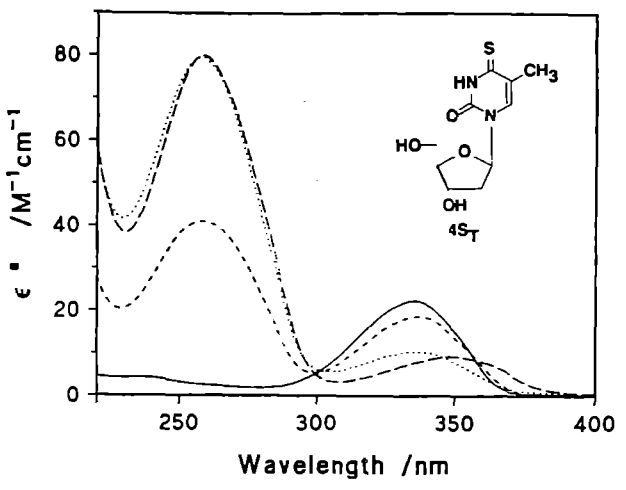

Figure 1. UV spectra at pH 7.2 of 4-thiothymidine (—) d(AG[^{4S}T]TC) (---), d(GACGA[^{4S}T]ATCGTC) (— — —) and d(GACGATA[^{4S}T]CGTC (....). [a]For single stranded DNA.

Table 1. Resonance Raman peaks and their vibrational assignments for 4-thiouridine [see section 1.7.2]. 4-thiothymidine in water and 4-thiothymidine in deuterium oxide (N3-d). § May be the other way around (see text).

Vibrational Mode	4-Thio-uridine	4-Thio-thymidine	N3-*d*'4-Thio-thymidine
Ring Stretch, ν_b^6 (C5=C6)	1619	1631	1632
ring stretch ν_a^6	1482	1477	1477
unknown	-	-	1404
N1-C1' stretch coupled with ring stretch $\nu_{\delta a}^6$	1372	1352	1366
C5-methyl stretch	-		1330
Kekule, Kk	1243	1233	1218
ring breath, Br^6, coupled with C=S stretch	1160	1158	1163
§ ring stretch, ν_b^6	-	1092	1090
§ ring deformation, Tr	-	1018	1017
unknown	-	865	-
C=S stretch coupled with ring breath, Br^6	709	707	699
ring deformation, δ_a^6	-	628	-

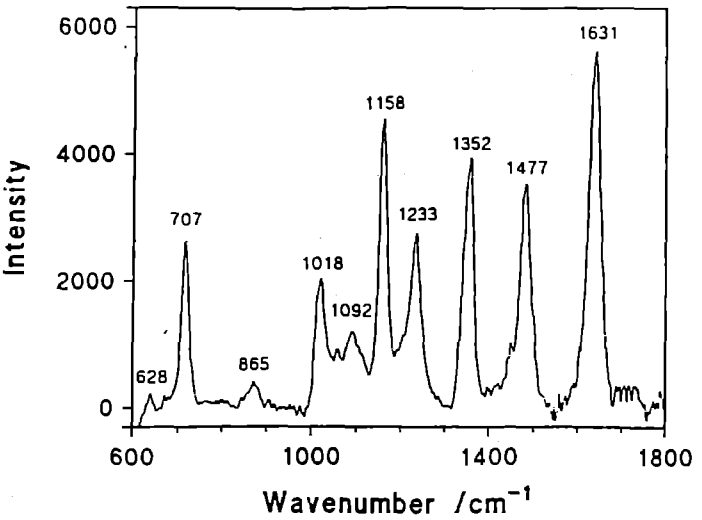

Figure 2. Final fluorescence subtracted and smoothed resonance Raman spectrum of 4-thiothymidine.

The free base 4-thiothymidine is a very strong Raman scatterer due to the large polarisability of the carbon sulphur double bond. When the incident light at 363.8 nm is used excellent resonance Raman spectra are obtained as shown in Figure 2. The spectrum obtained in Figure 2 used the rotating quartz cell apparatus (cell diameter 10 mm, height 3 mm) shown in Figure 3. The advantages of this system are that very small sample volumes (100 µl) can be used. The assignment of the peaks in the spectrum are given in Table 1. For comparison the spectrum of 4-thiothymidine in D_2O was also recorded. This replaces the N-3 proton with a deuteron and causes splitting of some of the peaks.

Spectra of d(AG[^{4S}T]TC), d(GACGA[^{4S}T]ATCGTC) and d(GACGATA[^{4S}T]CGTC) have also been recorded and that for the oligodeoxynucleotide is shown in Figure 4. The pentamer is single stranded whereas the two dodecamers are double stranded. The dodecamers also contain an EcoRV site (GATATC) modified with ^{4S}T. The assignments of the peaks are given in Table 2. The most striking features are shifts in the position of the C=S peak in the two dodacamers as compared to both the free deoxynucleoside and the single stranded pentamer. This is undoubtedly due to the Watson-Crick hydrogen bonding between the sulphur atom and the NH_2 group of its base pair deoxyadenosine on the opposite strand. It is possible to estimate the strength of these hydrogen bonds using either the estimate that there is a linear relationship between bond energy and wavelength shift (3) or assuming that the vibration behaves as a simple harmonic motion (4). This gives values of -6.7 to -8.4 kJ mol^{-1} for d(GACGA[^{4S}T]ATCGTC) and -3.4 to -4.2 kJ mol^{-1} for d(GACGATA[^{4S}T]CGTC). These values are of similar magnitude to those seen for Watson-Crick hydrogen bonds in DNA of -6.7 to -3.4 kJ mol^{-1} (5).

Finally the resonance Raman spectrum of d(GACGA[^{4S}T]ATCGTC) bound to the restriction endonuclease EcoRV is shown in Figure 5. The most interesting feature is that the C=S vibration is shifted to a value characteristic of a non Watson-Crick base paired species. This suggests that the Watson-Crick hydrogen bond between the underlined pair 5'-

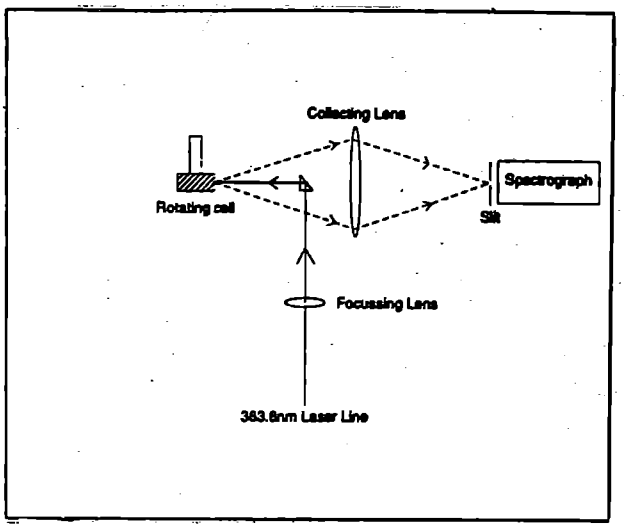

Figure 3. Schematic diagram of the experimental set-up for resonance Raman measurements. The laser is focussed onto the sample in the rotating cell and backscattered radiation is directed into the spectrograph slit.

GATTATC-3′/3′CTATAG-5′ is lost on binding to the protein. This is exactly what is seen by X-ray crystallography which shows dramatic oligodeoxynucleotide distortion centred on this central TA pair on EcoRV binding with loss of Watson-Crick hydrogen bonds (6).

Table 2 Resonance Raman peaks (cm^{-1}) and their vibrational assignments for oligodeoxynucleotides d(GACGA[^{4S}T]ATCGTC), d(GACGATA[^{4S}T]CGTC) and d(AG[^{4S}T]TC) in buffer α0.

Vibrational Mode	d(GACGA[^{4S}T]ATCGTC). [d(GCGATA[^{4S}T]CGTC) in brackets]	d(AG[^{4S}T]TC)
ring stretch $\nu_b{}^6$ (C5=C6)	1634 (1633)	1632
ring stretch, $\nu_b{}^6$	1469 (1470)	1474
ring stretch, $\nu_{\delta a}{}^6$ coupled with N1-C1′ stretch	1400 (1395)	-
C5-methyl stretch	1355 (1357)	1353
unknown	1243 (1247)	1254
Kekule, Kk	1205 (1211)	1230
ring breath, Br^6, coupled with C=S stretch	1158 (1159)	1157
ring stretch, $\nu_{\delta a}{}^6$	-	-
ring stretch, $\nu_{\delta a}{}^6$ plus PO_2^- stretch	1098 (1096)	1100
ring deformation, Tr	1013 (1014)	1018
unknown	-	-
C=S stretch coupled with ring breath, Br^6	699 (703)	706
ring deformation, $\delta_a{}^6$	625 (632)	-

Although this enzyme oligodeoxynucleotide spectrum needs improving and it is important to record the Raman Spectra of both bound d(GACGATA[^{4S}T]CGTC) and controls ie, d(GACCT[^{4S}T]AAGTC (oligonucleotides containing ^{4S}T but lacking the EcoRV site) it is clear that this technique can provide information about the conformation of enzyme-bound oligodeoxynucleotides.

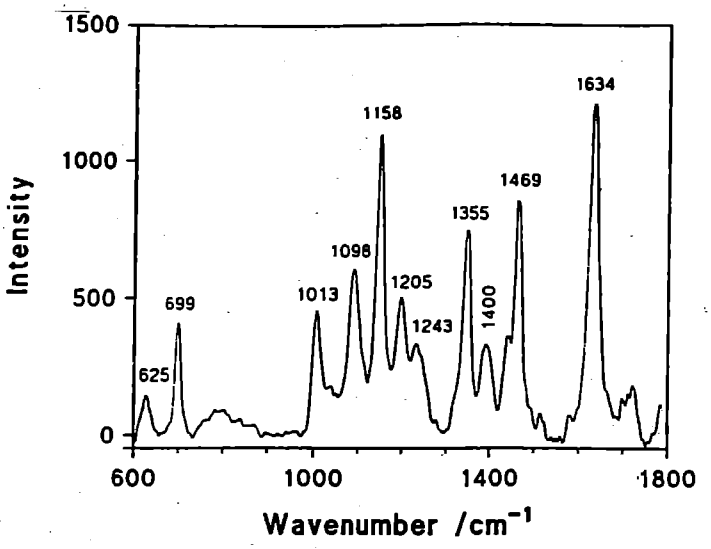

Figure 4. Resonance Raman spectrum of 540 μM double stranded d(GACGA[^{4S}T]ATCGTC) in buffer α0.

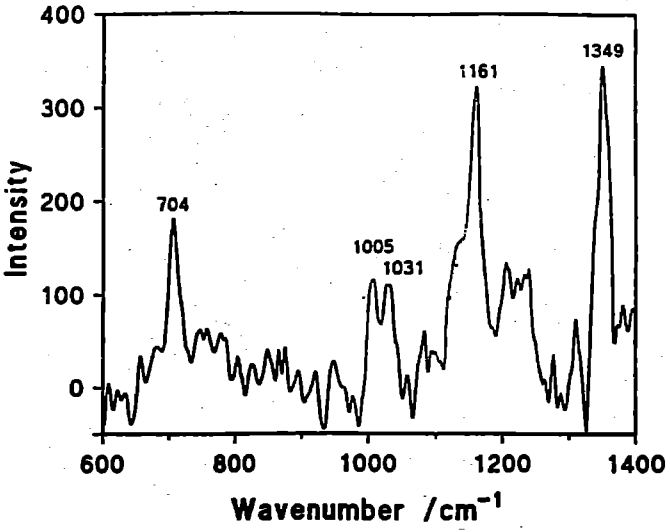

Figure 5. Final background subtracted and smoothed resonance Raman spectrum of endonuclease bound d(GACGA[^{4S}T]ATCGTC) [in the absence of magnesium].

REFERENCES

1. Y Nishimura, A Y Hirakawa, M Tsuboi, and S Nishimura, Nature 260, 173-174 (1976).

2. Y Nishimura, A Y Hirakawa, and M Tsuboi, Advances in Infrared and Raman Spectroscopy, (eds. R J M Clarke and R E Hester) Vol 5, (1978).

3. R M Badger and S M Bauer, J Chem Phys 5, 839-851, (1937).

4. P Gans, Vibrating Molecules, Chapman and Hall, London (1971).

5. S M Freier, N Sugimoto, A Sinclair, D Alkema, T Neilson, R Kierzek, M H Caruthers and D M Turner, Biochem. 25, 3214, (1986).

6. F K Winkler, Curr Opin Struct Biol 2, (1992) in press.

POTENTIAL 'FUNNEL' CHLOROPHYLLS IN PHOTOSYSTEM I

C.A. Potter[1,4], E.H. Evans[2,4], R.G. Brown[1,4], M.C.W. Evans[3,4], A.J. Langley[4], W. Shaikh[4] and W. Toner[4].

1. Lancashire Polytechnic, Preston, PR1 2TQ, U.K.
2. Liverpool Polytechnic, Liverpool L3 3AF, U.K.
3. University College, London, U.K.
4. Rutherford Appleton Laboratory,

Introduction:

In previous reports[1,2], we have described transients measured in Photosystem 1 (PS1) preparations from the cyanobacterium Chlorogloea fritschii. We have reported measurements made in the wavelength range 675-725 nm following excitation at 600 nm which exhibit a complex dependance on wavelength, probe delay, pump intensity and redox potential. In the 680 to 690 nm region the dominant feature at early times is a fast (<0.8ps[1]) rising bleach with a 10± 2 ps recovery which does not saturate at low pump intensities (component A). At 690 nm a minor saturating component is present with a prompt rise time and decay of 20-30 ps, (component B). In the 700 to 720 nm region the dominant feature at early times is a fast rise (<0.8ps[1]) with a 35± 5ps recovery (component C), whilst under reduced conditions an additional long lived component is present (component D). We have assigned the redox sensitive component D to the reaction centre chlorophyll, P700[3]. The fast decaying component A at 680 nm is best assigned to bulk light harvesting chlorophyll[3]. The assignments of components B and C are less clear, and the quantitative behaviour of these components is not always the same in different experimental sessions[2]. It has been suggested that an absorbance change at 690 nm should arise as a consequence of the reduction of a chlorophyll electron accepteor, A_0, reduced as a consequence of P700 oxidation[4]. This absorbance transient should therefore be redox sensitive, and should also be elicited by excitation of P700. An alternative assignment of both components C and D is of 'funnel' chlorophylls associated with energy transfer between the light harvesting chlorophyll and P700[3].

Results and Discussion

Samples were excited at 706 nm, exciting the reaction centre chlorophyll P700. Measurements were made at 680 nm, 690 nm and 720 nm. No absorption transient could be detected at 680 nm, but small transients were detected at 690 nm and 720 nm. These transients were substantially smaller than absorption transients measured at 706 nm following excitation at 600 nm[1]; approximately 10% of that extent. Figure 1(a) and (b) shows transients at 690 nm, excited at 706 nm under conditions where P700 was oxidised (480 mV ambient redox potential) or reduced (200 mV ambient redox

Fig. 1a.

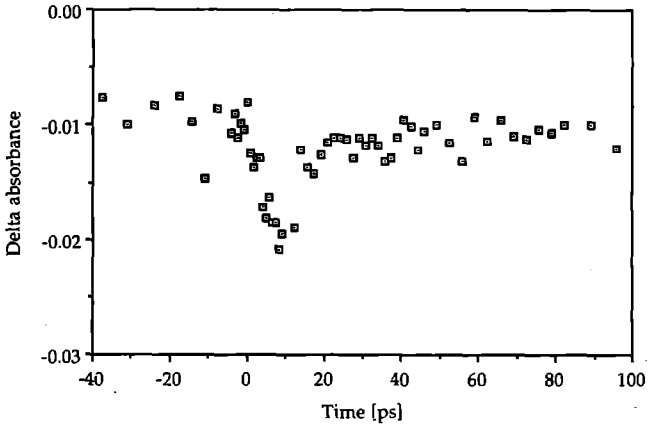

Fig. 1b.

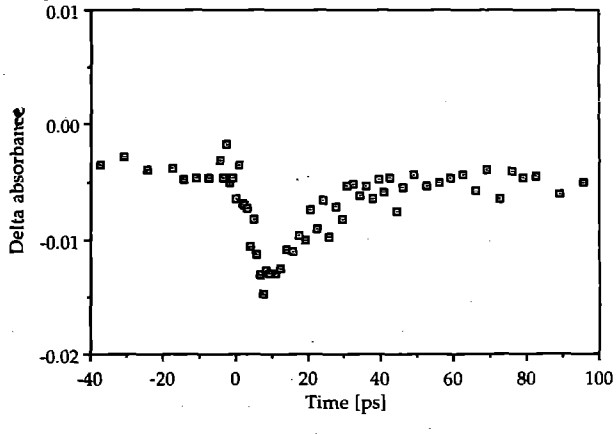

Figure 1
Transients measured in C.fritschii PS1 samples, pump wavelength 706 nm, probe wavelength 690 nm.
(a) oxidised sample (ambient redox potential 480 mV)
(b) reduced sample (ambient redox potential 200 mV).

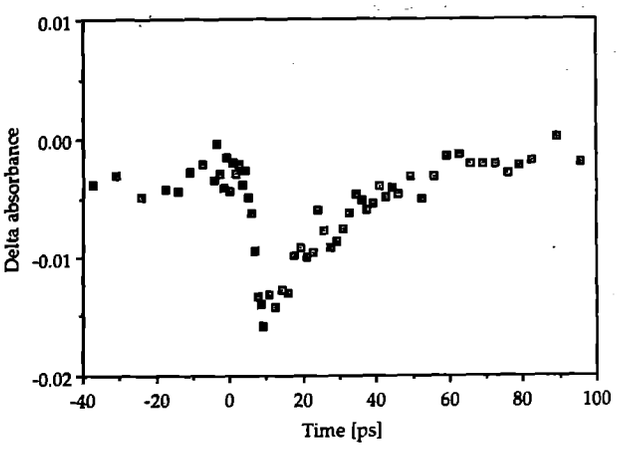

Fig. 2.

Figure 2
As in Figure 1(a), but probe wavelength 720 nm.

potential). There is no significant difference between these two transients, and it is therefore not possible to assign this spectral feature to the electron acceptor A_0, and we cannot confirm the results of Wasielewski et al[4]. The transient has a risetime of approximately 7ps and decays within 20-30ps. A similar transient is observed at 720 nm (Figure 2).

We are provisionally interpreting this data as further evidence of interactions between P700 and putative 'funnel' chlorophylls. We have previously suggested such a relationship for component C[3], and a proposal for such a 'funnel' at 690 nm has been made by Klug's group[5]. The data reported here may represent a back energy transfer between P700 and these funnels, occurring in 7ps. This reaction should not be favoured under previous experimental conditions when excitation of P700 was not direct but via the light harvesting chlorophyll (component A).

References

1. E.H. Evans et al, Annual Report to Central Laser Facility, p.66, 1990.
2. E.H. Evans et al, Annual Report to Central Laser Facility, p.171, 1991.
3. E.H. Evans et al, EBEC reports, 5, 174, 1988.
4. Wasielewski et al, Photosynth. Res. 12, 181, 1987.
5. D.R. Klug et al, Photosynth. Res. 22, 277, 1989.

The Kinetics and Mechanisms of Repair of UV induced Damage in mammalian Cell DNA.

R.A.Meldrum, J.Edgeton, W.Meaking and C.W.Wharton.

School of Biochemistry, University of Birmingham, PO Box 363, Birmingham B15 2TT.

The kinetics of enzvme repair of UV damage to mammalian cell DNA has been analysed further using the methods previously described (see RAL reports 1989, 1990 and 1991). Many complexities of the process have been revealed. It is clear that the kinetics and therefore the nature of the repair polymerases involved at different stages in the repair process are influenced by the amount of damage caused in the DNA and also the manner in which it is inflicted. Time profiles of ^{32}P-labelled nucleotide incorporation into DNA after UV damage are well illustrated in the previous RAL reports cited above. The effect of different doses of 248nm UV laser irradiation on the early time course profiles of repair of DNA damage was examined.

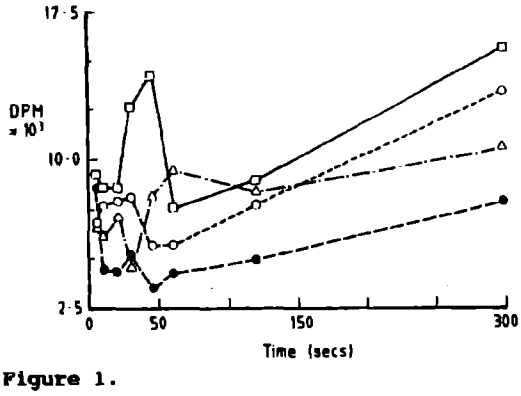

Figure 1.

Cells were electroporated to allow entry of ^{32}PddATP, irradiated with 248nm UV laser irradiation and quenched at the indicated times on the x axis. The dose rate of the UV light was kept constant. The y axis represents the radioactive label incorporated by each time point.

Square symbols and solid line 100J/m 248nm UV.

Circles and hatched line 50J/m 248nm UV.

Triangles and hatched and dottedline25J/m2 248nm UV.

Circles and hatched line no irradiation.

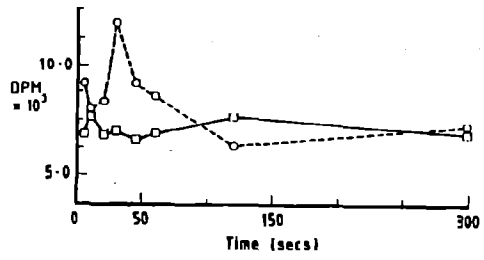

Figure 2.

Square symbols and solid line 10J/m^2 248nmUV.

Circles and hatched line 200J/m^2 248nm UV.

The initial transient commonly seen in time course profiles appears to be more pronounced at higher doses (see figure 1). It can be seen in figure 2 that a dose of 200J/m^2 produces a large transient but a reduced rise in the second steady state phase. This suggests that larger doses postpone the onset of the second phase of repair or reduce the rate at which the enzymes act in this phase.
Attenuation of the damaging laser beam (248nm) also influences the kinetics of repair of DNA (see figure 3). A high dose rate also appears to delay the onset of the steady state phase of repair . Lower dose rates show a much more rapid onset of the second phase of repair activity.

Effects of electroporation on the kinetic measurements of DNA repair.

Electroporation, which is used to introduce the negatively charged nucleotides and DNA nick trapping agent, itself produces complex effects on cells. These are as yet only partially understood. Electroporation has therefore formed a major part of this work. A field strength of 950 volts per centimetre has been found to produce a considerably large number of breaks in DNA and these require a significant time to repair. Also judging by viability studies (i.e. cloning of cells in agar), at this field strength, repair is not complete. Some DNA breaks occur at a field strength of 450 volts/cm but preliminary studies suggest these are repaired.

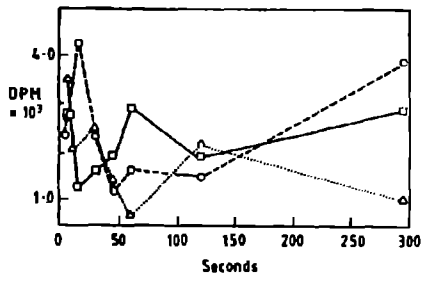

Figure 3

The total dose of 248nm UV irradiation was kept constant at 100 J/m2 but the dose rate a (i.e. the number of laser pulses required to deliver the total dose) was varied. Attenuation of the laser beam was achieved by passage of the laser beam through nitrous oxide.

Triangles and dotted line 1 laser pulse.

Squares and solid line 11 laser pulses.

Circles and hatched line 110 laser pulses.

Optimal poration, if judged by trypan blue inclusion, which has a molecular weight of 960,appears to be at a field strength of 950 volts/cm. Nucleotides and caged nucleotides have a molecular weight of around 500 and therefore adequate loading may be achieved at a lower voltage. Quantitative radiolabelled nucleotide studies suggest this is so but diffusion into the cell is considerably slower than at a higher voltage.

The nature of the breaks induced in the DNA by electroporation has not yet been determined. A gel electrophoresis assay which detects if a specific enzyme is activated was employed to determine if the breaks might be enzyme induced. The enzyme cuts DNA into pieces of specific length and the sizes of the pieces may be estimated from the bands seen in the gel. The DNA from electroporated cells did not form bands according to the pattern obtained when it has been cut by the enzyme therefore these breaks are not enzyme induced. Neutral sucrose gradients and alkaline sucrose gradients will be used to determine if the breaks are double stranded or single stranded.

Although in certain experiments performed previously, the kinetic measurements of DNA repair of UV damage may have been influenced by damage introduced by the electroporation procedure, it is clear that the UV damage produces the distinct phases of repair activity described (i.e. an initial transient followed by a steady state of repair), as cells with and without irradiation have been compared.

In fact, in most natural situations, DNA damage in mammalian cells will be mixed. Oxidative lesions are induced daily in the DNA of cells of most living organisms. To further clarify the polymerase activites stimulated by various forms of damage, the optimal voltage allowing maximum entry of the caged radioactive agent but minimal amount of DNA damage will have to be established. Studies with fluorescein labelled molecules of different sizes have shown that about 60% of the cells incorporate molecules of ca 600 molecular weight when a voltage of 500 volts per centimetre is applied to the cells. This field strength induces breaks in DNA approximately equivalent to that induced by 200 rads of gamma rays. It is unlikely that adequate loading of the DNA nick trapping agent will be achieved at a voltage which induces no DNA damage. Nevertheless, providing the damage is minimal, the caged reagent may be held inactive until this has repaired at which point the UV irradiation may be applied. and the caged reagent then activated in the appropriate manner. The recovery times for DNA breaks induced by various electric voltages is being estimated.

THE KINETICS AND MECHANISM OF THE REPAIR OF SOFT X-RAY DAMAGE IN MAMMALIAN CELLULAR DNA.

R A Meldrum[1], J Edgerton[1], W Meaking[1],C W Wharton[1], A Damerell[2], I C E Turcu[2],C Reason[2] & W Lester[2]

[1]School of Biochemistry, University of Birmingham, Birmingham B15 2TT
[2]Laser Support Facility, Rutherford Appleton Laboratory, Chilton, Didcot, OXON.

INTRODUCTION

As described in last year's report the repair of X-ray damage is a relatively fast process and is complete in several minutes. This contrasts with the repair of UV damage which takes many hours. In order to study the early events in the repair of X-ray damage it is essential to have an automated apparatus, which can treat samples in a matter of seconds or less. The design and application of this apparatus is described in this report. An important aspect of experimental methodology is the electroporation procedure which is used to permeabilise cells so that negatively charged reagents (such as dideoxyadenosine triphosphate (ddATP), which traps single strand breaks in DNA during repair) can be loaded into cells prior to experiments. In last year's report we described extensive experiments concerned with the electroporation of surface grown cells and were confident that a satisfactory procedure had been devised. Such hopes proved to be premature and much further work has now been done in attempts to achieve successful poration; the results of these and application to studies of DNA repair are described in this report. Finally we report some very recent studies which have employed the modified electroporation procedure as a component of the automated apparatus and have provided time courses of the incorporation of radiolabelled reagents into DNA during repair.

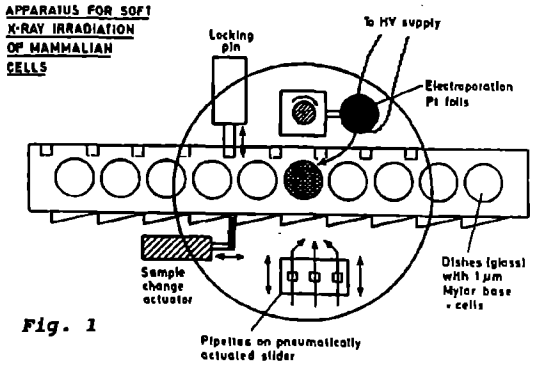

Fig. 1

THE AUTOMATED APPARATUS

The aim in the design of the apparatus was to allow exposure of the cell culture dishes, which have a 1 μm Hostaphan base, to an electrical discharge to effect permeabilisation, X-ray and 351 nm irradiation and quenching with 5M NAOH. The sequence of events is similar to that used in experiments on the effects of UV radiation but the design adopted for use with X-rays is substantially different. Vertical and horizontal views of the apparatus are shown in Figs. 1 & 2. All operations occur at the central position, in which the dish is positioned above the X-ray source. All movements are achieved by using pneumatic rams. The electroporation device, constructed with 2 mm spaced platinum foils (see below), is rotated out of position when not in use so that the 351 nm beam, which is used to decage break trapping reagent, can have unrestricted access to the sample from above. In early experiments the sample dish was placed on the side of the target chamber, but this did not allow a fluid covering over the monolayer of cells and so excluded electroporation in the irradiation position. Accordingly the Cu (tape) target rod, previously vertical, was reoriented to 45° so that the cell dishes could be presented in the horizontal plane. The apparatus, including the delivery of X-rays, is controlled by a 386 PC by means of a very general program that allows operations to be configured in any sequence. Thus for example, electroporation can be either before or after the X-ray dose. The X-ray dose is continuously monitored during an exposure and irradiation is terminated when the requested dose has been measured by a diode close to the cell layer. Recently the output of X-rays has been dramatically increased by using a picosecond pulse train for plasma generation. This aspect is described in last year's report and more recent developments elsewhere in this report.

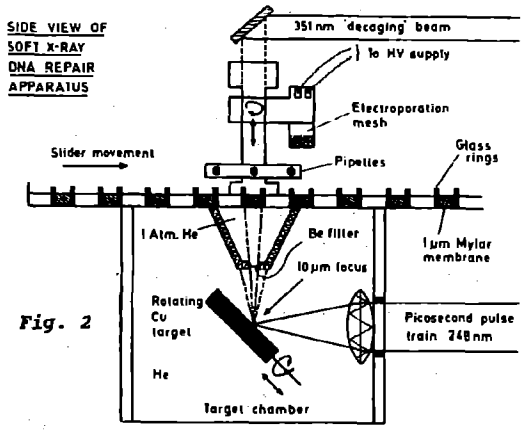

Fig. 2

FURTHER OPTIMISATION AND STUDY OF THE EFFECTS OF ELECTROPORATION IN A SURFACE LAYER OF CELLS.

Previously we have described an electroporation device in which 100 μm wires were strung on a former 2 mm apart. Each wire was connected alternately as an anode or cathode. The wires were placed over the surface of the cell monolayer and an electric discharge between the wires was found to permeabilise the cells well by the criterion of trypan blue uptake. Microscopic

examination of the porated cells revealed that they underwent a significant morphological change at voltages sufficient to induce trypan blue uptake and that there was signs of severe heat damage under the wires. It was clearly necessary to reduce the heating effect and this has been achieved by using a device constructed with platinum foils in place of the wires. The temperature jump consequent upon the electric discharge is now only ca. 7^{o}, compared with up to 20^{o} previously. Very effective permeabilisation appears to be achieved using this device and it is notable that the cells adhere to the Hostaphan film more tightly following the electric discharge.

REPAIR EXPERIMENTS

The automated apparatus has recently been used in a variety of repair experiments. Both caged and uncaged nucleoside triphosphates have been tested in the determination of repair time courses. In tests of the decaging methodology it was found that only samples that received both X-rays and 351 nm light, which decages the break trapping agent, incorporated significant amounts of photoreleased ^{3}HTTP.

The level of incorporation of TTP was some five times that in control samples and shows that the basis of the break trapping method is now established in X-ray experiments as was previously achieved in UV damage experiments, see 1987 CLF Report. Some time courses of repair, both in the form of rates of repair and accumulation of breaks have been obtained using the decaging method but these are as yet somewhat noise prone and require further optimisation.

TABLE 1. TEST OF DECAGING OF c-^{3}H-TTP AS A MEANS OF TRAPPING X-RAY INDUCED SINGLE STRAND IN DNA

3 H-TTP uptake in 5 min after damage dmp.

No X-rays, no 351nm	426
No X-rays, plus 351nm 1kJ/m2	481
400 rads X-rays, no 351nm	315
400 rads Xrays, plus 351nm	2401

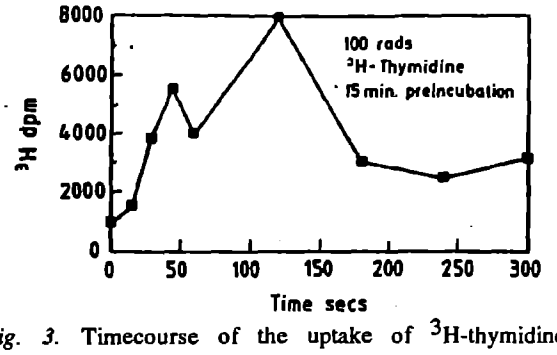

Fig. 3. Timecourse of the uptake of ^{3}H-thymidine triphosphate into X-ray damaged DNA of V79 cells. The cells were preincubated with thymidine,which is taken up by cells, for 15 min prior to X-ray exposure. The cells were not electroporated.

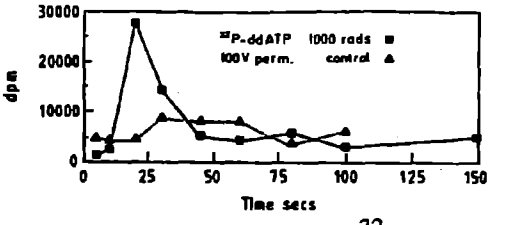

Fig.4. Time course of the uptake of ^{32}P-ddATP into X-ray damaged DNA of V79 cells.

Fig.4 shows a time course of the .incorporation of ^{32}P-ddATP following exposure to 1000 rads X-rays as well as a permeabilised, no X-ray control trace.

It is clear that there is a large transient uptake of ddATP which occurs rapidly following damage. As is seen in uv experiments, the unnatural chain terminating base that is incorporated in the rapid phase is removed almost equally rapidly. In this experiment the X-ray dose of 1 krad is large and would lead eventually to cell death for most cells. For this reason it is not easy to interpret the cellular events that give rise to the transient. Thus the loss of ddATP from the cellular DNA after rapid incorporation may reflect either a cellular degradation process related to cell death or to a panic response as seen in the repair of uv damage. During such a response DNA polymerase fidelity may be low initially, which allows incorporation of the unnatural base, but be 'switched on' after some 20 secs and result in excision of the unnatural base prior to a 'correct' repair.

REPAIR EXPERIMENTS USING ^{3}H-THYMIDINE.

V 79 cells grown as a surface layer become confluent after 2-3 days and at this time the intrinsic rate of DNA synthesis is very low. Thus replication DNA synthesis should not interfere with attempts to measure repair synthesis. Fig. 3 shows the result of an experiment in which cells were preincubated with thymidine for 15 min prior to X-irradiation in order to allow uptake of thymidine and accumulation of ^{3}H-TTP in the intracellular nucleotide pool. In this instance the dose of X-rays is quite low at 100 rads and shows that this is a sensitive way of following events after damage. A dose of 500 rads produced a much larger response but of exactly the same form. Notably the biphasic nature of the response, with a minimum at ca. 50 secs, was exactly replicated in both experiments. It will be necessary to check that this complex behaviour is not the result of some quirk of the experimental robot. An initial interpretation, ignoring for the time being the 50s 'glitch' would again suggest the involvement of fidelity modulation since thymidine is a natural base and would only be removed if it had previously been incorporated in place of one of the other bases. We regard the results we have obtained recently as being very encouraging and look forward to a more detailed analysis in the future.

DETERMINATION BY CROSS-LINKING OF RNA:RNA INTERACTIONS INVOLVED IN RNA SPLICING

R.A. Smith and I.C. Eperon

Department of Biochemistry, University of Leicester

INTRODUCTION

Splicing of pre-mRNA is the process in which the intron sequences of eukaryotic genes are removed from the initial transcripts, leaving the exon sequences as contiguous mRNA. The process of splicing is catalyzed by a large, complex assemblage known as the spliceosome, which incorporates four small ribonucleoprotein particles (the U1, U2, U4/U6 and U5 sn RNPs, each of which comprises one or two (U4/U6) RNA molecules of 106 to 196 nucleotides in association with up to ten polypeptides and additional proteins. The RNA components are essential for activity and, based on similarities with the RNA-catalyzed splicing reactions of some mitochondrial and chloroplast genes, it has been suggested that RNA is the reactive component (see, for example, ref. 1).

The roles of the RNA components are usually viewed in terms of their base-pairing properties. U1 snRNA base-pairs with the weakly conserved sequences at the 5′ splice site of the intron, and the strength of base-pairing can influence splice site preferences (ref. 2 and I.C. Eperon, D.C. Ireland, R.A. Smith and A.R. Krainer, manuscript in preparation). U2 snRNA base-pairs with the branch site, and this interaction can affect splice site choices [3,4,5] U4 snRNA base-pairs with U6 snRNA [6, 7] and U2 snRNA with U6 snRNA [8, 9, 10]. There is genetic evidence from yeast that U5 snRNA interacts with sequences in the 5′ and 3′ exons [11]. These interactions are dynamic, and change during splicing. It is not known which of these interactions are present simultaneously. Although genetic evidence can detect transient interactions (as, perhaps, for U5 with exon sequences), most of these interactions were found because extensive base-pairing was predicted; biochemical techniques usually detect only stable accumulated intermediates. Thus, a number of likely associations have not been detected yet.

We have been investigating the numbers and sites of snRNA interactions with substrate pre-mRNA by means of crosslinking with a psoralen, AMT, in the presence of ultra-violet light at λmax:365nm. We have confirmed the interactions of U1 snRNA with alternative 5′ splice sites and U2 snRNA with the branch site, and are studying the factors controlling this association. However, the efficiency of crosslinking is low, and limited by the intensity of U.V. The laser facility can offer intensities of irradiation which are 10^{10}-fold higher. Using this, we could address important questions about the number of simultaneous interactions with the pre-mRNA, undiscovered interactions between snRNAs in the spliceosome and the kinetic profile of base-pairing in the course of synchronized splicing reactions.

RESULTS

Preliminary experiments have been done with the 351 nm XeF excimer laser at RAL. Small scale (10 µl) reactions in nuclear extracts were initiated using ^{32}P-labelled pre-mRNA which had been transcribed *in vitro*. After incubation at 30°C for various times, the microtitre plate containing the reaction was irradiated at room temperature for various times. The temperature change was monitored in control reactions. After irradiation, a solution containing proteinase K and SDS was added to each reaction, and the samples were transported to Leicester for analysis by gel electrophoresis and autoradiography.

Six substrates were tested, with irradiation of 1.5mJ to 8J per sample. At the highest value, which corresponded to an intensity about four-fold greater than we used before, the efficiency of crosslinking began to approach that seen previously. The discrepancy may be attributable to the slightly different λmax of the two UV sources. Although it seemed clear that the intensity could be raised 10-20 fold and that this would produce much more crosslinking, it was noticed that 8J delivered over 10 seconds had raised the sample temperature by 4°C. Further work will require provision of circulating water underneath the microtitre plate, to prevent the increase in temperature. Such experiments are planned for the near future.

REFERENCES

1. Guthrie, C. (1991) *Science*, **253**, 157-163.
2. Zhuang, Y., and Weiner, A.M. (1986) *Cell* **46**, 827-835.
3. Parker, R., Siliciano, P.G., & Guthrie, C. (1987) *Cell* **49**, 229-239.
4. Zhuang, Y., and Weiner, A.M. (1989) *Genes Dev.* **3**, 1545-1552.
5. Wu, J., and Manley, J.L. (1989) *Genes Dev.* **3**, 1553-1561.
6. Hashimoto, C., and Steitz, J.A. (1984) *Nucleic Acids Res.* **12**, 3283-3293.
7. Bringmann, P., Appel, B., Rinke, J., Reuter, R., Theissen, H., & Luhrmann, R. (1984) *EMBO J.* **3**, 1357-1363.
8. Hausner, T.-P., Giglio, L.M., & Weiner, A.M. (1990) *Genes Dev.* **4**, 2146-2156.
9. Wu, J., and Manley, J.L. (1991) *Nature* **352**, 818-821.
10. Datta, B., and Weiner, A.M. (1991) *Nature* **352**, 821-824.
11. Newman, A.J. and Norman, C. (1992) *Cell*, **68**, 743-754.

MOLECULES IN INTENSE LASER FIELDS PROBED BY COVARIANCE MAPPING

E J Cartlidge[1], K Codling[2], G M Cross[2], L J Frasinski[2], P A Hatherly[2], A J Langley[1], W Shaikh[1] and M Stankiewicz[2]

[1]SERC Central Laser Facility, Rutherford Appleton Laboratory, Chilton, Didcot, Oxon, OX11 0QX, UK
[2]J J Thomson Physical Laboratory, University of Reading, Whiteknights, P O Box 220, Reading RG6 2AF, UK

ABSTRACT

The process of multielectron dissociative ionisation of molecules using picosecond laser pulses of intensity of $\geq 10^{15}$ W/cm^2 is poorly understood. Conventional multiphoton ionisation theory is not applicable here because the intense laser field cannot be considered as a small perturbation. Instead, one is forced to use simpler approaches, such as the field ionisation model or the Coulomb explosion model. A considerable experimental advance has been made by the introduction of the covariance mapping technique. When this technique is applied to ion time-of-flight spectra it allows unambiguous correlation of daughter fragments with parent molecular ions and provides a sound basis for future progress.

INTRODUCTION

When a molecule is placed in a picosecond laser pulse of focused intensity of the order of 10^{15} W/cm^2 or higher, then the process of multiple ionisation occurs and the molecule fragments into atomic ions (Frasinski *et al* 1987). Experimentally one can vary the peak intensity, the wavelength and the duration of the laser pulse and measure the charge state, the kinetic energy and angular distribution of the fragment ions. One can also study the similarities and the differences between various molecules (Hatherly *et al* 1988, Normand *et al* 1990). Some of the results are now understood but many of them remain unexplained.

IONISATION MODE

One may wonder why one studies molecules, when high-intensity experiments with atoms are difficult enough to explain. The reason is that in the case of molecules one has an additional source of information at one's disposal, that is the kinetic energy of the fragment ions; this gives an increased insight into the ionisation process. To illustrate the point let us go back a few years when it was uncertain if the process of multiple ionisation of atoms is direct (Luk *et al* 1983, 1985) or stepwise (L'Huillier *et al* 1983). If we take as an example the sextuple ionisation of xenon then in the first case the six electrons are removed together in some correlated manner and in the second case they peel off one after another.

To distinguish between the two possibilities we devised an experiment with hydrogen iodide, which is isoelectronic with xenon. If the ionisation mode is direct and six electrons are rapidly removed from HI, we will have H^+ sitting next to I^{5+} at the initial (i.e. neutral molecule) equilibrium internuclear distance. Due to strong Coulomb repulsion the proton is ejected with a high kinetic energy. On the other hand, if the ionisation is stepwise then after reaching the first or the second ionisation stage the molecule dissociates and the kinetic energy is smaller because of weaker Coulomb repulsion. Further ionisation of the iodine ion does not significantly increase the kinetic energy of the proton because the two fragments are already far apart.

In the experiment (Codling *et al* 1987) it was found that the kinetic energies of protons were quite low, suggesting that the ionisation is stepwise. By implication, the same was expected to be the case in Xe. However, before completing the experiment, theoretical arguments in favour of the stepwise mode were published by Lambropoulos (1985) and it is now widely accepted that the sequence of ionisation steps occur on the rising edge of the laser pulse at well-defined thresholds of the laser intensity.

In principle, the ionisation process can be fully described in terms of multiphoton theory (see, for example, Gontier *et al* 1984). In this approach the first-order transition probability from the initial, ground state of a neutral atom or a molecule to the final, ionised state involves a multiple sum over all intermediate resonances of the multiphoton field with the excites states of the system. The problem is that, especially in the case of molecules, one simply does not have the necessary information on the excited states. Moreover, at high laser intensities the energy levels are shifted by the dynamic Stark effect and the transition probability is no longer proportional to the laser intensity raised to the power of the number of photons absorbed. However, the most serious problem is that, as the laser intensity is increased, the higher order terms of the perturbation series are no longer negligible and the result becomes divergent.

An alternative approach is to use the field ionisation model, which applies particularly well at high intensities and low frequencies of the laser (Keldysh 1965). In this model the laser pulses are described by a classical electromagnetic wave—there are no photons—and only the electrons have quantum-mechanical properties. If one takes the xenon atom as an example then, without the laser field, one has the $5p^6$ electrons sitting in the potential well of the Xe^+ ion at the energy level defined by the ionisation potential of Xe. Introduction of an external field distorts the potential well and creates a potential barrier. When the field is increased to such a value that the top of the potential barrier is lowered to about 3 eV above the electron energy level, the electron tunnels through the potential barrier and escapes from the atom (Codling *et al* 1989, see also Corkum *et al* 1989). The remaining five electrons rapidly rearrange themselves and one now considers one of them in the Xe^{2+} potential well at an energy level lower than in the previous case due to the larger ionisation potential of Xe^+. As the field increases, the potential barrier decreases and the next ionisation occurs at the 3 eV barrier height. In this stepwise fashion, the electrons are removed one after another at the leading edge of the laser pulse. Of course, one has to remember that because the field oscillates with the appropriate optical or infra-red frequency, the tunnelling occurs only at the crests and the troughs of the wave.

A simpler, fully classical version of the field ionisation model requires the electrons to go over the potential barrier. Predictions of this model agree well with experimental appearance intensities of several charge states of the noble gases obtained with 1 ps laser pulses of 1 μm wavelength and intensities of up to 3×10^{16} W/cm^2 (Augst *et al* 1989). The fact that this agreement can be only marginally improved by allowing the electrons to tunnel through the potential barrier shows that one does have almost a classical situation at high laser intensities.

The field ionisation model is equally applicable to molecules, but

here one can expect some ionisation enhancement effects not present in atoms (Codling *et al* 1989). One such effect is that it is easier to ionise a molecule when the laser electric field is applied along the molecular axis than when the field is perpendicular to the axis. This is simply because in the first case the field acts over a larger distance and lowers the potential barrier more, thereby increasing the tunnelling probability. When the molecule starts to dissociate it becomes even more elongated, further enhancing the tunnelling process.

At small internuclear separations the valence electrons, driven by the oscillating external field, can move freely within the molecule. However, continued dissociation separates the molecule into atoms (ions) and free movement of the valence electrons is progressively restricted by the rising inner potential barrier (or barriers, in molecules such as N_2O). Because of their isolation by the potential barrier(s) separating the atoms the electrons can now gain energy from the laser and escape into the continuum.

FRAGMENTATION MODE

A fragment ion of particular mass, charge state and kinetic energy can usually be identified with the help of time-of-flight (TOF) spectroscopy (for more experimental details see, for example, Codling *et al* 1987 and Hatherly *et al* 1990). Additionally, one would like to correlate the fragments and identify their parent molecular ion. Unfortunately, the same fragment, for example N^+, can be produced in several fragmentation processes:

$$N_2^{2+} \rightarrow N^+ + N^+$$
$$N_2^{3+} \rightarrow N^{2+} + N^+$$
$$N_2^{4+} \rightarrow N^{3+} + N^+$$

This creates serious obstacles to definitive analysis of the fragmentation sequence, particularly in view of the broad, continuous range of ion kinetic energies. Moreover, since the TOF analyser is insensitive to neutral particles, the processes $N_2^+ \rightarrow N^+ + N$, $N_2^{2+} \rightarrow N^{2+} + N$, etc. cannot be ruled out. In order to resolve these ambiguities we devised a technique called covariance mapping (Frasinski *et al* 1989b). This technique relies on the fact that the shot-to-shot TOF spectra have large statistical fluctuations. In the conventional method these fluctuations are simply averaged over many laser shots and any correlations between the fragments are lost. If, however, we calculate a contribution to the covariance between each pair of TOF spectrum points *at each laser shot* then the result can be displayed as a map showing unambiguous correlations between the fragments.

In the visible, at around 600 nm, there is a predominance of charge-symmetric fragmentations in N_2 (Frasinski *et al* 1989a, Cornaggia *et al* 1990), CO (Frasinski *et al* 1989b, Lavancier *et al* 1991) and O_2 (Normand *et al* 1991). This means that, for example, N_2^{4+} ions fragment overwhelmingly into two N^{2+} ions and there is only a small contribution from the $N^{3+} + N^+$ channel. A matter of terminology: because parent ions of odd charge states cannot fragment into two equal charges, one must include as "charge-symmetric" fragmentations those processes where fragment charges differ by no more than one elementary charge, for example $N_2^{3+} \rightarrow N^{2+} + N^+$.

The preponderance of charge-symmetric fragmentation can be explained in terms of the field ionisation model. Charge-symmetric fragmentations are preferred because this is the state of lowest potential energy. For example, in order to create $N^{3+} + N^+$ from $N^{2+} + N^{2+}$ one has to add energy to the system. In the case of heteronuclear molecules, the differences in the ionisation potentials of the constituent atoms have to be taken into account. This can be seen in fragmentation of CO ions, where the $CO^{3+} \rightarrow C^{2+} + O^+$ channel is much stronger than the $CO^{3+} \rightarrow C^+ + O^{2+}$ channel because the ionisation potential of O^+ is higher that of C^+. The tendency towards charge-symmetric fragmentation can be also deduced from a more elaborate Thomas-Fermi-Dirac model (Brewczyk and Frasinski 1991).

There have been reports of charge-asymmetric fragmentation in the UV in the case of N_2 (Cornaggia *et al* 1990) and CO (Lavancier *et al* 1991) at 305 nm and in the case of N_2 at 248 nm (Boyer *et al* 1989). In order to check these reports we have performed covariance mapping experiments at the Saclay laboratory at 305 nm (Codling *et al* 1991). The results indicate that the claims of charge-asymmetry were incorrect. The reason for the earlier conclusions could be traced to ambiguities in interpretation of the conventional, one-dimensional TOF spectra.

Charge-symmetric fragmentations also appear to be the dominant mechanism in triatomic molecules (Frasinski *et al* 1991). In the case of N_2O, the $N_2O^{6+} \rightarrow N^{2+} + N^{2+} + O^{2+}$ channel is suprisingly strong. In fact the only other channel seen is a weak $N_2O^{2+} \rightarrow N^+ + NO^+$ channel. The lack of observation of channels involving N_2O^{3+}, N_2O^{4+} and N_2O^{5+} ions, which might be expected to be created in the periphery of the focal region of the laser, suggests that the N_2O^{6+} ion is produced by the simultaneous ejection of at least four electrons. This is contrary to the expected stepwise mode of ionisation and we have no convincing explanation for this surprising behaviour.

ANGULAR DISTRIBUTIONS

The drift tube used for covariance mapping is constructed in such a way that the ion TOF is linearly dependent on the initial momentum component along the drift tube axis but independent of the perpendicular component (Hatherly *et al* 1990). As a result the angular distributions of ions are folded with their kinetic energy distributions and in general it is not possible to untangle the two from the TOF spectrum. However, when both distributions are highly peaked, deconvolution is possible. In the typical case of the $CO^{3+} \rightarrow C^{2+} + O^+$ channel, it is found that the angular distribution of fragments can be approximated by a $\cos^8\theta$ function (Hatherly *et al* 1990), where θ is the angle between the initial momentum of the C^{2+} or O^+ fragment and the direction of the laser electric field.

One reason for high peaking of the angular distribution along the laser electric field has been already mentioned – a molecule is easier to ionise when the field is applied along the molecular axis. This process is followed by rapid axial recoil of the fragments. The second reason for a peaked distribution is that the molecule can be rotated by the laser field into this favourable orientation. To estimate this effect let us take an N_2 molecule and assume that the field polarizes the molecule, producing a modest shift of 0.1 of an elementary charge from one atom to the other. A typical laser field of 10 V/Å exerts a torque on the polarized molecule and rotates it by 90° in about 0.1 ps. Therefore, there is plenty of time for this process to occur during a typical 1 ps laser pulse.

KINETIC ENERGIES

To a first approximation, the ion kinetic energies can be explained by a simple Coulomb explosion model (Codling *et al* 1989), which represents the ions as point charges. Let us consider multielectron dissociative ionisation of N_2 as an example. When the molecule is ionised to the second ionisation stage the two N^+ ions repel each other, the internuclear distance increases and the ions gain kinetic energy. Meanwhile, the laser intensity increases and one of the N^+ ions is ionised to N^{2+}. The Coulomb repulsion, which to this point

has been falling with increasing internuclear distance, is now enhanced and the kinetic energy of the two ions is increased. The next ionisation steps follow and the final kinetic energy of the fragment ions depends on the internuclear distances at which each step occurred. Combining Newton's equation of motion with the experimentally determined fragment kinetic energies gives an approximate timescale for entire dissociation on the order of tens of femtoseconds.

Some doubts about validity of the Coulomb explosion model can be deduced from recent experiments performed by our group (Codling *et al* 1991) and the Saclay group (Cornaggia *et al* 1990 and Morellec's contribution to this volume). The experiments show that the kinetic energy of the fragments is independent of the pulse length in the range 0.2–2 ps. One expects that a change in the pulse length will affect the pulse risetime and if one lengthens the pulse, the intensity will increase more slowly. The intervals between the ionisation steps will be longer, the ionisation steps should occur at larger internuclear distances and the kinetic energy of the fragments should be smaller. This effect is not in fact observed but one has to remember that the experimental evidence is not definitive. This is because only the autocorrelation signal is available for short laser pulses and the exact pulse shape is not known in these experiments.

If, however, we accept the experimental evidence at face value then it is difficult to avoid the conclusion that something holds the molecular ions together and prevents them from rapidly dissociating. Normally, high ionisation stages of molecular ions are unstable but the strong laser field may conceivably create some sort of dynamic bound states. In other words, one might expect that, as the laser intensity is increased to the level of, say, the N_2^{4+} threshold and if the intensity is held constant thereafter, then the two N^{2+} ions would not fly apart but would stay at a well-defined internuclear distance for a time of the order of picoseconds.

Whatever the nature of these dynamic bound states, the binding force can only come from the electrons. It is interesting to note that even a single electron can provide a surprisingly effective binding of a diatomic molecular ion if the electron is constrained to stay mid-way between the two atomic ions. Representing the atomic ions as point charges of value q a distance r apart, a bound state exists if the attractive electron-ion force is no smaller than the repulsive ion-ion force, that is if $qe/(r/2)^2 \geq qq/r^2$. This gives $q \leq 4e$, which means that a single electron can bind a seven-times-ionised molecule.

The best promise for a detailed theoretical explanation of these processes appears to come from the bond softening model (Bucksbaum *et al* 1990). This model has been applied to H_2^+, where one considers the two lowest, the repulsive and the attractive, molecular potential curves dressed in the photon field. The field mixes the two states and changes curve crossings to avoided crossings. As a result there is a dynamic bound state created at about twice the normal equilibrium distance. So far, this model describes only dissociation at laser intensities of up to about 10^{14} W/cm^2 but there is a hope of including ionisation and going to higher intensities (see Giusti-Suzor's contribution to this volume).

CONCLUSIONS

At high laser intensities, it appears that the ionisation mode can be understood quite well in terms of the field ionisation model. The process is stepwise and the ultimate charge state is determined by the highest laser intensity to which the molecule is exposed. The fragmentation mode follows the path of the lowest potential energy, giving charge-symmetric fragments in the case of molecules made up of atoms with similar ionisation potentials. The ion angular distributions are highly peaked along the laser electric field because it is easier to ionise a molecule when the field is applied along the molecular axis. The field probably rotates those molecules which initially are not aligned with the field direction. There are some considerable doubts as to whether the Coulomb explosion model can explain the kinetic energies of the fragments. An alternative explanation would be to invoke the existence of dynamic bound states to explain the kinetic energies. Only when we understand the gross behaviour of a typical diatomic molecule in high-intensity laser pulses should we seek the explanation of any molecule-specific effects.

REFERENCES

Augst S, Strickland D, Meyerhofer D D, Chin S L and Eberly J H 1989 *Phys. Rev. Lett.* **63** *2212*

Boyer K, Luk T S, Solem J C and Rhodes C K 1989 *Phys. Rev.* A **39** 1186

Brewczyk M and Frasinski L J 1991 *J. Phys. B: At. Mol. Phys.* **24** L307

Bucksbaum P H, Zavriyev A, Muller H G and Schumacher D W 1990 *Phys. Rev. Lett.* **64** 1883

Codling K, Frasinski L J, Hatherly P and Barr J R M 1987 *J. Phys. B: At. Mol. Phys.* **20** L525

Codling K, Frasinski L J and Hatherly P A 1989 *J. Phys. B: At. Mol. Phys.* **22** L321

Codling K, Frasinski L J and Hatherly P A 1991 in *Multiphoton Processes* ed. by G Mainfray and P Agostini (Saclay: Commissariat a l'Énergie Atomique) p 205

Codling K, Cornaggia C, Frasinski L J, Hatherly P A, Morellec J and Normand D 1991 *J. Phys. B: At. Mol. Opt. Phys*, accepted

Corkum P B, Burnett N H and Brunel F 1989 *Phys. Rev. Lett.* **62** 1259

Cornaggia C, Lavancier J, Normand D, Morellec J and Liu H X 1990 *Phys. Rev.* A **42** 5464

Frasinski L J, Codling K, Hatherly P, Barr J, Ross I N and Toner W T 1987 *Phys. Rev. Lett.* **58** 2424

Frasinski L J, Codling K and Hatherly P A 1989a *Phys. Letters* A **142** 499

Frasinski L J, Codling K and Hatherly PA 1989b *Science* **246** 1029

Frasinski L J, Hatherly P A and Codling K 1991 *Physics Letters* A **156** 227

Gontier Y and Trahin M 1984 *Multiphoton Ionization of Atoms* ed S L Chin and P Lambropoulos (Toronto: Academic Press) pp 35–64

Hatherly P A, Frasinski L J, Codling K and Barr J R M 1988 *Chem. Phys. Letters* **149** 477–481

Hatherly P A, Frasinski L J, Codling K, Langley A J and Shaikh W 1990 *J. Phys. B: At. Mol. Phys.* **23** L291

Keldysh L V 1965 *Sov. Phys. JETP* **20** 1307

L'Huillier A, Lompre L A, Mainfray G and Manus C 1983 *Phys. Rev.* A **27** 2503

Lambropoulos P 1985 *Phys. Rev. Lett.* **55** 2141

Lavancier J, Normand D, Cornaggia C, Morellec J and Liu H X 1991 *Phys. Rev.* A **43** 1461

Luk T S, Pummer H, Boyer K, Shahidi M, Egger H and Rhodes C K 1983 *Phys. Rev. Lett.* **51** 110

Luk T S, Johann U, Egger H, Pummer H and Rhodes C K 1985 *Phys. Rev.* A **32** 214

Normand D, Cornaggia C, Lavancier J, Morellec J 1991 in *Multiphoton Processes* ed. by G Mainfray and P Agostini (Commissariat a l'Énergie Atomique) p 191

TRACE ANALYSIS USING LASER ABLATION RESONANT IONISATION SPECTROMETRY

K.W.D. Ledingham, I.S. Borthwick and R.P. Singhal

Department of Physics and Astronomy, University of Glasgow
Glasgow G12 8QQ, Scotland

INTRODUCTION

LIMA and LAMMA [1,2] are well established laser microprobe, trace analytical techniques in which a focussed, frequency quadrupled Nd:Yag laser is directed at the surface of a sample. The ions created are analysed by a reflectron time of flight mass spectrometer at sensitivities down to parts per million. The laser microprobe has been applied to a wide range of analytical problems. Its speed and versatility makes it an ideal technique for providing an initial assessment of a problem before more quantitative and time consuming methods are used. It is however essentially a qualitative technique. Although the laser microprobe is a sensitive analytical technique, it is necessary to understand in detail the mass removal and ionisation processes before the observed mass spectra can be related to the sample under study. These two processes are coupled and lead to matrix dependent ionisation which makes quantification difficult. An alternative approach is to seperate the ablation and ionisation processes in both time and space. Laser post ionisation of neutrals should potentially be less troubled with matrix problems and more sensitive than LIMA or LAMMA, since the numbers of neutral atoms created in the ablation process is often much greater than the number of ions. This is especially true at low ablation fluences where the neutral atom to ion yield is as high as 10^{3-4} [3]. Thus a more sensitive and quantitative procedure should be achieved by efficiently ionising the ablated neutral species with a delayed laser pulse tuned to a resonant transition wavelength of the specific atoms. This process has been called laser ablation resonant ionisation spectrometry (LARIS) and although a number of groups have successfully coupled resonant ionisation spectrometry (RIS) with laser ablation e.g [4] the procedure is poorly characterised. The purpose of this research was to evaluate and characterise LARIS as an analytical technique. Although at Glasgow we have all the equipment to operate a RIS system we did not have a Nd:Yag ablation laser of sufficient pulse energy stability to permit us to carry out the research and hence we applied to the Rutherford Laboratory laser loan pool for a JK HY750 Nd:YAG laser.

EXPERIMENTAL ARRANGEMENT

This has been described in detail elsewhere [5] and only the essential details will be described here. A schematic diagram of the Glasgow LARIS instrument is shown in fig.1. Samples were fixed to stainless steel stubs and then mounted on a XYZθ manipulator at the centre of a spherical sample chamber. The system is maintained at a pressure of 10^{-9} torr by turbomolecular and diffusion pumps. Sample changeover takes about 10 mins using a rapid transfer probe. The sample was vapourised using the JK HY750 Nd:Yag laser with a pulse duration of about 10ns. The harmonics at 532, 355 and 266nm were also used. The laser had an intercavity aperture to provide essentially TEM_{00} mode operation and the beam was focused using a 30cm lens to give a spot size of about 100μm. The ablation laser was directed at an angle of 45° to the sample surface and fluxes of up to 10^8 W/cm^2 were used to vapourise the sample. This is typically two orders of magnitude smaller than the ablation powers used in the LIMA process and guaranteed a large neutral to ion yield. Although at this power, significant cratering in the sample does not occur, it has been estimated by extrapolating from mass ablation rates at higher powers that between 10^{9-10} atoms of aluminium were ablated per shot.

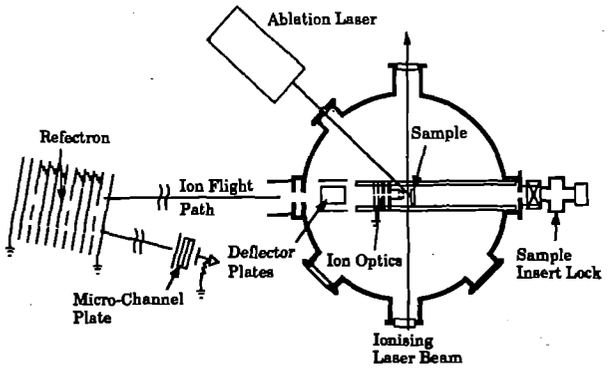

Figure 1

The post ablation ionising laser system consists of a Spectron SL2Q+SL3A Nd:Yag laser powering a Spectrolase 4000 dye laser with a bandwidth of 0.1cm^{-1} and an output energy of >1mJ pulse^{-1}. Frequency doubling crystals extended the wavelength down to between 250-350nm.

The reflectron time of flight mass spectrometer system has an overall length of 3m with a FWHM mass resolution of about 700 for ions of 50amu. A thin wire, 0.005cm in diameter, follows the ion flight path through the flight tube providing an electrostatic guide for the ions considerably increasing the transmission of the mass spectrometer.

The data acquisition system records and stores mass spectra and laser pulse energies on a pulse-to-pulse basis. A Lecroy 2261 transient recorder linked to a COMPAQ 386/25 forms the basis of the system. Ion signals from the Galileo multichannel plate detector are digitised by the transient recorder which provides 640 time channels (11 bit resolution) each of 10-100ns width.

The ionising laser is introduced into the sample chamber parallel to the surface of the sample stub. Principally the evaluation and characterising procedure consists of ablating different samples with various fluences and wavelengths and then ionising the emitted neutrals by either resonant or non-resonant multiphoton processes. The energies of the neutrals are determined by varying the delay time between the ablation and ionising lasers and plotting the the signal intensity of a specific mass as a function of delay time.

RESULTS AND DISCUSSION

Many different experiments were carried out during the course of this work and they will be presented in a comprehensive study of LARIS (manuscript in preparation). In this report only some of the more significant results will be presented.

In the following section, whenever the acronym LIMA is mentioned it should be understood that the ions produced directly in the ablation process are being discussed. On the other hand LARIS ions are laser ablated neutrals ionised by multiphoton resonant or non-resonant processes. The sample is normally kept at 2kV and the first optic maintained at about 1.4kV during LARIS analyses and since the post ablation ionisation is typically 3 mm above the sample surface, the LARIS ions fall through a potential of about 1.7kV. This ensures that the LARIS ions are reflected by the reflectron operated below 2kV while the majority of the higher energy LIMA ions are deposited on the earthed back plate. When the sample voltage is reduced to about 1.7 kV the LIMA ions are reflected by the electrostatic mirror and can be studied alone by switching off the post ablation lasers.

LIMA and LARIS comparison as a function of ablation laser flux. A 1mm thick aluminium sample was used for this study and the signals produced were compared as a function of laser flux. The ablation was carried out at 532nm and the post ablation ionisation was carried non-resonantly at 266nm. Both LIMA and LARIS signals increase

rapidly with increasing ablation fluence (a dependence of about 3 for aluminium). Other metals showed an even greater fluence dependence in agreement with other authors. As the ablation was increased however a small LIMA pulse leaked through the reflectron and dominated the LARIS signal at powers greater than 2 x 10^8 W/cm^2 and thus ablation power levels were always kept below this value.

LARIS signal as a function of ablation laser wavelength. Aluminium was again used as a sample and the ionisation was carried out non-resonantly using 266nm. The aluminium LARIS signal was studied as a function of time delay between the ionising and ablating laser pulses. The shape of the distribution was essentially unchanged as the ablation laser wavelength was varied between 226, 355, 532 and 1064nm. The shape can be described approximately by a Maxwellian velocity distribution from which the temperature of the neutral atoms may be derived. One of the important aspects of this measurement is that the optimum delay time for maximum signal size can be determined. Fig. 2 shows the aluminium distributions for the different ablation wavelengths.

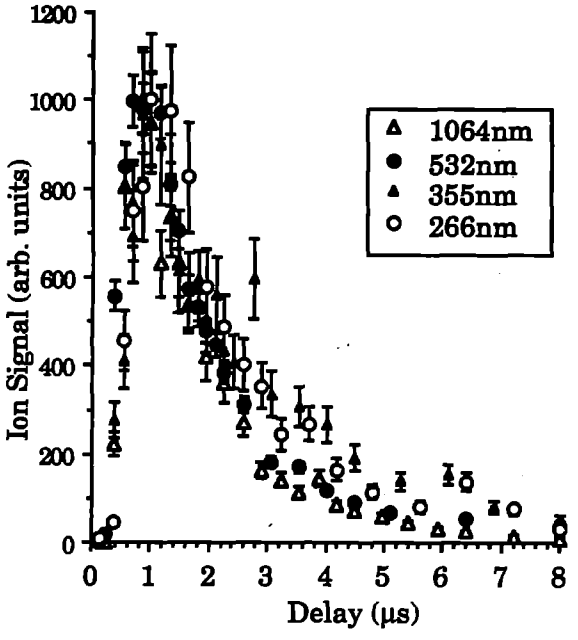

Figure 2

Bulk analysis using LARIS. Since laser ablation at power levels < 10^8 W/cm^2 removes only fractions of a monolayer per shot then to carry out bulk analysis using LARIS requires the removal of some layers before the typical bulk material is exposed. Trace elements in a number of different matrices were analysed e.g. steels, copper, aluminium and zinc. In one particular case, the isotopes ^{55}Mn and ^{54}Fe were compared in a NIST 1263a steel sample and it was only after some several thousand ablation shots that ion yields were stochiometrically characteristic of the bulk material.

Linearity and matrix independence of the LARIS signal. This is a very important aspect of all analytical procedures and an aim of the present research was to try to determine if the LARIS ion yields for trace elements were dependent on the sample matrix. Trace quantities of magnesium amd manganese were assayed in standard samples of aluminium supplied by Alusuisse-Lonza Services Ltd. The ionisation was carried out resonantly using two-photon processes: 280.2+355nm for manganese and 285.3+355nm for magnesium. Fig. 3 shows the ion signals as functions of concentrations of manganese and magnesium. The results must only be considered preliminary at this stage but the linearity over 4 orders of magnitude is reasonably good and more importantly perhaps one line can be drawn through all the points which indicates that any matrix problem is small. The same experiments have been carried out in other matrices, steel, copper and zinc and the results are still being assessed. Contamination free procedures have still to be optimised and it

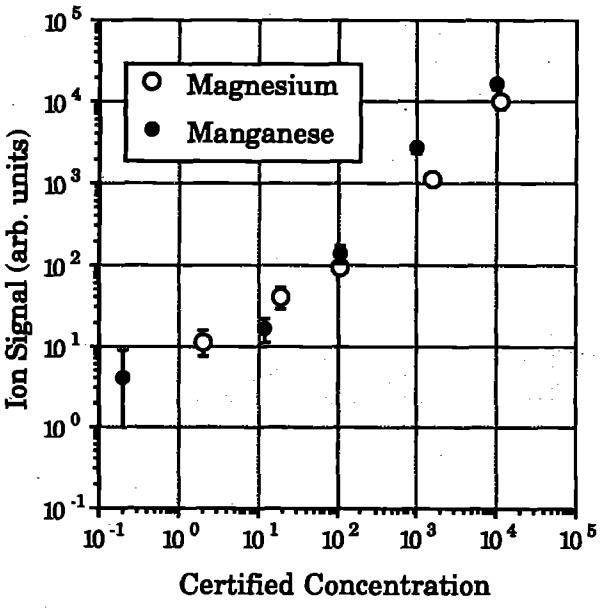

Figure 3

is expected that more linear and sensitive LARIS analyses can be carried out in the future.

A number of other experiments have also been carried out e.g. determining whether detected trace element ratios vary with ablation power, studying the variation of isotope ratios as a function of delay between the lasers and assessing the expected accuracy of LARIS analysis.

CONCLUSIONS AND FUTURE EXPERIMENTS

Laris has been shown to be a sensitive analytical technique capable of sensitivities down to ppm and below. There are inherent difficulties with the reproducibilty of the laser ablation process and it is hoped that these can be quantified by comparing LARIS with SIRIS, a similar technique in which the initial vapourisation is carried using an ion beam. These experiments will be initiated in the near future. It is also hoped to establish whether LARIS is less troubled with matrix problems than LIMA and initial results are encouraging.

REFERENCES

1) M.J. Southon, M.C. Witt, E.R. Wallach, J. Myatt, Vacuum 34 (1984) 903
2) G.Krier, F.R. Verdun, J.F. Muller, Z. Fresenius Anal. Chem. 322, (1985) 379.
3) I.S. Borthwick, K.W.D. Ledingham and R.P. Singhal *to be published.*
4) Mayo Santos, T.B.Lucatorto, G.S.Luther, Anal. Chem. 54, (1982) 553.
5) M. Towrie, S.L.T. Drysdale, R. Jennings, A.P. Land, K.W.D. Ledingham, P.T.McCombes, R.P.Singhal, M.H.C.Smyth and C.J.McLean Int. J. Mass Spectrom. Ion Process. 96, (1990), 309.

GENERATION OF INFRARED PICOSECOND PULSES BY STIMULATED RAMAN SCATTERING IN A MULTIPASS, HIGH PRESSURE CELL

C D Bain[1], P B Davies[2], T H Ong,[2] R N Ward[2] and A J Langley[3]
[1]Oxford
[2]Cambridge
[3]Rutherford Appleton Laboratory

Multiple-order stimulated Raman scattering is a well-established technique for shifting the output of tunable dye lasers into the near and mid-infrared. With *nanosecond* pulses, second and third-order Stokes scattering in hydrogen can generate pulses with energies in excess of a millijoule at wavelengths up to 10 μm. In a multiple-pass Raman cell, the photon conversion efficiency into third-order Stokes radiation can exceed 40%. The purpose of this study was to investigate the feasibility of generating *picosecond* pulses efficiently in the near and mid-IR by second-order (S_2) and third-order (S_3) stimulated Stokes scattering. The motivation for this study was the need for sufficient power in the near-IR to act as a pump in pump-probe experiments, and in the mid-IR for sum-frequency vibrational spectroscopy of surfaces.

Our study was limited to one gas (hydrogen) and one pump wavelength (600 nm). Nevertheless, we were able to generate >100 μJ/pulse of S_2 at 1.2 μm, with a quantum efficiency of 40%. S_3 radiation at 2.4 μm was readily produced, but only at low levels (<1 μJ/pulse).

To conduct this study, the output (~500 μJ/pulse, 600 nm, 10 Hz) from an amplified sync-pumped dye laser was focussed into the centre of a 2-metre long, multipass Raman cell (Fig.1) containing hydrogen at pressures up to 30 bar[(1)]. The beam diameter at the input window was typically 5 mm. The optical configuration was originally proposed by Herriot et al[(2)] the laser beam is focussed at the centre of the cell on each pass and successive reflections trace out circles on the end mirrors. A pick-off mirror attached to an encoder micrometer allows the beam to be directed out of the cell after any even number of passes. Up to 40 passes are possible, although the maximum output occurs at a lower number of passes (typically 16 for S[2]) due to the cumulative optical losses.

A summary of our observations follows:-

- At low pressures of hydrogen (~5 bar) there is little production of S_2. Several orders of anti-Stokes radiation are observed as ever increasing rings due to four-wave mixing, together with a cascade of rotationally shifted laser lines.

- At higher pressures rapid depletion of the pump beam shuts down the four-wave-mixing and the rotational Stokes scattering. At 30 bar the pump beam is largely converted to S_1 after 2 passes through the cell.

- S_2 radiation is initially generated in the form of a ring, which fills in from the centre on subsequent passes. The ring is indicative of four-wave mixing between the pump and S_1[(3)]. Four-wave mixing is poorly phase-matched in the forward direction but is nevertheless strong enough to act as a seed for stimulated Raman scattering, which ultimately accounts for the bulk of the energy in S2.

- Optimum conversion to S_2 (30 bar H_2,600μJ/pulse input power,16 passes) produced an estimated 120μJ/pulse at 1.2μm, after allowing for losses in the dispersing optics. This energy corresponds to a photon conversion efficiency of 40%.

- Generation of S_2 was most efficient for a pump pulse length of 3-5ps. External feedback in the dye laser, known to produce more stable pulses closer to the transform limit, improved the production of S_3, but had little effect on the efficiency of generation of S_2 under conditions of high conversion. There was,regrettably, insufficient time to measure the temporal width of the second-order Stokes radiation. Pulse compression is expected theoretically in transient SRS. Previous work in collaboration with Dr. Steve Meech at Heriot -Watt University has shown substantial pulse compression in S_2 (8 ps FWHM from a 19 ps pump). Similar compression in these experiments would yield pulse lengths of 1-2 ps.

- S_3 was detected after 6 passes at 30 bar, but the exponential growth in power characteristic of transient SRS under high amplification was not observed. Pulse-to-pulse fluctuations in energy were very large. It is not clear whether the S_3 detected is generated by 4-wave mixing or by SRS. Unlike S_2, the S_3 does not have a pronounced ring structure. The dispersion of hydrogen in the mid-infrared is less than in the visible and near-infrared, however, so the phase-matching angle for generation of S_3 by 4-wave mixing is likely to be smaller than for S_2, and the ring structure less pronounced.

In conclusion, second-order stimulated Stokes scattering in high pressure hydrogen is a feasible method for generating >100 μJ/pulse at 1.2 μm. Variation of the pump wavelength could provide tunable radiation at wavelengths up to 2 μm. The efficiency of conversion to third-order Stokes was disappointing. It is unlikely that optimisation of our current configuration would generate sufficient power in S_3 for non-linear vibrational spectroscopy of surfaces.

REFERENCES

1. Based on an original design by P Rabinowitz, B N Perry and N J Levinos, IEEE J Quantum Electronics, 22, 332 (1986).

2. D Herriott, H Kogelnik and R Kompfner, Appl Optics, 3, 523, (1964).

3. M D Duncan, R Mahon, L L Tankersley and J Reintjes, Opt Comm, 86, S38, (1991).

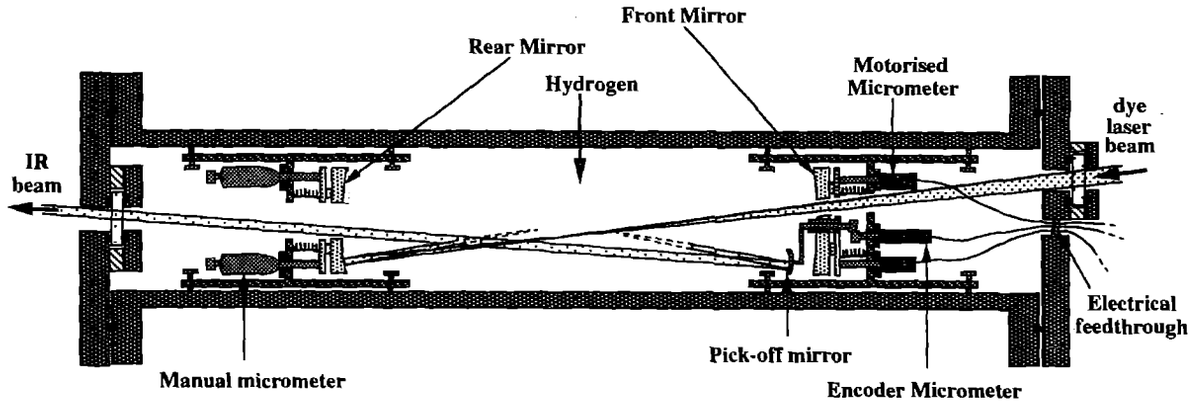

Fig.1 Schematic diagram of multipass Raman cell.

INVESTIGATIONS OF THE EXTREME MAGNETIC QUANTUM LIMIT OF HIGH MOBILITY GaAs-AlGaAs HETEROSTRUCTURES

A Usher, A S Plaut, M K Ellis, M Hayne and K Ploog*

Department of Physics, Exeter University
*University of Darmstadt

INTRODUCTION

We have mapped out a phase boundary diagram for the quantum condensates of a two dimensional (2-D) electron system, using photoluminescence as a probe. In order to make such a system condense magnetic fields of up to 17 Tesla are used in conjunction with temperatures as low as 400 milli-Kelvin. Under these extremes it is well known that the 2-D electron gas liquefies into an incompressible quantum fluid state whose quasiparticle excitations give rise to the fractional quantum Hall effect (FQHE)[1]. The fluid states are particularly stable when the lowest Landau level has an occupancy (filling factor) $\nu=p/q$ where p and q are integers and q is odd. Recent experiments have suggested that a further phase change occurs at low temperatures when the Landau level occupancy ν ($=hn_s/eB$, n_s the 2-D electron density) falls below a critical value $\nu_c \approx 0.25$ [2-5]. The new phase is pinned by disorder and therefore insulating at low electric fields [3,6]. It is thought to be either a 2-D electron solid, or a mixed 'hexatic liquid crystal' phase. Laughlin variational wavefunction calculations for the ground and excited states of the 2-D electron system [7] show that there should be a phase transition from the quantum fluid to solid at $\nu_c=0.1$, while more recent calculations yield $\nu_c=0.15$ [8]. Notwithstanding these calculations and measurements of the critical occupancy for electron solidification, there have been a number of observations of the FQHE quantum fluid at occupancies of 1/5 [2,3,9], and 1/7 and 1/9 [9].

THE EXPERIMENT

The system we have studied is a GaAs-AlGaAs single heterojunction with a δ-doping layer of beryllium in the GaAs 250Å from the interface. Argon ion laser light incident on the structure creates holes in the valence band of the AlGaAs some of which become bound to the (previously ionised) beryllium acceptors. A strong luminescence line is observed resulting from recombination of the 2-D electrons with these bound holes. The presence of the quantum fluid causes the position of the luminescence line to shift near fractional ν, and an analysis of this effect has been used to measure the energy gap between the quantum fluid ground state and its quasiparticle excitations [10]. The occurrence of the new phase (the solid, or mixed phase) is heralded by the appearance in the luminescence spectra of a new line about 1meV below the main line. In the regime investigated here, the new line forms a shoulder on the main one; at higher magnetic fields it becomes the dominant feature in the spectrum[5]. The new line appears below a critical temperature and below a critical value of ν, behaviour which is indicative of its association with a new phase. Further evidence for its association with a pinned phase is provided by a recent report in which the application of an electric field parallel to the 2-D electron system led to an enhancement of the intensity of the new line while leaving the old one unaffected [6]. This enhancement is interpreted as being caused by the depinning of the electron solid by the electric field. The present experiment consists of a systematic study of the relative strength of the new luminescence line compared with the main line, as a function of magnetic field and temperature.

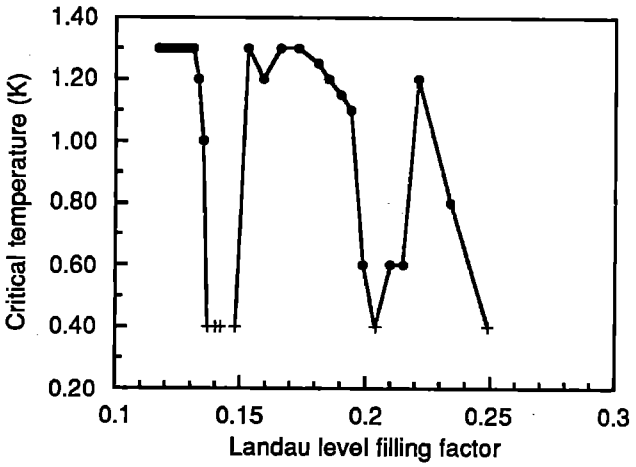

Figure 1. Electron solid phase boundary diagram

RESULTS

Figure 1 shows the phase boundary diagram for the quantum fluid and pinned solid (or mixed) phases [11]. The experimental points marked as filled circles show the critical temperature at which the new line appears, as a function of Landau level occupancy ν. The crosses indicate occupancies at which no critical temperature is observed. The values of ν are obtained from the positions of the luminescence shifts associated with the FQHE quantum fluid and are in agreement with low magnetic field Hall measurements. The important features of the diagram are:

1) There is no sign of the new line above $\nu=0.25$, even at the lowest experimental temperature (0.4K), in agreement with the results of previous experiments [2-5], and with recent theory [8].

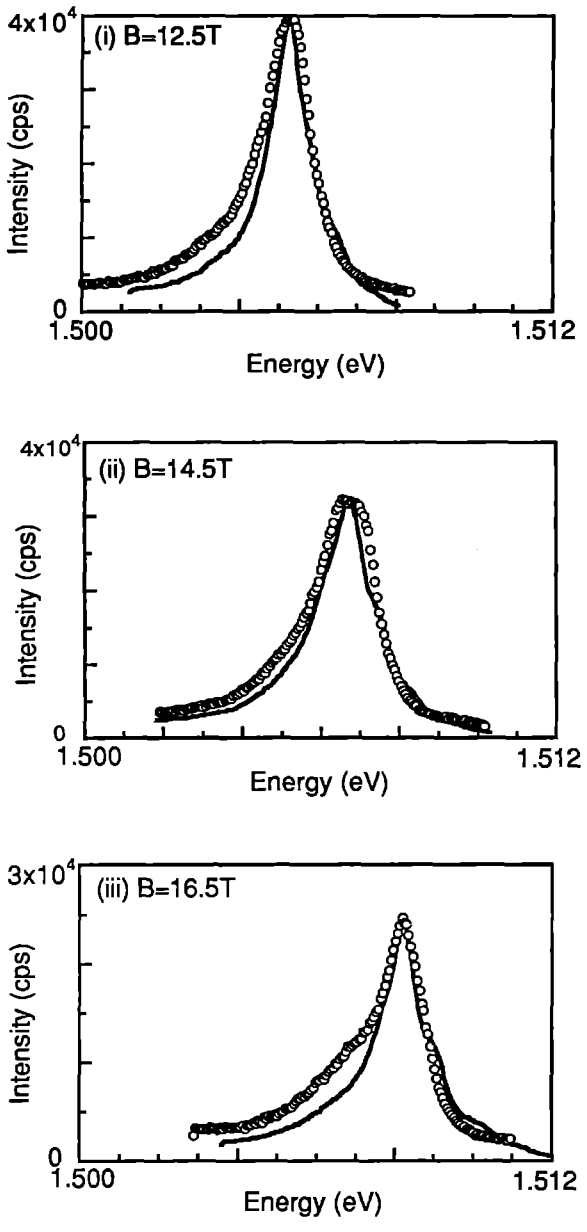

Figure 2: Spectra taken at 0.9K (open circles). Data for 4.25K are also shown for comparison (solid line).

2) The critical temperature shows a general increase with decreasing ν, and has a maximum value of 1.3K.

3) The new line also disappears at occupancies of 1/5 and 1/7, even at the lowest experimental temperature. This reentrant behaviour is theoretically quite unexpected and shows vividly the competition between the FQHE quantum fluid and the electron solid.

This competition is seen in the raw data of figure 2. Three luminescence spectra for 0.9K are shown, taken at (i) 12.5T, (ii) 14.5T and (iii) 16.5T. In each case, a 4.25K spectrum taken at the same field is shown for comparison. The high temperature spectra are provided for lineshape comparison of the low energy sides of the luminescence lines, and have been normalised to the heights of the low temperature data. (i) and (iii) show the expected increase in shoulder intensity at high magnetic field. However, the intensity of the shoulder in (ii) is weaker than in either (iii) or (i), despite the lower field of (i). The field of (ii) corresponds to ν=1/7, and coincides with a shift in the peak position of the main luminescence line, which indicates the formation of the 1/7 FQHE fluid state, and so we interpret the weakening of the shoulder around this field as an explicit demonstration of competition between the fluid and solid as ground states of the system at this occupancy.

CONCLUSIONS

We have made a systematic study of the luminescence signature of the solidification of 2-D electrons in a GaAs-AlGaAs heterojunction and have constructed the first experimental phase boundary diagram of this system. We observe a critical Landau level filling factor of 0.25. However, at fractional filling factors of 1/5 and 1/7, the FQHE quantum fluid remains the ground state of the system even at our lowest experimental temperature.

REFERENCES

1 Review: T Chakraborty and P Pietiläinen. 'The Fractional Quantum Hall Effect', Springer-Verlag, New York (1988).

2 H W Jiang, R L Willett, H L Stormer, D C Tsui, L N Pfeiffer and K W West. Phys. Rev. Lett. **65**, 633 (1990).

3 V J Goldman, M Santos, M Shayegan and J E Cunningham. Phys. Rev. Lett., **65**, 2189 (1990)

4 H W Jiang, H L Stormer, D C Tsui, L N Pfeiffer and K W West. Phys. Rev. **B44**, 8107 (1991).

5 H Buhmann, W Joss, K von Klitzing, I V Kukushkin,G Martinez, A S Plaut, K Ploog and V B Timofeev. Phys. Rev. Lett. **66**, 926 (1991).

6 I V Kukushkin, N J Pulsford, K von Klitzing, K Ploog, R J Haug, S Koch, V B Timofeev. Phys. Rev. **B45** in press (1992).

7 R B Laughlin. Phys. Rev. Lett. **50**, 1395 (1983).

8 P K Lam and S M Girvin, Phys. Rev. **B30**, 473 (1984).

9 H Buhmann, W Joss, K von Klitzing, I V Kukushkin, G Martinez, A S Plaut, K Ploog and V B Timofeev. Phys. Rev. Lett. **65**, 1056 (1990).

10 H Buhmann, W Joss, I V Kukushkin, V B Timofeev, K von Klitzing, A S Plaut, K Ploog, G Martinez. JETP Lett. **53** 449 (1991).

11 M Hayne, M K Ellis, A S Plaut, A Usher, K Ploog. Surface Science in press.

PHOTOLUMINESCENCE OF LPE-GROWN $InAs_{1-x-y}Sb_xP_y$

A Krier and D R Rowe

School of Physics and Materials, University of Lancaster

ABSTRACT

An investigation was made into the epitaxial growth and photoluminescence (PL) of $InAs_xSb_yP_{1-x-y}$ pn junctions grown by Liquid Phase Epitaxy (LPE). Photoluminescence emission was measured over the temperature range 78-295K. Four radiative transitions were observed in the spectrum at 78K, three of these were correlated with direct near band edge recombination, whilst a lattice defect was thought to be responsible for the weaker emission band at longer wavelengths. Increasing the sample temperature had the effect of shifting the main photoluminescence peak towards higher energies and quenching the PL emission arising from acceptors.

INTRODUCTION

There is at present considerable interest in the fabrication of optoelectronic devices for the middle infrared region (2-5μm) of the electromagnetic spectrum. Such devices have wide ranging applications for both gas detection using infrared absorption techniques, and also for long haul telecommunications. With regard to the latter, it has been estimated [1] that fluoride glass fibres should exhibit minimum attenuation losses ($<10^{-2}$dBkm^{-1}) at wavelengths of around 2.55μm, making them superior to conventional silica-based fibres currently operating at 1.55μm. Therefore, the distance over which a useful signal could be transmitted would be maximised if a combination of fluoride glass fibres and 2.55μm semiconductor lasers was utilised. Such a system could be used for example, for transatlantic communications without the need for repeater stations. The InAsSbP quaternary system can in principle provide semiconductor material with an appropriate energy gap for 2.55μm laser fabrication. Indeed, it can be shown using thermodynamic arguments [2], that the material composition $InAs_{.65}Sb_{.12}P_{.23}$, lattice matched to an InAs substrate should have an energy gap of 0.487eV, which corresponds to an emission wavelength of 2.55μm at room temperature. However, even though there are now new growth techniques, such as molecular beam epitaxy (MBE) and organo-metallic vapour phase epitaxy (OMVPE), available for semiconductor growth, there are as yet no reports of 2.55μm lasers operating at room temperature. Akiba et al [3] were able to achieve 2.5μm laser emission, but only by cooling their diodes to below 55K which makes such devices unattractive for use in practical systems. Although good quality InAsSbP has already been grown by OMVPE [4,5], no photoluminescence emission was reported from this material. Furthermore, the majority of work to date on LPE-grown InAsSbP has been concerned with material compositions corresponding to emission wavelengths beyond 3μm [6-11]. Here we report on the photoluminescence of material grown specifically for use as the active layer in 2.55μm semiconductor lasers.

EXPERIMENTAL PROCEDURES.

LIQUID PHASE EPITAXY

The quaternary InAsSbP layers studied in the present work were grown onto InAs substrates by liquid phase epitaxy (LPE), using the conventional sliding graphite boat technique [12]. The LPE apparatus itself was similar in design to that used previously by Nelson and White [13]. To provide good uniformity and reproducibility of the epitaxial material, the system was fully automated and controlled by a Quarndon QMS computer system . The liquid temperature was determined by direct observation of the melt whilst it was steadily heated, and was taken as that temperature at which the last melt crystals dissolved. In the ramp-cooling growth method employed here, the melts were first supercooled and then brought into contact with the substrate where they underwent a further controlled cooling.

The growth solutions were produced by dissolving appropriate amounts of InAs,InP and Sb in the indium metal and equilibrating at 650^{0}C for 1 hour. We used the phase diagram data of previous workers[4,14,15] to determine our growth melt compositions. A small amount ($5xlO^{-2}$%wt) of Zinc was added to the melt as a dopant to produce p-type layers while Tin (lxlO^{-2}%wt) was used as the n-type dopant. The resulting carrier concentrations were both estimated to be in the region of 1×10^{18} cm^{-3} , using the data of Brown and Porteous [16]. With these dopants it was possible to grow InAsSbP p-n homojunction structures for evaluation.

PHOTOLUMINESCENCE

In order to characterise the epitaxial material as closely as possible in relation to the p-n homojunction laser structure which will eventually be used for device fabrication, the photoluminescence measurements were made on as-grown unmetallised samples and the n-type InAs substrate material itself was also characterised for comparison. The experimental arrangement was as shown in the diagram of figure (1). The sample under investigation was excited with 488nm radiation from a Spectra Physics 2025 Argon ion laser (A) on loan from the Rutherford Central Laser Facility. The beam was chopped (B) and then filtered using an LP1 filter (C), to remove any spurious long wavelength components, before being focussed down into a 0.5mm diameter spot onto the sample (D). The maximum optical power density obtainable with this arrangement was estimated to be approximately 1×10^5 Wcm^{-2}. The sample under investigation was contained in an Oxford Instruments variable temperature liquid Nitrogen cryostat, and was held at selected fixed temperatures between 78K and 295K using helium exchange gas. After passing through the CaF_2 exit window of the cryostat the photoluminescence from the sample was focused by a series of CaF_2 lenses (E) and filtered using an RG850 filter (F) to remove any stray laser radiation before entering a Bentham M300E monochromator (G). The light was detected using a Lead Sulphide detector (H) and conventional phase sensitive detection techniques. Finally, the emission spectrum was recorded on a potentiometric chart recorder. To eliminate any atmospheric absorbtion effects, the whole of the optical path was enclosed and continuously flushed with dry nitrogen gas during the experiment.

Figure (1)

A schematic diagram showing the experimental apparatus used for the photoluminescence measurements.

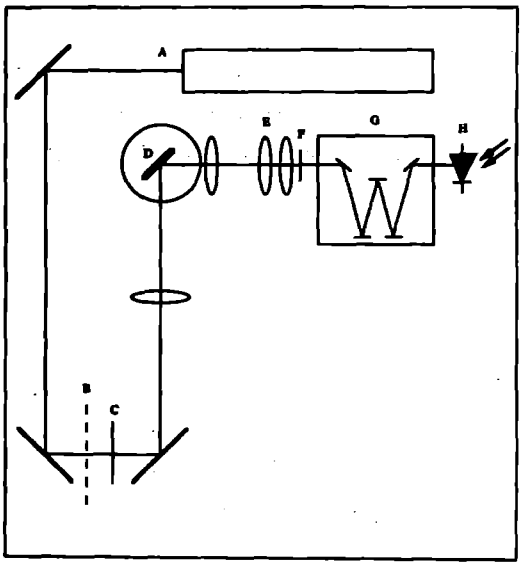

RESULTS

The as-grown epitaxial layers were smooth and shiny in appearance, but with some slight 'orange peel' surface structuring becoming evident when examined under the microscope. In general, the surface morphology was found to be heavily dependent on the degree of melt supercooling used during growth [17], and 10°C supercooling was found to be near optimum. The thicknesses of the n and p-type layers were determined by cleaving and then staining the samples with AB etchant [18]. This procedure typically revealed a 19 μm thick n-InAsSbP layer and a 5μm thick p-InAsSbP layer, which is consistent with the growth times used in our experiments. Both the interfaces were clearly visible and exhibited good planarity, x-ray analysis showed the layers to be near lattice matched.

The 77K photoluminescence spectra obtained from the quaternary InAsSbP epitaxial layer (solid curve) and the InAs substrate material (dashed curve) are shown for comparison in figure (2). The InAsSbP epilayer emission was found to be approximately 2.5 times brighter than the InAs substrate emission and peaked at 2.70μm (II), with two distinct shoulders at 2.80μm (III) and 2.65μm (I). The FWHM of the total emission was measured to be 138nm. In contrast, the InAs substrate photoluminescence consisted of only two somewhat broader emission bands centred at 2.48μm and 2.74μm it is interesting to note the large bandwidths of these PL peaks, since this effects is due to band filling at the high doping concentration ($n=2x10^{18}$ cm^{-3}) and is in agreement with previous findings [19]. At longer wavelengths an additional PL peak (IV) centred around 3.4μm was also observed in both the epitaxial InAsSbP and the InAs substrate material. Figure (3) shows the effects of temperature on the InAsSbP emission spectrum. As the sample temperature was increased the photoluminescence became less intense, the FWHM increased and the shoulder at 2.80μm was quenched.

Figure(2)

A comparison of the photoluminescence spectra of InAs and InAsSbP at 77K.

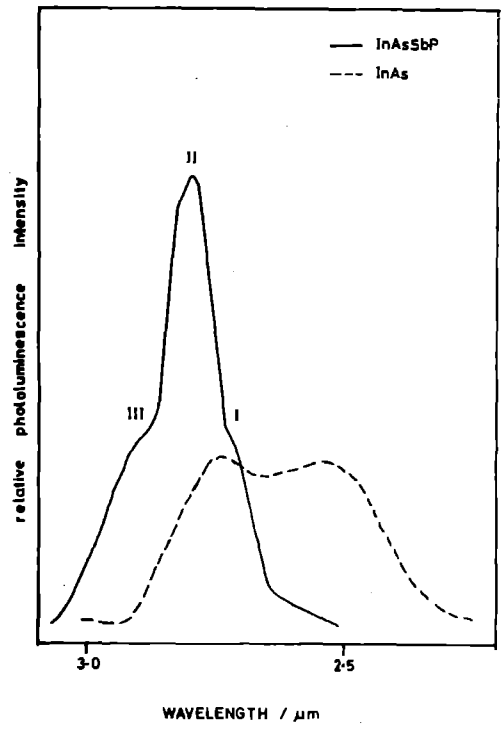

DISCUSSION

The room temperature photoluminescence spectra of the InAsSbP homostructures grown by liquid phase epitaxy peaked in the infrared at 2.68μm It was possible to calculate the material composition by using this value for the energy gap in Vegards law for a pseudoternary system, based on the bowing parameters given in [11]. This calculation relies on the $InAs_{1-x-y}Sb_xP_y$ being grown under the lattice matched

Figure(3)

Photoluminescence spectra from InAsSbP recorded at temperatures between 77K and 295K.

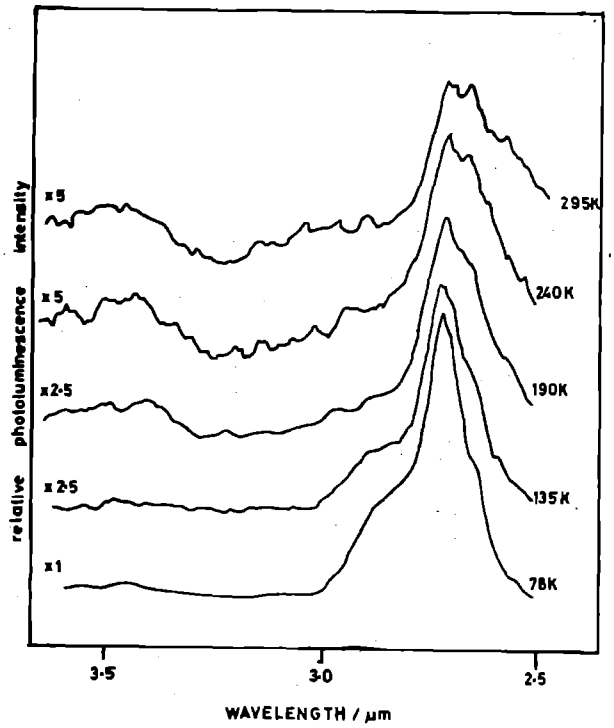

condition y=2.2x, which in our case is a valid approximation, based on x-ray analysis. In this way,the composition was determined to be $InAs_{.70}Sb_{.10}P_{.20}$, which is in fair agreement with the desired composition of $InAs_{.65}Sb_{.12}P_{.23}$ The 77K photoluminescence of this material revealed four radiative emission peaks which were tentatively identified in order of decreasing energy as follows;

(I) band to band emission, (II) donor level (9meV) to valence band, (III) donor level to acceptor level (16meV), and a much less intense peak (IV) most likely associated with a lattice defect.

The PL spectra indicate the presence of an acceptor level in the InAsSbP with an ionisation energy of approximately 16meV. The origin of this cannot be reliably identified but is most likely due to the intentionally added zinc (p-type) dopant. This is in good agreement with the findings of Melngailis and Rediker [20] who observed a zinc acceptor peak (16meV above the valence band) in the PL spectra of InAs. Secondary Ion Mass Spectrometry (SIMS) measurements on our samples revealed the existence of both zinc and silicon in the p-InAsSbP layer, with the zinc being present at a much higher concentration. Because zinc and silicon both give rise to acceptor levels at approximately the same energy [20,21] it is difficult to distinguish between them easily using photoluminescence. In our case the origin of the silicon contamination was most probably from the quartzware in our reactor and was therefore difficult to avoid. The nature of the donor level associated with transition II is less clear and requires further investigation.

The temperature dependence of the band gap energy of both the epitaxial InAsSbP and that of the InAs substrate material were investigated and observed to follow closely theory [22] based on the change in lattice parameter with temperature. In contrast however, it was found that the band gap variation in InAsSbP did not follow the above theory and in fact increased slightly with temperature. We believe this to be because as the temperature increases, the donor and acceptor levels become depopulated, leading to an increase in the occupancy of states in the conduction band and in the degenerate valence band respectively. This results in increased band filling, and hence PL emission at higher energy. This is consistent with thermal quenching of the donor-acceptor transition (III) in the PL spectra of figure(3). Furthermore, the thermal ionisation of donor levels with temperature results in a decrease in donor-valence band emission (II) and favours band-band emission

(I) at higher energy temperature, which is again consistent with our observations.

CONCLUSION

In summary, good quality lattice-matched $InAs_xSb_yP_{1-x-y}$ has been grown on InAs by liquid phase epitaxy and found to give room temperature photoluminescence at 2.68μm which was more efficient than the InAs substrate material. Room temperature and 77K PL spectra were studied and the main features of these spectra were tentatively identified with impurities in the epitaxial material. These results are encouraging because devices made from this type of material should allow the fabrication of 2.55μm homojunction semiconductor lasers suitable for fluoride fibre based telecommunications.

ACKNOWLEDGEMENTS

The authors wish to thank the the Rutherford Appleton Laboratory for the loan of the Ar ion laser. We also wish to thank the SERC for the CASE studentship and Laser Monitoring Systems Ltd. for supporting this work.

REFERENCES

1. P W France et al, "OH-Absorbtion in fluoride glass infrared fibres", Electron. Lett. Vol. 20, No. 14, pp. 607-608 (1984).

2. E R Gertner et al, "Liquid phase epitaxial growth of $InAs_xSb_yP_{1-x-y}$ layers on InAs", J. Elec. Mat. Vol .6, No. 2, pp. 163-172 (1977).

3. S Akiba et al, "InAsPSb/InAs Diode laser emitting in the 2.5μm range", Elec. Lett. Vol. 24, No .17, pp.1069-1071 (1988).

4. T Fukui and Y Horikoshi, "Organometallic VPE Growth of $InAs_{1-x-y}Sb_xP_y$ on InAs", Jpn. J. Appl . Phys. Vol. 20, No. 3, pp. 587-591 (1981).

5. T Fukui and Y Horikoshi, "InAs-InAsSbP heterostructures grown by organometallic vapour phase epitaxy", Inst . Phys. Conf. Ser. No. 63: Chap. 3 (1982).

6. L M Dolginov et al, "Efficient electron-beam-pumped $InAs_xSb_yP_{1-x-y}$ laser at 3.1-3.7μm", Sov. Tech. Phys. Lett. Vol. 4, No. 12, pp. 580-582 (1978).

7. N Kobayashi and Y Horikoshi, "DH Lasers, Fabricated by New III-V Semiconductor Material InAsSbP", Jap. J. App. Phys. Vol .19, No .10, pp. L641-L644 (1980)

8. P N Esina et al, "Long-Wavelength uncooled light-emitting diodes from $InAs_{1-x-y}Sb_xP$ solid solutions", Sov. Tech. Phys. Lett. Vol. 9, No. 4, pp. 167-168 (1983).

9. J L Benchimol et al, "Growth and modelling of InAsSbP/InAs double heterostructures," Inst .Phys. Conf.Ser . No. 83, Chap. 7, pp. 385-390 (1987)

10. N V Zotova et al, "Coherent emission at 3.9μm InAsSbP p-n structures", Sov.Tech. Phys. Lett. Vol. 12, No. 12, pp. 599-600 (1987).

11. A Krier, "Room-temperature $InAs_xSb_yP_{1-x-y}$ light-emitting diodes for $C0_2$ detection at 4.2μm", Appl. Phys. Lett. Vol. 56, No. 24, pp. 2428-2429(1990).

12. M B Panish et al, "Preparation of Multilayer LPE Heterostructures with Crystalline Solid Solutions of $Al_xGa_{1-x}As$: Heterostructure Lasers", Metallurgical Transactions, Vol. 2, pp. 795-801(1975).

13. A W Nelson and E A D White, "Automated LPE apparatus for the preparation of GaInAsP laser heterostructures", Br. Telecom. Technol. J. Vol. 1, No. 1, pp. 23-30 (1983).

14. B Benchimol et al, "Growth of InAsSbP/InAs heterostructures", SPIE. Vol .587 pp. 58-61 (1985).

15. J R Skelton, PhD Thesis (Oxford University) "Liquid phase epitaxy of III-V semiconductor materials and their development as emitters and detectors for middle infrared (2-5μm)", optical communications. (1984).

16. M A C S Brown and P Porteous, "The technology and properties of epitaxial indium arsenide lasers", Brit. J. Appl. Phys. Vol. 18, pp.1527-1535 (1967).

17. I Crossley and M B Small, "Some observations of the surface morphologies of GaAs Layers grown by Liquid Phase Epitaxy", J. Cryst. Growth, Vol .19, pp. 160-168 (1973).

18. M S Abrahams and C J Buiocchi, "Etching of Dislocations on the Low-Index faces of GaAs", J. Appl. Phys. Vol. 36, No. 9, pp. 2855-2863.(1965).

19. N V Zotova et al, "Photoluminescence of tin-doped n-type InAs crystals", Sov. Phys. Semicond. Vol. 9, No. 10, pp. 1275-1277 (1976).

20. I Melngailis and R H Rediker, "Properties of InAs Lasers", J. Appl. Phys. Vol. 37, pp. 899-911 (1965).

21. M I Guseva et al, "Radiative recombination in Indium arsenide implantation-doped with group IV elements", Sov. Phys. Semicond. Vol. 9, No. 5, pp. 591-592. (1975).

22. H C Casey and M B Panish, "Heterostructure Lasers Part B: Materials and operating Characteristics", Academic Press, pg 9.

LASER ANNEALING OF MAGNETO-OPTIC THIN FILM MEDIA AND CO GAS SENSORS

P.W. Haycock[+], A. Keeling[+], I. Ashcroft[+], R.H. Noyau[+],
S.D. Brown[+], E.W. Williams[+] and T. Thomson[*]
[+] Keele University
[*] University of Wales, Bangor

Over the past three years we have been carrying out experiments on the nanosecond pulsed laser-annealing of thin films of Tb-Fe-Co alloy. These have been sputtered between two protective layers onto glass substrates and are of the type used for erasable magneto-optic data storage media. The early experiments were performed using a Lambda-Physik FL2002 dye laser pumped by a Lumonics HyperEX 460 excimer laser at the Laser Support Facility. Anneals were carried out at 390nm and 830nm using energy densities of 2 mJ cm^{-2} to 18 mJ cm^{-2}. The sample was rastered under the beam in a variety of patterns and velocities in order to control the duration and frequency of elevated temperatures at any point on the surface. More recently we have made use of the Spectron SL801 Nd:YAG laser from the loan pool operating with the second harmonic at 532 nm.

From the earlier studies we knew that fairly high power anneals lead to loss of the perpendicular magnetic anisotropy of the films necessary for magneto-optic recording. This occured in samples where the transient temperature approched 830°C or above. Even in the these cases, the overall layering structure of the samples was not disturbed, as determined by neutron reflectivity measurements on CRISP at ISIS[1,2] and X-ray reflectivity at the Daresbury Laboratory[3,4].

More moderate power annealing has led to a variety of modifications to the hysteresis loop. In particular, it has been found to be possible to increase both the remanent magnetization and the coercivity by a careful choice of conditions. During the period of the loan we concentrated on optimizing the conditions for producing square magneto-optic hysteresis loops. These are obtained by measuring the optical Kerr rotation, θ_k from the sample as a function of applied magnetic field. Fig. 1 shows the hysteresis loops for an as-sputtered film (a) and one annealed at a moderate energy density (b). It can be seen that the squareness of the loop (i.e. $\theta_k/\theta_{k_{sat}}$ at zero applied field) has improved slightly in this case and it seems that samples with fairly high squareness can be improved. However, we can sputter films with initial squarenesses of unity and in that case the magnetic properties cannot be improved by pulsed nanosecond laser annealing.

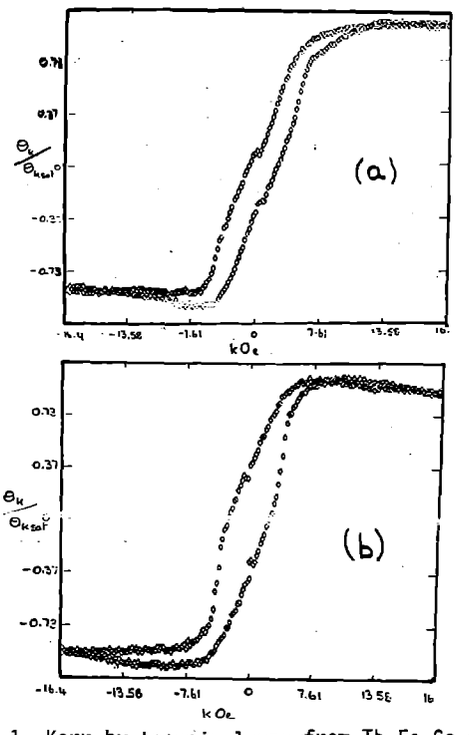

Fig. 1 Kerr hysteresis loops from Tb-Fe-Co films before (a) and after (b) laser annealing at moderate power density.

On the other hand, for magneto-optic recording purposes the optimum hysteresis loop may not be perfectly square since the magnetization of square loops is very time-dependent, particularly if the coercivity squareness (i.e. essentially the slope of the sides of the hysteresis loops) is also very high[5]. We are continuing to research into the time dependence of the magnetization and other parameters affecting the lifetime of magneto-optic storage media. If squarenesses of less than unity are required we will be able use laser annealing to degrade the magnetic properties in a controlled manner. Fig. 2 shows the results of such a process, using a lower power density than above.

In addition to annealing alloy films we have also been annealing multilayer magneto-optic samples These consist of alternate ultrathin (a few Å) layers of iron and terbium. As yet these experiments have been preliminary and we have no definitive results.

While the laser was in place at Keele we used it to laser anneal several other materials of interest. In particular,we have been processing a class of CO gas sensors being developed at Keele. These are particulate films which have to be

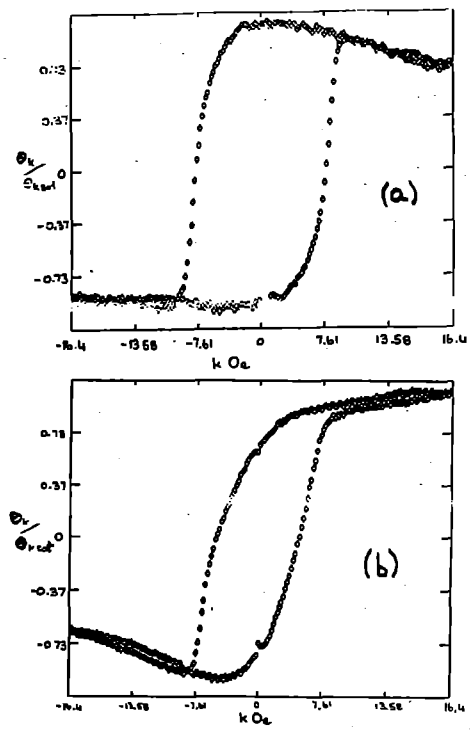

Fig. 2 Kerr hysteresis loops from Tb-Fe-Co films before (a) and after (b) laser annealing at lower power density.

annealed before use in order to fuse the grains together to give the required electrical characteristics. Our preliminary attempts at laser annealing the sensors have been very promising. Fig. 3 shows the results of laser anneals at three power densities, together with a sample annealed thermally. Further development of the technique is necessary to reduce the initial resistance, but if successful it will provide a much more rapid annealing process than the thermal annealing used at present.

Overall the results of the last three years have been very encouraging. We have shown that nanosecond pulsed laser annealing can be used for materials processing in the manufacture of magneto-optic recording media and CO gas sensors, although further development is required in both cases. Pulsed laser annealing has the advantages over thermal annealing of being rapid and volume specific in three dimensions so that only the particular volume of the sample to be processed is affected. The power from the energy pulse dissipates quickly in the surrounding material, causing little effect. The use of a compact YAG laser allows the process to be introduced in situ into manufacturing process without modification of the sample stage since the laser itself can be situated in a convenient position and only the beam is actually in situ.

REFERENCES

[1] P W Haycock, R H Moyau, T Thomson, G J Herdman, E W Williams and K. O'Grady, IEEE Transactions on Magnetics 26 1921 (1990).

[2] W G Stirling and E W Williams, ISIS Annual Report 1991, RB/1764.

[3] P W Haycock, S D Brown, A H Thomas, W G Stirling, E W Williams, T Thomson and K O'Grady, Synchrotron Radiation Appendix to the Daresbury Annual Report 1990/91, p.88.

[4] S D Brown, A H Thomas, C C Tang, I Ashcroft, A Keeling, P W Haycock, W G Stirling, E W Williams, T Thomson and A C Dent, Synchrotron Radiation Appendix to the Daresbury Annual Report 1990/91, in press.

[5] T Thomson, K O'Grady, S D Brown, P W Haycock and E W Williams, to be presented at INTERMAG '92, 13-16 April 1992, St. Louis, USA; also IEEE Trans. Mag., in press.

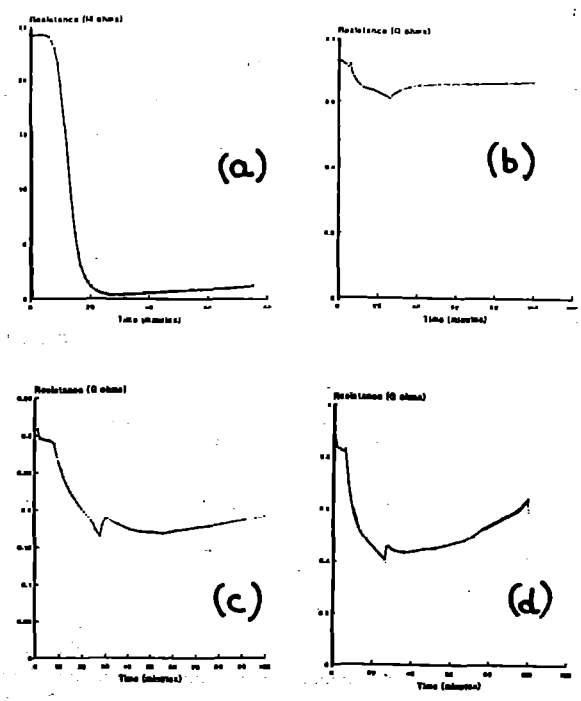

Fig. 3 Response of sensors to CO versus time after thermal anneal (a) and laser anneals at (b) 1.6mJ (c) 2.3mJ (d) 7.6mJ per pulse.

SCANNING TRANSMISSION X-RAY MICROSCOPY WITH A HIGH REPETITION RATE LASER-PLASMA SOURCE

A G Michette[1], M S Schulz[1], R E Burge[1], P Fluck[1], M T Browne[1] and I C E Turcu[2]

[1]Department of Physics, King's College London
[2]Rutherford Appleton Laboratory

INTRODUCTION

The first experiments with the King's College scanning transmission x-ray microscope (STXM) (designed for the undulator beamline at the Synchrotron Radiation Source (SRS), SERC Daresbury Laboratory) using the high repetition rate laser-plasma source at the LSF were reported in the CLF annual report for 1991.(1) This series of experiments suffered from several difficulties, because the STXM was neither designed nor optimised for use with a pulsed source, and it was not possible in the time available to make any significant modifications to the system. Despite this, it was possible to obtain some preliminary images.

One problem, with the detection system, involved a spurious pulse picked up by the proportional counter and preamplifier when the laser fired. This was reduced but not eliminated by careful screening. However it was discovered that this pulse was bidirectional and gave rise to a negligible contribution to the signal.

A more significant problem was noise in the images due to variation of source emission from shot to shot as well as the shot noise due to the number of photons collected during each pixel. Although the source emission was monitored it was not possible (in the time available) to modify the acquisition system to allow the effect of source emission to be removed so that only shot noise would remain.

In order to obtain the position of best focus, a 3 μm pinhole was scanned across the x-ray beam. Far from the focus of the zone plate the characteristic doughnut pattern (caused because the zone plate was centrally obstructed) was observed, while near focus there was a central bright region due to the focused X rays. The position of best focus was determined by minimizing the size of this bright region. Because of the target used to form the plasma (mylar tape) several x-ray lines contributed, although that at 3.37 nm line was sufficiently more intense that only its focus was obvious. The other (out of focus) lines, however, caused loss of contrast in the images.

In the second series of experiments, reported here, steps were taken to overcome these problems, and as a result much better images were obtained.

THE EXPERIMENTAL ARRANGEMENT

The arrangement used was as described in the 1991 Annual Report, with two main modifications. Firstly, the source emission was monitored with an x-ray diode, and the STXM software was modified to allow the image data to be normalised to this signal, thereby removing the effect of source noise. Secondly, the air gap between the chamber exit window and the detector was flushed with nitrogen, which acted as a filter to remove the effects of unwanted emission lines from the plasma. Additionally, the mechanism to drive the tape target was improved to prevent jamming caused by the take-up spool becoming full due to the distortion of the tape after irradiation by the focused laser beam. A full discussion of these modifications, and of the results obtained, is currently being prepared for publication.

RESULTS

Several images were obtained during this series of experiments. An example of a test image, after removal of source noise, is shown in figure 1; this is an electron microscope grid obtained with one pulse per pixel and a scanning step size of 0.63 μm. The fidelity of this image is much improved over that of similar ones obtained previously with many pulses per pixel, because of the improvements discussed above.

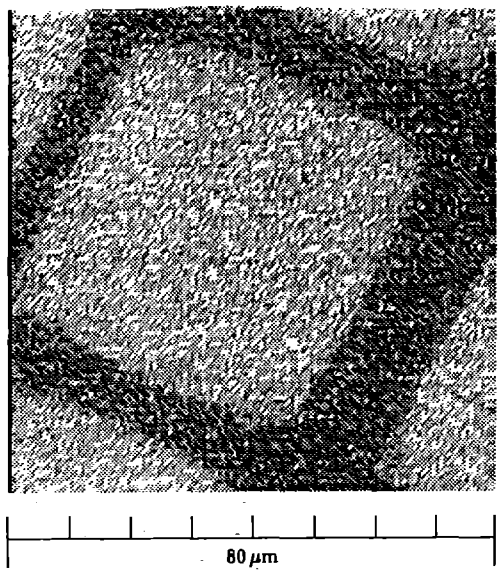

Fig. 1 An image of a grid, obtained with one pulse per pixel

In addition to test images of this type, images of real specimens have been obtained. These are still being analysed; images of silica gels, again obtained with one pulse per pixel, look similar to those obtained with a synchrotron source although the contrast is poorer (due to the x-ray wavelength used). A full description of the images obtained will be published later.

FUTURE WORK

The source/microscope combination used was still not fully optimised, and work in the immediate future will concentrate on rectifying this. In addition, it is planned to use the wide divergence of the laser-plasma source to allow stereo-pair imaging (figure 2), which is not possible with a synchrotron due to the high collimation of the x-ray beam.

ACKNOWLEDGEMENTS

The authors are grateful to many people at RAL and KCL for assistance with this project.

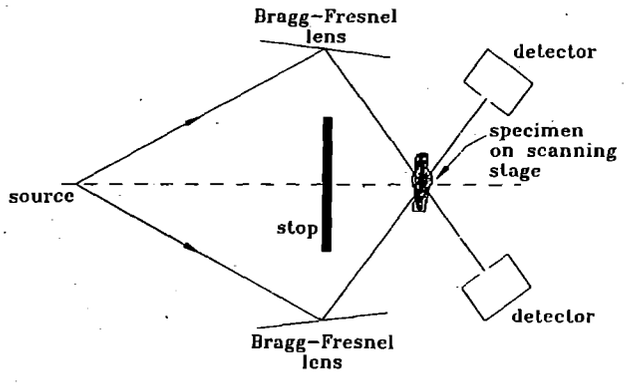

Fig. 2 A stereo-pair scanning transmission x-ray microscope

REFERENCES

1. A G Michette, M S Schulz and I C E Turcu, First experiments with a scanning transmission x-ray microscope on a high-repetition rate laser-plasma source, *Annual Report to the Laser Facility Committee 1991, RAL-91-025*, 208-9

CHIRPED PULSE AMPLIFICATION AT 249 nm

I N Ross[2], J Houliston[1], W Shaikh[2]

[1]University of Oxford
[2]Rutherford Appleton Laboratory

In the 1991 Annual Report[1], we reported on the first Chirped Pulse Amplification (CPA) experiment in which 3 ps, 600 nm pulses were stretched to 100 ps and recompressed to the original duration, within the measurement and fidelity limits. The CPA programme has been completed with two further experiments conducted at 249 nm with saturated amplification of 80 ps stretched pulses followed by faithful recompression to < 9 ps.

As described in Fig 1 the 5 ps, 746 nm, output of the synchronously pumped dye laser is amplified in a 3-stage dye amplifier and frequency converted to give 8 ps, 20 μJ pulses at 249 nm. The beam is expanded through the Questek discharge pumped KrF amplifier and recollimated at the output. The stretcher operates in a folded geometry[1] with a 3600 l/mm diffraction grating placed 24 cm from a 2 m focal length quartz spherical lens. A multilayer mirror is positioned at the focal plane of the lens with a light vertical tilt to separate the input and output beams. T he grating is used in second order near-Littrow diffraction geometry (angles of incidence and diffraction 54° and 64° respectively) with a diffraction efficiency of 10%. The 1 cm diameter stretched beam is amplified in a second Questek KrF amplifier to several times the saturation fluence (E_{sat} = 2 mJ/cm^2) before recompression. The compressor operates in a folded geometry with a 58 x 58 mm^2 3600 l/mm grating used in a similar diffraction grating geometry to the stretcher grating. A 90° quartz prism placed 180 cm from the compressor grating with the prism back edge perpendicular to the dispersion plane is used to retro-reflect the diffracted beam to the grating for recollimation.

Fig 1 248nm PICOSECOND CPA ARRANGEMENT.

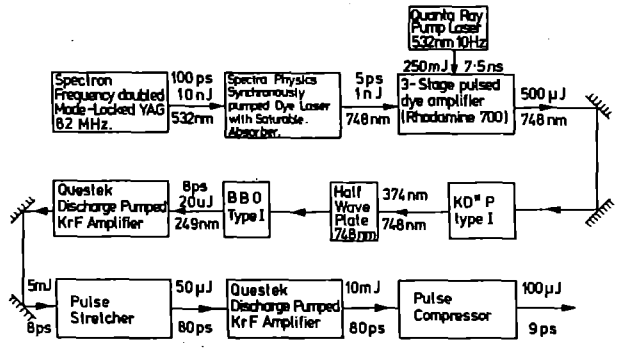

Fig 2 shows streak camera (Hadlands Imacon 200, 5 ps resolution) measurements of the input (with timing fiducial), amplified stretched and recompressed pulse durations. The measured stretch pulse duration is in agreement with the theoretically predicted value[2] which is determined from the pulse bandwidth (1 Å) and the stretcher geometry.

Fig 2 CPA AT 249nm (WITH SATURATED AMPLIFICATION).

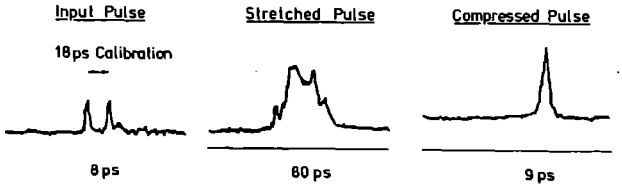

Faithful recompression is dependent on precise collimation of the input beam and accurate positioning of the stretcher back mirror. With good optical quality components in the system (particularly with respect to stretcher lens spherical aberration and diffraction grating flatness) faithful recompression is obtained without significant deterioration in beam focusability.

An important observation is that the recompressed pulse duration is not affected by saturated amplification of the stretched pulse, within the measurement limit. The stretcher introduces a linear positive chirp and under homogeneous saturated amplification the leading edge of the stretched pulse is amplified preferentially resulting in a significant change in spectral distribution as illustrated in Fig 3.

Fig 3 SATURATED AMPLIFICATION OF STRETCHED PULSE.

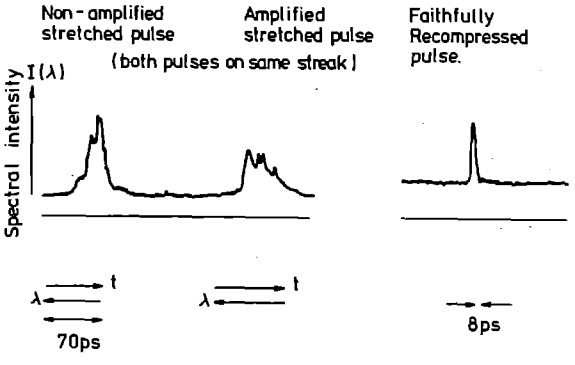

This CPA programme in conjunction with experiment reported elsewhere[3] (subpicosecond CPA with discharge pumped KrF amplifiers) has given confidence for the scheduled implementation of CPA for 100 fs operation of the Sprite Facility.

1. Annual Report 1991, RAL-91-025, 181.

2. Ibid, 112.

3. Annual Report 1992, Section B2.5.

PICOSECOND TIME-RESOLVED RESONANCE RAMAN SPECTROSCOPY APPARATUS A PROGRESS REPORT

P Matousek[1], A J Langley[1], A W Parker[1], W T Toner[1], M Towrie[1], I C E Turcu[1], M Wise[1], D Phillips[2], R E Hester[3], J N Moore[3] and S Umapathy[3]

[1]Rutherford Appleton Laboratory
[2]Imperial College, London
[3]University of York, York

This report outlines major modifications made to the time-resolved resonance Raman (TR^3) spectroscopy apparatus described in previous reports[1,2,3].

The present layout is shown in Figure 1.

The measurement of transient kinetics by time-resolved resonance Raman spectroscopy requires the collection of several spectra at various delay times typically taken over a period of several hours. Pump and probe powers should be kept as stable as possible during the experiment to simplify the interpretation of TR^3 spectra. Therefore efforts have been made to stabilise average pump and probe beam powers. An improvement from ±15% to ±2%, as measured over 3 hour run, has been achieved using a feedback stabiliser. The device monitors the dye amplifier output using a large area photodiode and accordingly partially blocks/unblocks the copper vapour laser beam to keep the average probe beam power constant.

The tunable range of the apparatus has been extended from the previous value of (610-620) nm to (550-655) nm (see Figure 2). This was achieved using six dye mixtures for the dye amplifier and 3 dyes for the cavity dumper. The fundamental output of the dye amplifier has a pulse energy exceeding 4 μJ in the whole tuning range. This is above the energy threshold required for TR^3 spectroscopy using this apparatus estimated from trans-Stilbene to be 2 μJ in the probe pulse and 0.2 μJ in the pump pulse. The pump beam is generated by second harmonic generation in a BBO crystal (type II) with conversion efficiency ca 10% in the whole tunable range. One set of reflecting mirrors and dichroic beamsplitters covers the present tuning range.

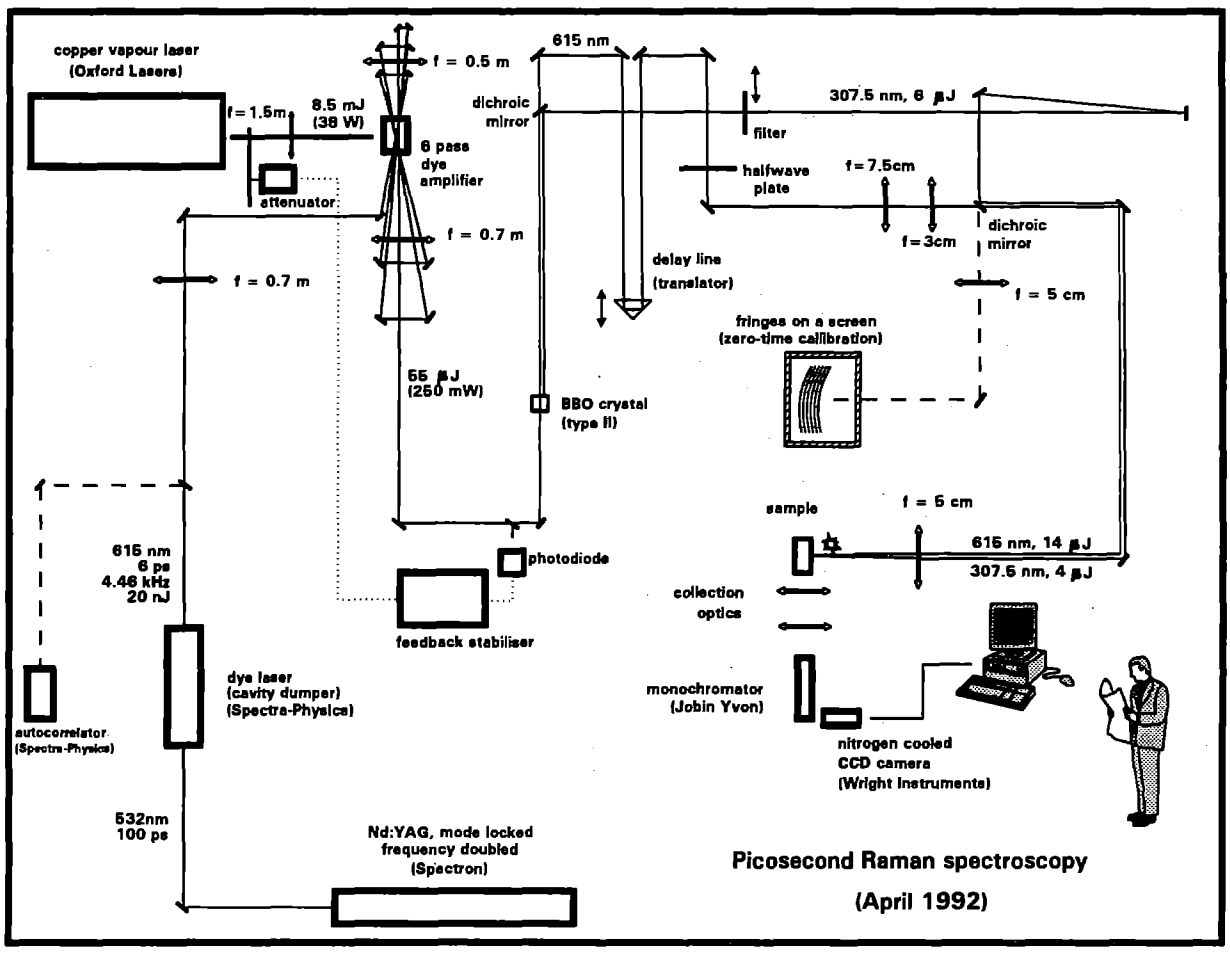

Figure 1. The layout of the ps-TR^3 spectroscopy apparatus.

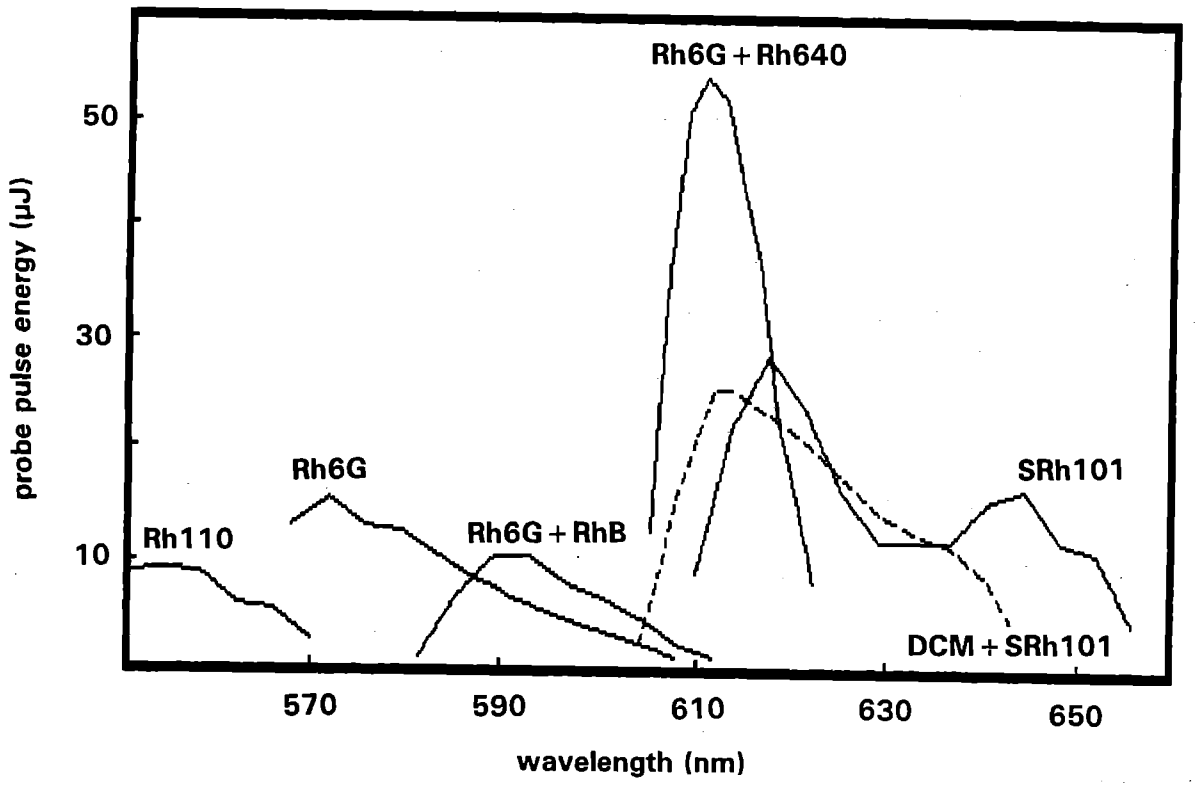

Figure 2. Tunability of the probe beam. The pump beam is generated by frequency doubling with 10% conversion efficiency.

The tunability was further extended by stimulated Raman generation in solvents. The technique was demonstrated using a 612 nm laser beam of 50 μJ pulse energy and 6 ps pulse width (FWHM). A 10cm focal length lens is used to focus the beam into an 11cm long cuvette containing dimethyl sulpoxide (grade 99.5%). The solvent was stirred to avoid overheating and bubbling in the beam waist. Stimulated Stokes emission shifted by ca 2960 cm^{-1} was generated with conversion efficiency of 18% and a bandwidth of 11 cm^{-1} (FWHM). The emission can be used as a probe beam or directly frequency doubled to obtain new pump or probe wavelength. In this case a wavelength of 373 nm was generated with 10% frequency doubling conversion efficiency from the Stokes emission.

The applicability of this technique for TR^3 spectroscopy was demonstrated using the dye amplifier output (612 nm) as probe and the second harmonic of the stimulated Raman line (373 nm) as pump beam. The TR^3 spectra of all-t b-apo-8'-carotenal in cyclohexane at 15 ps delay time between pump and probe beams were obtained (see Figure 3).

Details of experiments on trans-Stilbene and carotenoids carried out in collaboration with University of York and University of Keele can be found in the Chemistry Section of this Annual Report.

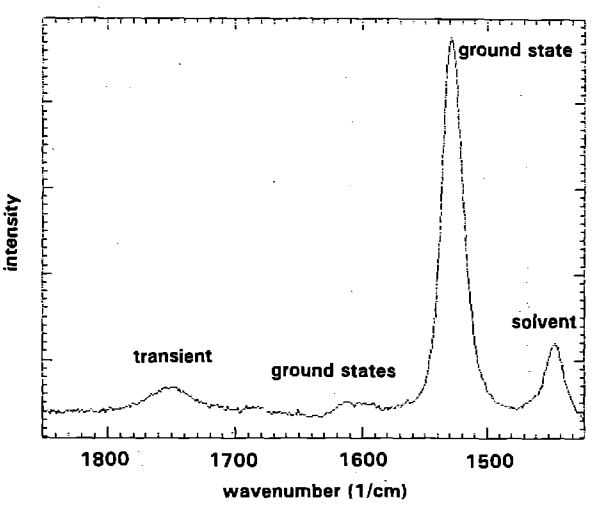

Figure 3. Transient Raman spectrum of all-t b-apo-8'-carotenal in cyclohexane (ca 1mM) at 15 ps delay time between pump (373 nm, 6 ps) and probe (612 nm, 6 ps). Accumulation time was 400 s.

REFERENCES

1. Central Laser Facility Annual Report 1989, Rutherford Appleton Laboratory, RAL-89-045, 1989.

2. Central Laser Facility Annual Report 1990, Rutherford Appleton Laboratory, RAL-90-026, 1990.

3. Central Laser Facility Annual Report 1991, Rutherford Appleton Laboratory, RAL-91-025, 1991.

TIME CORRELATED SINGLE PHOTON COUNTING

M. Towrie and S. Tavender.
Rutherford Appleton Laboratory

Time Correlated Single Photon Counting (TCSPC) provides a simple and direct means to study the rates of population decay from excited molecular species. The TCSPC apparatus based at RAL has been described previously in the 1990 and 1991 Annual Reports and to date has been used to study the fluorescence lifetimes of metallocenes (Perutz et al RAL report 1992).

Until recently the best time resolution for the apparatus was 180ps. A time resolution of 60ps was obtained when the microchannel plate was incorporated in similar apparatus at Imperial College. Investigations have isolated the main reasons for this difference and now values of better than 60ps are obtained on a routine basis.

The main contributions to the poor time resolution came from two sources, noise induced by the pre-amplifier arrangement after the microchannel plate photo multiplier (MCP) and light scattered from the walls of the sample cell and from the apertures and walls within the sample chamber. 80ps resolution was obtained by using pre-amplifiers with a combined rms noise output a factor of four lower than those used previously. Careful positioning of light baffles and slits gave a further 30% improvement.

The instrument response function (IRF) was studied as a function of the cavity dumper output power (equivalent to the photon count rate), the stability of the Spectron mode locked Nd:YAG pump laser and the cavity length of cavity dumper. The cavity dumper output power had the most significant effect, producing a peak shift and broadening of the IRF. This was thought to be due to a count rate dependent electric relaxation and thermal effects in the TAC. The long term stability of the apparatus was therefore improved by using a power stabiliser on the cavity dumper.

Figures 1a and b show the present optical and electrical arrangements of the TCSPC apparatus.

FIGURE 1a: The Optical Arrangement.

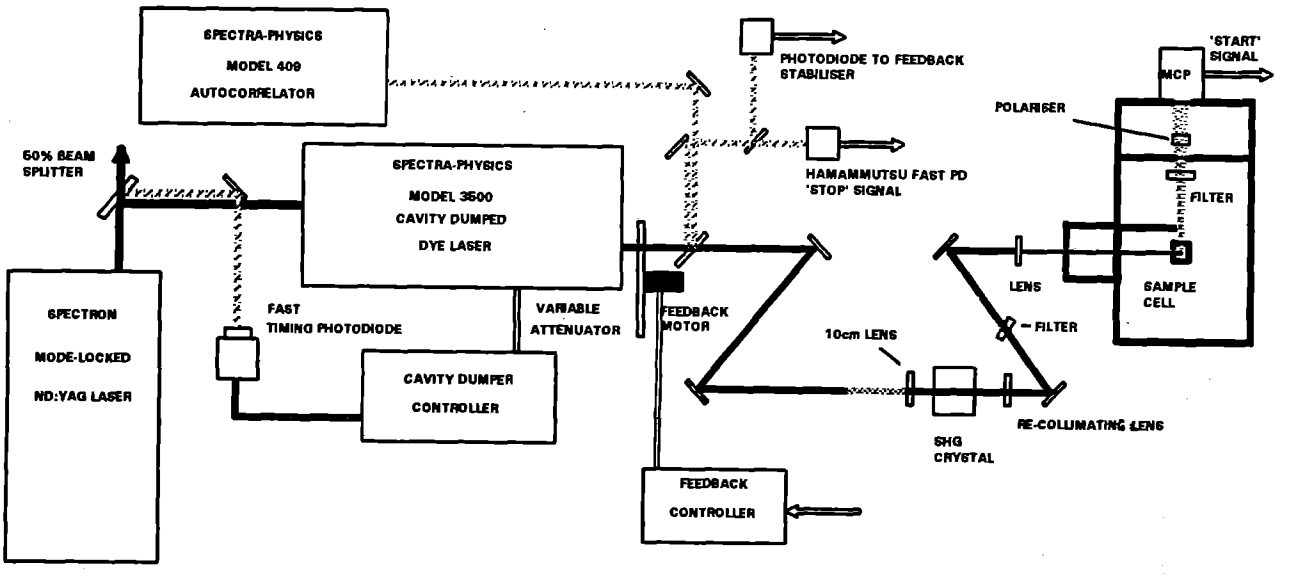

FIGURE 1b: The Electrical Arrangement.

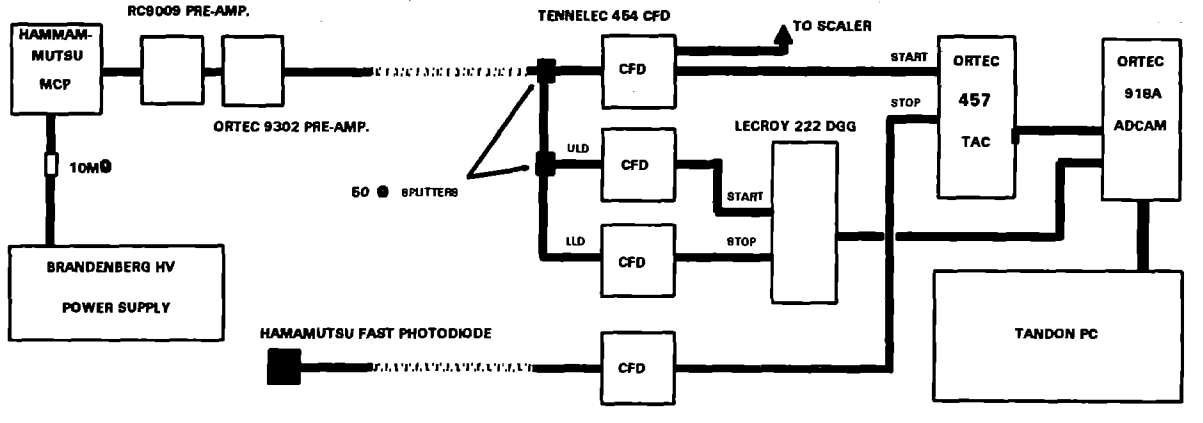

Signals from a Hammamutsu R2809U-07 MCP are amplified (X100) by two wide band pre-amplifiers in series, a Research Communications 9009 and an Ortec 9302. The signal is then split with one half going into a Tennelec 454 Constant Fraction Discriminator (CFD) to provide a start for the TAC and the other half, split again, passes into two further CFDs These are set to give an upper and lower threshold on the MCP signals. The lower threshold signal triggers, while the upper threshold inhibits, the output from a Lecroy 222 Dual Gate Generator. This output is then used as a coincidence gate for the Ortec ADCAM buffer. The Upper threshold has the effect of suppressing unwanted multi-photon events, and the lower level threshold of eliminating spurious 'near threshold' signals from the CFD.

A stop signal is generated from a biased Hammamutsu fast photo diode placed in a 4% split from the Cavity dumper output. Here again, the IRF would also be improved by the addition of upper and lower thresholds.

A flourescence lifetime measurement was made for Rhodamine 6G in a 2.4M solution of Potassium Iodide. The addition of KI to Rhodamine solutions has the effect of quenching the fluorescence from the S_1 to S_0 transition. At a concentration of 2.4M of KI the lifetime is reduced to around 50ps (J.M.Harris and F.E.Lytle). Polarisation effects were not considered.

The instrument response function with a FWHM of 60ps (shown in figure 2a) was produced by scattering the pump beam (wavelength 570nm) in a solution of Ludox. The flourescence data, fit to a triple exponential, is shown in figure 2b and gives a chi. squared value of 1.17 and lifetime values of 79ps, 324ps and 2810ps with normalised amplitudes of 1, 0.14 and 0.13 respectively.

Reference.

J.M.Harris and F.E. Lytle.
Rev. Sci. Instrum., Vol. 48(11), 1977.

FIGURE 2a: The Instrument Response Function for excitation at 570nm.

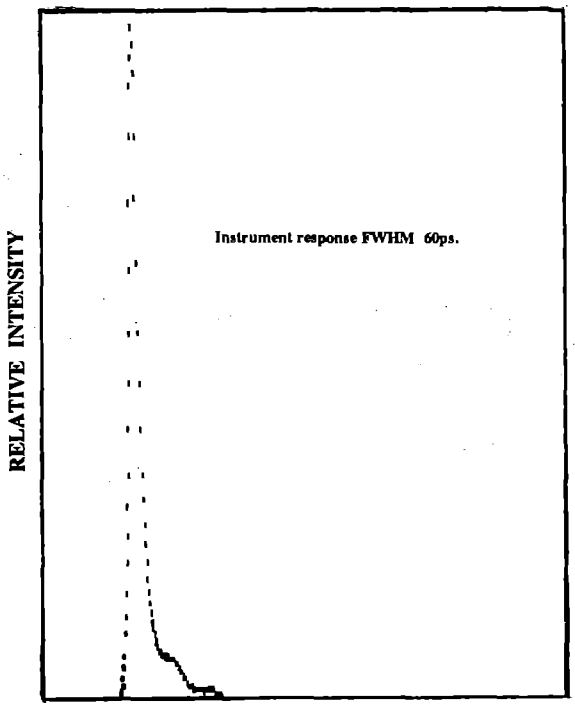

FIGURE 2b: Data fit to triple exponential.

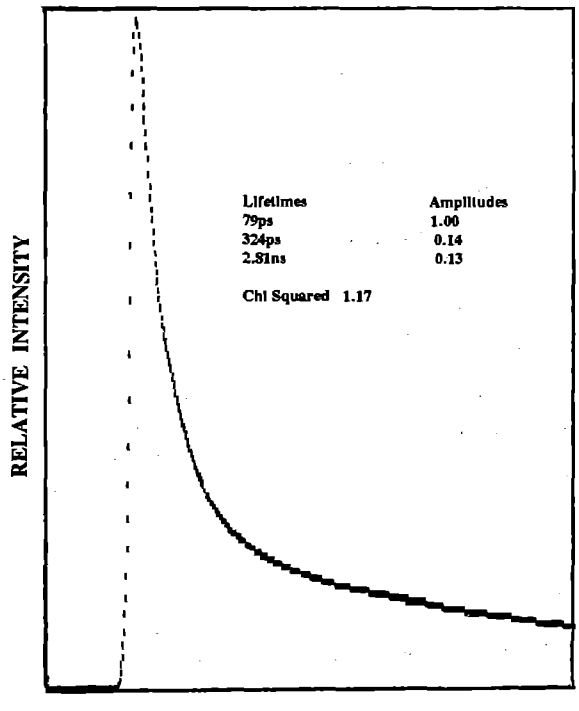

Development of a Diagnostic System to Monitor the Performance of a Picosecond Laser.

E J Cartlidge, A J Langley, C J Reason and W Shaikh.

Rutherford Appleton Laboratory

INTRODUCTION

Users of short pulse lasers are often concerned about the nature of the pulses they are using in their experiments. In principle full analysis of the pulse shape would allow experimenters to de-convolve their data and measure events occurring in times shorter than the pulse itself. Unfortunately with pulses of a few picoseconds and shorter this ideal is either impossible or at best difficult to achieve. There are however a range of techniques well reported in the literature which allow a considerable amount of information on the nature of short pulses to be extracted. These include second order intensity autocorrelation methods[1] which can provide a measure of pulse width when a pulse shape is assumed. Higher order autocorrelation measurements can provide at least some measure of the pulse asymmetry though are difficult in practice to carry out with low energy pulses[2]. Interferometric autocorrelation methods show the nature of chirp present on pulses and have been used to provide shape analysis of short pulses of around 100fs duration[3].

The LSF picosecond laser is used collectively by different research groups for a whole range of projects in physics, biology and chemistry. This clearly sets design constraints on the diagnostics system constructed to measure laser performance. Firstly because each experimental group may require pulse information in a different form. Secondly the diagnostic system must be capable of gathering data in-tandem with user experiments and thirdly it must be easy to operate and require minimum attention. With these constraints in mind we recently began building a system to measure CW, second-order intensity autocorrelation data together with single-shot measurements of pulse spectra.

THE DIAGNOSTIC SYSTEM

The system built thus far is shown schematically in figure 1. The single pulse spectra are measured using a home-built spectrometer with a resolution of ~15 GHz. The dispersed spectrum is detected by a Pulnix TM 765 CCD camera and the video signal transferred to a framestore in a Viglen III/LS personal computer for analysis. The hardware and image-analysis software was supplied by Oxford Framestores Applications (OFA) Ltd. The autocorrelation data are obtained using a Femtochrome Research scanning autocorrelator which has a resolution of 50fs. The autocorrelator signal is gathered and displayed by a Hewlett Packard 54600A digital oscilloscope before being transferred to the computer via the GPIB. The software to control the oscilloscope and acquire, store and display the data was written in-house but runs under the control of the OFA master system.

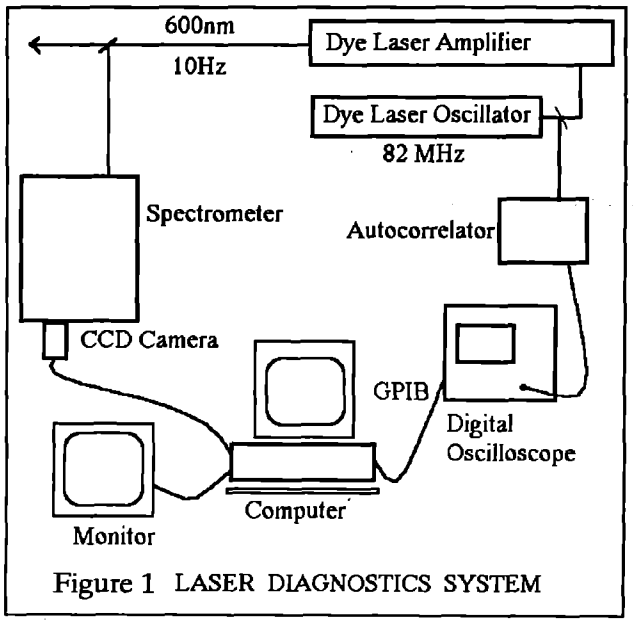

Figure 1 LASER DIAGNOSTICS SYSTEM

PERFORMANCE OF THE SYSTEM

The system has been tested with the laser operating in different conditions. Figure 2b. shows an autocorrelation trace (FWHM ~8.7ps) obtained with the sync-pumped dye laser operating with a wedge filter as the wavelength tuning element. The characteristic spike in the centre of the trace indicates the pulses to be noisy and non-transform limited. The measured

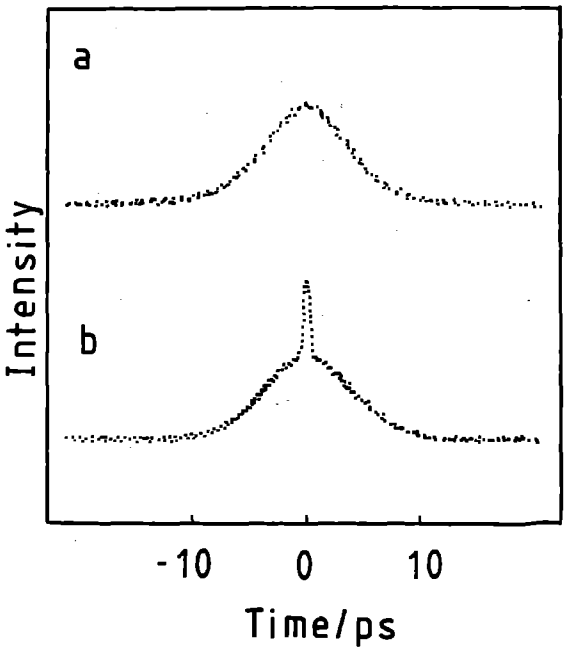

Figure 2 Autocorrelation data. (a) With external cavity feedback. (b) Without feedback.

spectra confirmed this and an example of one such spectrum is shown in figure 3b. Under these operating conditions every single-shot spectrum was different indicating each pulse to be a unique noise burst. The frequency range within which the spectrum lies gives a time-bandwidth product of ~10 and is far in excess of the 0.31 that would be expected for a smooth $sech^2$ pulse for example. However the width of the spectrum in figure 3b. ie ~2 x 10^{12}Hz is appropriate considering the 0.5ps wide noise-spike appearing in the autocorrelation.

The sync-pumped dye laser was also operated with feed-back from an external cavity. This is an established technique for stabilising the output of such lasers[4,5]. As expected the autocorrelation traces, see figure 2a., measured under these conditions lacked the central noise spike. The measured spectra were also markedly less noisy as is seen in figure 3a. Assuming the pulse shape to be $sech^2$ the time-bandwidth product for this data was 0.35 which is close to the value of 0.31[1] expected for such pulses. However the time-bandwidth products were observed to fluctuate between about 0.35 and 0.6 with a mean of 0.45. This may imply that the pulse duration or shape is fluctuating shot to shot.

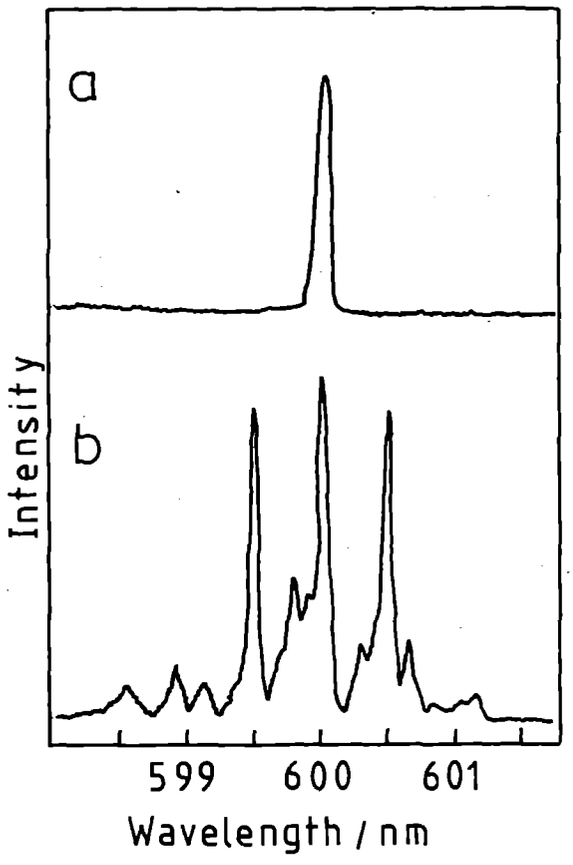

Figure 3 Spectra of Laser Pulses. (a) With feedback. (b) Without feedback.

FUTURE WORK

The system software will be modified to acquire the spectral and autocorrelation data-sets at the same time rather than in rotation as it does currently. It will also be developed to acquire diagnostic data during an experimental run so that the laser users can correlate their data with laser performance.

In due course we intend to build an averaging or single-shot second and third-order intensity autocorrelator for amplified pulses with the possibility of carrying out interferometric measurements where these are appropriate.

REFERENCES

1. K L Sala, G A Kenney-Wallace and G E Hall. "CW Autocorrelation Measurements of Picosecond Laser Pulses." IEEE Journal of Quantum Electronics QE-16, pp 909-997, 1980

2. L D Noordam, A ten Wolde and H B van Linden van den Heuvell. "Measurements of picosecond-Pulse Durations in the Ultraviolet." Rev.Sci.Instrum. Vol.60 (5), pp 835-838, 1989.

3. J-C M Diels, J J Fontaine, I C McMichael and F Simoni. "Control and Measurement of Ultrashort Pulse Shapes (in Amplitude and Phase) with Femtosecond Accuracy." Applied Optics Vol.20 (9), pp 1270-1282, 1985.

4. P Beaud, J Q Bi, W Hodel and H P Weber. Optics Comm. Vol.80, p31, 1990.

5. C J Hooker, J M D Lister and I N Ross, Variable length Transform-Limited Pulses from a Stabilised Synchronously-Pumped Mode-Locked Laser, Optics Communications, Vol 80, No 5,6, pp 375-380, 1991.

FEMTOSECOND SYSTEM DEVELOPMENT

C J Hooker and P Trenda

Rutherford Appleton Laboratory

INTRODUCTION

The previous subpicosecond source developed for the LSF [1] was a synchronously-pumped dye laser with an absorber jet in the cavity to act as a pulse-shortening device. The shortest pulses achieved using this system were around 90 femtoseconds, but the reliability and stability of the output were poor at that pulse length, and the system had to be operated at 200 fsec to obtain acceptably good behaviour. The reduction of wavelength tunability due to the saturable absorber and the difficulty of optimising both dye and absorber concentrations were also problems. The prospect of an alternative subpicosecond source using compressed, frequency-doubled, YAG pulses to synchronously pump a dye laser without the need for a saturable absorber was sufficiently attractive that an attempt was made to build such a system. In this report we describe this approach to obtaining subpicosecond pulses, and the results obtained so far.

SYSTEM DESCRIPTION

The main components of the present system are shown in Figure 1. The pulse compressor is a conventional fibre-grating device, manufactured by Femtochrome Research. The output of the modelocked CW YAG laser, normally about 8.5 Watts, is coupled into the optical fibre of the compressor, via a quarter-wave plate which provides isolation from back reflections from the fibre ends. A second quarter-wave plate restores linear polarisation after the fibre. The chirped pulses from the output end of the fibre traverse a four-pass grating compressor and are shortened to between 5 and 10 psec, the typical throughput efficiency of the complete device being about 35%. The compressed pulses are frequency-doubled in a KTP crystal, giving up to 600 mW average power in the second harmonic. Following the SHG stage it has been found necessary to include a "noise-eater" to reduce power fluctuations, which arise from mechanical vibrations in the YAG and are enhanced by the two non-linear processes to a level of around 20%, which is unacceptable for stable pumping of the dye laser. The noise-eater uses an acousto-optic modulator to diffract a variable fraction of the beam, which is dumped, while the undiffracted output is monitored by a photodiode which controls the modulator through a servo loop. Amplitude fluctuations in the main beam can be reduced to less than 1% at frequencies up to a few kHz, at the cost of a 25% loss in average power.

The dye laser is a Spectra-Physics model 375B, fitted with a sapphire jet to improve the stability of the dye stream. The three-plate birefringent filter (BRF) was modified by removing the two thicker plates, leaving the thinnest (~300 microns) as the sole wavelength tuning element. Subsequently a tuning wedge was substituted for the BRF. The output coupler mount was replaced with an alternative device having a micrometer control on the cavity length adjustment to provide increased sensitivity.

SYSTEM PERFORMANCE

When pumped with 400 mW of 532 nm light in compressed pulses, the average output power from the dye laser was between 80 and 100 mW, depending on wavelength. The output was fully tunable over the range of wavelengths between 575 and 625 nm. The pulse length was measured using a Femtochrome FR-103 XL autocorrelator, and was found to be 1.2 psec; the autocorrelator has a nominal resolution of 25 fsec. This pulse length was in fact determined by the transmission bandwidth of the BRF. The output exhibited fluctuations in average power of ±7% under the best obtainable operating conditions, and some variation in pulse length was also observed.

Replacing the BRF with a tuning wedge reduced the pulse length to 650 fsec; however, when the tuning wedge was removed, the laser became unstable and would not produce a modelocked pulse. A train of four Brewster-angle SF-10 prisms was introduced into the cavity to permit control of group-velocity dispersion, and the tuning wedge was replaced, after which the shortest measured pulse length was 400 fsec. This is the shortest pulse obtained so far, though the length was not constant, but varied between 400 and 600 fsec. Attempts to shorten the pulses further, using a slit positioned at the central plane of the prism sequence to control the bandwidth have so far been unsuccessful; as before, when the tuning wedge is removed the laser becomes unstable and does not sustain modelocking.

CONCLUSIONS

The stability of the dye laser ultimately depends on the stability of the pump. The output from the noise-eater is extremely stable and free from fluctuations in average power; however, we believe there are variations in pulse length which the noise-eater is unable to compensate for. As with the previous system of this type, lack of stability has proved to be its major problem. Although the laser would be adequate for development-type experiments, its long-term stability and reliability are not good enough for user experiments in the LSF. In view of the availability of Titanium-sapphire lasers capable of producing tunable 100 fsec pulses, it was felt that further work on this synchronously-pumped laser should be abandoned.

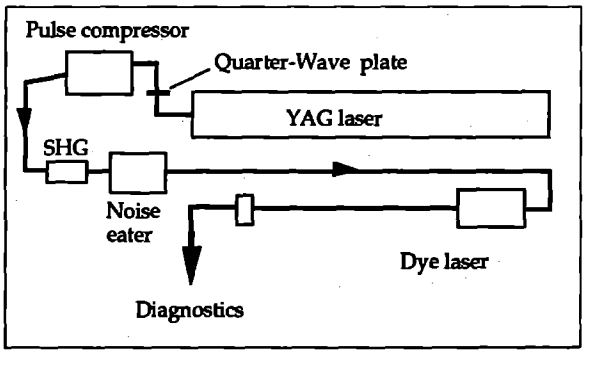

Figure 1. Schematic layout of the subpicosecond source.

REFERENCES

1. A J Langley and W Shaikh, Annual Report to the LFC (1990), RAL-90-026, p183

PERFORMANCE STUDY OF A 10 Hz PICOSECOND DYE-AMPLIFIER SYSTEM

A J Langley and W Shaikh

Laser Support Facility, Rutherford Appleton Laboratory

INTRODUCTION

The Laser Support Facility picosecond Pulsed Dye Amplifier (PDA) is used to amplify pulses of between 1 and 4 ps duration with energies around 1 nJ derived from a Synchronously Pumped Dye Laser (SPDL). We have used the PDA with different dyes to amplify various wavelengths between 550 nm and 850 nm though it is predominantly used near 600 nm. In some experiments the system is being used to amplify pulses at 746 nm which are then frequency tripled to 249 nm and amplified in a fluoride excimer-laser. We undertook a project to investigate the amplifiers performance at 746 nm and to compare it with that at 600 nm. The possibility of amplifying short-pulse, mode-locked Ti-sapphire lasers near 750 nm clearly provides further motivation for our better understanding the behaviour of our amplifier system.

THE AMPLIFIER SYSTEM

The PDA is pumped by up to 250 mJ of 532 nm radiation in a pulse of 7.5 ns from a 10 hZ injection-seeded, Q-switched, Nd:YAG (DCR3) laser with an unstable-resonator cavity. The output beam of this laser has a "doughnut" intensity distribution. There are three amplifier stages in the PDA the first two of which are pumped transversely and the final longitudinally. A diffraction limited pinhole is placed after the first amplifier at the focus of a 10 cm lens to minimise ASE transmission from the first gain length.

GAIN MEASUREMENTS

The specified gain of the PDA around 600 nm is ~0.5 x 10^6 giving final output energies of 500 µJ per pulse. However in practice, using the dye R640, 700 µJ is readily achieved at this wavelength. Gain saturation occurs for SPDL powers of ~30 mW equivalent to an oscillator energy per pulse of 0.37 nJ.

Using R700 as the amplifying medium, outputs were measured at 748 nm using a fast photodiode and calibrated ND filters. Results are shown in Figure 1. ASE levels were measured by blocking the oscillator beam and therefore only provide an upper estimate of real ASE levels. All three amplifier stages of the PDA appear to saturate at pump energies less than the maximum available. The saturation fluences for the amplified beam are ~1 mJ/cm^2 at the first and second amplifier stages and ~3.5 mJ/cm^2 at the third. The theoretical saturation fluence is given by $h\nu/\sigma$ where σ is the transition cross-section and ν the optical frequency[1]; from this the calculated saturation fluence for the dye R6G is 1.7 mJ/cm^2. Thus the measured saturation fluences compare well with those expected, assuming the dye R700 has a similar cross-section to R6G.

The total amplified energy achievable at 746 nm was around 1 mJ. Frequency doubling yielded energies of ~130 µJ at 374 nm using a 2-3 mm diameter beam and a 24 mm length KD*P crystal at a phase-matching angle of 47 degrees. Frequency mixing this doubled light in a 8 mm BBO crystal with the residual fundamental at 746 nm gave ~15 µJ at the tripled wavelength of 249 nm.

CONCLUSIONS

Ideally, the PDA should be operated near or above gain saturation so that the amplified pulse energy is less effected by fluctuations in the oscillator and pump energies. This may also help to avoid introducing chirp to the amplified pulse[2]. By attenuating the pump beam to the various amplifiers it is possible to optimise the gain and minimise levels of ASE. In practise we find that when very low levels of ASE are desired ie, <5% they can be achieved by simply reducing the pump energy to the first amplifier and spatially filtering the final output. This is because the ASE generated in the first gain-length is usually the most important.

Figure 1

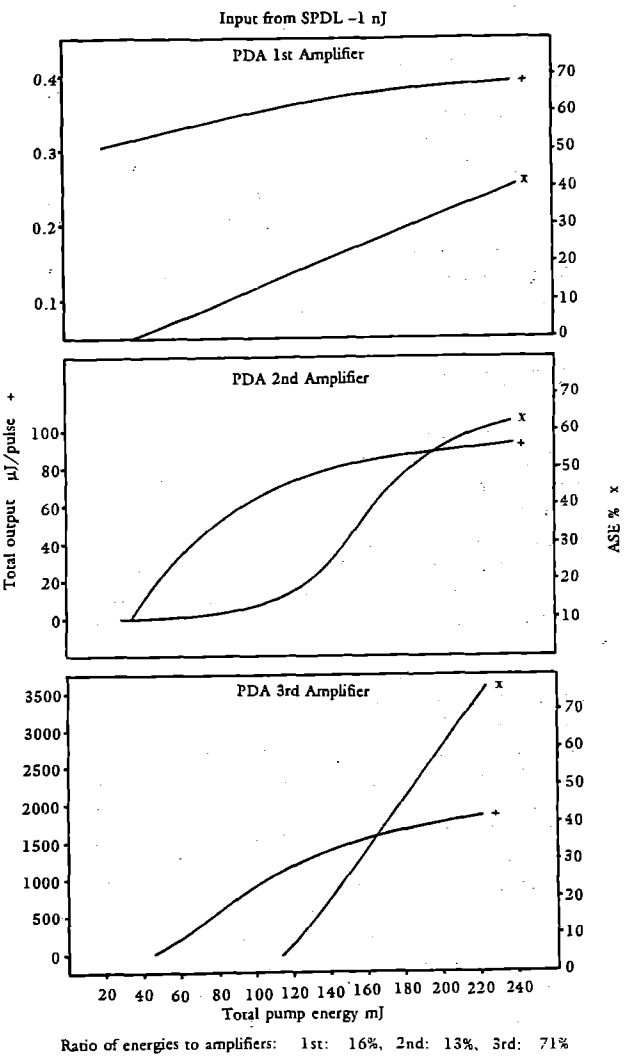

Ratio of energies to amplifiers: 1st: 16%, 2nd: 13%, 3rd: 71%

The final amplified output beam still shows some "doughnut" structure even though it is above gain saturation. Given the available pump energy to the final amplifier, it would be worthwhile investigating improvements in the near field quality of the amplified beam using a Bethune cell.

The gain measurements reported here demonstrate the possibility of pumping two dye amplifiers for multiple wavelength operation whilst achieving saturated gain albeit with less energy per amplified pulse.

REFERENCES

1. A E Siegman, "Lasers", University Science Books, California, (1986).

2. G Szabo, Z Bor and A, "Phase-Sensitive Single-Pulse Autocorrelator for Ultrashort Pulses", Optics Letters Vol 13, No 9, pp 746-748, (1988).

TIME RESOLVED STUDIES OF SINGLET OXYGEN, ($^1\Delta_g O_2$)

A. Beeby, S. Bishop, A.W.Parker*, M.S.C. Simpson and D.Phillips
Department of Chemistry, Imperial College, London SW7 2AY
* Rutherford Appleton Laboratory, Didcot, Oxon, OX11 0QX

Introduction

Singlet oxygen, ($^1\Delta_g$ O_2) is a highly reactive, shortlived intermediate, believed to be an important agent in the destructive effects seen in biological systems; in particular it is thought to be the major cytotoxic species involved in the photodynamic therapy of tumours. Singlet oxygen may be generated by energy transfer from an excited electronic state of a dye to ground state molecular oxygen ($^3\Sigma_g$ O_2), and is detected either by trapping with a suitable substrate or directly by the characteristic $^1\Delta_g$ -> $^3\Sigma_g$ phosphorescence at 1270nm. Using pulsed laser excitation of a photosensitiser and time resolved detection of the luminescence it is possible to gain information about the quantum yield of formation of $^1O_2$, and also the kinetics of non-radiative decay or quenching by added substrates. The lifetime of $^1O_2$ is strongly influenced by solvent; in CCl_4 the lifetime is 26ms but in solvents containing O-H or C-H groups the lifetime is much reduced because of efficient non-radiative relaxtion of the oxygen by an interaction with vibrational overtones of the solvent. Thus in H_2O the lifetime of $^1O_2$ is only 4μs compared to 55μs in D_2O. A major drawback with the direct observation of the luminescence is the very low luminescence efficiency, of the order of 10^{-5} to 10^{-6}, due to the transition being strongly forbidden. The time resolved detection of singlet oxygen requires a high sensitivity near infra-red detector with a fast, sub microsecond, time response. Commercially available photomultipliers have virtually no sensitivity in this region therefore a germanium photodiode was the preferred option.

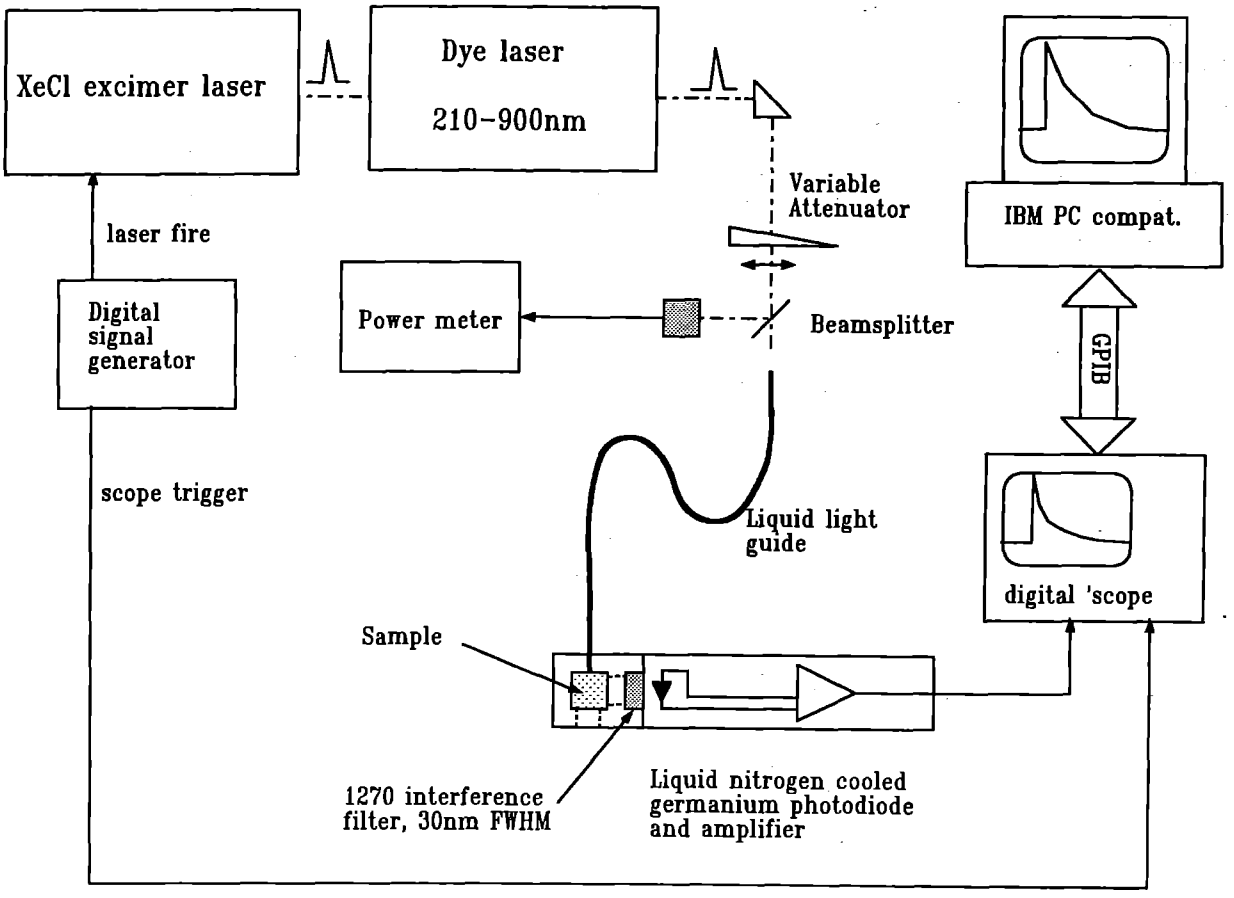

Figure 1. Schematic diagram of time resolved singlet oxygen detection apparatus based at Rutherford Appleton Laboratory..

Apparatus

The system based at RAL utilises a North Coast EO-817P liquid nitrogen cooled germanium photodiode and low noise amplifier combination. The sample, held in a 1cm cuvette, is irradiated by the output of either an excimer laser or excimer pumped dye laser, (10ns pulse duration, 10-2000μJ per pulse), delivered by a 5mm diameter liquid light guide which provides more reproducible and even illumination of the sample. The luminescence is monitored 90° to the excitation beam and scatted light and/or fluorescence is removed by a 1270nm interference filter with a 30nm bandpass. The output from the photodiode is processed by a digital storage oscilloscope, DSO, and the decay transferred to an IBM PC for data analysis. Synchronisation of the laser and the DSO was achieved using a digital signal generator.

Performance

The North Coast detector has a switchable time response, designated high and low; the responses to the scattered laser pulse have FWHM of 300 and 600ns respectively. Although the detector has greater sensitivity in low time response mode the output pulse suffers from a long lived tail which can interfere with the $^1O_2$ signal. To demonstrate the generation of $^1O_2$ a 10^{-6}M solution of zinc tetraphenylporpyhrin in aerated toluene was irradiated with a single 514nm pulse. The log plot of the 1270nm emission intensity shown in figure 2 shows a first order decay, with a lifetime of 26μs, over a period of 4 lifetimes which is approaching the limits of the 8-bit digitiser used in the DSO. When phthalocyanines are used as photosensitisers the observed emission at 1270nm contains a spike coincident with the laser pulse, attributed to fluorescence from the sensitiser. Conventional fluorescence spectra of these compounds shows no emission at these wavelengths although it is clear that the red edge does extend out into the near infra red. This is not necessarily a problem for the detection of $^1O_2$ since the fluorescence is very short lived. However, if the intensity of the spike is very much greater than that of the $^1O_2$ then the input amplifier of the DSO saturates and prevents data acquisition. The only way to avoid this is to reduce the pump light intensity. A decay from disulphonated aluminium phthalocyanine in D_2O is shown in figure 3 and clearly shows the spike and ringing due to the fluorescence.

The quantum yield of $^1O_2$ fomation, Φ_Δ, can be readily determined with this apparatus by comparing the gradients of the $^1O_2$ signal *vs* laser power graphs of a standard and unknown. It is important that the two samples are compared in the same solvent because the radiative rate constant of $^1O_2$ is solvent dependent. Using this method the values of Φ_Δ for acridine, tetraphenylporphyrin, zinc tetra-phenylporphyrin and C60 in toluene, pumped at 308nm were determined and are compared to the literature values in table 1.

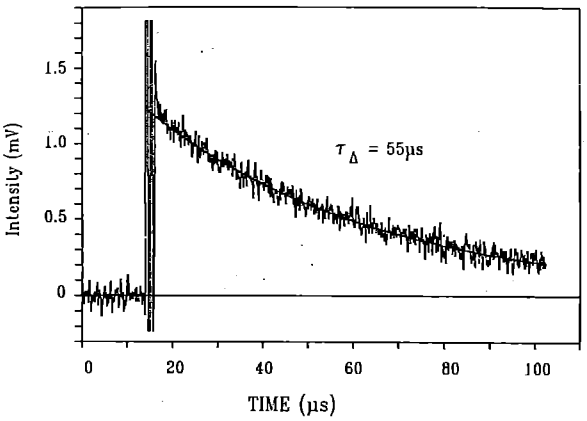

Figure 3. Decay of $^1O_2$ generated by disulphonated aluminium phthalocyanine in D_2O, pumped at 670nm, 16 pulses at 0.1mJ per pulse.

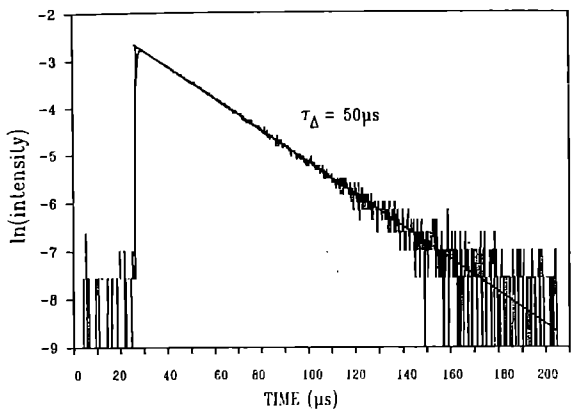

Figure 2, Decay of 1270nm emission of $^1O_2$ generated from ZnTPP in toluene, excitation 514nm, 1mJ single shot.

Table 1.

	Determined(±5%)	Lit.[Ref]
Acridine	0.84	0.84 [1]
H_2TPP	0.64	0.58 [2] & 0.62 [3]
ZnTPP	0.73	0.73 [2]
C60	0.78	0.76 [4]

References

1. R.W.Redmond and S.E.Braslavsky, Chem.Phys.Lett. (1988) 148 523
2. G.Rossbroich, N.A.Garcia and S.E.Braslavsky, J.Photochem. (1985) 31 37
3. R.Schmidt and E.Afshari, J.Phys. Chem. (1990) 94 4377-4378
4. J.W.Arbogast, A.P.Darmanyan, C.S.Foote, Y.Rubin F.N.Dieterich, M.M.Alverez, S.J.Anz and R.L.Whetten J.Amer.Chem.Soc (1991) 95 11-12

AMPLIFICATION OF 150 PICOSECOND PULSE TRAINS FOR HIGH AVERAGE POWER KrF LASER-PLASMA X-RAY GENERATION

I C E Turcu[1], I N Ross[1], M Steyer[1], M Amit[3], B Soom[4], K Osvay[1], A Hening[5], R Kaur[1] and S Quayum[1]

[1]Rutherford Appleton Laboratory, [2]School of Biochemistry, University of Birmingham, [3]Nuclear Research Centre-Negev, Beer-Sheva, Israel, [4]Institute of Laser Energetics, University of Rochester, USA, [5]Institute of Atomic Physics, Bucharest-Magurele, Romania

We continued the work presented in last year's Annual Report on the investigation of simple and efficient generation of picosecond pulses at 249 nm, their efficient amplification in a high repetition rate KrF amplifier and the use of the amplified pulse train to increase by a factor of 3 or more the efficiency of generating X-rays of keV photon energy.

The Quenched Dye Laser (QDL) was used to generate 150 ps pulses at 597 nm. These pulses passed through two dye amplifiers and a frequency-doubling crystal to generate a 10-20 μJ pulse at the KrF laser wavelength of 248.6 nm.

Two methods were investigated for the generation of trains of pulses:

(1) An active etalon with round-trip gain of unity was constructed around the second dye amplifier. The output consisted of 10 pulses 200 ps wide. 2 ns delay between pulses and an average of 10 μJ energy per pulse. This pulse train was amplified double-pass through the KrF amplifier to a total energy of 150-200 mJ. Conversion efficiencies of 1% for solid steel targets and 0.5% for copper tape targets are a factor of 3 higher than for 20 ns unmodulated KrF laser pulse.

(2) A passive "pulse-stacker" consisting of three 50% beam-splitters and four HR mirrors (all at 248 nm) was placed after the frequency doubling BBO crystal. For a 20 μJ, blue pulse input, the "pulse-stacker" generated four 1 μJ pulses. The interpulse time of 2.3 ns corresponds to $^1/_4$ of the round trip time of the injection mode-locked unstable resonator KrF amplifier. The amplifier output consists of 10 pulses with a total energy of 250 mJ. X-ray conversion efficiencies were similar with experiment (1) but more energy was extracted from the laser.

Both methods of pulse-train generation and amplification gave satisfactory results. A further factor of three increase in conversion efficiency is expected from perfecting the techniques, especially by restricting the amplified-spontaneous-emission level.

In conclusion the higher X-ray output and smaller amounts of target debris will greatly improve the microlithography and DNA repair experiments while the cleaner (lower background) X-ray spectrum will be beneficial for the scanning X-ray microscopy experiments.

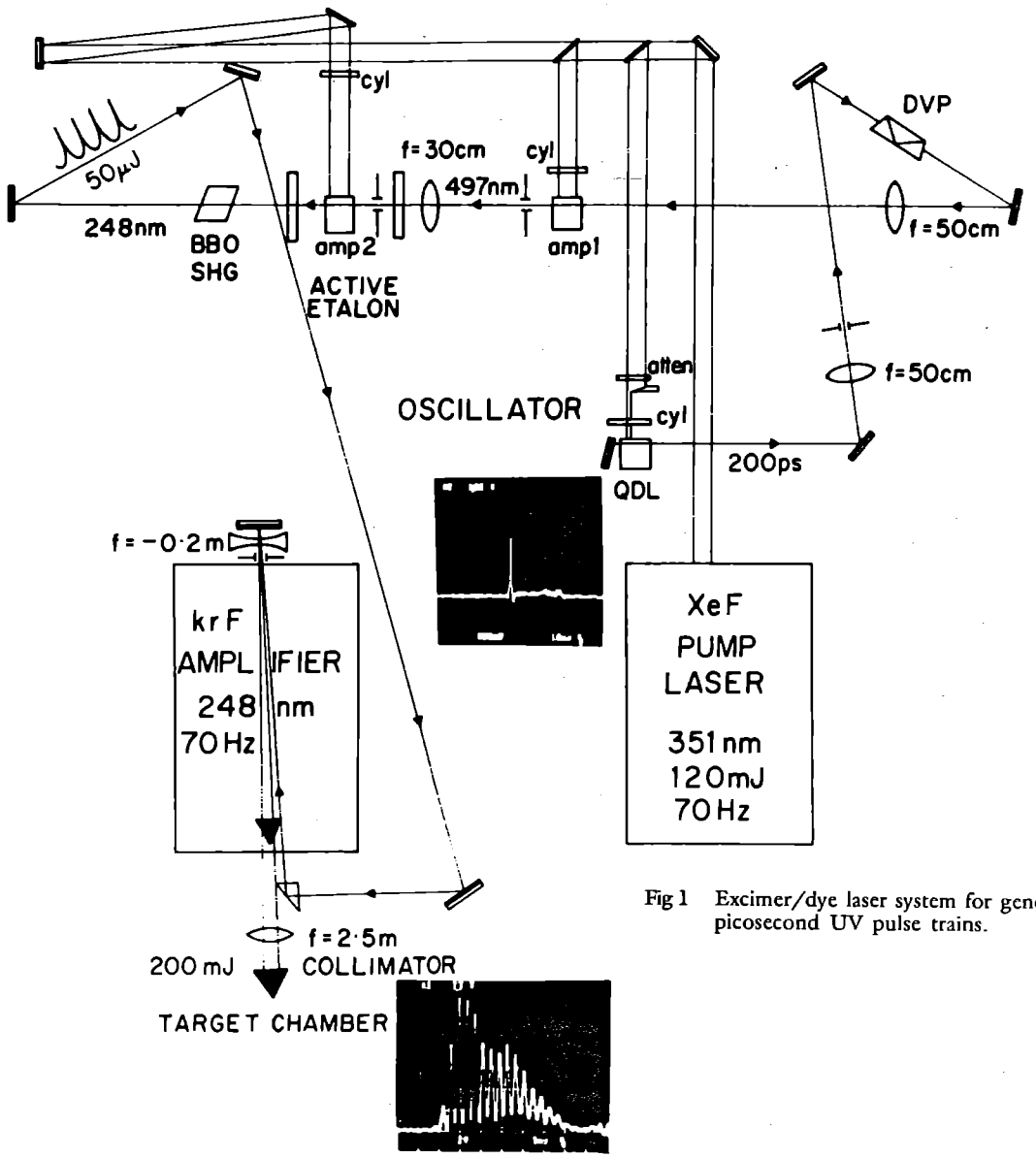

Fig 1 Excimer/dye laser system for generating picosecond UV pulse trains.

SPATIAL COHERENCE OF A REPETITIVE LASER-PLASMA POINT X-RAY SOURCE IN THE WATER WINDOW SPECTRAL REGION

H Daido[1], I C E Turcu[2], I N Ross[2], M S Schulz[3], M Steyer[2], M Amit[4], J G Watson[2] and R Kaur[2],

[1]Institute of Laser Engineering, Osaka University, Japan
[2]Rutherford Appleton Laboratory
[3]King's College London
[4]Nuclear Research Centre-Negev, Beer-Sheva, Israel

At Rutherford Appleton Laboratory, a pulse train of 20 ns duration which contained individual 200 ps pulses spaced by 2 ns was used to irradiate the target in order to improve the X-ray conversion efficiency. Two Questek excimer-laser systems with a quenched dye-laser system front end could be operated up to 100 Hz repetition rate. A 248 nm laser-pulse train with an energy of 130 mJ per shot was focused on a 15 μm-thick moving Mylar ($C_{10}H_8O_4$) tape target to a focal spot diameter of 10 μm by an f/3.6 optics. The peak intensity on the target was 10^{14} W/cm^2. The horizontal laser beam was incident at 45° in the vertical plane on the tape target, as shown in Fig 1. The water window X-rays were monitored with a 0.5 μm thick vanadium-filtered silicon PIN X-ray diode. The absolute emission of the carbon Lyman-α line was measured with a transmission grating spectrometer using calibrated Kodak S101-01 soft X-ray film to be ~ 3×10^{12} photons/shot/sr, giving a conversion efficiency of ~ 10^{-2}. The experiments were performed at 20 Torr of helium (flow rate: 5 l/mm) and 20 Torr of nitrogen with a similar flow rate in order to remove target debris. To generate a monochromatic source on the carbon VI Lyman-α line (wavelength - 3.37 nm), nitrogen gas is used in the target chamber as an X-ray filter suppressing the lines whose wavelengths are shorter than the nitrogen K-edge (wavelength = 3.1 nm) and attenuating longer wavelength carbon lines such as helium-α line (wavelength = 4.03 nm). The individual lines have inherently narrow spectral broadening of 10^4 derived from Doppler broadening and that of 10^3 if the dynamic-Stark broadening is taken into account. The monochromacity of the Lyman-α line suffered due to the adjacent line in the present experiment and should be improved in the future by isolating a single X-ray spectral line. The soft X-ray source sizes under both gas-flowing conditions were measured using a 200 nm aluminium filtered X-ray pinhole camera with a 6 μm diameter pinhole and a magnification of 8.8. The camera was placed along the same direction as the slit pairs, as shown in Fig 1, viewing the X-ray source at 45°. Under the nitrogen-flowing condition, 10 x 40 μm^2 elllipsoidal-shape images were taken which were 0.85 times smaller than those obtained under the helium conditions. The 10 μm width corresponds to the laser focal spot diameter while the 40 μm length stems from the expanding plasma plume which could be much reduced by shortening the laser pulse length further or by adjusting the viewing angle so that the camera points along the axis of the expanding plasma. The pinhole camera was also used to determine the shot-to-shot stability of the source position which was found to be ± 2 μm.

For a point quasimonochromatic X-ray source, good spatial coherence can be given within the angle defined as the source wavelength divided by its maximum size[2]. The well-known Young's interference experiment was performed to measure the spatial coherence. The distances between the X-ray source and the slits and the slits and the film were 31.7 and 33.4 cm respectively. Three slit pairs having an individual width of 0.5 μm and the separations of 10.5, 20.1 and 59.0 μm respectively, were made on the same 250 nm thick platinum foil using a gallium ion beam microfabrication machine. The slit pairs were separated by 0.7 mm from one another. Typical soft X-ray fringe patterns recorded on the calibrated S101-01 film under nitrogen and helium flowing conditions were taken with overlapped exposures (6 min at 20 Hz repetition rate). Fig 2 shows the X-ray fluence profile taken with the slit pairs whose separation are 10.5 μm. The observed data agree closely with the calculated fringe pattern if one assumes the dominant wavelength of 3.37 nm. The fluence profiles of these X-ray fringes are taken with a computer controlled densitometer which allows the calculation of the visibility and quantitative degree of spatial coherence at the position of the slit pair. The fringes of the slit pairs of 10.5 and 20.1 μm separation gave visibilities of 0.62 ± 0.1 and 0.33 ± 0.06 respectively.

In summary, we have demonstrated the coherence properties of the repetitive KrF laser plasma pointlike X-ray source emitting quasimonochromatic radiation at a 3.37 nm wavelength in the water window spectral region. Soft X-ray fringes of the Young's interference experiment were obtained with a visibility of 0.62 ± 0.1 with a slit pair of 10.5 μm separation at a distance of 31.7 cm from the source. The present X-ray source can be used to take a hologram or transmission scanning X-ray micrograph with a reasonable exposure time.

The authors wish to acknowledge M H Key, W T Toner, A G Michette, S Nakai, Y Kato, C Yamanaka, K Yamashita and T Namioka for thir help and encouragement for this work and also to acknowledge P Prewett, G Arthur, F Goodall, C Brown and P Charalambos for the microfabrication of the slit pairs. The SERC contribution to the work was partially supported by the UK Department of Trade and Industry through the EUREKA European research intiaitive (EU 213 excimer laser project).

REFERENCES

1. D G Goodwin and E E Fill, J Appl Phys 64, 1005 (1988).

2. G Zeng, H Daido, T Togawa, M Nakatsuka, S Nakai and H Aritome, J Appl Phys 69, 7460 (1991).

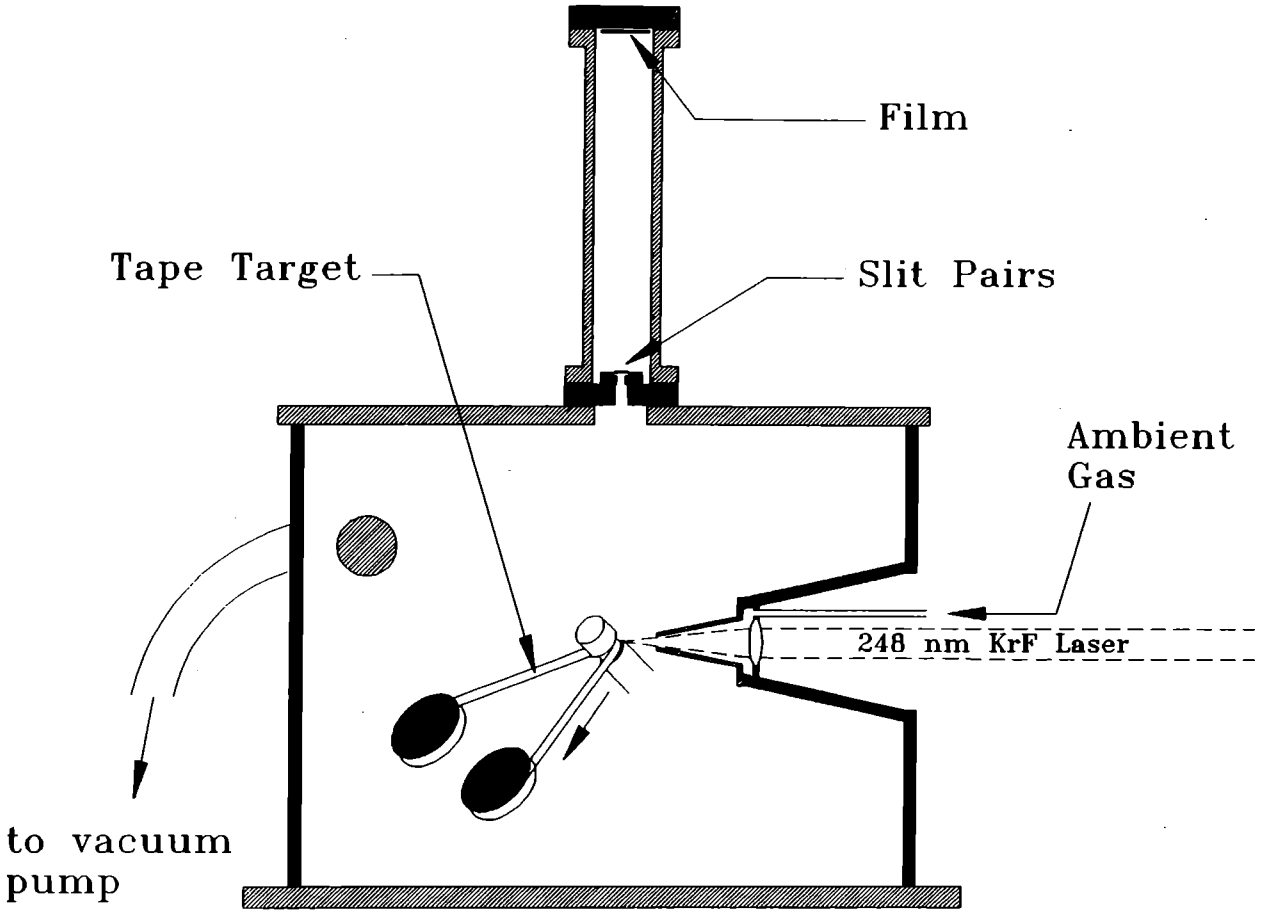

Fig 1 Schematic diagram of the experimental setup.

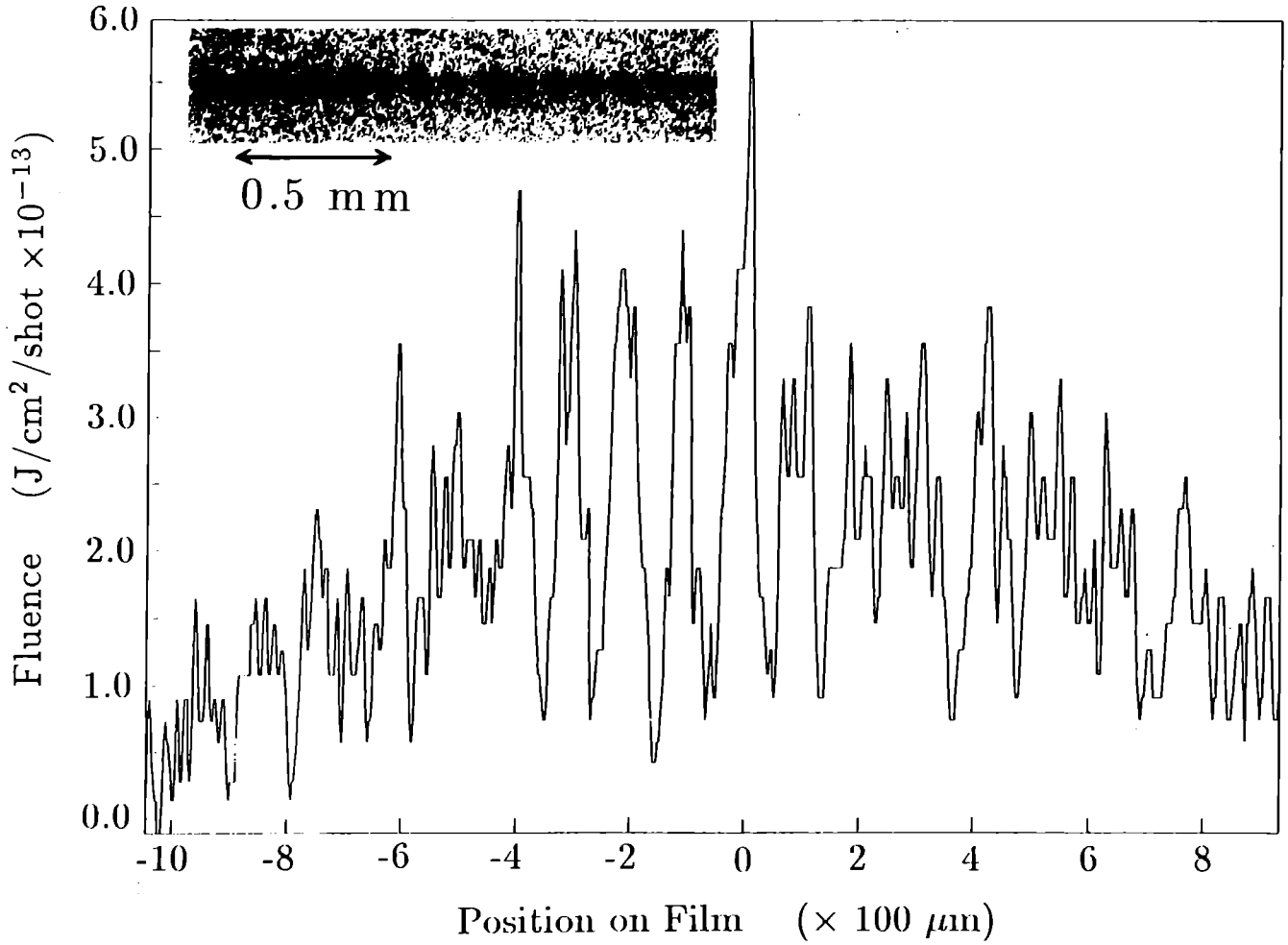

Fig 2 The fluence profile of soft X-ray fringes taken with 20 Torr of nitrogen. The separation of the slit pair was 10.5 μm.

AUTOMATIC SYSTEM FOR DNA REPAIR EXPERIMENTS BASED ON HIGH POWER KrF LASER-PLASMA X-RAY SOURCE

I C E Turcu[1], I N Ross[1], C J Reason[1], C W Wharton[2], J Edgerton[2], W Meaking[2], R A Meldrum[2], A R Damerell[1], W Lester[1], C Brown[1], K Miles[1], R Kaur[1], S Quayum[1],

[1]Rutherford Appleton Laboratory
[2]School of Biochemistry, University of Birmingham

To successfully apply the new source of X-rays (described in the previous report) to University user experiments, we designed, constructed and implemented an integrated fully computerised system comprising of laser-plasma X-ray source of 1 nm + excimer laser irradiation at 351 nm + biological rig for automatic processing of up to 10 dishes with live cells in solution, and atmospheric pressure. The biochemical application is: good time resolution measurements of repair-rate of DNA damaged with X-rays. Here are the new features of the system:

(1) Increased X-ray conversion efficiency at hv - 1.2 keV, resulting in up to 35 rad/shot (average 25 rad/shot) delivered through an aluminium plastic filter (1 μm parylene + 0.1 μm Al). Presently the X-ray source delivers a dose of 1 kilorad in two seconds (at 10 Hz) to a biological specimen in water placed at 40 cm from the source for uniform illumination. At 50 Hz a dose of 1 krad will require only 800 ms. The dose of 50-100 rad required in the present DNA experiments is delivered in 100-200 ms at 20 Hz.

(2) New target mechanism allowing long term operation (days) of copper tape-targets without opening chamber.

(3) New software to control the laser X-ray source-biochemical processes, allowing great flexibility in setting up different sequences for the 10 dishes exposed in one experiment.

(4) New electronics interfacing the computer to the system; new fast computer controlled laser shutters, increasing the exposure accuracy, lifetime of tape target and dyes in the picosecond front-end; new fast, computer controlled switch-out mirror at the output of the XeF pump laser, allowing the UV (351 nm) exposure of the dishes immediately after the X-ray exposure. The use of one laser for both dye pumping and UV exposure brings savings of the cost of one excimer: approximately £50K.

(5) New plunger for electrical permeabilisation of cells, using platinum foils (2 mm wide x 100 μm thick), 2 mm spacing, instead of wire electrodes. This proved very rugged in operation and handling.

(6) New safety features: perspex enclosure for the DNA exposure rig, to protect against beta radiation; perspex filter enclosure for the picosecond dye system to protect against UV (351 nm) and visible (496 nm) radiation; aluminium tubes enclosing the UV (351 nm) beam path to the dye lasers and to DNA rig.

In conclusion we have demonstrated for the first time, subsecond X-ray exposures + permeabilisation + UV exposure + full computer control of any desired biochemical + radiation sequence.

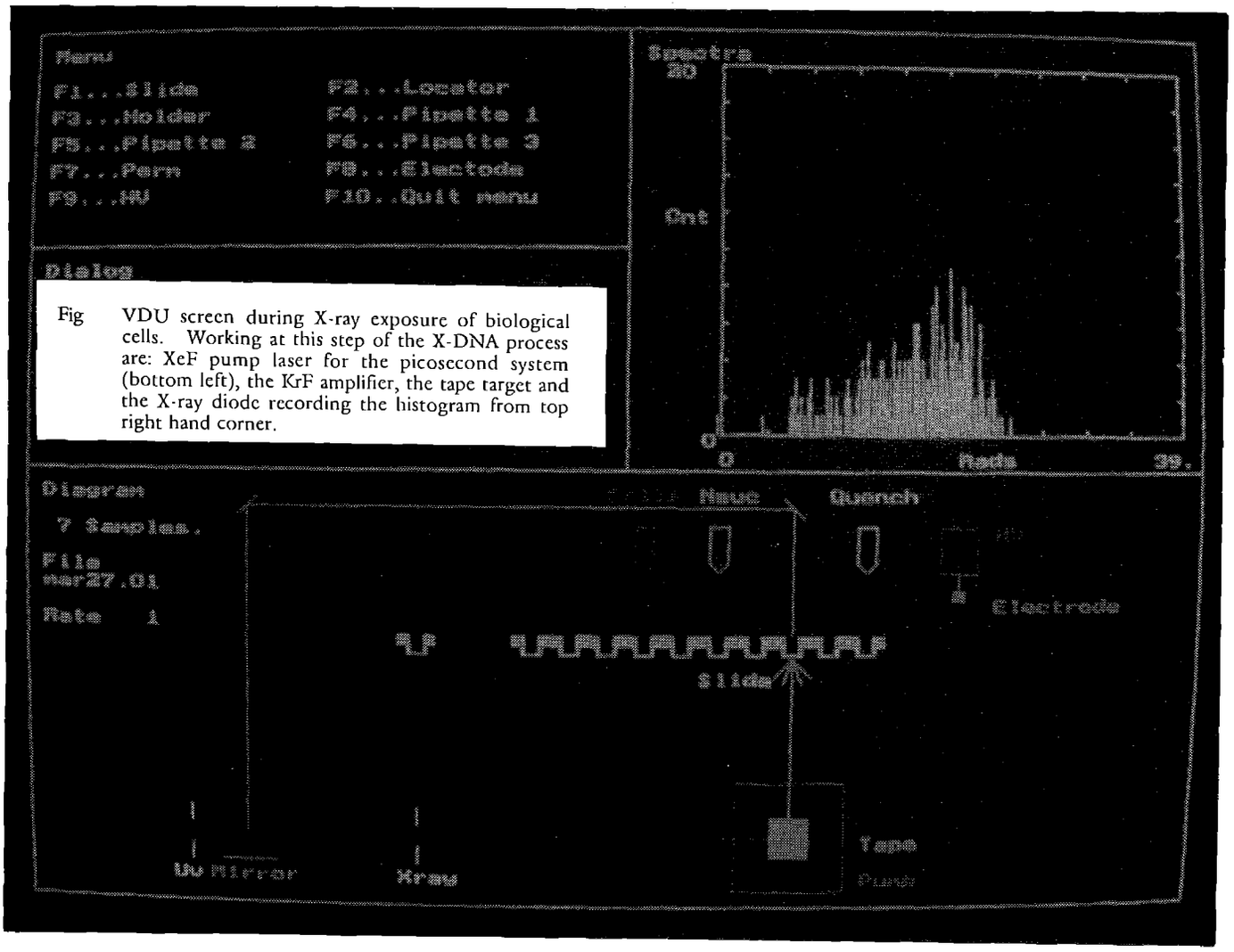

Fig VDU screen during X-ray exposure of biological cells. Working at this step of the X-DNA process are: XeF pump laser for the picosecond system (bottom left), the KrF amplifier, the tape target and the X-ray diode recording the histogram from top right hand corner.

KeV AND "WATER WINDOW" X-RAY EMISSION MEASUREMENTS WITH 4 ps KrF LASER PULSES

I C E Turcu[1], I N Ross[1], G J Tallents[2]

[1]Rutherford Appleton Laboratory
[2]Dept of Physics, University of Essex

Presently a sustained world-wide research effort is dedicated to the development of efficient, High Peak Average Power Laser Generated Plasma X-ray Sources for such applications as: microscopy*, biochemistry*, lithography*, surface physics, etc (* shows applications actively pursued in the LSF).

Nevertheless, using an irradiance of 10^{13} W/cm^2 on target with a laboratory sized commercial, repetitive, KrF (0.249 μm wavelength) excimer laser, a maximum of 0.2% conversion to Cu-L shell KeV X-rays from laser pulses of 500 mJ energy, 20 ns duration, was obtained, focused to 10 μm diameter spots on target[1]. Time resolved measurements in the KrF laser experiments showed that the KeV X-ray emission was cut off a few nanoseconds from the beginning of the laser pulse, such as the overall energy conversion efficiency was low while the peak power conversion efficiency was around 10%. This prompted the breakthrough experiment by the group at RAL and Imperial College[2] in which 100 ps XeCl excimer laser pulses of 10 mJ energy were focused to 10 μm spots on Fe and Cu targets to generate KeV X-rays with energy efficiencies of 4% and 1.4% respectively (an increase in efficiency of an order of magnitude compared to 20 ns, 500 mJ excimer pulses). Moreover, by using a new technique of injection modelocking the excimer laser with 100 ps pulses, over 100 mJ pulse-trains can be generated (good excimer energy extraction) and converted to KeV X-rays with an efficiency of 2.4% and 0.5% for Fe and Cu targets respectively[2]. The techniques of Ref 2 have been implemented over the past year in LSF LABA with the Questek excimer laser system capable of operating at 100 Hz repetition rate and 40 W average power at 0.249 nm wavelength. As a result the Birmingham University experiment on "Repair of soft X-ray DNA damage in surface adherent cells" can be performed with time resolutions of less than one second (the exposure time required to deliver an X-ray dose of 100 rad is 0.1 seconds).

The KrF laser-plasma X-ray generation experiments performed so far showed that for small focal spots on target (10 μm), a much shorter pulse (picoseconds) and higher irradiance (10^{14} W/cm^2) are required for maximum X-ray conversion efficiency, compared to large focal spot experiments (which require large energy/shot generated by large, single shot laser installations). The plasma physics in these experiments is rather complicated mainly because of the small focal spot. Nevertheless one could argue that since the 10 μm spot is much smaller than the characteristic length for lateral heat flow from a plasma[3], the large outward flux of heat should be balanced by a large input power density from the laser.

To test these ideas, we have performed some short pulse X-ray measurements in two half days during the "Chirp Pulse Amplification" experiment in November 1991, taking advantage of the four picosecond pulse at 0.249 nm wavelength and up to 10 Hz repetition, which was piped from Lab D to be amplified to 20 mJ in Lab A (the X-ray source laboratory). This pulse was focused by an f/3 aspheric singlet lens to 10 μm spots and maximum irradiance of 4E15 W/cm^2. To measure the conversion efficiency scaling with irradiance, the energy on target was varied by inserting an NO_2 absorber cell in the laser beam. The absolute X-ray emission was measured by filtered, calibrated PIN X-ray diodes from several tape targets: copper, aluminium and mylar. A Beryl crystal spectrometer was used to obtain Al-K shell and Cul-L shell spectra. The data analysis showed that the laser to X-ray energy conversion efficiency for all targets is very high (Fig 1).

(1) 10% for Cu L-shell (hν ≈1.2 keV), at an irradiance of 4E15, which is the maximum obtained with single shot glass lasers[4] with 15 J energy on target but an irradiance of only 5E12 W/cm^2. An X-ray spectrum was obtained - with only 120 laser shots of 15 mJ each - showing the characteristic neon-like structure but with strong Cu XXII lines indicated on increased plasma temperature, Fig 2.

(2) 7% for Carbon K-shell (hν≈0.4 keV). The efficiency increased only by a factor of 5 for an order of magnitude variation in irradiance.

(3) 0.4% for Aluminium K-shell (hν≈1.6 keV). No saturation with irradiance is observed. The electron density of the Al plasma was measured to be (1.6-2.0) E22 cm^{-3}, from the Stark broadening of the Helium-beta line of Al XIII.

In conclusion the use of 4 ps KrF pulses enhance the efficiency of the absorption X-ray source by a factor of 5. Coupled with the possibility of a smaller focal spot (hence X-ray source size) this could enhance the X-ray spectral brightness of the source by an order of magnitude.

REFERENCES

1. F O'Neill, G M Davies, M C Gower, I C E Turcu, M Lawless and M Williams, SPIE 831, 230 (1987).

2. F O'Neill, I C E Turcu, D Xenakis and M H R Hutchinson, Appl Phys Lett **55**, 2603 (1989).

3. P D Gupta, Y Y Tsui, R Popil, R Fedosejevs and A A Offenberger, Phys Fluids **30** 179 (1987).

4. M Chacker, H Pepin, V Bareau, S Boily, B Lafontaine, B Fabbro, I Thoubans, B Faral, J F Curie, D Nagel and M Peckerar, SPIE 733, 58 (1987).

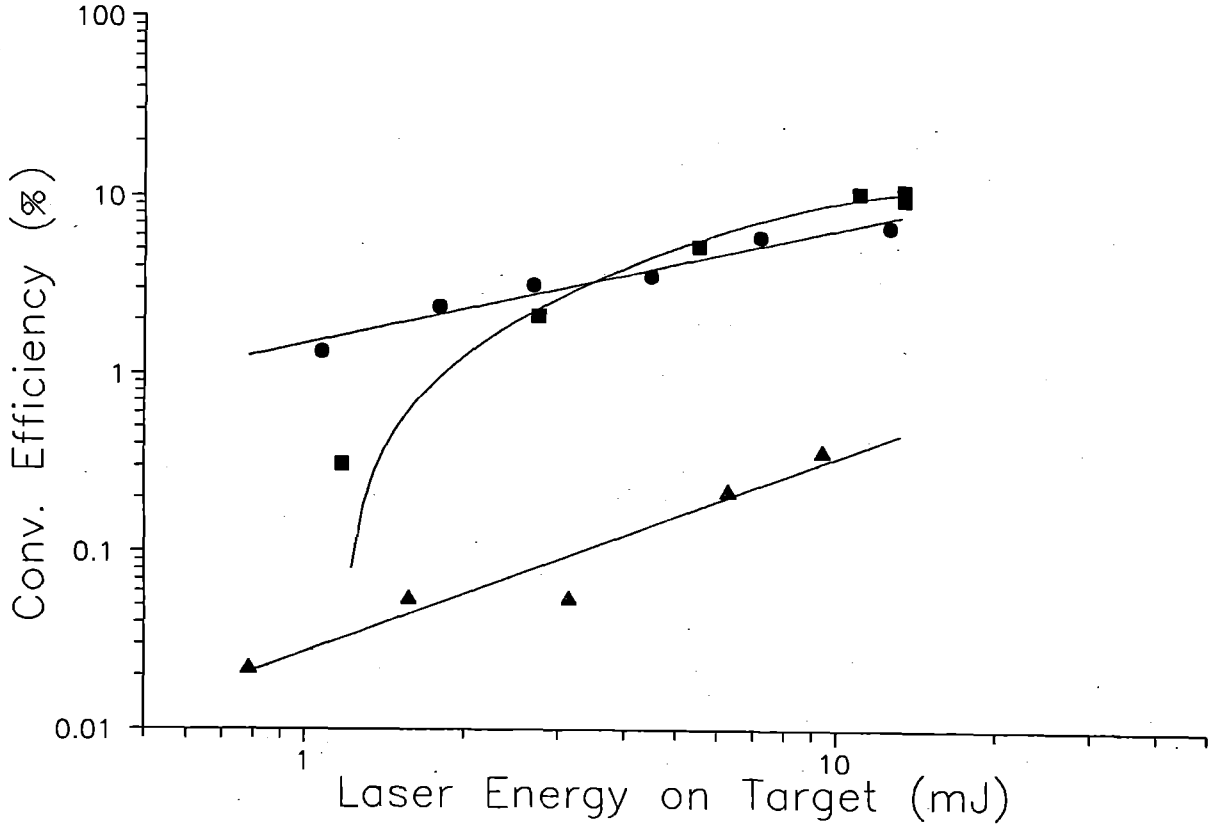

Fig 1 X-ray energy efficiency with 4 ps KrF pulses conversion recorded with filtered PIN X-ray diode. ■ Copper tape targets, 10 μm Befilter (hν ~ 1.2 keV), ▲Aluminium tape target, 10 μm Be filter (hν ~ 1.6 keV), • Mylar tape targets, 0.5 Vanadium filter (hν ~ 0.4 keV)

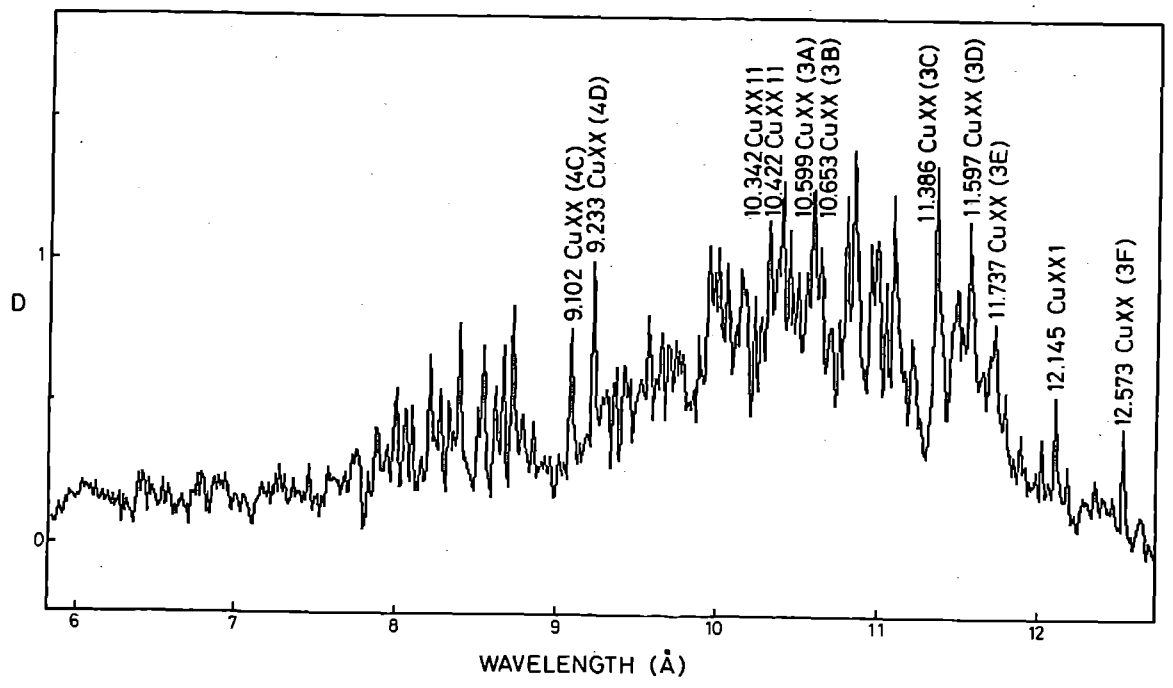

Fig 2 Copper spectrum obtained from 120 KrF shots of 15 mJ, 4 ps and recorded on Kodak DEF X-ray film with a Beryl crystal spectrometer filtered with 10 μm Beryllium.

LASER SUPPORT FACILITY OPERATIONS AND DEVELOPMENT

A total of 54 user experiments at RAL and 18 loans took place during the year. Applications exceeded allocations by a factor of 1.3. The distribution by subject area is given in Table I. The reliability of equipment at RAL continued to be very high. The first steps have been taken to replace some of the older loan pool lasers with the purchase of two new lasers. Developments of laser and experimental detection systems continued throughout the year and are reported individually elsewhere in this section.

Table 1

	Physics	Chemistry	Biology
Applications	20%	55%	25%

THE PICOSECOND LASER LABORATORY - Andrew J Langley and Waseem Shaikh

A total of 13 experiments were carried out using the picosecond facility. Once again these have ranged widely across the scientific disciplines with much of this work appearing in the current annual report.

The picosecond laser system has worked very reliably over the past year operating for over 95% of the available time. The Spectron mode-locked Nd:YAG laser has continued to be a reliable source to pump up to three picosecond dye-oscillators simultaneously. Over the past year we have operated the scheme where only one of the three oscillator systems is scheduled for user experiments at any one time with that experiment taking priority in terms of available resources. This has enabled available RAL and collaborating University staff to conduct off-line development using the other oscillators.

During the past year new wavelengths to meet the experimental needs of users have been generated with the 10 Hz laser system and are now available. Pulses of 10 mJ at 249 nm have been generated by frequency tripling picosecond pulses at 746 nm which then are sent via a 25 metre beam-pipe from the picosecond laboratory to a laboratory containing fluoride-excimer lasers for amplification. This has enabled researchers to carry out the CPA and X-ray generation experiments mentioned above. For transient absorption experiments we have generated pump pulses of ~50 μJ at 353 nm by doubling ~706 nm for simultaneous use with the probe wavelength at 425 nm generated by mixing 700 nm with residual 1064 nm Q-switched YAG radiation. Also for pump-probe experiments we have generated pump energies of ~50 μJ per pulse at 300 nm by frequency doubling 600 nm whilst simultaneously using continuum generation to generate sufficiently intense and stable probe pulses between 450 nm and 750 nm.

Developments to the pump and probe apparatus have included the commissioning of a new 33 MHz Viglen computer to replace the old IBM PC for data gathering and control. The system works well and users now have access to both RAL written software, which is best applied to investigate saturated or non-linear behaviour, and software donated by the Loughborough group. The latter group's software is best at obtaining data in a convenient, largely automatic way which novice users in particular will appreciate. The data gathered is compatible with both versions of the software.

The development of the Copper-Vapour-laser pumped dye-amplifier system has reached a most satisfactory stage with proven reliability for user experiments; several of which have been carried out this year. As appears elsewhere in this report (Section C4) the wavelength range has been extended and stability improved. Similarly, much progress has been made with the time-correlated single-photon counting apparatus. The time resolution has been improved to 60 ps and so has the long term stability.

Finally an area of development for which there has been considerable user pressure is the monitoring of picosecond laser performance. With this in mind we are developing a system for the simultaneous capture and storage of autocorrelation and spectral data during an experimental run. A description of the diagnostic system constructed and progress made thus far appears in Section C4 of this report.

NANOSECOND LASER FACILITY - Anthony W Parker and Susan M Tavender

The facility was fully scheduled throughout the year normally with two users working in parallel, sometimes three. Reliability continued to be very good with downtime due to laser faults less than 2%.

A near infra-red (800-1700 nm) fast response (200 ns) germanium photodiode (liquid nitrogen cooled) detector has been purchased. Full specifications of this detector and its use in measuring the yields and kinetics of singlet oxygen, $^1\Delta g\ O_2$, can be found in the report in section C4.

The high rep-rate laser plasma X-ray source (partly funded through the Eureka programme) has continued to be developed. New additions include the automatic X-ray exposure system for biological cells (built by the CLF workshop) and a new computer with revised software to drive the X-ray damage DNA experiment (described in section C2). The improved specifications for the X-ray source are; average power of 200 mW in 2π steradians in the water window and 20 mW in 2π steradians at $h\nu \sim 1$ keV. These powers have been achieved by using a 100 ps pulse train generated from a quenched dye laser (496 nm light which is frequency doubled to 248 nm for injection into the KrF excimer laser) system developed at RAL.

The ns-laser flash photolysis equipment has continued to be well used and groups are able to use this technique to complement their ns-TR[3] investigations.

The sample preparation laboratory has had a major reorganisation and has lost its 'corridor' image. Additional equipment includes an ice-maker and a vacuum prep-line. The running of preparation facilities is now helped by a new member of staff Mrs Irene Gray.

LOAN POOL - Mike Towrie

In early 1991 the LSF loan periods were increased from three to six months to economise on manpower while maintaining the level of scientific output from the use of loan pool lasers. In the past year 18 experiments, have been carried out or are at present under way.

This year has seen the replacement of the 12 year old JK2000 laser system with a new and efficient air cooled Quanta-Ray GCR-11-3 and PDL-3 dye laser system and the Lumonics HE460 Excimer laser with a Questek 2740 excimer laser.

In February 1992 the new lasers were installed, the Quanta-Ray system in Edinburgh where it is being used for the study of state-to-state chemical dynamics and the Questek excimer in Cambridge as a photolysis source for the generation of free-radicals, which are then studied with far infra-red spectroscopy.